MONONUCLEAR NONHEME IRON(II) MODEL COMPLEXES WITH MIXED N/S DONOR SETS: PRIMARY AND SECONDARY COORDINATION SPHERE EFFECTS

By

Leland Robert Widger

A dissertation submitted to The Johns Hopkins University in conformity with the requirements for the degree of Doctor of Philosophy

Baltimore, Maryland

January 2014

Abstract

Oxygen defines the aerobic environment in which much of life on earth exists. Nature has necessarily evolved a number of metalloenzyme-catalyzed reactions that utilize, as well as protect against, molecular oxygen (O_2) and its derivatives. Dioxygen is a particularly interesting molecule; it is found in nature mostly as a triplet diradical, rendering an otherwise powerful oxidizing agent relatively inert toward organic matter since reactions are spin-forbidden under standard conditions. However when activated by an appropriate catalyst (usually a transition metal), triplet oxygen can become extremely reactive in the form of singlet oxygen or one of a series of species that are collectively called "reactive oxygen species" (ROS). These ROS (superoxide, hydrogen peroxide, hydroxyl radical, organic peroxides and peroxynitrite) are responsible for performing some of the most important and recognizable reactions in biochemistry. In the Goldberg research group, we are particularly interested in unraveling the mysteries of what some refer to as the "oxygen economy," the many reactions which ultimately make up a global cycle between H_2O and O_2. One general class of enzymes that contribute to this cycle are the nonheme iron oxygenases, enzymes that active O_2 to oxidize a substrate utilizing a non-porphyrinoid iron center. The nonheme iron oxygenases encompass a massive variety of individual centers, each with its own unique ligand set and subsequent function. We are particularly interested in understanding the role of sulfur, which is present in some of these enzymes, and my interests have focused on building synthetic model systems inspired by two specific nonheme iron metalloenzymes that contain iron-sulfur centers: cysteine dioxygenase (CDO) and superoxide reductase (SOR). By making structural models of these systems we hope to build our understanding of the specific

ligand environment around the iron centers, and how they impart the observed reactivity and selectivity at the metal center.

One interesting property of metalloenzymes is their ability to incorporate redox cofactors or non-innocent ligands that have been implicated as critical aspects of various enzymatic reactivity. Chapter 2 discusses a study where an additional reducing equivalent was incorporated into a CDO model complex, known to undergo biomimetic S-oxygenation. The known iron(II) complex $[Fe^{II}(LN_3S)(OTf)]$ was used as starting material to prepare the new biomimetic (N_4S(thiolate)) iron(II) complexes $[Fe^{II}(LN_3S)(py)](OTf)$ and $[Fe^{II}(LN_3S)(DMAP)](OTf)$, where LN_3S is a tetradentate bis(imino)pyridine (BIP) derivative with a covalently tethered phenylthiolate donor. These complexes were characterized by X-ray crystallography, UV-vis, ^{1}H NMR, and Mössbauer spectroscopy, as well as electrochemistry. A nickel(II) analogue, $[Ni^{II}(LN_3S)](BF_4)$, was also synthesized and characterized by structural and spectroscopic methods. Cyclic voltammetric studies showed all of these complexes undergo a single reduction process with $E_{1/2}$ between -0.9 to -1.2 V versus Fc^+/Fc. Treatment of $[Fe^{II}(LN_3S)(DMAP)](OTf)$ with 0.5% Na/Hg amalgam gave the mono-reduced complex $[Fe(LN_3S)(DMAP)]^0$, which was characterized by X-ray crystallography, UV-vis, EPR (g = [2.155, 2.057, 2.038]) and Mössbauer (δ = 0.33 mm s^{-1}; ΔE_Q = 2.04 mm s^{-1}) spectroscopies. Computational methods (DFT) were also employed to model these complexes. The combined experimental and computational studies show that the iron(II) starting matierials are all 5-coordinate, high-spin (S = 2) Fe^{II} complexes, whereas $[Fe(LN_3S)(DMAP)]^0$ is best described as a 5-coordinate, intermediate-spin (S = 1) Fe^{II} complex antiferromagnetically coupled to a ligand radical. This unique electronic

configuration leads to an overall doublet spin (S_{total} = ½) ground state. The new ferrous starting complexes are shown to react with O_2 to give S-oxygenated products, as previously reported. In contrast, the mono-reduced analogue appears to react with O_2 to give a mixture of S- and Fe-oxygenates. The nickel(II) complex does not react with O_2, and even when the mono-reduced nickel complex is produced, it appears to undergo only outer-sphere oxidation with O_2.

Inspired by recent success in iron(II) mediated S(thiolate)-oxidation, we sought to determine if this methodology could be expanded to sulfide donors. Sulfide oxidation is an important strategy in organic chemistry, and more recently has attracted attention for its use in desulfurization of fossil fuels. In chapter 3, the unsymmetrical iron(II) bis(imino)pyridine complexes $[Fe^{II}(LN_3SMe)(H_2O)_3](OTf)_2$, and $[Fe^{II}(LN_3SMe)Cl_2]$ were synthesized and their reactivity with O_2 was examined. These complexes were characterized by single crystal X-ray crystallography, LDI-MS, ^{1}H-NMR and elemental analysis. The LN_3SMe ligand was designed to incorporate a single sulfide donor and relies on the bis(imino)pyridine scaffold. This scaffold was selected for its ease of synthesis and its well-precedented ability to stabilize Fe(II) ions. The reported complexes ware prepared via a metal-assisted template reaction from the unsymmetrical pyridyl ketone precursor 2-(O=CMe)-6-(2,6-(^{i}Pr$_2$-C$_6$H$_3$N=CMe)-C$_5$H$_3$N. Reaction of $[Fe^{II}(LN_3SMe)(H_2O)_3](OTf)_2$ with O_2 was shown to afford the S-oxygenated sulfoxide complex $[Fe(LN_3S(O)Me)(OTf)]^{2+}$, whereas $[Fe^{II}(LN_3SMe)Cl_2]$, under the same reaction conditions, afforded the corresponding sulfone complex $[Fe(LN_3S(O_2)Me)Cl]^{2+}$.

High-valent iron(IV)-oxo species are implicated as key intermediates in a number of enzymatic and synthetic systems. In chapter 4, the synthesis of the new ligand

N3Py^{amide}SR and its Fe^{II} complex [Fe^{II}(N3Py^{amide}SR)](BF$_4$)$_2$ are described. Reaction of [Fe^{II}(N3Py^{amide}SR)](BF$_4$)$_2$ with PhIO at –40 °C gives metastable [Fe^{IV}(O)(N3Py^{amide}SR)]$^{2+}$, containing a sulfide ligand and a single amide H-bond donor in proximity to the terminal oxo group. Direct evidence for H-bonding is seen in a structural analog, [Fe^{II}(Cl)(N3Py^{amide}SR)](BF$_4$)$_2$. The novel [Fe^{IV}(O)(N3Py^{amide}SR)]$^{2+}$ complex exhibits rapid O-atom transfer (OAT) toward external sulfide substrates, but no intramolecular OAT. However direct S-oxygenation does occur in the reaction of [Fe^{II}(N3Py^{amide}SR)](BF$_4$)$_2$ with mCPBA, yielding sulfoxide-ligated [Fe^{II} (N3Py^{amide}S(O)R)](BF$_4$)$_2$. Catalytic OAT with [Fe^{II}(N3Py^{amide}SR)](BF$_4$)$_2$ was also observed.

Iron(III)-(hydro)peroxo and (alkyl)-peroxo species are believed to be important species in a variety of reactions resulting from enzymatic O_2 activation. In chapter 5, two sulfide-incorporated N4Py derivatives, [Fe^{II}(N3PySR)(CH$_3$CN)](BF$_4$)$_2$ and [Fe^{II}(N3Py^{amide}SR)](BF$_4$)$_2$, were synthesized and characterized. These starting complexes, afforded rare examples of metastable Fe(III)-OOH and Fe(III)-OOtBu complexes containing equatorial sulfide ligands and a single H-bond donor in the second coordination sphere. These peroxo complexes were characterized by a range of spectroscopic methods and density functional theory (DFT). The influence of a sulfide ligand and of one H-bond donor on the stability and spectroscopic properties of these complexes was investigated.

Committee Members:

Professor David P. Goldberg

Professor Kenneth D. Karlin

Professor Marc M. Greenberg

Acknowledgements

First and foremost I would like to thank my advisor, Professor David Goldberg, for his mentorship through the past five years. Your passion for chemistry, attention to detail, creativity, insight, and commitment to teaching your students is always inspiring. I want to personally thank you for always pushing me to do my best work, your invaluable guidance, mentorship, and patience. I could not ask for a better role model to look up to, as I become a member of the scientific community. I also want to thank my thesis committee, Professor Kenneth Karlin and Professor Marc Greenberg for their advice, support, and guidance over the years.

Science is never a solo effort, and I could not have accomplished any of the work in this dissertation without so many of the wonderful people in this department, from so many different labs, as well as all of our outside collaborators. All of the Goldberg lab members, past and present, it has been a joy working with you. Thank you for always sharing ideas, helping out, proof reading, and being there for a good laugh. I would also like to thank my first-year mentor, Professor Thomas Lectka, along with Dr. Michael Scerba and Dr. Dan Pall for my training as a synthetic chemist.

Last but not least, I have to thank my family and friends. I never would have made it to this point in my life without the loving support and constant sacrifice of my wonderful parents, Gary and Sandy Widger, and my sister Jacky. The sacrifices you have made on our behalf are humbling. Dad, you are the greatest man I know, and if I can manage to become half the man you are it would be an accomplishment.

Table of Contents

Index of Figures

Chapter 1. Background and Significance

Index of Schemes

Index of Tables

Chapter 4. Dramatically Accelerated Selective Oxygen-Atom-Transfer by a Nonheme Iron(IV)-oxo complex: Tuning of the Primary and Secondary Coordination Spheres

Chapter 5. Synthesis and Characterization of Sulfide-ligated hydroperoxo and alkylperoxo iron(III) complexes with a Pendant Amide H-Bond Donor in the Second Coordination Sphere

Chapter 1. Background and Significance

1. 1. Introduction

The purpose of this chapter is to outline, in a broader sense, the underlying purpose, goals, and inspiration that govern the work described in this dissertation. Bioinorganic chemistry, or metallobiochemistry, is a large interdisciplinary field of study that encompasses research in molecular biology and enzymology, spectroscopy, crystallography, and synthetic chemistry in order to better understand the roles and functions of transition metal ions in biological systems. Transition metals play a variety of important roles in biology, and are absolutely essential components for life to exist. These biologically relevant metal ions include copper (Cu), zinc (Zn), iron (Fe), manganese (Mn), nickel (Ni), cobalt (Co), vanadium (V), molybdenum (Mo), and cadmium (Cd). Metal ions *in vivo* are often incorporated into metalloproteins (metal-containing proteins), and are responsible for structural support, protein folding, small-molecule transport/storage, electron transport, signal transduction, and an immense list of essential reactions. Reactions are carried out by metalloenzymes, which are metal-cofactor containing proteins capable of catalytic activity, and include electron transfer, hydrolysis, small-molecule (N_2, O_2, CO_2, H_2S) activation, C-H activation, detoxification reactions, and oxidation/reduction reactions including H_2O oxidation and O_2 reduction.[1]

Due to the essential nature of many reactions performed by metalloenzymes, improper, or loss of function has been implicated in many disease states. One purpose of studying these systems is to better understand the mechanism of action, how the enzyme performs the specific reaction. Among the questions to be addressed are the identities of the substrate(s) and metal ion, the structure of the active site, oxidation state of the metal

at each step of the reaction, and how the coordination environment around the metal center governs the specificity and reactivity observed. By understanding these fundamental aspects of metalloenzyme function, we hope to elucidate the pathways by which these processes are deactivated, corrupted, or otherwise contribute to the development of disease processes.

The large size, complex structure, and solubility constraints of native enzymes make them difficult to isolate, purify, and study. Model complexes are useful for addressing fundamental questions regarding the reactivity and spectroscopic properties of metal ions in well-defined coordination environments. Model systems tend to be synthetic small-molecule systems that are designed to replicate specific components of the first and/or secondary coordination sphere of a known system. Model complexes are generally easier to manipulate since they can be soluble in organic solvents, and the individual "ligands" can be covalently tethered or easy to control with stoichiometry, as opposed to the loose secondary interactions responsible for the folding of proteins. Information gleaned from model chemistry can be used as a comparison to the enzymatic system, and these mimics allow researchers to strip away additional factors that could encumber the study of these systems in proteins and examine the fundamental properties of these coordination units. This is meant to guide our asking of the right questions, gain understanding of the spectroscopy/reactivity of reactive intermediates, and to build a system we can control and manipulate to perform other desirable functions.

Non-heme iron metalloenzymes have garnered significant effort and study by bioinorganic chemists in recent years.[2-7] In particular, research in our group has focused on model systems inspired by the active sites in non-heme iron enzymes that contain

sulfur donors. This is however still a broad list, including everything from the well studied iron-sulfur clusters found in ferrodoxins,[8] hydrogenases[9] and nitrogenases;[10] to mononuclear centers with cysteine-based thiolate donors, such as those found in peptide deformylases,[11] nitrile hydratases,[12] isopenicillin N-synthases,[13] superoxide reductases[14] and cysteine dioxygenase.[15] These mononuclear sites all contain mixed nitrogen/sulfur (N/S) donor sets (**Figure 1. 1**) yet exhibit very different reactivity. Our research interests center around how this N/S motif controls reactivity of the iron centers with oxygen and its biologically-relevant derivatives.

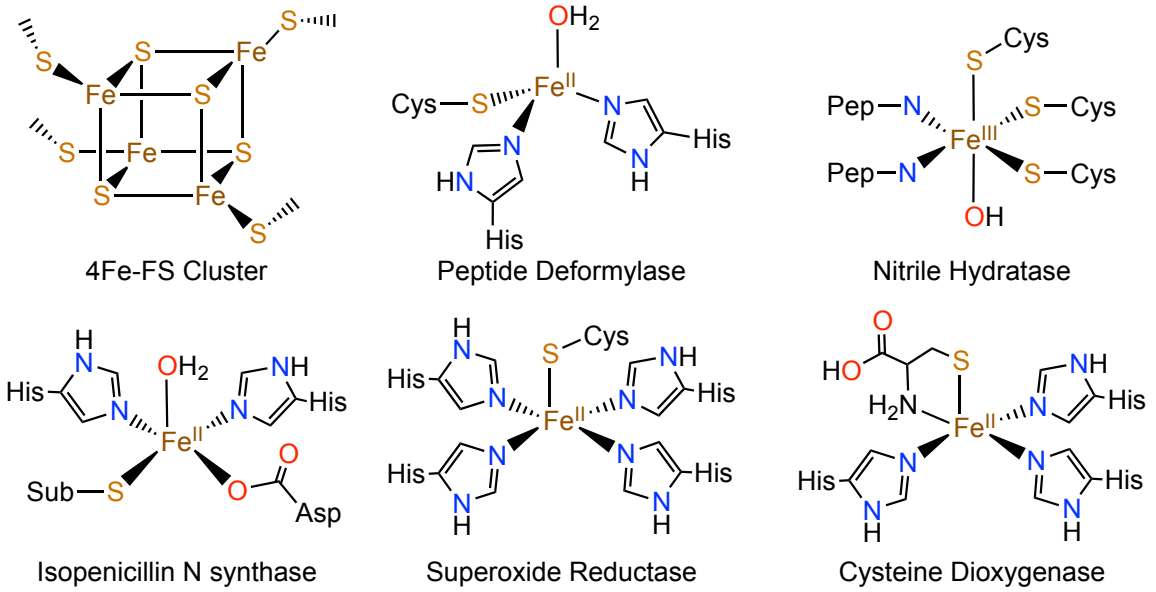

Figure 1. 1. Active site structures of selected non-heme iron metalloenzymes with mixed N/S donor sets.

Oxygen defines the aerobic environment in which much of life on earth exists. Therefore, nature has necessarily evolved a number of enzyme-catalyzed reactions that utilize, as well as protect against, molecular oxygen (O_2) and its derivatives. Dioxygen is a particularly interesting molecule; it is found in nature mostly as a triplet diradical, rendering an otherwise powerful oxidizing agent relatively inert toward organic matter

since reactions are spin-forbidden under standard conditions.[16] However, when activated by an appropriate catalyst (usually a transition metal), triplet oxygen can become extremely reactive in the form of singlet oxygen or one of a series of derivatives that are collectively called "reactive oxygen species" (ROS). These ROS (superoxide, hydrogen peroxide, hydroxyl radical, organic peroxides and peroxynitrite)[17] are responsible for performing some of the most important and recognizable reactions in biochemistry. My research in the Goldberg research group has focused on understanding the role of sulfur donors in the primary coordination sphere, and hydrogen-bond donors in the second coordination sphere, of nonheme iron model complexes. This work applies more broadly to understanding how nonheme iron oxygenases acitivate dioxygen, stabilize the resulting adducts, and direct oxidizing equivalents toward substrates. We hope that information gleaned from these studies will aid in unraveling the mysteries of what some refer to as the "oxygen economy," the many reactions which ultimately make up a global cycle between H_2O and O_2 (**Figure 1. 2**).

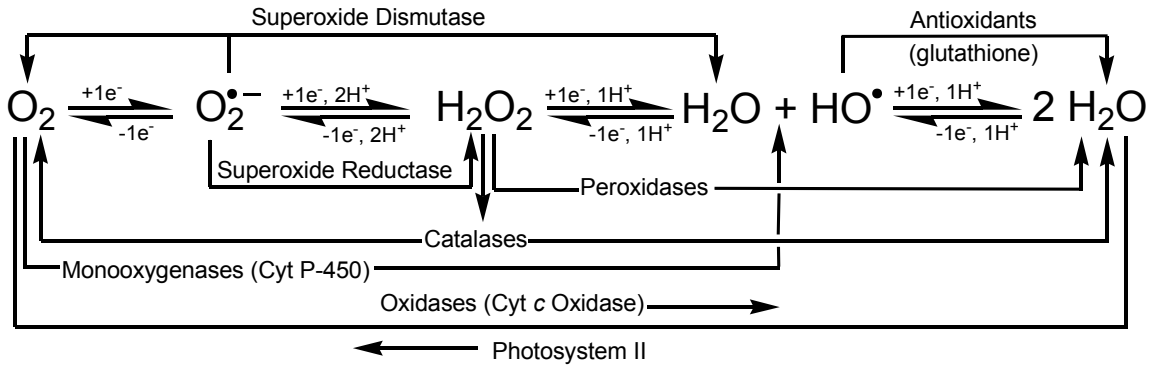

Figure 1. 2. "Global oxygen cycle" and representative enzymes that catalyze the reactions between O_2 and H_2O.

During the course of these reactions, the one or two electron reduction of O_2 can lead to undesired side reactions that cause the release of a ROS, which is toxic and

referred to as "oxidative stress." [18] These ROS, as well as their "downstream" products are capable of widespread damage to DNA, protein membranes and other cellular components that have been implicated in numerous disease states. Nature has developed many protective mechanisms to combat these ROS, yet they seem imperfect since ROS appear to play a role in neurodegenerative diseases,[19-21] diabetes[22] and some cancers.[23,24] Understanding the metalloenzymes which are responsible for the advantageous use, as well as protection against, oxygen species is critical to understanding (and hopefully treating) these diseases.

My interests have focused on building synthetic model systems inspired by the mononuclear non-heme active sites of two specific iron-sulfur containing metalloenzymes: cysteine dioxygenase (CDO) and superoxide reductase (SOR), both of which contain a four-nitrogen, one thiolate donor set, but catalyze two very different reactions. By making functional models of these systems we plan to increase our understanding of the specific ligand environment around the iron centers, and how they control the observed reactivity and selectivity at the metal center for the generation, stability, and reactivity of key Fe-O_x adducts (**Figure 1. 3**).

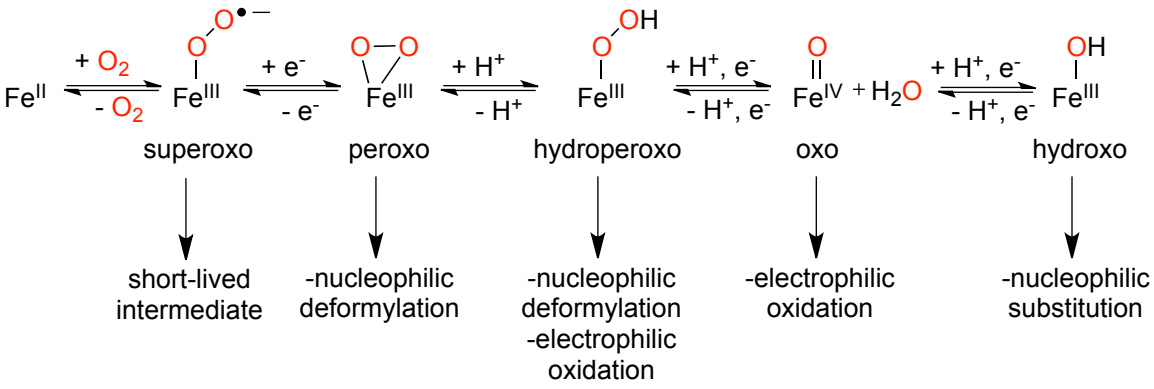

Figure 1. 3. General scheme for activation of O_2 by iron(II)-containing non-heme metalloenzymes, and the possible reactions with substrate for intermediate species.

1. 2. An example of mononuclear non-heme iron dioxygenases with mixed N/S ligation: Cysteine Dioxygenase (CDO)

Background

Careful regulation of intra and extracellular sulfur concentration is essential for proper cellular function.[25] Loss of these regulation pathways have been implicated in many disease states including cystinosis[26,27] and Hallervorden-Spatz syndrome,[28] as well as the more familiar Alzheimer's and Parkinson's diseases.[29,30] Cysteine dioxygenase catalyzes the first major step in cysteine catabolism in mammals, the oxidation of cysteine to cysteine sulfinic acid (CSA) by a molecule of dioxygen (**Figure 1. 4**).[31]

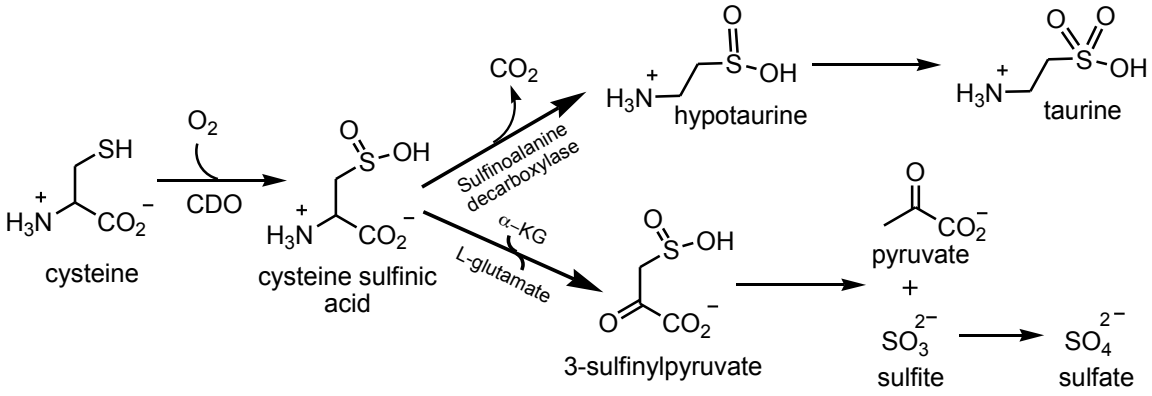

Figure 1. 4. Cysteine sulfinic acid (CSA) as a branch point for cysteine catabolism.

Structure of CDO

The structure of cysteine dioxygenase (**Figure 1. 5**) has been extensively studied since it was first isolated from rat liver in the 1960s[32-35] and was characterized for the first time by X-ray crystallography in 2006 (mouse, **Figure 1. 5**a).[36] Although CDO has significant sequence homology with other cuprin proteins,[37] it is a relatively recent addition to a small group of nonheme iron oxygenases that vary from the canonical 2-His-1-carboxylate "facial triad" binding motif, with a 3-His ligand environment.[38]

Several crystal structures of CDO have been solved from various sources: mouse, rat,[39] human[15] and *Ralstonia eutropha*.[40] The first (mouse) structure was solved by Phillips and coworkers (**Figure 1. 5**a), and contained a catalytically inactive Ni^{II}. The structure confirmed the second known example of the 3-His binding mode, although the coordination sphere contained three presumed aqua ligands. It also revealed a posttranslational modification of Cys93 and Tyr157, yielding a cysteinyltyrosine that is only conserved in eukaryotic CDOs. The role of this possible cofactor is still unclear,[41] but has otherwise only been observed in galactose oxidase[42] where it serves as a redox factor.[43] Collaboration between Simmons, Karplus and Stipanuk later produced the structure of the resting-state Fe^{II} enzyme with 1.5 Å resolution (**Figure 1. 5**b).[39] The rat CDO also had the cysteinyltyrosine crosslink and the 3-His facial triad, although this time with a single aqua ligand forming a tetrahedral iron site. A lower resolution (2.7 Å) structure for the cysteine bound, active form of human CDO (**Figure 1. 5**c), shows the cysteine displacing the solvent ligand and binding through the amine as well as through the thiolato-sulfur in a distorted tetragonal bipyramidal geometry.[15] It should be noted that the prokaryotic CDO structure from *Ralstonia eutropha*, was deposited in the PDB database and shows the resting state in a pseudo-octahedral geometry with two aqua ligands and one sulfate ion hydrogen bonded to Tyr157 (**Figure 1. 5**d). The cysteinyltyrosine crosslink is not present due to the replacement of Cys93 with a glycine, found in all known prokaryotic CDOs.[31]

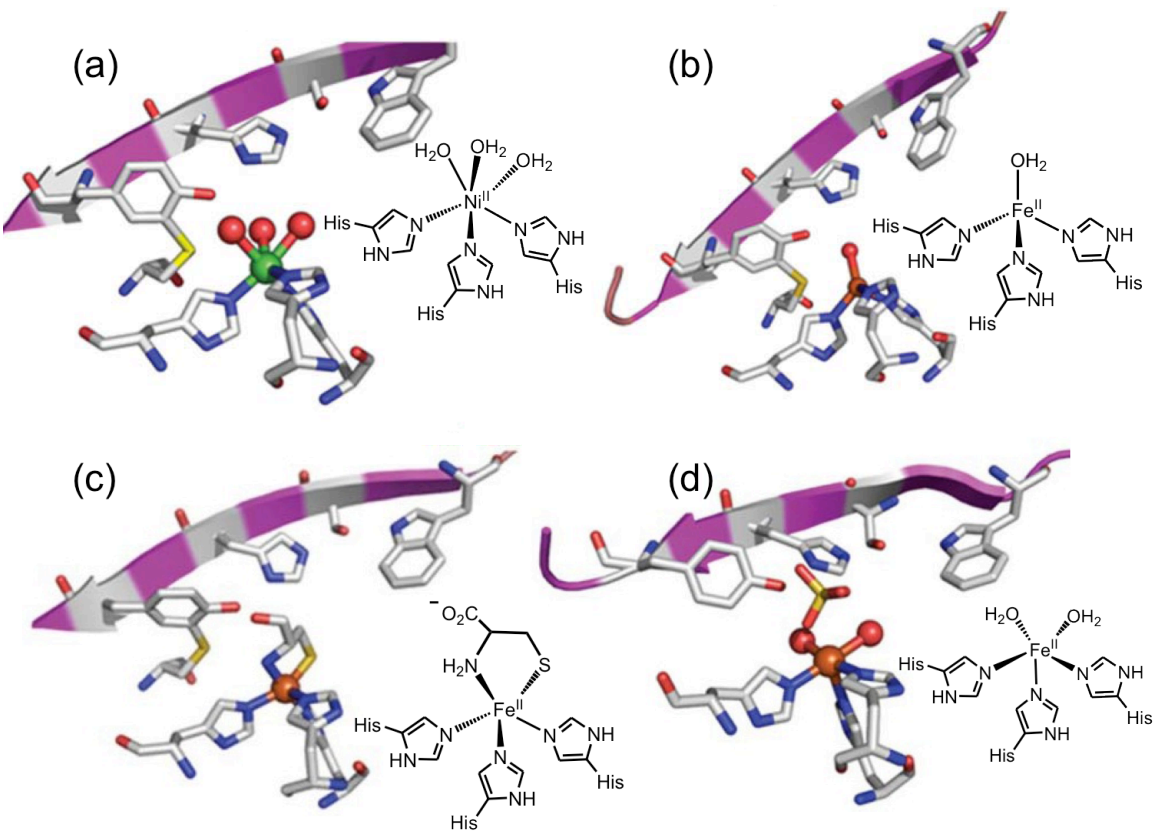

Figure 1. 5. X-ray structures of CDO. (a) $His_3Ni(OH_2)_3$ center and neighboring cysteinyltyrosine from mouse CDO. (b) $His_3Fe\text{-}OH_2$ center with neighboring cysteinyltyrosine from rat CDO. (c) His_3FeCys center and neighboring cysteinyltyrosine from human CDO. (d) $His_3Fe(OH_2)_2$ center with neighboring sulfate and tyrosine from Ralstonia eutropha CDO.

Mechanism of CDO

Mechanistic information for many non-heme iron dioxygenases is available,[4,7,16,44,45] but less is known about the mechanism of CDO. In general, non-heme dioxygenases operate under a common theme where O_2 activation occurs at a 5-coordinate ferrous center only after the substrate and cofactor (when required) are present. These dioxygenases can be divided into two groups based on mechanism, where

in the first group the substrate is activated for attack by O_2 (intradiol dioxygenases), and in the second O_2 is activated for attack by the substrate. These two main mechanistic groups can then be further divided depending on whether or not they require a redox cofactor, the latter case being made possible by a redox-active substrate.[31] Cysteine dioxygenase is of particular interest because it does not follow these general guidelines.[31] It is clear that CDO does not require an additional redox factor and the redox active cystenyltyrosine, which is conserved in eukaryotic CDOs, is absent in prokaryotes.[31] Although it can be envisioned that the conserved tyrosine (Tyr157) could act as an electron source with the formation of a tyrosyl radical, cysteine is also redox active and could be providing an electron to facilitate the formation of an iron(III)-peroxide species.

Experiments have been conducted, using site-directed mutagenesis, in an attempt to assess the impact of secondary coordination sphere effects on the mechanism of CDO, as well as other intriguing residues near the active site.[15] In the first set of experiments, Cys93 (the residue involved in cystenyltyrosine formation) was replaced with either serine or alanine. In addition Arg60, thought to be involved in substrate stabilization through hydrogen-bonding with the carboxylate, was replaced with glutamine or alanine. Both mutations led to a notable decrease in enzyme activity, to around 30 and 50% of wild type respectively, but most intriguing was the large decrease observed when Tyr157 was replaced with phenylalanine and enzyme fell to only ~5% of the wild type. These results suggest that the arginine may play a role in substrate stabilization within the active site hydrogen-bonding network. They also indicate that cysteine, which is responsible for cystenyltyrosine formation; aids in catalytic virility and that Tyr157 may play an even greater role in the catalytic cycle. Some of these results were confirmed by recent studies

where mutation of Cys93 to serine and Tyr157 to phenylalanine reduced enzyme activity to ~57% and 8%, respectively.[31] Notably, the K_m found for the Cys93 mutant was similar (1.6 versus 1.8 mM for wild-type) while the Tyr157 mutant was found to be only 0.17 mM, a full order of magnitude lower, indicating a critical role for Tyr157 in the catalytic reaction. The necessity of these residues in the secondary coordination sphere for enzymatic activity are indicative of important secondary interactions, such as H-bonding and/or redox activity, that are worthy of exploration through model chemistry.

One proposed mechanism for CDO[36] (**Figure 1. 6**) starts with displacement of solvent molecule(s) to enable bidentate cysteine binding, with the carboxylate interacting with Arg60. The deprotonation of the cysteine ammonium ion may be facilitated by some combination of His155, cysteinyltyrosine and/or water/hydroxide to facilitate substrate binding. Reduction of oxygen to superoxide is facilitated via oxidation of Fe^{II} to Fe^{III}. The Fe^{III}-superoxide is immediately reduced to Fe^{II}-superoxide by the thiolate which combine to form a cyclic peroxo complex. Homolytic O-O bond cleavage forms a sulfoxy cation and an iron-oxyl species, which react to form the sulfinate before ligand substitution to release CSA and regenerate the resting enzyme.

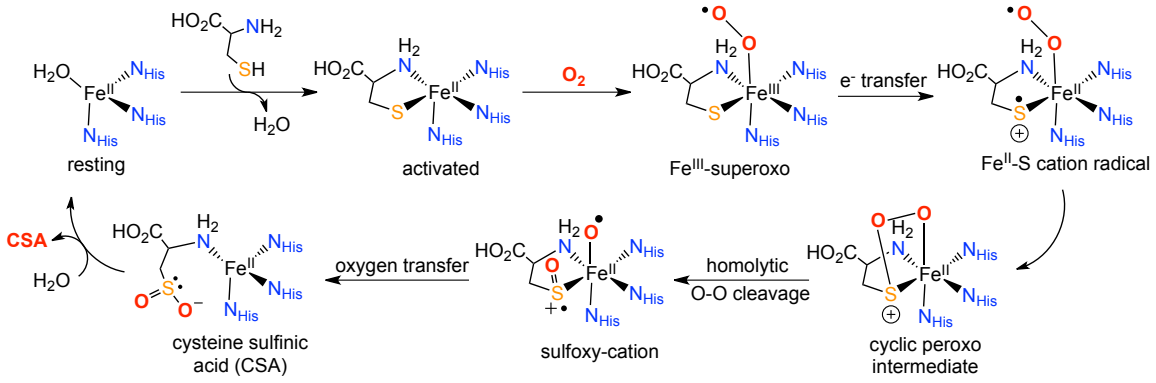

Figure 1. 6. CDO mechanism proposed by McCoy, et. al.[36]

A second possible mechanism was proposed[15] where cysteine binding (as S-H) is in a geometry that allows the carboxyl group to participate in hydrogen bonding with the highly conserved Tyr157, Tyr58, and His155 residues. Dioxygen binds end-on to the ferrous center forming a Fe^{III}-superoxo intermediate, stabilized by hydrogen-bonding to the cysteinyltyrosine. Homolytic O-O bond cleavage then forms a single sulfur-oxygen bond accompanied by hydrogen atom abstraction from Tyr157, forming a tyrosyl radical and an oxyferryl species. The tyrosyl radical then abstracts the thiol S-H hydrogen atom allowing the oxyferryl to attack the cysteine sulfur before reductive elimination forms the S=O bond and completes the cycle (**Figure 1. 7**).

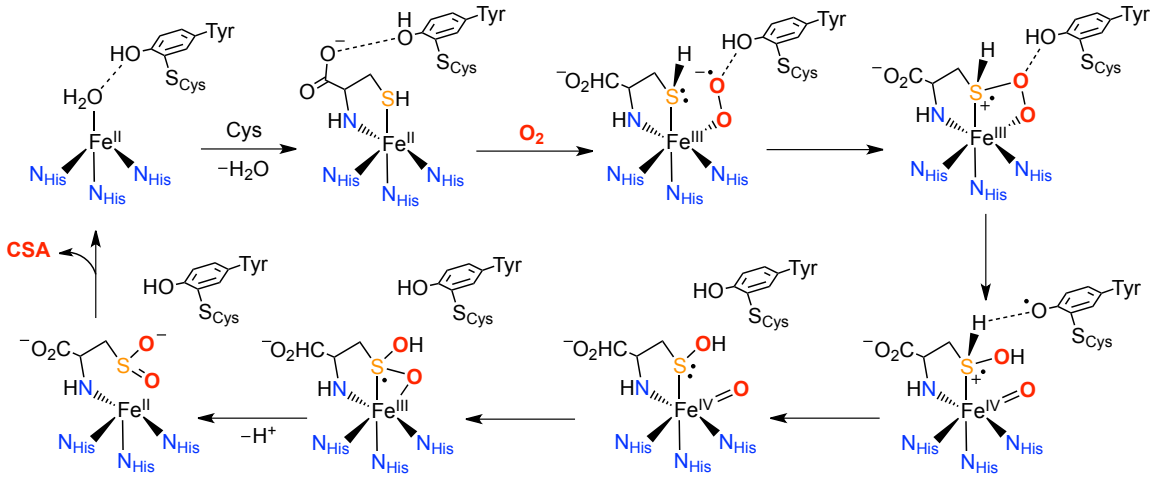

Figure 1. 7. CDO mechanism proposed by Ye, et. al.[15]

Further complication comes from XAS data which suggests the possibility of a very different situation for the binding, or lack there-of, of the cysteine substrate.[31] Data for the resting ferrous enzyme was in agreement with the Ni^{II} structure, consistent with three His residues and three aqua ligands. Upon anaerobic addition of saturating amounts of cysteine, structural changes were observed but were only consistent with oxygen and nitrogen ligands. No evidence of a sulfur ligand was seen. Even though it is possible for

the motion of weakly coordinating absorbing and scattering atoms to lose signal, sulfur is fully capable of reacting with activated oxygen species under standard metal free conditions and a sulfur-free coordination sphere should not be dismissed.

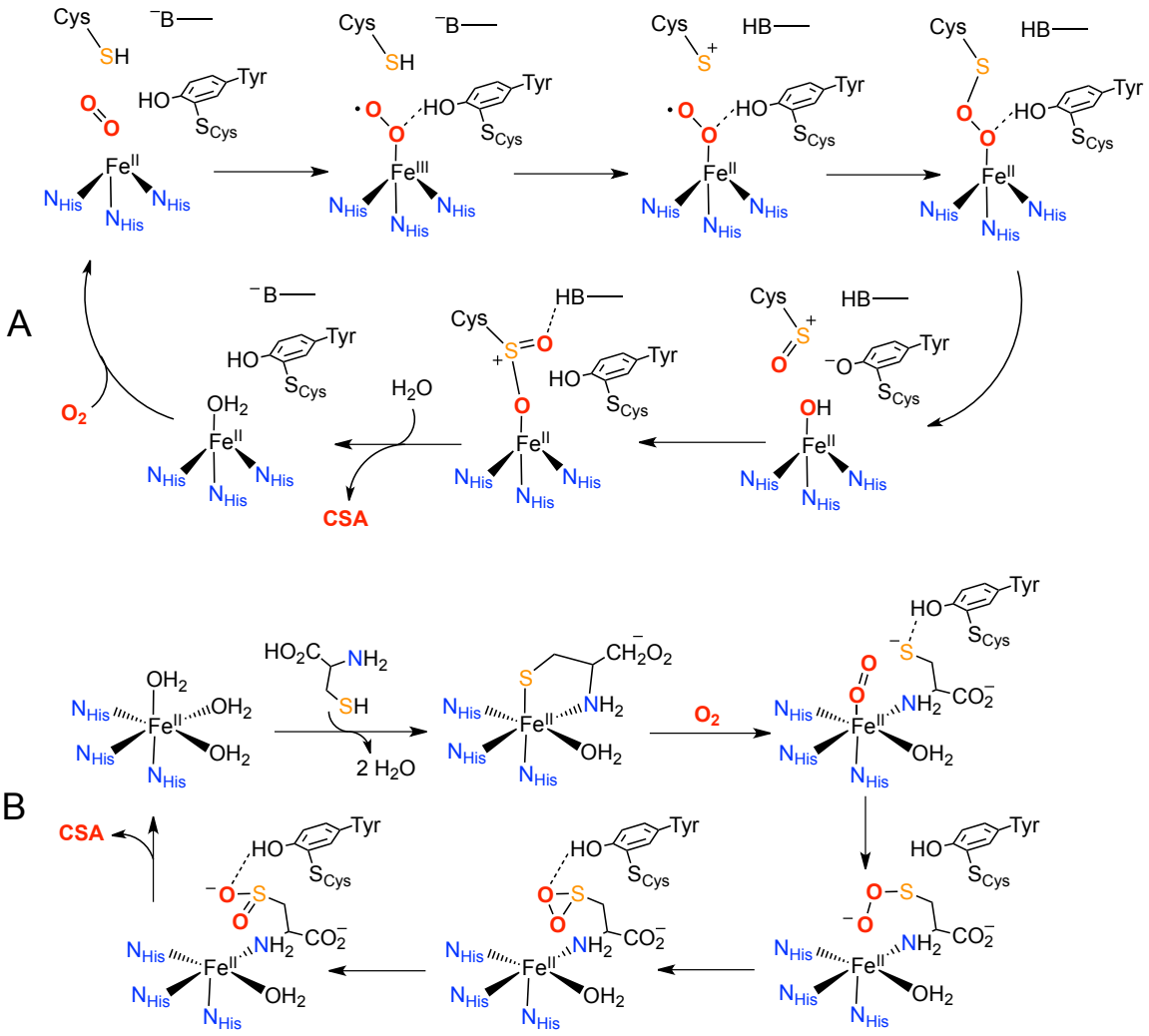

Figure 1. 8. Proposed mechanisms for CDO that do not invoke direct Fe-S interaction. Adapted from Ref 39 (**A**) and Ref 31 (**B**).

This possibility has led to two distinct mechanistic proposals, which do not invoke a direct Fe-S interaction (**Figure 1. 8**). The first involves the activation of oxygen by Fe^{II} to form an Fe^{III}-superoxo complex which oxidizes the nearby cysteine thiolate. Radical coupling between the resulting thiyl radical and superoxo complex is followed by

rearrangement to a sulfenyl cation and Fe^{II}-OH complex. Nucleophilic attack on the sulfenyl cation and release of CSA completes the cycle.[39] The other mechanistic possibility[31] would have the substrate bind via both amine and thiolate groups in a six-coordinate complex with one aqua ligand. In this scenario, the thiolate would be weakly bound so it could be displaced to allow binding of oxygen. The fact that this thiolate is weakly coordinating would be consistent with both its presence in the X-ray structure and its absence in the EXAFS experiments. This displaced thiolate, stabilized by Tyr157, could nucleophilically attack the bound O_2 ligand and oxidize to CSA.

Despite the XAS data and mechanistic proposals that invoke a non-coordinating thiolate, Jameson and co-workers have recently conducted studies on the properties of iron(II)-CDO binding to cysteine and homocysteine.[46] These studies showed that iron(II)-CDO bound cysteine with a $K_d \sim 10$ mM, and also bound homocysteine. The resulting substrate-bound complexes were characterized by Mössbauer spectroscopy, which was consistent with bidentate cysteine and homocysteine binding. Further single-turnover experiments on formation of the catalytically competent Fe(II):CDO:cysteine ES complex revealed a single $K_d \sim 65$ μM and $k_1 = 7.3 \times 10^4$ M^{-1} s^{-1}.[47] In addition, careful analysis of the Mössbauer data revealed that formation of the ES complex was actually two distinct species. Computational and mutagenesis studies revealed that cystienyltyrosine crosslink formation is not necessary for the formation of these two distinct species, but that protonation of Tyr157 is. Although these two separate species were not definitively identified, addition of dioxygen to the ES complex rapidly yields the resting-state Fe(II)-CDO enzyme with stoichiometric CSA , and does not accumulate any sufficient intermediate for detection. Although further work is needed to identify the

nature of these species, reports from Jameson and coworkers indicate important roles for both the Cys thiolate donor and secondary residues, including the cysteinyl-tyrosine crosslink.

Recent work from de Visser and coworkers sought to clarify some of the debate surrounding the CDO mechanism by preforming quantum mechanics/molecular mechanics (QM/MM) using an enzyme monomer and a large QM active region (**Figure 1. 9**).[48] In this report, de Visser found a stepwise mechanism in which the bound Cys(thiolato) sulfur is attacked by the distal oxygen atom of the iron-superoxo complex. The resulting cyclic intermediate then undergoes O-O bond cleavage to form an S-bound sulfoxide and iron(IV)-oxo complex. Sulfoxide rotation to the O-bound form allows for transfer of the second oxygen atom to form the iron(II)-slufenate, and release of the product (CSA) regenerates the resting iron(II) enzyme. The only mechanistically relevant structural evidence was obtained from crystals of rat CDO soaked in cysteine, which yield an unusual persufenate intermediate.[49] It is still unclear whether this represents a viable intermediate on the reaction pathway, but this computational evidence from deVisser suggests this lies on a high-energy pathway and is likely not catalytically competent.[48]

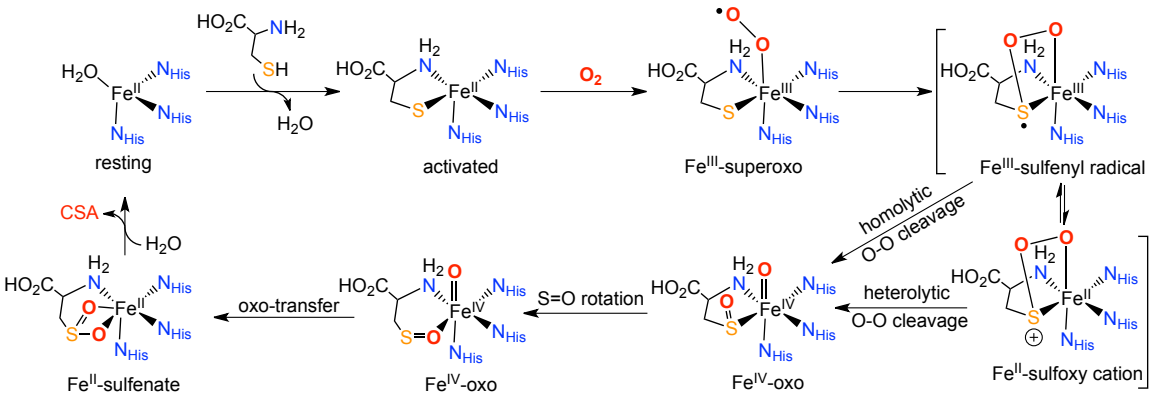

Figure 1. 9. Proposed mechanism of CDO.

Model Chemistry

There is extensive literature on synthetic S-oxygenation of metal-thiolate and thioether complexes utilizing Ni^{II}, Pt^{II}, Pd^{II}, $Cu^{I/II}$, Fe^{III}, Ru^{II}, and Re^{V}, but only a few which utilize O_2 as the oxidant.[50-51] Following an initial report by Maroney,[52] Grapperhaus and Darensbourg have extensively studied nickel(II) mediated sulfur-oxygenation by a variety of oxidants, showing reactivity in some cases.[53-61] Copper(I) and (II) oxygenation of sulfur ligands has been reported by Nicholas,[62] Réglier,[63] Karlin[64] and others. Prior to recent reports from our lab, the reaction of O_2 with Fe^{II}-SR complexes has led only to the formation of Fe^{III}-O-Fe^{III} complexes, in lieu of S-oxygenates (**Figure 1. 10**).[65] In this work, Darensbourg observed that the site of O-capture (Fe vs S) in the reaction of Fe^{II}-SR + O_2 resulted in the exclusive selection of Fe over S. Other recent reports by Grapperhaus and Kodanko, among others, have also shown interesting Fe-S reactivity. As a model for NHase, Grapperhaus and coworkers prepared pentadentate iron(III) complexes with two amines, two thiolates, and one thioether group as donors to give $(N_2S_3)Fe^{III}(X)$ ($X = Cl^-$, CN^-).[66] These complexes were shown to react differently with O_2 (**Figure 1. 11**), where the l.s. cyano complex $(N_2S_3)Fe^{III}(CN)$ gave S-oxygenates, and the h.s. chloride complex $(N_2S_3)Fe^{III}(Cl)$ gave only iron-oxo clusters and disulfide products with no eveidence of S-oxygenation. Kodanko and coworkers studied the oxidation of glutathione (GSH) by $[Fe^{IV}(O)(N4Py)]^{2+}$ (**Figure 1. 11**),[67] and were able to characterize a l.s. ferric intermediate assigned as $[Fe^{III}(SG)(N4Py)]^{2+}$ that decayed to the final products $[Fe^{II}(H_2O)(N4Py)]^{2+}$ and the disulfide GSSG. Our recent findings, described below, establish that an Fe^{II}-SR complex, in the appropriate ligand environment, can selectively react with O_2 to yield S-oxygenates.[68]

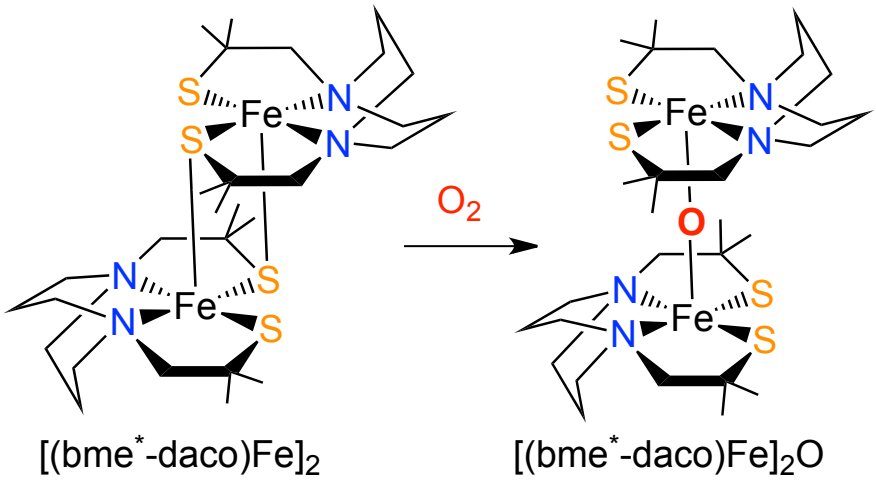

Figure 1. 10. Reaction of $[(bme^{*}\text{-daco})Fe]_2$ with dioxygen gives exclusively Fe^{III}-O-Fe^{III}. Adapted from Ref 65.

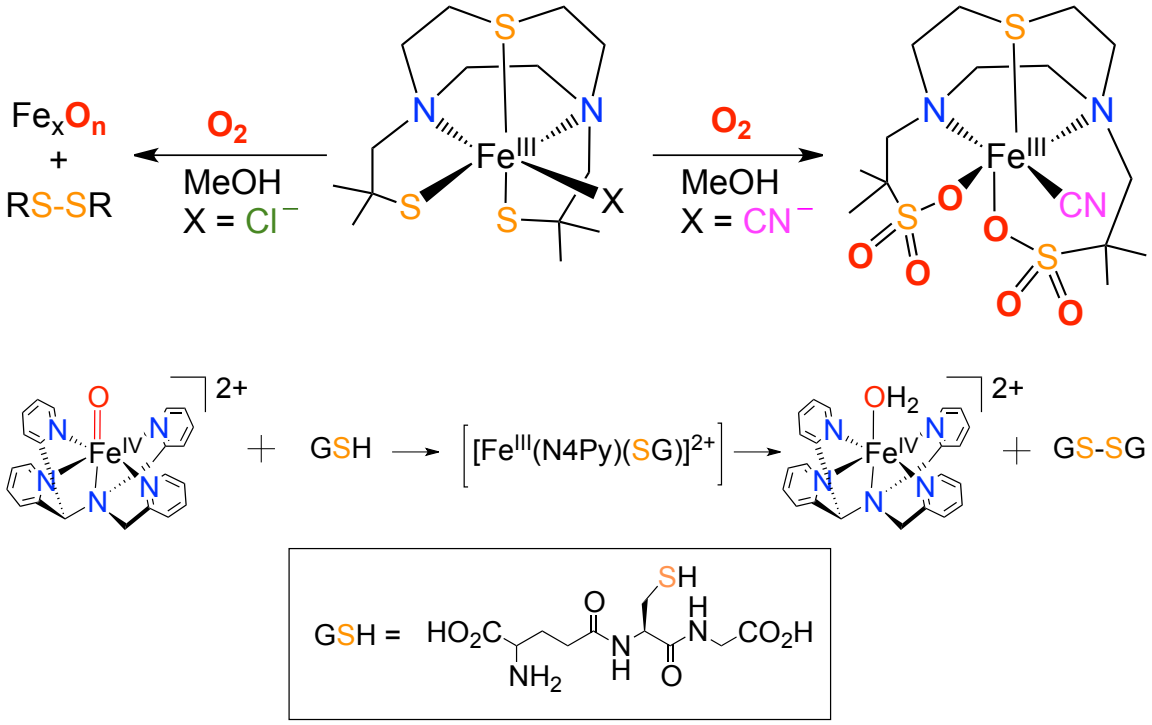

Figure 1. 11. Reactivity of $[(N_2S_3)Fe^{III}(X)]$ (X = Cl^-, CN^-) complexes with O_2 (top), Oxidation of glutathione (GSH) by $[Fe^{IV}(O)(N4Py)]^{2+}$ (bottom).

In recent reports from Nam and coworkers, chromium was used in lieu of iron to give a functional chemical model of CDO (**Figure 1. 12**, bottom).[69,70] The starting

chromium(II) complex $[Cr^{II}(14\text{-TMC})(Cl)]^+$ reacted with O_2 to form a meta-stable intermediate that was identified as the biomimetic Cr(III)-superoxo complex $[Cr^{III}(O_2)(14\text{-TMC})(Cl)]^+$ by UV-vis, ESI-MS, resonance Raman, and X-ray crystallography. Although there is no pendant sulfur donor, as in Cys-bound CDO, for biologically-relevant oxygen-atom transfer, the chromium(III)-superoxo complex does preform OAT to thioanisole and triphenylphosphine. Interestingly, the active oxidant in this reaction is proposed to be the Cr(III)-superoxo and the product is the Cr(IV)-oxo. This is in contrast to most mechanistic proposals for CDO, where the Fe(III)-superoxo would be reduced to the Fe(III)-(hydro)peroxo and undergo O-O bond cleavage to afford the Fe(IV)-oxo complex as the active oxidant.

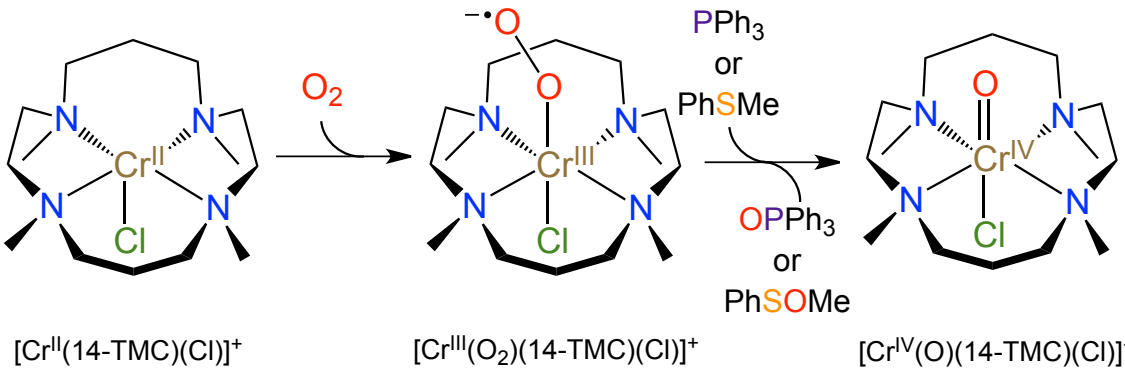

Figure 1. 12. Reaction of $[Cr^{II}(14\text{-TMC})(Cl)]^+$ to form $[Cr^{III}(O_2)(14\text{-TMC})(Cl)]^+$ and subsiquent OAT to PPh_3 and PhSMe. Adapted from Refs 67,68.

In the first report of iron(II) mediated S-oxyenation by O_2, we utilized an unsymmetrical bis(imino)pyridine (BIP) system with a pendant S(thiolato) donor incorporated into the coordination sphere (**Figure 1. 13**).[68] Reaction of the $[Fe^{II}(LN_3S)(OTf)]$ complex with excess O_2 at ambient temperature and pressure afforded the S-oxygenated sulfonate (RSO_3^-) product, $[Fe^{II}(LN_3SO_3)]^+$, which was identified by a combination of LDI-MS and imine hydrolysis followed by recovery of the organic ligand

fragment. In a subsiquent study (**Figure 1. 13**), the symmetrical ^{iPr}BIP ligand was utilized with an exogenous phenylthiolate (PhS^-) donor.[71] In this case, the couterion (OTf^- vs Cl^-) was shown to influence the geometry of PhS^- binding, where the thiolate donor was positioned *cis* or *trans* to the putative O_2 binding site, respectively. When the thiolate donor was positioned cis to the binding site, S-oxygenation was observed leading again to the sulfonate product, while the trans complex did not exhibit S-oxidized products but was proposed instead to lead to the formation of an iron(IV)-oxo intermediate.

Although encouraged by these results, we desired to obtain complexes that would give the biologically-relevant sulfinate (SO_2^-) product, in stead of over-oxidizing to the sulfonate. The first report of iron(II)-mediated S-oxygenation to give the sulfinate product came from Limberg and coworkers, where a trispyrazolylborato iron(II) complex was shown to bind cysteine ethyl ether to generate an N_4S complex that reacted with O_2 to give the biomimetic sulfinate product (**Figure 1. 13**).[72] Shortly thereafter a second report, from our lab, utilized the pentadentate N3PyS ligand to make the thiolate-ligated $[Fe^{II}(N3PyS)(CH_3CN)](BF_4)_2$. This new N_4S complex also afforded the doubly oxygenated sulfinate product when allowed to react with O_2 (**Figure 1. 13**). Stabilization of the product by binding of a thiocyanate anion allowed for the first structurally characterized iron(II)-sulfenate, $[Fe^{II}(N3PySO_2)(SCN)]$.[73]

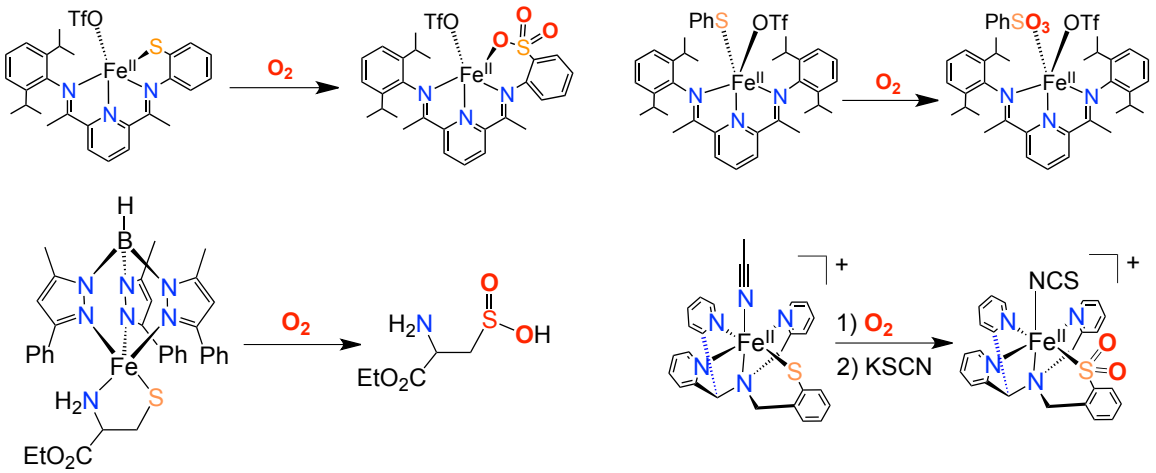

Figure 1. 13. Reported examples of iron(II) in S-oxygenation with O_2. Top: Bis(imino)pyridine derived N_3S(thiolate) donors give sulfonate products (Goldberg). Bottom: Pentadentate N_4S(thiolate) ligands that yield sulfinate products (left = Limberg, right = Goldberg).

1. 3. Superoxide Reductase

Background

Superoxide ($O_2^{\bullet -}$) is generated in mammalian mitochondria and at the surface of bacterial cytoplasmic membranes as a side product of dioxygenic respiration.[74] The diffusion of this superoxide into the intracellular space and the resulting reactions are believed to be the source of "oxidative stress" implicated in many disease states. In mammals, and other aerobic organisms, superoxide detoxification is accomplished by dismutation to H_2O_2 and O_2, with superoxide dismutases (SODs) (Equation 1. 1). However in anaerobic bacteria and archea an alternative strategy is necessary in order to avoid the production of O_2, which would be toxic to the obligate anaerobes. This reaction is catalyzed by a class of metalloenzymes, appropriately named superoxide reductases (SORs), which mediate the one electron reduction of superoxide directly to H_2O_2 (Equation 1. 2). SORs are of

particular interest because they show remarkable selectivity for superoxide and demonstrate virtually no dismutation activity.[74]

$$2O_2^{\bullet -} + 2H^+ \xrightarrow[\text{disproportionation}]{\text{SOD}} O_2 + H_2O_2$$

Equation 1. 1

$$O_2^{\bullet -} + 2H^+ + e^- \xrightarrow[\text{reduction}]{\text{SOR}} H_2O_2$$

Equation 1. 2

Structure of SOR

Superoxide Reductases are divided into three main classes, I, II, and III.[14] Class I (2Fe-SORs) contain two iron centers, the catalytically active $Fe(N_{His})_4(S_{Cys})$ domain and an additional $Fe(S_{Cys})_4$ center in a distorted tetrahedral geometry.[75] Classes II and III (1Fe-SORs) both contain a single $Fe(N_{His})_4(S_{Cys})$ center, while Class III SORs have an additional N-terminal domain.[14] Although the $Fe(S_{Cys})_4$ domain in Class I SORs resembles the electron transfer domain in rubedoxin, the function of this center remains illusive. This domain absent in Class II and III SORs, and at a distance of >20 Å from the catalytic site, is likely too far away to be competent for electron transfer.[76] Additionally, when the $Fe(S_{Cys})_4$ site is removed by mutagenesis, the 2Fe-SOR remained fully active.[77]

The structure of the catalytically active $Fe(N_{His})_4(S_{Cys})$ SOR domain (**Figure 1. 14**) has been extensively studied through the five X-ray structures which have been solved.[14,78-80] The reduced (active) form (SOR_{red}) contains a high-spin ferrous center in a square pyramidal geometry with four equatorial histidines and an axial cysteinate residue, which is *trans* to the open binding site. The open site on iron center is located at the solvent-exposed surface of the protein, with the S-thiolato donor protected inside the protein. It is also interesting to note that there are two backbone peptide amide N-H

groups within H-bonding distance of the Cys donor, likely to mediate the donating ability of this ligand.[81] The oxidized form, SOR_{ox}, contains a high-spin iron(III) center bound in an octahedral geometry, with a highly conserved glutamate residue (Glu 47) from a nearby flexible loop coordinated in the axial binding site.[78] Another notable structural feature is the highly conserved Lys 48 (**Figure 1. 14**b), located in the secondary coordination sphere of the active iron site.[82] There are several possible roles that can be envisioned for a cationic residue capable of donating protons in this reaction, and mechanistic studies (*vide infra*) suggest it is a vital component for proper SOR function.

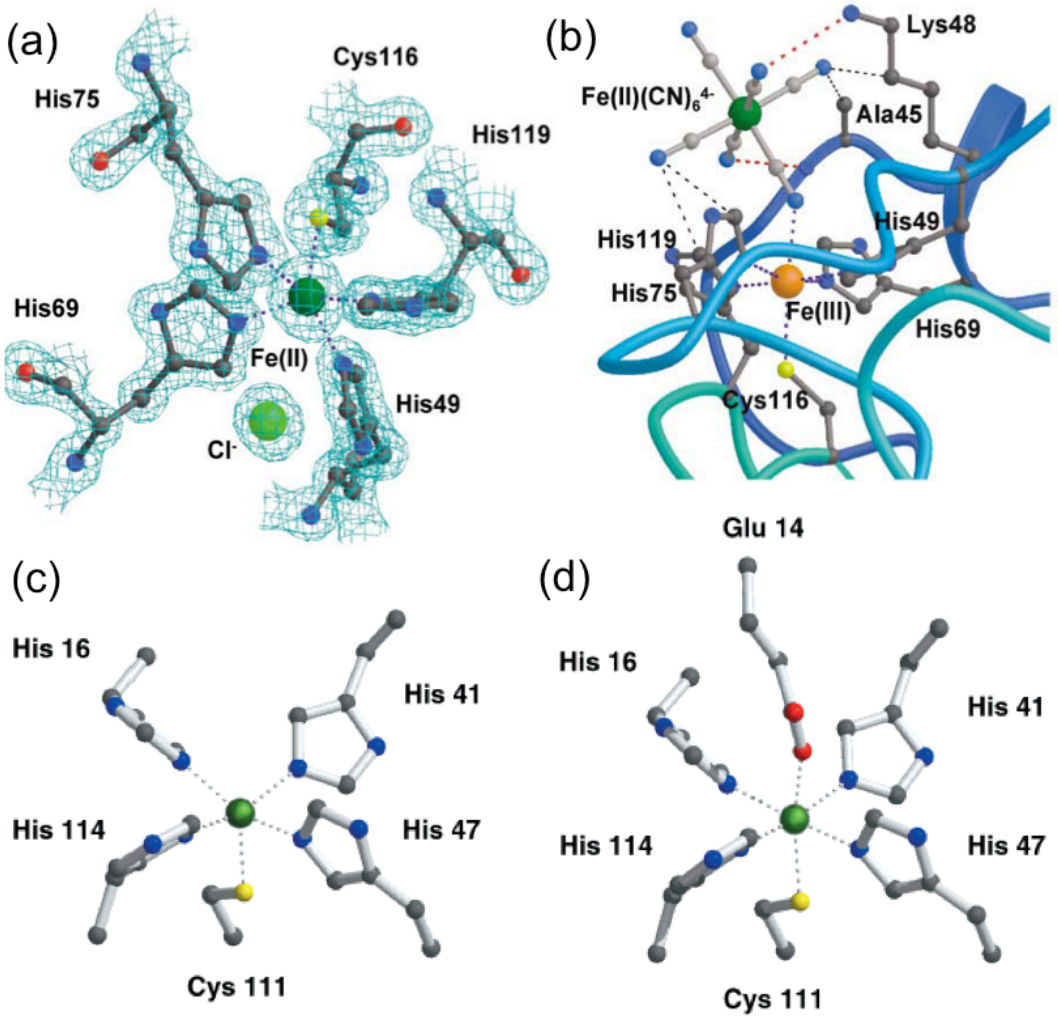

Figure 1. 14. Structure of SOR. (a) Electron density map of chloride-bound active (reduced) SOR.[80] (b) Ferrocyanide-bound oxidized SOR shows bent, end-on binding geometry.[80] (c) Structure of active (reduced) SOR[78]. (d) Structure of resting (oxidized) SOR.[78]

Mechanism of SOR

Although SOR has been extensively studied in vitro and in vivo as well as through synthetic and theoretical modeling, there are many aspects of the catalytic cycle that remain elusive. It has been shown that the active enzyme (SOR_{red}, **Figure 1. 14**c) binds superoxide at diffusion-controlled rates and produces an intermediate displaying a

new charge transfer band (λ_{max} = 600 nm, ε = 3500 M^{-1} cm^{-1}).[83] Based on spectroscopic data, this active intermediate was postulated as ferric-peroxo or –hydroperoxo adduct, and has been observed in all classes of SORs.[82,84] The putative Fe^{III}-OO(H) adduct then releases H_2O_2 at a rate of 40-50 s^{-1}, decaying to a new species characteristic of iron(III) complexes (λ_{max} = 645 nm, ε = 2000 M^{-1} cm^{-1}) identified as the ferric SOR_{ox} (**Figure 1. 14**d).[85-87] With the crystal structures of the resting and product states of SOR solved, efforts have shifted to determining the function of key residues identified in the active site, and specific properties of intermediates in the catalytic cycle (**Figure 1. 15**).

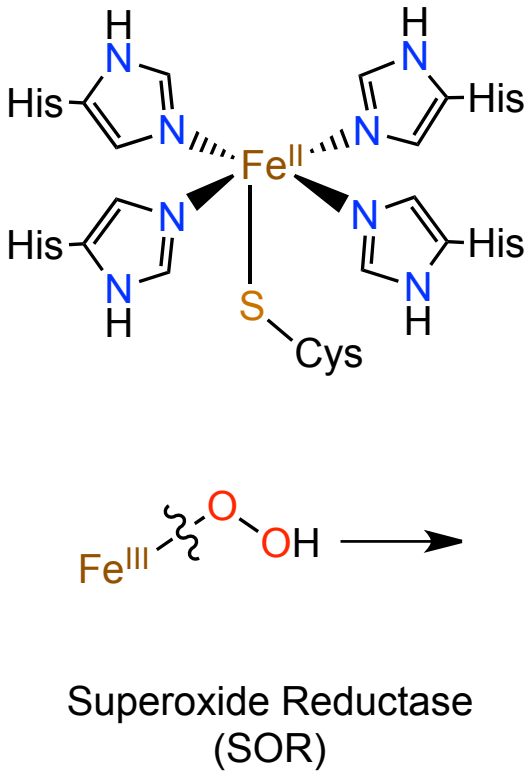

Figure 1. 15. Resting state structure of SOR, with the key (Fe-O) bond cleavage step for reduction.

There are two highly conserved residues in the secondary coordination sphere, Glu47 and Lys48, suggesting that they are important to SOR activity. Even though two

protons are necessary for the overall reduction of superoxide to hydrogen peroxide (Equation 1. 2), Kurtz and Emerson used deuterium isotope effects to show that neither Glu47 or Lys48 are involved in the rate determining protonation step.[88] Instead, it is suggested that solvent is the actual proton source for superoxide reduction, based on the sensitivity of the decay of the key intermediate toward the addition of various proton sources, HX ($X = F^-$, HCO_2^-, N_3^-). Although no additional intermediates are observed in the decay of the Fe^{III}-OO(H) species in the native enzyme, the presence of exogenous anions (F^-, HCO_2^-, PO_4^-, N_3^-) inhibit Glu47 binding and suggest there may be an additional, solvent-bound, species formed first that is rapidly scavenged by glutamate to form the Glu-bound ferric state (**Figure 1. 17**).

Site-directed mutagenesis of Lys48 to isoleucine leads to a 20-30 fold decrease in enzyme activity, indicating an important role in catalytic turnover other than proton donation. Recent work from Bonnot and coworkers demonstrated that in a Lys48 knockout, the major product was no longer H_2O_2 (<15% H_2O_2 detected). Instead, the Lys48 mutant was shown to catalyze olefin epoxidation, implicating the presence of an iron(IV)-oxo species, from O-O bond cleavage, along the reaction pathway.[89] The Lys48 residue therefore is postulated to be critical in the H-bonding network between solvent molecules that serves as the proton source for superoxide reduction and the proximal oxygen of the Fe^{III}-OO(H) intermediate, which leads to Fe-O cleavage in lieu of O-O bond cleavage. However, structural evidence for these proposed intermediates have not been obtained, and many questions remain regarding the binding mode, spin state, protonation state, and the nature of the necessary protonation events.

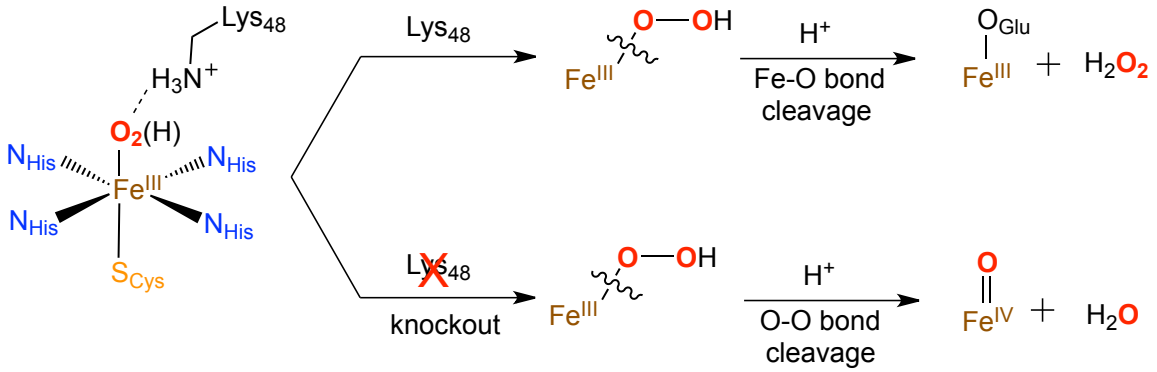

Figure 1. 16. Effect of Lys_{48} on SOR reactivity. Wild-type SOR (top pathway), Lys_{48} SOR knockout (bottom pathway).

The rich reactivity of SORs makes this system an alluring target for synthetic modeling studies. Although our lab has had success studying hydro-[90] and alkyl-[91-94]-peroxo complexes, we continue to synthesize new N_4S ligand systems in an effort to study the role of sulfur and H-bond donors in the generation, stabilization, and reactivity of Fe-O_x adducts.

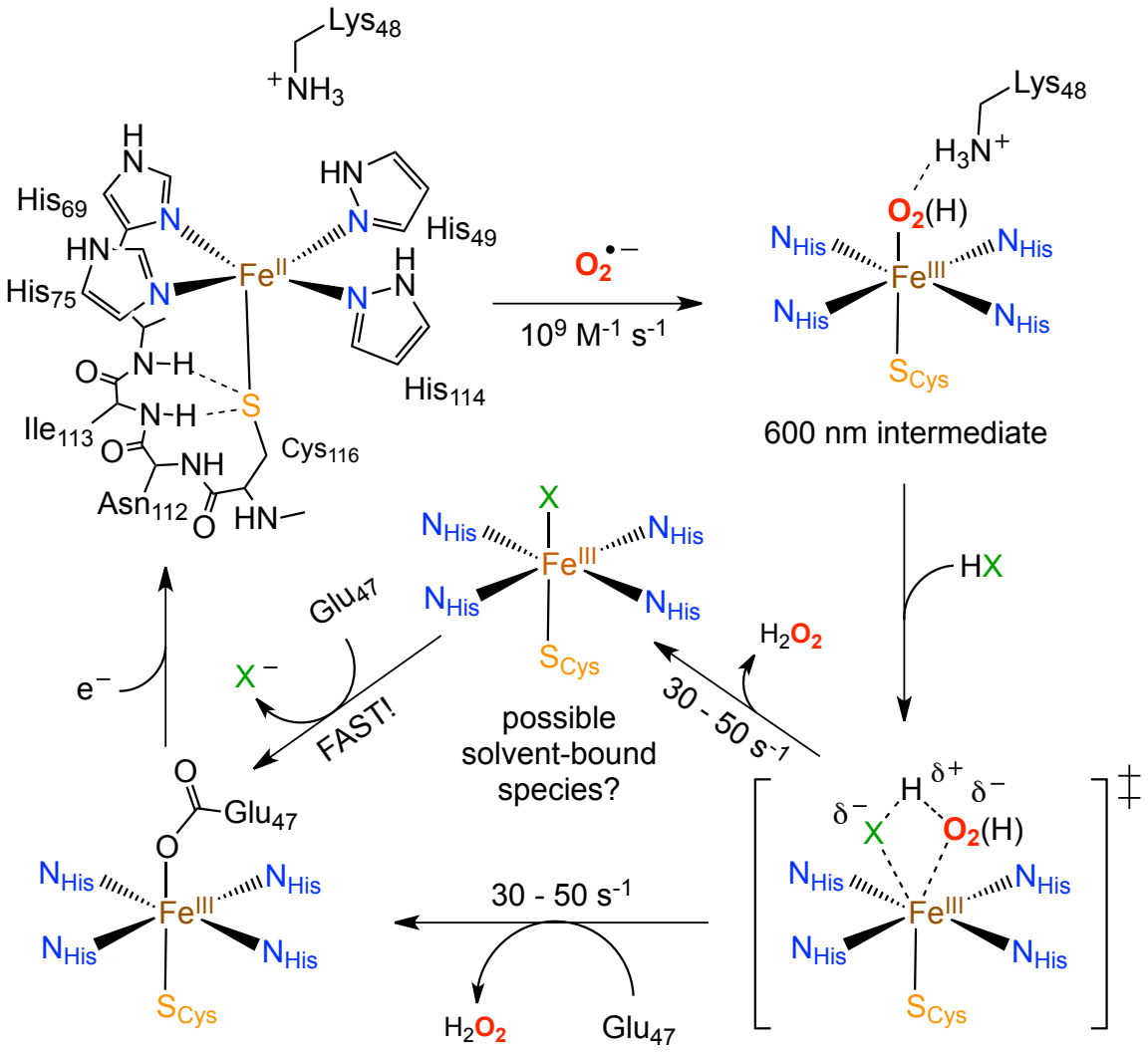

Figure 1. 17. Proposed mechanism of SOR, highlighting the importance of H-bonding interactions in the secondary coordination sphere.

Model Chemistry

There are relatively few examples of Fe^{III}-peroxo compounds that have been well characterized due to their thermal instability, high reactivity and photolability.[95] Examples of successful characterization of these species by Que[96] and Kovacs[97-99] have greatly expanded our understanding of the behavior and spectroscopic properties of these intermediates. For example, Que and coworkers were able to demonstrate the differences

between a side-on ferric peroxide [$Fe^{III}(\eta^2\text{-}O_2)$] and the protonated hydroperoxide species [$Fe^{III}(\eta^1\text{-}OOH)$] with his "$N_4$Py" system (**Figure 1. 18**). In this example, the side-on peroxide is high-spin (S = $^5/_2$), has higher energy $\nu_{O\text{-}O}$ stretching frequency (827 cm^{-1}) and lower energy $\nu_{Fe\text{-}O}$ stretching (495 cm^{-1}) while the protonated hydroperoxide is low spin (S = ½), has a lower $\nu_{O\text{-}O}$ frequency (790 cm^{-1}) and a higher $\nu_{Fe\text{-}O}$ frequency (632 cm^{-1}).

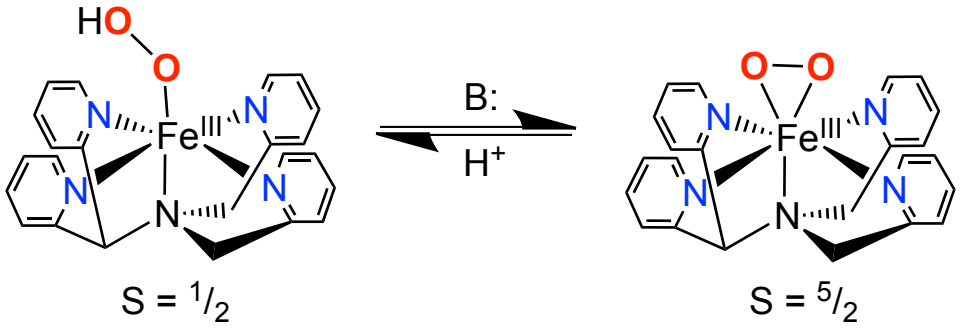

Figure 1. 18. Que's end-on and side-on peroxide N4Py complexes. Adapted from Ref [96].

Professor Kovacs was able to report the first thiolate containing complex that affords an Fe^{III}-hydroperoxide intermediate [$Fe^{III}(S^{Me2}N_4(tren)(OOH))]^+$ (**Figure 1. 19**) from superoxide and extensively characterized the species in THF at -90 °C (λ_{max} = 452 nm, ε = 2780 M^{-1} cm^{-1}, g = 2.14, 1.97).[98] XAS studies showed scattering from one sulfur donor at 2.33(2) Å and four nitrogen donors at 2.01(1) Å, with improved fitting upon the addition of two Fe-O shells (1.86(3) and 2.78(3) Å) suggesting an end-on Fe-OOH structure as expected. Although the thiolate in this complex is *cis* to the hydroperoxo binding site, the intermediate was also found to be low-spin (S = ½) with a $\nu_{O\text{-}O}$ frequency (Fermi doublet, 788 and 781 cm^{-1}) in good agreement with Que's compound. Addition of acid to the hydroperoxo-iron(III) was shown by ^{1}H-NMR and catalase assay to release the biomimetic product H_2O_2 and generate the solvent-bound ferric product.

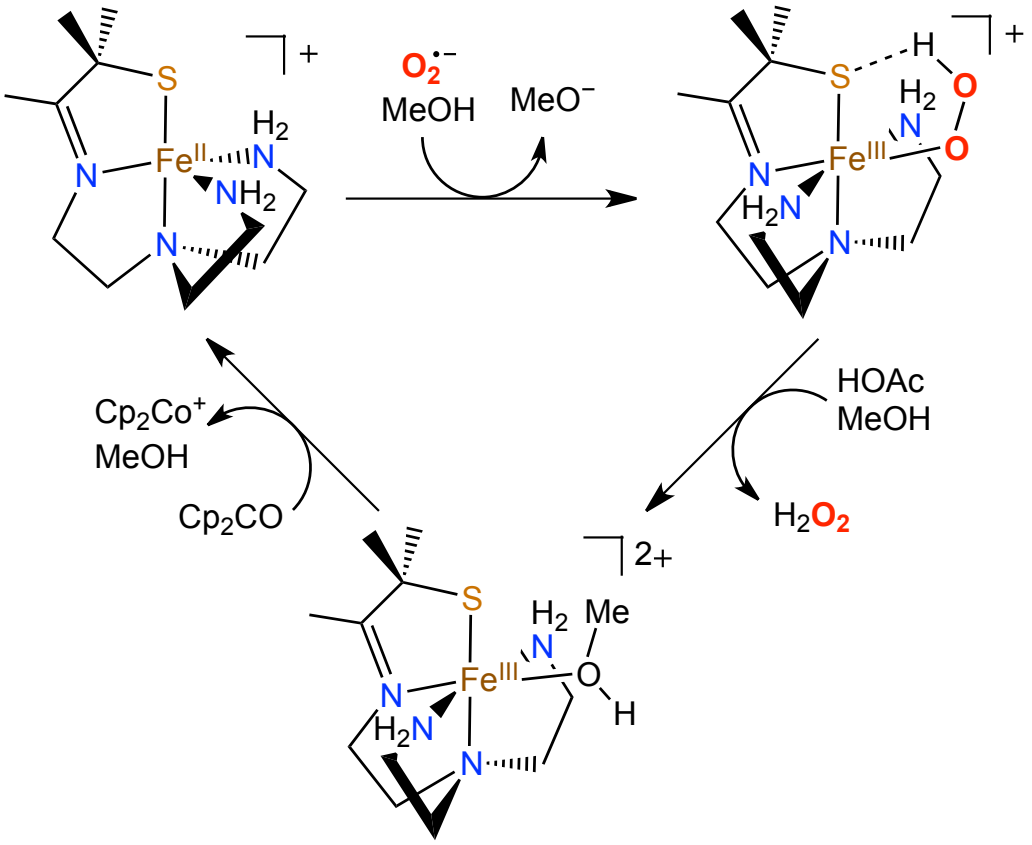

Figure 1. 19. Catalytic cycle of Kovacs' cis-thiolate ligated complex involving reduction of superoxide, protonation and Cp_2Co reduction to release H_2O_2. Adapted from Ref 98.

Kovacs was later able to demonstrate analogous superoxide reduction activity in a *trans*-thiolate complex, $[Fe^{II}(cyclam\text{-}PrS)]^+$ (**Figure 1. 20**).[99] Here, the incorporation of a pendant thiolate donor on a tetradentate cyclam ligand allows for a more biomimetic binding geometry where the four N-donors are in the equatorial plane with the tholate opposite of the proposed binding site. This complex reacts at -78 °C with superoxide in protic solvents, such as MeOH, to give the corresponding hydroperoxo-iron(III) complex $[Fe^{III}(cyclam\text{-}PrS)(OOH)]^+$. In this case the hydroperoxo complex exhibited an EPR signal (g = 7.72, 5.40, 4.15) and rR vibrational data ($\nu_{Fe\text{-}O}$ = 419 cm^{-1}, $\nu_{O\text{-}O}$ = 891 cm^{-1}) that are characteristic of high-spin Fe^{III}–OOH complexes. Again, addition of AcOH was

shown to release H_2O_2 and generate the acetate bound $[Fe^{III}(cyclam\text{-}PrS)(AcO)]^+$ that resembles the catalytically-relevant species in SOR. Furthermore, the use of the reductant Cp_2Co to regenerate the ferrous starting material allowed for modest catalytic activity, achieving 5 complete turnovers.

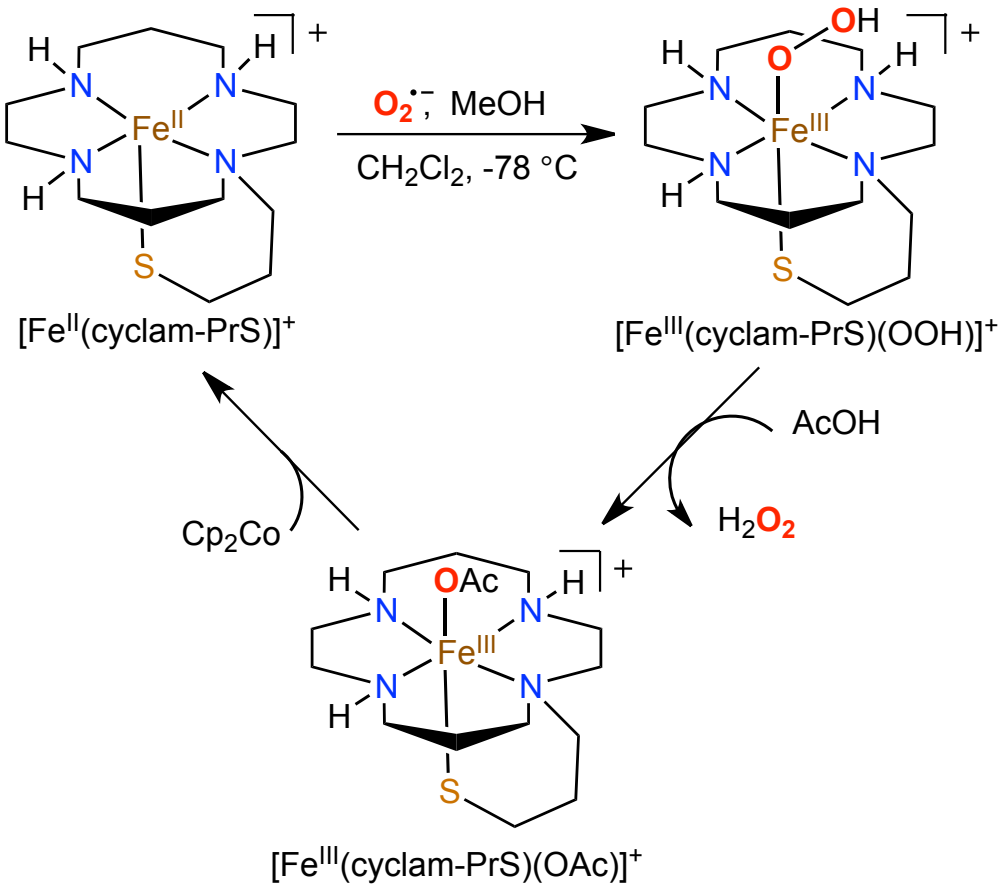

Figure 1. 20. Catalytic cycle of superoxide reduction to release H_2O_2 with $[Fe^{II}(cyclam\text{-}PrS)]^+$. Adapted from Ref 99.

A few model systems have also been reported where the thiolato-S donor is not covalently tethered to the ligand. The use of an exogenous anionic donor makes a series of compounds easily accessible that vary the electronics of the thiolate donor and allow for direct comparison of the effect of the thiolate on the stability and spectroscopic properties of peroxo compounds. In one such report, Que and coworkers utilized

$[Fe^{II}(L^{8}Py_2)(X)]^+$ (X = OTf, OBn, SAr) to generate a series of high-spin ferric-alkylperoxo species, $[Fe^{II}(L^{8}Py_2)(X)(OOtBu)]^+$, at -80 °C (**Figure 1. 21**A).[100] They were able to show that increasing the donating ability, or Lewis basicity, of the sixth ligand actually stabilized the resulting Fe^{III}-OOR complexes. This trend is completely opposite than observed in previously reported low-spin Fe-OO(H/R), complexes where increasing Lewis basicity destabilized intermediates via the "push" effect observed in heme systems that promote O-O bond cleavage.[101,102] This stark difference in reactivity is attributed to the change in spin state from l.s. to h.s. Resonance Raman has shown that l.s. Fe-OOR complexes exhibit relatively stronger Fe-O vibrations and weaker O-O vibrations, thereby promoting O-O bond cleavage to generate the Fe^{IV}=O complex (**Figure 1. 21**B).[103-105] High-spin complexes however, exhibit the opposite trend, where the Fe-O bond is weaker and the O-O bond is stronger, favoring Fe-O bond cleavage as is necessary in SOR for H_2O_2 release. Electron donation to the metal center in these h.s. Fe^{III}–OOR complexes lowers the $Fe^{III/II}$ potential, thereby slowing decay.

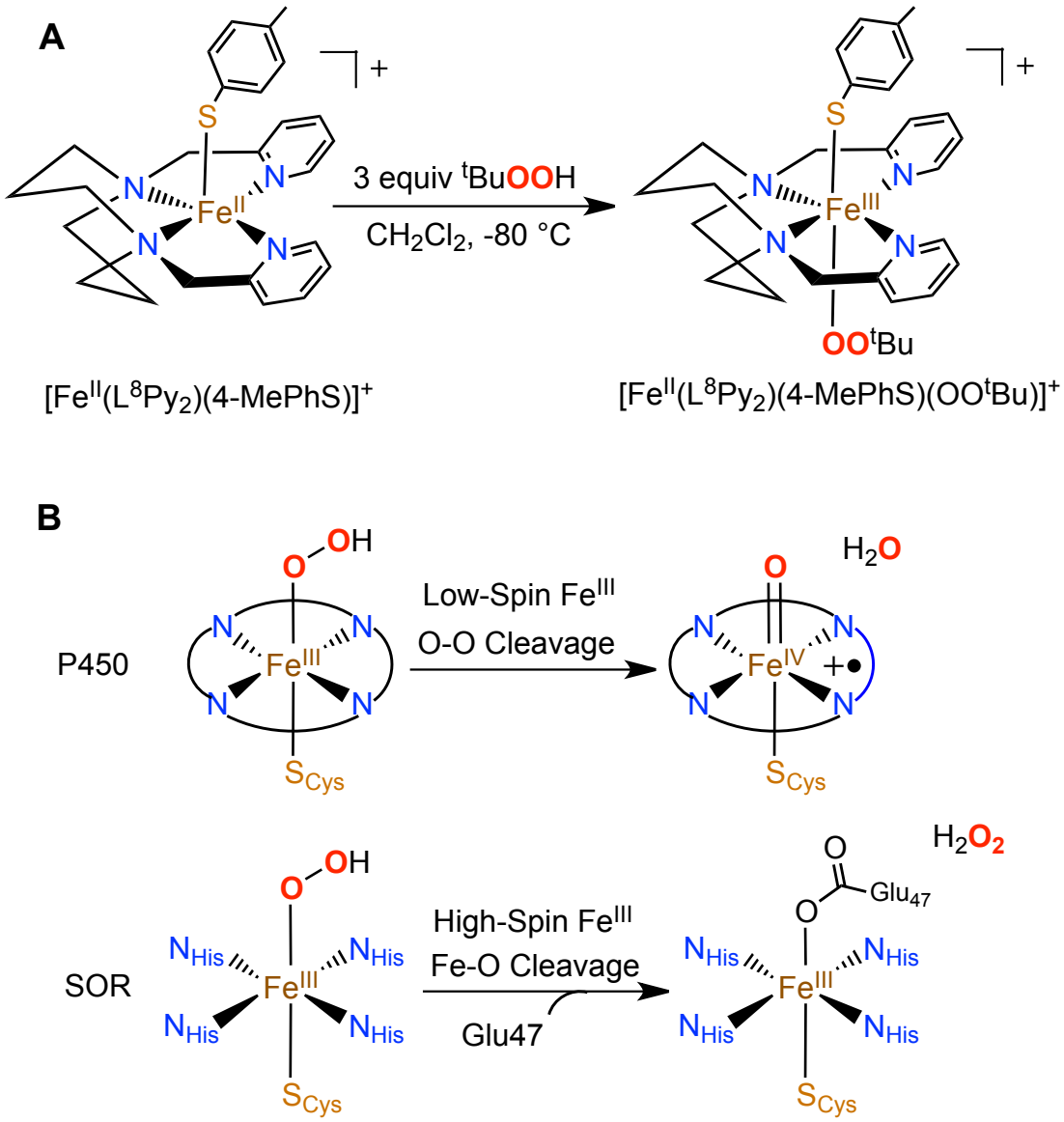

Figure 1. 21. A) Reaction of $[Fe^{II}(L^{8}Py_2)(4\text{-MePhS})]^{+}$ with tBuOOH to generate $[Fe^{II}(L^{8}Py_2)(4\text{-MePhS})(OOtBu)]^{+}$, at -80 °C. Adapted from Ref [100]. B) Examples of how spin-state effects reactivity: O-O bond cleavage in P450 versus Fe-O bond cleavage in SOR.

Other recent reports from our lab (**Figure 1. 22**) describe the synthesis of a series of Fe^{II}-N_4S complexes, based on the $[Fe^{II}([15]aneN_4)(SAr)]^+$ platform, that serve as precursors for the generation of alkylperoxo-iron(III) complexes with varying electronics of the sulfur donor (SAr, where Ar = C_6H_5, C_6H_4-*p*-Cl, C_6H_4-*p*-NO_2, C_6H_4-*p*-OMe, C_6H_4-*p*-C_6F_5).[91,92] Reaction of the iron(II) complexes with alkylperoxides (^{t}BuOOH, CmOOH) generates metastable Fe^{III}-OOR complexes that are characterized by UV-vis, EPR, and resonance Raman spectroscopy. The series of $[Fe^{II}([15]aneN_4)(SAr)(OO^tBu)]^+$ complexes are shown to contain l.s. iron(III) centers with alkylperoxo-to-iron(III) LMCT bands from 508 – 530 nm. The resonance Raman data show that over the entire series, the Fe-O bonds are dramatically weakened relative to other reported ls Fe^{III}-OOR complexes, and that the ν(Fe-O) shifts to lower energy with increasing donating character of the thiolate ligand while the ν(O-O) energies remain relatively unchanged over the series. These complexes were structurally characterized by X-ray absorption spectroscopy (XAS) and density functional theory (DFT) methods, confirming the presence of a ligated thiolate and giving matching Fe-O, Fe-N, and Fe-S distances.[94] Interestingly, another report showed that a new complex, $[Fe^{II}(Me_4[15]aneN_4)(SPh)](BPh_4)$, where the equatorial amine donors are all methylated reacted with ^{t}BuOOH to generate a hs Fe^{III}-OO^tBu complex.[93] In this case, there was also a non-thiolate ligated analogue synthesized and characterized, allowing for direct comparison of the effect of S-ligation on the properties of the Fe^{III}-OO^tBu species. Overall, the reports on these $[15]aneN_4$ complexes are the only example where the effect of *trans* ligation to peroxo-iron(III) moieties has been directly studied in structurally-equivalent high-spin and low-spin complexes.

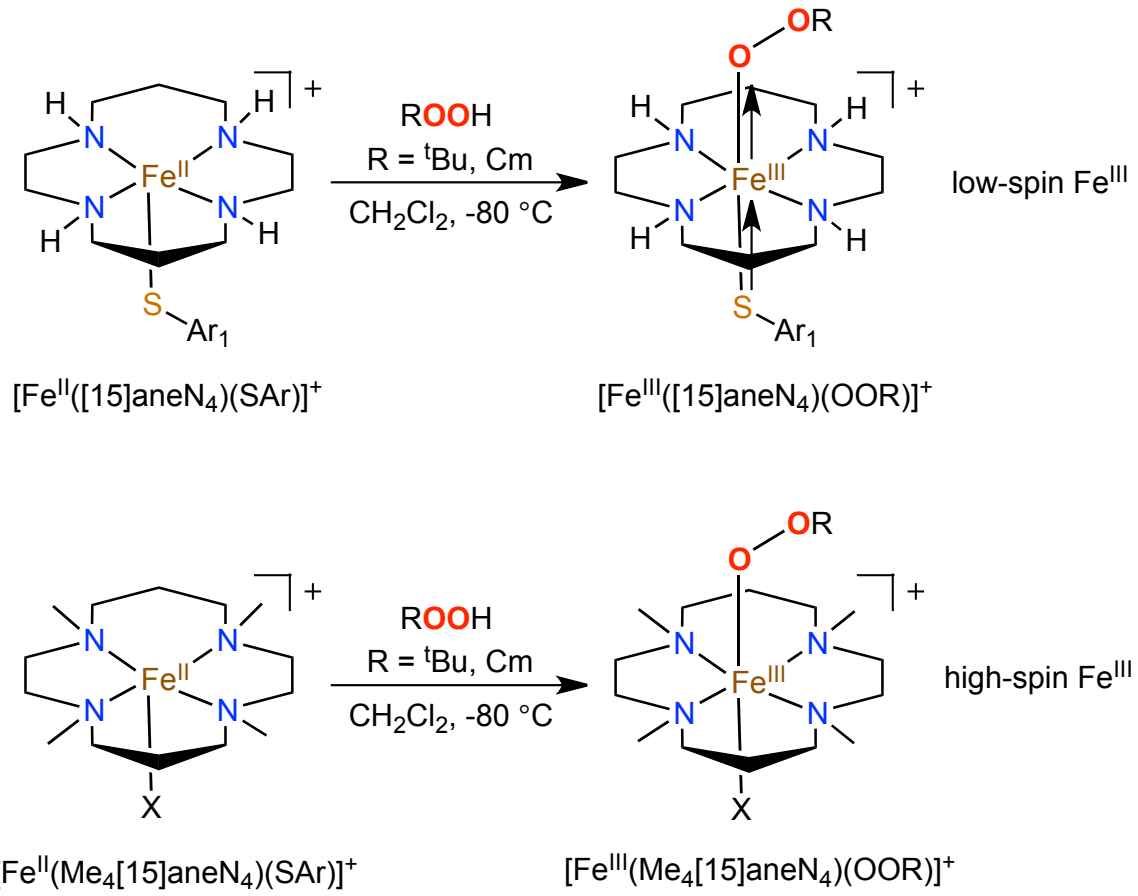

Figure 1. 22. Reaction of $[Fe^{II}([15]aneN_4)(SAr)]^+$ (top) and $[Fe^{II}(Me_4[15]aneN_4)(SAr)]^+$ (bottom) with alkylperoxides to generate their respective high- and low-spin Fe^{III}-OOR complexes, $[Fe^{II}([15]aneN_4)(SAr)(OOR)]^+$ and $[Fe^{II}(Me_4[15]aneN_4)(SAr)(OOR)]^+$. Ar = C_6H_5, C_6H_4-*p*-Cl, C_6H_4-*p*-NO_2, C_6H_4-*p*-OMe, C_6H_4-*p*-C_6F_5; X = OTf, SC_6H_5, SC_6H_4-*p*-Cl, SC_6H_4-*p*-NO_2.

1. 4. References

(1) Lippard, S.J.; Berg, J. M. *Principles of Bioinorganic Chemistry*; University Science Books, California, 1994; pp 1-20.

(2) Solomon, E. I.; Decker, A.; Lehnert, N. *Proc. Natl. Acad. Sci. U. S. A.* **2003**, *100*, 3589.

(3) Kovaleva, E. G.; Neibergall, M. B.; Chakrabarty, S.; Lipscomb, J. D. *Acc. Chem. Res.* **2007**, *40*, 475.

(4) Costas, M.; Mehn, M. P.; Jensen, M. P.; Que, L., Jr. *Chem. Rev.* **2004**, *104*, 939.

(5) Abu-Omar, M. M.; Loaiza, A.; Hontzeas, N. *Chem. Rev.* **2005**, *105*, 2227.

(6) Bollinger, J. M., Jr.; Krebs, C. *J. Inorg. Biochem.* **2006**, *100*, 586.

(7) Ryle, M. J.; Hausinger, R. P. *Curr. Opin. Chem. Biol.* **2002**, *6*, 193.

(8) Fukuyama, K.; Matsubara, H.; Tsukihara, T.; Katsube, Y. *J. Mol. Biol.* **1989**, *210*, 383.

(9) Florin, L.; Tsokoglou, A.; Happe, T. *J. Biol. Chem.* **2001**, *276*, 6125.

(10) Seefeldt, L. C.; Dance, I. G.; Dean, D. R. *Biochemistry* **2004**, *43*, 1401.

(11) Rao, P. V.; Holm, R. H. *Chem. Rev.* **2004**, *104*, 527.

(12) Serero, A.; Giglione, C.; Meinnel, T. *J. Mol. Biol.* **2001**, *314*, 695.

(13) Roach, P. L.; Clifton, I. J.; Hensgens, C. M. H.; Shibata, N.; Schofield, C. J.; Hajdu, J.; Baldwin, J. E. *Nature* **1997**, *387*, 827.

(14) Santos-Silva, T.; Trincão, J.; Carvalho, A. L.; Bonifácio, C.; Auchère, F.; Raleiras, P.; Moura, I.; Moura, J. J. G.; Romão, M. J. *J. Biol. Inorg. Chem.* **2006**, *11*, 548.

(15) Ye, S.; Wu, X.; Wei, L.; Tang, D. M.; Sun, P.; Bartlam, M.; Rao, Z. H. *J. Biol. Chem.* **2007**, *282*, 3391.

(16) Solomon, E. I.; Brunold, T. C.; Davis, M. I.; Kemsley, J. N.; Lee, S. K.; Lehnert, N.; Neese, F.; Skulan, A. J.; Yang, Y. S.; Zhou, J. *Chem. Rev.* **2000**, *100*, 235.

(17) Valentine, J. S.; Wertz, D. L.; Lyons, T. J.; Liou, L. L.; Goto, J. J.; Gralla, E. B. *Curr. Opin. Chem. Biol.* **1998**, *2*, 253.

(18) Kurtz, D. M., Jr. *Acc. Chem. Res.* **2004**, *37*, 902.

(19) Ihara, Y.; Chuda, M.; Kuroda, S.; Hayabara, T. *J. Neurol. Sci.* **1999**, *170*, 90.

(20) Kocatürk, P. A.; Akbostanci, M. C.; Tan, F.; Kavas, G. Ö. *Pathophysiology* **2000**, *7*, 63.

(21) Marklund, S. L.; Adolfsson, R.; Gottfries, C. G.; Winblad, B. *J. Neurol. Sci.* **1985**, *67*, 319.

(22) Maritim, A. C.; Sanders, R. A.; Watkins, J. B. *J. Biochem. Mol. Toxicol.* **2003**, *17*, 24.

(23) Toh, Y.; Kuninaka, S.; Mori, M.; Oshiro, T.; Ikeda, Y.; Nakashima, H.; Baba, H.; Kohnoe, S.; Okamura, T.; Sugimachi, K. *Oncology* **2000**, *59*, 223.

(24) Burdon, R. H. *Free Radical Biol. Med.* **1995**, *18*, 775.

(25) Moriarty-Craige, S. E.; Jones, D. P. *Annu. Rev. Nutr.* **2004**, *24*, 481.

(26) Kalatzis, V.; Cherqui, S.; Antignac, C.; Gasnier, B. *EMBO J.* **2001**, *20*, 5940.

(27) Kalatzis, V.; Antignac, C. *Nephrol., Dial., Transplant.* **2002**, *17*, 1883.

(28) Perry, T. L.; Norman, M. G.; Yong, V. W.; Whiting, S.; Crichton, J. U.; Hansen, S.; Kish, S. J. *Ann. Neurol.* **1985**, *18*, 482.

(29) Pean, A. R.; Parsons, R. B.; Waring, R. H.; Williams, A. C.; Ramsden, D. B. *J. Neurol. Sci.* **1995**, *129*, 107.

(30) Parsons, R. B.; Waring, R. H.; Ramsden, D. B.; Williams, A. C. *Neurotoxicology* **1998**, *19*, 599.

(31) Joseph, C. A.; Maroney, M. J. *Chem. Commun.* **2007**, 3338.

(32) Yamaguch.K; Sakakiba.S; Koga, K.; Ueda, I. *Biochim. Biophys. Acta* **1971**, *237*, 502.

(33) Lombardi, J. B.; Turini, P.; Biggs, D. R.; Singer, T. P. *Physiol. Chem. Phys. Med. NMR* **1969**, *1*, 1.

(34) Ewetz, L.; Sorbo, B. *Biochim. Biophys. Acta.* **1966**, *128*, 296.

(35) Sorbo, B.; Ewetz, L. *Biochem. Biophys. Res. Commun.* **1965**, *18*, 359.

(36) McCoy, J. G.; Bailey, L. J.; Bitto, E.; Bingman, C. A.; Aceti, D. J.; Fox, B. G.; Phillips, G. N. *Proc. Natl. Acad. Sci. U. S. A.* **2006**, *103*, 3084.

(37) Gough, J.; Karplus, K.; Hughey, R.; Chothia, C. *J. Mol. Biol.* **2001**, *313*, 903.

(38) Jongkees, S. A. K.; Jameson, G. N. L. *Chem. N. Z.* **2007**, *71*, 79.

(39) Simmons, C. R.; Liu, Q.; Huang, Q. Q.; Hao, Q.; Begley, T. P.; Karplus, P. A.; Stipanuk, M. H. *J. Biol. Chem.* **2006**, *281*, 18723.

(40) Simmons, C. R.; Karplus, P. A.; Stipanuk, M. H., 1.5 Å Resolution CDO structure deposited in PDB.

(41) Straganz, G. D.; Nidetzky, B. *Chembiochem* **2006**, *7*, 1536.

(42) Ito, N.; Phillips, S. E. V.; Stevens, C.; Ogel, Z. B.; Mcpherson, M. J.; Keen, J. N.; Yadav, K. D. S.; Knowles, P. F. *Nature* **1991**, *350*, 87.

(43) Firbanks, S. J.; Rogers, M. S.; Wilmot, C. M.; Dooley, D. M.; Halcrow, M. A.; Knowles, P. F.; McPherson, M. J.; Phillips, S. E. V. *Proc. Natl. Acad. Sci. U. S. A.* **2001**, *98*, 12932.

(44) Koehntop, K. D.; Emerson, J. P.; Que, L., Jr. *J. Biol. Inorg. Chem.* **2005**, *10*, 87.

(45) Neidig, M. L.; Solomon, E. I. *Chem. Commun.* **2005**, 5843.

(46) Tchesnokov, E. P.; Wilbanks, S. M.; Jameson, G. N. L. *Biochemistry* **2012**, *51*, 257.

(47) Tchensnokov, E.; Siakkou, E.; Souness, R.; Turner, R.; Fellner, M.; Wilbanks, S. M.; Jameson, G. N. L. **2013**, *Unpublished Results*.

(48) Kumar, D.; Thiel, W.; de Visser, S. P. *J. Am. Chem. Soc.* **2011**, *133*, 3869.

(49) Simmons, C. R.; Krishnamoorthy, K.; Granett, S. L.; Schuller, D. J.; Dominy, J. E.; Begley, T. P.; Stipanuk, M. H.; Karplus, P. A. *Biochemistry* **2008**, *47*, 11390.

(50) Connick, W. B.; Gray, H. B. *J. Am. Chem. Soc.* **1997**, *119*, 11620.

(51) Lippert, C. A.; Soper, J. D. *Inorg. Chem.* **2010**, *49*, 3682.

(52) Kumar, M.; Colpas, G. J.; Day, R. O.; Maroney, M. J. *J. Am. Chem. Soc.* **1989**, *111*, 8323.

(53) Farmer, P. J.; Solouki, T.; Mills, D. K.; Soma, T.; Russell, D. H.; Reibenspies, J. H.; Darensbourg, M. Y. *J. Am. Chem. Soc.* **1992**, *114*, 4601.

(54) Farmer, P. J.; Solouki, T.; Soma, T.; Russell, D. H.; Darensbourg, M. Y. *Inorg. Chem.* **1993**, *32*, 4171.

(55) Buonomo, R. M.; Font, I.; Maguire, M. J.; Reibenspies, J. H.; Tuntulani, T.; Darensbourg, M. Y. *J. Am. Chem. Soc.* **1995**, *117*, 5427.

(56) Darensbourg, M. Y.; Tuntulani, T.; Reibenspies, J. H. *Inorg. Chem.* **1995**, *34*, 6287.

(57) Grapperhaus, C. A.; Darensbourg, M. Y.; Sumner, L. W.; Russell, D. H. *J. Am. Chem. Soc.* **1996**, *118*, 1791.

(58) Grapperhaus, C. A.; Darensbourg, M. Y. *Acc. Chem. Res.* **1998**, *31*, 451.

(59) Mullins, C. S.; Grapperhaus, C. A.; Frye, B. C.; Wood, L. H.; Hay, A. J.; Buchanan, R. M.; Mashuta, M. S. *Inorg. Chem.* **2009**, *48*, 9974.

(60) Herdt, D. R.; Grapperhaus, C. A. *Dalton Trans.* **2012**, *41*, 364.

(61) Mullins, C. S.; Grapperhaus, C. A.; Kozlowski, P. M. *J. Biol. Inorg. Chem.* **2006**, *11*, 617.

(62) Zhou, L.; Powell, D.; Nicholas, K. M. *Inorg. Chem.* **2006**, *45*, 3840.

(63) Champloy, F.; Benali-Cherif, N.; Bruno, P.; Blain, I.; Pierrot, M.; Reglier, M.; Michalowicz, A. *Inorg. Chem.* **1998**, *37*, 3910.

(64) Lee, Y.; Lee, D. H.; Sarjeant, A. A. N.; Zakharov, L. N.; Rheingold, A. L.; Karlin, K. D. *Inorg. Chem.* **2006**, *45*, 10098.

(65) Musie, G.; Lai, C. H.; Reibenspies, J. H.; Sumner, L. W.; Darensbourg, M. Y. *Inorg. Chem.* **1998**, *37*, 4086.

(66) O'Toole, M. G.; Kreso, M.; Kozlowski, P. M.; Mashuta, M. S.; Grapperhaus, C. A. *J. Biol. Inorg. Chem.* **2008**, *13*, 1219.

(67) Campanali, A. A.; Kwiecien, T. D.; Hryhorczuk, L.; Kodanko, J. J. *Inorg. Chem.* **2010**, *49*, 4759.

(68) Jiang, Y. B.; Widger, L. R.; Kasper, G. D.; Siegler, M. A.; Goldberg, D. P. *J. Am. Chem. Soc.* **2010**, *132*, 12214.

(69) Cho, J.; Woo, J.; Nam, W. *J. Am. Chem. Soc.* **2012**, *134*, 11112.

(70) Cho, J.; Woo, J.; Nam, W. *J. Am. Chem. Soc.* **2010**, *132*, 5958.

(71) Badiei, Y. M.; Siegler, M. A.; Goldberg, D. P. *J. Am. Chem. Soc.* **2011**, *133*, 1274.

(72) Sallmann, M.; Siewert, I.; Fohlmeister, L.; Limberg, C.; Knispel, C. *Angew. Chem. Int. Ed.* **2012**, *51*, 2234.

(73) McQuilken, A. C.; Jiang, Y. B.; Siegler, M. A.; Goldberg, D. P. *J. Am. Chem. Soc.* **2012**, *134*, 8758.

(74) Kurtz, D. M. *J. Inorg. Biochem.* **2006**, *100*, 679.

(75) Adams, M. W. W.; Jenney, F. E.; Clay, M. D.; Johnson, M. K. *J. Biol. Inorg. Chem.* **2002**, *7*, 647.

(76) Emerson, J. P.; Coulter, E. D.; Phillips, R. S.; Kurtz, D. M. *J. Biol. Chem.* **2003**, *278*, 39662.

(77) Emerson, J. P.; Cabelli, D. E.; Kurtz, D. M. *Proc. Natl. Acad. Sci. U. S. A.* **2003**, *100*, 3802.

(78) Yeh, A. P.; Hu, Y. L.; Jenney, F. E.; Adams, M. W. W.; Rees, D. C. *Biochemistry* **2000**, *39*, 2499.

(79) Matias, P. M.; Morais, J.; Coelho, A. V.; Meijers, R.; Gonzalez, A.; Thompson, A. W.; Sieker, L.; LeGall, J.; Carrondo, M. A. *J. Biol. Inorg. Chem.* **1997**, *2*, 507.

(80) Adam, V.; Royant, A.; Nivière, V.; Molina-Heredia, F. P.; Bourgeois, D. *Structure* **2004**, *12*, 1729.

(81) Mathé, C.; Weill, C. O.; Mattioli, T. A.; Berthomieu, C.; Houée-Levin, C.; Tremey, E.; Nivière, V. *J. Biol. Chem.* **2007**, *282*, 22207.

(82) Lombard, M.; Houée-Levin, C.; Touati, D.; Fontecave, M.; Nivière, V. *Biochemistry* **2001**, *40*, 5032.

(83) Brines, L. M.; Kovacs, J. A. *Eur. J. Inorg. Chem.* **2007**, 29.

(84) Abreu, I. A.; Xavier, A. V.; LeGall, J.; Cabelli, D. E.; Teixeira, M. *J. Biol. Inorg. Chem.* **2002**, *7*, 668.

(85) Coulter, E. D.; Emerson, J. P.; Kurtz, D. M.; Cabelli, D. E. *J. Am. Chem. Soc.* **2000**, *122*, 11555.

(86) Nivière, V.; Lombard, M.; Fontecave, M.; Houée-Levin, C. *FEBS Lett.* **2001**, *497*, 171.

(87) Kurtz, D. M.; Coulter, E. D. *J. Biol. Inorg. Chem.* **2002**, *7*, 653.

(88) Huang, V. W.; Emerson, J. P.; Kurtz, D. M. *Biochemistry* **2007**, *46*, 11342.

(89) Bonnot, F.; Molle, T.; Ménage, S.; Moreau, Y.; Duval, S.; Favaudon, V.; Houée-Levin, C.; Nivière, V. *J. Am. Chem. Soc.* **2012**, *134*, 5120.

(90) Jiang, Y. B.; Telser, J.; Goldberg, D. P. *Chem. Commun.* **2009**, 6828.

(91) Krishnamurthy, D.; Kasper, G. D.; Namuswe, F.; Kerber, W. D.; Sarjeant, A. A. N.; Moënne-Loccoz, P.; Goldberg, D. P. *J. Am. Chem. Soc.* **2006**, *128*, 14222.

(92) Namuswe, F.; Kasper, G. D.; Sarjeant, A. A. N.; Hayashi, T.; Krest, C. M.; Green, M. T.; Moënne-Loccoz, P.; Goldberg, D. P. *J. Am. Chem. Soc.* **2008**, *130*, 14189.

(93) Namuswe, F.; Hayashi, T.; Jiang, Y. B.; Kasper, G. D.; Sarjeant, A. A. N.; Moënne-Loccoz, P.; Goldberg, D. P. *J. Am. Chem. Soc.* **2010**, *132*, 157.

(94) Stasser, J.; Namuswe, F.; Kasper, G. D.; Jiang, Y. B.; Krest, C. M.; Green, M. T.; Penner-Hahn, J.; Goldberg, D. P. *Inorg. Chem.* **2010**, *49*, 9178.

(95) Girerd, J. J.; Banse, F.; Simaan, A. J. *Struct. Bonding* **2000**, *97*, 145.

(96) Roelfes, G.; Vrajmasu, V.; Chen, K.; Ho, R. Y. N.; Rohde, J. U.; Zondervan, C.; la Crois, R. M.; Schudde, E. P.; Lutz, M.; Spek, A. L.; Hage, R.; Feringa, B. L.; Münck, E.; Que, L., Jr. *Inorg. Chem.* **2003**, *42*, 2639.

(97) Shearer, J.; Nehring, J.; Lovell, S.; Kaminsky, W.; Kovacs, J. A. *Inorg. Chem.* **2001**, *40*, 5483.

(98) Shearer, J.; Scarrow, R. C.; Kovacs, J. A. *J. Am. Chem. Soc.* **2002**, *124*, 11709.

(99) Kitagawa, T.; Dey, A.; Lugo-Mas, P.; Benedict, J. B.; Kaminsky, W.; Solomon, E.; Kovacs, J. A. *J. Am. Chem. Soc.* **2006**, *128*, 14448.

(100) Bukowski, M. R.; Halfen, H. L.; van den Berg, T. A.; Halfen, J. A.; Que, L., Jr. *Angew. Chem. Int. Ed.* **2005**, *44*, 584.

(101) Payeras, A. M. I.; Ho, R. Y. N.; Fujita, M.; Que, L., Jr. *Chem.-Eur. J.* **2004**, *10*, 4944.

(102) Kaizer, J.; Costas, M.; Que, L., Jr. *Angew. Chem. Int. Ed.* **2003**, *42*, 3671.

(103) Lehnert, N.; Ho, R. Y. N.; Que, L., Jr.; Solomon, E. I. *J. Am. Chem. Soc.* **2001**, *123*, 8271.

(104) Ho, R. Y. N.; Roelfes, G.; Feringa, B. L.; Que, L., Jr. *J. Am. Chem. Soc.* **1999**, *121*, 264.

(105) Lehnert, N.; Neese, F.; Ho, R. Y. N.; Que, L., Jr.; Solomon, E. I. *J. Am. Chem. Soc.* **2002**, *124*, 10810.

Chapter 2. Synthesis and Ligand Non-Innocence of Thiolate-Ligated (N4S) Iron(II) and Nickel(II) Bis(imino)pyridine Complexes

This work was co-written with the following authors and is published under the following citation:

Leland R. Widger, Yunbo Jiang, Maxime A. Siegler, Devesh Kumar, Reza Latifi, Sam P. de Visser, Guy N. L. Jameson, and David P. Goldberg.

Inorg. Chem., **2013**, *52* (18), 10467–10480

2. 1. Introduction

Thiolate-ligated nonheme iron sites play key roles in biology, exhibiting diverse structural features as well as contributing to a wide range of reactivity.[1-7] The mononuclear, thiolate-ligated nonheme iron enzymes superoxide reductase,[8-12] nitrile hydratase,[13-15] and cysteine dioxygenase (CDO)[16-23] utilize single iron sites coordinated in mixed N/S ligand environments. Work by some of us has focused on the preparation of synthetic analogs of these sites, including some of the first structural and functional models of CDO.[1,24-33] A bis(imino)pyridine (BIP) ligand scaffold was employed, leading to the synthesis of $Fe^{II}(LN_3S)$ complexes that mimicked certain structural and functional features of CDO.[24,25] The key thiolate donor was incorporated into these complexes by either covalent attachment to the BIP backbone, or by addition of an exogenous phenylthiolate (PhS^-) ligand to the iron(II) center, yielding $Fe^{II}(N_3S)$ complexes in both cases. These complexes were among the first mononuclear thiolato-iron(II) complexes to selectively react with O_2 to give S-oxygenated products, reproducing the gross reactivity of the enzymatic system. However, the Cys-bound iron(II) form of CDO contains an iron center held in an (N_4S) donor set, comprised of 3 His ligands and one Cys substrate chelated through both the amino and sidechain S groups. Thus work in the Goldberg group is currently focused on the design and synthesis of $Fe^{II}(N_4S)$ complexes in which a

fourth neutral N donor is included in the first coordination sphere to more closely match the active site of CDO prior to S-oxygenation.

This chapter describes the synthesis, spectroscopic characterization and O_2 reactivity of a new series of $Fe^{II}(N_4S)$ complexes (**Figure 2. 1**) that contain a covalently-linked, BIP-derived ligand providing an N_3S(thiolate) donor set (LN_3S^-), and a fourth N donor derived from exogenous pyridine derivatives. The general synthetic strategy was to incorporate a fourth N donor without the need for covalent modification of the BIP backbone. This strategy proved productive, and the new iron(II) complexes $[Fe^{II}(LN_3S)(py)](OTf)$ and $[Fe^{II}(LN_3S)(DMAP)](OTf)$ were synthesized and characterized by X-ray crystallography, NMR, electrochemistry, Mössbauer spectroscopy and density functional theory (DFT) calculations. A nickel(II) analog, $[Ni^{II}(LN_3S)](BF_4)$, was also prepared for comparative spectroscopic and reactivity studies.

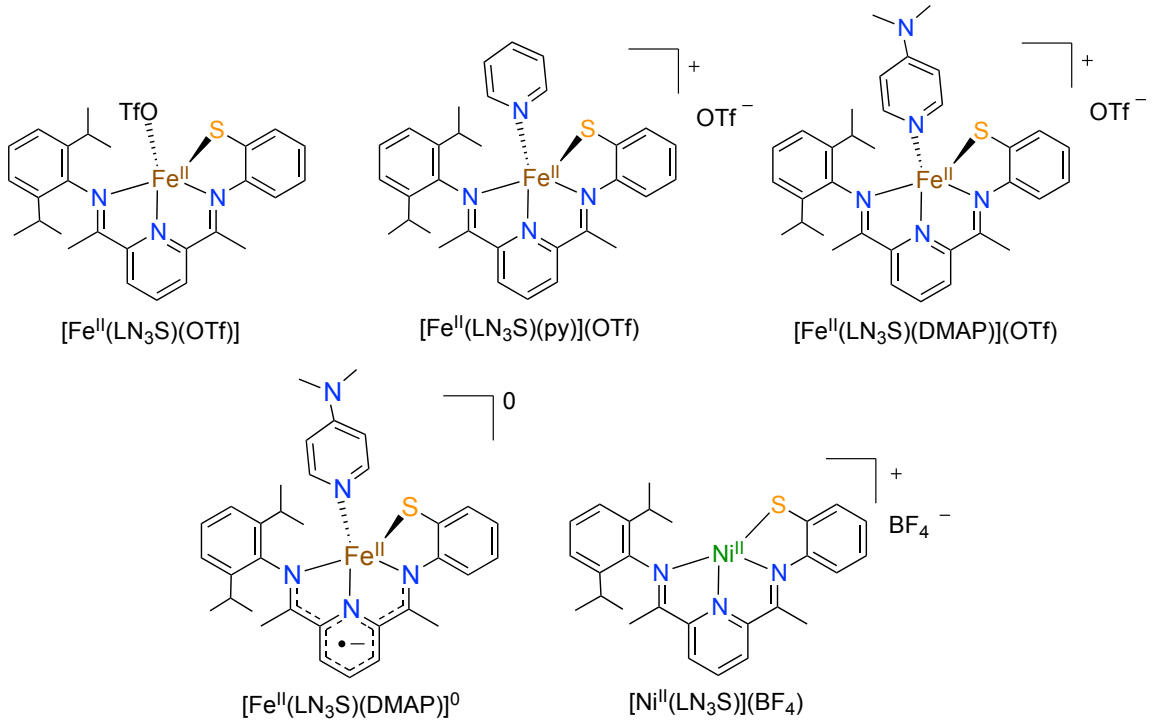

Figure 2. 1. Complexes discussed in this chapter.

The BIP platform is also well known to behave as a non-innocent ligand, allowing for the storage of multiple reducing equivalents on the ligand backbone. The BIP framework has been shown to accept up to three electrons, which are stabilized by delocalization over the conjugated ligand scaffold. [34-45] However, the reduced analogs of these BIP complexes are generally restricted to derivatives in which only minor changes to the aryl substitution patterns on the imino positions have been made, with no major modification of the chelating abilities of the BIP framework. There is significant interest in the development of non-innocent, polydentate ligands for their use as redox-active partners in combination with metal ions to assist with various chemical transformations such as the reduction of small-molecules (e.g. CO_2, N_2) and other redox reactions. With the thiolate-modified LN_3S system in hand, I thus wanted to determine if it could also function as a non-innocent ligand, perhaps stabilizing one or more reducing equivalents across the ligand backbone. A question to be addressed concerns the influence of the additional, covalently-linked phenylthiolate arm on the stability, spin delocalization, and spectroscopic and redox properties of possible (multi)reduced ligand-metal complexes. It is also of interest to determine if multiple reducing equivalents stored on both the ligand and the metal can be employed together for the activation of O_2, and how this combination will affect subsequent S- or metal-based oxygenation steps.

The new complexes $[Fe^{II}(LN_3S)(py)]OTf$, $[Fe^{II}(LN_3S)(DMAP)]OTf$ and $[Ni^{II}(LN_3S)]BF_4$, were shown to accept a single electron to give the respective mono-reduced products. In one case, successful crystallization of the mono-reduced species was achieved, and the structure of $[Fe(LN_3S)(DMAP)]^0$ was obtained by X-ray crystallography. A detailed experimental and computational (DFT) investigation into the

electronic and structural properties of $[Fe(LN_3S)(DMAP)]^0$, as well as the other mono-reduced analogs, was conducted, revealing a number of insights regarding the interplay between the structures and the electronic configurations of these complexes. The influence of the stong field thiolate donor, the extent of non-innocence in the BIP ligand, and the oxidation and spin state of the metal center are addressed. A major finding from these studies is that $[Fe(LN_3S)(DMAP)]^0$, based on experimental and computational results, is a mono-reduced bis(imino)pyridine complex with an intermediate-spin iron(II) center coupled with a stable ligand-based radical.

The O_2 reactivity of these complexes was also examined, and for the starting iron(II) complexes $[Fe^{II}(LN_3S)(py)]OTf$ and $[Fe^{II}(LN_3S)(DMAP)]OTf$, selective S-oxygenation to give sulfonato (RSO_3^-) products was observed, as seen previously for $[Fe^{II}(LN_3S)(OTf)]$.[24] In contrast, the mono-reduced complex $[Fe(LN_3S)(DMAP)]^0$ reacts with O_2, leading to a mixture of products that suggest both Fe- and S-oxygenation readily occur for this mono-reduced species. However, both the Ni^{II} complex $[Ni^{II}(LN_3S)](BF_4)$, and its mono-reduced analog, do not exhibit any S- or metal-based oxygenation in the presence of O_2 even after prolonged reaction times. This lack of reactivity is in contrast to the iron analogs, as well as some nickel-thiolate complexes that do react with O_2 to give S-oxygenated sulfinato and sulfonato products, although these reactions can be sluggish.[46-54]

2. 2. Experimental

General Procedures

All reagents were purchased from commercial vendors and used without further purification unless noted otherwise. All reactions were carried out under an atmosphere

of N_2 inside a glovebox or under Ar by standard Schlenk and vacuum line techniques. UV-visible spectra were recorded on an Agilent 8453 photodiode array spectrophotometer. Electron paramagnetic resonance (EPR) spectra were obtained on a Bruker EMX EPR spectrometer controlled with a Bruker ER 041 X G microwave bridge at 15 K. The EPR spectrometer was equipped with a continuous-flow liquid He cryostat and an ITC503 temperature controller made by Oxford Instruments, Inc. NMR was performed on a Bruker Avance 400 MHz FT-NMR spectrometer at 25 ºC. Elemental analysis was performed by Atlantic Microlab Inc., Norcross, GA. LDI-ToF mass spectra were obtained using a Bruker Autoflex III Maldi ToF/ToF instrument (Billerica, MA). Samples were dissolved in CH_2Cl_2 and deposited on the target plate in the absence of any added matrix. Samples were irradiated with a 355 nm UV laser and mass-analyzed by ToF mass spectrometry in the reflectron mode. $Fe^{II}(LN_3S)(OTf)$ was prepared according to literature procedure.[24] ^{57}Fe Mössbauer spectra were recorded on a Mössbauer spectrometer from SEE Co. (Science Engineering & Education Co., MN) equipped with a closed cycle refrigerator system from Janis Research Co. and SHI (Sumitomo Heavy Industries Ltd.). Approximately 10 mg of sample was placed in a custom sample holder made from Teflon and specifically designed for solid samples. Data were collected in constant acceleration mode in transmission geometry with an applied field of 47 mT parallel to the γ-rays. The zero velocity of the Mössbauer spectra refers to the centroid of the room temperature spectrum of a 25 μm metallic iron foil. Analysis of the spectra was conducted using the WMOSS program (SEE Co., formerly WEB Research Co., Edina, MN).

Computational Methods

Density functional theory calculations were performed by Devesh Kumar, Reza Latifi, and Sam P. de Visser using methods and procedures we have tested and calibrated previously.[55,56] The complexes were calculated in several possible spin states. The spin state ordering of transition metal complexes can be dependent on the DFT functional chosen, and thus we tested several different methods for our calculations. In an initial set of calculations, the unrestricted hybrid density functional method B3LYP was used in combination with an LACVP basis set on the metal and 6-31G on the rest of the atoms (basis set B1) for geometry optimizations and frequencies.[57-59] Optimized structures were employed as the starting point for single point calculations using (*a*) the LACV3P+ basis set on the metal and 6-311+G* on the rest of the atoms; (*b*) the M06/B1 method;[60] (*c*) B3LYP/B1 with the polarized continuum model with a dielectric constant of $e = 5.7$. In a second set of calculations we used the unrestricted BP86 density functional method[61,62] in combination with an LACV3P+ basis set on the metal and 6-311+G* on the rest of the atoms; basis set B2. Full geometry optimizations were run in *Jaguar* 7.6 and followed by a frequency calculation using these methods.[63] Single point calculations with dispersion corrected DFT were performed as proposed by Schwabe and Grimme,[64] however, this had a negligible effect on the spin state ordering and relative energies.

Synthesis of Reported Compounds

Synthesis of $[Fe^{II}(LN_3S)(py)]OTf$

Crystalline $[Fe^{II}(LN_3S)(OTf)]$ (100 mg, 0.16 mmol) was dissolved in CH_2Cl_2 and pyridine (15 μL, 0.19 mmol) was added. After stirring for 2 h, the solution was filtered through celite. Slow vapor diffusion of diethyl ether or layering with pentane gave the desired

product as dark brown plates suitable for X-ray diffraction in 97% yield (110 mg). ^{1}H NMR (CD_2Cl_2): δ 107.0, 95.4, 91.6, 45.2, 13.1, 11.6, 3.1, 1.3, -4.1, -10.3, -16.2, -30.4. LDIMS (+): *m/z* 484.2 ([M – py – OTf]$^+$). *Anal*. *Calc*. for $Fe^{II}(L_3NS)(py)(OTf)$ •CH_2Cl_2 ($C_{34}H_{37}Cl_2F_3FeN_4O_3S_2$): C, 51.20; H, 4.68; N, 7.02. Found: C, 51.21; H, 4.88; N, 7.67.

Synthesis of $[Fe^{II}(LN_3S)(DMAP)]OTf$

Crystalline $[Fe^{II}(LN_3S)(OTf)]$ (110 mg, 0.17 mmol) was dissolved in CH_2Cl_2 and DMAP (25 mg, 0.21 mmol) was added. After stirring for 2 h, the solution was filtered through celite. Slow vapor diffusion of diethyl ether or layering with pentane gave the product as black plates suitable for X-ray diffraction in 95% (125 mg). ^{1}H NMR (CD_2Cl_2): δ 128.0, 102.4, 92.8, 37.6, 19.4, 10.4, 8.4, 3.1, 1.4, -4.9, -7.7, -10.4, -13.7, -22.8. LDIMS (+): *m/z* 484.2 ([M – DMAP – OTf]). *Anal*. *Calc*. for $Fe^{II}(LN_3S)(DMAP)(OTf)$ ($C_{35}H_{40}F_3FeN_5O_3S_2$): C, 55.63; H, 5.34; N, 9.27. Found: C, 55.37; H, 5.29; N, 9.07.

Synthesis of $[Fe(LN_3S)(DMAP)]$• $2Et_2O$

Crystalline $[Fe^{II}(LN_3S)(DMAP)](OTf)$ (125 mg, 0.17 mmol) was combined with 1.5 equiv of 0.5% Na/Hg amalgam (6.0 mg Na^0, 1.15 g Hg) and suspended in 5 mL of Et_2O. Upon stirring, the insoluble starting material (3) slowly dissolves into solution as it reacts, giving a dark green/brown solution. After stirring for 2 h, the reaction mixture was filtered through celite, layered with pentane, and placed in the freezer for several days, giving the product as dark brown crystals suitable for X-ray diffraction (38 mg, 37% yield). UV-vis (nm): 566, 625, 785 (ε = 890 $M^{-1}cm^{-1}$). ^{1}H NMR (THF-d_8): δ 95.7, 33.8, 24.7, 5.8. ^{19}F NMR (THF-d_8): δ -79.3. EPR: g = 2.155, 2.057, 2.038. Mössbauer: $\Gamma_{L=R}$ = 0.8 mm s^{-1}, δ = 0.33 mm s^{-1}, ΔE_Q = 2.04 mm s^{-1}. *Anal*. *Calc*. for [4 + Et_2O + 0.25 NaOTf] ($C_{38.25}H_{50}F_{0.75}FeN_5Na_{0.25}O_{1.75}S_{1.25}$): C, 63.48; H, 6.96; N, 9.68. Found: C, 62.85; H, 6.74; N,

9.73. Crystalline samples of $[Fe^{II}(LN_3S)(DMAP)]\bullet 2Et_2O$ co-precipitate with a small amount of white solid impurity that could not be separated from the product. The impurity was identified as NaOTf by ^{19}F NMR (**Figure 2. 24**). Inclusion of 0.25 equiv of NaOTf was necessary to obtain a good fit for elemental analysis.

Synthesis of $[Ni^{II}(LN_3S)]BF_4$

An amount of 2-(O=CMe)-6-(2,6-(^{i}Pr2-C_6H_3N=CMe)-C_5H_3N (50 mg, 0.155 mmol) and $Ni^{II}(BF_4)_2\bullet 6H_2O$ (55.4 mg, 0.163 mmol) was suspended in EtOH (5 mL) and heated at 80 ºC for 30 min. The solids slowly dissolved to give a deep green solution, and then a solution of 2-aminothiophenol (17 μL, 0.155 mmol) and triethylamine (22 μL, 0.155 mmol) in EtOH (1 mL) was added to the reaction mixture. The reaction was allowed to stir at 80 ºC for 24 h before being cooled to room temperature and concentrated. The resulting solid residue was brought into a glovebox where it was redissolved in a minimum amount of CH_2Cl_2 and filtered through Celite. Slow vapor diffusion of diethyl ether into the filtrate yielded the product (96 mg, 94% yield) as dark red crystals suitable for X-ray analysis, together with colorless crystals of $Et_3NH\bullet BF_4$. Samples for elemental analysis were prepared by manual separation of crystals of $[Ni^{II}(L_3NS)](BF_4)$ from the colorless $Et_3NH\bullet BF_4$ crystals. ^1H NMR (CD_2Cl_2): δ 8.30 (br, 1H), 7.89 (br, 2H), 7.35 (t, 1H), 7.22 (d, 2H), 7.09 (d, 1H), 6.92 (t, 1H), 6.82-6.72 (m, 2H), 3.18 (br), 2.69 (s, 3H), 2.14 (s, 3H), 2.14 (s, 3H), 1.50 (d, 6H), 1.33 (br), (1.17 (d, 6H). LDIMS (+): *m/z* 488.3 $[M - BF_4]^+$. *Anal. Calc.* for $[Ni^{II}(L_3NS)](BF_4)\bullet CH_2Cl_2$ ($C_{28}H_{32}BCl_2F_4N_3NiS$): Predicted: C, 51.03; H, 4.89; N, 6.38. Found: C, 51.28; H 4.76; N, 6.66.

O_2 Reactivity

Reactions of $[Fe^{II}(LN_3S)(py)](OTf)$, $[Fe^{II}(LN_3S)(DMAP)](OTf)$, and $[Ni^{II}(L_3NS)](BF_4)$ with excess O_2 were conducted as previously reported for $[Fe^{II}(LN_3S)(OTf)]$ in CH_2Cl_2.[24] The one-electron reduced complexes were reacted with O_2 by freshly preparing solutions of $[Fe^{II}(LN_3S)(DMAP)]^0$ or reduced $[Ni^{II}(L_3NS)](BF_4)$ via Na/Hg amalgam in Et_2O followed by filtration through Celite, as described for the synthesis of $[Fe^{II}(LN_3S)(DMAP)]^0$. Reaction mixtures following O_2 addition were then analyzed directly by LDI-MS.

2. 3. Results and Discussion

Synthesis of Iron(II) and Nickel(II) Complexes

The synthesis of the unsymmetrical, thiolate-ligated complex $[Fe^{II}(LN_3S)(OTf)]$ was accomplished by reacting the imino-ketone precursor[65] 2-(O=CMe)-6-(2,6-($^iPr_2$-C_6H_3N=CMe)-C_5H_3N with the commercially available 2-aminothiophenol and $Fe(OTf)_2$ in a metal-assisted template reaction as previously described.[24] We sought to determine if this complex could be used as a precursor to generate Fe^{II} complexes with biologically relevant $[N_4S]$ donor sets via substitution at the OTf^- position. Displacement of the OTf^- ligand in $[Fe^{II}(LN_3S)(OTf)]$ was an attractive route when compared to the more challenging strategy involving multi-step organic synthesis to produce covalently linked N_4S-donating ligands (**Scheme 2. 1**).[26,66-68] Addition of one equivalent of either pyridine or *N*,*N'*-dimethylaminopyridine (DMAP) to dark red-purple $[Fe^{II}(LN_3S)(OTf)]$ in CH_2Cl_2 at room temperature does not result in any color change. However, vapor diffusion of diethyl ether into the reaction mixture after stirring for 2 h afforded single crystals as dark brown plates of the pyridine-ligated $[Fe^{II}(LN_3S)(py)](OTf)$, and black plates in the case of

the DMAP-ligated [$Fe^{II}(LN_3S)$(DMAP)](OTf). These crystals yielded the X-ray structures of [$Fe^{II}(LN_3S)$(py)](OTf) and [$Fe^{II}(LN_3S)$(DMAP)](OTf) (**Figure 2. 2** and **Figure 2. 3**) (vide infra), confirming that the OTf^- anion was displaced by the pyridine derivatives. For large-scale preparations of [$Fe^{II}(LN_3S)$(py)](OTf) and [$Fe^{II}(LN_3S)$(DMAP)](OTf), layering of pentane was used in place of vapor diffusion of Et_2O to give both [$Fe^{II}(LN_3S)$(py)](OTf) and [$Fe^{II}(LN_3S)$(DMAP)](OTf) in high yield.

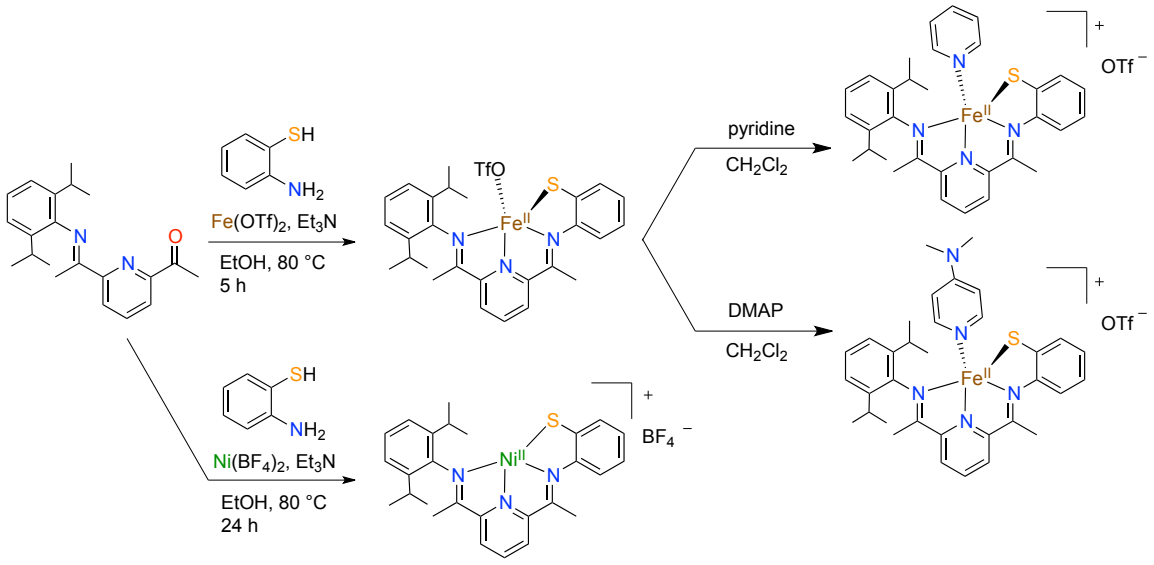

Scheme 2. 1. Synthesis of Iron(II) and Nickel(II) Complexes.

The synthesis of the Ni^{II} analog of [$Fe^{II}(LN_3S)$(OTf)] was also targeted for comparison of spectroscopic features and its reactivity toward O_2. The use of $Ni^{II}(BF_4)_2$ in place of $Fe^{II}(OTf)_2$ in (**Scheme 2. 1**) results in a dark green solution. Vapor diffusion of Et_2O afforded dark red crystals together with clusters of large colorless needles. The red crystals were separated by hand and analyzed by X-ray crystallography revealing the Ni^{II} complex [$Ni^{II}(LN_3S)$](BF$_4$) (see **Figure 2. 4**). The colorless crystals were presumed to be $Et_3NH^+BF_4^-$, the expected byproduct of the template reaction. Peaks corresponding to $Et_3NH^+BF_4^-$ were confirmed in the ^{1}H NMR of [$Ni^{II}(LN_3S)$](BF$_4$) (**Figure 2. 6**). The co-

precipitation of $Et_3NH^+BF_4^-$ could not be avoided even upon successive recrystallizations, and therefore it was necessary to isolate complex $[Ni^{II}(LN_3S)](BF_4)$ by manual separation of crystalline material for elemental analysis and further reactivity studies.

X-ray Structures of the Iron(II) and Nickel(II) Complexes

The X-ray structures for the iron(II) complexes $[Fe^{II}(LN_3S)(py)](OTf)$ and $[Fe^{II}(LN_3S)(DMAP)](OTf)$ are shown in **Figure 2. 2** and **Figure 2. 3**, respectively. Selected bond distances and angles are given in **Table 2. 1** and **Table 2. 2**. The structures reveal that the triflate ligand has been displaced in each case by the heterocyclic N donor to afford the 5-coordinate $Fe^{II}(N_4S(\text{thiolate}))$ products. There is a clear preference for forming the 5-coordinate complexes over the 6-coordinate species, in which the OTf^- would be retained in the first coordination sphere. The Fe-N distances of 2.073(5) – 2.196(5) Å for $[Fe^{II}(LN_3S)(py)](OTf)$ and 2.0667(14) – 2.2179(15) Å for $[Fe^{II}(LN_3S)(DMAP)](OTf)$ are indicative of high-spin (S = 2) Fe^{II} complexes. The pyridine-derived Fe-N bonds are shorter than the imine nitrogen-to-iron distances in both $[Fe^{II}(LN_3S)(py)](OTf)$ and $[Fe^{II}(LN_3S)(DMAP)](OTf)$, whereas the Fe-S bonds are nearly identical. There is minimal effect of substitution of the *para* position of the pyridine derivatives on the bond lengths in $[Fe^{II}(LN_3S)(py)](OTf)$ and $[Fe^{II}(LN_3S)(DMAP)](OTf)$. An analysis of the bond angles for $[Fe^{II}(LN_3S)(py)](OTf)$ and $[Fe^{II}(LN_3S)(DMAP)](OTf)$ and their t values ($[Fe^{II}(LN_3S)(py)](OTf)$: t = 0.15; $[Fe^{II}(LN_3S)(DMAP)](OTf)$: t = 0.18; where $\tau = 0$ for square pyramidal and $\tau = 1$ for trigonal bipyramidal)[69] show that in both cases the Fe^{II} ions are held in a distorted square pyramidal geometry, with the pyridine derivatives occupying the axial position. The molecular structure of **1** has been reported,[24] and select bond distances are reproduced in **Table 2. 1**. The Fe-N distances are very

similar to those found in $[Fe^{II}(LN_3S)(py)](OTf)$ and $[Fe^{II}(LN_3S)(DMAP)](OTf)$, whereas the Fe-S distance appears slightly shorter. The parent complex, $[Fe^{II}(LN_3S)(OTf)]$, exhibits a more idealized square pyramidal geometry than $[Fe^{II}(LN_3S)(py)](OTf)$ or $[Fe^{II}(LN_3S)(DMAP)](OTf)$, and a comparison of the τ values for these complexes reveals that the geometry becomes more distorted from square pyramidal with increasing axial ligand donor strength ($\tau_{(OTf)} = 0.12 < \tau_{(py)} = 0.15 < \tau_{(DMAP)} = 0.18$). In all three complexes, the pyridine diimine backbone remains planar, while the ferrous ion sits 0.276 Å above the N_3 plane for $[Fe^{II}(LN_3S)(OTf)]$, but less out of plane for $[Fe^{II}(LN_3S)(py)](OTf)$ (0.116 Å) and $[Fe^{II}(LN_3S)(DMAP)](OTf)$ (0.200 Å). In addition, the thiolate donor never sits in the ideal equatorial position, but rather lies well below the N_3 plane. For $[Fe^{II}(LN_3S)(OTf)]$ and $[Fe^{II}(LN_3S)(py)](OTf)$ the N_{plane}–S distance is 0.824 and 1.18 Å, respectively, while for $[Fe^{II}(LN_3S)(DMAP)](OTf)$ it is significantly more distorted with $d(N_{plane}–S)$ = 1.8 Å. The C_{imine}-N and C_{imine}-C_{ipso} bond distances for the ligand are similar for all three complexes (**Table 2. 1**), and are consistent with a neutral-ligand bis(imino)pyridine backbone ($LN_3S^–$).[34,43]

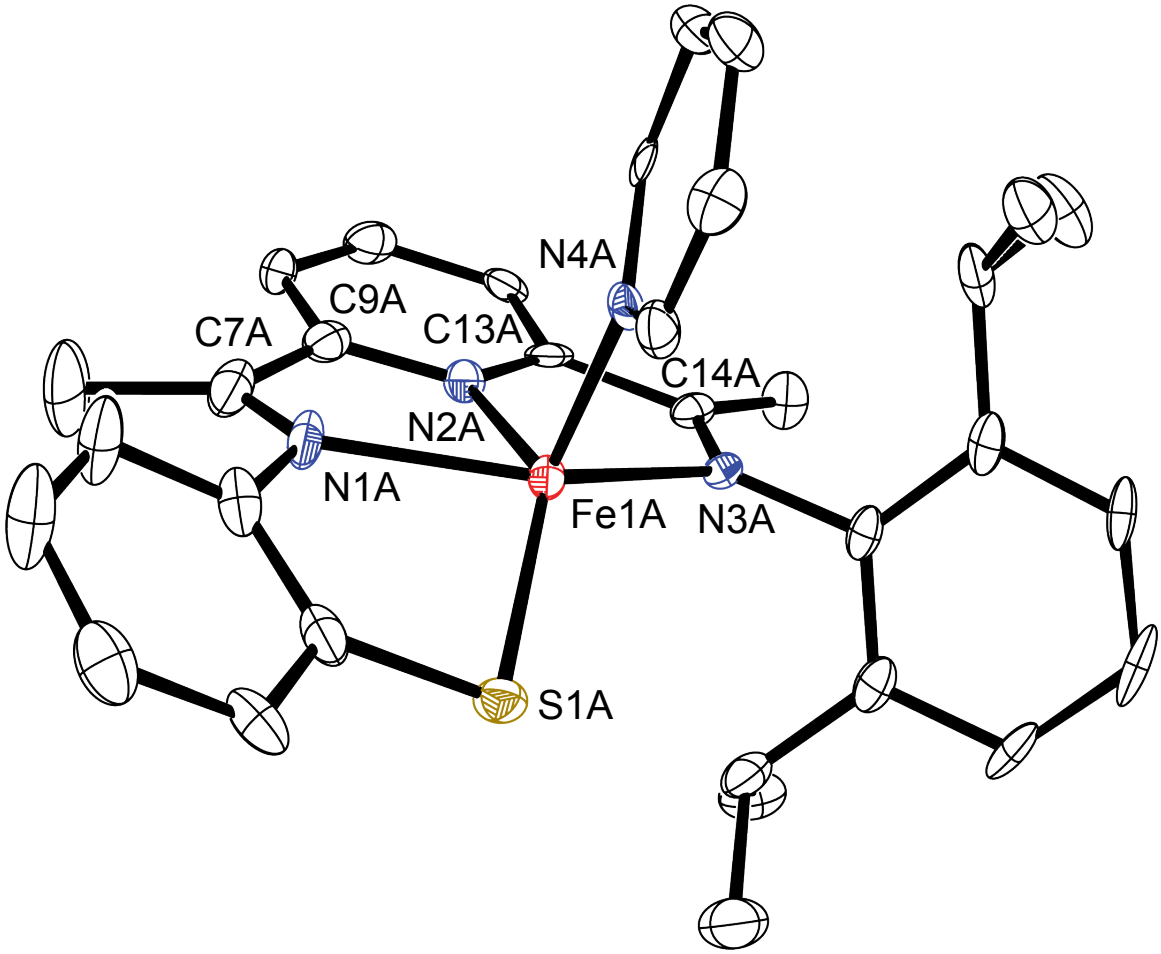

Figure 2. 2. Displacement ellipsoid plot for the cation of $[Fe^{II}(LN_3S)(py)](OTf)$ (50% probablility level). The H atoms are removed for clarity.

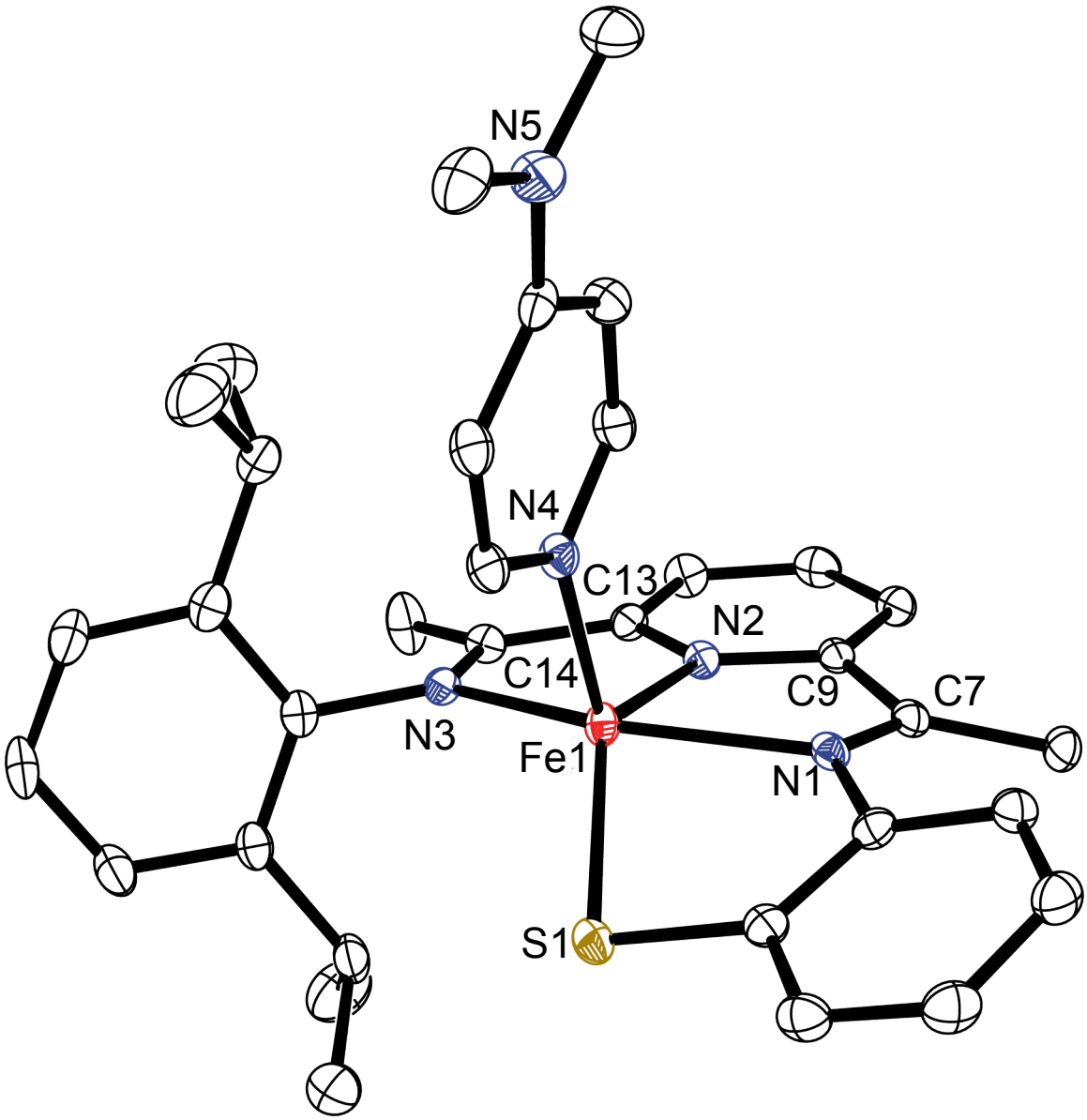

Figure 2. 3. Displacement ellipsoid plot for the cation of $[Fe^{II}(LN_3S)(DMAP)](OTf)$ (50% probablility level). The H atoms are removed for clarity.

Table 2. 1. Selected Bond Distances (Å) for $[Fe(LN_3S)]^{n+}$ Complexes

	$[Fe^{II}(LN_3S)(OTf)]^a$	$[Fe^{II}(LN_3S)(py)]OTf$	$[Fe^{II}(LN_3S)(DMAP)]OTf$	$[Fe^{II}(LN_3S)(DMAP)]^0$
Fe1–N1	2.188(2)	2.173(5)	2.1859(15)	1.9255(15)
Fe1–N2	2.072(2)	2.090(5)	2.0960(14)	1.8278(15)
Fe1–N3	2.184(2)	2.196(5)	2.2179(15)	1.9179(16)
Fe1–N4	N/A	2.073(5)	2.0667(14)	2.0508(16)
Fe1–S1	2.2942(8)	2.3246(18)	2.3295(5)	2.2179(5)
Fe–O1	2.0870(18)	N/A	N/A	N/A
N1–C7 (imine)	1.293(3)	1.298(8)	1.292(2)	1.347(2)
C7(imine)– C9(ipso)	1.480(4)	1.485(9)	1.486(2)	1.432(3)
C9(ipso)–N2(pyr)	1.343(3)	1.342(8)	1.341(2)	1.376(2)
N3–C14(imine)	1.284(3)	1.275(7)	1.290(2)	1.341(2)
C14(imine)–C13(ipso)	1.483(4)	1.494(8)	1.487(3)	1.426(3)
C13(ipso)–N2(pyr)	1.334(3)	1.334(8)	1.343(2)	1.381(2)

[a]Ref 24

Table 2. 2. Selected Bond Angles (°) for $[Fe(LN_3S)]^{n+}$ Complexes

	$[Fe^{II}(LN_3S)(py)]OTf$	$[Fe^{II}(LN_3S)(DMAP)]OTf$	$[Fe^{II}(LN_3S)(DMAP)]^0$
N4–Fe1–N2	109.79(19)	112.91(6)	99.92(6)
N4–Fe1–N1	95.3(2)	99.69(6)	95.84(6)
N2–Fe1–N1	74.0(2)	73.08(5)	81.26(7)
N4–Fe1–N3	99.29(19)	99.82(6)	99.88(6)
N2–Fe1–N3	73.4(2)	73.94(6)	80.65(7)
N1–Fe1–N3	147.24(19)	146.17(5)	157.78(7)
N4–Fe1–S1	106.05(15)	107.20(4)	105.25(5)
N2–Fe1–S1	138.08(14)	135.18(4)	153.58(5)
N1–Fe1–S1	81.79(15)	81.40(4)	88.27(5)
N3–Fe1–S1	121.28(13)	118.28(4)	102.49(5)

The X-ray structure for the Ni^{II} complex $[Ni^{II}(LN_3S)](BF_4)$ is shown in **Figure 2. 4**. Selected bond distances and angles for $[Ni^{II}(LN_3S)](BF_4)$ are given in **Table 2. 3**. The molecular structure of $[Ni^{II}(LN_3S)](BF_4)$ shows a square planar geometry for the Ni^{II} ion. The observed Ni-N distances are 1.8151(14) – 1.9159(15) Å, and are somewhat shorter (~0.1 – 0.4 Å) than other BIP-derived nickel(II) complexes.[45,70-73] The Ni-S distance of 2.1386(5) Å is significantly shorter than the Fe^{II}–S distances seen for the iron(II) complexes, as are the Ni–N distances. The bond angles about the Ni^{II} center deviate slightly from the idealized square-planar geometry (82.44 – 102.37°), likely due to the constraints imposed by the three 5-membered chelate rings. The Ni^{II} ion and S atom sit directly in the plane of the bis(imino)pyridine ligand as seen by Ni–N_3(plane) and S-N_3(plane) distances of 0.030 Å and 0.082 Å, respectively. This structure contrasts those

found for the iron(II) derivatives, where both the metal ion and sulfur donor lie significantly out of the bis(imino)pyridine plane for these 5-coordinate complexes.

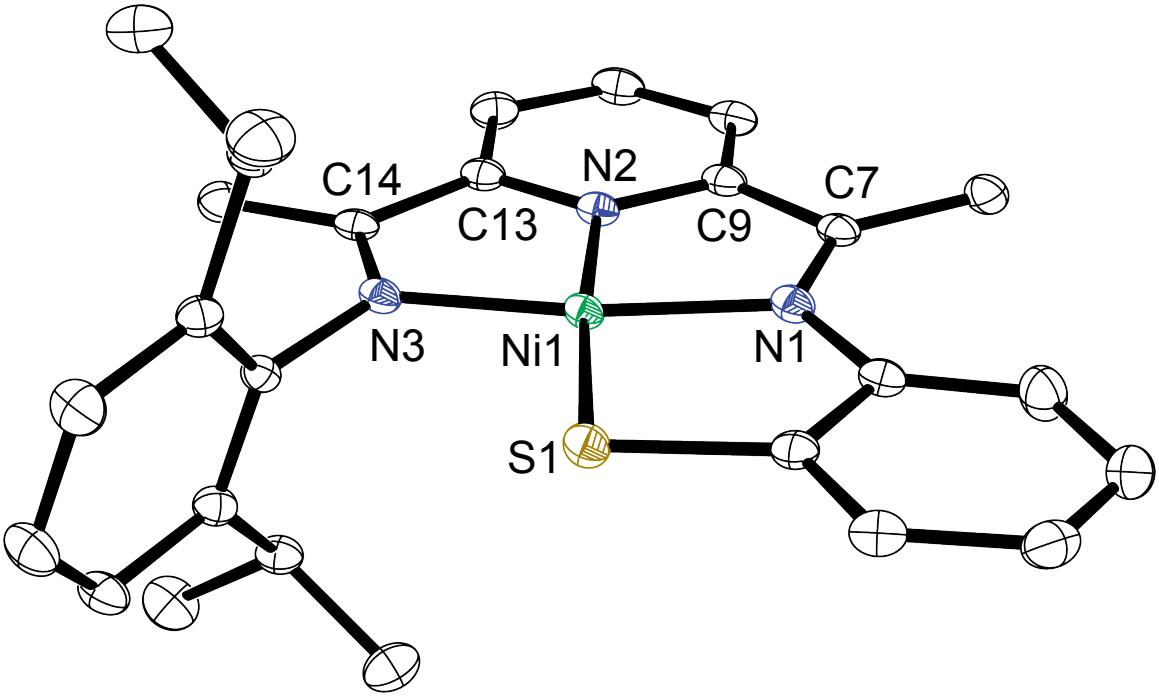

Figure 2. 4. Displacement ellipsoid plot for the cation of $[Ni^{II}(LN_3S)](BF_4)$ (50% probablility level). The H atoms are removed for clarity.

Table 2. 3. Selected Bond Distances (Å) and Angles (°) for $[Ni^{II}(LN_3S)](BF_4)$

	distance (Å)		angle (°)
Ni1–N1	1.8981(15)	N2–Ni1–N1	83.56(6)
Ni1–N2	1.8151(14)	N2–Ni1–N3	82.44(6)
Ni1–N3	1.9159(15)	N1–Ni1–N3	165.91(6)
Ni1–S1	2.1386(5)	N2–Ni1–S1	175.17(5)
N1–C7 (imine)	1.312(2)	N1–Ni1–S1	91.64(5)
C7(imine)–C9(ipso)	1.480(2)	N3–Ni1–S1	102.37(5)
C9(ipso)–N2(pyr)	1.341(2)		.
N3-C14(imine)	1.299(2)		
C14(imine)–C13(ipso)	1.480(2)		
C13(ipso)–N2(pyr)	1.338(2)		

NMR Spectroscopy

The paramagnetic ^{1}H NMR spectra for the $[Fe^{II}(LN_3S)(X)]^{n+}$ complexes in CD_2Cl_2 are shown in **Figure 2. 5**. Each complex exhibits sharp, paramagnetically shifted peaks over a broad range (130 to -30 ppm), indicative of high-spin (S = 2) Fe^{II} complexes. Detailed ^{1}H NMR assignments have been made for bis(imino)pyridine iron(II) complexes that carry the same aryl imino substituents.[34,65,74,75] These data can be used as a guide for interpreting the spectra for the current complexes, although the unsymmetrical structures of the $[Fe^{II}(LN_3S)(X)]^{n+}$ complexes make their ^{1}H NMR patterns too difficult to definitively assign. For all three complexes, the downfield region (130 to 80 ppm) contains three sharp peaks, with the exception of $[Fe^{II}(LN_3S)(DMAP)](OTf)$, in which the most downfield resonance at 130 ppm is significantly broadened. In comparison to

symmetrical (BIP)FeX_2 complexes, two of the three resonances in this region can be assigned to the *meta* and *para* pyridyl backbone protons, with the most intense resonance (82.8, 95.4, and 92.8 ppm for $[Fe^{II}(LN_3S)(OTf)]$, $[Fe^{II}(LN_3S)(py)](OTf)$, and $[Fe^{II}(LN_3S)(DMAP)](OTf)$, respectively) likely arising from the *meta* protons that are apparently not split in the local symmetry. We tentatively assign the third resonance to a proton on the phenylthiolate ring. No peaks appear in the spectrum for $[Fe^{II}(LN_3S)(OTf)]$ between 80 and 20 ppm, whereas $[Fe^{II}(LN_3S)(py)](OTf)$ shows a broad peak at 45.2 ppm and $[Fe^{II}(LN_3S)(DMAP)](OTf)$ exhibits a sharp peak at 37.6 ppm and a broad feature at 43.5 ppm. The latter peaks for $[Fe^{II}(LN_3S)(py)](OTf)$ and $[Fe^{II}(LN_3S)(DMAP)](OTf)$ can be assigned to the axial pyridine ligands, which are absent in $[Fe^{II}(LN_3S)(OTf)]$. This assignment was confirmed by the generation in situ of $[Fe^{II}(LN_3S)(py)](OTf)$ with the addition of one equiv of pyridine-d_5 to $[Fe^{II}(LN_3S)(OTf)]$. As seen in **Figure 2. 5**, the spectrum for deuterated $[Fe^{II}(LN_3S)(py\text{-}d_5)](OTf)$ is a good match for $[Fe^{II}(LN_3S)(py)](OTf)$ except for the disappearance of the resonance at 45.2 ppm. The broadness of the py peak and the absence of distinct signals for the *ortho*, *meta* and *para* protons suggest that the py ligand in $[Fe^{II}(LN_3S)(py)](OTf)$ is labile on the NMR timescale. In contrast two peaks are seen for $[Fe^{II}(LN_3S)(DMAP)](OTf)$ in the region of the axial DMAP donor, and one is relatively sharp, suggesting that DMAP is significantly less labile than py, and consistent with it being a more strongly donating py derivative. Further upfield, the diisopropyl methyl groups can easily be assigned to the intense singlets between 1.20 – 1.36 ppm, and the peaks found from -14 to -16 ppm are assigned to the *para* C-H on the iPr_2Ph substituent based on earlier work.[34,65,74,75] The upfield

resonances at -21.9, -30.3, and -22.8 ppm, likely arise from the isopropyl methine protons.

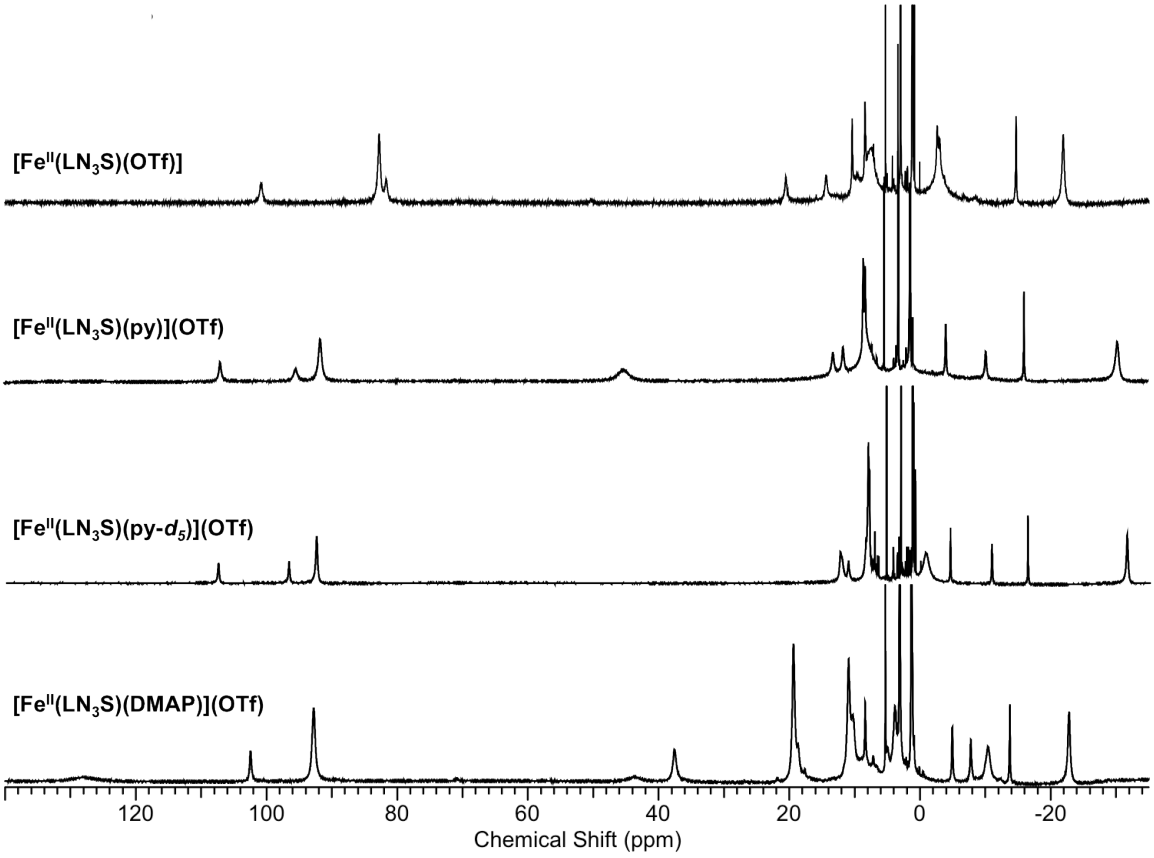

Figure 2. 5. ^{1}H-NMR spectra of $[Fe^{II}(LN_3S)(L)]^{n+}$ complexes in CD_2Cl_2 at 25 °C.

The ^{1}H NMR spectrum of the diamagnetic $[Ni^{II}(LN_3S)](BF_4)$ is shown in **Figure 2. 6**. The peaks for the pyridyl protons are seen at δ 8.30 and 7.88, and the diisopropylphenyl peaks are assigned to δ 7.35 (t, 1H) and 7.22 (d, 2H). Other peaks in the aromatic region include δ 7.09 (d, 1H), 6.92 (t, 1H), and overlapping peaks at 6.79 (d, 1H) and 6.75 (t, 1H), which can be attributed to the phenylthiolate ring. The peaks found at 3.18 and 1.33 ppm come from a small amount of $Et_3NH^+BF_4^-$ impurity (vide supra), and the peak at 3.18 ppm likely masks the isopropyl methine C-H peaks for $[Ni^{II}(LN_3S)](BF_4)$. The ketimine CH_3 resonances are located at δ 2.70 (s, 3H) and 2.14 (s,

3H). There are two distinct isopropyl CH_3 peaks found at δ 1.50 (d, 6H) and 1.17 (d, 6H), indicating restricted rotation of the diisopropylphenyl substituent about the N_{imino}–C_{ipso} bond.

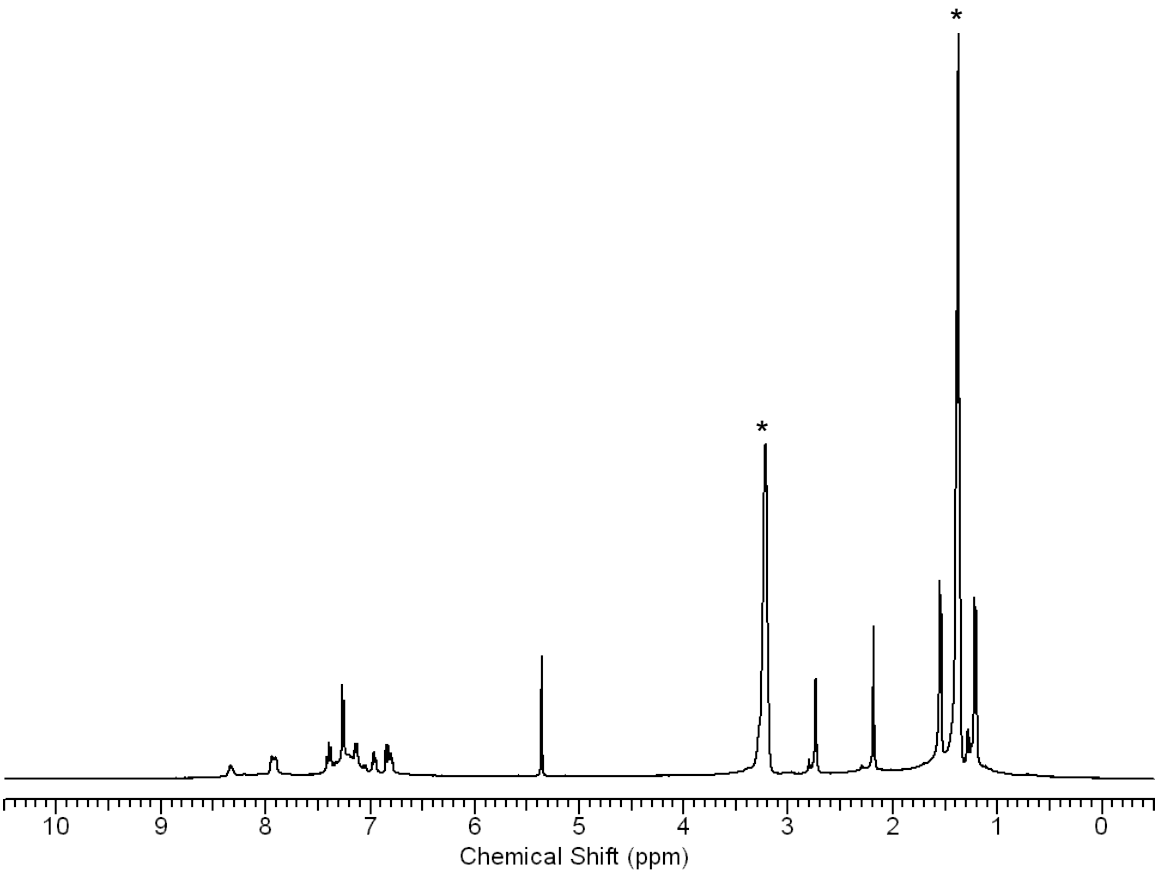

Figure 2. 6. ^{1}H NMR spectrum of $[Ni^{II}(LN_3S)](BF_4)$ in CD_2Cl_2 at 25 °C. $Et_3NH^+BF_4^-$ impurity (*).

Electrochemistry

Cyclic voltammetry of the iron(II) and nickel(II) complexes was measured to gain insights regarding the influence of the exogenous py derivatives and covalently tethered phenylthiolato donor on the redox properties of these complexes. The cyclic voltammograms for the iron(II) and nickel(II) compounds are shown in **Figure 2. 7**. The triflate complex $[Fe^{II}(LN_3S)(OTf)]$ and the pyridine complex $[Fe^{II}(LN_3S)(py)](OTf)$

exhibit quasireversible waves at $E_{½}$ = -1.1 V, while the DMAP complex $[Fe^{II}(LN_3S)(DMAP)](OTf)$ reveals a more negative $E_{½}$ = -1.2 V. No other obvious redox processes for these complexes are present within the solvent window for CH_3CN. The fact that the $E_{½}$ values for $[Fe^{II}(LN_3S)(OTf)]$ and $[Fe^{II}(LN_3S)(py)](OTf)$ are the same suggest that the axial pyridine donor in $[Fe^{II}(LN_3S)(py)](OTf)$ does not exhibit any influence on the redox potential, but is also consistent with the pyridine ligand dissociating to some extent in solution as indicated by the NMR data. Substitution of py for DMAP does have a clear impact, shifting the redox potential by ~100 mV more negative in $[Fe^{II}(LN_3S)(DMAP)](OTf)$ as compared to $[Fe^{II}(LN_3S)(py)](OTf)$. This result is consistent with DMAP being a more strongly donating ligand than unsubstituted pyridine. The nickel(II) complex is the easiest to reduce in the series, with $E_{1/2}$ = -0.9 V.

Non-innocent BIP ligands have been shown previously to undergo up to three sequential reductions in which the electrons are delocalized over the BIP backbone.[34-45] The negative $E_{1/2}$ values for the $[Fe^{II}(LN_3S)(X)]^{n+}$ complexes are consistent with ligand-based reduction, and covalent attachment of the phenylthiolate group exerts a strong influence on the redox properties in comparison to other BIP complexes.[25] The non-thiolate-ligated BIP complexes typically show two reversible reduction waves, whereas these complexes exhibit only one reduction process, suggesting that the next reduction, if it exists, lies outside the solvent window. Similarly, the nickel(II) analogue $[Ni^{II}(LN_3S)](BF_4)$ exhibits only one redox process at -0.9 V, which is within the range of ligand-based reductions for the iron complexes, but is more positive by $\geq$ 200 mV. These data show that the BIP-derived ligand of the Ni^{II} complex is significantly easier to reduce than the $[Fe^{II}(LN_3S)(X)]^{n+}$ derivatives.

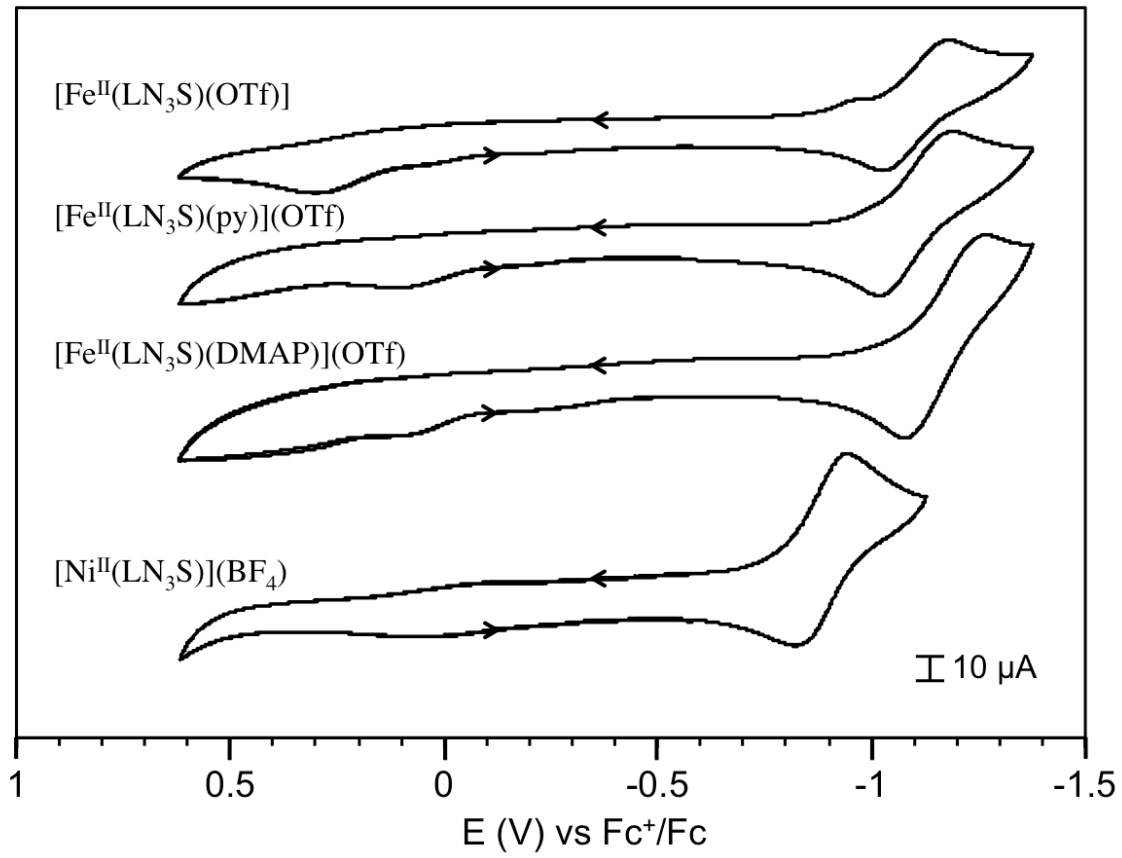

Figure 2. 7. Cyclic voltammograms of compounds iron(II) and nickel(II) LN_3S complexes in MeCN. $E_{½}$: $[Fe^{II}(LN_3S)(OTf)]$ = -1.1 V, $[Fe^{II}(LN_3S)(py)](OTf)$ = -1.1 V, $[Fe^{II}(LN_3S)(DMAP)](OTf)$ = -1.2 V, $[Ni^{II}(LN_3S)](BF_4)$ = -0.9 V; ΔE_p: $[Fe^{II}(LN_3S)(OTf)]$ = 120 mV, $[Fe^{II}(LN_3S)(py)](OTf)$ = 130 mV, $[Fe^{II}(LN_3S)(DMAP)](OTf)$ = 130 mV, $[Ni^{II}(LN_3S)](BF_4)$ = 66 mV. Working electrode: glassy carbon; counter electrode: platinum; reference electrode: Ag/Ag^+. Electrolyte: $LiClO_4$, 100 mM. Scan rate: 100 mV/s.

One-Electron Reduction of the Iron(II) and Nickel(II) Complexes

A summary of the possible redox transformations for the phenylthiolate-appended $[M(LN_3S)(L)]^+$ complexes are shown in **Scheme 2. 2**. The CV data (*vide supra*) show well-separated, quasi-reversible reduction waves, indicating that one-electron-reduced

complexes should be synthetically accessible. The lack of a second reduction process suggests that the one-electron-reduced complexes can be isolated without the complication of forming two-electron-reduced species, in contrast to other BIP complexes.[39] A number of methods have been employed to reduce M^{n+}(BIP) complexes, including treatment with aluminum/lithium alkyl reagents, $NaBEt_3H$, KC_8, and Na/Hg amalgam.[35,70,76,77] The latter method was a convenient choice for the controlled reduction of the thiolate-ligated complexes described here.

Reduction of the DMAP complex $[Fe^{II}(LN_3S)(DMAP)](OTf)$ was accomplished by stirring a suspension of $[Fe^{II}(LN_3S)(DMAP)](OTf)$ in Et_2O over a slight excess of 0.5% Na/Hg amalgam, affording the one-electron-reduced $[Fe(LN_3S)(DMAP)]^0$ as shown in **Scheme 2. 3**. The progress of the reaction is easily followed by the colorless ethereal suspension of $[Fe^{II}(LN_3S)(DMAP)](OTf)$ converting to a deep green, homogeneous solution. The UV-vis spectrum following the Na/Hg reduction is shown in **Figure 2. 8**, where the solvent is THF instead of Et_2O to maintain the solubility of $[Fe^{II}(LN_3S)(DMAP)](OTf)$. Distinct features appear at 566, 625, and 785 nm that are indicative of $[Fe(LN_3S)(DMAP)]^0$. It should be noted that solutions of $[Fe(LN_3S)(DMAP)]^0$ in either THF or Et_2O are extremely air-sensitive, and will decompose upon prolonged standing even at -35 °C in a drybox freezer, as seen by spontaneous conversion of dark green solutions of $[Fe(LN_3S)(DMAP)]^0$ to a brown precipitate. Crystals for X-ray diffraction can be grown from layering of pentane into Et_2O at -35 °C, but the crystals must be obtained within 48 hours or decomposition occurs and no crystalline product will form. Crystalline $[Fe(LN_3S)(DMAP)]^0$ is also difficult to isolate outside of the mother liquor without further decomposition. Attempts

to scale up the reaction failed to give crystalline product, instead leading to more rapid decomposition.

A number of reduced Fe(BIP) complexes have been reported, most involving doubly-reduced species relative to the M^{II} complexes analogous to $[Fe^{II}(LN_3S)(L)]^{n+}$. However, a few examples of mono-reduced and triply-reduced, Fe(BIP) complexes have been described.[37-39] The mono-reduced Fe(BIP) complexes were prepared by either reduction of iron(II) starting materials (e.g. $[(^{iPr}BIP)Fe^{II}Cl_2] + e^- \rightarrow [(^{iPr}BIP)FeCl]^0$), or oxidation of doubly-reduced (formally Fe^0) Fe(BIP) complexes (e.g. $[(^{iPr}BIP)Fe(N_2)]^0 \rightarrow [(^{iPr}BIP)Fe(OEt_2)]^+ + e^-$), and in both cases yield 4-coordinate iron complexes.[37-39] The 5-coordinate complexes $[(^{iPr}BIP)Fe(Br)(THF)]$ and $[(^{iPr}BIP)Fe(CO)_2]^+$, were prepared via one-electron oxidation of their respective doubly-reduced precursors, while $[(^{Et}BIP)Fe(Cl)(Et_2O)]$ was prepared by reduction of the starting material.[37,40,78] However, the doubly-reduced species in general are more easily obtained than the mono-reduced analogs, and careful stoichiometric control must be used to synthesize mono-reduced complexes. In contrast, the putative doubly-reduced analog of $[Fe^{II}(LN_3S)(DMAP)](OTf)$ is not accessible as seen by electrochemistry, and thus reduction of $[Fe^{II}(LN_3S)(DMAP)](OTf)$ leads to the selective isolation of a rare 5-coordinate, mono-reduced complex.

Attempted reductions of the iron(II) complexes $[Fe^{II}(LN_3S)(OTf)]$ and $[Fe^{II}(LN_3S)(py)](OTf)$ suspended in Et_2O led to similar deep green solutions as seen for $[Fe(LN_3S)(DMAP)]^0$, but the products were highly soluble even in mixtures with pentane, and crystals could not be isolated. The nickel(II) complex $[Ni^{II}(LN_3S)](BF_4)$, which is insoluble in Et_2O, reacts similarly with Na/Hg amalgam to give a homogenous bright

green solution which presumably contains the mono-reduced nickel analog. This product was also highly soluble and could not be crystallized, but provides a useful comparison to iron-containing $[Fe(LN_3S)(DMAP)]^0$, and therefore it was prepared in situ from $[Ni^{II}(LN_3S)](BF_4)$ and characterized by EPR spectroscopy (vide infra).

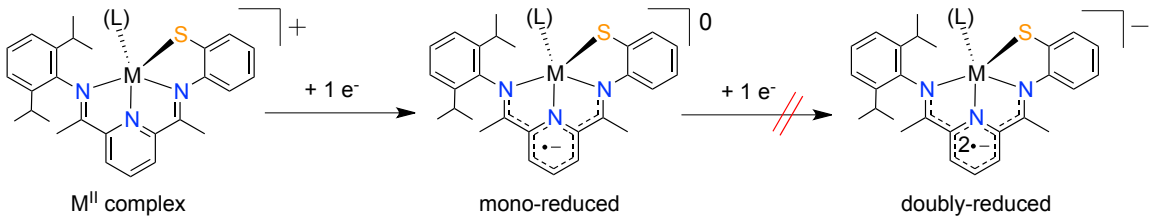

Scheme 2. 2. Reduction of Thiolate-Incorporated M^{II} Bis(imino)pyridine Complexes

X-ray Structure of Mono-Reduced $[Fe(LN_3S)(DMAP)]^0$

The crystal structure of $[Fe(LN_3S)(DMAP)]^0$ (**Figure 2. 9**) shows an overall neutral iron complex with no additional counterions. Charge balance therefore indicates that this complex is the one-electron-reduced analog of the cation of $[Fe^{II}(LN_3S)(DMAP)](OTf)$. The DMAP is retained in the axial position and together with the LN_3S ligand gives a 5-coordinate iron center. Selected bond distances and angles are given in **Table 2. 1** and **Table 2. 2**. The Fe and S atoms in $[Fe(LN_3S)(DMAP)]^0$ have moved toward the equatorial plane of the bis(imino)pyridine backbone (Fe–N_3(plane) = 0.254 Å and S-N_3(plane) = 0.411 Å) as compared to $[Fe^{II}(LN_3S)(DMAP)](OTf)$. This flattening of the geometry around the iron center is characterized by a change in tau value from t = 0.18 for $[Fe^{II}(LN_3S)(DMAP)](OTf)$, to t = 0.08 for $[Fe(LN_3S)(DMAP)]^0$. There is a significant shortening of the Fe-N and Fe-S bonds for LN_3S, with the Fe-S bond decreasing by 0.1 Å and the Fe-N bonds decreasing by 0.3 Å. These changes are opposite to what would be expected for a metal-centered reduction to give a formal high-spin iron(I) complex, and are more consistent with ligand-based reduction.

It has been shown that the C-C and C-N bond distances in BIP complexes are indicative of ligand reduction and an analysis of ligand backbone distances is essential when assigning the locus of reduction in these complexes.[37-43] To gain insight into the electronic structure of $[Fe(LN_3S)(DMAP)]^0$, it is useful to compare metrical parameters with other structurally characterized 5-coordinate mono-reduced complexes reported in the literature. The complexes $[Fe(^{iPr}BIP)(Br)(THF)]$[78] and $[Fe(^{Et}BIP)(Cl)]$[40] exhibit similar C_{imine}-N_{imine}, C_{imine}-C_{ipso}, and C_{ipso}-$C_{pyridyl}$ bond distances in the BIP backbone that are consistent with one-electron ligand reduction. In contrast, $[Fe(^{iPr}BIP)(CO)_2](BAr^F_4)$[37], another mono-reduced complex, has bond distances closer to a non-reduced BIP ligand and has been assigned as an iron(I) complex. The critical metrical parameters for $[Fe(LN_3S)(DMAP)]^0$ are highlighted in the structural fragments shown in **Figure 2. 10**, in which $[Fe(LN_3S)(DMAP)]^0$ can be compared with its non-reduced precursor $[Fe^{II}(LN_3S)(DMAP)](OTf)$. The C-$N_{imine}$ and C-$N_{pyridyl}$ bonds are elongated, while the C_{imine}-C_{ipso} bonds are shortened in $[Fe(LN_3S)(DMAP)]^0$ as compared to $[Fe^{II}(LN_3S)(DMAP)](OTf)$. These changes in the ligand backbone clearly point to the complex undergoing ligand-based reduction upon conversion of $[Fe^{II}(LN_3S)(DMAP)](OTf)$ to $[Fe(LN_3S)(DMAP)]^0$. A careful comparison of the bond distances in $[Fe(LN_3S)(DMAP)]^0$ to those reported in the literature suggests the ligand in $[Fe(LN_3S)(DMAP)]^0$ is similar to a two-electron reduced BIP ligand. However, $[Fe(LN_3S)(DMAP)]^0$ would need to be formulated as an Fe^{III} complex with a doubly-reduced $(LN_3S)^{3-}$ ligand, which is unlikely given that iron(III) complexes are often not stable in the presence of monoanionic thiolate donors. Further evidence from Mössbauer spectrosocopy and DFT calculations point to $[Fe(LN_3S)(DMAP)]^0$ as being an iron(II)

complex with a one-electron reduced ligand (vide infra). The phenylthiolate-appended LN_3S ligand appears capable of behaving as a non-innocent ligand by accommodating a reducing equivalent delocalized over the BIP backbone.

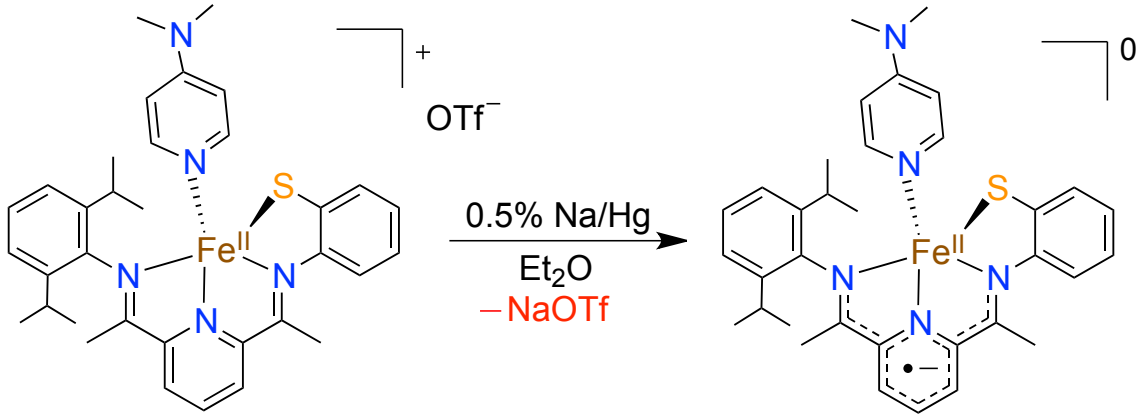

Scheme 2. 3. Synthesis of the Mono-Reduced Complex $[Fe(LN_3S)(DMAP)]^0$

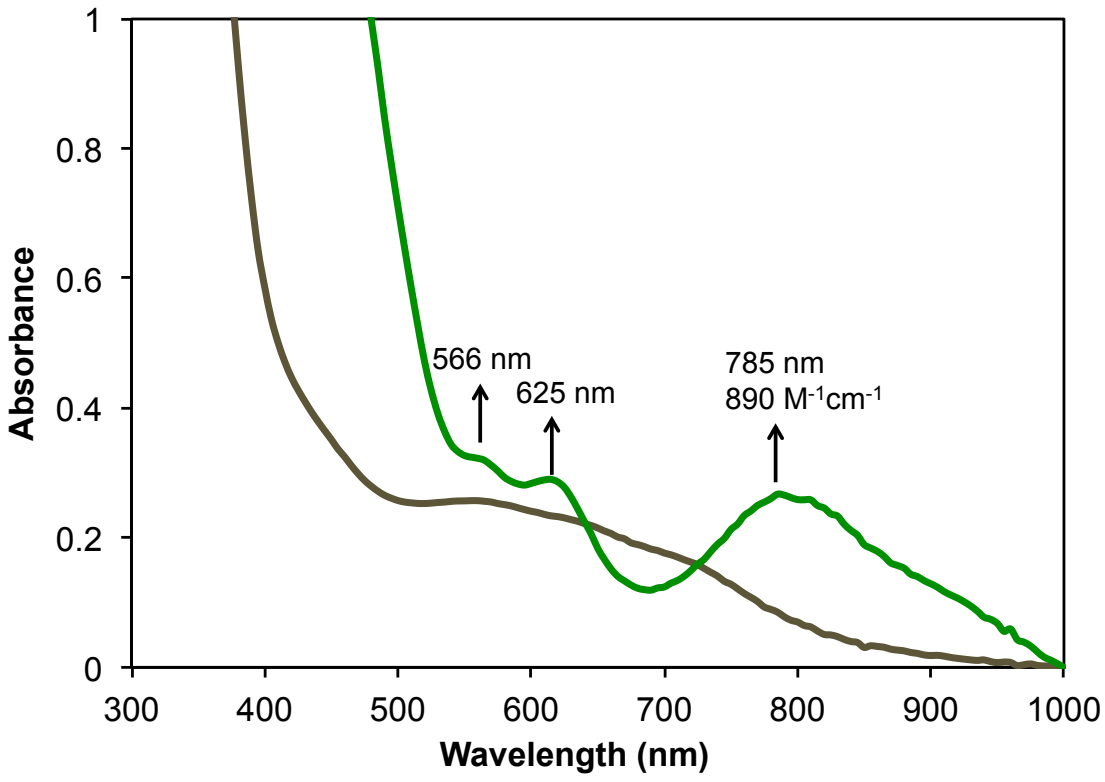

Figure 2. 8. UV-vis spectral change for the conversion of $[Fe^{II}(LN_3S)(DMAP)](OTf)$ (brown) to $[Fe(LN_3S)(DMAP)]^0$ (green) with 0.5% Na/Hg amalgam in THF.

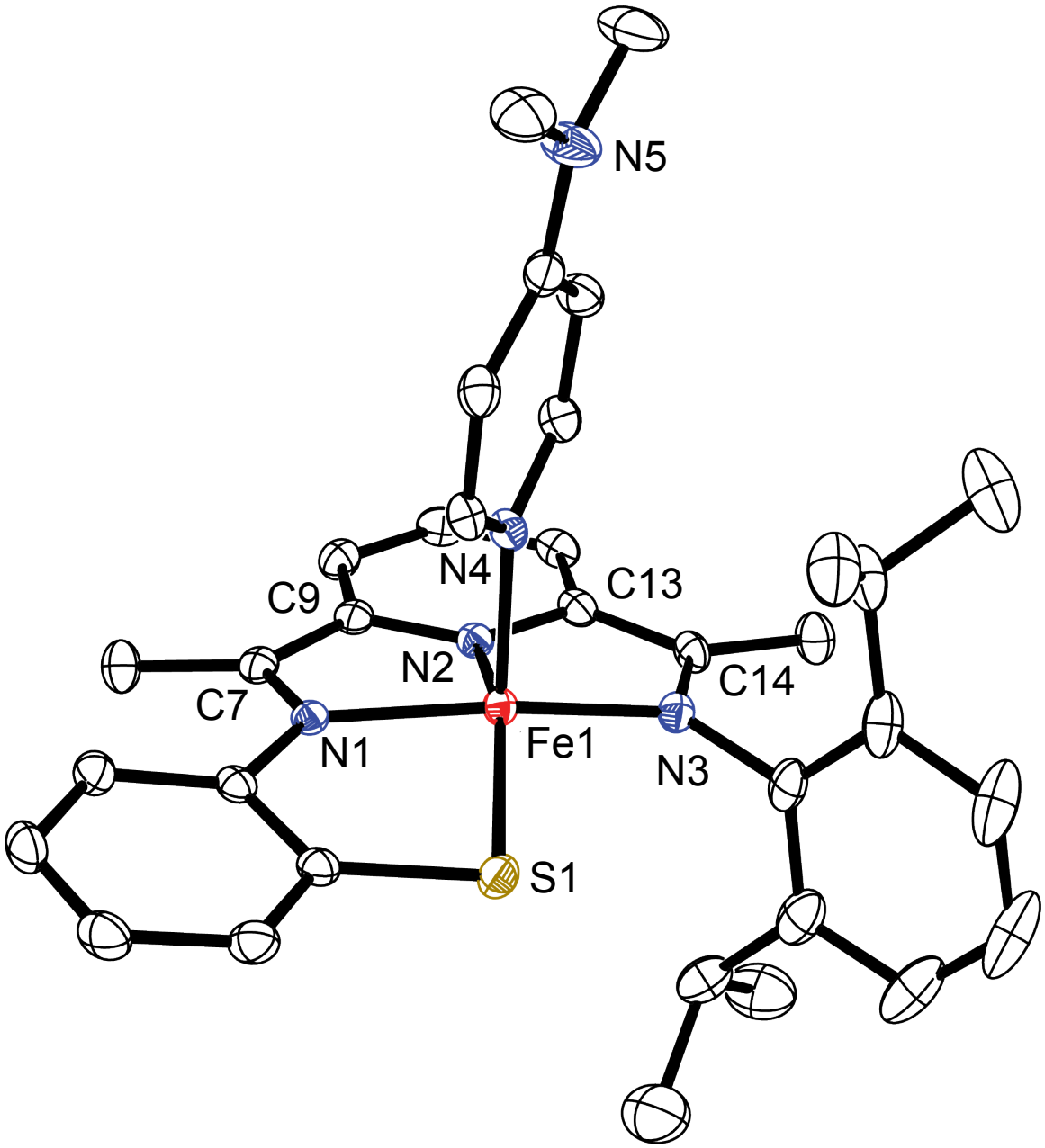

Figure 2. 9. Displacement ellipsoid plot for $[Fe(LN_3S)(DMAP)]^0$ (50% probability level). The H atoms are removed for clarity.

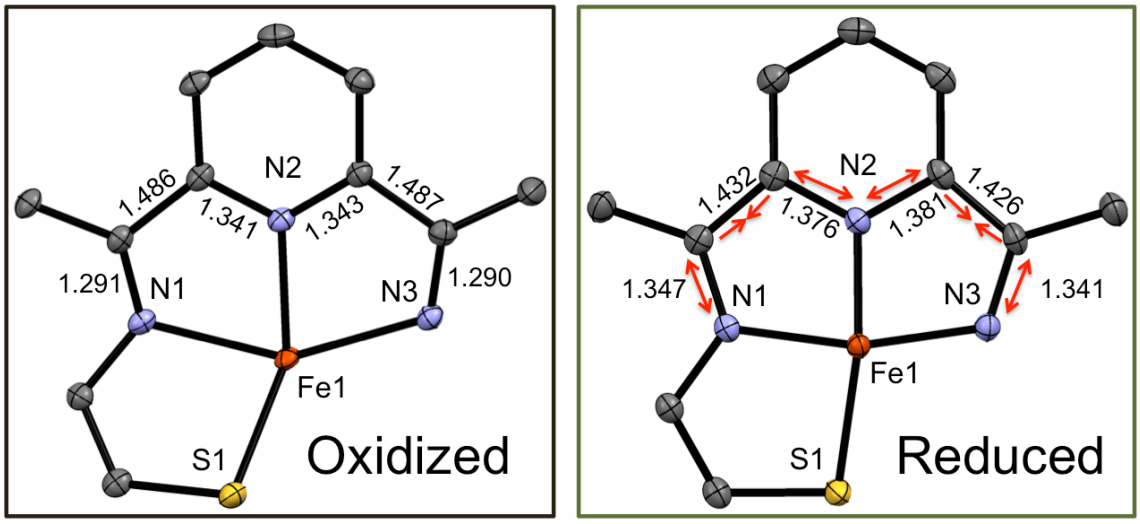

Figure 2. 10. Comparison of selected ligand bond lengths for [Fe(LN$_3$S)(DMAP)](OTf) (left) and [Fe(LN$_3$S)(DMAP)]^0 (right).

EPR Spectroscopy

Further information regarding the electronic structure of the mono-reduced [Fe(LN$_3$S)(DMAP)]^0 was obtained by EPR spectroscopy. Crystalline [Fe(LN$_3$S)(DMAP)]^0 was dissolved in Et$_2$O and EPR data were recorded at 15 K. A nearly axial EPR spectrum was observed, and a good simulation was obtained for an S = ½ system with g values of 2.155, 2.057, and 2.038 (**Figure 2. 11**). The S = ½ ground state could arise from a low-spin (ls) iron(I) center resulting from metal-based reduction, a ls-iron(II) (S = 0) center with a ligand-based radical, or an intermediate-spin (is) iron(II) (S = 1) center antiferromagnetically coupled to a ligand-based radical. An additional possibility is a high-spin (hs) iron(II) (S = 2) antiferromagnetically coupled to a ligand-based radical, but this configuration would give rise to a total spin ground state of S = 3/2, which should exhibit g values spread over a much wider range than observed in **Figure 2. 11**.[38] To make a definitive assignment, it is useful to draw comparisons with

other mono-reduced BIP-iron complexes. For the mono-reduced complex [(^{iPr}BIP)Fe(CO)$_2$](BAr$^F_4$), a rhombic EPR spectrum with g = 2.111, 2.043, 1.994 is observed and attributed to a low-spin Fe^I configuration with an S = ½ ground state.[37] In contrast, the mono-reduced [(^{iPr}BIP)Fe(OEt$_2$)](BAr$^F_4$) exhibits an EPR spectrum assigned to an S = 3/2 species derived from a high-spin Fe^{II} ion antiferromagnetically coupled to the BIP radical anion.[38] The spectrum in **Figure 2. 11** does not match the spectra for either of the former complexes. These results suggest that the LN$_3$S complex [Fe(LN$_3$S)(DMAP)]^0, which contains a covalently tethered phenylthiolate group, exhibits a new electronic configuration consisting of either ls-Fe^{II} and a ligand-based radical or an is-Fe^{II} center antiferromagnetically coupled to a ligand-based radical, not previously observed in other mono-reduced complexes.

The in situ reduction of the nickel complex [Ni^{II}(LN$_3$S)](BF$_4$) helps clarify the EPR properties and electronic ground states of the LN$_3$S complexes described in this work. The mono-reduced analog of [Ni^{II}(LN$_3$S)](BF$_4$), [Ni(LN$_3$S)]^0, was generated in situ and its EPR spectrum is shown in **Figure 2. 12**. A sharp singlet at g = 2.00 (Dpp = 20 G) is observed and can be assigned to a purely ligand-based radical.[70] Such a spectrum would be expected for [Fe(LN$_3$S)(DMAP)]^0 if this complex contained an ls-Fe^{II} ion and a single, unpaired e$^-$ delocalized over the LN$_3$S ligand. Taken together, these data suggest that [Fe(LN$_3$S)(DMAP)]^0 may be best described as an intermediate-spin iron(II) ion antiferromagnetically coupled with a ligand radical, giving rise to the axial EPR spectrum in **Figure 2. 11**.

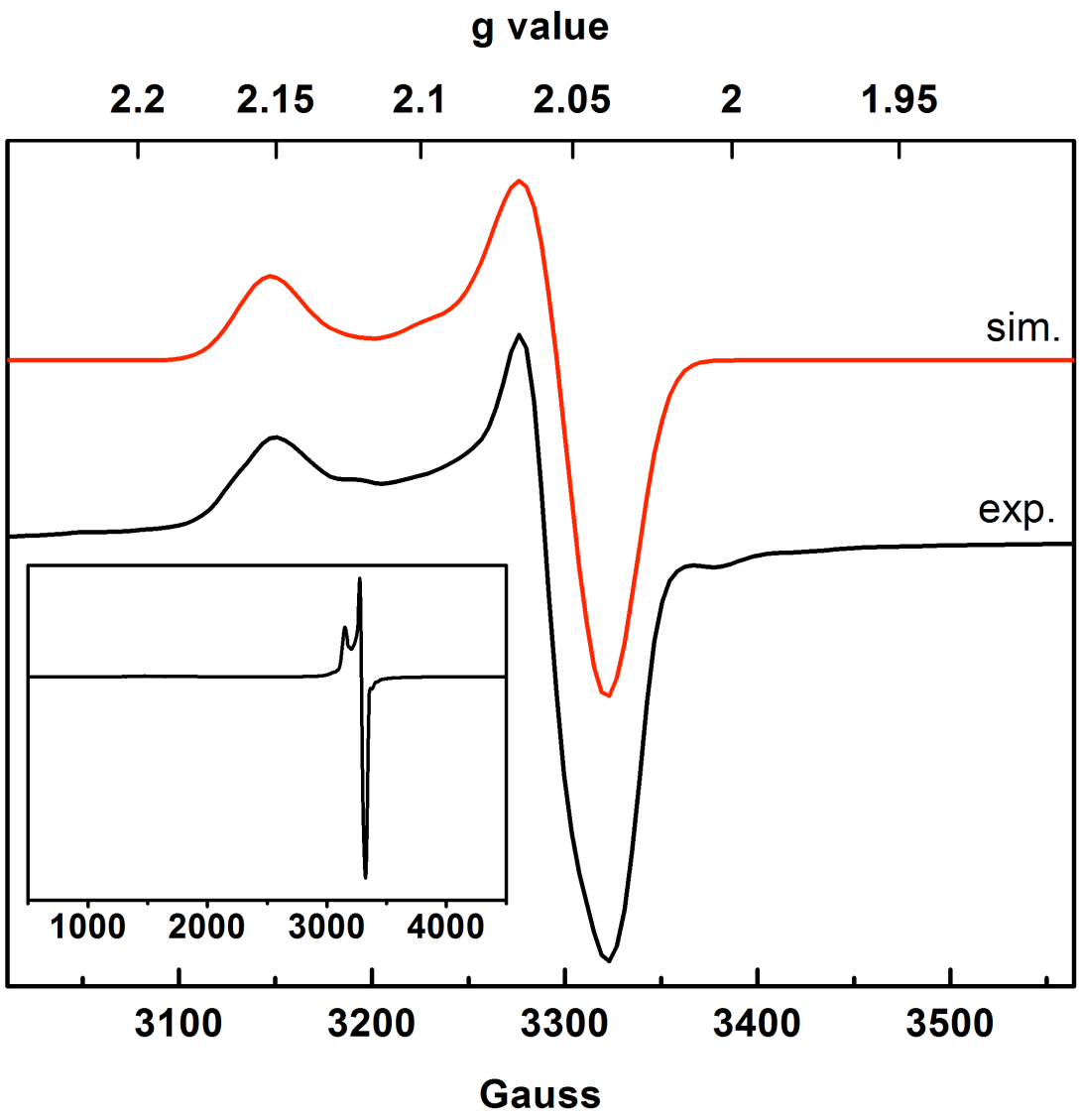

Figure 2. 11. X-band EPR spectrum of $[Fe(LN_3S)(DMAP)]^0$ (2.4 mM) in Et_2O at 15 K (black line). Inset: full-range experimental spectrum. Parameters: frequency, 9.479 GHz; microwave power, 2 mW; modulation amplitude, 10 G; modulation frequency, 100 kHz. Parameters for simulation (red line): S = ½; g = [2.155, 2.057, 2.038]; Lorentzian linewidths, W = 33, 32, and 30 G.

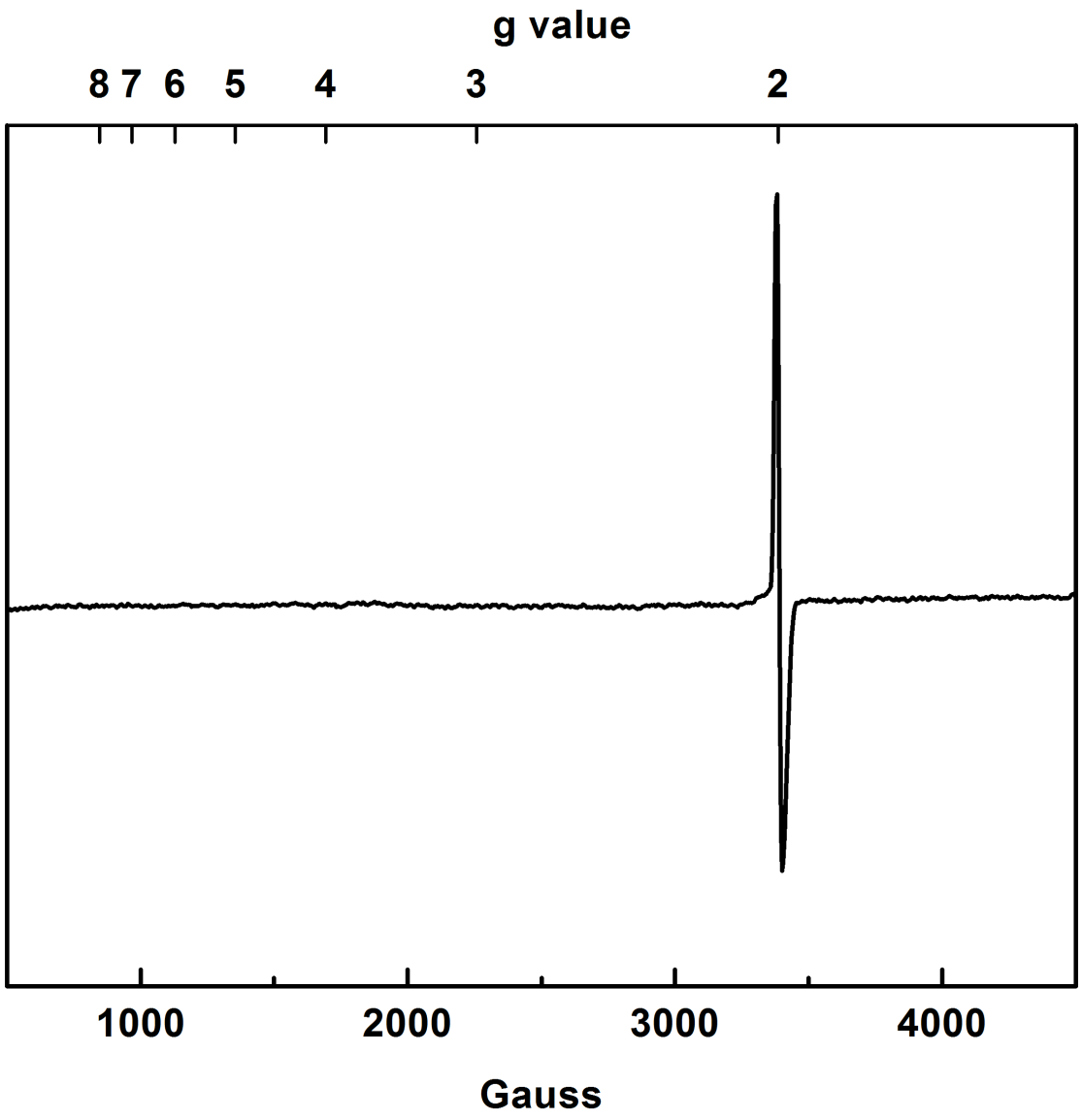

Figure 2. 12. X-band EPR spectrum of $[Ni^{II}(LN_3S)](BF_4)$ (3.0 mM) + Na/Hg (0.5%) amalgam in THF at 16 K. Parameters: frequency, 9.479 GHz; microwave power, 2 mW; modulation amplitude, 10 G; modulation frequency, 100 kHz.

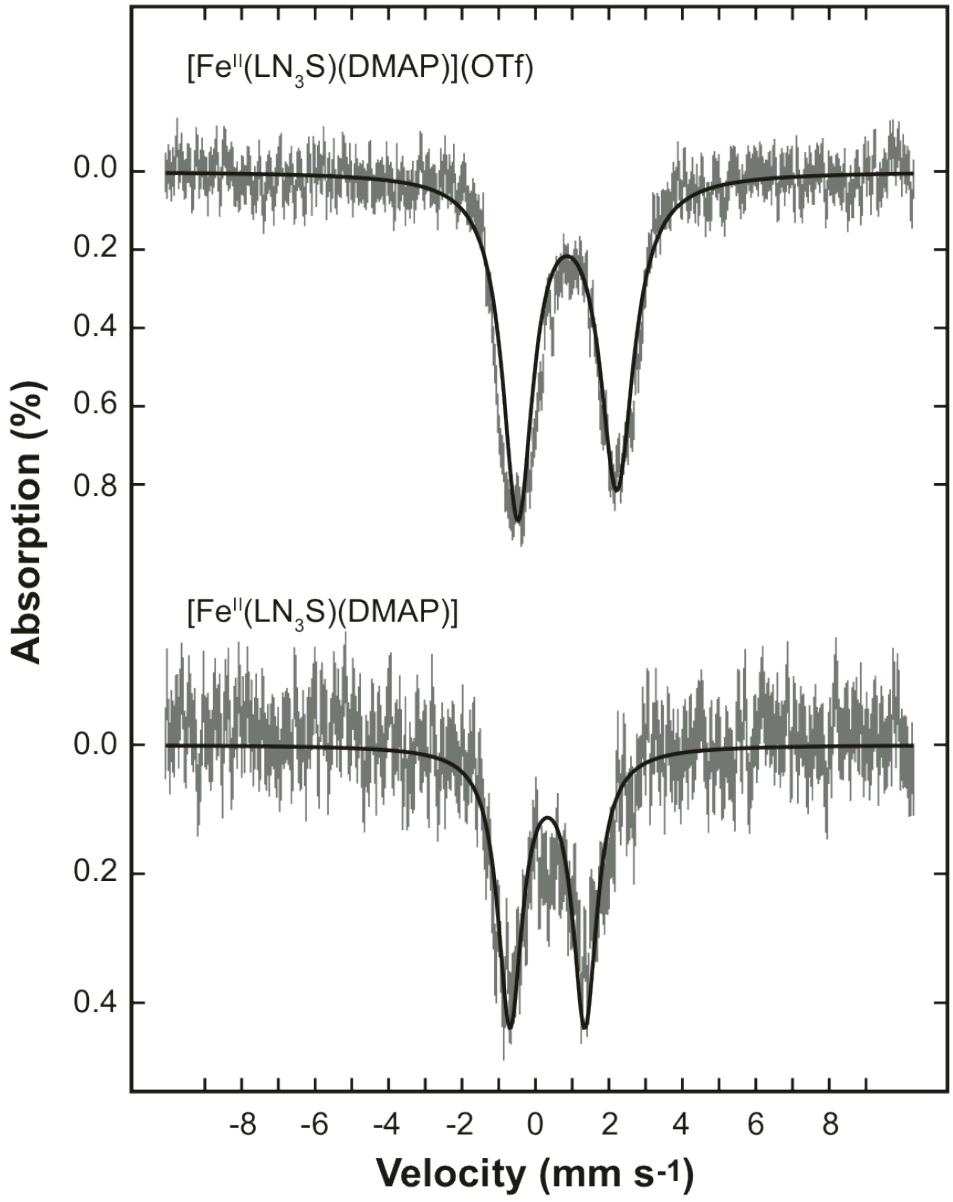

Figure 2. 13. Mössbauer spectra at 5.3 K in a weak applied field (47 mT) of [Fe(LN$_3$S)(DMAP)](OTf) (starting material) and [Fe(LN$_3$S)(DMAP)]^0 (mono-reduced). Both spectra consist of broad quadrupole doublets ($\Gamma_{L=R}$ = 0.8 mm s^{-1}). Complex [Fe(LN$_3$S)(DMAP)](OTf) has parameters that can be assigned to a high-spin iron(II) species: (δ = 0.87 mm s^{-1}; ΔE_Q = 2.70 mm s^{-1}), while [Fe(LN$_3$S)(DMAP)]^0 is consistent with an intermediate-spin iron(II) species coupled to a S=½ radical: (δ = 0.33 mm s^{-1}; ΔE_Q = 2.04 mm s^{-1}).

Mössbauer Spectroscopy

Mössbauer spectra of microcrystalline samples of complexes [Fe(LN_3S)(DMAP)](OTf) and [Fe(LN_3S)(DMAP)]^0 with natural abundance ^{57}Fe were collected at 5.3 K and with a weak applied field (47 mT) and are given in **Figure 2. 13**. Mössbauer parameters for these complexes, together with complexes from the literature are given in **Table 2. 4** and **Table 2. 5**. Both [Fe(LN_3S)(DMAP)](OTf) and [Fe(LN_3S)(DMAP)]^0 produced spectra that consisted of broad quadrupole doublets. The broad spectra may be attributed to the fact that the samples for [Fe(LN_3S)(DMAP)](OTf) and [Fe(LN_3S)(DMAP)]^0 were mixtures of both crystalline and amorphous solids. The spectrum of [Fe(LN_3S)(DMAP)](OTf) can be fitted to a quadrupole doublet with parameters that are highly distinctive[79] for a high-spin iron(II) ion (δ = 0.87 mm s^{-1}; ΔE_Q = 2.70 mm s^{-1}). However, the isomer shift is on the low end of the expected range, and this lowering is likely caused by both covalency of the thiolate iron bond and the five-coodinate nature of the complex. We previously reported an analogous ^{iPr}BIP complex, [Fe^{II}(^{iPr}BIP)(SPh)Cl], which contains an exogenous thiolate donor in place of the tethered PhS$^-$ group in LN_3S and Cl$^-$ as the fifth ligand, and its Mössbauer spectrum was collected and is displayed in **Figure 2. 14**.[25] Complex [Fe(LN_3S)(DMAP)](OTf) and [Fe^{II}(^{iPr}BIP)(SPh)Cl] exhibit similar isomer shifts and quadrupole splittings, suggesting that substitution of the neutral DMAP ligand with the anionic Cl$^-$ ligand has little effect on the Mössbauer spectra and hence electronic structure. These complexes can also be compared favorably with data for the thiolate-ligated non-heme iron enzymes CDO[20] and SOR.[80]

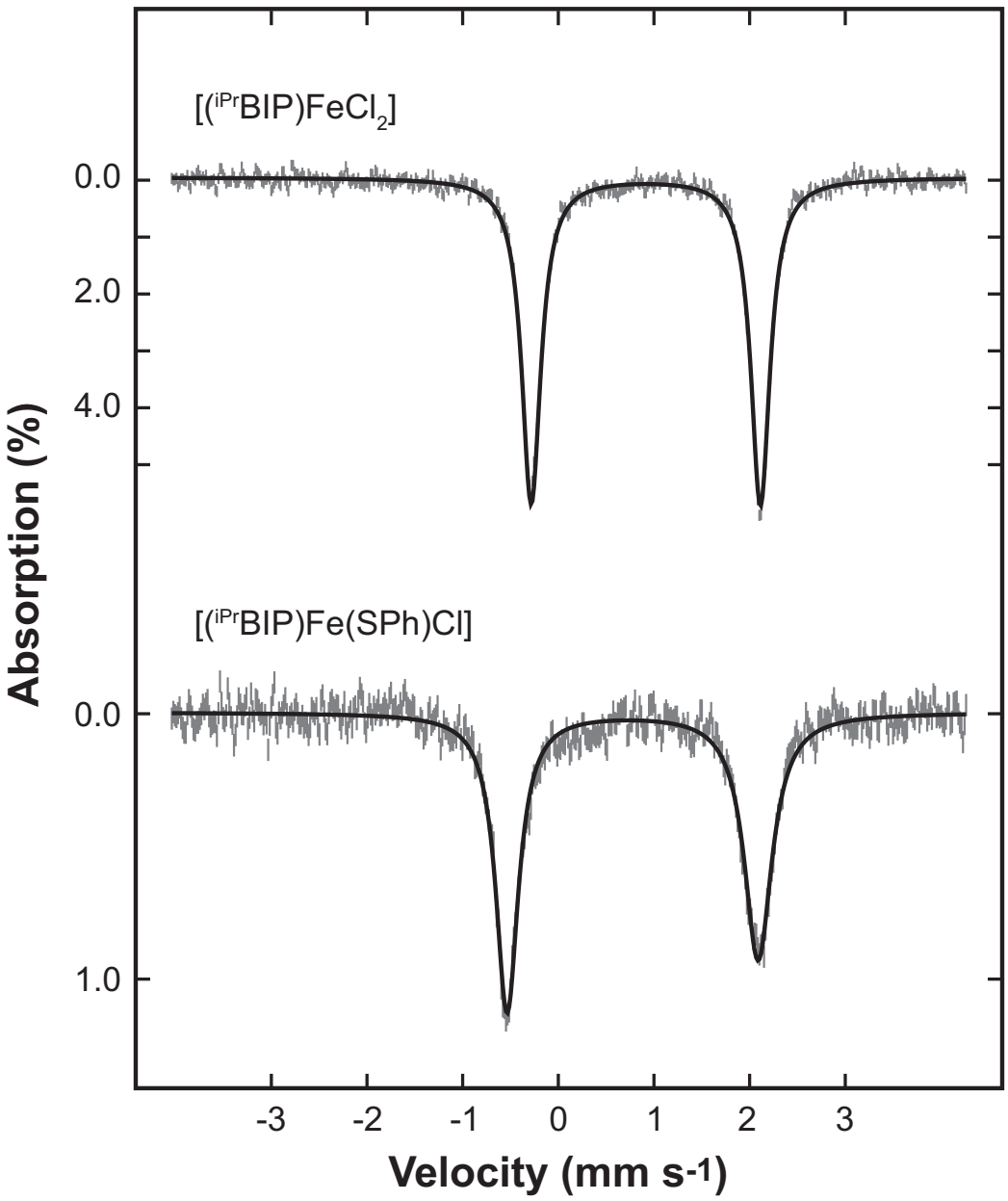

Figure 2. 14. ^{57}Fe Mössbauer spectra of [(^{iPr}BIP)FeCl$_2$] and [(^{iPr}BIP)Fe(SPh)Cl] measured at 5.6 K and with an applied field of 47 mT parallel to the γ-rays. Both spectra can be fitted to sharp quadrupole doublets with parameters given in **Table 2. 4**. The starting material [(^{iPr}BIP)FeCl$_2$] was measured for completeness, although it was previously reported [ref 40].

We next examined the one-electron-reduced complex $[Fe(LN_3S)(DMAP)]^0$ by Mössbauer spectroscopy. Analysis of crystalline $[Fe(LN_3S)(DMAP)]^0$ affords a Mössbauer spectrum distinct from $[Fe(LN_3S)(DMAP)](OTf)$, with a significant decrease in both isomer shift and quadrupole splitting (δ = 0.33 mm s^{-1}; ΔE_Q = 2.04 mm s^{-1}). Comparison with the mono- and doubly-reduced complexes in **Table 2. 5** show that $[Fe(LN_3S)(DMAP)]^0$ exhibits Mössbauer parameters in between those of mono-reduced $[(BIP)Fe(CO)_2]^+$, which contains two strong-field CO donors and an ls-Fe^I center, and mono-reduced $[(BIP)Fe(OEt_2)]^+$, which has a single, weak-field Et_2O donor and an hs-Fe^{II} ion. Surprisingly, the isomer shift and quadrupole splitting values for $[Fe(LN_3S)(DMAP)]^0$ are in fact closest to those seen for the *doubly-reduced* complexes, which have been assigned as intermediate-spin (is) iron(II) species with diradical ligands. The Mössbauer data for $[Fe(LN_3S)(DMAP)]^0$ thus point to an is-Fe^{II} center as the best assignment for this complex, and this conclusion is in good agreement with both the structural and EPR data. The strong-field thiolate ligand in $[Fe(LN_3S)(DMAP)]^0$, coupled with the relatively weak-field DMAP donor, gives rise to this unique electronic configuration.

Table 2. 4. ^{57}Fe Mössbauer Parameters for Selected High-Spin Iron(II) Complexes

	δ (mm s^{-1})	ΔE_Q (mm s^{-1})	Ground State	Reference
$[Fe^{II}(LN_3S)(DMAP)](OTf)$	0.87	2.70	2	This work
$[(^{iPr}BIP)FeCl_2]$	0.89	2.40	2	39
$[(^{iPr}BIP)FeCl_2]$	0.92	2.40	2	This work
$[(^{iPr}BIP)Fe(SPh)Cl]$	0.78	2.62	2	This work
$[(^{Mes}BIP)FeCl_2]$	0.90	1.12	2	81

Table 2. 5. ^{57}Fe Mössbauer Parameters for Mono- and Doubly-Reduced BIP-Iron Complexes

	δ (mm s^{-1})	ΔE_Q (mm s^{-1})	S_{total}	S_{Fe}	S_{ligand}	Reference
Mono-reduced complexes						
$[Fe^{II}(LN_3S)(DMAP)]^0$	0.33	2.04	½	1	½	This work
$[(^{iPr}BIP)Fe(CO)_2](BAr^F{}_4)$	0.17	0.62	½	½	0	37
$[(^{iPr}BIP)Fe(OEt_2)](BAr^F{}_4)$	1.13	2.51	3/2	2	½	38
$[(^{iPr}BIP)FeCl]$	0.77	0.73	3/2[c]	2	½	39
Doubly-reduced complexes						
$[(^{iPr}BIP)Fe(DMAP)]$	0.31	1.94	0	1	1	39
$[(^{iPr}BAP)Fe(DMAP)]$[a]	0.30	2.04	0	1	1	82
$[(^{iPr}BIP)Fe(CO)_2]$	0.03	1.17	1	0	1	39, 82

[a]BAP = bis(aldimino)pyridine

Computational Studies

The iron(II) and nickel(II) complexes, and their mono-reduced analogs, were studied by DFT calculations to gain further insight into their structures and electronic configurations. The optimized geometries of $[(LN_3S)Fe^{II}(DMAP)]^+$ and $[Ni^{II}(LN_3S)]^+$ were calculated with the B3LYP functional on all low-lying spin states and are given in **Figure 2. 15**. A quintet spin ground state (S = 2, hs-Fe^{II}) was found for $[Fe^{II}(LN_3S)(DMAP)]^+$. At ΔE+ZPE level of theory, the quintet state ($^5[Fe^{II}(LN_3S)(DMAP)]^+$) for the iron(II) complex is more stable than either the triplet state (S = 1, is-Fe^{II}, ($^3[Fe^{II}(LN_3S)(DMAP)]^+$) or the singlet state ($^1[Fe^{II}(LN_3S)(DMAP)]^+$) by 13.8 and 17.0 kcal mol^{-1}. Inclusion of dispersion corrections further increases the

energy gaps to 21.6 and 32.7 kcal mol^{-1}, respectively. These results indicate that the singlet and triplet spin states should be inaccessible at room temperature, and match nicely with the experimental observations (structural parameters, ^1H NMR) that show **3** has an hs-Fe^{II} ground state. The Fe-N bond lengths in the DFT-optimized structure of $^5[Fe^{II}(LN_3S)(DMAP)](OTf)$ range from 2.092 – 2.279 Å, and are in good agreement with the X-ray structure (Fe-N for $[Fe^{II}(LN_3S)(DMAP)]^+$: 2.073(5) – 2.196(5)). The Fe-S distance of 2.407 Å for $^5[Fe^{II}(LN_3S)(DMAP)]^+$ in **Figure 2. 15** is slightly elongated compared to the X-ray structure (Fe-S = 2.3246(18) Å). Note that when geometry optimizations for $[Fe^{II}(LN_3S)(DMAP)]^+$ were run with a pure density functional such as BP86 instead of B3LYP, a different spin state ordering was found, in which a degenerate singlet/triplet ground state was obtained and the quintet spin state was calculated to be much higher in energy (see Appendix C). Consequently, pure density functional methods such as BP86 give results that are inconsistent with the experimental findings, and therefore we did not proceed further with these kinds of methods.

For the nickel(II) complex $[Ni^{II}(LN_3S)]^+$, a closed-shell singlet spin state ($S = 0$) was found to be the ground state. We also calculated the triplet and quintet spin states for $[Ni^{II}(LN_3S)]^+$, but found these states lie higher in energy than $^1[Ni^{II}(LN_3S)]^+$ by 4.2 and 33.3 kcal mol^{-1}, respectively. No changes in spin state ordering were found for this complex when alternative density functional methods were employed. The optimized geometry for the ground state singlet is approximately square planar, consistent with the X-ray structure. The Ni-N distances for $^1[Ni^{II}(LN_3S)]^+$ are in excellent agreement with those derived from the crystal structure (**Table 2. 3**), although the Ni–S distance is slightly elongated (DFT: 2.201 Å; Expt: 2.1386(5) Å), similar to the trend seen for the

Fe-S distance in $^{5}[Fe^{II}(LN_3S)(DMAP)](OTf)$ versus the X-ray structure. The DFT calculations at the B3LYP level of theory often slightly overestimate metal-sulfur bond lengths.[83] The other main structural features, and importantly the spin ground states, are well reproduced by the calculations.

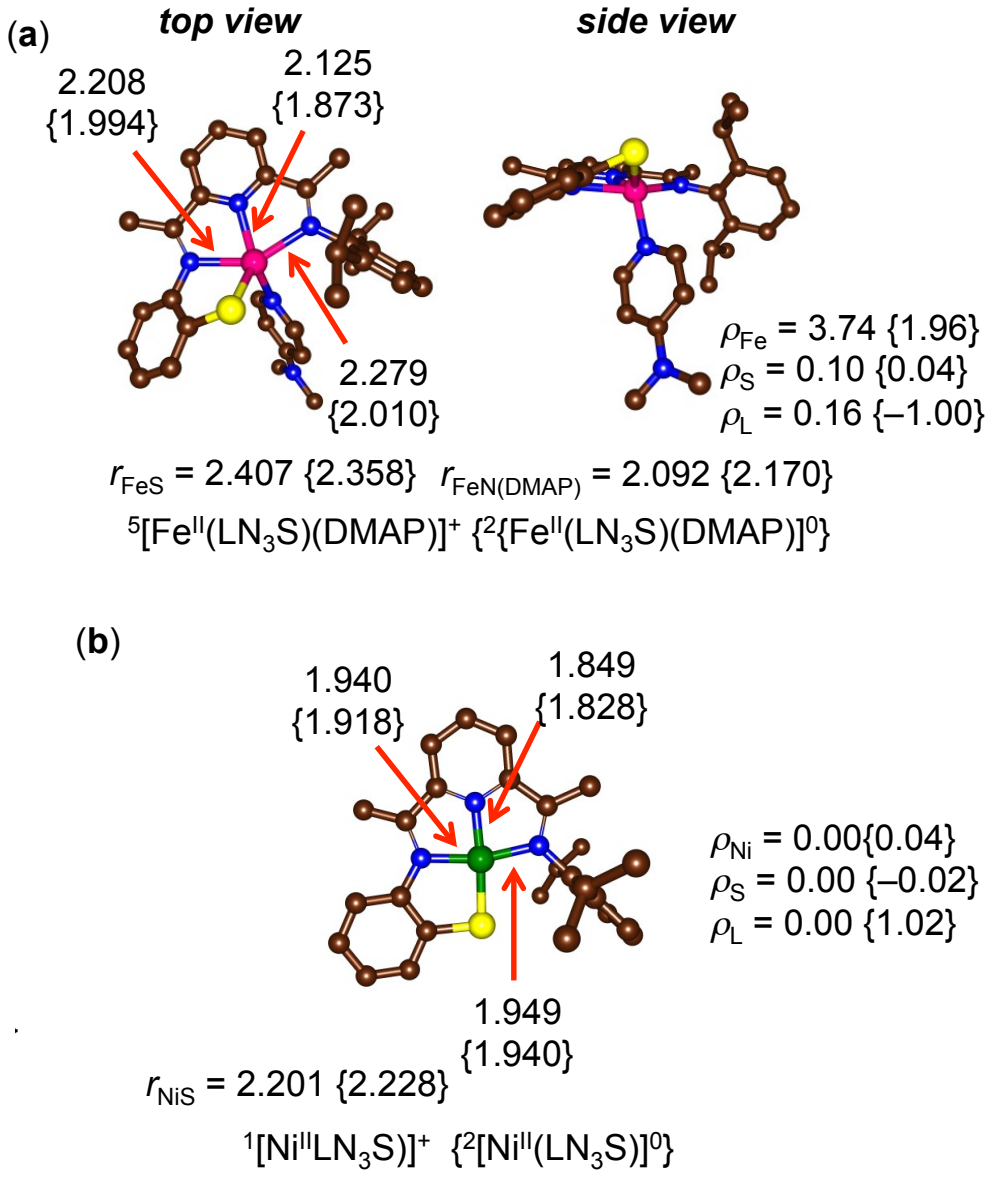

Figure 2. 15. Optimized UB3LYP/B1 geometries of $^{5}[Fe^{II}(LN_3S)(DMAP)]^{+}$ and $^{1}[Ni^{II}(LN_3S)]^{+}$, and their reduced complexes with bond lengths in angstroms. Also given are group spin densities.

The mono-reduced complex $[Fe^{II}(LN_3S)(DMAP)]^0$ was also studied at the B3LYP level of theory, taking into consideration the possible doublet (S = ½) and quartet (S = 3/2) spin states for this complex. Calculations were initiated by using the coordinates from the X-ray structure of $[Fe^{II}(LN_3S)(DMAP)]^0$ as a starting point, and the results led to an overall doublet spin ground state (S = ½) for the mono-reduced complex. The doublet spin state is found to be stabilized by 6.3 kcal mol^{-1} over the quartet spin state, and solvent corrections raise this energy gap to 6.5 kcal mol^{-1}, however dispersion corrections reduce it to 0.6 kcal mol^{-1}. The computationally-derived S = ½ ground state thus matches that derived from the EPR spectrum observed in **Figure 2. 11** for complex $[Fe^{II}(LN_3S)(DMAP)]^0$. The bond distances for the doublet spin ground state of $[Fe^{II}(LN_3S)(DMAP)]^0$ are shown in **Figure 2. 15**, and both the Fe-N and Fe-S distances are significantly shortened compared to the starting complex $[Fe^{II}(LN_3S)(DMAP)]^+$. The Fe-N bond lengths for the in-plane LN_3S ligand are in good agreement with the structural parameters for $[Fe^{II}(LN_3S)(DMAP)]^0$ (**Table 2. 1**), but the Fe-S distance is somewhat longer, following the trend seen for $[Fe^{II}(LN_3S)(DMAP)]^+$ and $[Ni^{II}(LN_3S)]^+$. In addition the Fe-N distance for the axial DMAP ligand is also slightly elongated (DFT: 2.170; Expt: 2.0508(16) Å).

The molecular orbital diagram for the doublet spin ground state of $[Fe^{II}(LN_3S)(DMAP)]^0$ is given in **Figure 2. 16** together with the MO diagram for the quintet spin ground state of starting complex $[Fe^{II}(LN_3S)(DMAP)]^+$. For complex $[Fe^{II}(LN_3S)(DMAP)]^0$, the computational results are consistent with an is-Fe^{II} (S_{Fe} = 1) center antiferromagnetically coupled with a ligand-based radical to give an overall doublet spin (S_{total} = ½) ground state. As seen in **Figure 2. 16**, two a spin electrons reside

in metal-based orbitals, while a predominantly ligand-based orbital (π^*_L) contains one β spin electron. The two unpaired electrons on the metal are reflected by a calculated spin density of $\rho_{Fe} = 1.96$, whereas the unpaired electron on the ligand leads to $\rho_{LN3S} = -1.00$ (**Figure 2. 15**). In contrast, the MO diagram for $[Fe^{II}(LN_3S)(DMAP)]^+$ reveals four half-filled (a spin) metal-based orbitals resulting in $\rho_{Fe} = 3.74$, as expected for a hs-Fe^{II} center. The calculations show that one-electron reduction of $[Fe^{II}(LN_3S)(DMAP)]^+$ occurs by the filling of a low-lying virtual ligand (π^*_L) orbital in preference to filling of an empty metal-based orbital, confirming the non-innocent nature of the LN_3S ligand. The spin state change that occurs at the iron center upon reduction of $[Fe^{II}(LN_3S)(DMAP)]^+$ (hs-Fe^{II}) to $[Fe^{II}(LN_3S)(DMAP)]^0$ (is-Fe^{II}) appears to be a consequence of the destabilization of the σ^*_{xy} orbital. This destabilization is likely brought on by an increase in ligand field strength for the one-electron-reduced LN_3S ligand and a consequent shortening of the Fe-N and Fe-S bonds. Destabilization of σ^*_{xy} leads to depopulation of this orbital and occupation of the lower-lying π^*_{yz} orbital, resulting in an overall is-Fe^{II} center. Finally, the ligand-based β electron in $[Fe^{II}(LN_3S)(DMAP)]^0$ is mainly located on the bis(imino)pyridine backbone, which leads to the significant bond length perturbations shown in **Figure 2. 18**, where the backbones for $^5[Fe^{II}(LN_3S)(DMAP)]^+$ and $^2[Fe^{II}(LN_3S)(DMAP)]^0$ are compared. The trends in the perturbations provide a satisfying match to what is seen experimentally in **Figure 2. 10** and help to further validate the DFT results. The close agreement of the calculated ligand backbone bond distances (**Figure 2. 18**) with the X-ray structure of $[Fe^{II}(LN_3S)(DMAP)]^0$ provides additional evidence for the assignment of $[Fe^{II}(LN_3S)(DMAP)]^0$ as a one-electron reduced ligand radical coupled to an is-Fe^{II} ion ($\rho_{Fe} = 1.96$, $\rho_L = -1.00$; **Figure 2. 15**a).

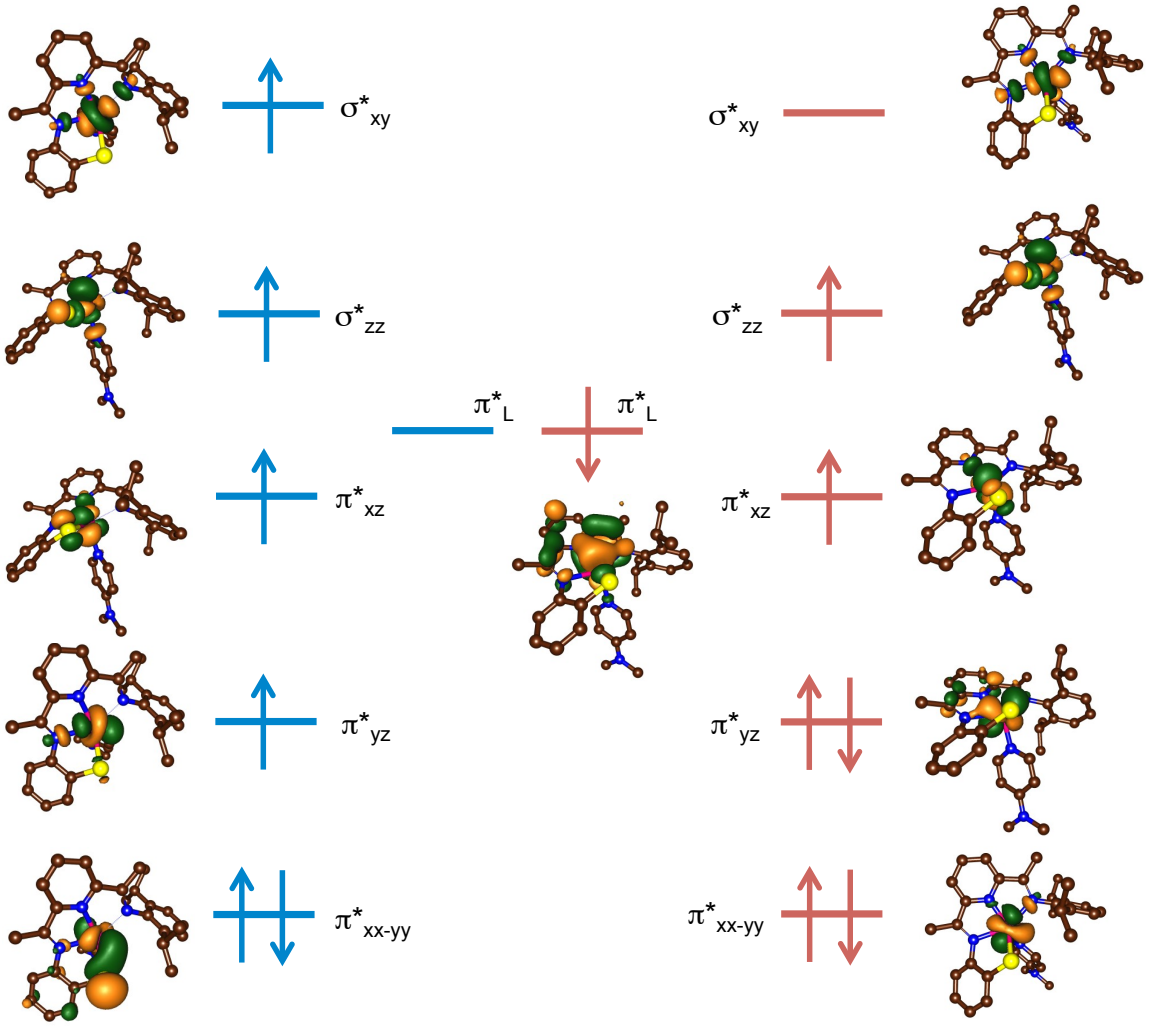

Figure 2. 16. Orbital diagrams of $^{5}[Fe^{II}(LN_3S)(DMAP)]^{+}$ (left) and $^{2}[Fe^{II}(LN_3S)(DMAP)]^{0}$ (right).

The mono-reduced product of $^{1}[Ni^{II}(LN_3S)]^{+}$, $[Ni^{II}(LN_3S)]^{0}$, was also investigated by DFT, giving the optimized geometry for the doublet spin ground state of $^{2}[Ni^{II}(LN_3S)]^{0}$ shown in **Figure 2. 15**. In this case, there are only very minor perturbations on the metal-ligand bond lengths as compared to the non-reduced starting material. Analysis of the spin density shows that the extra electron clearly lies on the LN_3S ligand and not the closed-shell nickel center, with an a electron occupying a π^*_L orbital (**Figure 2. 17**). The DFT calculations for the mono-reduced nickel complex provide further confirmation that

LN_3S functions easily as a non-innocent ligand, and the ligand-based radical predicted by DFT is in full agreement with the sharp organic radical seen in the EPR spectrum for mono-reduced $[Ni^{II}(LN_3S)]^0$ (**Figure 2. 12**).

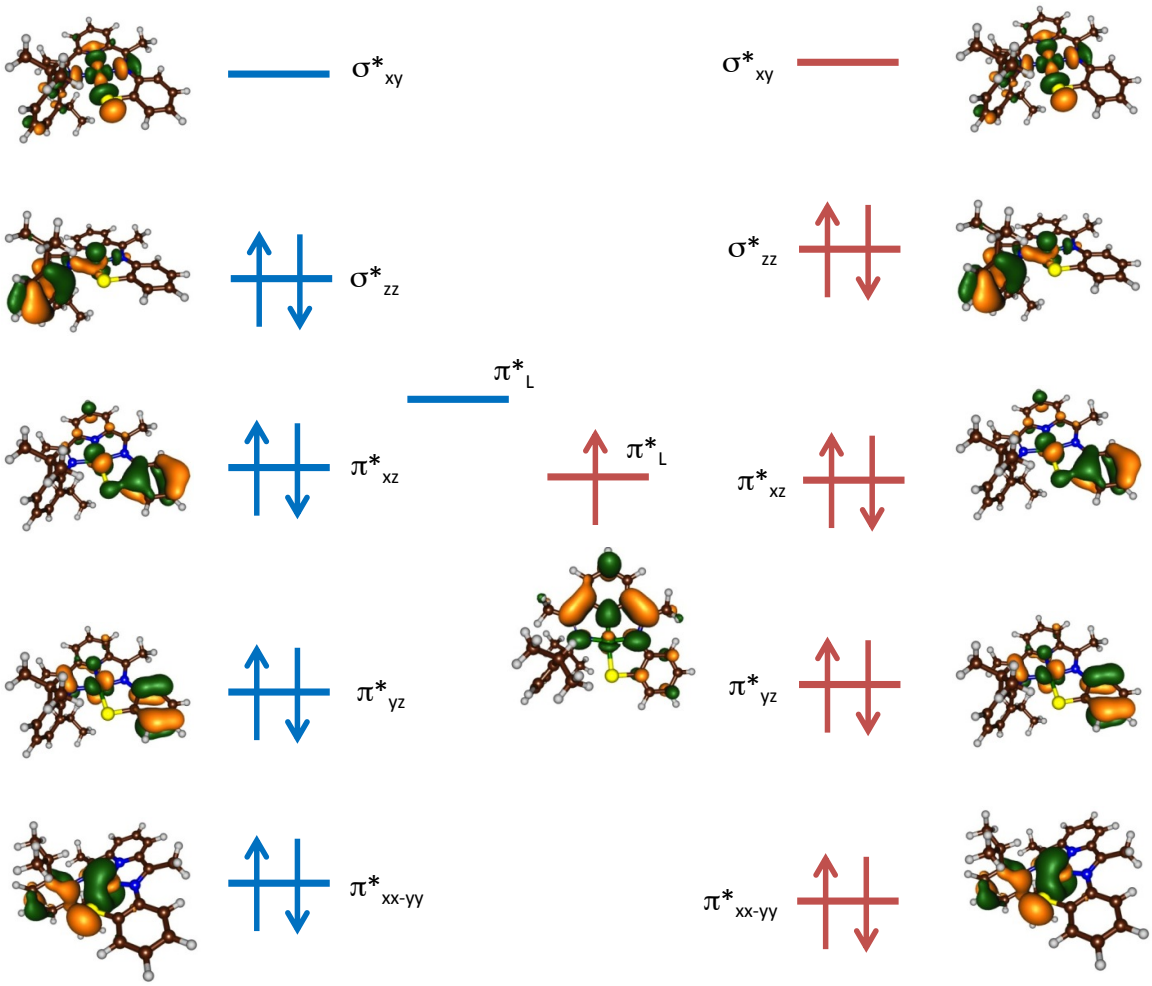

Figure 2. 17. Orbital diagram of $^1[Ni^{II}(LN_3S)]^+$ (left-hand-side) and $^2[Ni^{II}(LN_3S)]^0$ (right-hand-side).

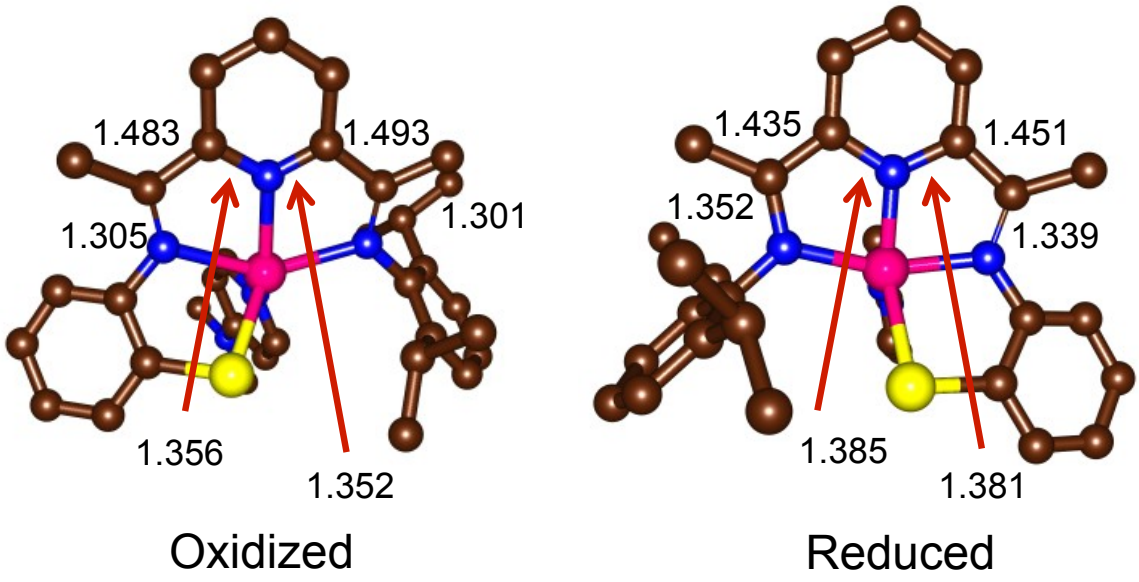

Figure 2. 18. Optimized UB3LYP/B1 geometries of $^{5}[Fe^{II}(LN_3S)(DMAP)]^{+}$ and $^{2}[Fe^{II}(LN_3S)(DMAP)]^{0}$, highlighting BIP ligand backbone bond lengths in angstroms.

O_2 Reactivity

We previously found that $[Fe^{II}(LN_3S)(OTf)]$ reacts with excess O_2 in CH_2Cl_2 to give an S-oxygenated sulfonate complex, providing the first example of an Fe^{II}-thiolate complex that reacts with O_2 to give selective S-oxygenation.[24] This reaction mimicked some of the general features of the reaction seen for CDO, but was lacking in the fact that the donor set at the metal center was N_3S(thiolate), not N_4S(thiolate), and the S-oxygenated product was a triply-oxygenated RSO_3^- complex, as opposed to the doubly-oxygenated RSO_2^- product generated by the enzymatic system. In a subsequent report, we prepared an improved N_4S(thiolate) iron(II) model complex based on the tripodal N4Py ligand, $[Fe^{II}(N3PyS)(solvent)]^{+}$, and found that it reacts with O_2 to give a biomimetic, doubly-oxygenated sulfinato-iron(II) complex.[26] We thus sought to test the new

N_4S(thiolate) iron(II) complexes $[Fe^{II}(LN_3S)(py)](OTf)$ and $[Fe^{II}(LN_3S)(DMAP)](OTf)$ to determine their reactivity toward O_2.

Reactions of $[Fe^{II}(LN_3S)(py)](OTf)$ and $[Fe^{II}(LN_3S)(DMAP)](OTf)$ with excess O_2 in CH_2Cl_2 were analyzed directly by LDIMS. The mass spectral data (**Figure 2. 19** and **Figure 2. 20**) show dominant ions that correspond to the triply-oxygenated sulfonato-iron(II) complex, $[Fe(LN_3SO_3)]^+$ (m/z = 532). This oxygenation pattern is the same as that seen for $[Fe^{II}(LN_3S)(OTf)]$.[24] Conversion of $[Fe^{II}(LN_3S)(OTf)]$ to an N_4S(thiolate) coordination environment by addition of py or DMAP does not alter the O_2 reactivity such that S-oxygenation results in a doubly-oxygenated sulfinato product as seen for our other N_4S(thiolate) system.[25]

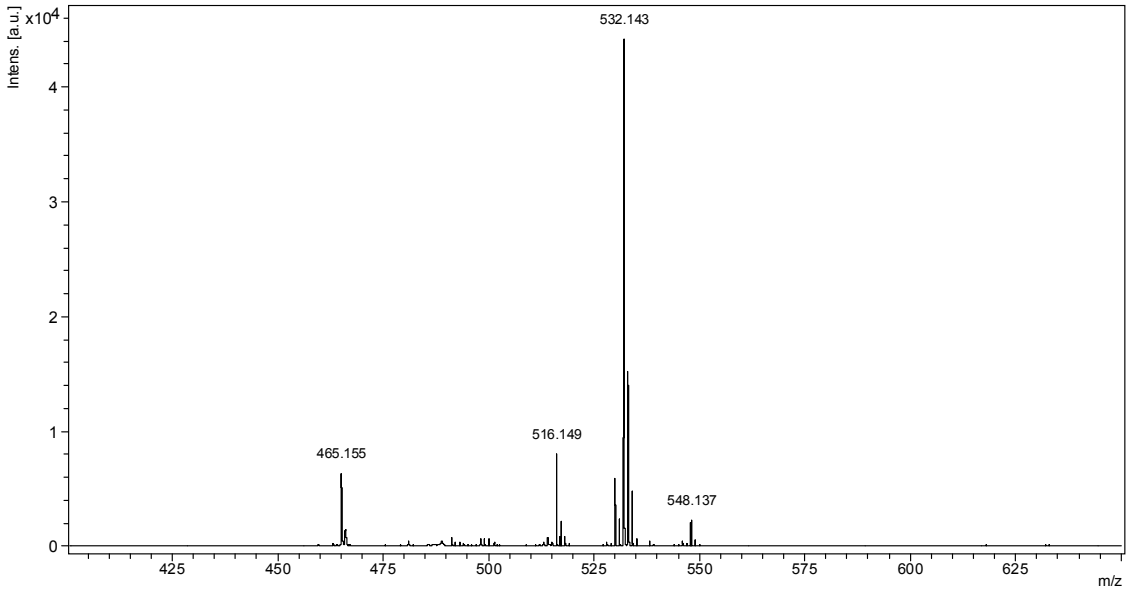

Figure 2. 19. LDIMS(+) of $[Fe^{II}(LN_3S)(py)](OTf)$ + excess O_2 after 24 h in CH_2Cl_2. m/z = 516.15 ($[M + 2O – py – OTf]^+$), 532.14 ($[M + 3O – py – OTf]^+$).

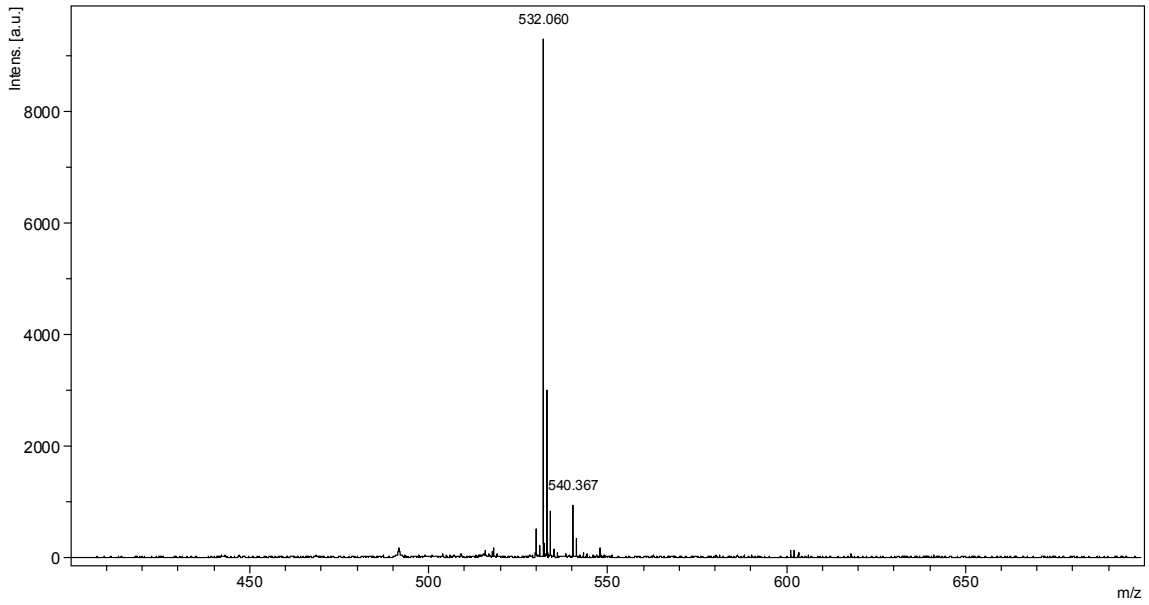

Figure 2. 20. LDIMS(+) of $[Fe^{II}(LN_3S)(DMAP)](OTf)$ + excess O_2 after 24 h in CH_2Cl_2. m/z = 532.06 ($[M + 3O – DMAP – OTf]^+$).

Some nickel(II) thiolate complexes can undergo S-oxygenation, most likely through a mechanism involving direct attack of O_2 on the coordinated sulfur atom, while other Ni^{II}-thiolates are inert toward O_2, and orbital compositions have been analyzed to explain these differences in O_2 reactivity.[46-54] We did not observe any reaction between complex $[Ni^{II}(LN_3S)](BF_4)$ and excess O_2 in CH_2Cl_2, even after prolonged stirring for several days. Solutions of the mono-reduced nickel(II) complex $[Ni(LN_3S)]^0$ generated from Na/Hg amalgam in THF were next tested for their reactivity toward O_2. In this case a rapid reaction with O_2 was indeed observed by an immediate color change from bright to dark green, but LDI-MS analysis of the reaction mixture revealed only a peak (m/z = 488.3, **Figure 2. 21**) for the starting material $[Ni^{II}(LN_3S)](BF_4)$, suggesting only outer-sphere oxidation had occurred. In contrast, a related Ni^{II}(BIP) complex undergoes outer-sphere reduction to give a one-electron reduced product that then reacts with O_2 via an inner-sphere mechanism to afford ligand-oxidized products.[70]

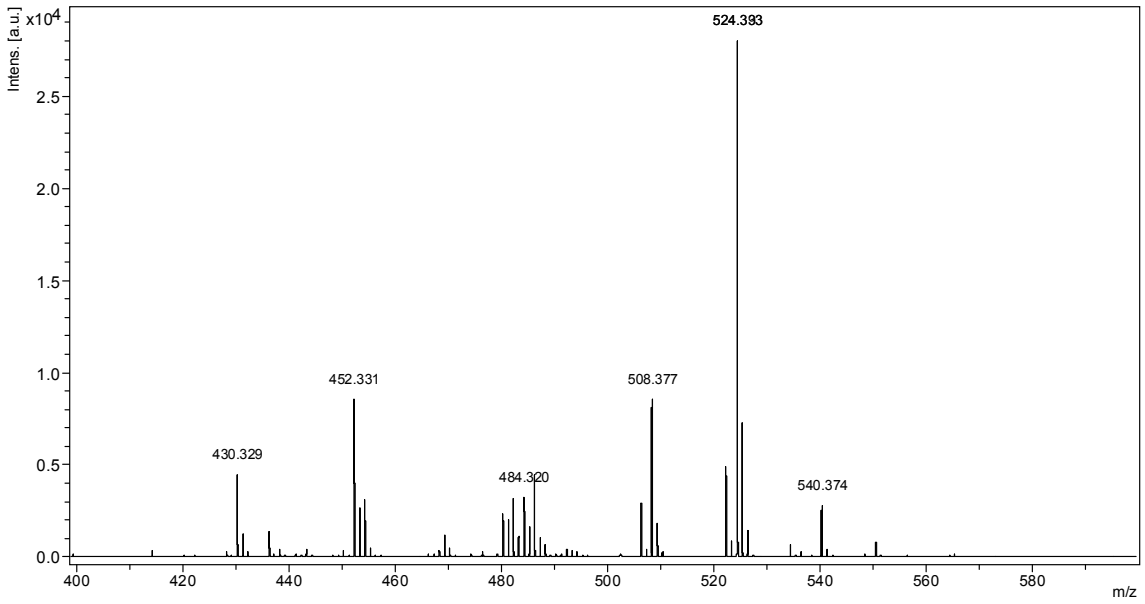

Figure 2. 21. LDIMS(+) of $[Ni^{II}(LN_3S)](BF_4)$ + excess Na/Hg, followed by exposure to excess O_2 in Et_2O. m/z = 488.3 ($[M - BF_4]^+$).

The mono-reduced compound $[Fe^{II}(LN_3S)(DMAP)]^0$ also exhibits rapid reactivity with O_2. Exposure of solutions of $[Fe^{II}(LN_3S)(DMAP)]^0$ in Et_2O to air, or bubbling O_2, leads to an immediate color change from dark green to brown with concurrent formation of a brown precipitate. Analysis by LDI-MS reveals a mixture that can be assigned to Fe-oxygenates and S-oxygenates, with multiple major peaks assigned to $[SOFe^{III}\text{-}O\text{-}Fe^{III}SO]^{2+}$ (m/z = 508.3), $[SO_2Fe^{III}\text{-}O\text{-}Fe^{III}SO_2]^{2+}$ (m/z = 524.4), and $[SO_3Fe^{III}\text{-}O\text{-}Fe^{III}\text{-}SO_3]^{2+}$ (m/z = 540.4), see **Figure 2. 22**. While the $[Fe^{II}(LN_3S)(L)]^+$ complexes exhibit S-centered oxidation, the mono-reduced complex $[Fe^{II}(LN_3S)(DMAP)]^0$ appears to show significant oxidation at the iron center. This represents a significant change in the observed reactivity of these complexes as a result of the change in electronic structure.

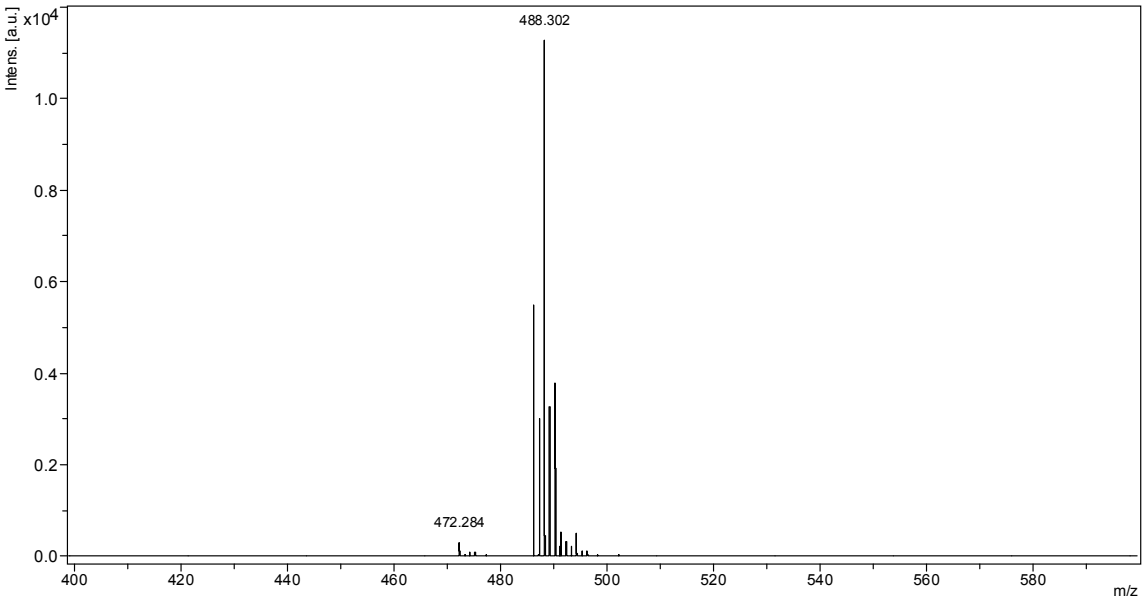

Figure 2. 22. LDIMS(+) of $[Fe^{II}(LN_3S)(DMAP)]^0$ + excess O_2 in Et_2O. m/z = 484.3 ($[M - DMAP - OTf]^+$), m/z = 508.3 ($[LN_3SOFe^{III}\text{-}O\text{-}Fe^{III}SOLN_3]^{2+}$), m/z = 524.4 ($[LN_3SO_2Fe^{III}\text{-}O\text{-}Fe^{III}SO_2LN_3]^{2+}$), and m/z = 540.4 ($[LN_3SO_3Fe^{III}\text{-}O\text{-}Fe^{III}\text{-}SO_3LN_3S]^{2+}$).

2. 4. Conclusions

The triflate-ligated ferrous complex $[Fe^{II}(LN_3S)(OTf)]$ serves as a useful precursor for the facile synthesis of the biomimetic N_4S(thiolate) complexes $[Fe^{II}(LN_3S)(DMAP)](OTf)$ and $[Fe^{II}(LN_3S)(DMAP)](OTf)$. Template assembly with nickel(II) tetrafluoroborate leads to the Ni^{II} analog $[Ni^{II}(LN_3S)](BF_4)$. Structural and spectroscopic methods show that the iron complexes are 5-coordinate, high-spin (S = 2) iron(II) species, while the nickel complex is a 4-coordinate square-planar nickel(II) species. Electrochemical measurements revealed that these complexes uniformly exhibit only one reversible reduction wave between -0.9 and -1.2 V vs Fc^+/Fc within the CH_3CN solvent window. Bulk chemical reduction of $[Fe^{II}(LN_3S)(DMAP)](OTf)$ by Na/Hg amalgam gives the extremely air-sensitive, mono-reduced complex $[Fe(LN_3S)(DMAP)]^0$,

which was isolated and crystallographically characterized. No evidence for a two-electron reduced product was observed, in line with the electrochemical analysis. This behavior contrasts other bis(imino)pyridine complexes, which typically can house up to two or three reducing equivalents beginning at the $M^{2+}(BIP^0)$ redox level, and have been shown to form two-electron reduced products from Na/Hg reduction. It can be concluded that the anionic thiolate arm appended to the new LN_3S system likely causes multiple reductions to be thermodynamically unfavorable. The X-ray structure of $[Fe^{II}(LN_3S)(DMAP)]^0$ shows it is a 5-coordinate complex, with one DMAP ligand remaining coordinated in the axial position following reduction. The electronic structure of the mono-reduced complex $[Fe^{II}(LN_3S)(DMAP)]^0$ was firmly established through a combination of structural analysis, EPR and Mössbauer spectroscopies as well as computational (DFT) methods. The ground state of $[Fe^{II}(LN_3S)(DMAP)]^0$ is clearly a doublet state that arises from an intermediate-spin (S = 1) iron(II) center antiferromagnetically coupled to a ligand-based radical. The spin state of the iron center is reflected in the unusual Mössbauer parameters for this mono-reduced BIP complex, with δ = 0.33 mm s^{-1} and ΔE_q = 2.04 mm s^{-1}. These parameters differ significantly from other mono-reduced Fe(BIP) complexes that exhibit either hs-Fe^{II} (S = 2) or ls-Fe^{II} (S = 0) configurations, and in fact fall in line with the doubly-reduced Fe(BIP) species which have been previously assigned as is-Fe^{II} complexes carrying diradical ligands. The computational studies show that the doublet spin ground state is comprised of two α electrons occupying metal-based orbitals of d_{z2} and d_{xz} parentage and one β electron residing on a ligand-based π^* orbital with most of the spin density localized on the bis(imino)pyridine backbone and not on the phenylthiolate arm. The DFT results are

nicely validated by their agreement with the findings from Mössbauer and EPR spectroscopies, as well as by their reproduction of the experimentally observed, yet subtle bond length distortions that occur in the BIP backbone upon one-electron reduction. This study shows that the tetradentate LN_3S ligand can serve as a non-innocent ligand in the same fashion as the parent BIP system, but in this case only accepts one electron delocalized over the ligand backbone. Taken together, our experimental and computational data strongly suggest that mono-reduction of the starting iron(II) complex provides the first example of an intermediate-spin iron(II) complex antiferromagnetically coupled with a ligand-based radical.

The O_2 reactivity of the new Fe^{II} complexes $[Fe^{II}(LN_3S)(py)](OTf)$ and $[Fe^{II}(LN_3S)(DMAP)](OTf)$ appears to mirror that of $[Fe^{II}(LN_3S)(OTf)]$ to give sulfonato-iron complexes. Interestingly, the thiolate-ligated Ni^{II} complex $[Ni^{II}(LN_3S)](BF_4)$ is completely unreactive toward O_2, as opposed to some thiolate-ligated Ni^{II} complexes that can become oxygenated at the sulfur positions. The mono-reduced iron complex $[Fe^{II}(LN_3S)(DMAP)]^0$ is extremely air-sensitive and rapidly reacts with O_2, but instead of leading only to *S*-oxygenation, yields a mixture of products involving both Fe-centered and S-centered oxygenates. Now that the ability to store reducing equivalents on thiolate-appended BIP ligands has been established, future work may involve designing systems where reducing equivalents on both the non-innocent ligand and the metal can be harnessed in a more controlled fashion for O_2 activation.

2. 5. References

(1) McQuilken, A. C.; Goldberg, D. P. *Dalton Trans*. **2012**, *41*, 10883.

(2) Fox, B. G. *Iron cofactors: Non-heme Handbook of Proteins John Wiley & Sons Ltd., Chichester, UK*, 2007; pp 611-618.

(3) Kovacs, J. A.; Brines, L. M. *Acc. Chem. Res*. **2007**, *40*, 501.

(4) Mascharak, P. K. *Coord. Chem. Rev*. **2002**, *225*, 201.

(5) Solomon, E. I.; Decker, A.; Lehnert, N. *Proc. Natl. Acad. Sci. U. S. A*. **2003**, *100*, 3589.

(6) Ryle, M. J.; Hausinger, R. P. *Curr. Opin. Chem. Biol*. **2002**, *6*, 193.

(7) Bruijnincx, P. C. A.; van Koten, G.; Gebbink, R. J. M. K. *Chem. Soc. Rev*. **2008**, *37*, 2716.

(8) Nivière, V.; Bonnot, F.; Bourgeois, D. *Handbook of Metalloproteins* **2011**, 246.

(9) Yeh, A. P.; Hu, Y. L.; Jenney, F. E.; Adams, M. W. W.; Rees, D. C. *Biochemistry* **2000**, *39*, 2499.

(10) Matias, P. M.; Morais, J.; Coelho, A. V.; Meijers, R.; Gonzalez, A.; Thompson, A. W.; Sieker, L.; LeGall, J.; Carrondo, M. A. *J. Biol. Inorg. Chem*. **1997**, *2*, 507.

(11) Santos-Silva, T.; Trincão, J.; Carvalho, A. L.; Bonifàcio, C.; Auchére, F.; Raleiras, P.; Moura, I.; Moura, J. J. G.; Romão, M. J. *J. Biol. Inorg. Chem*. **2006**, *11*, 548.

(12) Adam, V.; Royant, A.; Nivière, V.; Molina-Heredia, F. P.; Bourgeois, D. *Structure* **2004**, *12*, 1729.

(13) Kobayashi, M.; Nagasawa, T.; Yamada, H. *Trends Biotechnol*. **1992**, *10*, 402.

(14) Endo, I.; Nojiri, M.; Tsujimura, M.; Nakasako, M.; Nagashima, S.; Yohda, M.; Odaka, M. *J. Inorg. Biochem.* **2001**, *83*, 247.

(15) Kobayashi, M.; Shimizu, S. *Nat. Biotechnol.* **1998**, *16*, 733.

(16) de Visser, S. P.; Kumar, D., Eds.; *Iron-Containing Enzymes: Versatile Catalysts of Hydroxylation Reactions in Nature*; Royal Society of Chemistry: Cambridge, U.K., 2011.

(17) Joseph, C. A.; Maroney, M. J. *Chem. Commun.* **2007**, 3338.

(18) Straganz, G. D.; Nidetzky, B. *Chembiochem* **2006**, *7*, 1536.

(19) Siakkou, E.; Rutledge, M. T.; Wilbanks, S. M.; Jameson, G. N. L. *Biochim. Biophys. Acta, Proteins Proteomics* **2011**, *1814*, 2003.

(20) Tchesnokov, E. P.; Wilbanks, S. M.; Jameson, G. N. L. *Biochemistry* **2012**, *51*, 257.

(21) McCoy, J. G.; Bailey, L. J.; Bitto, E.; Bingman, C. A.; Aceti, D. J.; Fox, B. G.; Phillips, G. N. *Proc. Natl. Acad. Sci. U. S. A.* **2006**, *103*, 3084.

(22) Simmons, C. R.; Liu, Q.; Huang, Q. Q.; Hao, Q.; Begley, T. P.; Karplus, P. A.; Stipanuk, M. H. *J. Biol. Chem.* **2006**, *281*, 18723.

(23) Ye, S.; Wu, X.; Wei, L.; Tang, D. M.; Sun, P.; Bartlam, M.; Rao, Z. H. *J. Biol. Chem.* **2007**, *282*, 3391.

(24) Jiang, Y. B.; Widger, L. R.; Kasper, G. D.; Siegler, M. A.; Goldberg, D. P. *J. Am. Chem. Soc.* **2010**, *132*, 12214.

(25) Badiei, Y. M.; Siegler, M. A.; Goldberg, D. P. *J. Am. Chem. Soc.* **2011**, *133*, 1274.

(26) McQuilken, A. C.; Jiang, Y. B.; Siegler, M. A.; Goldberg, D. P. *J. Am. Chem. Soc.* **2012**, *134*, 8758.

(27) Kovacs, J. A. *Science* **2003**, *299*, 1024.

(28) Kovacs, J. A. *Chem. Rev.* **2004**, *104*, 825.

(29) Artaud, I.; Chatel, S.; Chauvin, A. S.; Bonnet, D.; Kopf, M. A.; Leduc, P. *Coord. Chem. Rev.* **1999**, *192*, 577.

(30) Cho, J.; Woo, J.; Nam, W. *J. Am. Chem. Soc.* **2012**, *134*, 11112.

(31) Sallmann, M.; Siewert, I.; Fohlmeister, L.; Limberg, C.; Knispel, C. *Angew. Chem. Int. Ed.* **2012**, *51*, 2234.

(32) Gonzalez-Ovalle, L. E.; Quesne, M. G.; Kumar, D.; Goldberg, D. P.; de Visser, S. P. *Org. Biomol. Chem.* **2012**, *10*, 5401.

(33) Kumar, D.; Sastry, G. N.; Goldberg, D. P.; de Visser, S. P. *J Phys Chem A* **2012**, *116*, 582.

(34) Britovsek, G. J. P.; Bruce, M.; Gibson, V. C.; Kimberley, B. S.; Maddox, P. J.; Mastroianni, S.; McTavish, S. J.; Redshaw, C.; Solan, G. A.; Stromberg, S.; White, A. J. P.; Williams, D. J. *J. Am. Chem. Soc.* **1999**, *121*, 8728.

(35) Scott, J.; Gambarotta, S.; Korobkov, I.; Budzelaar, P. H. M. *Organometallics* **2005**, *24*, 6298.

(36) Scott, J.; Gambarotta, S.; Korobkov, I.; Knijnenburg, Q.; de Bruin, B.; Budzelaar, P. H. M. *J. Am. Chem. Soc.* **2005**, *127*, 17204.

(37) Tondreau, A. M.; Milsmann, C.; Lobkovsky, E.; Chirik, P. J. *Inorg. Chem.* **2011**, *50*, 9888.

(38) Tondreau, A. M.; Stieber, S. C. E.; Milsmann, C.; Lobkovsky, E.; Weyhermuller, T.; Semproni, S. P.; Chirik, P. J. *Inorg. Chem.* **2013**, *52*, 635.

(39) Bart, S. C.; Chlopek, K.; Bill, E.; Bouwkamp, M. W.; Lobkovsky, E.; Neese, F.; Wieghardt, K.; Chirik, P. J. *J. Am. Chem. Soc.* **2006**, *128*, 13901.

(40) Bouwkamp, M. W.; Bart, S. C.; Hawrelak, E. J.; Trovitch, R. J.; Lobkovsky, E.; Chirik, P. J. *Chem. Commun.* **2005**, 3406.

(41) Bart, S. C.; Lobkovsky, E.; Bill, E.; Wieghardt, K.; Chirik, P. J. *Inorg. Chem.* **2007**, *46*, 7055.

(42) Stieber, S. C. E.; Milsmann, C.; Hoyt, J. M.; Turner, Z. R.; Finkelstein, K. D.; Wieghardt, K.; DeBeer, S.; Chirik, P. J. *Inorg. Chem.* **2012**, *51*, 3770.

(43) Darmon, J. M.; Turner, Z. R.; Lobkovsky, E.; Chirik, P. J. *Organometallics* **2012**, *31*, 2275.

(44) Enright, D.; Gambarotta, S.; Yap, G. P. A.; Budzelaar, P. H. M. *Angew. Chem. Int. Ed.* **2002**, *41*, 3873.

(45) de Bruin, B.; Bill, E.; Bothe, E.; Weyhermuller, T.; Wieghardt, K. *Inorg. Chem.* **2000**, *39*, 2936.

(46) Farmer, P. J.; Solouki, T.; Mills, D. K.; Soma, T.; Russell, D. H.; Reibenspies, J. H.; Darensbourg, M. Y. *J. Am. Chem. Soc.* **1992**, *114*, 4601.

(47) Farmer, P. J.; Solouki, T.; Soma, T.; Russell, D. H.; Darensbourg, M. Y. *Inorg. Chem.* **1993**, *32*, 4171.

(48) Darensbourg, M. Y.; Tuntulani, T.; Reibenspies, J. H. *Inorg. Chem.* **1995**, *34*, 6287.

(49) Buonomo, R. M.; Font, I.; Maguire, M. J.; Reibenspies, J. H.; Tuntulani, T.; Darensbourg, M. Y. *J. Am. Chem. Soc.* **1995**, *117*, 5427.

(50) Grapperhaus, C. A.; Darensbourg, M. Y.; Sumner, L. W.; Russell, D. H. *J. Am. Chem. Soc.* **1996**, *118*, 1791.

(51) Grapperhaus, C. A.; Darensbourg, M. Y. *Acc. Chem. Res.* **1998**, *31*, 451.

(52) Mullins, C. S.; Grapperhaus, C. A.; Frye, B. C.; Wood, L. H.; Hay, A. J.; Buchanan, R. M.; Mashuta, M. S. *Inorg. Chem.* **2009**, *48*, 9974.

(53) Herdt, D. R.; Grapperhaus, C. A. *Dalton Trans.* **2012**, *41*, 364.

(54) Mullins, C. S.; Grapperhaus, C. A.; Kozlowski, P. M. *J. Biol. Inorg. Chem.* **2006**, *11*, 617.

(55) Kumar, D.; Karamzadeh, B.; Sastry, G. N.; de Visser, S. P. *J. Am. Chem. Soc.* **2010**, *132*, 7656.

(56) Vardhaman, A. K.; Sastri, C. V.; Kumar, D.; de Visser, S. P. *Chem. Commun.* **2011**, *47*, 11044.

(57) Becke, A. D. *J. Chem. Phys.* **1993**, *98*, 1372.

(58) Lee, C. T.; Yang, W. T.; Parr, R. G. *Phys. Rev. B* **1988**, *37*, 785.

(59) Hay, P. J.; Wadt, W. R. *J. Chem. Phys.* **1985**, *82*, 299.

(60) Grimme, S.; Antony, J.; Ehrlich, S.; Krieg, H. *J. Chem. Phys.* **2010**, *132*, 154104.

(61) Becke, A. D. *Phys. Rev. A* **1988**, *38*, 3098.

(62) Perdew, J. P. *Phys. Rev. B* **1986**, *33*, 8822.

(63) *Jaguar, version 7.9.*; Schrodinger, LLC: New York, NY, 2011.

(64) Schwabe, T.; Grimme, S. *Phys. Chem. Chem. Phys.* **2007**, *9*, 3397.

(65) Bianchini, C.; Mantovani, G.; Meli, A.; Migliacci, F.; Zanobini, F.; Laschi, F.; Sommazzi, A. *Eur. J. Inorg. Chem.* **2003**, 1620.

(66) Fiedler, A. T.; Halfen, H. L.; Halfen, J. A.; Brunold, T. C. *J. Am. Chem. Soc.* **2005**, *127*, 1675.

(67) Theisen, R. M.; Shearer, J.; Kaminsky, W.; Kovacs, J. A. *Inorg. Chem.* **2004**, *43*, 7682.

(68) Shearer, J.; Nehring, J.; Lovell, S.; Kaminsky, W.; Kovacs, J. A. *Inorg. Chem.* **2001**, *40*, 5483.

(69) Addison, A. W.; Rao, T. N.; Reedijk, J.; Vanrijn, J.; Verschoor, G. C. *J. Chem. Soc., Dalton Trans.* **1984**, 1349.

(70) Manuel, T. D.; Rohde, J. U. *J. Am. Chem. Soc.* **2009**, *131*, 15582.

(71) Fan, R. Q.; Fan, R. J.; Lv, Z. W.; Yang, Y. L.; An, F.; Gu, D. M. *J. Coord. Chem.* **2007**, *60*, 919.

(72) Dunn, T. J.; Ramogida, C. F.; Simmonds, C.; Paterson, A.; Wong, E. W. Y.; Chiang, L.; Shimazaki, Y.; Storr, T. *Inorg. Chem.* **2011**, *50*, 6746.

(73) Chen, Y. J.; Hao, P.; Zuo, W. W.; Gao, K.; Sun, W. H. *J. Organomet. Chem.* **2008**, *693*, 1829.

(74) Bryliakov, K. P.; Talsi, E. P.; Semikolenova, N. V.; Zakharov, V. A. *Organometallics* **2009**, *28*, 3225.

(75) Britovsek, G. J. P.; Gibson, V. C.; Spitzmesser, S. K.; Tellmann, K. P.; White, A. J. P.; Williams, D. J. *J. Chem. Soc., Dalton Trans.* **2002**, 1159.

(76) Bart, S. C.; Lobkovsky, E.; Chirik, P. J. *J. Am. Chem. Soc.* **2004**, *126*, 13794.

(77) Nakajima, Y.; Nakao, Y.; Sakaki, S.; Tamada, Y.; Ono, T.; Ozawa, F. *J. Am. Chem. Soc.* **2010**, *132*, 9934.

(78) Trovitch, R. J.; Lobkovsky, E.; Chirik, P. J. *J. Am. Chem. Soc.* **2008**, *130*, 11631.

(79) Gutlich, P.; Bill, E.; Trautwein, A. X. *Mossbauer Spectroscopy and Transition Metal Chemistry: Fundamentals and Applications*; Springer-Verlag: Berlin Heidelberg, 2011.

(80) Moura, I.; Tavares, P.; Moura, J. J. G.; Ravi, N.; Huynh, B. H.; Liu, M. Y.; Legall, J. *J. Biol. Chem.* **1990**, *265*, 21596.

(81) Britovsek, G. J. P.; Clentsmith, G. K. B.; Gibson, V. C.; Goodgame, D. M. L.; McTavish, S. J.; Pankhurst, Q. A. *Catal. Commun.* **2002**, *3*, 207.

(82) Russell, S. K.; Milsmann, C.; Lobkovsky, E.; Weyhermuller, T.; Chirik, P. J. *Inorg. Chem.* **2011**, *50*, 3159.

(83) Kumar, D.; Thiel, W.; de Visser, S. P. *J. Am. Chem. Soc.* **2011**, *133*, 3869.

2. 6. Appendix A: Supplementary spectra

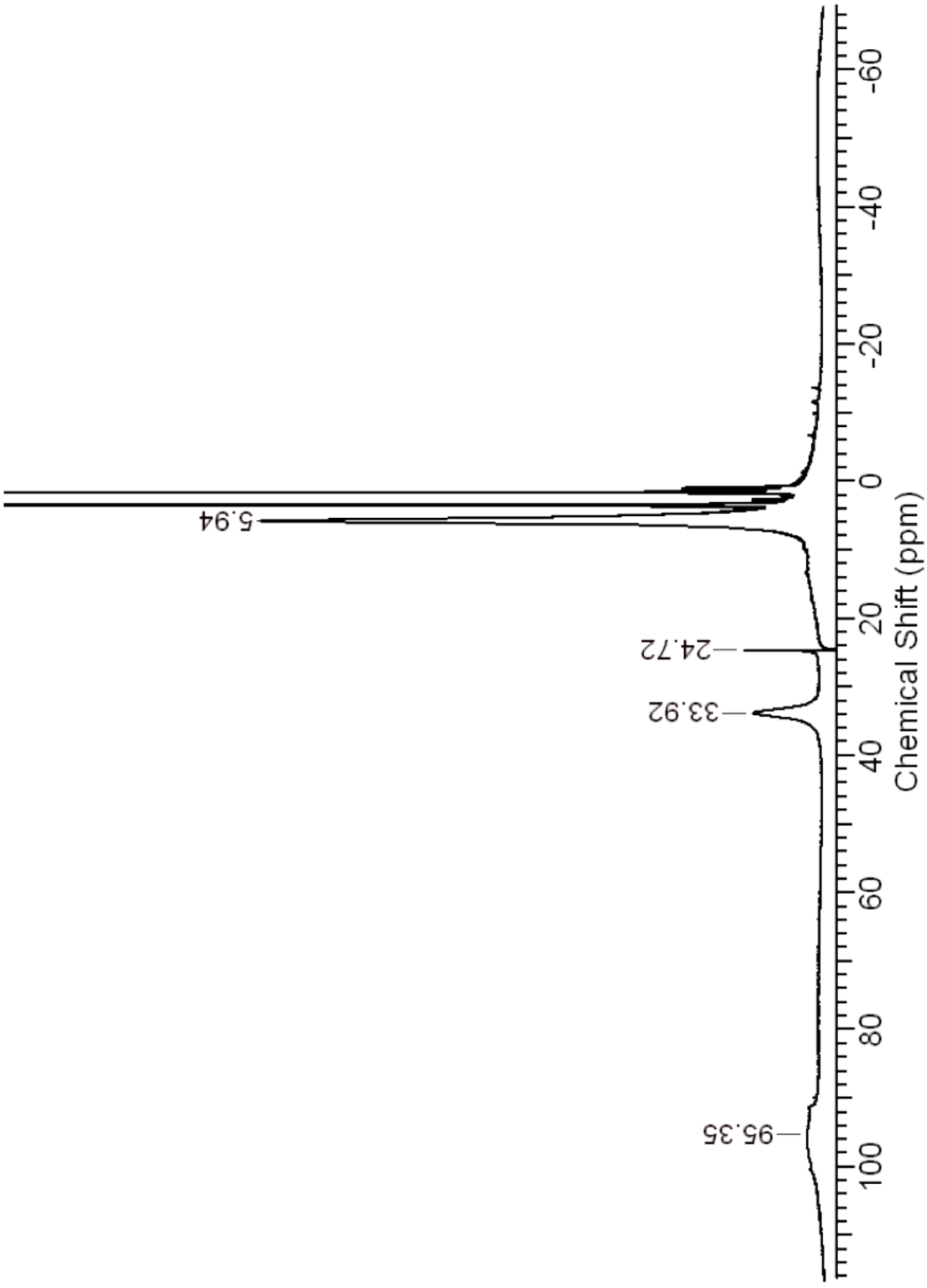

Figure 2. 23. ^{1}H NMR spectrum of $[Fe^{II}(LN_3S)(DMAP)]^0$ (25 °C, THF-d_8).

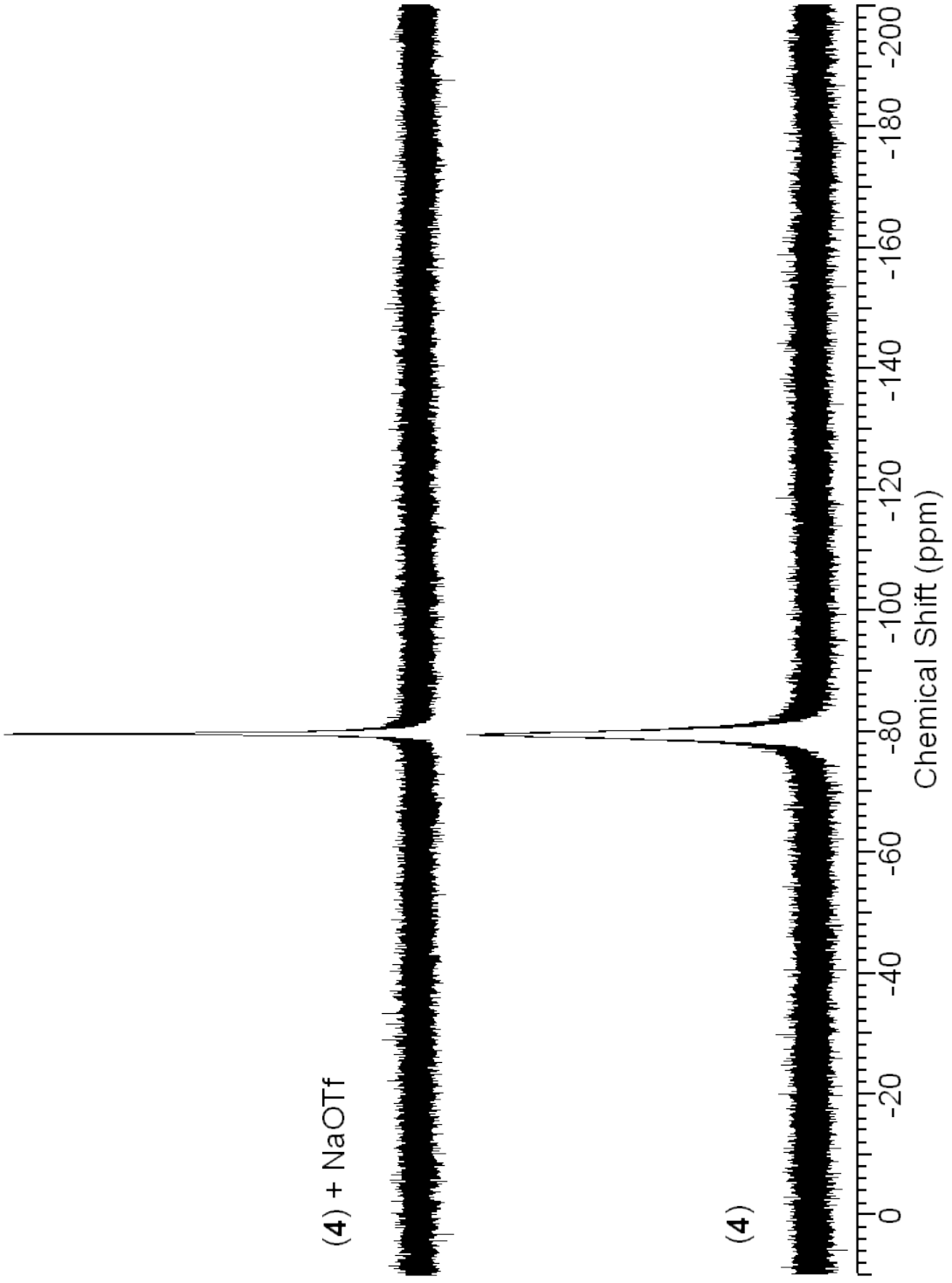

Figure 2. 24. ^{19}F NMR spectra (25 °C, THF-d_8) of $[Fe^{II}(LN_3S)(DMAP)]^0$ (bottom) and $[Fe^{II}(LN_3S)(DMAP)]^0$ + NaOTf (excess)(top).

2. 7. Appendix B: X-ray Crystallography

General

All reflection intensities were measured at 110(2) K using a KM4/Xcalibur (detector: Sapphire3) with enhance graphite-monochromated Mo *K*α radiation (λ = 0.71073 Å) under the program CrysAlisPro (Versions 1.171.33.48, 1.171.33.55, and 1.171.34.49, Agilent Technologies). The program CrysAlisPro (Versions 1.171.33.48, 1.171.33.55, and 1.171.34.49, Agilent Technologies) was used to refine the cell dimensions. Data reduction was done using the program CrysAlisPro (Versions 1.171.33.48, 1.171.33.55, and 1.171.34.49, Agilent Technologies). The structures were solved with the program SHELXS-97[1] and were refined on F^2 with SHELXL-97.[1] Analytical numeric absorption corrections based on a multifaceted crystal model were applied using CrysAlisPro (Versions 1.171.33.48, 1.171.33.55, and 1.171.34.49, Agilent Technologies). The temperature of the data collection was controlled using the system Cryojet (manufactured by Oxford Instruments). The H-atoms were placed at calculated positions using the instructions AFIX 13, AFIX 23, AFIX 43 or AFIX 137 with isotropic displacement parameters having values 1.2 or 1.5 times *U*eq of the attached C atoms.

Crystal structure of $[Fe^{II}(LN_3S)(py)](OTf)$

The structure is ordered. The crystal that was mounted on the diffractometer was twinned. The twin relationship was resolved using the program TwinRotMat from Platon;[2] the two twinned components are related by a twofold axis along the a* direction. The structure is also racemically twinned. The fractional contribution of the three components (*i.e.*, the BASF batch scale factor) refined to 0.185(8), 0.546(13), 0.212(13). Fw = 712.62, dark brown thick plate, 0.41 × 0.20 × 0.10 mm^3, monoclinic, *Pc* (no. 7), *a* =

17.6133(5), b = 10.4554(2), c = 18.8663(4) Å, β = 105.548(3)°, V = 3347.17(13)Å^3, Z = 4, D_x = 1.414g cm^{-3}, μ = 0.632 mm^{-1}, abs. corr. range: 0.632– 0.827. 26684 Reflections were measured up to a resolution of (sin $\theta/\lambda)_{max}$ = 0.59 Å^{-1}. 11193 Reflections were unique (R_{int} = 0.0652), of which 8793 were observed [$I > 2\sigma(I)$]. 844 Parameters were refined with 282 restraints. $R1/wR2$ [$I > 2\sigma(I)$]: 0.0471/0.1068. $R1/wR2$ [all refl.]: 0.0661/0.1136. S = 0.993. Residual electron density found between –0.75 and 0.78 eÅ^{-3}.

Crystal structure of [Fe^{II}(LN$_3$S)(DMAP)](OTf)

The structure is ordered. Fw = 755.69, black plate, 0.49 × 0.36 × 0.07 mm^3, monoclinic, $C2/c$ (no. 15), a = 30.8054(16), b = 10.2837(2), c = 25.181(4) Å, β = 116.305(6)°, V = 7151.1(12)Å^3, Z = 8, D_x = 1.404 g cm^{-3}, μ = 0.596 mm^{-1}, abs. corr. range: 0.802–0.962. 29265 Reflections were measured up to a resolution of (sin $\theta/\lambda)_{max}$ = 0.62 Å^{-1}. 7007 Reflections were unique (R_{int} = 0.0400), of which 5442 were observed [$I > 2\sigma(I)$]. 450 Parameters were refined. $R1/wR2$ [$I > 2\sigma(I)$]: 0.0314/0.0756. $R1/wR2$ [all refl.]: 0.0474/0.0796. S = 1.026. Residual electron density found between –0.46 and 0.30 eÅ^{-3}.

Crystal structure of [Fe^{II}(LN$_3$S)(DMAP)]^0

The structure is ordered. The asymmetric unit contains one molecule of Fe complex and two uncoordinated diethyl ether solvent molecules. Fw = 754.86, dark brown lath, 0.49 × 0.21 × 0.07 mm^3, monoclinic, $P2_1/c$ (no. 14), a = 19.5713(4), b = 10.9561(2), c = 19.7953(3) Å, β = 103.7517(18) °, V = 4122.94(13) Å^3, Z = 4, D_x = 1.216 g cm^{-3}, μ = 0.457 mm^{-1}, abs. corr. range: 0.871–0.977. 37056 Reflections were measured up to a resolution of (sin $\theta/\lambda)_{max}$ = 0.61 Å^{-1}. 7886 Reflections were unique (R_{int} = 0.0433), of

which 6329 were observed [$I > 2\sigma(I)$]. 472 Parameters were refined. $R1/wR2$ [$I > 2\sigma(I)$]: 0.0379/0.0823. $R1/wR2$ [all refl.]: 0.0542/0.0879. S = 1.035. Residual electron density found between –0.30 and 0.47 e $Å^{-3}$.

Crystal structure of $[Ni^{II}(LN_3S)](BF_4)$

The structure is ordered. Fw = 659.05, red plate, 0.56 × 0.33 × 0.07 mm^3, monoclinic, $P2_1/c$ (no. 14), a = 15.13933(17), b = 13.80648(15), c = 13.94752(16) Å, β = 95.0548(10)°, V = 2903.98(6) $Å^3$, Z = 4, D_x = 1.507 g cm^{-3}, μ = 0.974 mm^{-1}, abs. corr. range: 0.728–0.951. 39899 Reflections were measured up to a resolution of $(\sin \theta/\lambda)_{max}$ = 0.68 $Å^{-1}$. 7712 Reflections were unique (R_{int} = 0.0522), of which 5909 were observed [$I > 2\sigma(I)$]. 367 Parameters were refined. $R1/wR2$ [$I > 2\sigma(I)$]: 0.0352/0.0937. $R1/wR2$ [all refl.]: 0.0497/0.0974. S = 1.018. Residual electron density found between –0.63 and 0.80 e $Å^{-3}$.

References:

(1) Sheldrick, G. M. *Acta Cryst*. **2008**, *64,* 112-122

(2) Spek, A. L. *Acta Cryst*. **2009,** *65,* 148-155.

2. 8. Appendix C: Density Functional Theory

Table 2. 6. Absolute energies, zero-point energies and free energies of DFT calculated structures. Also given are dispersion corrected energies (E_{disp}) and solvent energy (E_{solv}). Geometries optimized at UB3LYP/B1.

	E (B1)	ZPE (B1)	G (B1)	E_{solv}	E (B2)	E_{disp} (B2)
Nickel(II) Complexes						
$^{1}[Ni^{II}(LN_3S)]^{+}$	-1778.285310	0.518848	-1777.828539	-45.7729	-1778.896295	-1777.390861
$^{3}[Ni^{II}(LN_3S)]^{+}$	-1778.275937	0.517597	-1777.821860	-45.1618	-1778.888356	-1777.370593
$^{5}[Ni^{II}(LN_3S)]^{+}$	-1778.225293	0.516065	-1777.774736	-39.5319	-1778.840463	-1777.313815
$^{2}[Ni^{II}(LN_3S)]^{0}$	-1778.473189	0.516086	-1778.017698	-13.4556	-1779.091135	-1778.473189
Iron(II) Complexes						
$^{1}[Fe^{II}(LN_3S)(DMAP)]^{+}$	-2114.598946	0.684178	-2113.986084	-44.0630	-2115.392667	-2113.402611
$^{3}[Fe^{II}(LN_3S)(DMAP)]^{+}$	-2114.603486	0.684355	-2113.993085	-44.5044	-2115.397990	-2113.420448
$^{5}[Fe^{II}(LN_3S)(DMAP)]^{+}$	-2114.621034	0.683054	-2114.015586	-46.0380	-2115.418699	-2113.453619
$^{4}[Fe^{II}(LN_3S)(DMAP)]^{0}$	-2114.762060	0.679341	-2114.159079	-17.8990	-2115.566541	-2113.597691
$^{2}[Fe^{II}(LN_3S)(DMAP)]^{0}$	-2114.775209	0.681040	-2114.170098	-18.1525	-2115.578244	-2113.600308

In au, In kcal mol^{-1}.

Table 2. 7. Relative energies (in kcal mol^{-1}) for iron and nickel complexes. Geometries optimized at UB3LYP/B1.

	ΔE (B1)	ΔE+ZPE (B1)	ΔE (B2)	ΔE+ZPE (B2)	ΔG (B1)	ΔG (B2)	ΔE_{disp}	ΔE_{disp}+ ZPE	ΔE+ZPE $+E_{solv}$
Nickel(II) Complexes									
$^{1}[Ni^{II}(LN_3S)]^{+}$	0.00	0.00	0.00	0.00	0.00	0.00	0.00	0.00	0.00
$^{3}[Ni^{II}(LN_3S)]^{+}$	5.88	5.10	4.98	4.20	4.19	3.29	12.72	11.93	4.81
$^{5}[Ni^{II}(LN_3S)]^{+}$	37.66	35.92	35.03	33.29	33.76	31.13	48.35	46.60	39.53
$^{2}[Ni^{II}(LN_3S)]^{0}$	-117.90	-119.63	-122.26	-124.00	-118.70	-123.07	-679.17	-680.91	-91.68
Iron(II) Complexes									
$^{1}[Fe^{II}(LN_3S)(DMAP)]^{+}$	13.86	14.57	16.34	17.04	18.51	20.99	32.01	32.71	19.02
$^{3}[Fe^{II}(LN_3S)(DMAP)]^{+}$	11.01	11.83	13.00	13.81	14.12	16.10	20.81	21.63	15.34
$^{5}[Fe^{II}(LN_3S)(DMAP)]^{+}$	0.00	0.00	0.00	0.00	0.00	0.00	0.00	0.00	0.00
$^{4}[Fe^{II}(LN_3S)(DMAP)]^{0}$	-102.36	-105.39	-109.11	-112.14	-108.56	-115.31	-122.41	-125.45	-85.98
$^{2}[Fe^{II}(LN_3S)(DMAP)]^{0}$	-110.61	-112.58	-116.45	-118.42	-115.47	-121.32	-124.06	-126.03	-92.51

Cartesian coordinates of DFT optimized structures.

$^{1}[Fe^{II}(LN_3S)(DMAP)]^{+}$

26	-0.057725000	0.104267000	0.093772000
16	-0.638085000	0.607789000	2.247171000
6	1.070785000	0.431960000	2.887571000
6	1.425977000	0.951851000	4.138232000
6	2.751008000	0.888360000	4.581767000
6	3.741692000	0.317893000	3.769575000
6	3.401440000	-0.223880000	2.529314000
6	2.060865000	-0.196822000	2.090196000
6	2.121316000	-1.676142000	0.122147000
6	3.271346000	-2.561183000	0.515648000
6	1.377938000	-1.949687000	-1.117295000
6	1.654153000	-2.910400000	-2.102678000
6	0.759928000	-3.064087000	-3.170190000
6	-0.408909000	-2.289958000	-3.237467000
6	-0.645446000	-1.344345000	-2.232962000
6	-1.833494000	-0.485111000	-2.055236000
6	-2.956739000	-0.563138000	-3.048828000
6	-2.949941000	1.108247000	-0.622223000
6	-3.101989000	2.394170000	-1.194134000
6	-4.212599000	3.159976000	-0.800368000
6	-5.138557000	2.675040000	0.121238000
6	-4.966602000	1.405730000	0.674506000
6	-3.875531000	0.596394000	0.324127000
6	-2.115826000	2.987160000	-2.203395000
6	-2.774550000	3.220714000	-3.584751000
6	-1.500768000	4.305840000	-1.679482000
6	-3.753185000	-0.810461000	0.916302000
6	-4.670619000	-1.810346000	0.168969000
6	-4.046582000	-0.849790000	2.432328000
6	1.444834000	1.600911000	-2.069002000
6	2.222917000	2.611550000	-2.605859000
6	2.593584000	3.729375000	-1.804220000
6	2.119431000	3.716173000	-0.461442000
6	1.340674000	2.668156000	-0.005668000
6	3.826500000	4.726824000	-3.687526000
6	3.703107000	5.896792000	-1.439151000
7	1.604649000	-0.690025000	0.837876000
7	0.261014000	-1.179242000	-1.234941000
7	-1.810335000	0.268742000	-0.978150000
7	0.990237000	1.603951000	-0.786307000
7	3.354822000	4.753193000	-2.295684000

1	0.661685000	1.416406000	4.750701000
1	3.014164000	1.300000000	5.550429000
1	4.775295000	0.302989000	4.096863000
1	4.182201000	-0.623625000	1.895955000
1	3.330885000	-2.664726000	1.601803000
1	4.234658000	-2.168134000	0.165009000
1	3.150409000	-3.559866000	0.088662000
1	2.540097000	-3.528866000	-2.040128000
1	0.964155000	-3.798330000	-3.940553000
1	-1.114881000	-2.427579000	-4.046488000
1	-3.291016000	-1.599332000	-3.175281000
1	-2.624637000	-0.204570000	-4.031315000
1	-3.808423000	0.039162000	-2.734614000
1	-4.349846000	4.149118000	-1.224396000
1	-5.990768000	3.282341000	0.407878000
1	-5.689852000	1.035687000	1.391889000
1	-1.294819000	2.276907000	-2.339616000
1	-2.038929000	3.611726000	-4.298068000
1	-3.193410000	2.297604000	-4.000060000
1	-3.588898000	3.950813000	-3.514993000
1	-0.733567000	4.668604000	-2.373687000
1	-1.040675000	4.166295000	-0.697143000
1	-2.262347000	5.088226000	-1.587345000
1	-2.716626000	-1.141842000	0.785103000
1	-4.549249000	-2.818860000	0.580970000
1	-4.448250000	-1.852067000	-0.903389000
1	-5.723537000	-1.525154000	0.278676000
1	-3.827245000	-1.849208000	2.824746000
1	-3.427217000	-0.130328000	2.974600000
1	-5.099845000	-0.638158000	2.649760000
1	1.166267000	0.752279000	-2.679500000
1	2.537509000	2.532743000	-3.637124000
1	2.345337000	4.523644000	0.220635000
1	0.961289000	2.658228000	1.006802000
1	4.468029000	3.857399000	-3.876915000
1	4.409714000	5.626224000	-3.882447000
1	2.988025000	4.705714000	-4.394655000
1	4.298342000	6.604429000	-2.015245000
1	4.294201000	5.582059000	-0.570598000
1	2.805657000	6.417061000	-1.083152000

^{3}[Fe^{II}(LN$_3$S)(DMAP)]$^{+}$

26	-0.031419000	-0.092564000	-0.108969000
16	-0.302641000	0.050276000	2.244436000
6	1.494602000	0.171957000	2.506742000
6	2.044279000	0.740461000	3.665669000
6	3.429387000	0.836938000	3.817716000

6	4.291531000	0.376275000	2.808286000
6	3.765618000	-0.209597000	1.657902000
6	2.368180000	-0.326262000	1.506883000
6	2.126355000	-1.925913000	-0.335705000
6	3.361959000	-2.740688000	-0.072070000
6	1.165814000	-2.324282000	-1.361706000
6	1.238317000	-3.405717000	-2.263020000
6	0.151500000	-3.659350000	-3.100480000
6	-1.004318000	-2.853510000	-3.044997000
6	-1.025819000	-1.785738000	-2.148883000
6	-2.121858000	-0.808137000	-1.934714000
6	-3.379907000	-0.946244000	-2.741265000
6	-2.842562000	1.192211000	-0.788729000
6	-2.876477000	2.302084000	-1.673718000
6	-3.786516000	3.333839000	-1.388063000
6	-4.629641000	3.275224000	-0.279393000
6	-4.578331000	2.174011000	0.575703000
6	-3.688248000	1.113226000	0.347254000
6	-1.993284000	2.428177000	-2.921373000
6	-2.834520000	2.381601000	-4.221923000
6	-1.147417000	3.723563000	-2.904685000
6	-3.701292000	-0.107470000	1.270303000
6	-4.830391000	-1.092043000	0.872594000
6	-3.828435000	0.269127000	2.762495000
6	1.834024000	1.920441000	-1.381595000
6	2.523494000	3.104588000	-1.573040000
6	2.223923000	4.239841000	-0.764857000
6	1.191421000	4.066134000	0.200515000
6	0.547405000	2.846967000	0.321890000
6	3.952204000	5.566493000	-1.913458000
6	2.558157000	6.571425000	-0.046546000
7	1.721277000	-0.875477000	0.371374000
7	0.049614000	-1.546390000	-1.357883000
7	-1.891827000	0.113199000	-1.026963000
7	0.854122000	1.765168000	-0.449154000
7	2.888363000	5.426854000	-0.908966000
1	1.378592000	1.108965000	4.437833000
1	3.841131000	1.283315000	4.716987000
1	5.365257000	0.482126000	2.917005000
1	4.432659000	-0.530832000	0.867195000
1	3.608610000	-2.736156000	0.993377000
1	4.236830000	-2.358147000	-0.613724000
1	3.214756000	-3.778848000	-0.380355000
1	2.119424000	-4.032991000	-2.303390000
1	0.191781000	-4.488523000	-3.797133000
1	-1.850165000	-3.062841000	-3.686830000

1	-3.806432000	-1.947043000	-2.602698000
1	-3.170323000	-0.827046000	-3.810714000
1	-4.125829000	-0.207692000	-2.451313000
1	-3.836315000	4.191844000	-2.050007000
1	-5.327526000	4.082775000	-0.083959000
1	-5.241440000	2.133117000	1.431863000
1	-1.291764000	1.586002000	-2.938483000
1	-2.179633000	2.417814000	-5.100537000
1	-3.447437000	1.477775000	-4.289192000
1	-3.510916000	3.242354000	-4.275783000
1	-0.467119000	3.739333000	-3.764346000
1	-0.552781000	3.803135000	-1.991834000
1	-1.783326000	4.613498000	-2.972859000
1	-2.746611000	-0.631593000	1.150144000
1	-4.804827000	-1.977130000	1.518558000
1	-4.737473000	-1.427791000	-0.166603000
1	-5.813639000	-0.619670000	0.983844000
1	-3.695297000	-0.624829000	3.380867000
1	-3.064998000	0.995112000	3.055061000
1	-4.815688000	0.684778000	2.995483000
1	2.067767000	1.049913000	-1.983442000
1	3.290134000	3.145904000	-2.334196000
1	0.895490000	4.874145000	0.854580000
1	-0.223850000	2.694816000	1.065371000
1	4.778711000	4.870641000	-1.722766000
1	4.347878000	6.580927000	-1.873635000
1	3.571389000	5.390312000	-2.926974000
1	3.193217000	7.414673000	-0.316467000
1	2.730589000	6.338859000	1.011357000
1	1.512786000	6.878367000	-0.172491000

^{5}[Fe^{II}(LN$_3$S)(DMAP)]$^{+}$

26	-0.002937000	-0.009402000	0.016732000
16	-0.010515000	0.022503000	2.423179000
6	1.815407000	-0.002461000	2.525723000
6	2.482175000	0.563832000	3.622835000
6	3.877142000	0.543765000	3.700360000
6	4.639564000	-0.039477000	2.675777000
6	3.999291000	-0.625726000	1.585451000
6	2.590312000	-0.619976000	1.505144000
6	2.074598000	-2.225936000	-0.265420000
6	3.167980000	-3.228769000	-0.006104000
6	1.054394000	-2.508046000	-1.304523000
6	1.104353000	-3.582449000	-2.210968000
6	0.042612000	-3.768851000	-3.098299000
6	-1.057721000	-2.900296000	-3.070353000
6	-1.050698000	-1.838941000	-2.156880000

6	-2.147476000	-0.834983000	-2.021944000
6	-3.378168000	-0.997325000	-2.871374000
6	-2.875635000	1.216101000	-0.962907000
6	-2.944341000	2.255972000	-1.928610000
6	-3.784970000	3.347459000	-1.651084000
6	-4.532038000	3.413833000	-0.475999000
6	-4.449912000	2.380196000	0.459256000
6	-3.622482000	1.268319000	0.244350000
6	-2.136334000	2.266991000	-3.233046000
6	-3.055472000	2.283778000	-4.479913000
6	-1.156167000	3.462535000	-3.289426000
6	-3.594279000	0.117608000	1.253085000
6	-4.736464000	-0.891641000	0.966569000
6	-3.652818000	0.589552000	2.721378000
6	1.839896000	2.121469000	-1.156229000
6	2.450726000	3.355329000	-1.283499000
6	1.935735000	4.480524000	-0.575114000
6	0.786772000	4.241305000	0.236289000
6	0.241752000	2.974291000	0.312227000
6	3.701949000	5.924011000	-1.505689000
6	1.956409000	6.850818000	0.086831000
7	1.858101000	-1.130907000	0.410713000
7	-0.004008000	-1.661092000	-1.320552000
7	-1.958626000	0.109743000	-1.147375000
7	0.744835000	1.905466000	-0.373201000
7	2.509523000	5.716623000	-0.668492000
1	1.895140000	1.022572000	4.409847000
1	4.373224000	0.992215000	4.554626000
1	5.722792000	-0.030554000	2.726451000
1	4.587818000	-1.044300000	0.776887000
1	3.541632000	-3.131123000	1.015441000
1	4.020054000	-3.093422000	-0.685700000
1	2.800644000	-4.251002000	-0.137023000
1	1.952077000	-4.254732000	-2.221924000
1	0.065413000	-4.590094000	-3.805358000
1	-1.890947000	-3.049790000	-3.743752000
1	-3.797051000	-2.003047000	-2.746984000
1	-3.145179000	-0.866602000	-3.935076000
1	-4.141171000	-0.268777000	-2.597251000
1	-3.853025000	4.156118000	-2.371224000
1	-5.177731000	4.265748000	-0.289629000
1	-5.037502000	2.435921000	1.368213000
1	-1.528720000	1.356255000	-3.278670000
1	-2.455842000	2.216239000	-5.395806000
1	-3.769538000	1.454825000	-4.475630000
1	-3.632071000	3.213462000	-4.530723000

1	-0.557857000	3.417484000	-4.207916000
1	-0.475530000	3.464148000	-2.433715000
1	-1.699188000	4.413907000	-3.291780000
1	-2.644042000	-0.416307000	1.124851000
1	-4.681009000	-1.735368000	1.664601000
1	-4.683723000	-1.289135000	-0.054555000
1	-5.716072000	-0.412557000	1.088247000
1	-3.500613000	-0.264241000	3.390716000
1	-2.869582000	1.323454000	2.936874000
1	-4.625208000	1.030972000	2.970277000
1	2.228856000	1.260738000	-1.685520000
1	3.320465000	3.445331000	-1.919427000
1	0.332186000	5.035178000	0.810852000
1	-0.611728000	2.776713000	0.948187000
1	4.544614000	5.313527000	-1.160633000
1	3.998280000	6.970677000	-1.451655000
1	3.499138000	5.683283000	-2.555878000
1	2.552160000	7.739219000	-0.121288000
1	1.985389000	6.665017000	1.167336000
1	0.920458000	7.058387000	-0.205645000

^{2}[Fe(LN$_3$S)(DMAP)]^{0}

26	3.405019000	9.865004000	8.809484000
16	4.305090000	9.362658000	6.688066000
6	6.007685000	9.776179000	7.193207000
6	7.010347000	10.001495000	6.234513000
1	6.759229000	9.880987000	5.185992000
6	8.296368000	10.393116000	6.614375000
1	9.053952000	10.569279000	5.856111000
6	8.599308000	10.583781000	7.970624000
1	9.584428000	10.926814000	8.271168000
6	7.623925000	10.344196000	8.940599000
1	7.858987000	10.535113000	9.979152000
6	6.331295000	9.908963000	8.572368000
6	5.382223000	9.244332000	10.750912000
6	6.665084000	8.889367000	11.457438000
1	7.383385000	8.442192000	10.763122000
1	6.469884000	8.165629000	12.251631000
1	7.150576000	9.758922000	11.918101000
6	4.103776000	9.042603000	11.405828000
6	3.845028000	8.631016000	12.716456000
1	4.656022000	8.466619000	13.414975000
6	2.510574000	8.426585000	13.124975000
1	2.304751000	8.106735000	14.140462000
6	1.453597000	8.615506000	12.227644000
1	0.430767000	8.433949000	12.537955000
6	1.731261000	9.031971000	10.915763000

6	0.824386000	9.232240000	9.822108000
6	-0.652915000	8.980382000	9.992117000
1	-1.093958000	9.678241000	10.716501000
1	-0.838931000	7.966359000	10.368860000
1	-1.188300000	9.092885000	9.048505000
6	0.621365000	9.775092000	7.467905000
6	-0.025678000	11.005985000	7.187737000
6	-0.782509000	11.114822000	6.008743000
1	-1.285868000	12.050805000	5.786083000
6	-0.902807000	10.045098000	5.123723000
1	-1.494177000	10.147946000	4.218427000
6	-0.257204000	8.841474000	5.407612000
1	-0.351388000	8.011232000	4.715934000
6	0.512678000	8.679123000	6.570544000
6	0.059241000	12.209028000	8.129455000
1	0.772450000	11.960228000	8.920809000
6	-1.305853000	12.516475000	8.792412000
1	-2.057006000	12.783810000	8.038226000
1	-1.213886000	13.361315000	9.487193000
1	-1.686141000	11.655408000	9.351472000
6	0.589119000	13.467512000	7.405464000
1	1.545115000	13.265254000	6.915258000
1	0.737028000	14.284156000	8.122740000
1	-0.117144000	13.817323000	6.642261000
6	1.170522000	7.326470000	6.858507000
1	1.917181000	7.483563000	7.643670000
6	0.134309000	6.302057000	7.383303000
1	-0.371594000	6.661508000	8.285303000
1	0.626917000	5.352093000	7.625564000
1	-0.633109000	6.101317000	6.624294000
6	1.913063000	6.750222000	5.633525000
1	1.222422000	6.489427000	4.821628000
1	2.444321000	5.834605000	5.920570000
1	2.650347000	7.461745000	5.254168000
6	4.193715000	12.731648000	7.856091000
1	4.420849000	12.165371000	6.961638000
6	4.457947000	14.091826000	7.936538000
1	4.902655000	14.585189000	7.083424000
6	4.142738000	14.809053000	9.120027000
6	3.567432000	14.055708000	10.177874000
1	3.300637000	14.518867000	11.117772000
6	3.342538000	12.696694000	10.012663000
1	2.908057000	12.109492000	10.813074000
6	4.987432000	16.900329000	8.126864000
1	5.987421000	16.517443000	7.884609000
1	5.083997000	17.949534000	8.407080000

1	4.370320000	16.845986000	7.221194000
6	4.045609000	16.863836000	10.477347000
1	2.976212000	16.781939000	10.711093000
1	4.285715000	17.921289000	10.363860000
1	4.615006000	16.473836000	11.331796000
7	5.270514000	9.657233000	9.481897000
7	3.045861000	9.262877000	10.546351000
7	1.414748000	9.620788000	8.669556000
7	3.639493000	12.021621000	8.873309000
7	4.379679000	16.161892000	9.236576000

^{4}[Fe(LN$_3$S)(DMAP)]^{0}

26	3.400952000	9.807009000	8.788791000
16	4.358193000	9.360841000	6.682691000
6	6.037748000	9.805906000	7.236227000
6	7.055657000	10.068569000	6.304977000
1	6.832386000	9.956321000	5.249382000
6	8.320539000	10.492353000	6.719986000
1	9.089754000	10.700954000	5.982238000
6	8.584157000	10.676662000	8.084658000
1	9.550229000	11.047290000	8.412551000
6	7.593992000	10.396208000	9.028359000
1	7.797468000	10.584345000	10.074080000
6	6.324450000	9.927634000	8.624438000
6	5.350379000	9.237446000	10.782240000
6	6.626595000	8.884311000	11.503079000
1	7.363905000	8.469051000	10.809954000
1	6.429339000	8.134886000	12.274206000
1	7.090759000	9.748771000	11.997329000
6	4.064516000	9.052580000	11.427245000
6	3.799515000	8.665171000	12.745473000
1	4.605367000	8.495960000	13.449167000
6	2.457974000	8.495587000	13.148124000
1	2.239091000	8.205814000	14.169897000
6	1.406477000	8.675564000	12.238703000
1	0.381669000	8.516215000	12.554348000
6	1.692726000	9.051603000	10.916755000
6	0.788996000	9.214835000	9.810523000
6	-0.687454000	8.967184000	9.990671000
1	-1.169278000	9.790873000	10.535434000
1	-0.866049000	8.051211000	10.565443000
1	-1.191346000	8.870323000	9.028169000
6	0.561419000	9.730055000	7.444128000
6	-0.098173000	10.955802000	7.165349000
6	-0.865016000	11.055703000	5.993093000
1	-1.377749000	11.987252000	5.772492000
6	-0.978555000	9.983891000	5.108145000

1	-1.579377000	10.078999000	4.208534000
6	-0.309110000	8.790593000	5.381741000
1	-0.391139000	7.962205000	4.685829000
6	0.471599000	8.638804000	6.538599000
6	0.007717000	12.167748000	8.094015000
1	0.714101000	11.913818000	8.889793000
6	-1.350378000	12.516988000	8.748384000
1	-2.086999000	12.811128000	7.990725000
1	-1.235901000	13.355967000	9.446756000
1	-1.764047000	11.667099000	9.300769000
6	0.570049000	13.403505000	7.354106000
1	1.525886000	13.173187000	6.876139000
1	0.729092000	14.229653000	8.058487000
1	-0.122135000	13.753895000	6.578887000
6	1.176434000	7.307332000	6.811065000
1	1.925962000	7.486192000	7.588847000
6	0.184603000	6.244765000	7.345004000
1	-0.313956000	6.579561000	8.260949000
1	0.711634000	5.308752000	7.567909000
1	-0.591128000	6.027094000	6.599857000
6	1.927623000	6.766594000	5.575221000
1	1.239093000	6.490426000	4.767237000
1	2.492796000	5.867501000	5.848422000
1	2.637428000	7.505764000	5.195177000
6	4.163511000	12.766657000	7.829291000
1	4.308136000	12.198774000	6.918333000
6	4.446499000	14.124967000	7.885750000
1	4.818086000	14.616876000	6.997350000
6	4.244133000	14.841946000	9.093781000
6	3.759457000	14.091533000	10.198915000
1	3.581049000	14.556275000	11.158864000
6	3.510231000	12.733511000	10.051444000
1	3.148834000	12.145202000	10.887600000
6	4.992729000	16.933847000	8.022404000
1	5.952081000	16.538101000	7.665194000
1	5.139563000	17.978312000	8.297834000
1	4.276403000	16.898352000	7.191105000
6	4.294501000	16.894684000	10.457903000
1	3.248034000	16.836176000	10.787366000
1	4.550264000	17.946950000	10.329172000
1	4.928143000	16.484634000	11.256298000
7	5.251234000	9.644679000	9.509681000
7	3.016340000	9.269279000	10.567942000
7	1.357814000	9.591115000	8.638818000
7	3.696298000	12.058646000	8.889989000
7	4.502254000	16.193577000	9.189168000

$^{1}[Ni^{II}(LN_3S)]^{+}$

28	-0.007258000	0.013535000	-0.005032000
16	-0.034175000	0.028760000	2.196102000
7	1.932508000	0.021646000	-0.039660000
7	0.164247000	0.096180000	-1.843929000
7	-1.907010000	-0.009153000	-0.440267000
6	1.778314000	-0.070714000	2.352748000
6	2.354570000	-0.154498000	3.626107000
6	3.733003000	-0.320451000	3.769271000
6	4.553612000	-0.422559000	2.634409000
6	4.001681000	-0.318815000	1.361303000
6	2.609358000	-0.106397000	1.200469000
6	2.435100000	0.209484000	-1.253269000
6	3.871753000	0.453497000	-1.607753000
6	1.416977000	0.207713000	-2.331545000
6	1.581520000	0.298749000	-3.721988000
6	0.436039000	0.278835000	-4.535721000
6	-0.849601000	0.182247000	-3.981653000
6	-0.956658000	0.094596000	-2.587291000
6	-2.164611000	0.015879000	-1.728594000
6	-3.527957000	-0.020897000	-2.345063000
6	-2.964520000	-0.080126000	0.558920000
6	-3.405528000	-1.351881000	0.994310000
6	-4.418794000	-1.385612000	1.965007000
6	-4.957969000	-0.210635000	2.490223000
6	-4.481724000	1.029604000	2.063479000
6	-3.469042000	1.127294000	1.096435000
6	-2.813923000	-2.661774000	0.467406000
6	-2.172442000	-3.488066000	1.607657000
6	-3.867957000	-3.499334000	-0.295488000
6	-2.951131000	2.503780000	0.671597000
6	-2.410360000	3.305732000	1.879076000
6	-4.034929000	3.309508000	-0.084225000
1	1.713305000	-0.110220000	4.498792000
1	4.165831000	-0.393421000	4.761117000
1	5.618395000	-0.591907000	2.744315000
1	4.652202000	-0.443880000	0.510899000
1	4.348298000	1.115448000	-0.879100000
1	3.950284000	0.927025000	-2.588305000
1	4.451965000	-0.477789000	-1.645145000
1	2.563596000	0.377607000	-4.168826000
1	0.549433000	0.344485000	-5.611485000
1	-1.727964000	0.178902000	-4.614011000
1	-4.307664000	-0.069287000	-1.586006000
1	-3.694113000	0.872471000	-2.960152000
1	-3.626410000	-0.893352000	-3.003338000

1	-4.782875000	-2.344741000	2.316864000
1	-5.741302000	-0.261584000	3.239004000
1	-4.895475000	1.936764000	2.490127000
1	-2.010369000	-2.417500000	-0.238414000
1	-1.409020000	-2.905144000	2.132455000
1	-2.923087000	-3.804478000	2.340346000
1	-1.703166000	-4.391442000	1.201056000
1	-4.307920000	-2.939289000	-1.129061000
1	-4.685832000	-3.802295000	0.367823000
1	-3.411693000	-4.410558000	-0.698364000
1	-2.108118000	2.355635000	-0.014672000
1	-1.625110000	2.749046000	2.399649000
1	-1.992486000	4.260544000	1.539519000
1	-3.205684000	3.529257000	2.598725000
1	-3.632122000	4.273236000	-0.415540000
1	-4.895862000	3.512511000	0.562597000
1	-4.402801000	2.770804000	-0.965553000

$^{3}[Ni^{II}(LN_3S)]^{+}$

28	-0.034329000	-0.049379000	0.167310000
16	0.309679000	0.540273000	2.315832000
7	2.046871000	-0.190642000	-0.035840000
7	0.178235000	0.178023000	-1.783980000
7	-2.052486000	-0.004857000	-0.473926000
6	2.047184000	-0.032537000	2.359383000
6	2.688781000	-0.164349000	3.599448000
6	3.991522000	-0.660906000	3.674313000
6	4.675514000	-1.032778000	2.505692000
6	4.068853000	-0.876580000	1.261313000
6	2.758866000	-0.356474000	1.168901000
6	2.496125000	0.073055000	-1.238935000
6	3.928645000	0.319872000	-1.622367000
6	1.434147000	0.196132000	-2.277036000
6	1.616805000	0.334401000	-3.663403000
6	0.484215000	0.447520000	-4.479881000
6	-0.806735000	0.422225000	-3.928055000
6	-0.930418000	0.276943000	-2.541051000
6	-2.200298000	0.202891000	-1.753305000
6	-3.511552000	0.340824000	-2.469603000
6	-3.152246000	-0.083499000	0.463769000
6	-3.450643000	-1.355183000	1.013381000
6	-4.472272000	-1.431519000	1.969978000
6	-5.155108000	-0.288594000	2.390127000
6	-4.821765000	0.956854000	1.858568000
6	-3.816482000	1.094468000	0.886960000
6	-2.702480000	-2.624622000	0.599124000
6	-2.008999000	-3.295051000	1.809560000

6	-3.630481000	-3.624844000	-0.129276000
6	-3.437429000	2.494753000	0.395440000
6	-2.747878000	3.303994000	1.522213000
6	-4.649612000	3.270757000	-0.169696000
1	2.151897000	0.107671000	4.500896000
1	4.468665000	-0.774574000	4.641580000
1	5.674592000	-1.449039000	2.568349000
1	4.590840000	-1.203963000	0.371895000
1	4.488976000	0.735497000	-0.780840000
1	3.994405000	1.026165000	-2.453830000
1	4.432952000	-0.604607000	-1.933237000
1	2.607115000	0.348126000	-4.099328000
1	0.606704000	0.553823000	-5.551627000
1	-1.678987000	0.507816000	-4.562904000
1	-4.348760000	0.171787000	-1.792588000
1	-3.614858000	1.343549000	-2.903212000
1	-3.578144000	-0.380391000	-3.293348000
1	-4.731903000	-2.395251000	2.394848000
1	-5.938865000	-0.367970000	3.135925000
1	-5.342855000	1.841597000	2.207501000
1	-1.915811000	-2.340064000	-0.112541000
1	-1.328009000	-2.600536000	2.314161000
1	-2.743273000	-3.638259000	2.547186000
1	-1.434289000	-4.169234000	1.481488000
1	-4.099293000	-3.171723000	-1.010131000
1	-4.431517000	-3.974423000	0.531946000
1	-3.061985000	-4.503130000	-0.456209000
1	-2.708818000	2.396108000	-0.417961000
1	-1.859108000	2.788030000	1.901804000
1	-2.442087000	4.289207000	1.151215000
1	-3.431163000	3.458678000	2.365012000
1	-4.321328000	4.232116000	-0.580843000
1	-5.387945000	3.483857000	0.610726000
1	-5.157101000	2.712737000	-0.964462000

$^{5}[Ni^{II}(LN_3S)]^{+}$

28	-0.016898000	0.039749000	0.112814000
16	0.220913000	0.081112000	2.463796000
7	2.017657000	0.019176000	0.003859000
7	0.178655000	0.107500000	-1.801310000
7	-2.023112000	0.003076000	-0.468471000
6	1.990944000	-0.099806000	2.426644000
6	2.660622000	-0.226591000	3.670977000
6	4.022995000	-0.453030000	3.722305000
6	4.744026000	-0.575024000	2.510397000
6	4.121945000	-0.437083000	1.273019000

6	2.735755000	-0.157107000	1.172075000
6	2.486506000	0.192896000	-1.288676000
6	3.921831000	0.439894000	-1.663350000
6	1.459196000	0.208372000	-2.289940000
6	1.602876000	0.314859000	-3.701753000
6	0.473722000	0.308349000	-4.508939000
6	-0.828719000	0.209616000	-3.949923000
6	-0.940758000	0.115169000	-2.569565000
6	-2.189465000	0.034064000	-1.770091000
6	-3.521795000	-0.003357000	-2.461031000
6	-3.118827000	-0.072989000	0.479540000
6	-3.542564000	-1.345502000	0.933531000
6	-4.561726000	-1.389069000	1.897819000
6	-5.131652000	-0.219602000	2.402672000
6	-4.681659000	1.023395000	1.956111000
6	-3.664742000	1.128019000	0.993739000
6	-2.920540000	-2.650406000	0.429932000
6	-2.233589000	-3.427023000	1.579392000
6	-3.959362000	-3.542097000	-0.291007000
6	-3.179692000	2.511243000	0.552415000
6	-2.601186000	3.315026000	1.741940000
6	-4.299382000	3.310840000	-0.156222000
1	2.073655000	-0.157769000	4.579535000
1	4.530411000	-0.555686000	4.673896000
1	5.807704000	-0.786705000	2.541174000
1	4.717798000	-0.567759000	0.384949000
1	4.403159000	1.124601000	-0.956861000
1	3.992720000	0.896696000	-2.652202000
1	4.516205000	-0.482901000	-1.692595000
1	2.584504000	0.388502000	-4.151781000
1	0.584210000	0.381773000	-5.584339000
1	-1.701604000	0.213388000	-4.589875000
1	-4.338765000	-0.060206000	-1.741689000
1	-3.662439000	0.893094000	-3.076724000
1	-3.584724000	-0.871098000	-3.128763000
1	-4.909518000	-2.351330000	2.258491000
1	-5.919302000	-0.276702000	3.146440000
1	-5.122458000	1.927907000	2.361659000
1	-2.142366000	-2.400362000	-0.302459000
1	-1.474235000	-2.813309000	2.078065000
1	-2.960167000	-3.737742000	2.338439000
1	-1.748511000	-4.330521000	1.192242000
1	-4.432264000	-3.013897000	-1.126654000
1	-4.753471000	-3.858309000	0.394728000
1	-3.479436000	-4.445608000	-0.683824000
1	-2.366449000	2.375158000	-0.171563000

1	-1.788465000	2.769814000	2.235462000
1	-2.209516000	4.278201000	1.395064000
1	-3.369910000	3.520505000	2.495211000
1	-3.917089000	4.277322000	-0.503575000
1	-5.135079000	3.508053000	0.524681000
1	-4.696884000	2.768378000	-1.021502000

$^{2}[Ni^{II}(LN_3S)]^{0}$

28	-0.013957000	0.025414000	-0.001634000
16	-0.030839000	0.066877000	2.225441000
7	1.903410000	0.004452000	-0.027447000
7	0.161599000	0.106577000	-1.819808000
7	-1.901308000	-0.001277000	-0.449025000
6	1.776896000	-0.078168000	2.372997000
6	2.366997000	-0.180511000	3.640330000
6	3.742117000	-0.375657000	3.776297000
6	4.541731000	-0.489850000	2.630739000
6	3.974230000	-0.374275000	1.361892000
6	2.587739000	-0.132172000	1.205012000
6	2.430227000	0.177447000	-1.267187000
6	3.881966000	0.402079000	-1.593422000
6	1.441137000	0.191739000	-2.316281000
6	1.590815000	0.273054000	-3.710222000
6	0.450861000	0.262029000	-4.530013000
6	-0.843485000	0.183233000	-3.977280000
6	-0.970362000	0.109497000	-2.589004000
6	-2.159092000	0.047627000	-1.760808000
6	-3.537477000	0.039066000	-2.360865000
6	-2.961587000	-0.076050000	0.532491000
6	-3.393719000	-1.347751000	0.980472000
6	-4.410799000	-1.397039000	1.946245000
6	-4.973713000	-0.229828000	2.463970000
6	-4.514306000	1.014171000	2.030206000
6	-3.499673000	1.119886000	1.065699000
6	-2.769533000	-2.646943000	0.466896000
6	-2.074442000	-3.423196000	1.610653000
6	-3.805754000	-3.537605000	-0.258087000
6	-2.997492000	2.501368000	0.640277000
6	-2.398069000	3.276047000	1.837763000
6	-4.108246000	3.327303000	-0.051147000
1	1.729725000	-0.123992000	4.516313000
1	4.183500000	-0.459526000	4.764474000
1	5.606608000	-0.678378000	2.722593000
1	4.614256000	-0.506634000	0.504266000
1	4.341153000	1.102781000	-0.888567000
1	3.981936000	0.829203000	-2.594261000

1	4.472365000	-0.523797000	-1.572825000
1	2.575237000	0.335273000	-4.158418000
1	0.569228000	0.317564000	-5.606130000
1	-1.717858000	0.185236000	-4.617410000
1	-4.305623000	-0.015136000	-1.588739000
1	-3.710738000	0.945192000	-2.954991000
1	-3.664030000	-0.819928000	-3.032020000
1	-4.756781000	-2.362302000	2.302481000
1	-5.758698000	-0.289560000	3.211641000
1	-4.941099000	1.919092000	2.451190000
1	-1.992286000	-2.382198000	-0.257650000
1	-1.320049000	-2.796923000	2.097177000
1	-2.797096000	-3.744917000	2.370627000
1	-1.581647000	-4.320186000	1.215116000
1	-4.278907000	-3.007080000	-1.092978000
1	-4.600439000	-3.860227000	0.425709000
1	-3.321964000	-4.438271000	-0.655382000
1	-2.188512000	2.356081000	-0.083457000
1	-1.587099000	2.704341000	2.299505000
1	-1.996706000	4.240171000	1.501365000
1	-3.157489000	3.478063000	2.603098000
1	-3.712025000	4.293711000	-0.385925000
1	-4.939287000	3.527226000	0.636349000
1	-4.516306000	2.804219000	-0.924080000

2. 9. Appendix D: Additional structures from reduced bis(imino)pyridine complexes

When [Fe^{II}(LN_3S)(DMAP)](OTf) is reduced with excess Na/Hg amalgam in CH_3CN and crystallized from CH_3CN/Et_2O, a new compound is obtained as light green single crystals. The new complex ([Fe($L^{2H}N_3S$)(DMAP)(OTf)]) is shown in **Figure 2. 25**, although data collection was not completed and only a partial data set (49.7%) was obtained. In this complex, one of the imine C=N bonds has been reduced, with the proton source likely from residual water in the CH_3CN solvent. In this structure, the DMAP donor has moved from the axial position in the starting material to an equatorial position in the plane of the BIP ligand. The thiolate and triflate anions occupy the axial positions, resulting in a 6-coordinate Fe^{II} complex. Selected bond distances and angles are given in **Table 2. 8**, and the Fe-N distances (2.111(4) - 2.248(3) Å) are consistent with a hs Fe^{II} center.

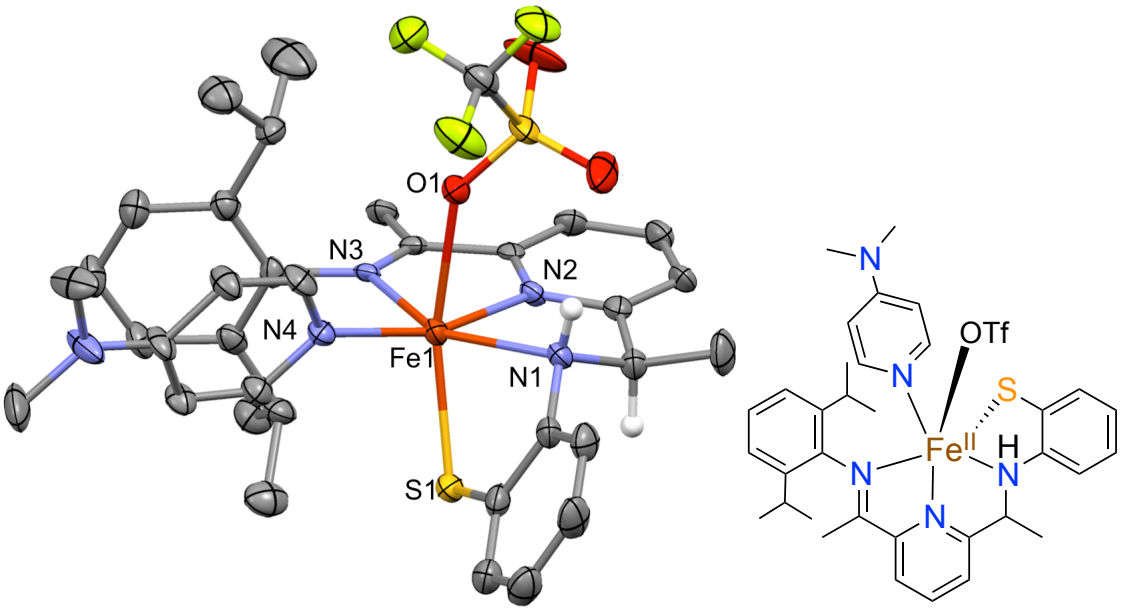

Figure 2. 25. Displacement ellipsoid of [Fe($L^{2H}N_3S$)(DMAP)(OTf)] (50% probability level) based on refinement for 49.7% of data collection, R_1 [$I > 2\sigma(I)$] = 4.7%.

Table 2. 8. Selected bond distances (Å) and angles (°) for [Fe($L^{2H}N_3S$)(DMAP)(OTf)]

Bond Lengths		Bond Angles	
Fe1-N1	2.219(3)	N1-Fe1-N3	148.46(14)
Fe1-N2	2.111(4)	N1-Fe1-O1	81.59(11)
Fe1-N3	2.248(3)	N1-Fe1-S1	79.50(10)
Fe1-N4	2.134(7)	N2-Fe1-N1	75.89(13)
Fe1-O1	2.387(3)	N2-Fe1-N3	73.17(12)
Fe- S1	2.4224(17)	N2-Fe1-O1	84.61(12)
		N2-Fe1-N4	162.3(5)
		N2-Fe1-S1	97.69(10)
		N3-Fe1-O1	89.55(11)
		N3-Fe1-S1	110.44(9)
		N4-Fe1-O1	83.9(6)
		N4-Fe1-N3	93.4(5)
		N4-Fe1-N1	115.5(5)
		N4-Fe1-S1	97.7(5)
		O1-Fe1-S1	159.74(7)

Reduction of [$Fe^{II}(LN_3S)$(OTf)] with excess Na/Hg amalgam in THF, followed by successive recrystallizations with Et_2O afforded a small amount of dark crystals suitable for X-ray diffraction. The new compound, [Fe($L^{2H}N_3S$)(THF/H_2O)(OTf)], has two molecules in the asymmetric unit with different donors, THF (**Figure 2. 26**) or H_2O

(**Figure 2. 27**), in the equatorial position. This compound also appears to have been reduced at the imine C=N position, and shows the thiolate and triflate donors occupying the axial positions. Relevant bond distances for the two components of [Fe($L^{2H}N_3S$)(THF/H_2O)(OTf)] are given in **Table 2. 9**, and the Fe-N distances are consistent with a hs Fe^{II} center in both complexes.

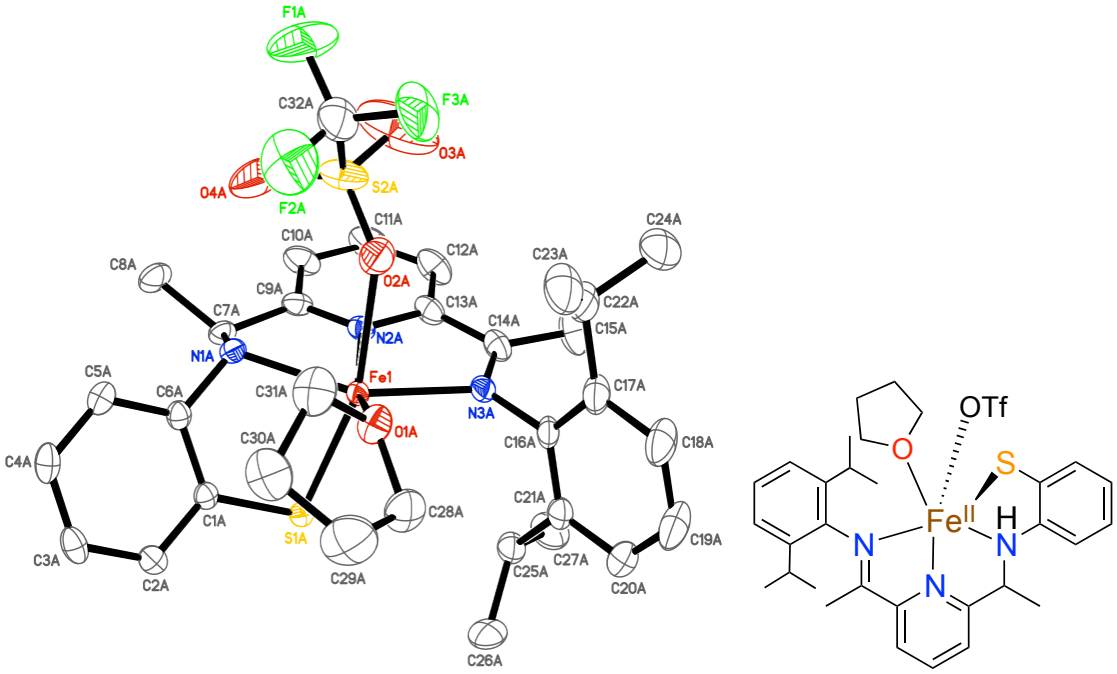

Figure 2. 26. Thermal ellipsoid plot (50% probability level) of [Fe($L^{2H}N_3S$)(THF)(OTf)]. H-atoms have been removed for clarity.

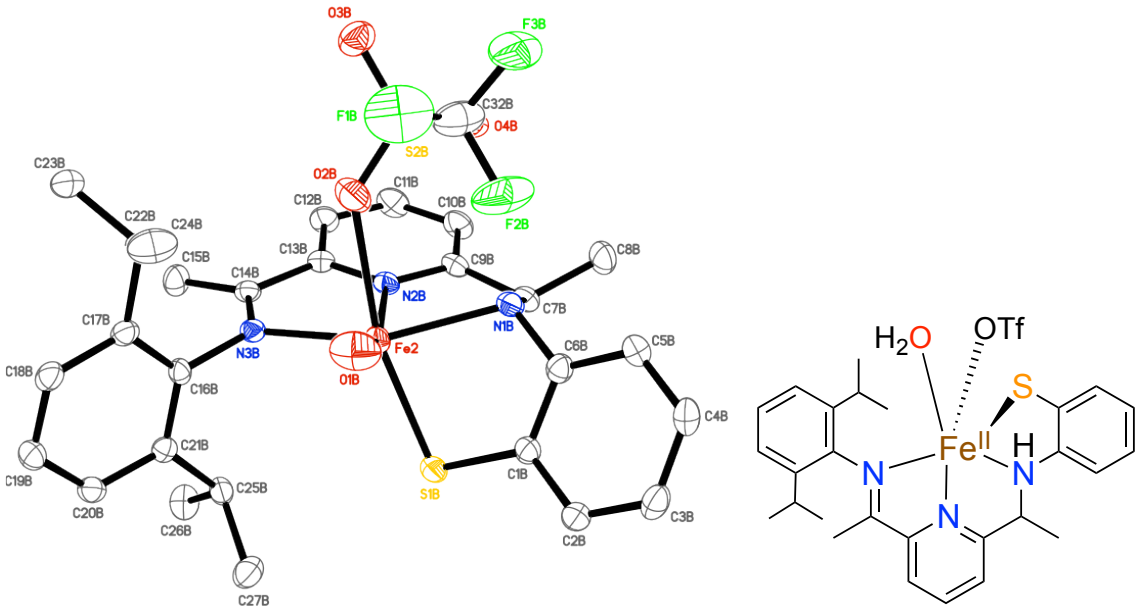

Figure 2. 27. Thermal ellipsoid plot of [Fe($L^{2H}N_3S$)(H_2O)(OTf)], where O8 is from a coordinated H_2O molecule. H-atoms have also been removed for clarity.

Table 2. 9. Selected bond distances (Å) for the independent components of [Fe($L^{2H}N_3S$)(THF/H_2O)(OTf)]

[Fe($L^{2H}N_3S$)(THF)(OTf)]		[Fe($L^{2H}N_3S$)(THF/H_2O)(OTf)]	
Fe1-N2A	2.084(2)	Fe2-O1B	2.058(2)
Fe1-O1A	2.0996(19)	Fe2-N2B	2.084(2)
Fe1-N3A	2.169(2)	Fe2-N3B	2.205(2)
Fe1-N1A	2.207(2)	Fe2-N1B	2.237(2)
Fe1-S1A	2.3588(7)	Fe2-S1B	2.3611(8)

We have successfully employed a metal-assisted template reaction for the synthesis of a number of bis(imino)pyridine compounds. On rare occasions however,

unexpected products are obtained. The new complex [$Fe^{II}(LN_3S)(2\text{-}NH_3\text{-}SPh)$] (**Figure 2. 28**) shows an additional equivalent of 2-aminothiophenol coordinated in lieu of the trifluoromethanesulfonate counterion. It is likely that this complex was formed when excess 2-aminothiophenol was inadvertently added to the reaction mixture for the synthesis of [$Fe^{II}(LN_3S)(OTf)$].[9] These types of complexes where two different S-donors are coordinated could be of interest in future studies. An independent synthesis of [$Fe^{II}(LN_3S)(2\text{-}NH_3\text{-}SPh)$] has not been attempted, however it is likely that a reaction mixture comprising 2:1 (2-aminothiophenol : $Fe(OTf)_2$) would be favorable for the formation of this complex. Selected bond distances for [$Fe^{II}(LN_3S)(2\text{-}NH_3\text{-}SPh)$] are given in **Table 2. 10**.

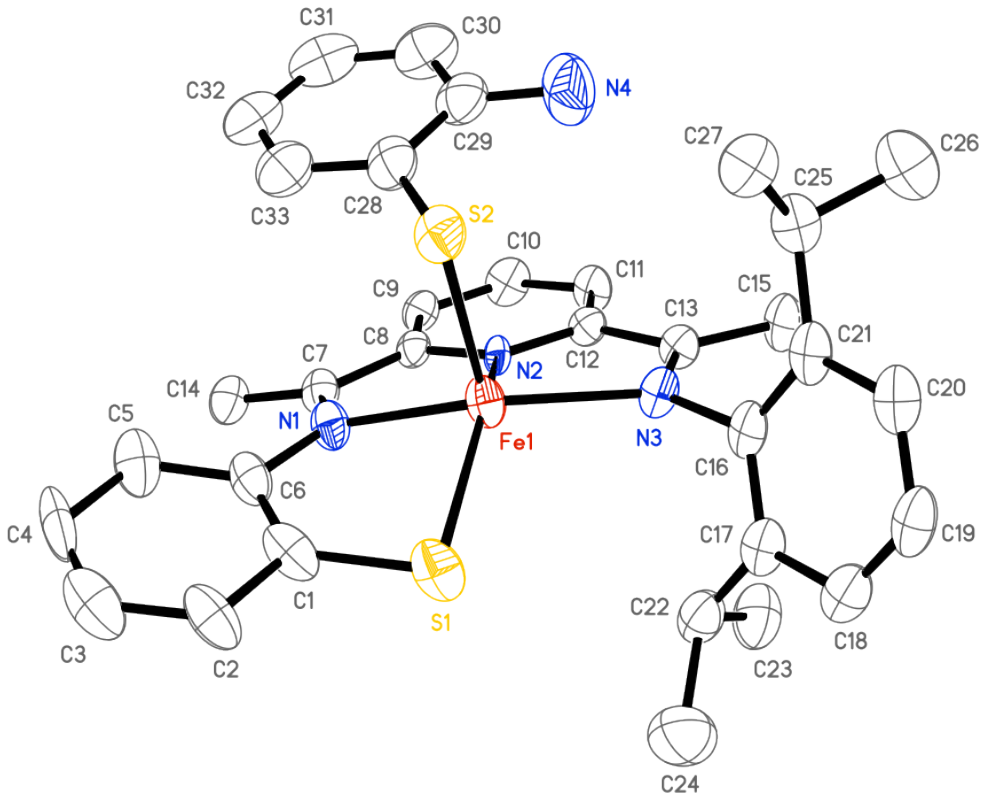

Figure 2. 28. Thermal ellipsoid plot of [$Fe^{II}(LN_3S)(2\text{-}NH_3\text{-}SPh)$]. H-atoms are removed for clarity.

Table 2. 10. Selected bond distances (Å) and angles (°) for [$Fe^{II}(LN_3S)(2\text{-}NH_3\text{-}SPh)$]

Bond Distances		Bond Angles	
Fe1-N2	2.050(3)	N2-Fe1-N1	73.98(14)
Fe1-N1	2.158(4)	N2-Fe1-N3	74.34(13)
Fe1-N3	2.190(4)	N1-Fe1-N3	144.86(14)
Fe1-S2	2.3242(16)	N2-Fe1-S2	103.08(11)
Fe1-S1	2.3400(14)	N1-Fe1-S2	95.77(11)
		N3-Fe1-S2	105.85(11)
		N2-Fe1-S1	136.12(11)
		N1-Fe1-S1	81.89(11)
		N3-Fe1-S1	111.75(10)
		S2-Fe1-S1	115.53(5)
		C1-S1-Fe1	95.70(18)
		C28-S2-Fe1	100.15(17)

The dimeric complex [$(Fe^{II}LN_3S)_2OH$](OTf) (**Figure 2. 29**) was also obtained from a metal-assisted template synthesis of [$Fe^{II}(LN_3S)$(OTf)],[9] likely when solvents were not vigorously dried. This structure is particularly interesting because it shows that these complexes can form dimeric structures despite the diisopropyl aryl groups that were incorporated to prevent such interactions.

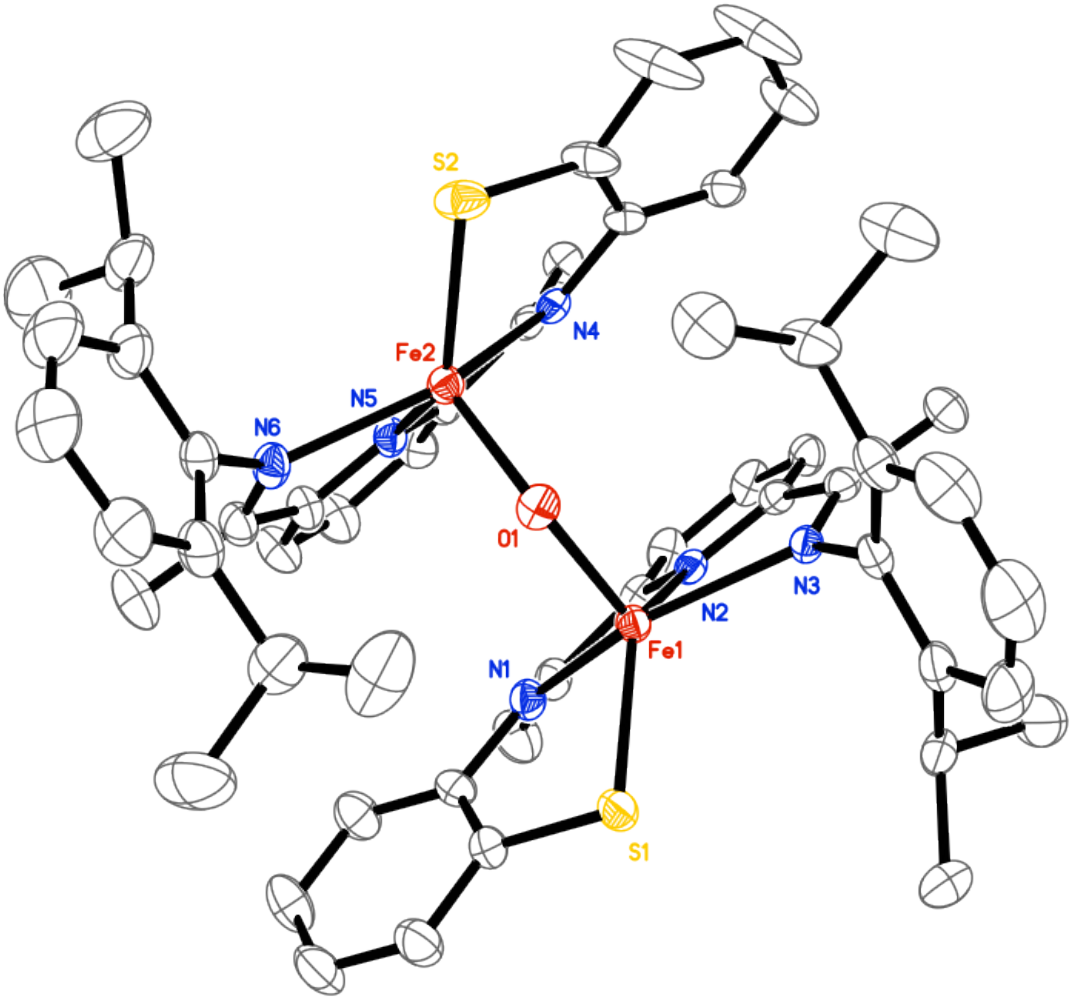

Figure 2. 29. Thermal ellipsoid plot of $[(Fe^{II}LN_3S)_2OH](OTf)$. H-atoms are removed for clarity.

Table 2. 11. Selected bond distances (Å) and angles (°) for [($Fe^{II}LN_3S)_2OH$](OTf)]

Bond Distances		Bond Angles	
Fe1-O1	1.952(2)	O1-Fe1-N2	112.76(8)
Fe1-N2	2.070(2)	O1-Fe1-N1	107.45(8)
Fe1-N1	2.190(2)	N2-Fe1-N1	73.75(8)
Fe1-N3	2.218(2)	O1-Fe1-N3	97.31(8)
Fe1-S1	2.3012(8)	N2-Fe1-N3	74.01(8)
Fe2-O1	1.9518(19)	N1-Fe1-N3	144.99(8)
Fe2 N5	2.072(2)	O1-Fe1-S1	112.52(6)
Fe2-N4	2.190(2)	N2-Fe1-S1	132.99(6)
Fe2-N6	2.227(2)	N1-Fe1-S1	81.38(6)
Fe2-S2	2.3028(8)	N3-Fe1-S1	111.83(6)
		O1-Fe2-N5	111.56(8)
		O1-Fe2-N4	107.39(8)
		N5-Fe2-N4	73.43(8)
		O1-Fe2-N6	96.56(8)
		N5-Fe2-N6	73.93(9)
		N4-Fe2-N6	144.79(8)
		O1-Fe2 -2	113.56(6)
		N5-Fe2-S2	133.09(7)
		N4-Fe2-S2	81.55(6)
		N6-Fe2-S2	112.39(6)

Experimental Methods

X-Ray Crystallography. Preformed by Dr. Maxime A. Siegler. All reflection intensities were measured using a KM4/Xcalibur (detector: Sapphire3) with enhance graphite-monochromated Mo *K*α radiation (λ = 0.71073 Å) under the program CrysAlisPro (Version 1.171.34.44 Oxford Diffraction Ltd., 2010). The program CrysAlisPro (Version 1.171.34.44, Oxford Diffraction Ltd., 2010) was used to refine the cell dimensions. Data reduction was done using the program CrysAlisPro (Version 1.171.34.44, Oxford Diffraction Ltd., 2010). The structure was solved with the program SHELXS-97 (Sheldrick, 2008) and was refined on F^2 with SHELXL-97 (Sheldrick, 2008). Analytical numeric absorption corrections based on a multifaceted crystal model were applied using CrysAlisPro (Version 1.171.34.44, Oxford Diffraction Ltd., 2010). The temperature of the data collection was controlled using the system Cryojet (manufactured by Oxford Instruments). The H atoms were placed at calculated positions using the instructions AFIX 13, AFIX 23, AFIX 43 or AFIX 137 with isotropic displacement parameters having values 1.2 or 1.5 times *U*eq of the attached C or N atoms.

[Fe($L^{2H}N_3S$)(DMAP)(OTf)] (x0943a)

An amount of [Fe^{II}(LN_3S)(DMAP)](OTf) (126 mg, 0.17 mmol) was dissolved in 2 mL CH_3CN. A slight excess of 0.5% Na/Hg amalgam (0.26 mmol, 1.5 equiv) was added and stirred vigorously for 2 h. The crude mixture was filtered, and vapor diffusion of Et_2O into the resulting solution gave light green crystals of [Fe($L^{2H}N_3S$)(DMAP)(OTf)] suitable for X-ray diffraction. Data collection was not completed, and the structure was not refined further.

[Fe($L^{2H}N_3S$)(THF/H_2O)(OTf)] (x0787a).

An amount of [$Fe^{II}(LN_3S)$(OTf)] (161 mg, 0.25 mmol) was suspended in 2 mL THF. A slight excess of 0.5% Na/Hg amalgam (0.38 mmol Na, 1.5 equiv) was added and the suspension was stirred vigorously for 2 h. The crude mixture was filtered, and successive recrystallizations with Et_2O gave black crystals of [Fe($L^{2H}N_3S$)(DMAP)(OTf)] suitable for X-ray diffraction.

Data were collected at 110(2) K after the crystal had been flash-cooled from room temperature. The structure was solved and refined in the centrosymmetric space group $P2_1/c$ with $Z' = 1$. The asymmetric unit contains one molecule of the compound $C_{32}H_{40}F_3FeN_3O_4S_2$ (*i.e.*, the Fe complex with the coordinated THF molecule and the weakly coordinated triflate counterion), one molecule of the compound $C_{27}H_{34}F_3FeN_3O_4S_2$ (*i.e.*, the Fe complex with the coordinated water molecule and the weakly coordinated triflate counterion), and one uncoordinated ether molecule. The structure is mostly ordered except for both triflate counterions that are both disordered over two orientations [occupancy factor of the major component: 0.682(3)], and for the isopropyl group C25A→C27A [occupancy factor of the major component: 0.63(2)]. The coordinated water molecule is H-bond donor to the uncoordinated ether molecule *via* one O–H···O hydrogen bond. The H-atoms of the coordinated water molecule were initially found from difference Fourier maps, and their positions were restrained so that the O–H and H···H distances refine to 0.84(3) and 1.33 (3) Å, respectively (note: the H···H distance must be ~ 1.33 Å so that H–O–H is ~ 104.5°). The final refinement against F^2 was good. The *R* factor [$F^2 > 2\sigma(F^2)$] is about 0.044. The final difference Fourier map was relatively flat. The other residual peaks were no larger than 0.83 e $Å^{-3}$. $C_{64}H_{84}F_6Fe_2N_6O_9S_4$, Fw =

1435.31, black lath, 0.37 × 0.16 × 0.12 mm^3, monoclinic, $P2_1/c$ (no. 14), a = 11.8863(2), b = 33.6943(6), c = 17.1746(3) Å, β = 92.9031(16)°, V = 6869.6(2) $Å^3$, Z = 4, D_x = 1.388 g cm^{-3}, μ = 0.618 mm^{-1}, abs. corr. range: 0.845–0.943. 46384 Reflections were measured up to a resolution of $(\sin \theta/\lambda)_{max}$ = 0.62 $Å^{-1}$. 13509 Reflections were unique (R_{int} = 0.0412), of which 10424 were observed [$I > 2\sigma(I)$]. 946 Parameters were refined with 596 restraints. $R1/wR2$ [$I > 2\sigma(I)$]: 0.0441/0.1046. $R1/wR2$ [all refl.]: 0.0647/0.1135. S = 1.013. Residual electron density found between −0.82 and 0.83 e $Å^{-3}$.

[$Fe^{II}(LN_3S)(2\text{-}NH_3\text{-}SPh)$]. (x0633a).

See procedure for [$Fe^{II}(LN_3S)(OTf)$],[9] use 2.0 equiv of 2-aminothiophenol to reproduce this complex.

Data were collected at 110(2) K after the crystal had been flash-cooled from room temperature. The structure of the compound $C_{33}H_{36}FeN_4S_2$ was solved and refined in the centrosymmetric space group $C2/c$ with Z' = 1. The structure of x0633a is ordered. A first refinement against F^2 was not entirely satisfactory because some residual electron density were found in two voids located at (0.5, 0, 0.3) and (0, 0.5, 0.124), which include 134 electrons in a volume of 843 $Å^3$ per void. Each void contains some disordered solvent molecule diethyl ether. In order to maximize the data/parameter ratio (the crystal diffracted poorly, *i.e.* $2\theta_{max}$ = 44º), the contribution of such solvent molecules was then taken out for the subsequent stages of the refinement using the program SQUEEZE. The final refinement against F^2 was fair. The R factor [$F^2 > 2\sigma(F^2)$] is about 0.047. The final difference Fourier map was flat. The residual peaks were found no larger than 0.28 e $Å^{-3}$. $C_{33}H_{36}FeN_4S_2$, Fw = 608.63 *, black needle, 0.72 × 0.07 × 0.05 mm^3, monoclinic, $C2/c$

(no. 15), a = 29.1967(13), b = 15.9817(7), c = 17.0174(8) Å, β = 112.931(5)°, V = 7313.0(6) Å^3, Z = 8, D_x = 1.106 g cm^{-3},* μ = 0.551 mm^{-1},* abs. corr. range: 0.778–0.972. 17140 Reflections were measured up to a resolution of (sin $\theta/\lambda)_{max}$ = 0.53 Å^{-1}. 4491 Reflections were unique (R_{int} = 0.0679), of which 2780 were observed [$I > 2\sigma(I)$]. 367 Parameters were refined. $R1/wR2$ [$I > 2\sigma(I)$]: 0.0469/0.1168. $R1/wR2$ [all refl.]: 0.0826/0.1231. S = 0.925. Residual electron density found between −0.29 and 0.28 e Å^{-3}. * excluding the solvent contribution.

[(Fe^{II}LN$_3$S)$_2$OH](OTf) (x0811a).

See procedure for [Fe^{II}(LN$_3$S)(OTf)],[9] may try using EtOH from bottle or adding a small amount of H_2O to reproduce. This complex was not pursued for further characterization.

Data were collected at 110(2) K after the crystal had been flash-cooled from room temperature. The structure was solved and refined in the centrosymmetric space group $P\bar{1}$ with Z' = 1. The asymmetric unit contains Fe complex, on triflate counterion, and some solvent molecules. The structure is partly disordered. The asymmetric unit contains one half occupied molecule of diethylether that is found at some sites of inversion symmetry (i.e., ½ ½ 0). The unresolved residual electron density is likely to be some diethylether and/or THF molecules that are found to be severely disordered. A first refinement against F^2 was not completely satisfactory because some residual electron density was found in one void located at (0.5 0 0.5), which includes 152 electrons in a volume of 468 Å^3. This contribution was then taken out for the subsequent stages of the refinement using the program SQUEEZE. The final refinement against F^2 was good. The R factor [$F^2 > 2\sigma(F^2)$] is about 0.045. The final difference Fourier map was flat. The residual peaks were no larger than 0.35 e Å^{-3}. Fw = 2344.08 (this number should be

smaller by a factor of two, see below for explanation),* black needle, 0.44 × 0.09 × 0.04 mm^3, triclinic, $P\bar{1}$ (no. 2), a = 12.0041(4), b = 12.7182(4), c = 22.8080(7) Å, α = 86.292(2), β = 76.080(3), γ = 71.695(3)°, V = 3208.60(18) $Å^3$, Z = 1 (the Z number is actually 2, but was assigned as 1 because the checkcif test does not allow half integers in the chemical formula moiety), D_x = 1.213 g cm^{-3},* μ = 0.604 mm^{-1},* abs. corr. range: 0.835–0.979. 30308 Reflections were measured up to a resolution of $(\sin \theta/\lambda)_{max}$ = 0.59 $Å^{-1}$. 11298 Reflections were unique (R_{int} = 0.0481), of which 7939 were observed [$I > 2\sigma(I)$]. 721 Parameters were refined with 27 restraints. $R1/wR2$ [$I > 2\sigma(I)$]: 0.0450/0.0993. $R1/wR2$ [all refl.]: 0.0720/0.1055. S = 0.984. Residual electron density found between −0.45 and 0.35 e $Å^{-3}$. * excluding the contribution of the unresolved residual electron density

Chapter 3. Sulfide oxidation by O_2: Synthesis, structure and reactivity of novel sulfide-incorporated iron(II) bis(imino)pyridine complexes

This work was co-written with the following authors and is published under the following citation:

Leland R. Widger, Maxime A. Siegler, and David P. Goldberg

Polyhedron, **2013**, *58*, 179–189

3. 1. Introduction

There is broad interest in understanding the mechanisms by which metalloenzymes activate O_2 and control reactivity with substrates.[1] Many non-heme iron oxygenases that carry out these reactions typically employ a 2-His-1-carboxylate motif around the catalytically active iron center. One exception is cysteine dioxygenase (CDO), which contains a high-spin ferrous center bound by three His residues in a facial triad and one water molecule completing a pseudo-tetrahedral coordination sphere. This $(His)_3Fe^{II}(H_2O)$ center likely activates O_2 upon binding of the cysteine substrate, and is responsible for catalyzing the oxidation of cysteine to cysteine sulfinic acid (**Figure 3. 1**). Mechanistic information for many non-heme iron dioxygenases is available,[2-7] but little is known about the mechanism of CDO. There is debate in the literature about the nature of the possible O_2 derived intermediate(s) in the catalytic cycle of CDO.[8-18] As the first step in mammalian cysteine catabolism, CDO activity is critical for proper cellular function. Loss of this activity has been implicated in many disease states including cystinosis,[19,20] Hallervoden-Spatz syndrome,[21] Alzheimer's and Parkinson's disease.[22,23]

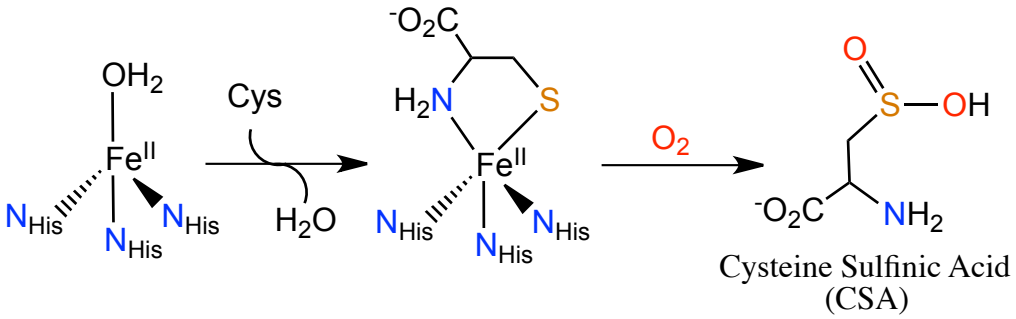

Figure 3. 1. Oxidation of cysteine to cysteine sulfinic acid by CDO.

In addition to the biological relevance of sulfur-oxidation, sulfoxides are valued synthetic intermediates to organic chemists[24,25] and are important in many pharmaceutically active compounds (**Figure 3. 2**a).[26-28] Sulfur oxidation is a well-known and widely used synthetic strategy for a variety of applications in organic chemistry,[29] but the use of stoichiometric amounts of harsh or toxic oxidizing agents (**Figure 3. 2**b) and the difficulty of stopping oxidation at the sulfoxide[30,31] presents challenges that have attracted the interest of inorganic chemists. Furthermore, sulfoxidation catalysts have recently attracted a great deal of attention for use in desulfurization of fossil fuels with O_2 and other applications to reduce toxicity (**Figure 3. 2**c).[28,32,33]

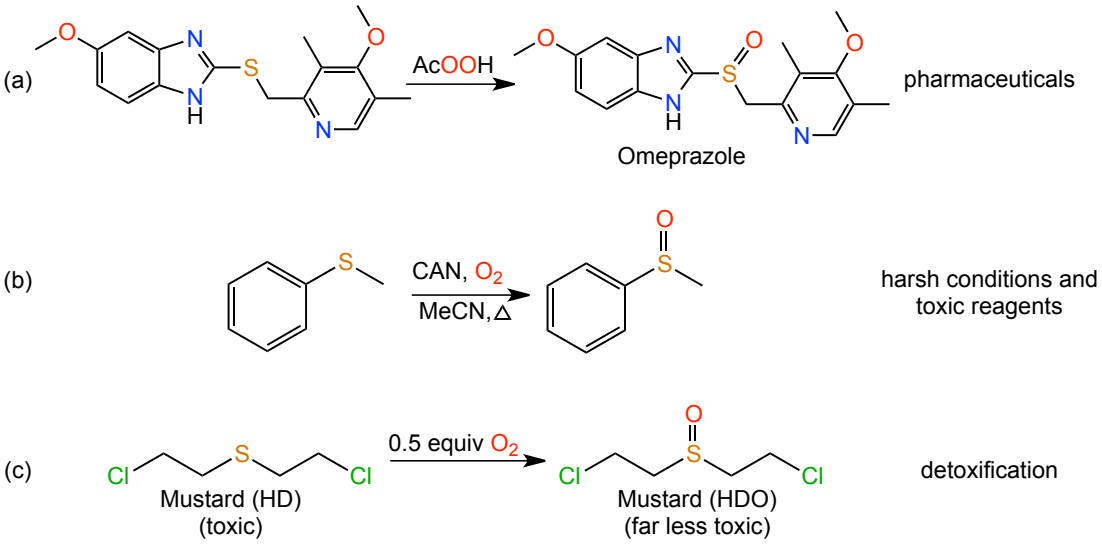

Figure 3. 2. Examples of sulfoxides in synthetic chemistry and detoxification processes.

Some metal-based systems have been developed to oxidize sulfides under mild conditions. Some of these systems perform as catalysts for asymmetric sulfide oxidation, and a few can utilize dioxygen as the oxidant.[34-60] There are only a few reports of iron-based sulfoxidation catalysts, but all of these systems utilize Fe^{III} centers in lieu of Fe^{II}.[41,49,51,52] Molecular O_2 is used in some of these cases as a co-oxidant with an Fe^{III} source and an additional oxidant generated in situ. For example, Wang and coworkers have reported a catalytic Fe_2O_3 system where molecular oxygen is proposed to work in concert with the Fe^{III} catalyst to generate peracid oxidants in situ from various aldehydes.[44,45] These peracids, much like mCPBA, are ultimately responsible for sulfide oxidation. Despite the efficiency of the Wang Fe_2O_3/O_2/aldehyde system, only modest yields are observed for sulfone products. In addition, peracids are not selective for sulfides, and are well known to be efficient reagents for olefin epoxidation, Baeyer-Villiger oxidation of ketones, and oxidation of secondary alcohols, even in the absence of a metal catalyst.[43] This limited functional group tolerance severely restricts the scope under which this methodology could be used in a synthetic scenario. In other systems reported by Rossi et al.,[49,51,61,62] aerobic oxidation is carried out by catalytic amounts of NO_2 (which is in equilibrium with N_2O_4), generated by an $FeBr_3$ catalyst from HNO_3. In these reports, once NO_2/N_2O_4 is generated there is an aerobic catalytic cycle of NO_x species which gives NO and the S-oxygenated product. NO then reacts with O_2 to regenerate NO_2 and turnover the system (**Figure 3. 3**). Recent mechanistic studies have actually shown that these types of systems, originally reported with $FeBr_3$ to initiate the catalytic reaction, can in fact proceed in the absence of a metal-based catalyst.[61,63] Catalytic systems based solely on these types of gaseous equilibria are sensitive to a

variety of environmental conditions, and are likely to be deactivated in many industrial circumstances.[52]

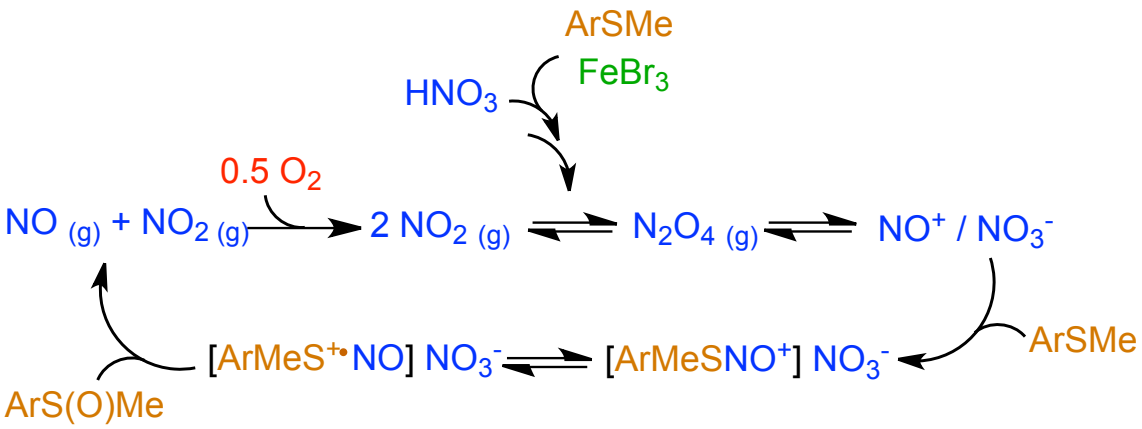

Figure 3. 3. Proposed catalytic mechanism of aerobic sulfoxidation by NO_x species.[61]

Recent work in our lab has focused on the development of iron(II) complexes with mixed N/S donor sets to serve as structural and functional models for a variety of non-heme metalloenzymes, including non-heme iron oxygenases which utilize O_2 for substrate oxidation reactions. Previous reports from our lab have included examples where an Fe^{II} center was shown to mediate sulfur oxygenation of thiolate ligands.[64-66] In these reports, discrete thiolate-ligated Fe^{II} complexes reacted with O_2 at room temperature and atmospheric pressure to give the corresponding Fe^{II}-sulfonato or sulfinato complexes. In addition to being among the first reports of this reactivity,[64-67] the assignment of an oxidation state for the product as Fe^{II} was interesting due to the similarity with the iron(II) resting state in CDO. We were interested in synthesizing a modified $Fe^{II}(LN_3SMe)X_2$ system which incorporated sulfides in place of the thiolate donors to determine the effect on S-oxygenation reactivity. Herein we report the synthesis, characterization, and O_2 reactivity of two novel methyl-sulfide iron(II) complexes. The unsymmetrical bis(imino)pyridine complexes $[(Fe^{II}(LN_3SMe)(H_2O)_3](OTf)_2$ (**Figure 3.**

4.) and $[Fe^{II}(LN_3SMe)Cl_2]$ (**Figure 3. 5.**), were synthesized by metal-assisted template reactions. The $[(Fe^{II}(LN_3SMe)(H_2O)_3](OTf)_2$ and $[Fe^{II}(LN_3SMe)Cl_2]$ complexes were characterized by single crystal X-ray crystallography, LDI-MS, ^{1}H-NMR, and elemental analysis. While $[(Fe^{II}(LN_3SMe)(H_2O)_3](OTf)_2$ reacts with O_2 at modestly elevated temperature to afford the sulfoxide complex $[(Fe(LN_3SOMe)(OTf)]^{2+}$, The chloride complex $[Fe^{II}(LN_3SMe)Cl_2]$, under the same conditions, yields the sulfone complex $[Fe(LN_3SO_2Me)Cl]^{2+}$.

3. 2. Experimental

General Remarks

All reagents were purchased from commercial vendors and used without further purification unless noted otherwise. All reactions were carried out under an atmosphere of N_2 inside a glovebox or under Ar by standard Schlenk and vacuum line techniques unless otherwise noted. Dioxygen gas (2.6 Grade) was purchased from BOC Gases and dried by passage through a column of Drierite. $H_2{}^{18}O$ (97%) was purchased from Cambridge Isotope Laboratories, Inc. Iron(II) trifluoromethanesulfonate (98%) was purchased from Strem. Iron(II) chloride (98%), 2-(methylthio)aniline (97%), and 2,6-diacetylpyridine (99%) were purchased from Sigma-Aldrich. 2,6-diisopropylaniline (92%) was purchased from Acros. Dichloromethane was purified via a Pure-Solv Solvent Purification System from Innovative Technology, Inc. Methanol, ethanol, and triethylamine were distilled over CaH_2. All solvents were degassed by repeated cycles of freeze-pump-thaw and stored in an N_2-filled glovebox. 2-(O=CMe)-6-(2,6-(^{i}Pr$_2$-C_6H_3N=CMe)-C_5H_3N was synthesized according to the published procedure (C. Bianchini, G. Mantovani, A. Meli, F. Migliacci, F. Zanobini, F. Laschi, A. Sommazzi,

Eur. J. Inorg. Chem. (2003) 1620). LDI-TOF mass spectra were obtained using a Bruker Autoflex III Maldi ToF/ToF instrument (Billerica, MA). Samples were dissolved in CH_2Cl_2 and deposited on the target plate. Samples were irradiated with a 355 nm UV laser and mass analyzed by ToF mass spectrometry in the reflectron/linear mode. High resolution EI mass spectra were obtained using a VG70S double-focusing magnetic sector mass spectrometer (VG Analytical, Manchester, UK, now Micromass/Waters) equipped with an MSS data acquisition system (MasCom, Bremen, Germany). Attenuated total reflectance (ATR) infrared spectra of neat crystalline material and crude reaction mixtures were obtained with a Golden Gate Reflectance diamond cell in a Nexus 670 Thermo-Nicolet FTIR spectrometer. Crude reaction mixtures were deposited on the reflectance window as a solution in CH_2Cl_2 and allowed to dry to a residue. Electron paramagnetic resonance (EPR) spectra were obtained on a Bruker Elexsys E580 EPR spectrometer with a Bruker super high Q resonator (SHQE) at 15 K. The EPR spectrometer was equipped with an Oxford Instruments ESR900 liquid helium flow cryostat.

Synthesis of reported compounds

$[Fe^{II}(LN_3SMe)(H_2O)_3](OTf)_2 \bullet Et_3NHOTf$

An amount of 2-(O=CMe)-6-(2,6-(^{i}Pr$_2$-C_6H_3N=CMe)-C_5H_3N (200 mg, 0.62 mmol) and $Fe(OTf)_2$ (230 mg, 0.65 mmol) were suspended in EtOH (10 mL) and heated at 60 ºC for 1 h. The solids slowly dissolved to give a deep purple solution, and a solution of 2-(methylthio)aniline (73 μL, 0.62 mmol) and triethylamine (22 μL, 0.62 mmol) in EtOH (1 mL) was added to the reaction mixture. The reaction was stirred at 80 ºC for 24 h to give a dark red solution that was then cooled to room temperature. The crude reaction

mixture was evaporated to dryness and the resulting solid residue was brought into a glovebox, where it was dissolved in a minimum amount of CH_2Cl_2 and filtered through Celite. The filtrate was layered with pentane to give 650 mg (95% yield) of $[Fe^{II}(LN_3SMe)(H_2O)_3](OTf)_2 \bullet Et_3NHOTf$ as a dark red residue. Single crystals (red-purple blocks) suitable for X-ray diffraction were grown from slow vapor diffusion of diisopropyl ether into a solution of $[Fe^{II}(LN_3SMe)(H_2O)_3](OTf)_2$ in MeCN. LDIMS (+): *m/z* 648.3 [M-3H_2O-OTf]+. ATR-IR, ν (cm^{-1}): 3275, 2974, 1589, 1468, 1371, 1291, 1210, 1166, 1098, 1024, 803, 766, 636. *Anal. Calc*. for $[Fe^{II}(L_3NSMe)(H_2O)_3](OTf)_2 \bullet 0.5\ Et_3NH^+OTf^-$ ($C_{33.5}H_{47}F_{7.5}FeN_{3.5}O_{10.5}S_{3.5}$): Predicted: C, 41.17; H, 4.85; N, 5.02. Found: C, 41.29; H 5.02; N, 5.24. Note: Although the X-ray structure of $[Fe^{II}(LN_3SMe)(H_2O)_3](OTf)_2$ contains one Et_3NH^+ OTf^- per Fe, samples for elemental analysis contain crystalline material along with inseparable residue. Elemental data for the bulk material fits best for 0.5 Et_3NH^+ OTf^- per Fe.

$[Fe^{II}(LN_3SMe)Cl_2] \bullet MeOH$

An amount of 2-(O=CMe)-6-(2,6-(^{i}Pr2-C_6H_3N=CMe)-C_5H_3N (200 mg, 0.62 mmol) and $FeCl_2$ (230 mg, 0.65 mmol) were suspended in EtOH (10 mL) and heated at 60 ºC for 1 h. The solids slowly dissolved to give a deep blue solution, and a solution of 2-(methylthio)aniline (73 μL, 0.62 mmol) and triethylamine (22 μL, 0.62 mmol) in EtOH (1 mL) was added to the reaction mixture. The reaction was stirred at 80 ºC for 24 h and then cooled to room temperature. The crude reaction mixture was evaporated to dryness and the resulting solid residue was brought into a glovebox where it was dissolved in a minimum amount of CH_2Cl_2 and filtered through Celite. Layering the filtrate with pentane gave 250 mg (72% yield) of $[Fe^{II}(LN_3SMe)Cl_2] \bullet MeOH$ as a dark blue residue.

Single crystals of $[Fe^{II}(LN_3SMe)Cl_2]$•MeOH for X-ray diffraction were prepared by slow vapor diffusion of diisopropyl ether into a MeOH solution of $[Fe^{II}(LN_3SMe)Cl_2]$•MeOH. LDIMS (+): *m/z* = 534.3 [M-Cl]+. ATR-IR, ν (cm^{-1}): 2964, 1585, 1463, 1370, 1318, 1269, 1204, 1105, 1059, 939, 803, 778, 738. *Anal. Calc.* for $[Fe^{II}(L_3NSMe)Cl_2]$•MeOH ($C_{29}H_{37}Cl_2FeN_3OS$): Predicted: C, 57.82; H, 6.19; N, 6.97. Found: C, 57.74; H 6.30; N, 7.03.

2-(methylsulfinyl)aniline

An amount of 2-(methylthio)aniline (44 mg, 0.316 mmol) was dissolved in 7 mL of CH_2Cl_2 and *m*CPBA (55 mg, 0.316 mmol) was added dropwise as a solution in 3 mL of CH_2Cl_2. After stirring for several minutes, TLC analysis indicated the reaction was complete, and the product was purified by column chromatography on silica (EtOAc / hexanes) to give 10 mg (20% yield) of a pale solid. ^{1}H-NMR ($CDCl_3$) (@ 25 ºC) δ 7.27-7.22 (m, 2H), 6.75 (t, 1H), 6.69 (d, 1H), 2.93 (s, 3H). MS (EI+) *m/z* 155.1 [M^+].

O_2 Reactivity

General Remarks

All O_2 reactions were carried out in a sealed reaction vessel, equipped with a vacuum port that was connected above the Teflon screw-cap. Solutions of compounds **1** and $[Fe^{II}(LN_3SMe)Cl_2]$•MeOH in CH_2Cl_2 were transferred to the flask, and then the flask was charged with O_2 by bubbling directly into the CH_2Cl_2 solution for 5 min. The vessel was then sealed and heated to 60 °C for several days. Typical reaction times varied from 24 to 96 h, depending on concentration and reaction scale.

Oxidation of $[Fe^{II}(L_3NSMe)(H_2O)_3](OTf)_2$•0.5 $Et_3NH^+OTf^-$ with O_2

An amount of $[Fe^{II}(L_3NSMe)(H_2O)_3](OTf)_2$•0.5 $Et_3NH^+OTf^-$ (50.0 mg, 51 μmol) was dissolved in 5 mL of CH_2Cl_2 and transferred to a pressure vessel equipped with a vacuum port. Excess O_2(g) was bubbled into the solution for 5 min and the vessel was put under an atmosphere of O_2 before being sealed and heated to 60 ºC. The reaction was monitored by removal of aliquots of the reaction mixture for analysis by LDI-MS. Complete disappearance of the starting material was observed after 96 h. The crude reaction mixture was then stirred with 5 mL of 1 M HCl for 1 h before being neutralized with $NaHCO_3$. The organic layer was then collected, dried, and 2-(methylsulfinyl)aniline was purified by column chromatography on silica with EtOAc / hexanes. ^{1}H-NMR ($CDCl_3$) (@ 25 ºC) δ 7.23-7.22 (m, 2H), 6.75 (t, 1H), 6.69 (d, 1H), 2.93 (s, 3H). This spectrum matched that of an authentic sample of 2-(methylsulfinyl)aniline, prepared as described above.

$H_2{}^{18}O$ labeling

An amount of $[Fe^{II}(L_3NSMe)(H_2O)_3](OTf)_2$•0.5 $Et_3NH^+OTf^-$ (34 mg, 35 μmol) was dissolved in 3.0 mL of CH_2Cl_2 and $H_2{}^{18}O$ (60 μL, 100 equiv) was added. The mixture was transferred to a reaction vessel and $^{16}O_2$(g) was bubbled through the solution for 5 min. The vessel was sealed and heated to 60 ºC for 96 h. The LDI-MS of the crude reaction mixture showed an isotopic cluster at *m/z* 684.1 for the unlabeled sulfoxide **3**, and no significant peak corresponding to ^{18}O incorporation at *m/z* 686.1 was observed.

Oxidation of $[Fe^{II}(LN_3SMe)Cl_2]$•MeOH with O_2

An amount of $[Fe^{II}(LN_3SMe)Cl_2]$•MeOH (14.0 mg, 23 μmol) was dissolved in 5.0 mL of CH_2Cl_2 and transferred to a pressure vessel equipped with a side-arm. Excess O_2(g) was

bubbled into the solution for 5 min and the vessel was put under a slight positive pressure of O_2 before being sealed and heated to 60 ºC. The reaction was monitored by LDI-MS over the course of several days. After 96 h the reaction was complete as evidenced by the absence of peaks for either the sulfide starting material or sulfoxide intermediate observed in the LDI-MS spectrum. The crude reaction mixture was then stirred with 5 mL of 1 M HCl for 1 h before being neutralized with $NaHCO_3$. The organic layer was then collected and dried. The ^{1}H-NMR spectrum of the crude mixture allowed for the identification of the S-oxygenated product, 2-(methylsulfonyl)aniline, δ ($CDCl_3$) = 3.06. This peak corresponds to the literature value.[68]

3. 3. Results and Discussion

Synthesis of LN_3SMe Complexes

The bis(imino)pyridine (BIP) ligand scaffold has been widely used due to its ease of synthesis, and facile steric and electronic modification to give a range of ligand variants. In fact, from commercially available 2,6-diacetylpyridine and 2 equiv of a primary amine, it is possible to synthesize a large array of symmetrical BIP ligands in one pot in a matter of hours. The challenge lies in the synthesis of unsymmetrical derivatives, of interest to us so as to be able to incorporate sulfur-containing functional groups around the metal center. For our purposes regarding iron-oxygen chemistry, a key requirement for a ligand system is to be able to include significant steric protection around the metal center to help prevent the formation of polymeric Fe complexes. We were therefore fortunate to come across the unsymmetrical precursor 2-(O=CMe)-6-(2,6-(^{i}Pr$_2$-C_6H_3N=CMe)-C_5H_3N, reported by Bianchini and coworkers,[69] which is easily prepared by mixing 2,6-diacetylpyridine and 2,6-diisopropylaniline in MeOH with catalytic formic

acid. The product is insoluble in MeOH and precipitates out of solution before it can react further. This precursor includes pre-organized steric shielding via the 2,6-diisopropylphenyl substituent, and it provides a convenient way for installing a single sulfur-containing group through the available ketone (see **Scheme 3. 1** and **Scheme 3. 2**).

We have previously reported the difficulty in direct condensation, or even reductive amination, of the second amine onto this unsymmetrical precursor.[70] The difficulty we encountered while attempting to synthesize these ligands resulted from the reversibility of the Schiff-base reactions. Extended exposure of the unsymmetrical precursor to Schiff base reaction conditions may lead to scrambling of the imine groups, giving intractable mixtures of labile imine products.[70] However, pre-binding a metal ion to the 2-(O=CMe)-6-(2,6-(^{i}Pr2-C_6H_3N=CMe)-C_5H_3N precursor alleviates this problem, and by using this metal template method we have been successful at synthesizing several unsymmetrical, BIP-derived compounds with an array of metal ions.

A template reaction was carried out to synthesize the new iron(II)-sulfide complexes $[Fe^{II}(LN_3SMe)(H_2O)_3](OTf)_2$, and $[Fe^{II}(LN_3SMe)Cl_2]$. The appropriate Fe^{II} salt ($Fe(OTf)_2$ or $FeCl_2$) was suspended in EtOH with 2-(O=CMe)-6-(2,6-($^{i}Pr_2$-C_6H_3N=CMe)-C_5H_3N and heated to 60 °C for 1 h, or until all of the solids dissolved. As the solids dissolve, the solution becomes deep purple or blue in color for the trifuloromethanesulfonate or chloride complexes, respectively. This step is followed by addition of 2-(methylthio)aniline added together with Et_3N, and the reaction mixture is allowed to stir at 80 °C for 24 h. The crude reaction mixture is then concentrated to a residue and transferred to the glovebox for crystallization. Single crystals suitable for X-ray structure determination were grown from vapor diffusion of diisopropyl ether into

solutions of $[Fe^{II}(LN_3SMe)(H_2O)_3](OTf)_2$ (in MeCN) and $[Fe^{II}(LN_3SMe)Cl_2]$ (in MeOH). Crystallographic data for complexes $[Fe^{II}(LN_3SMe)(H_2O)_3](OTf)_2$ and $[Fe^{II}(LN_3SMe)Cl_2]$ are summarized in **Table 3. 1**.

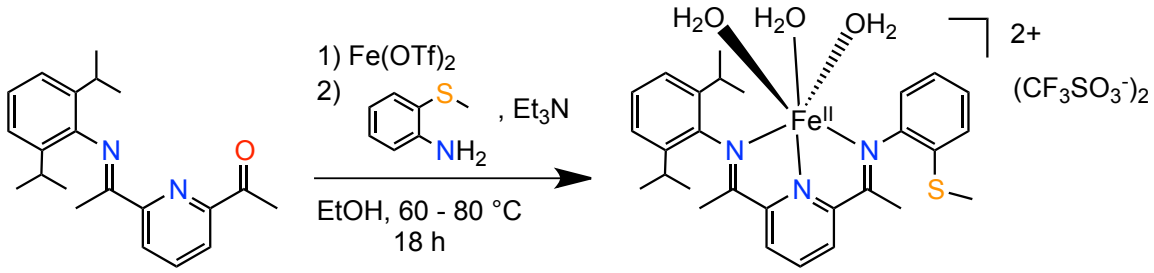

Scheme 3. 1. Synthesis of $[Fe^{II}(LN_3SMe)(H_2O)_3](OTf)_2$.

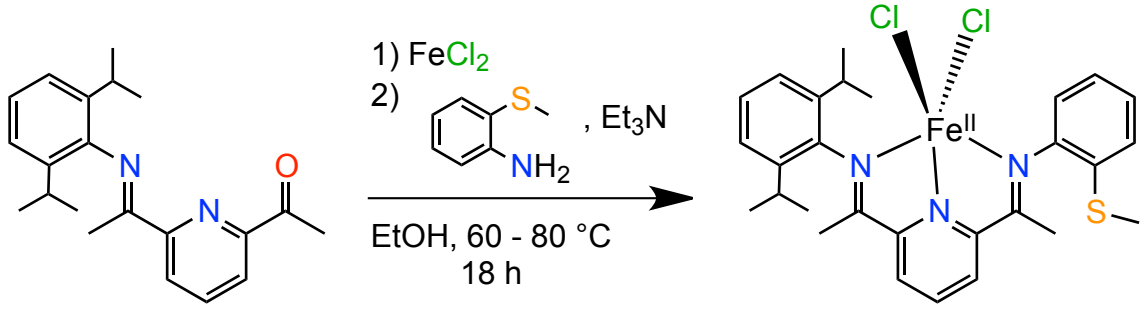

Scheme 3. 2. Synthesis of $[Fe^{II}(LN_3SMe)Cl_2]$.

X-ray crystallography

The ferrous center of $[Fe^{II}(LN_3SMe)(H_2O)_3](OTf)_2$ is bound in a distorted octahedral geometry by the three neutral N donors from the BIP ligand and three water molecules (**Figure 3. 4**). Although Fe^{II}-bis(imino)pyridine complexes are usually found in five-coordinate geometries, there are a few reported examples of octahedral complexes.[65,71] The aryl diisopropyl group is projected orthogonal to the N_3 plane, which contains the iron ion. The three water molecules lie in a plane completing the octahedral coordination environment; the locations of all H atoms from the three water ligands were

easily derived from the difference Fourier maps. The sulfide moiety is not bound to the iron center, being displaced by the water molecules from the coordination sphere. The asymmetric unit contains three trifluoromethanesulfonate anions, one triethylammonium cation, and the Fe complex, leading to the assignment of the metal center as iron(II).

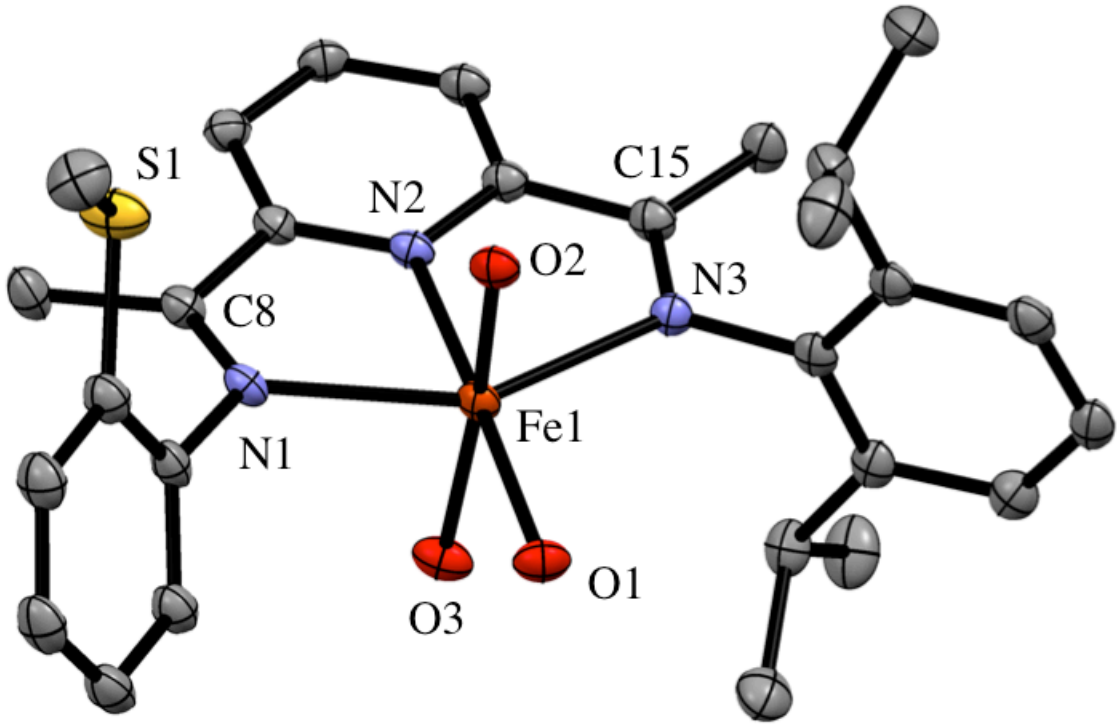

Figure 3. 4. Displacement ellipsoid plot (50% probability level) of the cation of $[Fe^{II}(LN_3SMe)(H_2O)_3](OTf)_2$. H-atoms are removed for clarity.

The structure of $[Fe^{II}(LN_3SMe)Cl_2]$ is shown in

Figure 3. 5. The three neutral bis(imino)pyridine N donors and two chloride anions bind the ferrous center in a distorted square pyramidal geometry ($\tau = 0.18$). The diisopropyl groups are projected orthogonal to the N_3 plane in which the iron sits, and as in $[Fe^{II}(LN_3SMe)(H_2O)_3](OTf)_2$ the sulfide moiety is not bound to the iron center. One

chloride counterion occupies the axial position while the second occupies a pseudoequatorial position completing the square pyramid. Additionally there is one uncoordinated lattice solvent methanol molecule per Fe complex in the structure of $[Fe^{II}(LN_3SMe)Cl_2]$.

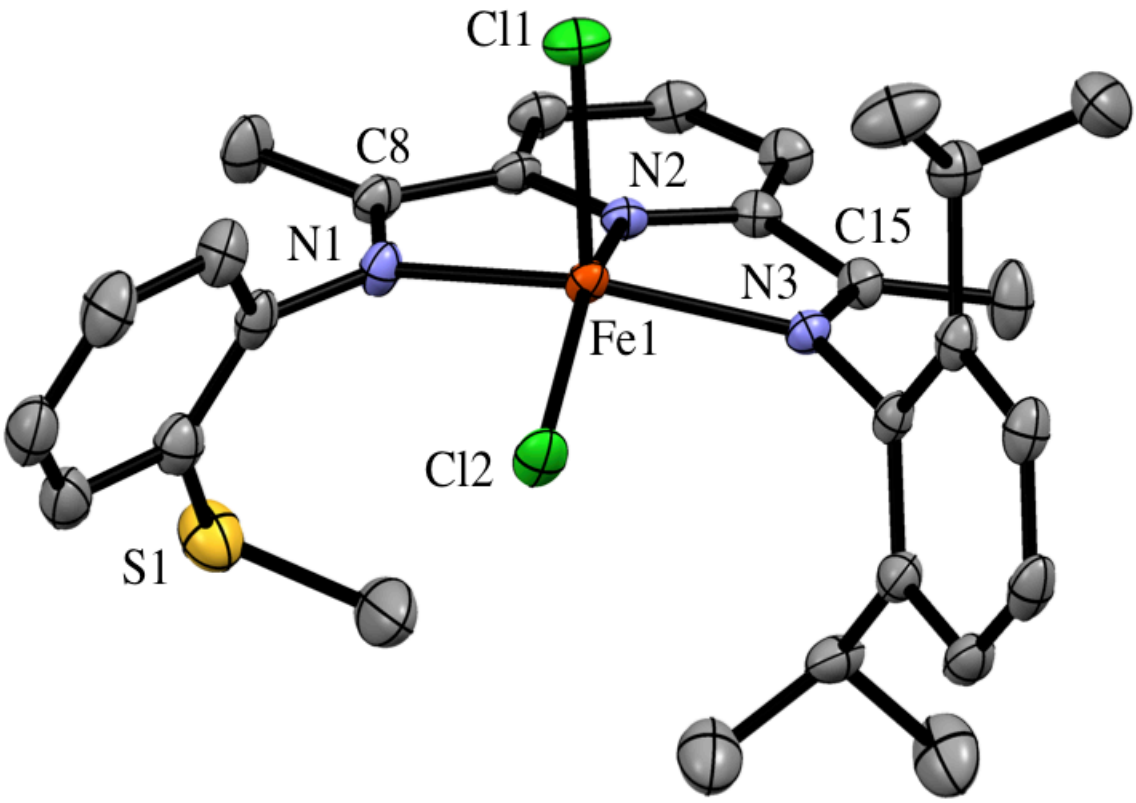

Figure 3. 5. Displacement ellipsoid plot (50% probability level) of $[Fe^{II}(LN_3SMe)Cl_2]$. H-atoms are removed for clarity.

Table 3. 1. Summary of the crystallographic data.

	$[Fe^{II}(LN_3SMe)(H_2O)_3](OTf)_2 \bullet Et_3NHOTf$	$[Fe^{II}(LN_3SMe)Cl_2] \bullet MeOH$
Formula	$[C_{37}H_{55}FeN_4O_{12}S_4F_9]$	$[C_{29}H_{37}Cl_2FeN_3OS]$
Formula weight	1102.94	602.43
T (K)	110	110
Color	Red-purple	Dark blue
Class	monoclinic	monoclinic
Space group	$P2_1/n$	$P2_1/c$
a (Å)	13.73725(19)	9.86440(19)
b (Å)	16.1292(2)	16.3351(2)
c (Å)	22.9656(3)	18.2562(2)
β (°)	95.0312(13)	94.1396(15)
V (Å^3)	5068.90(12)	2934.07(7)
Z	4	4
ϱ (g cm^{-3})	1.445	1.364
μ (mm^{-1})	0.553	0.794
θ (°)	25	26.25
No. reflections collected	36550	24149
No. unique reflections	8932	5932
R_{int}	0.0459	0.0274
No. variable parameters	821	358
R_1 [$I > 2\sigma(I)$]	0.0450	0.0422
wR_2 [$I > 2\sigma(I)$]	0.1222	0.1078
R_1 [all data]	0.0642	0.0467
wR_2 [all data]	0.1292	0.1103
Goodness-of-fit (GOF) on F^2	1.041	1.084
Largest difference in hole and peak (eA^{-3})	–0.58 and 0.65	–0.83 and 1.03

Bond distances for $[Fe^{II}(LN_3SMe)(H_2O)_3](OTf)_2$ and $[Fe^{II}(LN_3SMe)Cl_2]$ are consistent with high-spin ferrous centers[72] and are in good agreement with similar bis(imino)pyridine compounds reported in the literature.[65,71,73] A comparison of bond lengths from the cations of $[Fe^{II}(LN_3SMe)(H_2O)_3](OTf)_2$ and $[Fe^{II}(LN_3SMe)Cl_2]$ with closely related compounds in the literature are summarized in **Table 3. 2**. The comparable symmetrical analogue of complex $[Fe^{II}(LN_3SMe)(H_2O)_3](OTf)_2$, $[Fe^{II}(^{i\text{Pr}}BIP)(H_2O)_2(NCCH_3)](OTf)_2$, reported previously by our lab[65] has an additional diisopropyl phenyl group in lieu of the aryl sulfide substitution. In addition, $[Fe^{II}(^{i\text{Pr}}BIP)(H_2O)_2(NCCH_3)](OTf)_2$ has two axial water ligands and an equatorial coordinated acetonitrile molecule, while $[Fe^{II}(LN_3SMe)(H_2O)_3](OTf)_2$ has 3 coordinated water molecules. Fe-N_{imine} and Fe-N_{pyr} distances of 2.276(3), 2.280(3) and 2.075 Å are in good agreement with the observed Fe-N distances of 2.245(2), 2.234(2) and 2.102(2) Å in $[Fe^{II}(LN_3SMe)(H_2O)_3](OTf)_2$. Fe-$OH_2$ distances in the symmetrical $[Fe^{II}(^{i\text{Pr}}BIP)(H_2O)_2(NCCH_3)](OTf)_2$ complex are 2.075(2) and 2.161(2) Å, very close to the observed Fe-OH_2 distances in $[Fe^{II}(LN_3SMe)(H_2O)_3](OTf)_2$ of 2.086(2), 2.098(2) and 2.116(2) Å, while N_{imine}-C_{imine} distances are very much comparable. Similar results are derived from comparison of $[Fe^{II}(LN_3SMe)Cl_2]$ with the closely related symmetrical bis(diisopropylphenyl) compound $[Fe^{II}(^{i\text{Pr}}BIP)Cl_2]$, first reported by Brookhart and coworkers[73] (see **Table 3. 2**). The observed bond angles in $[Fe^{II}(LN_3SMe)(H_2O)_3](OTf)_2$ and $[Fe^{II}(LN_3SMe)Cl_2]$ are also in good agreement with their close analogues from the literature (**Table 3. 2**).

Table 3. 2. Selected bond distances (Å) and bond angles (°) for iron(II) complexes.

	$[Fe^{II}(LN_3SMe)(H_2O)_3](OTf)_2$	$[Fe^{II}(^{iPr}BIP)(H_2O)_2(NCCH_3)](OTf)_2$[a]	$[Fe^{II}(LN_3SMe)Cl_2]$	$[Fe^{II}(^{iPr}BIP)Cl_2]$[b]
Fe1-N1	2.245(2)	2.276(3)	2.200(2)	2.222(4)
Fe1-N2	2.102(2)	2.086(3)	2.094(2)	2.091(4)
Fe1-N3	2.234(2)	2.280(3)	2.186(2)	2.225(5)
Fe1-O1	2.086(2)	2.075(2)	N/A	N/A
Fe1-O2	2.098(2)	2.161(2)	N/A	N/A
Fe1-O3	2.116(2)	N/A	N/A	N/A
Fe-N4	N/A	2.105(5)	N/A	N/A
Fe-Cl1	N/A	N/A	2.3297(7)	2.3173(19)
Fe-Cl2	N/A	N/A	2.2611(7)	2.2627(17)
N1-C8	1.281(4)	1.286(4)	1.287(4)	1.301(7)
N3-C15	1.287(4)	1.284(4)	1.288(3)	1.295(7)
N1-Fe1-N2	73.30(8)	74.20(10)	73.14(8)	73.67(16)
N1-Fe1-N3	146.95(8)	147.36(9)	141.43(8)	140.23(16)
N2-Fe1-N3	73.89(8)	74.03(10)	73.11(7)	72.59(16)
N2-Fe1-O1	176.45(9)	102.98(10)	N/A	N/A
N2-Fe1-O2	96.69(8)	83.08(9)	N/A	N/A
N2-Fe1-O3	89.82(9)	N/A	N/A	N/A
N2-Fe1-N4	N/A	168.56(10)	N/A	N/A
N2-Fe1-Cl1	N/A	N/A	99.60(6)	94.52(13)
N2-Fe1-Cl2	N/A	N/A	152.16(6)	147.90(13)
O1-Fe1-O2	86.79(8)	173.40(10)	N/A	N/A
Cl1-Fe1-Cl2	N/A	N/A	108.06(3)	117.58(7)
O1-Fe1-N4	86.64(9)	87.59(10)	N/A	N/A
O2-Fe1-N4	170.14(8)	86.58(10)	N/A	N/A

[a] Ref 65. [b] Ref 73.

In the solid-state structure of $[Fe^{II}(LN_3SMe)(H_2O)_3](OTf)_2$, there does not appear to be any π-stacking interactions between the individual cations of $[Fe^{II}(LN_3SMe)(H_2O)_3](OTf)_2$, as all of the aryl groups are significantly offset from each other. In fact, the individual cations are angled away from each other in order to accommodate an extensive H-bonding network (**Figure 3. 6**). In this network, two of the three trifluoromethanesulfonate anions (containing S2 and S4) are found to be H-bond acceptors in two O–H**---**O hydrogen bonds, for which the coordinated water molecules (O1, O2 and O3) are donors. One of the trifluoromethanesulfonate ions bridges the cations of $[Fe^{II}(LN_3SMe)(H_2O)_3](OTf)_2$ between O2**---**O5 and O4**---**O3 through H-bonds, where O2 and O3 are the two axially coordinated water molecules, and O4 and O5 are from the trifluoromethanesulfonate ion. The remaining trifluoromethanesulfonate anion (containing S3) is found to be an H-bond acceptor in O_{water}–H**---**O and N–H**---**O H-bonding interactions (the triethylammonium cation is the donor in the latter). Distances and angles for H-bonds in the solid-state structure of $[Fe^{II}(LN_3SMe)(H_2O)_3](OTf)_2$ are given in **Table 3. 3**. All values are consistent with good H-bonding interactions and are in good agreement with accepted values (D-A ≈ 2.6 – 2.7 Å, DHA ≥ 160°) although some variation is expected based on the nature of the individual H-bond.

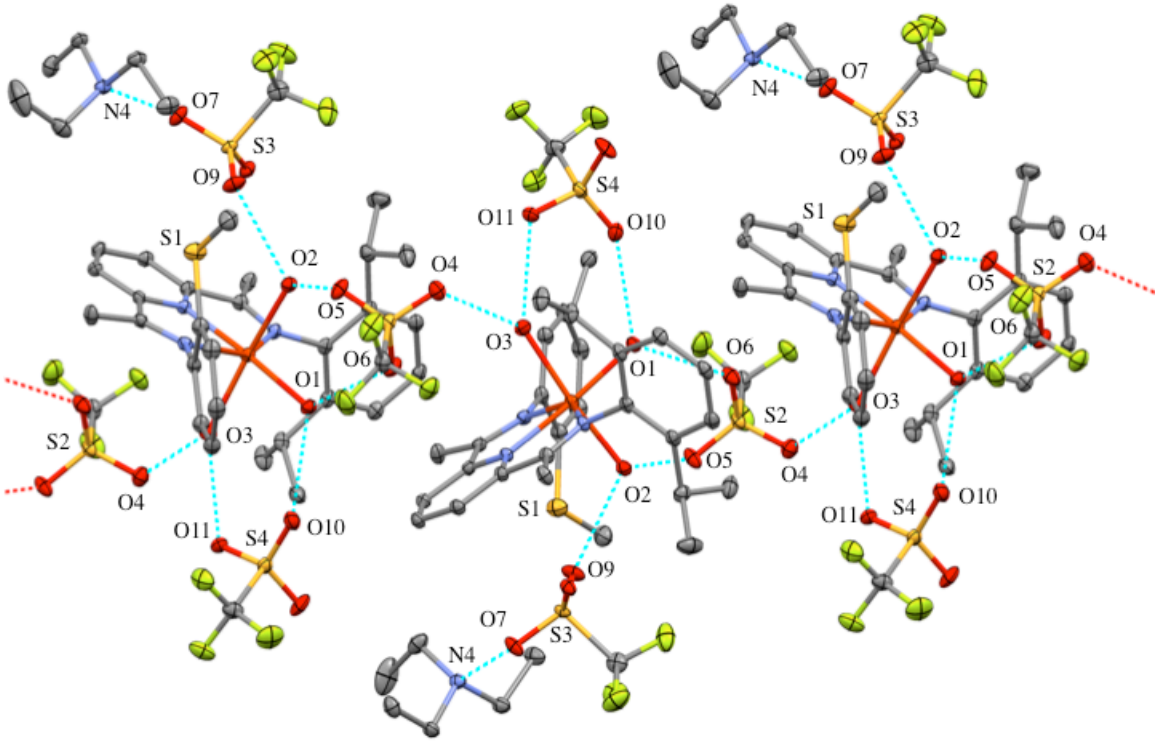

Figure 3. 6. Hydrogen bonding network in the crystal lattice of $[Fe^{II}(LN_3SMe)(H_2O)_3](OTf)_2$. Disorder and H-atoms were removed for clarity.

Table 3. 3. Selected bond distances (Å) and angles (°) for H-bonding interactions in the solid-state structure of $[Fe^{II}(LN_3SMe)(H_2O)_3](OTf)_2$.

Donor Atom (D)	Hydrogen Atom (H)	Acceptor Atom (A)	Distance D-H (Å)	Distance H-A (Å)	Distance D-A (Å)	Angle DHA (°)
O1	H1W1	O6	0.82(2)	1.95(2)	2.759(3)	174(4)
O1	H1W2	O10	0.84(2)	1.99(3)	2.793(3)	160(4)
O1	H1W2	O10’	0.84(2)	1.94(2)	2.77(2)	174(4)
O2	H2W1	O9	0.85(2)	1.90(2)	2.745(6)	171(3)
O2	H2W1	O9’	0.85(2)	1.81(3)	2.636(19)	163(4)
O2	H2W2	O5	0.79(2)	2.01(2)	2.789(3)	171(4)
O3	H3W1	O4	0.82(2)	2.07(3)	2.864(3)	157(3)
O3	H3W2	O11	0.84(2)	1.87(3)	2.702(4)	170(4)
N4	H4A	O7	0.93	1.90	2.755(6)	152

NMR Spectroscopy

Compounds $[Fe^{II}(LN_3SMe)(H_2O)_3](OTf)_2$ and $[Fe^{II}(LN_3SMe)Cl_2]$ were characterized by ^{1}H-NMR spectroscopy. Both compounds exhibit paramagnetically shifted peaks, consistent with the assignment of high-spin Fe^{II} from metal-ligand bond distances. The ^{1}H-NMR spectrum for $[Fe^{II}(LN_3SMe)(H_2O)_3](OTf)_2$ exhibits peaks that are paramagnetically shifted from 90 ppm to -42 ppm, while for $[Fe^{II}(LN_3SMe)Cl_2]$ a wider spread of resonances are observed, from 97 ppm to -38 ppm (**Figure 3. 7** and **Figure 3. 8**). The spectra for compounds $[Fe^{II}(LN_3SMe)(H_2O)_3](OTf)_2$ and $[Fe^{II}(LN_3SMe)Cl_2]$ are significantly more complex relative to related, symmetrical BIP complexes that we have prepared,[65] likely due to the desymmetrized nature of $[Fe^{II}(LN_3SMe)(H_2O)_3](OTf)_2$ and $[Fe^{II}(LN_3SMe)Cl_2]$, as well as the possibility for ligand exchange at the metal center on the NMR timescale. Although individual resonances cannot be assigned in the spectra of

$[Fe^{II}(LN_3SMe)(H_2O)_3](OTf)_2$ and $[Fe^{II}(LN_3SMe)Cl_2]$, the spectra are consistent and reproducible for analytically pure samples.

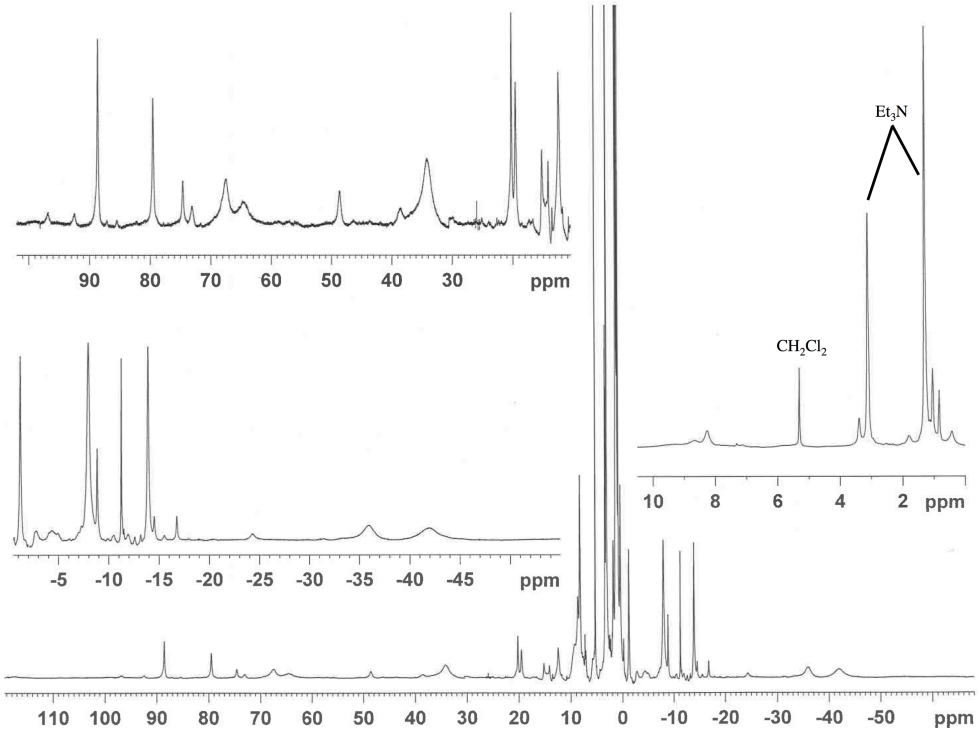

Figure 3. 7. ^{1}H-NMR of $[Fe^{II}(LN_3SMe)(H_2O)_3](OTf)_2$ •Et_3NHOTf in CD_2Cl_2.

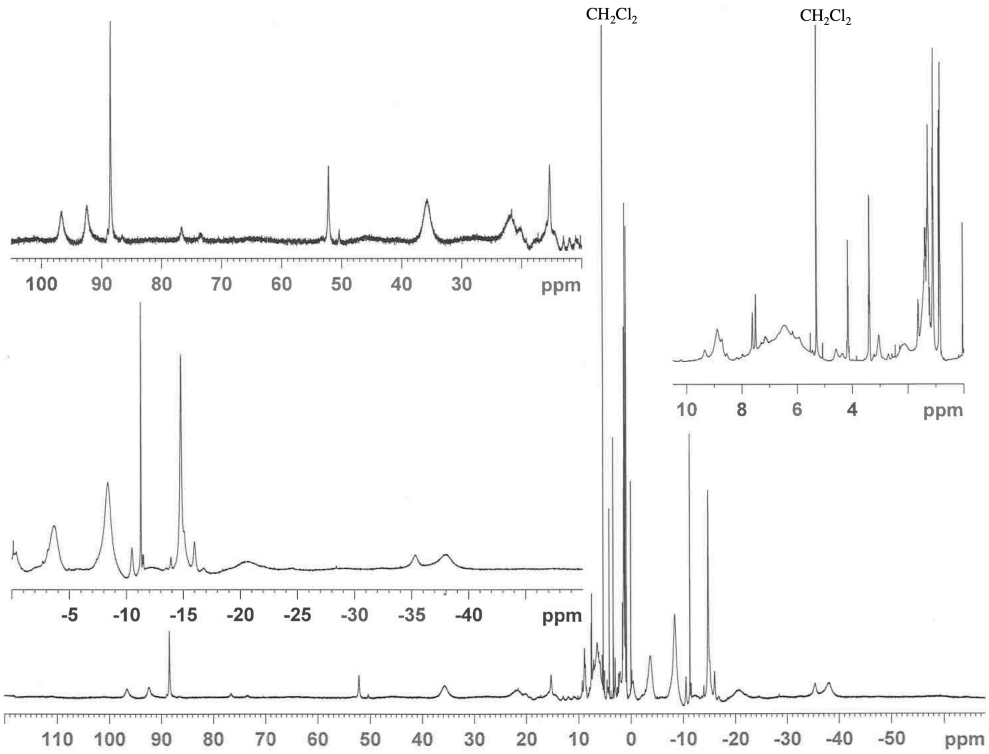

Figure 3. 8. ^{1}H-NMR of $[Fe^{II}(LN_3SMe)Cl_2]$•MeOH in CD_2Cl_2.

O_2 Reactivity

Although $[Fe^{II}(LN_3SMe)(H_2O)_3](OTf)_2$ is unreactive toward O_2 at ambient temperature and pressure, a new sulfoxide product is generated at modestly elevated temperature in CH_2Cl_2, as seen in **Scheme 3. 3**. The reaction of $[Fe^{II}(LN_3SMe)(H_2O)_3](OTf)_2$ to $[Fe(LN_3SOMe)(OTf)]^+$ was followed by LDI-MS. As shown in **Figure 3. 9**, a loss of the starting material at *m/z* 648.1 ($[M - 3\ H_2O - OTf]^+$) is seen over 4 days, along with the appearance of a singly-oxygenated sulfoxide species, $[Fe(LN_3SOMe)(OTf)]^+$, at *m/z* = 664.4 ($[M]^+$). Further analysis (vide infra) reveals that this complex is likely an Fe^{III} species which was reduced and observed as a monocation in the LDI-MS experiment.

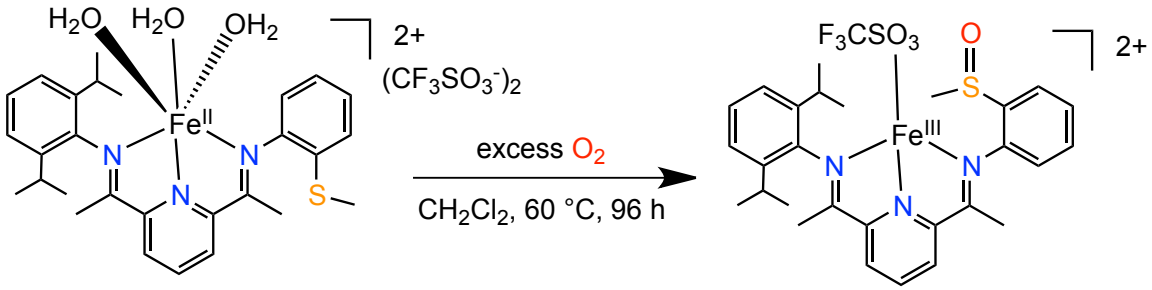

Scheme 3. 3. Reaction of $[Fe^{II}(LN_3SMe)(H_2O)_3]^{2+}$ with O_2 to form sulfoxide complex $[Fe(LN_3S(O)Me)(OTf)]^{2+}$.

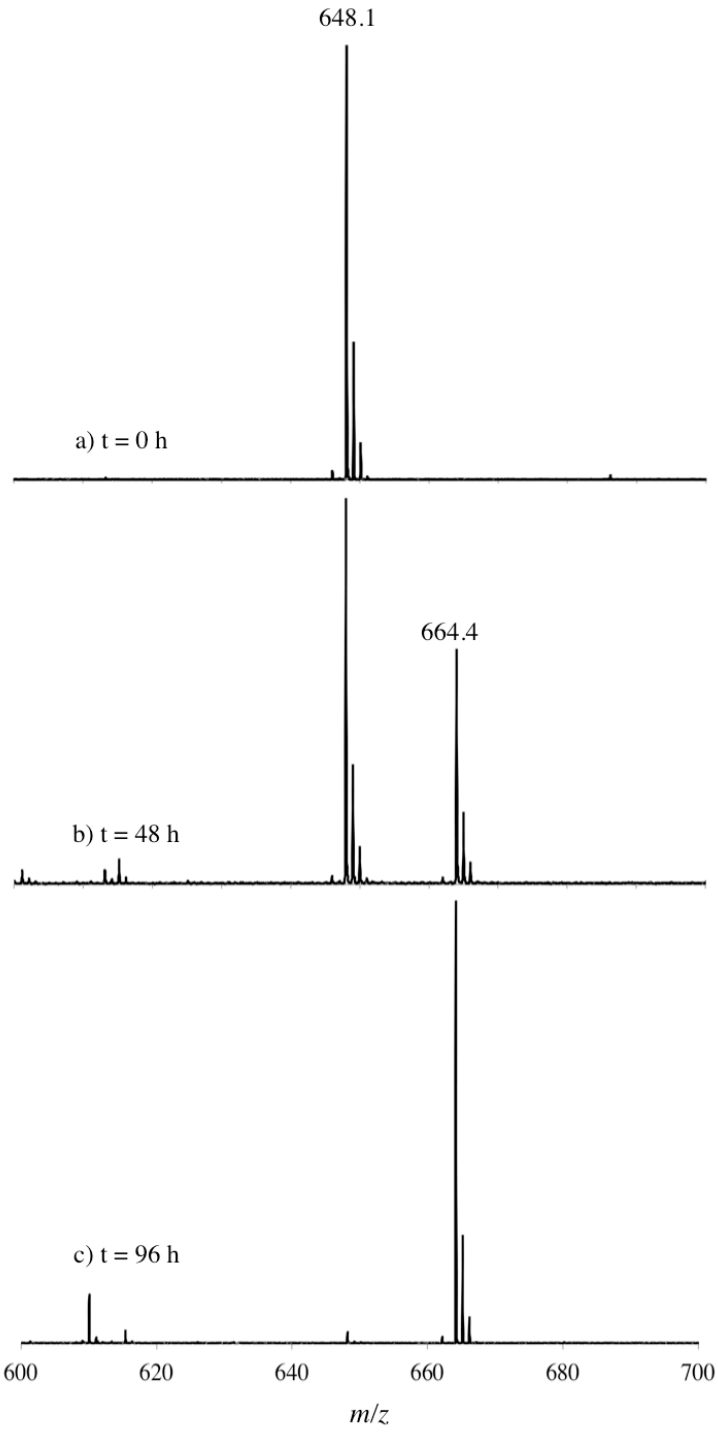

Figure 3. 9. Reaction of $[Fe^{II}(LN_3SMe)(H_2O)_3](OTf)_2$ with excess O_2 in CH_2Cl_2 at 60 °C as monitored by LDI-MS. The peak at *m/z* 648.1 is assigned to $[Fe^{II}(LN_3SMe)(OTf)]^+$, and the peak at *m/z* 664.4 is assigned to $[Fe(LN_3S(O)Me)(OTf)]^+$.

The $Fe^{II}(LN_3SMe)Cl_2$ complex also exhibits reactivity toward O_2. Solutions of $[Fe^{II}(LN_3SMe)Cl_2]$ react with excess O_2 at 60 °C in a closed reaction vessel to afford the sulfone **4** in 96 h (**Scheme 3. 4**). **Figure 3. 10** shows the loss of $[Fe^{II}(LN_3SMe)Cl_2]$ (*m/z* 534.4, $[Fe^{II}(LN_3SMe)Cl]^+$) with the concurrent appearance of a peak at *m/z* 566.4, corresponding to the doubly-oxygenated species $[Fe(LN_3S(O_2)Me)Cl]^+$. As in the case of $[Fe(LN_3S(O)Me)(OTf)]^+$, this complex is assigned as an Fe^{III} product but is presumed to be reduced in the LDI-MS experiment to the corresponding monocation. Spectra taken at early time points (0 - 48 h) reveal the presence of a singly oxygenated (possibly sulfoxide) intermediate (*m/z* 550.4, $[Fe(LN_3S(O)Me)Cl]^+$) along with sulfide starting material and sulfone product. This intermediate species is not observed in significant quantities, and after 96 h only the doubly-oxygenated sulfone product $[Fe(LN_3S(O_2)Me)Cl]^+$ was observed (**Figure 3. 10**). Attempts to improve the yield of the putative singly-oxygenated complex (*m/z* 550.4) by performing the reaction at lower temperature and pressure gave only small amounts of this species and the doubly-oxygenated product. No significant improvement in yield could be obtained.

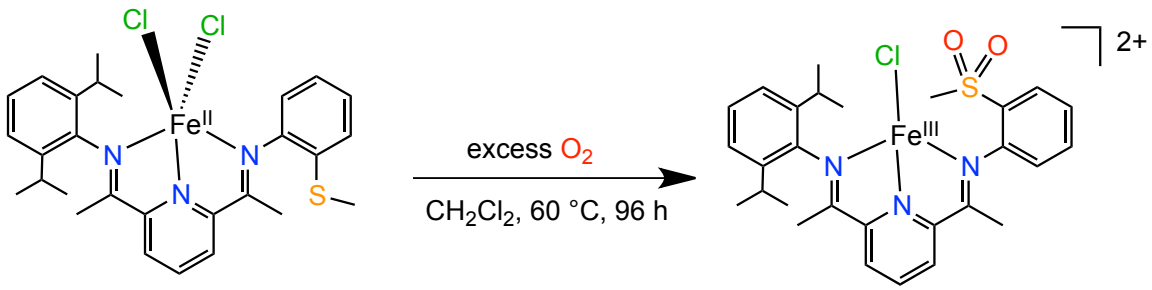

Scheme 3. 4. Reaction of $[Fe(LN_3S(O_2)Me)Cl_2]$ with O_2 to form the sulfone complex $[Fe(LN_3S(O_2)Me)Cl]^{2+}$.

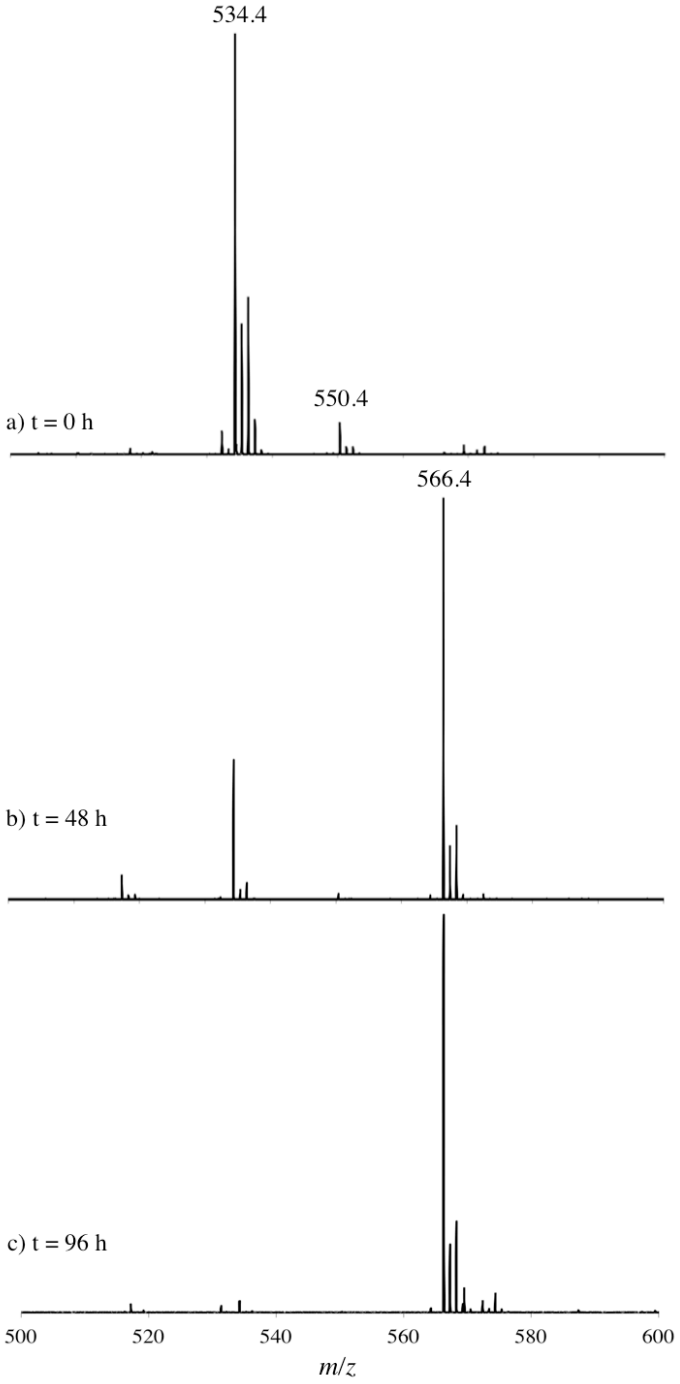

Figure 3. 10. Reaction of $[Fe(LN_3S(O_2)Me)Cl_2]$ with excess O_2 in CH_2Cl_2 at 60 °C as monitored by LDI-MS. The peak at *m/z* 534.4 is assigned to $[Fe(LN_3SMe)Cl]^+$, and the peak at *m/z* 566.4 is assigned to doubly-oxygenated $[Fe(LN_3S(O_2)Me)Cl]^+$. The small peak at *m/z* 550.4 is assigned to singly-oxygenated $[Fe(LN_3S(O)Me)Cl]^+$.

Control experiments were conducted, and exposure of 2-aminothiophenol to excess O_2 under the same conditions for 3 d resulted in no observed sulfoxide or sulfone products as measured by ^{1}H-NMR. These control reactions indicated that the presence of the ferrous complexes $[Fe^{II}(LN_3SMe)(H_2O)_3](OTf)_2$ and $Fe(LN_3S(O_2)Me)Cl_2$ were necessary for the observed reactivity. The reaction of $[Fe^{II}(LN_3SMe)(H_2O)_3](OTf)_2$ was also run in the presence of excess $H_2{}^{18}O$ (100 equiv). This experiment was performed to confirm that dioxygen, and not exogenous water, was the source of the oxygen atom in the sulfoxide complex, and to determine if O-atom exchange with water could occur during the *S*-oxygenation reaction. High-valent ferryl (Fe=O) species are known to rapidly exchange with H_2O in nonheme iron complexes, resulting in the incorporation of oxygen derived from water in oxidized substrates.[74-76] No ^{18}O incorporation into $[Fe(LN_3S(O)Me)(OTf)]^+$ was observed by LDI-MS in the presence of $^{18}OH_2$. This result indicates that O_2 is the sole source of oxygen in the *S*-oxygenation reaction, and suggests that ferryl intermediates do not play a significant role. In addition, water (in small amounts) does not appear to have any inhibitory effect on this reaction.

Product characterization

In our previous S-oxygenation studies, the final product(s) were shown to be in the iron +2 oxidation state, making these complexes good functional models for CDO, and opening up the possibility for catalytic activity. Product complexes $[Fe(LN_3S(O)Me)(OTf)]^{2+}$ and $[Fe(LN_3S(O_2)Me)Cl]^{2+}$ exhibit featureless absorption spectra (**Figure 3. 19** and **Figure 3. 20**), and also give paramagnetic ^{1}H-NMR spectra (**Figure 3. 21** and **Figure 3. 22**) with no discernable resonances that can be assigned to ligand-based peaks. ^{1}H-NMR spectra of $[Fe(LN_3S(O)Me)(OTf)]^{2+}$ and

$[Fe(LN_3S(O_2)Me)Cl]^{2+}$ are significantly different from the sharp, paramagnetically shifted spectra that is characteristic of high-spin iron(II), as seen in the starting materials $[Fe^{II}(LN_3SMe)(H_2O)_3](OTf)_2$ and $Fe(LN_3S(O_2)Me)Cl_2$ (**Figure 3. 7** and **Figure 3. 8**). These featureless ^{1}H-NMR spectra are consistent with high-spin (S = 5/2) iron(III)-containing complexes. The X-band EPR spectrum of $[Fe(LN_3S(O)Me)(OTf)]^{2+}$ (**Figure 3. 11**) reveals an intense signal near g_{eff} = 4.28 that is typical for a rhombic, hs-Fe^{III} ion. There is also a strong feature at g_{eff} = 2 that may arise from hs-Fe^{III}, ls-Fe^{III} or intermolecular interactions.[77-81] The EPR spectrum for $[Fe(LN_3S(O_2)Me)Cl]^{2+}$ (**Figure 3. 12**) exhibits similar peaks near g_{eff} = 4.29 and 2.01, and while detailed simulations of these spectra have not been attempted, they are clearly consistent with the S-oxygenated products $[Fe(LN_3S(O)Me)(OTf)]^{2+}$ and $[Fe(LN_3S(O_2)Me)Cl]^{2+}$ being in the hs-Fe^{III} oxidation state. In contrast, the EPR spectra of the starting complexes $[Fe^{II}(LN_3SMe)(H_2O)_3](OTf)_2$ and $Fe(LN_3S(O_2)Me)Cl_2$, which are overlayed with the spectra from $[Fe(LN_3S(O)Me)(OTf)]^{2+}$ and $[Fe(LN_3S(O_2)Me)Cl]^{2+}$, show only very weak signals in the same regions, which can be attributed to a small amount of oxidation by air during sample preparation.

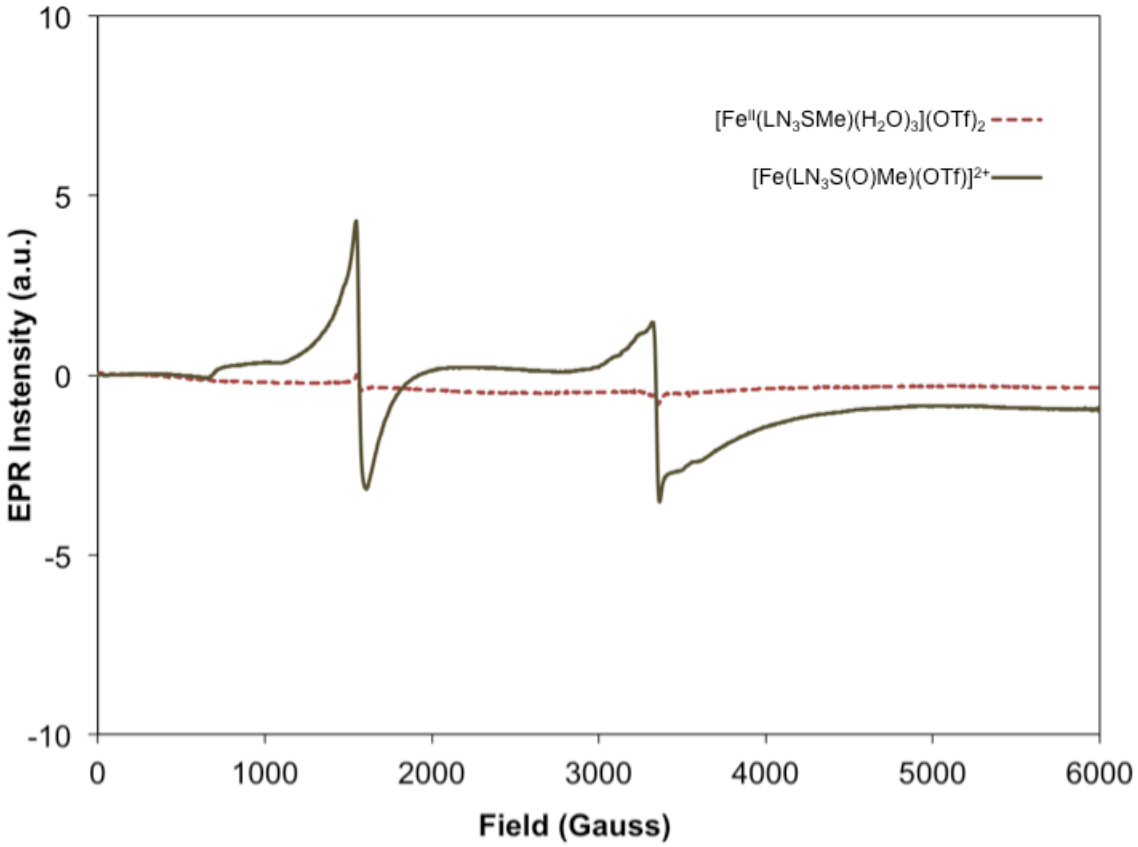

Figure 3. 11. X-band EPR spectra of $[Fe^{II}(LN_3SMe)(H_2O)_3](OTf)_2$ and $[Fe(LN_3S(O)Me)(OTf)]^{2+}$ in CH_2Cl_2 at 15 K.

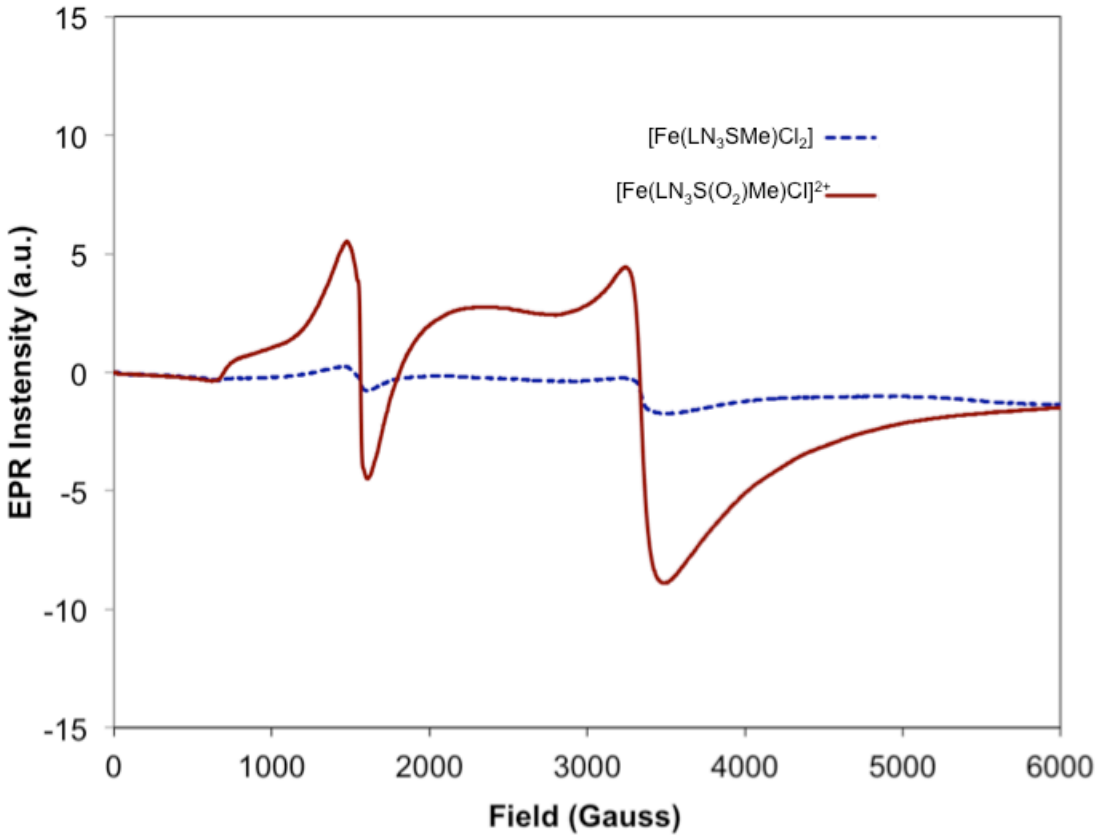

Figure 3. 12. X-band EPR spectra of $[Fe(LN_3SMe)Cl_2]$ and $[Fe(LN_3S(O_2)Me)Cl]^{2+}$ in CH_2Cl_2 at 15 K.

A UV-Vis titration for iron(II) was employed to confirm the oxidation state of the Fe product in these sulfide oxygenation reactions. It is well known that 1,10-phenanthroline is a strong chelator for iron(II) and iron(III), forming highly colored $[Fe(phen)_3]^{2+}$ and $[Fe(phen)_3]^{3+}$ complexes, which exhibit distinct spectra (**Figure 3. 13**). Titration of the iron from the crude reaction mixture of $[Fe(LN_3S(O_2)Me)Cl]^{2+}$ with 5.0 equiv of 1,10-phenanthroline (**Figure 3. 14**) and comparison of the absorbance at $\lambda = 510$ nm (the marker band for $[Fe(phen)_3]^{2+}$) with a calibration curve (**Figure 3. 23**), revealed that there is < 6% Fe^{II} in this solution. These data confirm that $[Fe(LN_3S(O_2)Me)Cl]^{2+}$ contains a ferric (Fe^{III}) center.

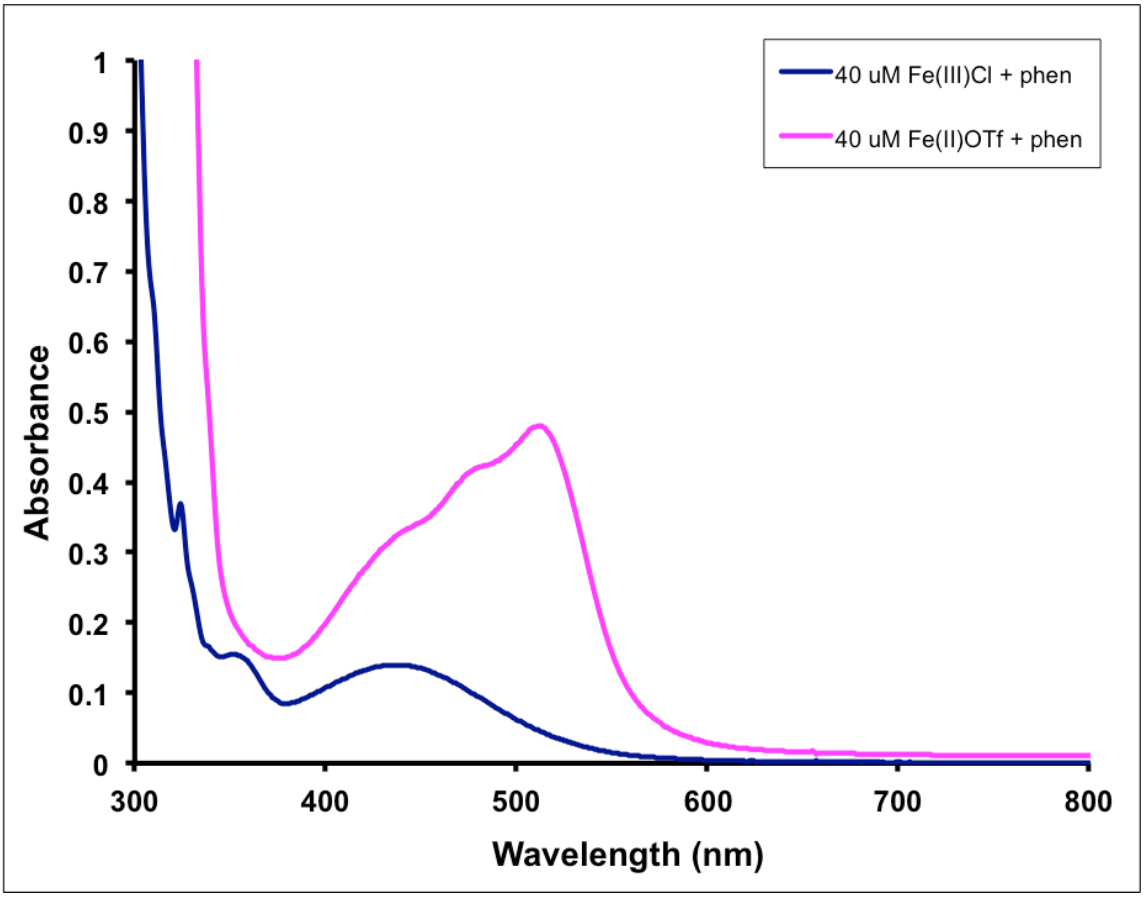

Figure 3. 13. Comparison of the UV-Vis spectra of $[Fe(phen)_3]^{3+}$ (blue) and $[Fe(phen)_3]^{2+}$ (pink) (40 μM in Fe). Samples were prepared by mixing $FeCl_3$ or $Fe(OTf)_2$ salt with 5.0 equiv of 1,10-phenanthroline and mixing for 5 min in CH_2Cl_2.

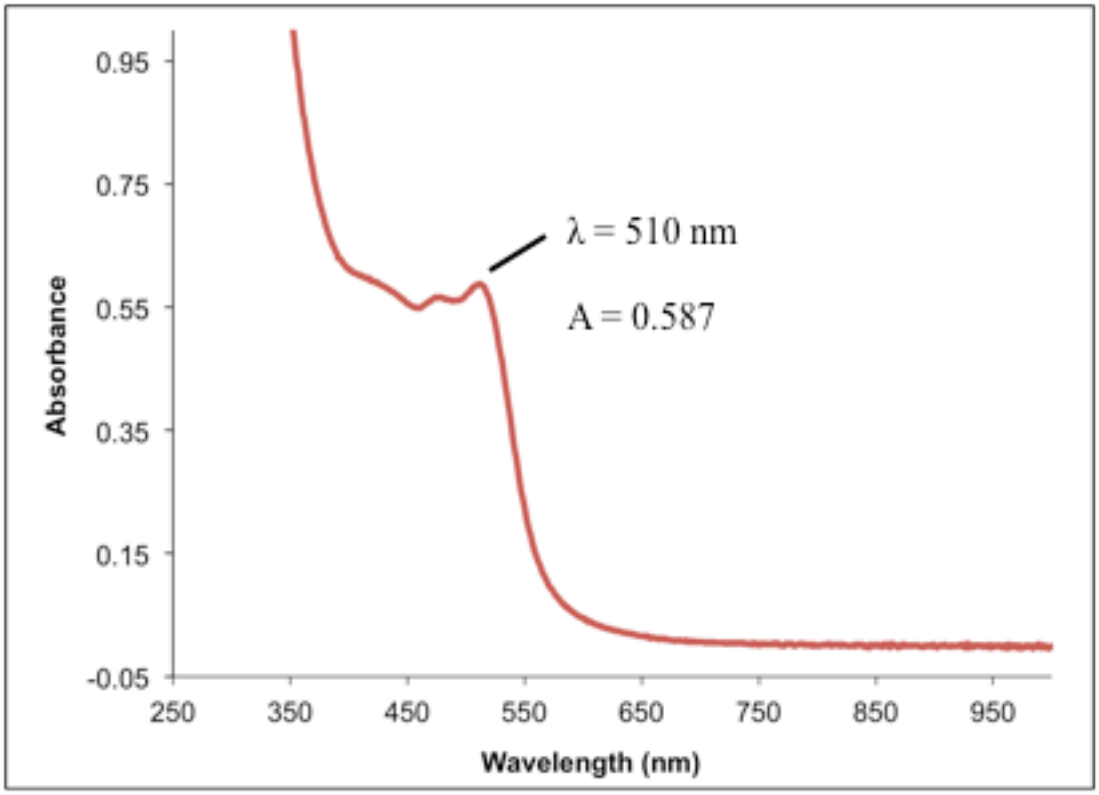

Figure 3. 14. UV-Vis spectrum of $[Fe(LN_3S(O_2)Me)Cl]^{2+}$ with 5.0 equiv of 1,10-phen in CH_2Cl_2.

Attempts to crystallize the sulfoxide and sulfone products in **Scheme 3. 3** and **Scheme 3. 4** were unsuccessful, and identification of S-oxygenates by IR spectroscopy proved inconclusive (**Figure 3. 24** – **Figure 3. 27**) due to overlapping features. However, the S-oxygenated products were easily identified when the ligand was separated from the metal center and hydrolyzed with aqueous acid into its component organic fragments (**Scheme 3. 5**). The relevant organic compounds are distinguishable by the respective ^{1}H-NMR chemical shifts of the $RSCH_3$ moiety. The chemical shift for the methyl sulfide of the starting material, 2-(methylthio)aniline, is $\delta(CDCl_3)$ = 2.34 (s, 3H), while the corresponding sulfoxide (2-(methylsulfinyl)aniline) and sulfone (2-(methylsulfonyl)aniline) products have chemical shifts $\delta(CDCl_3)$ = 2.93 (s, 3H) and 3.03

(s, 3H),[68] respectively. Demetalation of the crude reaction mixture of $[Fe(LN_3S(O)Me)(OTf)]^+$ was accomplished by stirring with 1 M HCl, neutralization with $NaHCO_3$, and separation of the organic layer. Due to the polar nature of the sulfoxide moiety, 2-(methylsulfinyl)aniline was easily separated from other organic material via column chromatography on silica (EtOAc/hexanes) and its structure confirmed by ^{1}H-NMR (**Figure 3. 15**), $\delta(CDCl_3)$ = 2.93 (s, 3H). Final recovery of 2-(methylsulfinyl)aniline was low (≤ 10%), contrasting the apparent good conversion observed in the LDI-MS (vide infra).

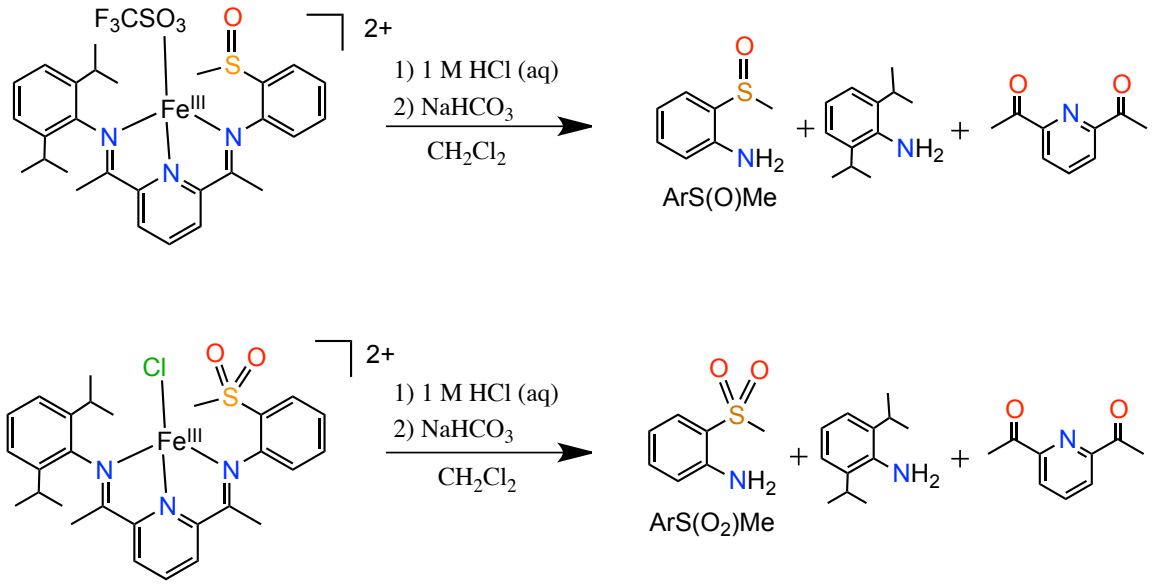

Scheme 3. 5. Hydrolysis of bis(imino)pyridine complexes.

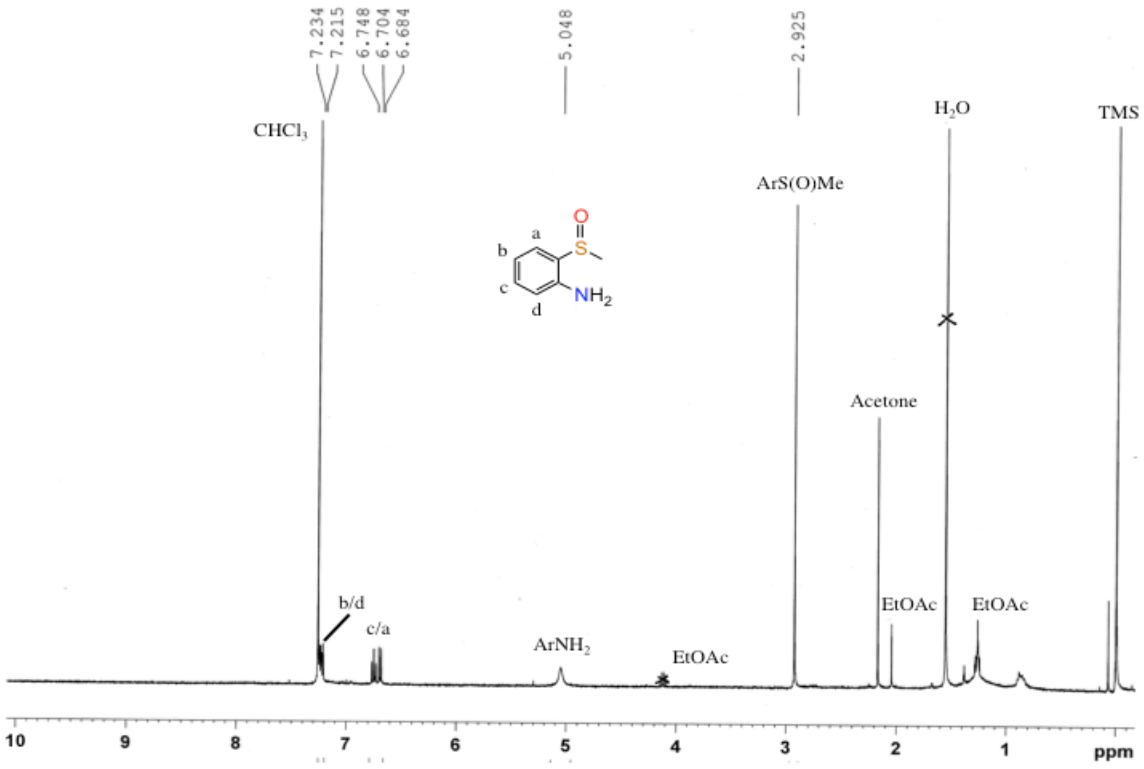

Figure 3. 15. ^{1}H-NMR spectrum of 2-(methylsulfinyl)aniline recovered following demetalation of $[Fe(LN_3S(O)Me)(OTf)]^{2+}$.

The demetalation of the reaction mixture of $[Fe(LN_3S(O_2)Me)Cl]^{+}$ was performed as above, but in this case the S-oxygenated fragment, 2-(methylsulfonyl)aniline, co-eluted with other organics and therefore its purification by chromatography was not successful. However, in the crude ^{1}H-NMR spectrum (**Figure 3. 16**) following demetalation, we can clearly identify the characteristic resonance of the sulfone (δ ($CDCl_3$) = 3.05), with only minor contributions from the starting sulfide or sulfoxide methyl groups.

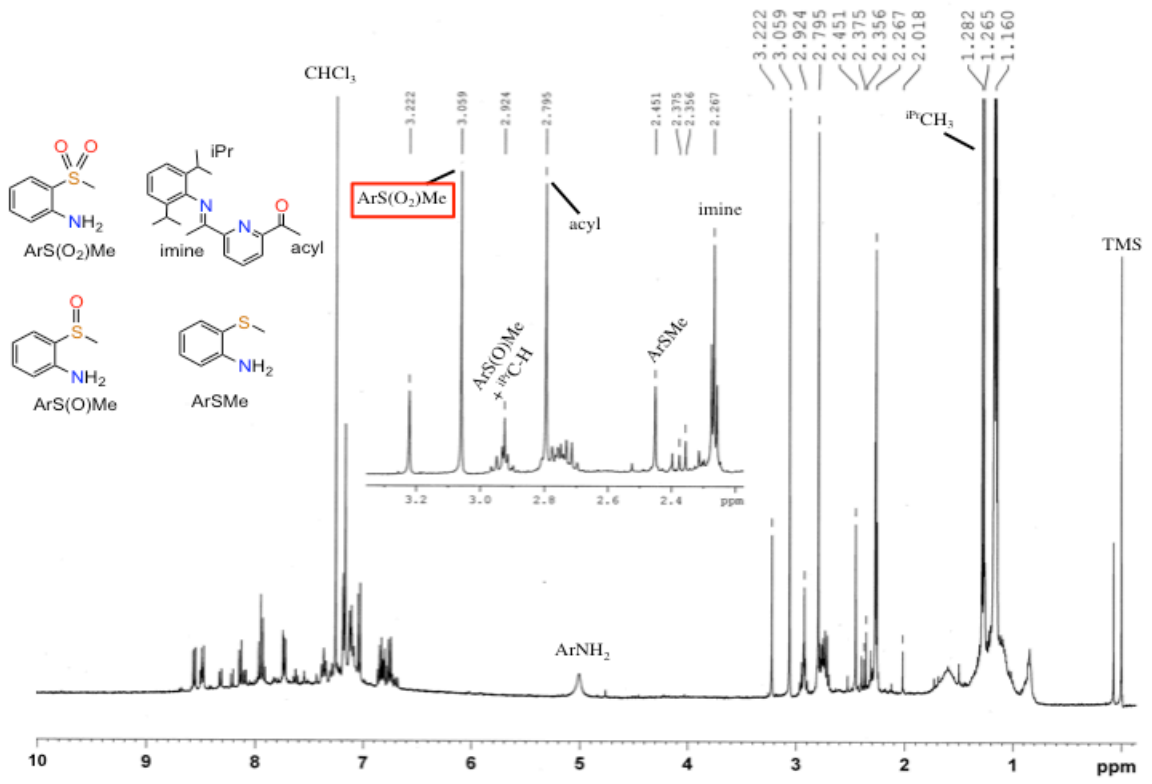

Figure 3. 16. ^{1}H-NMR spectrum of the crude mixture following demetalation of $[Fe(LN_3S(O_2)Me)Cl]^{2+}$. The 2-(methylsulfonyl)aniline is identified at 3.06 ppm, with minor peaks arising from the intermediate sulfoxide (2.92 ppm) and starting sulfide (2.36 ppm).

Given the above results, ^{1}H-NMR experiments were conducted in an effort to quantitate the crude products immediately following aqueous workup but prior to chromatographic separation (**Figure 3. 17** and **Figure 3. 18**). The addition of CH_3NO_2 as an external standard ($\delta(CDCl_3)$ = 4.32) and comparison with the S-oxygenated products (2-(methylsulfinyl)aniline or 2-(methylsulfonyl)aniline, ($\delta(CDCl_3)$ = 2.92 or 3.05, respectively) gives only modest yields of sulfoxide (15%) and sulfone (29%). However, low recovery of other organic ligand fragments was also observed when compared with

the CH_3NO_2 standard, indicating that the polar, amino-functionalized fragments are likely lost in the aqueous workup. A comparison of the methyl resonances from the sulfoxide and sulfone with the recovered 2,6-diisopropylaniline resonance ($\delta(CDCl_3)$ = 1.27, d 12H) as an internal standard indicate a higher overall yield of the sulfoxide (51%) and sulfone (45%) products.

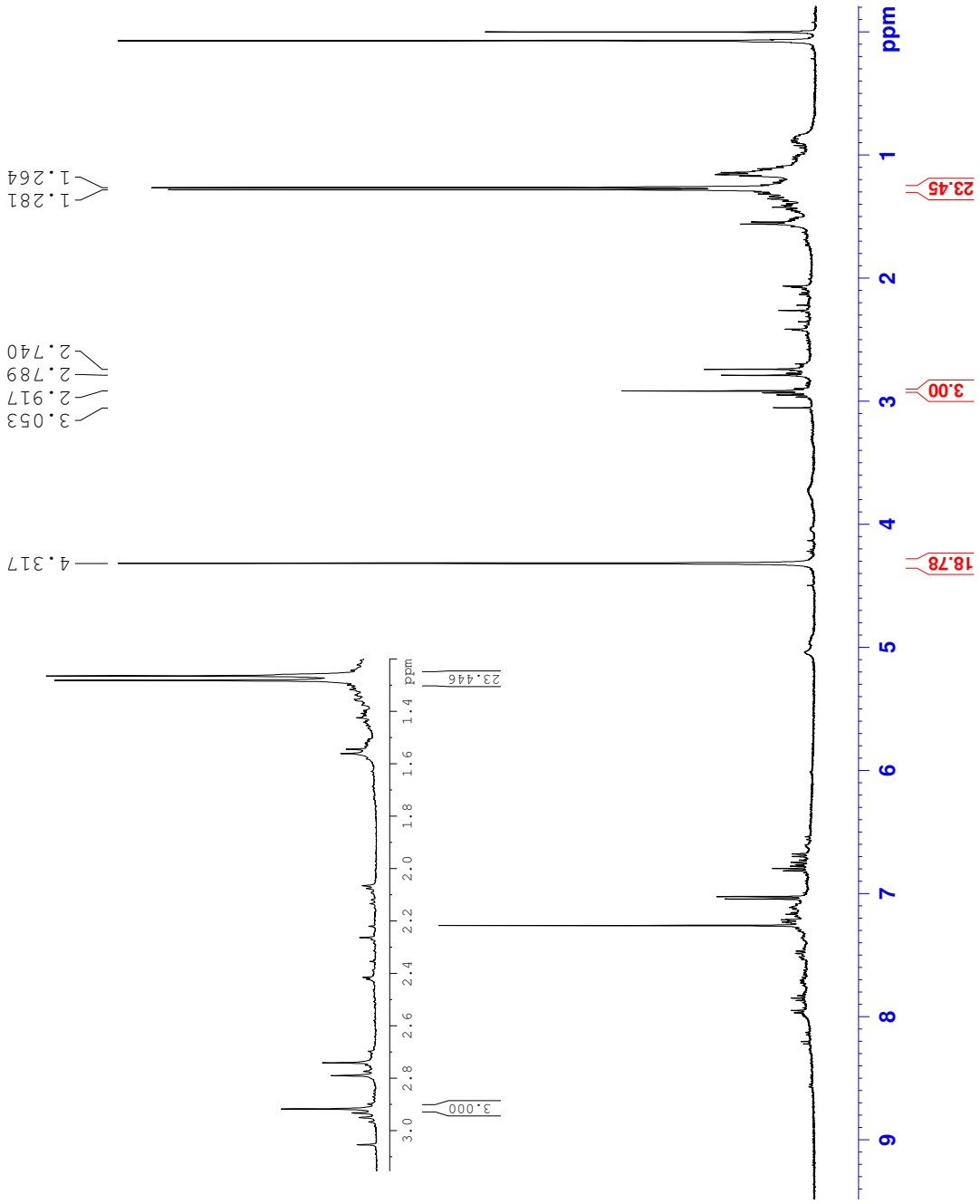

Figure 3. 17. ^{1}H-NMR spectrum of the crude products following acid demetalation/hydrolysis of $[Fe(LN_3S(O)Me)(OTf)]^{2+}$. The sulfoxide product, 2-(methylsulfinyl)aniline, shows a characteristic methyl peak at 2.92 ppm. The diisopropyl resonance for 2,6-diisopropylaniline is observed at 1.27 ppm. Nitromethane (4.32 ppm, 1.0 equiv based on $[Fe^{II}(LN_3SMe)(H_2O)_3](OTf)_2$) was added as external standard.

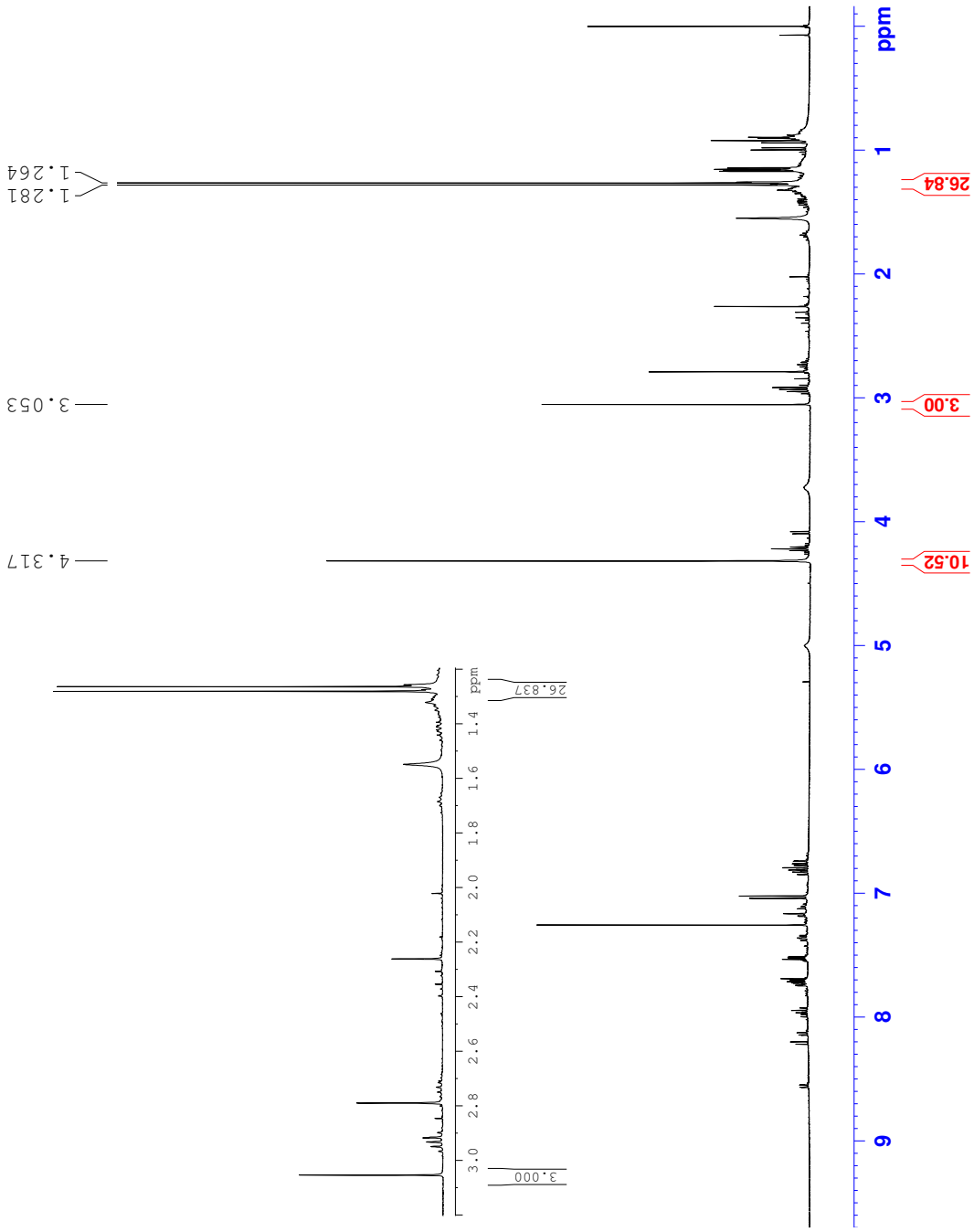

Figure 3. 18. ^{1}H-NMR spectrum of the crude products following acid demetalation/hydrolysis of $[Fe(LN_3S(O_2)Me)Cl]^{2+}$. The sulfone product, 2-(methylsulfonyl)aniline, shows a characteristic methyl peak at 3.05 ppm. The diisopropyl resonance for 2,6-diisopropylaniline is observed at 1.27 ppm. Nitromethane (4.32 ppm, 1.0 equiv based on $Fe^{II}(LN_3SMe)Cl_2$) was added as external standard.

3. 4. Conclusions

Herein we have reported the synthesis of two unsymmetrical sulfide-incorporated, bis(imino)pyridine complexes which are accessible via a metal-assisted template reaction. Complexes $[Fe^{II}(LN_3SMe)(H_2O)_3](OTf)_2$ and $Fe^{II}(LN_3SMe)Cl_2$ were characterized by single crystal X-ray crystallography. These complexes react with O_2 at modestly elevated temperature to yield S-oxygenated sulfoxide or sulfone complexes. The identities of the products were determined by mass spectrometry and ^{1}H-NMR studies. UV-Vis quantitation of the iron(II) ions with 1,10-phenanthroline in the reaction mixture of $[Fe(LN_3S(O_2)Me)Cl]^{2+}$ indicated that $[Fe(LN_3S(O_2)Me)Cl]^{2+}$ should contain mainly iron(III) ions. EPR spectroscopy of reaction mixtures following oxygenation confirmed the presence of hs-Fe^{III} complexes in the case of both $[Fe(LN_3S(O)Me)(OTf)]^{2+}$ and $[Fe(LN_3S(O_2)Me)Cl]^{2+}$. Sulfide oxidation was confirmed by demetalation and hydrolysis of the bis(imino)pyridine ligands in $[Fe(LN_3S(O)Me)(OTf)]^{2+}$ and $[Fe(LN_3S(O_2)Me)Cl]^{2+}$. The ^{1}H-NMR of the ligand fragments allowed for identification of the sulfoxide and sulfone products from complexes $[Fe(LN_3S(O)Me)(OTf)]^{2+}$ and $[Fe(LN_3S(O_2)Me)Cl]^{2+}$, respectively. The S-oxygenation reaction for sulfide ligands with dioxygen as the oxidant/O-atom source was demonstrated for two nonheme iron(II) complexes. The nature of the complexes (chloride versus triflate starting materials) determines the extent of S-oxygenation, resulting in either sulfoxide or sulfone products. Selective oxidation of organic substrates such as sulfides is an important and desirable property of metal-mediated oxygenations, and the reactivity reported here warrants further investigation.

3. 5. References

(1) Bollinger, J. M., Jr.; Krebs, C. *J. Inorg. Biochem.* **2006**, *100*, 586.

(2) Solomon, E. I.; Brunold, T. C.; Davis, M. I.; Kemsley, J. N.; Lee, S. K.; Lehnert, N.; Neese, F.; Skulan, A. J.; Yang, Y. S.; Zhou, J. *Chem. Rev.* **2000**, *100*, 235.

(3) Costas, M.; Mehn, M. P.; Jensen, M. P.; Que, L., Jr. *Chem. Rev.* **2004**, *104*, 939.

(4) Koehntop, K. D.; Emerson, J. P.; Que, L., Jr. *J. Biol. Inorg. Chem.* **2005**, *10*, 87.

(5) Neidig, M. L.; Solomon, E. I. *Chem. Commun.* **2005**, 5843.

(6) Ryle, M. J.; Hausinger, R. P. *Curr. Opin. Chem. Biol.* **2002**, *6*, 193.

(7) Kovaleva, E. G.; Lipscomb, J. D. *Nat. Chem. Biol.* **2008**, *4*, 186.

(8) Pierce, B. S.; Gardner, J. D.; Bailey, L. J.; Brunold, T. C.; Fox, B. G. *Biochemistry* **2007**, *46*, 8569.

(9) Joseph, C. A.; Maroney, M. J. *Chem. Commun.* **2007**, 3338.

(10) McCoy, J. G.; Bailey, L. J.; Bitto, E.; Bingman, C. A.; Aceti, D. J.; Fox, B. G.; Phillips, G. N. *Proc. Natl. Acad. Sci. U. S. A.* **2006**, *103*, 3084.

(11) Simmons, C. R.; Liu, Q.; Huang, Q. Q.; Hao, Q.; Begley, T. P.; Karplus, P. A.; Stipanuk, M. H. *J. Biol. Chem.* **2006**, *281*, 18723.

(12) Ye, S.; Wu, X.; Wei, L.; Tang, D. M.; Sun, P.; Bartlam, M.; Rao, Z. H. *J. Biol. Chem.* **2007**, *282*, 3391.

(13) Crawford, J. A.; Li, W.; Pierce, B. S. *Biochemistry* **2011**, *50*, 10241.

(14) Kumar, D.; Thiel, W.; de Visser, S. P. *J. Am. Chem. Soc.* **2011**, *133*, 3869.

(15) Tchesnokov, E. P.; Wilbanks, S. M.; Jameson, G. N. L. *Biochemistry* **2012**, *51*, 257.

(16) Imsand, E. M.; Njeri, C. W.; Ellis, H. R. *Arch. Biochem. Biophys.* **2012**, *521*, 10.

(17) McDonald, A. R.; Bukowski, M. R.; Farquhar, E. R.; Jackson, T. A.; Koehntop, K. D.; Seo, M. S.; De Hont, R. F.; Stubna, A.; Halfen, J. A.; Münck, E.; Nam, W.; Que, L., Jr. *J. Am. Chem. Soc.* **2010**, *132*, 17118.

(18) Saget, T.; Lemouzy, S. J.; Cramer, N. *Angew. Chem. Int. Ed.* **2012**, *51*, 2238.

(19) Kalatzis, V.; Cherqui, S.; Antignac, C.; Gasnier, B. *Embo J.* **2001**, *20*, 5940.

(20) Kalatzis, V.; Antignac, C. *Nephrol., Dial., Transplant.* **2002**, *17*, 1883.

(21) Perry, T. L.; Norman, M. G.; Yong, V. W.; Whiting, S.; Crichton, J. U.; Hansen, S.; Kish, S. J. *Ann. Neurol.* **1985**, *18*, 482.

(22) Pean, A. R.; Parsons, R. B.; Waring, R. H.; Williams, A. C.; Ramsden, D. B. *J. Neurol. Sci.* **1995**, *129*, 107.

(23) Parsons, R. B.; Waring, R. H.; Ramsden, D. B.; Williams, A. C. *Neurotoxicology* **1998**, *19*, 599.

(24) Cremlyn, R.J. *An Introduction to Oragnosulfur Chemistry*, John Wiley & Sons, **1996;** pp 1-250.

(25) *Organosulfur Chemistry*, Page, P. Academic Press: Great Britain, **1998**; Vol. 2, pp 1-309.

(26) Fernandez, I.; Khiar, N. *Chem. Rev.* **2003**, *103*, 3651.

(27) Carreno, M. C. *Chem. Rev.* **1995**, *95*, 1717.

(28) Campos-Martin, J. M.; Capel-Sanchez, M. C.; Fierro, J. L. G. *Green Chem.* **2004**, *6*, 557.

(29) Block, E. *Reactions of Organosulfur Compounds*; New York: Academic Press; Vol. 1978.

(30) Riley, D.; Stern, M.; Ebner, J. In *Activation of Dioxygen and Homogeneous Catalytic Oxidation*; Plenum Press: New York, NY, USA, 1993, p 31.

(31) Beller, M. B., C., *Transition Metals for Organic Synthesis*, 1998.

(32) Te, M.; Fairbridge, C.; Ring, Z. *Appl. Catal., A* **2001**, *219*, 267.

(33) Li, C.; Jiang, Z. X.; Gao, J. B.; Yang, Y. X.; Wang, S. J.; Tian, F. P.; Sun, F. X.; Sun, X. P.; Ying, P. L.; Han, C. R. *Chem.-Eur. J.* **2004**, *10*, 2277.

(34) Ricci, L. C.; Comasseto, V.; Andrade, L. H.; Capelari, M.; Cass, Q. B.; Porto, A. L. M. *Enzyme Microb. Technol.* **2005**, *36*, 937.

(35) Lee, H. B.; Ren, T. *Inorg. Chim. Acta* **2009**, *362*, 1467.

(36) Khavrutskii, I. V.; Maksimov, G. M.; Kholdeeva, O. A. *React. Kinet. Catal. Lett.* **1999**, *66*, 325.

(37) Clennan, E. L.; Zhou, W. H.; Chan, J. *J. Org. Chem.* **2002**, *67*, 9368.

(38) Choudary, B. M.; Reddy, C. R. V.; Prakash, B. V.; Kantam, M. L.; Sreedhar, B. *Chem. Commun.* **2003**, 754.

(39) Chen, L.; Yang, Y.; Jiang, D. L. *J. Am. Chem. Soc.* **2010**, *132*, 9138.

(40) Baciocchi, E.; Chiappe, C.; Del Giacco, T.; Fasciani, C.; Lanzalunga, O.; Lapi, A.; Melai, B. *Org. Lett.* **2009**, *11*, 1413.

(41) Legros, J.; Bolm, C. *Angew. Chem. Int. Ed.* **2003**, *42*, 5487.

(42) Boring, E.; Geletii, Y. V.; Hill, C. L. *J. Am. Chem. Soc.* **2001**, *123*, 1625.

(43) Rao, T. V.; Sain, B.; Kumar, K.; Murthy, P. S.; Rao, T. S. R. P.; Joshi, G. C. *Synth. Commun.* **1998**, *28*, 319.

(44) Wang, F.; Zhang, H.; Song, G. Q.; Lu, X. L. *Synth. Commun.* **1999**, *29*, 11.

(45) Song, G. Q.; Wang, F.; Zhang, H.; Lu, X. L.; Wang, C. *Synth. Commun.* **1998**, *28*, 2783.

(46) Bagherzadeh, M.; Amini, M. *Inorg. Chem. Commun.* **2009**, *12*, 21.

(47) Ji, H. B.; Wang, T. T.; Wang, L. F.; Fang, Y. X. *React. Kinet. Catal. Lett.* **2007**, *90*, 259.

(48) Bosch, E.; Kochi, J. K. *J. Org. Chem.* **1995**, *60*, 3172.

(49) Martin, S. E.; Rossi, L. I. *Tetrahedron Lett.* **2001**, *42*, 7147.

(50) Gao, J. B.; Lu, L.; Zhou, W. J.; Gao, G. H.; He, M. Y. *J. Porous Mater.* **2008**, *15*, 127.

(51) Kinen, C. O.; Rossi, L. I.; de Rossi, R. H. *Green Chem.* **2009**, *11*, 223.

(52) Okun, N. M.; Tarr, J. C.; Hilleshiem, D. A.; Zhang, L.; Hardcastle, K. I.; Hill, C. L. *J. Mol. Catal. A: Chem.* **2006**, *246*, 11.

(53) Santoni, G.; Licini, G.; Rehder, D. *Chem.-Eur. J.* **2003**, *9*, 4700.

(54) Nakajima, K.; Kojima, M.; Toriumi, K.; Saito, K.; Fujita, J. *Bull. Chem. Soc. Jpn.* **1989**, *62*, 760.

(55) Mba, M.; Pontini, M.; Lovat, S.; Zonta, C.; Bernardinelli, G.; Kundig, P. E.; Licini, G. *Inorg. Chem.* **2008**, *47*, 8616.

(56) Maurya, M. R.; Khan, A. A.; Azam, A.; Kumar, A.; Ranjan, S.; Mondal, N.; Pessoa, J. C. *Eur. J. Inorg. Chem.* **2009**, 5377.

(57) Lippold, I.; Becher, J.; Klemm, D.; Plass, W. *J. Mol. Catal. A: Chem.* **2009**, *299*, 12.

(58) Werncke, C. G.; Limberg, C.; Knispel, C.; Metzinger, R.; Braun, B. *Chem.-Eur. J.* **2011**, *17*, 2931.

(59) Guo, C. Y.; Wang, Y. Y.; Xu, K. Z.; Zhu, H. L.; Liu, P.; Shi, Q. Z.; Peng, S. M. *Polyhedron* **2008**, *27*, 3529.

(60) Lovat, S.; Mba, M.; Abbenhuis, H. C. L.; Vogt, D.; Zonta, C.; Licini, G. *Inorg. Chem.* **2009**, *48*, 4724.

(61) Kinen, C. O.; Rossi, L. I.; de Rossi, R. H. *J. Org. Chem.* **2009**, *74*, 7132.

(62) Rossi, L. I.; Martin, S. E. *Appl. Catal., A* **2003**, *250*, 271.

(63) Luo, Z.; Geletii, Y. V.; Hillesheim, D. A.; Wang, Y. M.; Hill, C. L. *ACS Catal.* **2011**, *1*, 1364.

(64) Jiang, Y. B.; Widger, L. R.; Kasper, G. D.; Siegler, M. A.; Goldberg, D. P. *J. Am. Chem. Soc.* **2010**, *132*, 12214.

(65) Badiei, Y. M.; Siegler, M. A.; Goldberg, D. P. *J. Am. Chem. Soc.* **2011**, *133*, 1274.

(66) McQuilken, A. C.; Jiang, Y. B.; Siegler, M. A.; Goldberg, D. P. *J. Am. Chem. Soc.* **2012**, *134*, 8758.

(67) Sallmann, M.; Siewert, I.; Fohlmeister, L.; Limberg, C.; Knispel, C. *Angew. Chem. Int. Ed.* **2012**, *51*, 2234.

(68) Andersen, K. K.; Chumpradit, S.; Mcintyre, D. J. *J. Org. Chem.* **1988**, *53*, 4667.

(69) Bianchini, C.; Mantovani, G.; Meli, A.; Migliacci, F.; Zanobini, F.; Laschi, F.; Sommazzi, A. *Eur. J. Inorg. Chem.* **2003**, 1620.

(70) Badiei, Y. M.; Jiang, Y. B.; Widger, L. R.; Siegler, M. A.; Goldberg, D. P. *Inorg. Chim. Acta* **2012**, *382*, 19.

(71) Britovsek, G. J. P.; England, J.; Spitzmesser, S. K.; White, A. J. P.; Williams, D. J. *Dalton Trans.* **2005**, 945.

(72) Krishnamurthy, D.; Sarjeant, A. N.; Goldberg, D. P.; Caneschi, A.; Totti, F.; Zakharov, L. N.; Rheingold, A. L. *Chem.-Eur. J.* **2005**, *11*, 7328.

(73) Small, B. L.; Brookhart, M.; Bennett, A. M. A. *J. Am. Chem. Soc.* **1998**, *120*, 4049.

(74) Nam, W. *Acc. Chem. Res.* **2007**, *40*, 522.

(75) Seo, M. S.; In, J. H.; Kim, S. O.; Oh, N. Y.; Hong, J.; Kim, J.; Que, L., Jr.; Nam, W. *Angew. Chem. Int. Ed.* **2004**, *43*, 2417.

(76) Que, L., Jr. *Acc. Chem. Res.* **2007**, *40*, 493.

(77) Weisser, J. T.; Nilges, M. J.; Sever, M. J.; Wilker, J. J. *Inorg. Chem.* **2006**, *45*, 7736.

(78) Guerra, K. P.; Delgado, R. *Polyhedron* **2008**, *27*, 2265.

(79) Taylor, S. W.; Chase, D. B.; Emptage, M. H.; Nelson, M. J.; Waite, J. H. *Inorg. Chem.* **1996**, *35*, 7572.

(80) Meyer, K.; Bill, E.; Mienert, B.; Weyhermuller, T.; Wieghardt, K. *J. Am. Chem. Soc.* **1999**, *121*, 4859.

(81) Comba, P.; Gahan, L. R.; Mereacre, V.; Hanson, G. R.; Powell, A. K.; Schenk, G.; Zajaczkowski-Fischer, M. *Inorg. Chem.* **2012**, *2012*, 12195.

3. 6. Appendix

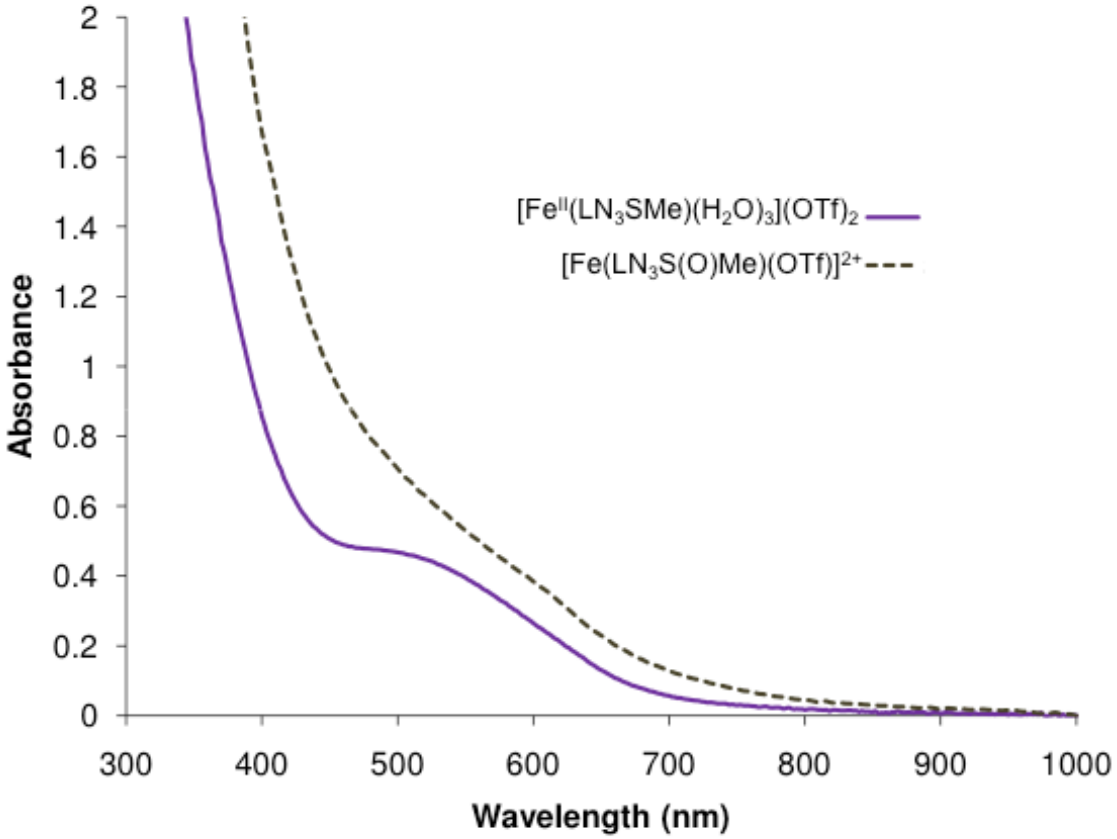

Figure 3. 19. Room temperature electronic absorption spectra of $[Fe^{II}(LN_3SMe)(H_2O)_3](OTf)_2$ and $[Fe(LN_3S(O)Me)(OTf)]^{2+}$.

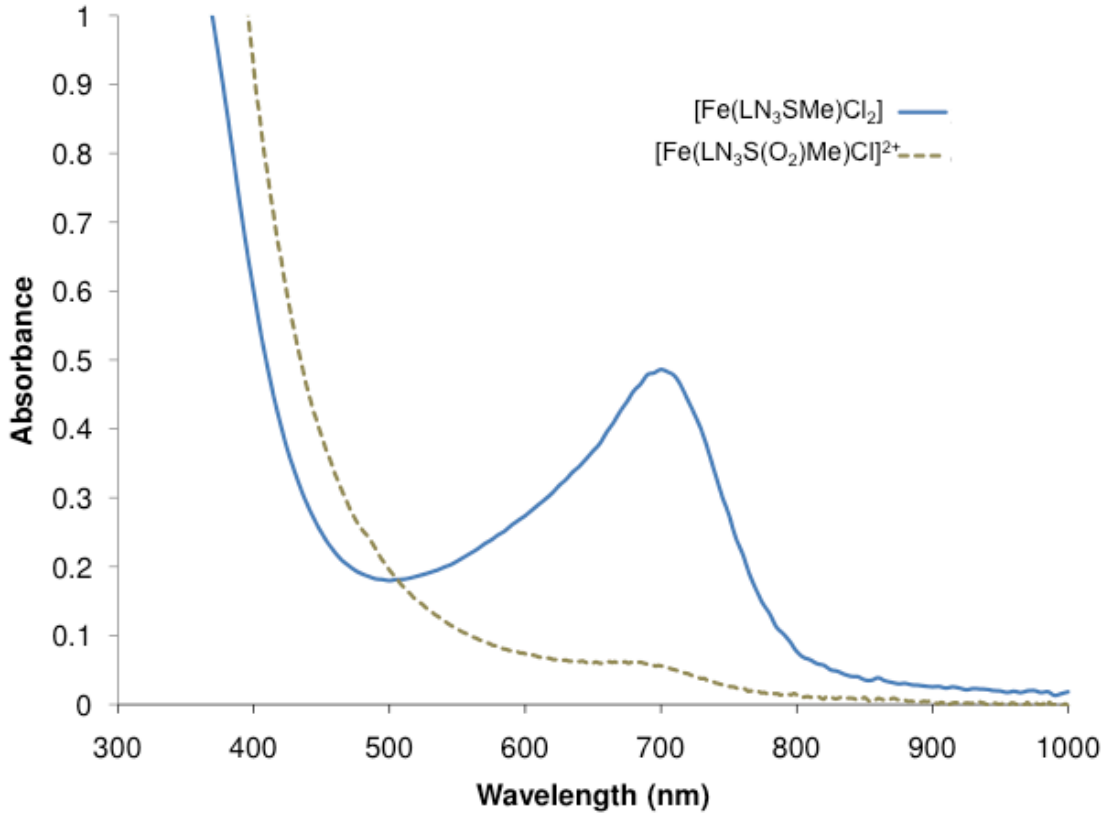

Figure 3. 20. Room temperature electronic absorption spectra of $Fe^{II}(LN_3SMe)Cl_2$ and $[Fe(LN_3S(O_2)Me)Cl]^{2+}$.

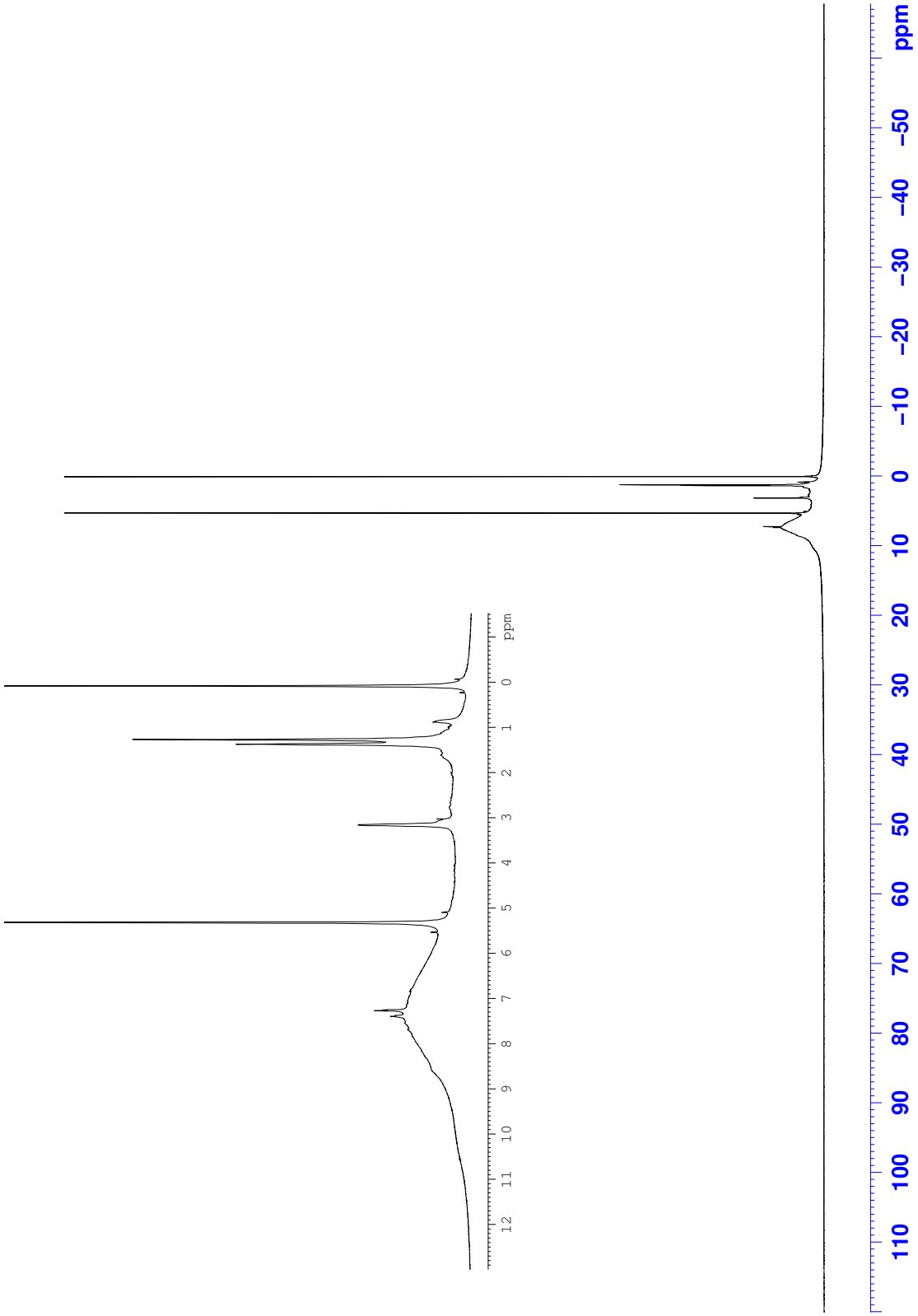

Figure 3. 21. ^{1}H-NMR spectrum of $[Fe(LN_3S(O)Me)(OTf)]^{2+}$ in CD_2Cl_2.

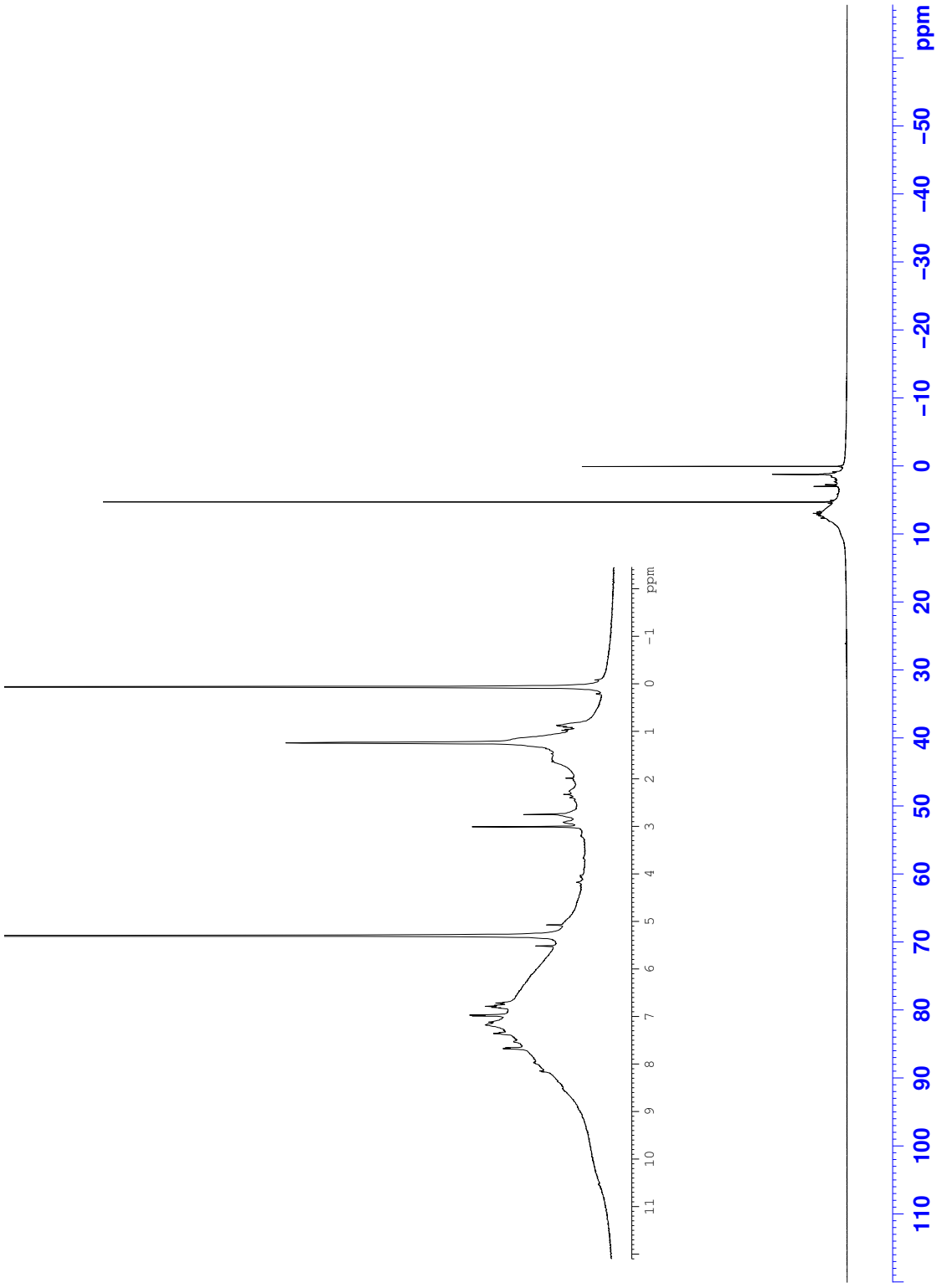

Figure 3. 22. ^{1}H-NMR spectrum of $[Fe(LN_3S(O_2)Me)Cl]^{2+}$ in CD_2Cl_2.

(a)

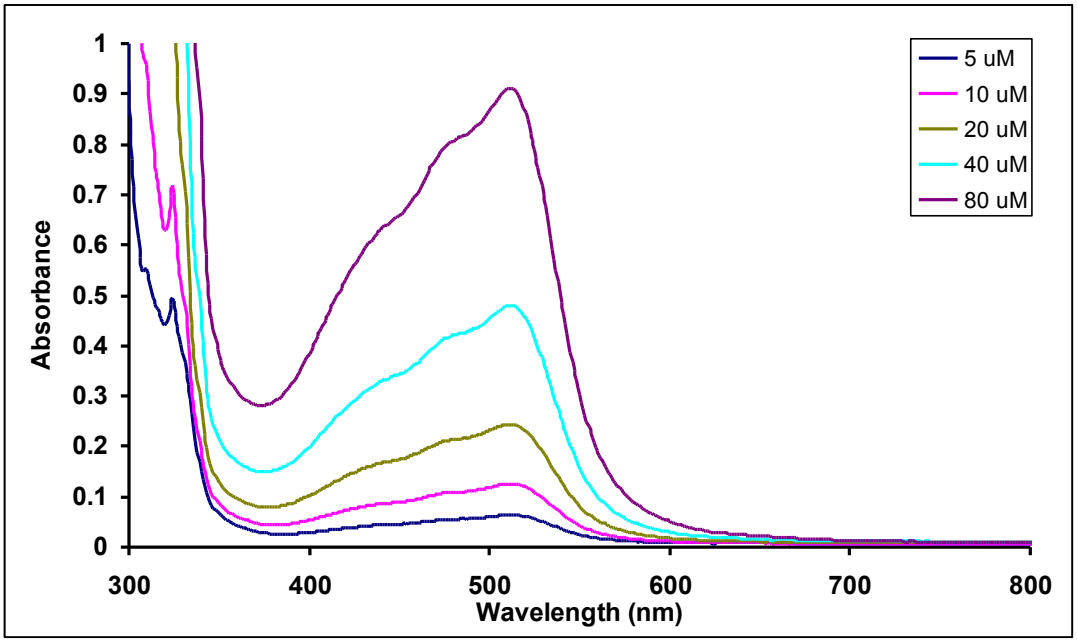

(b)

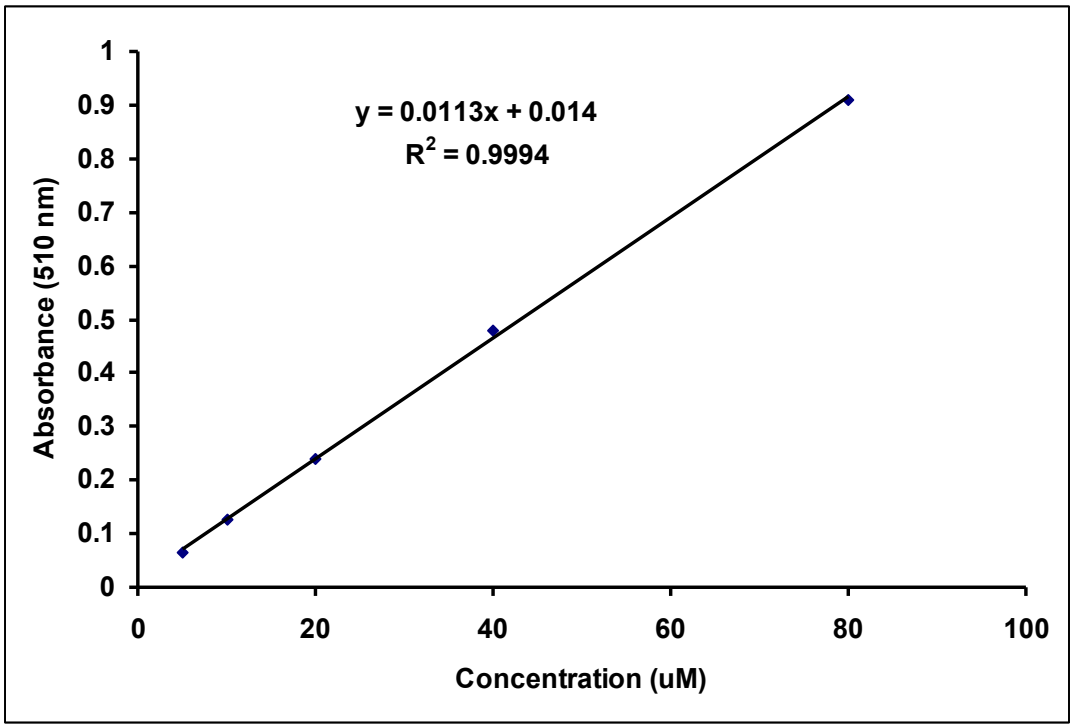

Figure 3. 23. a) Room temperature electronic absorption spectra of $Fe^{II}(OTf)_2$ (5 – 80 μM) + 1,10-phenanthroline (5.0 equiv) in CH_2Cl_2. b) Calibration curve of absorbance at 510 nm versus [$Fe^{II}(OTf)_2$] obtained from the data in (a).

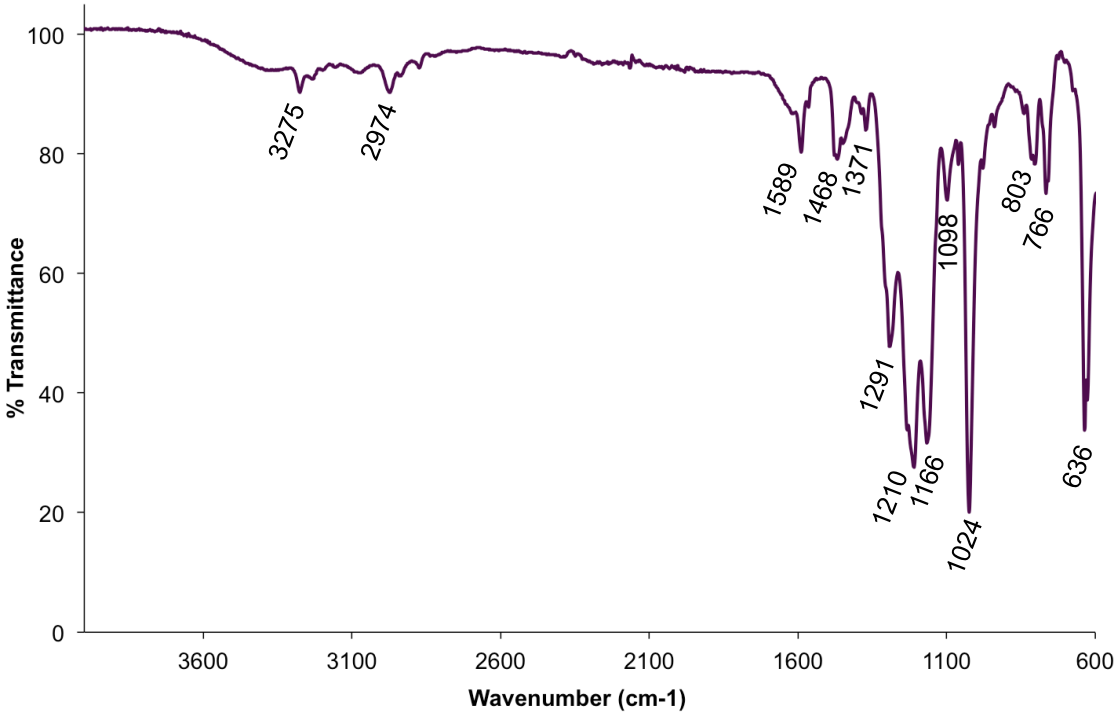

Figure 3. 24. ATR-IR spectrum of crystalline $[Fe^{II}(LN_3SMe)(H_2O)_3](OTf)_2$.

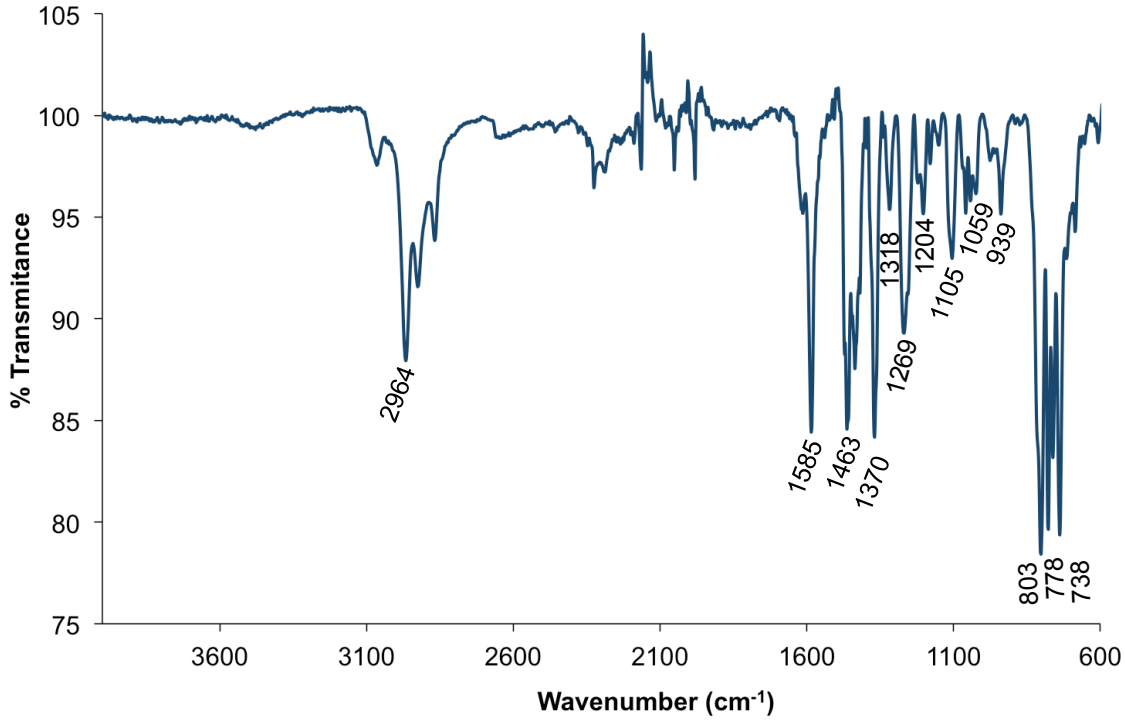

Figure 3. 25. ATR-IR spectrum of crystalline $Fe^{II}(LN_3SMe)Cl_2$.

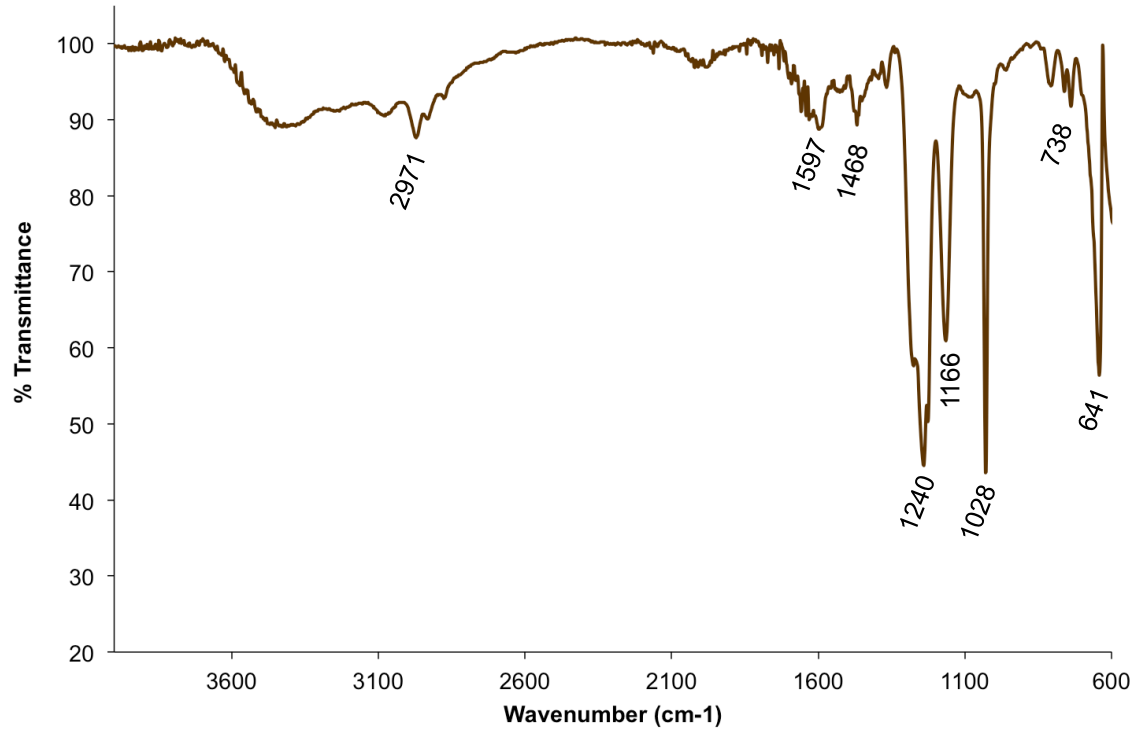

Figure 3. 26. ATR-IR spectrum of crude solid residue containing $[Fe(LN_3S(O)Me)(OTf)]^{2+}$.

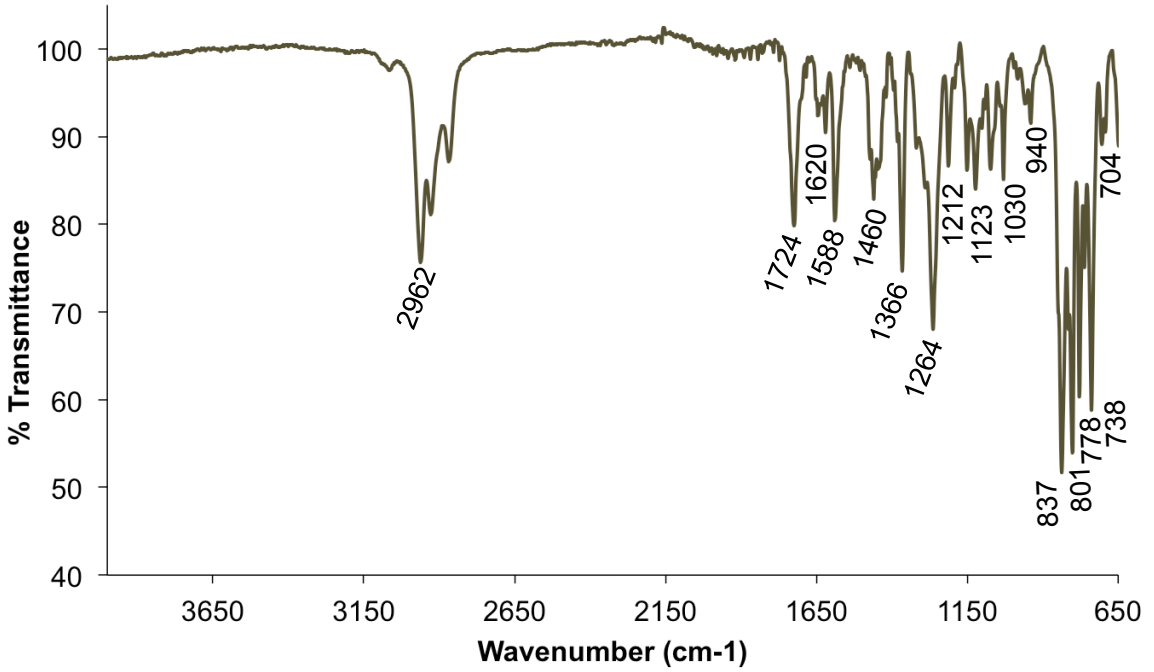

Figure 3. 27. ATR-IR spectrum of crude solid residue containing $[Fe(LN_3S(O_2)Me)Cl]^{2+}$.

Chapter 4. Dramatically Accelerated Selective Oxygen-Atom-Transfer by a Nonheme Iron(IV)-oxo Complex: Tuning of the Primary and Secondary Coordination Spheres

This work was co-written with the following authors and is published under the following citation:

Leland R. Widger, Casey G. Davies, Tzuhsiung Yang, Maxime A. Siegler, Oliver Troeppner, Guy N. L. Jameson, Ivana Ivanović-Burmazović, and David P. Goldberg

J. Am. Chem. Soc., revised version returned

4. 1. Introduction

Determining the influence of both first- and second-coordination sphere elements on nonheme iron-O_x species has been the focus of much recent effort.[1-3] Well characterized, high-valent $Fe^{IV}(O)$ complexes are known, but most of these systems contain structurally similar polyamino/pyridyl ligands.[1] Very few $Fe^{IV}(O)$ complexes have been reported with heteroatoms other than nitrogen in the first coordination sphere. The inclusion of sulfur donors is important for modeling key metal-sulfur interactions in nonheme enzymes, but is challenging because of the inherent problems associated with the facile oxidation of sulfur.[4-11] In earlier work we described an Fe^{II} complex with a thiolato donor built into the first coordination sphere, $N3PyS^-$ (**Figure 4. 1**), which undergoes facile O_2-mediated *S*-oxygenation.[5] This complex provided a functional model of the nonheme iron enzyme cysteine dioxygenase (CDO), but no $Fe^{IV}(O)$ intermediate was detected. In contrast, the $Fe^{IV}(O)$ complex of the all-nitrogen analog N4Py is well-characterized.[12,13]

Encouraged by our success in ligand design to incorporate an S-bound substrate mimic, we have made further efforts to control the reactivity of nonheme Fe centers by tuning both the first and second coordination spheres through ligand modification.[14] In

the present work, a new thioether, amide-appended ligand N3Py^{amide}SR (**Figure 4. 1**) has been prepared from the N3PyS scaffold. The thiolato donor was converted to a thioether group to discourage S oxidation in the first-coordination sphere and potentially allow for the stabilization of an Fe^{IV}(O)complex, similar to the proposed protective function of N-H---S hydrogen bonds in thiolate-ligated metalloenzymes.[15-17] In addition, a pendant amide group was installed in the second-coordination sphere to examine the influence of a single H-bond donor on the reactivity of Fe/O$_x$ intermediates, including Fe^{IV}(O) species. The influence of multiple H-bond donors on sterically encumbered metal-oxygen species has been examined, but there remains relatively little known about the influence of a single H-bond donor on sterically accessible MO$_x$ sites.[18-23]

The new ligand N3Py^{amide}SR was used to prepare the Fe^{II} complex [Fe^{II}(N3Py^{amide}SR)](BF$_4$)$_2$. The Fe^{II} complex reacts with PhIO to give a metastable ferryl complex at low temperature, [Fe^{IV}(O)(N3Py^{amide}SR)]$^{2+}$. This species is a rare example of a well characterized Fe^{IV}(O) complex with sulfur ligation.[24-26] Remarkably, [Fe^{IV}(O)(N3Py^{amide}SR)]$^{2+}$ shows no propensity for *intramolecular* sulfoxidation, but instead exhibits extremely rapid *intermolecular* O-atom transfer (OAT) to external thioether substrates. In addition, the rates of OAT are dramatically accelerated when compared to the same reaction exhibited by other Fe^{IV}(O) complexes, and this increase in reactivity is likely due, at least in part, to the presence of the designed NH---O=Fe hydrogen bond.

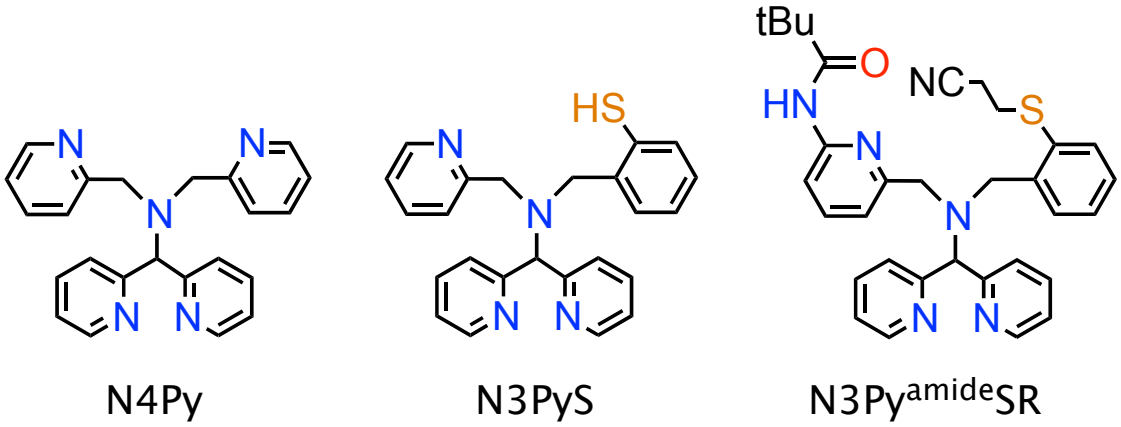

Figure 4. 1. Ligands discussed in the present study.

4. 2. Experimental

General Procedures

All reagents were purchased from commercial vendors, and used without further purification unless otherwise noted. Dichloromethane and diethyl ether were purified via a Pure-Solv Solvent Purification System from Innovative Technology, Inc. Methanol and acetonitrile were distilled over CaH_2. All solvents were degassed by repeated cycles of freeze-pump-thaw and stored in an N_2-filled drybox. Iron-57 metal (95.63%) was purchased from Cambridge Isotope Laboratories, Inc.; tetrafluoroboric acid (48% w/w) was purchased from Aldrich. Reactions requiring inert atmosphere were performed in an N2-filled drybox or with standard Schlenk techniques. Iodosobenzene,[27] 3-((2-(hydroxymethyl)phenyl)thio)propanenitrile,[28] di(2-pyridyl)methanamine,[29] and N-(6-(bromomethyl)-2-pyridyl)pivalamide[14] were prepared according to reported procedures.

Physical Methods

UV-visible spectra were recorded on a Varian Cary 50 spectrophotometer. NMR spectra were recorded on a Bruker Avance 400 MHz FT-NMR spectrometer at 25 °C. Elemental

analysis was performed by Atlantic Microlab Inc., Norcross, GA. Electron paramagnetic resonance (EPR) spectra were obtained on a Bruker EMX EPR spectrometer controlled with a Bruker ER 041 X G microwave bridge at 15 K. The EPR spectrometer was equipped with a continuous-flow liquid He cryostat and an ITC503 temperature controller made by Oxford Instruments, Inc. Mössbauer spectra were recorded on a spectrometer from SEE Co. (Science Engineering & Education Co., MN) equipped with a closed cycle refrigerator system from Janis Research Co. and SHI (Sumitomo Heavy Industries Ltd.). MS measurements were performed on a UHR-ToF Bruker Daltonik (Bremen, Germany) maXis, which was coupled to a Bruker cryospray unit, an ESI-ToF MS capable of resolution of at least 40.000 FWHM. Detection was in positive-ion mode and the source voltage was 4.5 kV. The flow rates were 200 μL/hour. The dry-gas temperature (N_2) was held at -40 °C and the spray-gas temperature was held at -35 °C. The machine was calibrated prior to every experiment via direct infusion of the Agilent ESI-ToF low concentration tuning mixture, which provided an m/z range of singly charged peaks up to 2700 Da in both ion modes.

Computational Methods

The structure of $[Fe^{II}(N3Py^{amide}SR)]^{2+}$ and $[Fe^{IV}(O)(N3Py^{amide}SR)]^{2+}$ in various spin states were investigated by computational methods: $[Fe^{II}(N3Py^{amide}SR)]^{2+}$ in the singlet and $[Fe^{IV}(O)(N3Py^{amide}SR)]^{2+}$ in the triplet and quintet spin states. Calculations utilized density functional theory (DFT) as implemented in the Gaussian-09 and Orca-2.6.35 program packages.[30,31] The geometry of $[Fe^{II}(N3Py^{amide}SR)]^{2+}$ was fully optimized (without constraints) with 6-31G(d) basis set[32-34] implemented on all atoms with DFT at the unrestricted hybrid density functional level B3LYP. Single point energies with zero-

point energy corrections were calculated using these optimized geometries. Calculations were preformed on the $Fe^{IV}(O)$ complex, $[Fe^{IV}(O)(N3Py^{amide}SR)]^{2+}$, in the Orca-3.0.0 program package. The geometry of $[Fe^{IV}(O)(N3Py^{amide}SR)]^{2+}$ was calculated for both the triplet and quintet spin states. The geometries were optimized (without constraints) with LANLDZ on the iron and 6-31G on the rest of the atoms, including the auxiliary basis sets def2-SVP/J and def2-SVP/K for the RIJCOSX approximation,[35,36] with DFT at the unrestricted hybrid density functional level B3LYP. Optimized structures of $[Fe^{IV}(O)(N3Py^{amide}SR)]^{2+}$ were employed as the starting point for single point calculations using LANLTZ+ on the iron and 6-311+G* on the rest of the atoms. Calculated Mössbauer parameters were obtained from the optimized geometries using the Orca-2.6.35 and Orca-3.0.0 program packages. These calculations used the B3LYP method in conjunction with the CP(PPP)[37] basis set on Fe and TZVP[38] basis set on all remaining atoms. The quadrupole splitting (ΔE_Q) was obtained directly, and the isomer shift (δ) was obtained from the calculated spin density at the iron nucleus ρ_0(Fe) using a previously determined calibration curve.[39]

Synthesis of Reported Compounds

Aldehyde (i)

An amount of 3-((2-(hydroxymethyl)phenyl)thio)propanenitrile (5.7 g, 29.5 mmol) was dissolved in CH_2Cl_2 (100 mL) and added to a stirring suspension of pyridinium chlorochromate (9.5 g, 44.1 mmol) in CH_2Cl_2 (300 mL). The mixture was stirred for several hours before being diluted with Et_2O, filtered through Celite and concentrated. The crude product was purified by column chromatography on silica (EtOAc/hexanes) to give the desired product as a white solid (5.1 g, 90%). ^{1}H-NMR ($CDCl_3$): δ 10.31 (s, 1

H), 7.82 (m, 1 H), 7.53 (m, 1 H), 7.41 (d, J = 8.1 Hz, 1H), 7.35 (t, J = 7.5 Hz, 1H), 3.18 (t, J = 7.2 Hz, 2 H) 2.67 (t, J = 7.2 Hz, 2 H); ^{13}C NMR ($CDCl_3$): δ 191.6, 138.5, 134.6, 132.8, 129.7, 127.3, 126.6, 117.9, 29.5, 18.0.

Secondary amine (ii)

Aldehyde (i) (2.73 g, 14.3 mmol) and di(2-pyridyl)methanamine (2.64 g, 14.3 mmol) were dissolved in a 1:1 mixture of $CHCl_3$/MeOH (80 mL). A small amount of 4 Å molecular sieves was added and the reaction was allowed to stir overnight under Ar atmosphere. An amount of $NaBH_4$ (540 mg, 14.3 mmol) was added in small portions and the reaction mixture was allowed to stir for 3 h before being filtered through Celite and concentrated. The resulting residue was dissolved in $CHCl_3$, washed with water, dried and concentrated. Purification by column chromatography on neutral alumina (EtOAc/hexanes) gave the desired product as a yellow solid (2.06 g, 40%). ^{1}H NMR ($CDCl_3$): δ 8.59 (m, 2 H) 7.65 (m, 2 H) 7.48 – 7.41 (m, 4 H) 7.29 – 7.25 (m, 2 H) 7.17 (m, 2 H) 5.15 (s, 1 H) 3.96 (s, 2 H) 3.10 (t, J=7.3 Hz, 2 H) 2.55 (t, J=7.3 Hz, 2 H); ^{13}C NMR ($CDCl_3$): δ 161.7, 149.5, 142.3, 136.9, 132.9, 132.4, 130.5, 128.4, 128.3, 122.7, 122.5, 118.4, 69.0, 50.35, 30.64, 18.41.

N3Py^{amide}SR

Secondary amine (ii) (1.23 g, 3.4 mmol) was dissolved in MeCN (100 mL) before Cs_2CO_3 (1.7 g, 5.2 mmol), N-(6-(bromomethyl)-2-pyridyl)pivalamide (925 mg, 3.4 mmol), and NaI (767 mg, 5.1 mmol) were added. The mixture was stirred under Ar atmosphere for 24 h before additional portions of Cs_2CO_3 (1.7 g, 5.2 mmol), and NaI (767 mg, 5.1 mmol) were added. After stirring for an additional 48 h, the crude reaction mixture was filtered through Celite and concentrated. The residue was dissolved in

$CHCl_3$, washed with H_2O, dried and concentrated. Purification by column chromatrography on neutral alumina (EtOAc/hexanes) gave the desired product as a pale yellow solid (1.1 g, 60%). ^{1}H NMR ($CDCl_3$): δ 8.56 (m, 2 H), 8.01 (m, 1 H), 7.97 (br, 1 H), 7.78 (dd, J = 7.6, 1.5 Hz, 1 H), 7.67 - 7.55 (m, 5 H), 7.30 (dd, J = 7.6, 1.3 Hz, 1 H), 7.24 – 7.12 (m, 5 H), 5.34 (s, 1 H), 4.03 (s, 2 H), 3.86 (s, 2 H), 3.00 (t, J = 7.3 Hz, 2 H) 2.48 (t, J = 7.3 Hz, 2 H) 1.32 (s, 9 H); ^{13}C NMR ($CDCl_3$): δ 177.2, 160.2, 158.2, 150.8, 149.4, 141.2, 138.7, 136.4, 132.5, 131.4, 129.9, 127.9, 127.7, 124.1, 122.4, 118.8, 118.2, 112.0, 72.5, 56.8, 53.9, 39.9, 36.9, 30.0, 27.7, 18.2.

$[Fe^{II}(N3Py^{amide}SR)](BF_4)_2 \bullet CH_3CN$

An amount of the free ligand ($N3Py^{amide}SR$) (1.0 g, 1.82 mmol) was dissolved in MeCN and $Fe(BF_4)_2 \bullet 6H_2O$ (615 mg, 1.82 mmol) was added. The yellow solution immediately changed to an orange color, and was then stirred for 2 h. The mixture was concentrated to a residue, which was dissolved in a minimum amount of MeCN. Vapor diffusion of Et_2O into this solution gave the desired complex as dark red crystals suitable for X-ray diffraction (1.25 g, 88%). UV-Vis (MeCN): 350 nm (4700 $M^{-1}cm^{-1}$), 450 nm (6000 $M^{-1}cm^{-1}$); ^{1}H NMR (CD_3CN, 25 °C): δ 68.3, 45.0, 36.6, 29.8, 29.0, 27.6, 26.9, 23.1, 16.9, 15.6, 11.7, 10.4, 9,6, 7.3, 7.0, 6.6, 6.3, 4.3, 3.3, 1.0, -13.5; Anal. Calc. for $[Fe^{II}(N3Py^{amide}SR)](BF_4)_2]$ ($C_{32}H_{34}B_2F_8FeN_6OS$): C, 49.26; H, 4.39; N, 10.77. Found: C, 48.59; H, 4.37; N, 10.63. m/z (ESI-ToF, -40 °C) = 303.0917 $[M - 2BF_4]^{2+}$.

Generation of $[Fe^{IV}(O)(N3Py^{amide}SR)]^{2+}$ for characterization by UV-vis spectroscopy.

An amount of $Fe^{II}(N3Py^{amide}SR)](BF_4)_2$ (0.8 mg, 1.0 μmol) was dissolved in MeCN (5.0 mL), and cooled to -40 °C in a flask equipped with a submersible UV-vis probe. A stock solution of PhIO in MeOH was freshly prepared, and then 0.1 mL of this PhIO solution

(0.12 μmol, 1.2 equiv) was added. The reaction mixture changed in color from orange to yellow over 30 min. Monitoring the reaction by UV-vis spectroscopy revealed the disappearance of the characteristic peaks for $[Fe^{II}(N3Py^{amide}SR)](BF_4)_2$ (350, 450 nm), and the appearance of a new peak at 750 nm, corresponding to $[Fe^{IV}(O)(N3Py^{amide}SR)]^{2+}$.

$[Fe^{II}(Cl)(N3Py^{amide}SR)](BF_4)$

An amount of the ligand (iii) (12.3 mg, 0.016 mmol) was dissolved in 2 mL of MeCN and $FeCl_2$ (2.2 mg, 0.017 mmol) was added. The mixture was allowed to stir for 1 h, and $NaBF_4$ (1.9 mg, 0.017 mmol) was added. After stirring for an additional 2 h the solution was filtered through Celite, and vapor diffusion of Et_2O gave the desired product as yellow crystals suitable for X-ray diffraction (8.3 mg, 67%). ^{1}H NMR (CD_3CN): δ 63.3, 56.4, 41.4, 35.3, 28.9, 26.1, 25.2, 16.4, 14.2, 12.5, 12.0, 8.2, 7.9, 7.7, 7.3, 6.0, 3.6, 3.4, 1.2, 0.9, -1.6; UV-vis: λ_{max} = 358 nm, ε = 5000 M^{-1} cm^{-1}; Anal. Calc. for $[Fe^{II}(Cl)(N3Py^{amide}SR)](BF_4)$ ($C_{32}H_{34}B_2ClF_8FeN_6OS$): C, 47.12; H, 4.20; N, 10.30. Found: C, 47.61; H, 4.30; N, 10.04. *m/z* (LDI-MS) = 641.0 $[M - BF_4]+$.

$[Fe^{II}(N3Py^{amide}S(O)R)](BF_4)_2 \bullet 0.5\ CH_3CN$

An amount of $Fe^{II}(N3Py^{amide}SR)](BF_4)_2$ (9 mg, 0.012 mmol) was dissolved in MeCN (0.5 mL) and a solution of 75% m-CPBA (10.6 mg, 0.062 mmol) in MeCN (0.5 mL) was added. After stirring for 2 h, the green solution was concentrated and the residue was dissolved in CH_2Cl_2 and filtered through Celite. Successive vapor diffusion of Et_2O afforded X-ray quality crystals (4.7 mg, 49% yield). ^{1}H NMR (CD_3CN): δ 69.1, 67.0, 63.7, 60.7, 60.0, 58.9, 57.3, 56.8, 56.3, 55.9, 53.2, 46.0, 41.3, 33.6, 32.8, 31.8, 25.5, 22.3, 19.4, 18.7, 12.5, 10.0, 9.4, 9.0, 8.3, 8.1, 7.8, 7.7, 7.0, 6.5, 5.9, 5.4, 4.9, 4.0, 3.4, 3.0, 2.9, 2.5, 1.1; UV-vis: λ_{max} = 700 nm, ε = 1000 M^{-1} cm^{-1}; Anal. Calc. for

$[Fe^{II}(N3Py^{amide}S(O)R)](BF_4)_2$ •0.5 CH_3CN•0.8 CH_2Cl_2] ($C_{33.8}H_{37.1}B_2C_{11.6}F_8FeN_{6.5}O_2S$): C, 45.89; H, 4.23; N, 10.29. Found: C, 46.02; H, 4.14; N, 9.96. *m/z* (LDI-MS) = 621.5 [M – H – $2BF_4$]$^+$. Note: Unresolved residual electron density, presumed to be disordered CH_2Cl_2, was found in the crystal structure of $[Fe^{II}(N3Py^{amide}S(O)R)](BF_4)_2$ (see the X-ray crystallography section for further details). The elemental analysis was consistent with this assignment, in which a small amount of CH_2Cl_2 was added to obtain a good fit.

Mössbauer Spectroscopy

$^{57}Fe(BF_4)_2$

An amount of $^{57}Fe^0$ metal (50 mg, 0.9 mmol) was combined with aqueous HBF_4 (48% w/w, 2.0 equiv, 0.23 mL). The suspension was diluted with H_2O (0.27 mL) and heated to boiling on a sand bath. The solid slowly dissolved with heating, and care was taken to minimize solvent loss due to evaporation on the small scale. The pale blue solution was diluted to a final volume of 5.0 mL with MeCN. The final concentration of $^{57}Fe(BF_4)_2$, based on measured $^{57}Fe^0$, was 0.18 *M*.

$[^{57}Fe^{II}(N3Py^{amide}SR)](BF_4)_2$

The $N3Py^{amide}SR$ ligand (**iii**) (5.0 mg, 0.01 mmol) was dissolved in a small amount of MeCN and freshly prepared $^{57}Fe(BF_4)_2$ (1.0 equiv, 56 μL of a 0.18 *M* stock solution) was added. The mixture immediately turned dark orange and the resulting solution was diluted with MeCN to a final volume of 2.5 mL, giving a 4.0 mM solution of the starting $[^{57}Fe^{II}(N3Py^{amide}SR)](BF_4)_2$ complex.

[$^{57}Fe^{IV}$(O)(N3Py^{amide}SR)]$(BF_4)_2$

A solution of [$^{57}Fe^{II}$(N3Py^{amide}SR)]$(BF_4)_2$ (0.4 mL, 4 mM) was loaded directly into a Teflon Mössbauer sample cup cooled to -40 °C in an MeCN/dry ice bath using a custom brass sample holder. A stock solution of PhIO was prepared by dissolving PhIO (2.0 mg, 9 μmol) in MeOH (0.38 mL). The PhIO solution (0.1 mL, 1.0 equiv) was injected directly into the sample cup and mixed well by bubbling with Ar. After standing at -40 °C for 45 min, the sample was frozen in liquid N_2 using the custom holder, and stored at 77 K until measurements were preformed.

Kinetic Studies

General Methods

Kinetic measurements for the reactions of [Fe^{IV}(O)(N3Py^{amide}SR)]$^{2+}$ with substrates were performed on a Varian Cary 50 spectrophotometer (kinetics mode) in CH_3CN/CH_3OH at -40 °C. Reaction rates and pseudo-first-order rate constants (k_{obs}) were measured by the growth of the absorption band at 450 nm corresponding to the return of [Fe^{II}(N3Py^{amide}SR)]$^{2+}$. Monitoring the disappearance of the 750 nm band corresponding to [Fe^{IV}(O)(N3Py^{amide}SR)]$^{2+}$ gave the same results. All reactions were performed under pseudo-first-order conditions where the concentration of substrate was at least 20-fold greater than the concentration of iron complex.

Reaction of [Fe^{IV}(O)(N3Py^{amide}SR)]$^{2+}$ with PhSMe at -40 °C

A solution of [Fe^{II}(N3Py^{amide}SR)]$(BF_4)_2$ (5.0 mL, 0.54 mM) in CH_3CN was cooled to -40 °C in a flask equipped to accept a submersible UV-vis probe (2 mm path length). A solution of PhIO (0.9 mg, 4.1 μmol) was then added in 0.25 mL of MeOH, and the

reaction mixture was stirred at -40 °C for 30 min or until the full formation of $[Fe^{IV}(O)(N3Py^{amide}SR)]^{2+}$ was observed by UV-vis spectroscopy. A solution of PhSMe in CH_3CN (1.0 $x10^{-2}$ – 5.0 $x10^{-2}$ M, 0.1 mL total volume) was added, and the change in absorbance at 450 nm was monitored for ~500 s (Appendix A, **Figure 4. 15**). The UV-vis spectral changes for a representative reaction are shown in **Figure 4. 5**, and reveal two kinetic phases. The first phase shows good isosbestic behavior for the conversion of $[Fe^{IV}(O)(N3Py^{amide}SR)]^{2+}$ to $[Fe^{II}(N3Py^{amide}SR)](BF_4)_2$, followed by a second phase in which the original isosbestic point at 322 nm is lost. The first kinetic phase was assigned to the reaction $[Fe^{IV}(O)(N3Py^{amide}SR)]^{2+}$ + PhSMe → $[Fe^{II}(N3Py^{amide}SR)]^{2+}$ + PhS(O)Me, and typically corresponded to 60 – 70% reaction completion. These data were easily modeled with a single exponential function as described below. The origin of the second, slower kinetic phase was not determined. The plot of ΔA (450 nm) versus time for the first phase was fit to the following single exponential function:

$$\boldsymbol{A_t = (\Delta A)e^{-k_{obs}t} + A_f} \qquad \text{(equation 4. 1)}$$

where A_t = absorbance at time t; ΔA = total change in absorbance from $t = 0$ to t = final; A_f = absorbance at final time t; and k_{obs} = pseudo-first-order rate constant.

The k_{obs} values obtained from the fits to equation 4. 1, which corresponded to 5 half lives *of that initial reaction*, were plotted versus [PhSMe] (**Figure 4. 6**), and found to give a linear relationship. The slope yields the second-order rate constant k = 4.3 M^{-1} s^{-1} for the reaction between $[Fe^{IV}(O)(N3Py^{amide}SR)]^{2+}$ and PhSMe.

Reaction of $[Fe^{IV}(O)(N3Py^{amide}SR)]^{2+}$ with 2,4-di-tert-butyl phenol at -40 °C

A solution of $[Fe^{II}(N3Py^{amide}SR)](BF_4)_2$ in MeCN (4.0 mL, 0.5 mM) was cooled to -40 °C in a flask equipped to accept a submersible UV-vis probe. PhIO (0.54 mg, 2.5 μmol) was added as a solution in 0.1 mL of MeOH and allowed to stir for 30 min until full formation of $[Fe^{IV}(O)(N3Py^{amide}SR)]^{2+}$ was observed by UV-vis spectroscopy. A solution of 2,4-di-tert-butyl phenol (1.0 mmol, 500 equiv) in CH_2Cl_2 (700 μL) was added and the growth of the absorbance at 450 nm was monitored for 80 min (**Figure 4. 9**). Total recovery of $[Fe^{II}(N3Py^{amide}SR)]^{2+}$ was 98% as measured by the absorbance of the final peak at 650 nm (e = 6000 M^{-1} cm^{-1}). The growth of the absorbance at 450 nm was fit using a single exponential function to give a $k_{obs} = 4.0x10^{-3}$ s^{-1} (**Figure 4. 9**).

Yield of PhS(O)Me in the reaction of 2 + PhSMe in CH_3CN/CH_3OH at -40 °C

An amount of $[Fe^{IV}(O)(N3Py^{amide}SR)](BF_4)_2$ (1.3 mg, 1.8 μmol) was dissolved in CD_3CN (0.25 mL), and cooled to -40 °C in an acetonitrile/dry ice bath. The oxidant, PhIO (0.47 mg, 2.1 μmol), was added as a solution in MeOD (50 μL), and allowed to stand at -40 °C for 45 min. The solution lightened in color from orange to yellow. Thioanisole (PhSMe, 10.0 equiv, 2.09 μL) was then added as a solution in CD_3CN (50 μL), and the reaction mixture was allowed to stand at -40 °C for 30 min before warming to room temperature. Peaks in the ^1H NMR spectrum corresponding to PhSMe and PhS(O)Me were integrated, showing PhS(O)Me was formed in 80% yield (versus iron).

Catalytic oxidations

An amount of $[Fe^{IV}(O)(N3Py^{amide}SR)](BF_4)_2$ (1.0 mg, 1.4 μmol) was dissolved in 0.3 mL CD_3CN, and placed in an NMR tube. Thioanisole (100 equiv, 16 μL) was added as a solution in CD_3CN (100 μL), and then the oxidant PhIO (50 equiv, 15.1 mg) was added

as a solution in MeOD (250 μL). Immediately upon addition of the oxidant, there is a transient color change to yellow, followed by a darkening toward orange. After 30 min, the solution is pale yellow in color, likely due to catalyst decomposition. The reaction mixture was allowed to stand for a total of 2 h. Comparison of the ^{1}H NMR peaks for PhSMe and PhS(O)Me reveal PhS(O)Me was produced in 85% yield as compared to oxidant, which corresponds to ~43 turnovers (**Figure 4. 10**).

4. 3. Results and Discussion

Synthesis and Characterization

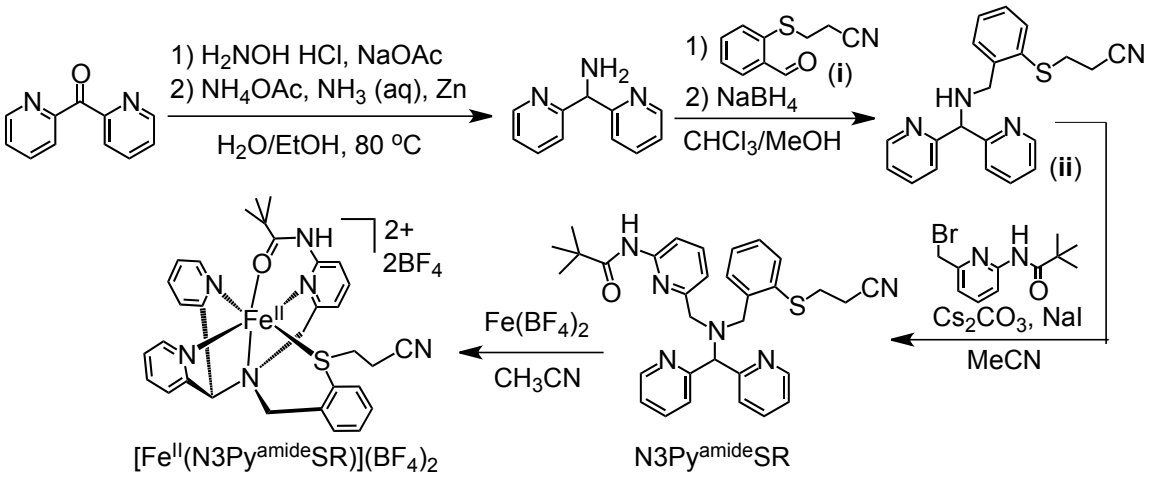

Scheme 4. 1. Synthesis of $N3Py^{amide}SR$ and $[Fe^{II}(N3Py^{amide}SR)](BF_4)_2$.

Reaction of $N3Py^{amide}SR$ with $Fe^{II}(BF_4)_2$ in MeCN led to the isolation of crystalline $[Fe^{II}(N3Py^{amide}SR)](BF_4)_2$ (88%). The X-ray structure of $[Fe^{II}(N3Py^{amide}SR)](BF_4)_2$ at 110 K (**Figure 4. 2**) reveals an octahedral Fe^{II} complex with the amide group coordinated in the open site. Bond distances for $[Fe^{II}(N3Py^{amide}SR)](BF_4)_2$ (**Table 4. 2**) are consistent with low-spin (ls) Fe^{II} (S = 0), and Mössbauer spectroscopy at 5 K reveals a sharp, well-resolved doublet (δ = 0.47 mm s^{-1}; ΔE_Q =0.77 mm s^{-1}, **Figure 4. 3**) typical for ls-Fe^{II}. However, the room temperature ^{1}H

NMR spectrum for $[Fe^{II}(N3Py^{amide}SR)](BF_4)_2$ reveals paramagnetically shifted peaks, and further work is needed to definitively assign the spin state at higher temperatures for this complex.

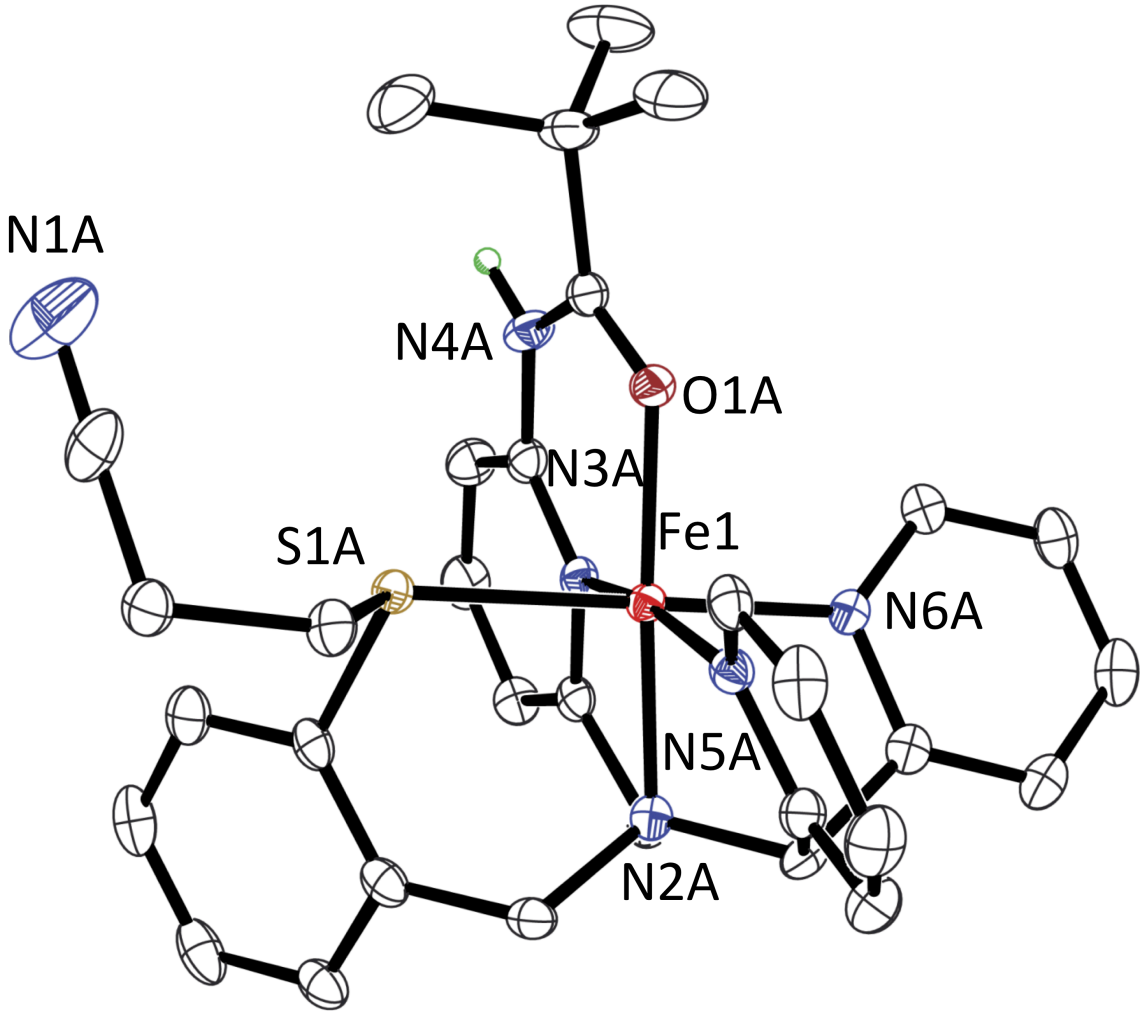

Figure 4. 2. Displacement ellipsoid plots (50% probability level) of the dication $[Fe^{II}(N3Py^{amide}SR)]^{2+}$. H-atoms omitted for clarity, except for the amide N-H.

Reaction of $[Fe^{II}(N3Py^{amide}SR)](BF_4)_2$ with PhIO (1.2 equiv, dissolved in minimal MeOH) in MeCN at -40 °C leads to the rapid decay of the peaks for $[Fe^{II}(N3Py^{amide}SR)](BF_4)_2$ at 350 and 450 nm (ε = 5 x 10^3, 6 x 10^3 M^{-1} cm^{-1} respectively), and the isosbestic production of a new peak at 750 nm (ε = 400 M^{-1} cm^{-1}) (**Figure 4. 3**).

This broad, weak band in the near-IR region is characteristic of non-heme $Fe^{IV}(O)$ complexes.[1] The new species with λ_{max} = 750 nm is stable at –40 °C for hours, but immediately decays upon warming above –30 °C. This behavior contrasts that of $[Fe^{IV}(O)(N4Py)]^{2+}$, which is stable at room temperature ($t_{1/2}$ = 60 h).[12] Analysis of the reaction mixture by low-temperature, high-resolution ESI-MS (+ mode) (–40 °C) shows a parent ion at *m/z* 311.0914 (**Figure 4. 14**) and isotope pattern corresponding to the dicationic $[Fe(O)(N3Py^{amide}SR)]^{2+}$ (**Figure 4. 3**). The 750 nm species is EPR silent (X-band, 15 K), consistent with an integer- spin $Fe^{IV}(O)$ complex. Confirmation of the nature of the new species from $[Fe^{II}(N3Py^{amide}SR)](BF_4)_2$ + PhIO was obtained through Mössbauer spectroscopy, which shows a well-resolved doublet (δ = 0.04 mm s^{-1}, ΔE_Q = 0.80 mm s^{-1}, (**Figure 4. 3**). These parameters, especially the low isomer shift, are definitive for an $Fe^{IV}(O)$ complex.[1,2] The lack of peaks for $[Fe^{II}(N3Py^{amide}SR)](BF_4)_2$ indicates that the Fe^{II} complex has been quantitatively converted to the $Fe^{IV}(O)$ complex $[Fe^{IV}(O)(N3Py^{amide}SR)]^{2+}$.

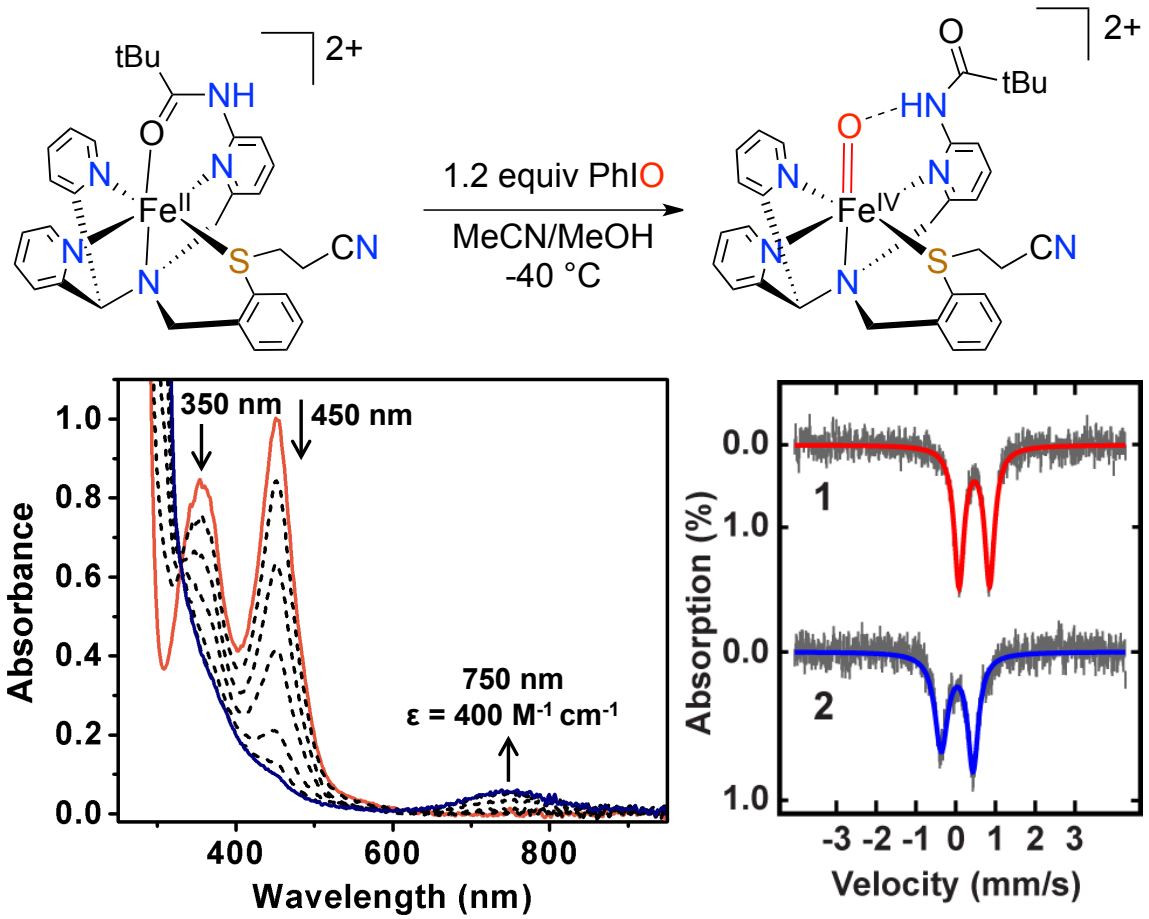

Figure 4. 3. Synthesis of $[Fe^{IV}(O)(N3Py^{amide}SR)]^{2+}$ (top); UV-vis spectral changes for the conversion of $[Fe^{II}(N3Py^{amide}SR)](BF_4)_2$ to $[Fe^{IV}(O)(N3Py^{amide}SR)]^{2+}$ (bottom, left); Mössbauer spectra (47 mT) for $[Fe^{II}(N3Py^{amide}SR)](BF_4)_2$ and $[Fe^{IV}(O)(N3Py^{amide}SR)]^{2+}$ (bottom, right) at 5 K in CH_3CN.

A structural analog of metastable $[Fe^{IV}(O)(N3Py^{amide}SR)]^{2+}$ was synthesized from $FeCl_2$, $N3Py^{amide}SR$, and anion metathesis with $NaBF_4$, affording orange, crystalline $[Fe^{II}(Cl)(N3Py^{amide}SR)](BF_4)$. The X-ray structure of $[Fe^{II}(Cl)(N3Py^{amide}SR)](BF_4)$ (**Figure 4. 4**) shows that the carbonyl group has been displaced by Cl^-. Importantly, the free amide N-H group is clearly oriented for hydrogen bonding to the terminal Cl^- (Cl---H-N = 2.497 Å; Cl-H-N = 167.53°).[40,41] The structure of $[Fe^{II}(Cl)(N3Py^{amide}SR)](BF_4)$

fully supports the proposed structure for $[Fe^{IV}(O)(N3Py^{amide}SR)]^{2+}$, in which the pendant N-H amide forms a stable, 6-membered H-bond ring with the terminal oxo ligand.

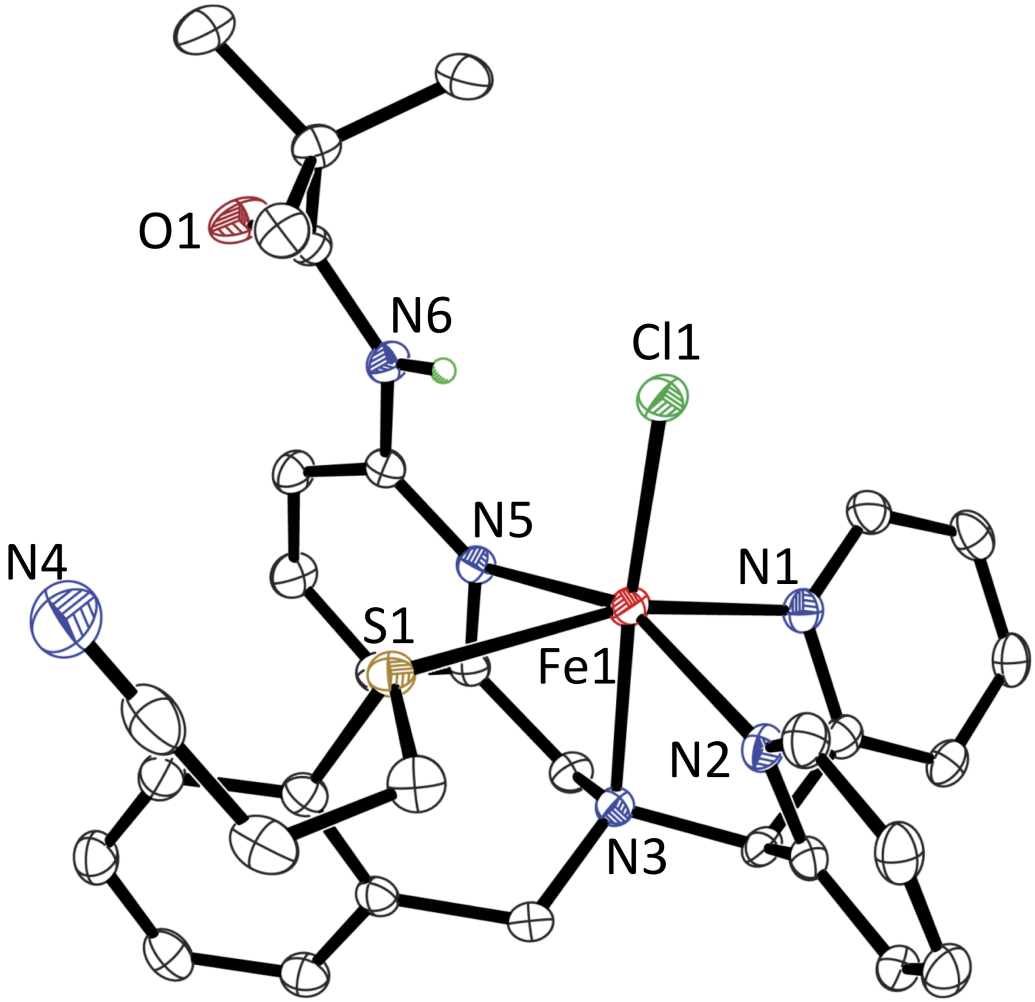

Figure 4. 4. Displacement ellipsoid plots (50% probability level) of the cation of $[Fe^{II}(Cl)(N3Py^{amide}SR)](BF_4)$. H-atoms omitted for clarity, except for the amide N-H.

Reactivity

We have previously shown that the thiolato donor in $[Fe^{II}(N3PyS)]^{+}$ is S-oxygenated by O_2, as is the coordinated S-Cys donor in CDO.[5,42,43] Thus it is notable that protection of the thiolato donor to a thioether allows for a metastable $Fe^{IV}(O)$ complex to be trapped at low temperature, exhibiting no *intramolecular* S-oxygenation. However,

when $[Fe^{IV}(O)(N3Py^{amide}SR)]^{2+}$ is exposed to *external* thioether substrates, rapid OAT occurs. Reaction of $[Fe^{IV}(O)(N3Py^{amide}SR)]^{2+}$ with PhSMe at -40 °C leads to the fast decay of the 750 nm band and isosbestic return of the starting Fe^{II} complex $[Fe^{II}(N3Py^{amide}SR)]^{2+}$ (82% recovery in 30 min) (**Figure 4. 5**). Analysis by ^{1}H NMR showed PhS(O)Me was produced in 80% yield (Equation 4. 2).

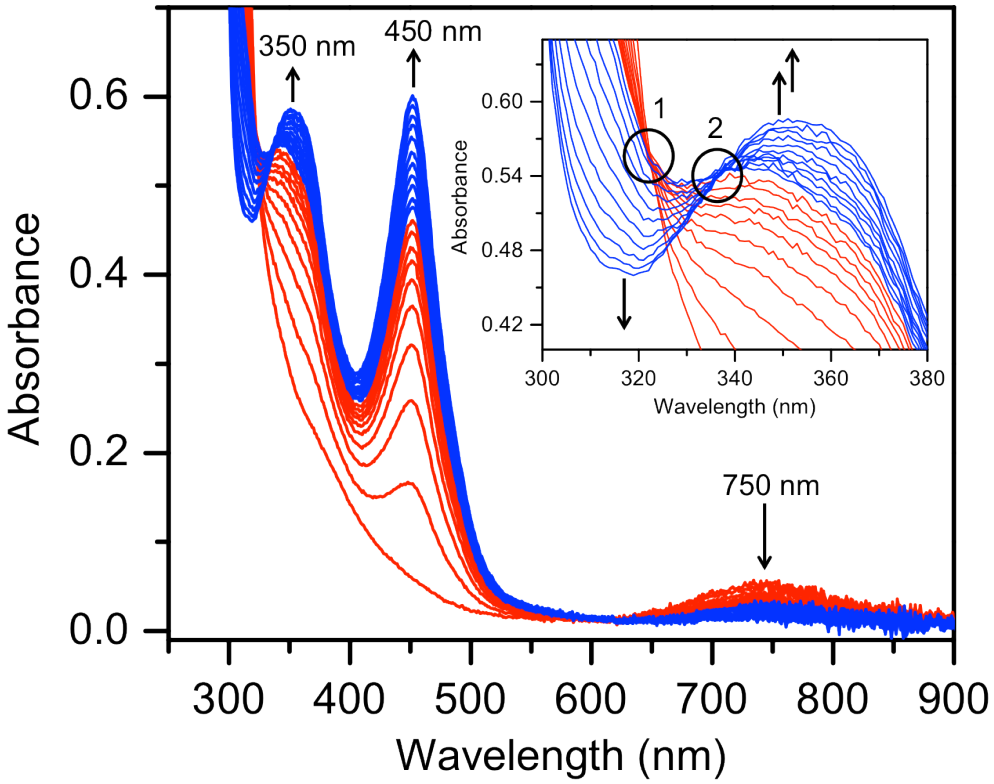

Figure 4. 5. UV-vis spectral changes over 30 min for the reaction of $[Fe^{IV}(O)(N3Py^{amide}SR)]^{2+}$ (0.39 mM) with PhSMe (21.6 mM) in CH_3CN/CH_3OH at -40 °C. Red spectra = first kinetic phase, blue spectra = second kinetic phase. Inset: spectral changes for 300 - 380 nm showing the two isosbestic points (circles) for the first kinetic phase (322 nm), and the second kinetic phase (337 nm).

$$[Fe^{IV}(O)(N3Py^{amide}SR)]^{2+} + PhSMe \longrightarrow [Fe^{II}(N3Py^{amide}SR)]^{2+} + PhS(O)Me$$
(82%) (80%)

Equation 4. 2

The kinetics of intermolecular sulfoxidation were monitored by UV-vis under pseudo-first-order conditions, and could be well fit to a single exponential model (**Figure 4. 15**). A linear dependence was found for k_{obs} versus [PhSMe], yielding a second-order rate constant of k = 4.3 M^{-1} s^{-1} (**Figure 4. 6**). The rate constants for other nonheme $Fe^{IV}(O)$ complexes are given in **Table 4. 1**. The $[Fe^{IV}(O)(N3Py^{amide}SR)]^{2+}$ complex shows dramatically enhanced OAT reactivity, exhibiting a nearly 70-fold rate enhancement at –40 °C vs the parent $[Fe^{IV}(O)(N4Py)]^{2+}$ at 0 °C.[44] The reaction between $[Fe^{IV}(O)(N4Py)]^{2+}$ and PhSMe at –40 °C was run as a direct comparison, but we observed no spectroscopic change under these conditions over 40 min. The only example in **Table 4. 1** that also exhibits significantly increased reactivity is found in row 3, in which the strong proton donor $HClO_4$ is postulated to activate the $Fe^{IV}(O)$ complex through monoprotonation of the oxo ligand ($[(N4Py)Fe^{IV}(OH)]^{3+}$).[45] We suggest that the unique amide H-bond donor in $[Fe^{IV}(O)(N3Py^{amide}SR)]^{2+}$ may activate the terminal oxo ligand in an analogous fashion, increasing the electrophilicity of the oxo ligand.

Table 4. 1. Second order rate constants for OAT of various Fe(IV)-oxo complexes to thioanisole

Complex	k(M^{-1} s^{-1})	T(°C)	ref
$[Fe^{IV}(O)(N3Py^{amide}SR)]^{2+}$	4.3	–40	This work
$[Fe^{IV}(O)(N4Py)]^{2+}$ (+ $HClO_4$)	8.7 x10^{-1} (1.5 x10^{3})	25	45
$[(Fe^{IV}(O)(N4Py)]^{2+}$	6.5 x10^{-2}	0	44
$[Fe^{IV}(O)(TMC)]^{2+}$	2.9 x10^{-2}	35	45
$[Fe^{IV}(O)(TPA)]^{2+}$	4.4 x10^{-1}	–45	44
$[Fe^{IV}(O)(TBC)]^{2+}$	3.5 x10^{-1}	–10	46

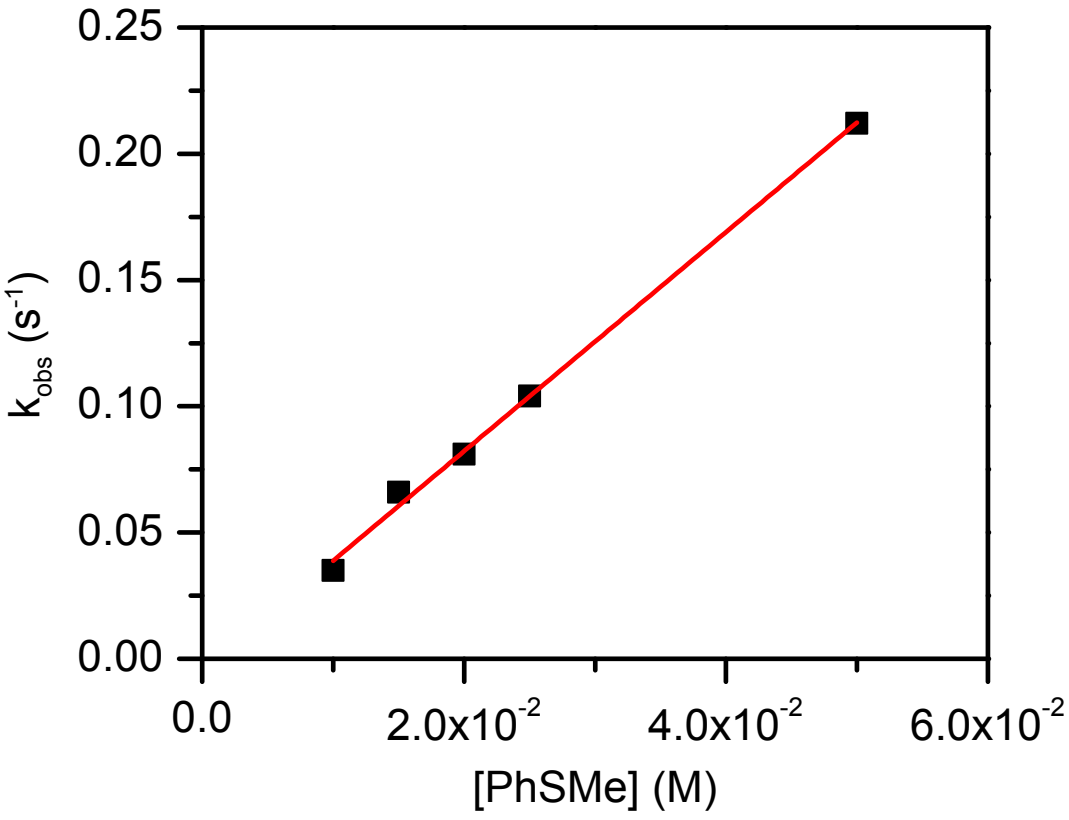

Figure 4. 6. Plot of k_{obs} vs [PhSMe] (squares) and best fit (red line).

The choice of oxidant for $[Fe^{II}(N3Py^{amide}SR)](BF_4)_2$ is critical to the reaction pathway. If PhIO is replaced with the more powerful oxidant mCPBA (**Scheme 4. 2**), the UV-vis signature for the ferryl complex is not obtained, but instead an intense band at 700 nm (1000 $M^{-1}\,cm^{-1}$) is produced **Figure 4. 7**). This new species is thermally stable, unlike $[Fe^{IV}(O)(N3Py^{amide}SR)]^{2+}$, and an X-ray structure of this product (**Figure 4. 7**, **Figure 4. 16**) reveals that the ligated sulfide has been *S*-oxygenated to sulfoxide, affording $[Fe^{II}(N3Py^{amide}S(O)R)]^{2+}(BF_4)_2$. The major isomer of $[Fe^{II}(N3Py^{amide}S(O)R)]^{2+}(BF_4)_2$ is S-bound, while a minor isomer is O-bound to iron (**Figure 4. 16**). This complex also provides an authentic iron(II)-sulfoxide complex with a characteristic UV- vis band at λ_{max} = 700 nm. The complete absence of this peak during the formation of $[Fe^{IV}(O)(N3Py^{amide}SR)]^{2+}$ or its subsequent reactions with external substrates confirms that intramolecular S-oxygenation does not occur for $[Fe^{IV}(O)(N3Py^{amide}SR)]^{2+}$. The susceptibility of the coordinated thioether to sulfoxidation with mCPBA further emphasizes the remarkable stability of $[Fe^{IV}(O)(N3Py^{amide}SR)]^{2+}$ toward intramolecular OAT.

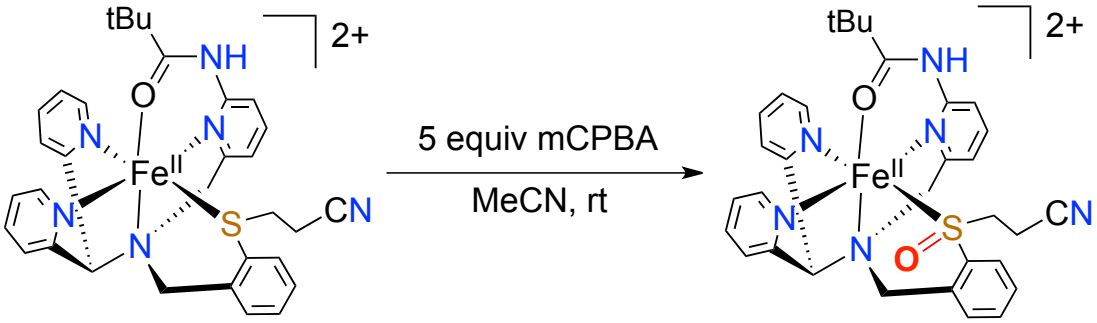

Scheme 4. 2. Reaction of $[Fe^{II}(N3Py^{amide}SR)]^{2+}$ with excess mCPBA to form the ligand oxidized product $[Fe^{II}(N3Py^{amide}S(O)R)]^{2+}$.

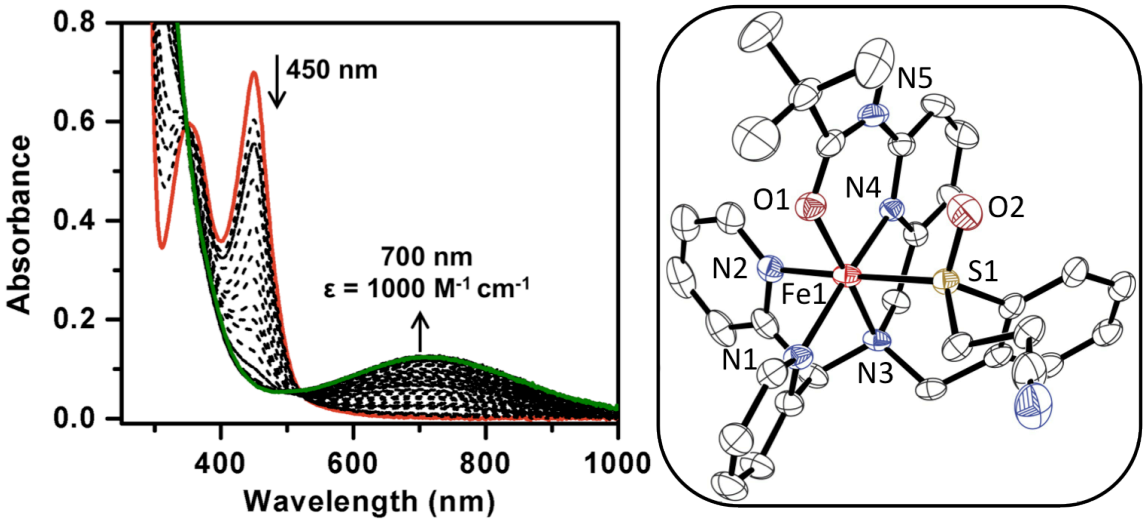

Figure 4. 7. UV-vis spectral changes for the formation of $[Fe^{II}(N3Py^{amide}S(O)R)]^{2+}$ (left); and displacement ellipsoids (50% probability level) for the dication of $[Fe^{II}(N3Py^{amide}S(O)R)]^{2+}$ showing the major S-bound isomer, with H-atoms omitted for clarity, except for the amide N-H (right).

A preliminary examination of $[Fe^{IV}(O)(N3Py^{amide}SR)]^{2+}$ for its ability to abstract hydrogen atoms reveals strongly muted reactivity. Addition of the H-atom donor 2,4-di-*tert*-butylphenol to $[Fe^{IV}(O)(N3Py^{amide}SR)]^{2+}$ at –40 °C leads to the slow decay of the 750 nm band and return of the peaks for $[Fe^{II}(N3Py^{amide}SR)]^{2+}$ (**Figure 4. 8**). The reaction rate with a large excess of phenol (500 equiv) leads to a k_{obs} of only 4.0 x 10^{-3} s^{-1} (**Figure 4. 9**), which is 2.5 times slower than H-atom transfer (HAT) to $[Fe^{IV}(O)(TMC)(NCCH_3)]^{2+}$ at 0 °C for the same phenol.[47] This observation is in line with calculations that predict that H-bonds in nonheme $Fe^{IV}(O)$ and $Mn^{IV}(O)$ complexes should lower H-atom abstraction reactivity.[48] These results also argue against the involvement of a high-spin $^5[Fe^{IV}(O)]$ ground state (or accessible quintet excited state) in the reactivity of $[Fe^{IV}(O)(N3Py^{amide}SR)]^{2+}$, because a $^5[Fe^{IV}(O)]$ species should exhibit accelerated HAT.[14,49,50]

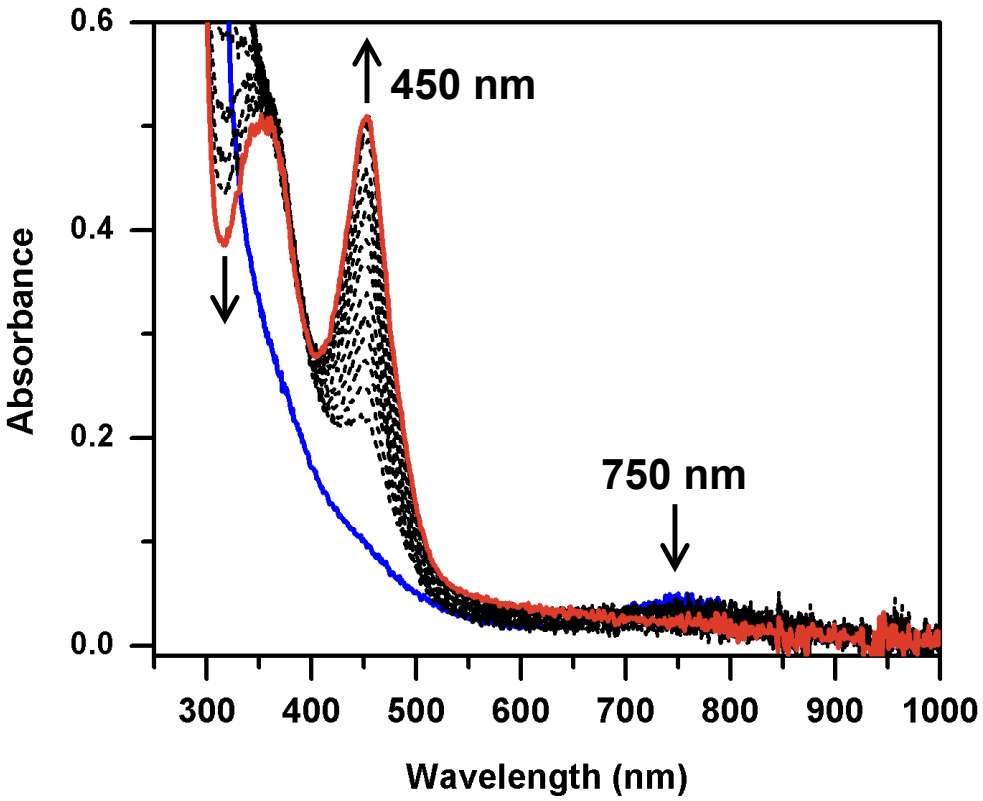

Figure 4. 8. UV-vis spectral changes of $[Fe^{IV}(O)(N3Py^{amide}SR)]^{2+}$ + 2,4-di-tert-butyl (500 equiv) phenol over 80 min in CH_3CN/CH_3OH at -40 °C.

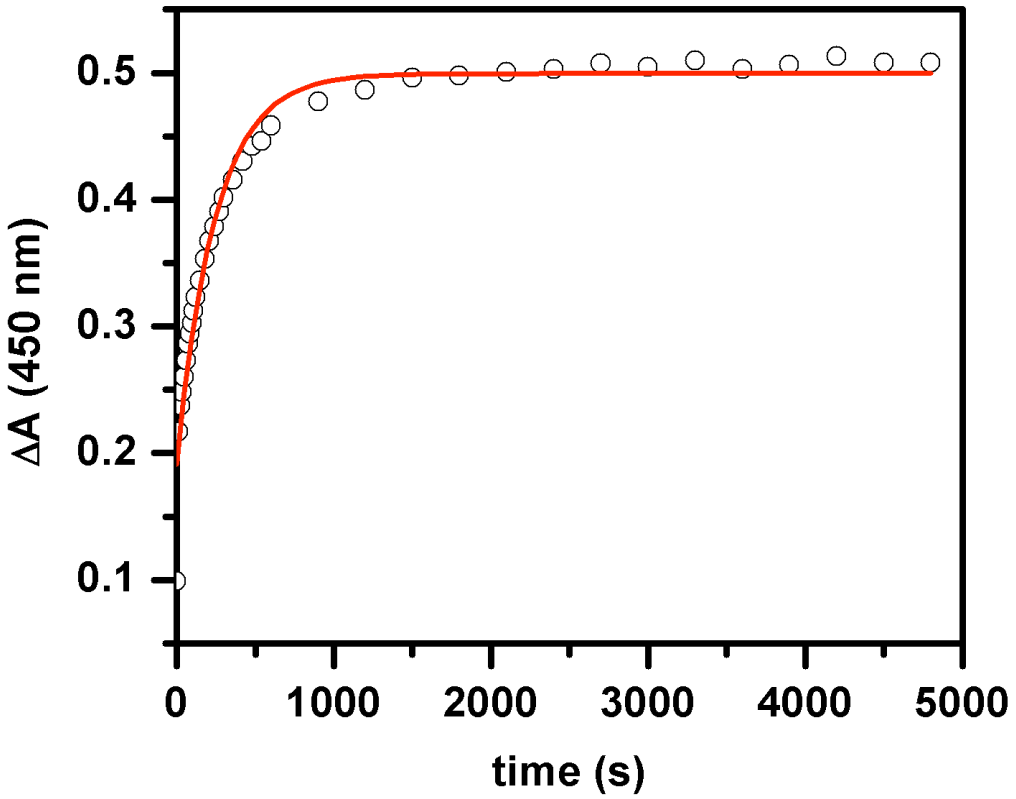

Figure 4. 9. Plot of the change in absorbance at 450 nm for the reaction of $[Fe^{IV}(O)(N3Py^{amide}SR)]^{2+}$ + 2,4-di-tert-butyl phenol (500 equiv) in CH_3CN/CH_3OH at -40 °C. Experimental = Open circles, best fit = red line.

Finally, the efficient intermolecular OAT facilitated by $[Fe^{IV}(O)(N3Py^{amide}SR)]^{2+}$ to PhSMe can be exploited for catalytic sulfoxidation. The starting $[Fe^{II}(N3Py^{amide}SR)](BF_4)_2$ complex was combined with excess PhSMe (100 equiv) at room temperature and then treated with PhIO (50 equiv). A transient color change signaling the formation of $[Fe^{IV}(O)(N3Py^{amide}SR)]^{2+}$ was observed, followed by an immediate return of the orange color for $[Fe^{II}(N3Py^{amide}SR)]^{2+}$. Product analysis by ^1H NMR gave 40 turnovers of PhS(O)Me in 2 h (**Figure 4. 10**), before catalyst decomposition. These results demonstrate that $[Fe^{II}(N3Py^{amide}SR)](BF_4)_2$ is able to function as a potent catalyst for the oxidation of thioethers.

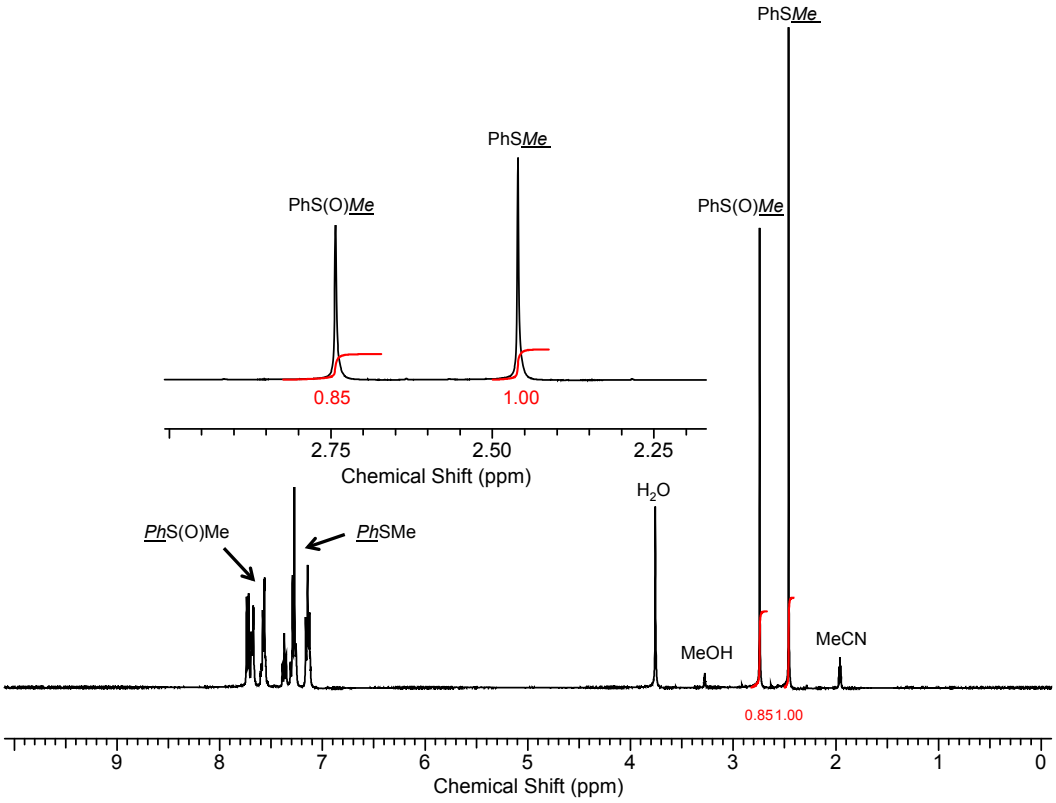

Figure 4. 10. ^{1}H NMR spectrum of the catalytic oxidation of thioanisole with $[Fe^{II}(N3Py^{amide}SR)](BF_4)_2$ as catalyst and PhIO as oxidant in CD_3CN/CD_3OD at 25 °C (PhSMe : PhIO : Fe^{II} = 100 : 50 : 1). Phenylmethyl sulfoxide (PhS(O)Me, 2.73 ppm) is formed in 85% yield (versus oxidant), as compared to the thioanisole (PhSMe, 2.44 ppm), integrations are shown in red.

Density Functional Calculations

The structures and Mössbauer parameters for $[Fe^{II}(N3Py^{amide}SR)]^{2+}$ and $[Fe^{IV}(O)(N3Py^{amide}SR)]^{2+}$ were examined by density functional theory (DFT) methods. The optimized ground-state structures are presented in **Figure 4. 11**, and relevant bond distances and angles compared with the data from the X-ray structures available in **Table 4. 2**. The bond distances compare favorably except for the Fe-S distances, which are

known to be over-estimated by DFT calculations.[43] Geometry optimization for $[Fe^{IV}(O)(N3Py^{amide}SR)]^{2+}$ (**Figure 4. 11**) confirms the proposed structure, including the amide NH---O H-bond, and a triplet ground state is found for $[Fe^{IV}(O)(N3Py^{amide}SR)]^{2+}$ with a close-lying quintet ($^5[Fe^{IV}(O)(N3Py^{amide}SR)]^{2+}$) excited state 2.3 kcal mol^{-1} higher in energy (**Table 4. 3**). Mössbauer parameters calculated by using the optimized structures are compared in **Table 4. 4**. The Mössbauer parameters of the $^1Fe^{II}$ complex (δ = 0.39 mm s-1, ΔE_Q = 0.82 mm s^{-1}) are predicted with a calculated isomer shift within 0.08 mm s^{-1} and the quadrupole splitting within 0.06 mm s^{-1} of experiment. The Mössbauer parameters for the $Fe^{IV}(O)$ complex were calculated with the optimized structure obtained from the higher-level calculations described in the Computational Methods section. The isomer shift of $^3Fe^{IV}$ is underestimated by only 0.01 mm s^{-1} by DFT, while the quadrupole splitting is underestimated by 0.25 mm s^{-1}. These calculated parameters are a reasonable fit to the experimental data, and are well within the error seen in the literature (**Table 4. 5**).[51,39]

The experimental isomer shift for $[Fe^{IV}(O)(N3Py^{amide}SR)]^{2+}$ falls within the range for $^3[Fe^{IV}(O)]$ complexes as well as the low end of the range for $^5[Fe^{IV}(O)]$ complexes (Table S4), and thus the Mössbauer data alone do not conclusively show a triplet ground state. However, the DFT-derived Mössbauer parameters for $^3[Fe^{IV}(O)(N3Py^{amide}SR)]^{2+}$ are a good match for the experimental values (calcd: δ = 0.03 mm s^{-1}, ΔE_Q = 0.55 mm s^{-1}), whereas the calculated parameters for $^5[Fe^{IV}(O)(N3Py^{amide}SR)]^{2+}$ deviate significantly from experiment. Moreover, almost all well-defined $^5[Fe^{IV}(O)]$ species are 5-coordinate, whereas the optimized geometry for $[Fe^{IV}(O)(N3Py^{amide}SR)]^{2+}$ is 6-coordinate. These data,

together with the DFT calculations and reactivity studies (vide infra), provide strong evidence that the ground state for $[Fe^{IV}(O)(N3Py^{amide}SR)]^{2+}$ is most likely the triplet state.

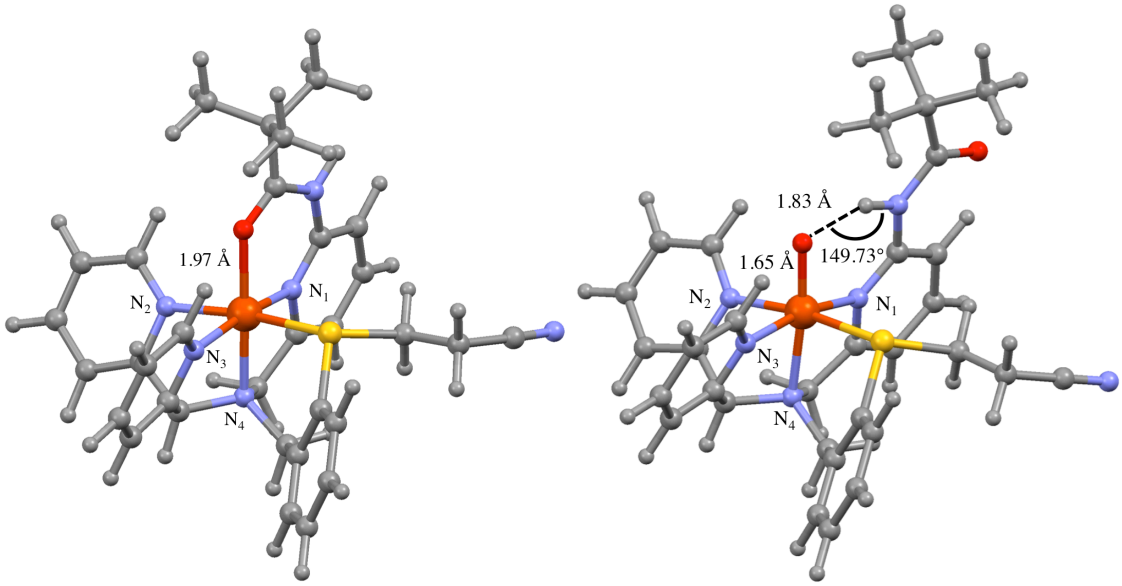

Figure 4. 11. DFT optimized structures of $^{1}[Fe^{II}(N3Py^{amide}SR)]^{2+}$ (left) using the B3LYP/6-31G(d) functional on all atoms), and $^{3}[Fe^{IV}(O)(N3Py^{amide}SR)]^{2+}$ (right) calculated with LANLDZ on the iron and 6-31G on the rest of the atoms, including the auxiliary basis sets def2-SVP/J and def2-SVP/K for the RIJCOSX approximation, with DFT at the unrestricted hybrid density functional level B3LYP.

Table 4. 2. Comparison of selected bond distances (Å) and angles (°) from the X-ray crystal structure of $[Fe^{II}(N3Py^{amide}SR)](BF_4)_2$, and those calculated for the ls Fe^{II} starting material ($^1[Fe^{II}(N3Py^{amide}SR)]^{2+}$), ls $Fe^{IV}(O)$ ($^3[Fe^{IV}(O)(N3Py^{amide}SR)]^{2+}$) and hs $Fe^{IV}(O)$ ($^5[Fe^{IV}(O)(N3Py^{amide}SR)]^{2+}$).

	Fe^{II} (X-ray)	$^1Fe^{II}$ [a]	$^3Fe^{IV}$ [b]	$^5Fe^{IV}$ [b]
Fe-O	1.95	1.97	1.65	1.65
Fe-N4	1.98	2.02	2.09	2.08
Fe-N3	1.92	1.99	1.99	2.07
Fe-N2	1.96	2.01	1.98	2.19
Fe-N1	1.97	1.95	2.03	2.05
Fe-S	2.29	2.41	2.45	2.75
C=O	1.25	1.25	N/A	N/A
Fe=O---H	N/A	N/A	1.83	1.88
O---H-N	N/A	N/A	149.73°	149.14°

[a] 6-31G(d) basis set. [b] LANLDZ on the iron and 6-31G basis set on the rest of the atoms, including the auxiliary basis sets def2-SVP/J and def2-SVP/K for the RIJCOSX approximation. See Computational Methods for complete details.

Table 4. 3. Calculated absolute and relative energies of the ls (S =1) and hs (S = 2) forms of $[Fe^{IV}(O)(N3Py^{amide}SR)]^{2+}$. [a] Sum of electronic energy and zero-point energy in atomic energy units.

	E^a (Eh)	ΔE (kcal mol^{-1})
$^3[Fe^{IV}(O)(N3Py^{amide}SR)]^{2+}$	-2238.635984	0
$^5[Fe^{IV}(O)(N3Py^{amide}SR)]^{2+}$	-2238.632402	+2.3

[a] Sum of electronic energy, zero-point energy, and thermal energy in atomic energy units.

Table 4. 4. Comparison of the experimental (exp.) and calculated (calc.) Mössbauer parameters for $[Fe^{II}(N3Py^{amide}SR)]^{2+}$ and $[Fe^{IV}(O)(N3Py^{amide}SR)]^{2+}$.

	$^1[Fe^{II}(N3Py^{amide}SR)]^{2+}$		$^3Fe^{IV}$	$^5Fe^{IV}$	$[Fe^{IV}(O)(N3Py^{amide}SR)]^{2+}$
	calc.	exp.	calc.		exp.
δ (mm s^{-1})	0.39	0.47	0.03	0.12	0.04
ΔE_Q (mm s^{-1})	0.82	0.77	0.55	−1.26	0.80

Table 4. 5. Comparison of Low-Spin and High-Spin Mossbauer parameters for selected reported $Fe^{IV}(O)$ complexes.

	δ (mm s^{-1})	ΔE_Q (mm s^{-1})	Citation
Low-Spin (S = 1)			
$[Fe^{IV}(O)(N4Py)]^{2+}$	−0.04	0.93	12
$[Fe^{IV}(O)(TPA)(NCCH_3)]^{2+}$	0.01	0.92	52
$[Fe^{IV}(O)(cyclam\text{-}CH_2CO_2)]^{+}$	0.01	1.37	53
$[Fe^{IV}(O)(N3Py^{amide}SR)]^{2+}$	0.04	0.80	This work
$[Fe^{IV}(O)(TMC)(NCCH_3)]^{2+}$	0.17	1.24	54
$[Fe^{IV}(O)(^{Me,H}Pytacn)]^{2+}$	0.05	0.73	55
$[Fe^{IV}(O)(BisPi1)]^{2+}$	0.02	0.69	56
$[Fe^{IV}(O)(TBC)(NCCH_3)]^{2+}$	0.22	0.97	49
High-Spin (S = 2)			
$[Fe^{IV}H3buea(O)]^{-}$	0.02	0.43	20
$[Fe^{IV}(O)(TMG_3tren)]^{2+}$	0.09	−0.29	57
$[Fe^{IV}(O)(tpa^{Ph})]^{-}$	0.09	0.51	58
CytC3•Fe(II)•RKG•L-Aba-*S*-CytC2•Br^{-} Species 1	0.23	0.81	59
$TyrH^{1}$	0.25	−1.27	60
Prolyl-4-Hydroxylase	0.30	−0.82	61
TauD	0.31	0.88	62
CytC3•Fe(II)•RKG•L-Aba-*S*-CytC2•Br^{-} Species 2	0.31	1.06	59
$[Fe^{IV}(O)(H_2O)_5]^{2+}$	0.38	−0.33	63

4. 4. Conclusions

The new findings reported here are summarized schematically in **Figure 4. 12**. We have shown that a rare, metastable non- heme $Fe^{IV}(O)$ complex can be generated with a pendant thioether donor in the first coordination sphere. Despite the fact that $[Fe^{IV}(O)(N3Py^{amide}SR)]^{2+}$ does not undergo intramolecular S-oxygenation, it does facilitate the rapid sulfoxidation of external thioether substrates. The dramatic rate enhancement in OAT facilitated by $[Fe^{IV}(O)(N3Py^{amide}SR)]^{2+}$ is similar to that seen for $[Fe^{IV}(O)(N4Py)]^{2+}$ upon addition of strong H^+ donors, suggesting that the inclusion of the amide H-bond donor in the second coordination sphere enhances OAT reactivity through a similar increase in electrophilicity of the terminal oxo ligand. However other factors may contribute to the strong increase in reactivity seen for $[Fe^{IV}(O)(N3Py^{amide}SR)]^{2+}$, including the accessibility of a high-spin quintet state. The metal-oxo group may also be more exposed in $[Fe^{IV}(O)(N3Py^{amide}SR)]^{2+}$ as compared to $[Fe^{IV}(O)(N4Py)]^{2+}$ because of replacement of an equatorial pyridine donor with a less sterically encumbered sulfide donor, allowing for easier approach of substrate. The remarkable reactivity seen for $[Fe^{IV}(O)(N3Py^{amide}SR)]^{2+}$ provides motivation for further examination of first- and second-coordination sphere effects in this, and other nonheme iron model complexes.

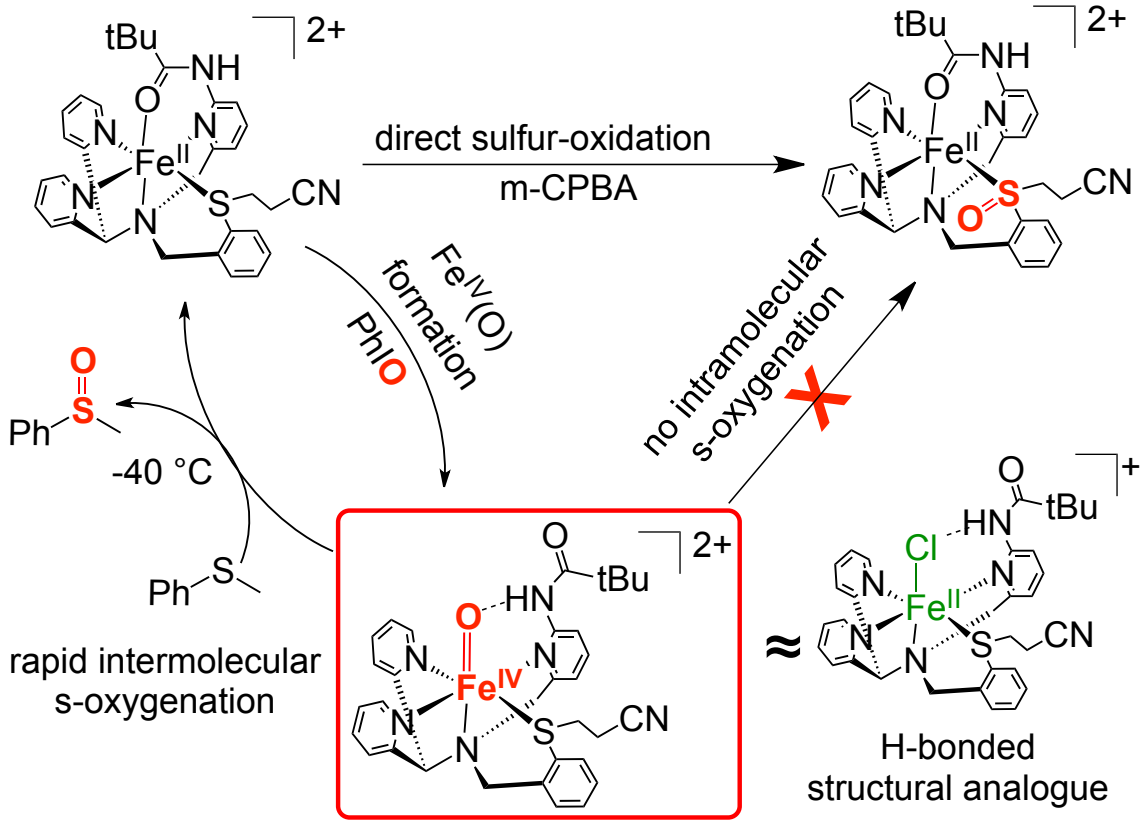

Figure 4. 12. Summary of reactivity for $[Fe^{II}(N3Py^{amide}SR)](BF_4)_2$ and $[Fe^{IV}(O)(N3Py^{amide}SR)]^{2+}$.

4. 5. References

(1) McDonald, A. R.; Que, L., Jr. *Coord. Chem. Rev.* **2013**, *257*, 414.

(2) Shook, R. L.; Borovik, A. S. *Inorg. Chem.* **2010**, *49*, 3646.

(3) de Visser, S. P.; Rohde, J. U.; Lee, Y. M.; Cho, J.; Nam, W. *Coord. Chem. Rev.* **2013**, *257*, 381.

(4) McQuilken, A. C.; Goldberg, D. P. *Dalton Trans.* **2012**, *41*, 10883.

(5) McQuilken, A. C.; Jiang, Y. B.; Siegler, M. A.; Goldberg, D. P. *J. Am. Chem. Soc.* **2012**, *134*, 8758.

(6) Jiang, Y. B.; Widger, L. R.; Kasper, G. D.; Siegler, M. A.; Goldberg, D. P. *J. Am. Chem. Soc.* **2010**, *132*, 12214.

(7) Sallmann, M.; Siewert, I.; Fohlmeister, L.; Limberg, C.; Knispel, C. *Angew. Chem. Int. Ed.* **2012**, *51*, 2234.

(8) Badiei, Y. M.; Siegler, M. A.; Goldberg, D. P. *J. Am. Chem. Soc.* **2011**, *133*, 1274.

(9) Liu, T. B.; Li, B.; Singleton, M. L.; Hall, M. B.; Darensbourg, M. Y. *J. Am. Chem. Soc.* **2009**, *131*, 8296.

(10) O'Toole, M. G.; Kreso, M.; Kozlowski, P. M.; Mashuta, M. S.; Grapperhaus, C. A. *J. Biol. Inorg. Chem.* **2008**, *13*, 1219.

(11) Lugo-Mas, P.; Taylor, W.; Schweitzer, D.; Theisen, R. M.; Xu, L.; Shearer, J.; Swartz, R. D.; Gleaves, M. C.; DiPasquale, A.; Kaminsky, W.; Kovacs, J. A. *Inorg. Chem.* **2008**, *47*, 11228.

(12) Kaizer, J.; Klinker, E. J.; Oh, N. Y.; Rohde, J. U.; Song, W. J.; Stubna, A.; Kim, J.; Münck, E.; Nam, W.; Que, L., Jr. *J. Am. Chem. Soc.* **2004**, *126*, 472.

(13) Klinker, E. J.; Kaizer, J.; Brennessel, W. W.; Woodrum, N. L.; Cramer, C. J.; Que, L., Jr. *Angew. Chem. Int. Ed.* **2005**, *44*, 3690.

(14) Sahu, S.; Widger, L. R.; Quesne, M. G.; de Visser, S. P.; Matsumura, H.; Moënne-Loccoz, P.; Siegler, M. A.; Goldberg, D. P. *J. Am. Chem. Soc.* **2013**, *135*, 10590.

(15) Zheng, P.; Takayama, S. I. J.; Mauk, A. G.; Li, H. B. *J. Am. Chem. Soc.* **2012**, *134*, 4124.

(16) Dey, A.; Okamura, T.; Ueyama, N.; Hedman, B.; Hodgson, K. O.; Solomon, E. I. *J. Am. Chem. Soc.* **2005**, *127*, 12046.

(17) Chiou, S. J.; Innocent, J.; Riordan, C. G.; Lam, K. C.; Liable-Sands, L.; Rheingold, A. L. *Inorg. Chem.* **2000**, *39*, 4347.

(18) Lacy, D. C.; Mukherjee, J.; Lucas, R. L.; Day, V. W.; Borovik, A. S. *Polyhedron* **2013**, *52*, 261.

(19) Gupta, R.; Lacy, D. C.; Bominaar, E. L.; Borovik, A. S.; Hendrich, M. P. *J. Am. Chem. Soc.* **2012**, *134*, 9775.

(20) Lacy, D. C.; Gupta, R.; Stone, K. L.; Greaves, J.; Ziller, J. W.; Hendrich, M. P.; Borovik, A. S. *J. Am. Chem. Soc.* **2010**, *132*, 12188.

(21) Sen Soo, H.; Komor, A. C.; Iavarone, A. T.; Chang, C. J. *Inorg. Chem.* **2009**, *48*, 10024.

(22) Wada, A.; Harata, M.; Hasegawa, K.; Jitsukawa, K.; Masuda, H.; Mukai, M.; Kitagawa, T.; Einaga, H. *Angew. Chem. Int. Ed.* **1998**, *37*, 798.

(23) Kim, S.; Saracini, C.; Siegler, M. A.; Drichko, N.; Karlin, K. D. *Inorg. Chem.* **2012**, *51*, 12603.

(24) McDonald, A. R.; Bukowski, M. R.; Farquhar, E. R.; Jackson, T. A.; Koehntop, K. D.; Seo, M. S.; De Hont, R. F.; Stubna, A.; Halfen, J. A.; Münck, E.; Nam, W.; Que, L., Jr. *J. Am. Chem. Soc.* **2010**, *132*, 17118.

(25) Annaraj, J.; Kim, S.; Seo, M. S.; Lee, Y. M.; Kim, Y.; Kim, S. J.; Choi, Y. S.; Jang, H. G.; Nam, W. *Inorg. Chim. Acta* **2009**, *362*, 1031.

(26) Bukowski, M. R.; Koehntop, K. D.; Stubna, A.; Bominaar, E. L.; Halfen, J. A.; Münck, E.; Nam, W.; Que, L., Jr. *Science* **2005**, *310*, 1000.

(27) Blackmond, D. G.; Hodnett, N. S.; Lloyd-Jones, G. C. *J. Am. Chem. Soc.* **2006**, *128*, 7450.

(28) Thapper, A.; Behrens, A.; Fryxelius, J.; Johansson, M. H.; Prestopino, F.; Czaun, M.; Rehder, D.; Nordlander, E. *Dalton Trans.* **2005**, 3566.

(29) Najera, C.; Gil-Molto, J.; Karlstrom, S. *Adv Synth Catal* **2004**, *346*, 1798.

(30) Frisch, M.J.; et al. *Gaussian 09,* Revision A.1; Gaussian, Inc.: Wallingford, CT, **2009**.

(31) Neese, F. *WIREs Comput. Mol. Sci.* **2012**, *2*, 73.

(32) Francl, M. M.; Pietro, W. J.; Hehre, W. J.; Binkley, J. S.; Gordon, M. S.; Defrees, D. J.; Pople, J. A. *J. Chem. Phys.* **1982**, *77*, 3654.

(33) Hehre, W. J.; Ditchfie.R; Pople, J. A. *J. Chem. Phys.* **1972**, *56*, 2257.

(34) Rassolov, V. A.; Pople, J. A.; Ratner, M. A.; Windus, T. L. *J. Chem. Phys.* **1998**, *109*, 1223.

(35) Neese, F.; Wennmohs, F.; Hansen, A.; Becker, U. *Chem. Phys.* **2009**, *356*, 98.

(36) Kendall, R. A.; Früchtl, H. A. *Theor. Chem. Acc.* **1997**, *97*, 158.

(37) Sinnecker, S.; Slep, L. D.; Bill, E.; Neese, F. *Inorg. Chem.* **2005**, *44*, 2245.

(38) Schafer, A.; Horn, H.; Ahlrichs, R. *J. Chem. Phys.* **1992**, *97*, 2571.

(39) RoÃàmelt, M.; Ye, S.; Neese, F. *Inorg. Chem.* **2008**, *48*, 784.

(40) Sickerman, N. S.; Park, Y. J.; Ng, G. K. Y.; Bates, J. E.; Hilkert, M.; Ziller, J. W.; Furche, F.; Borovik, A. S. *Dalton Trans.* **2012**, *41*, 4358.

(41) Aullon, G.; Bellamy, D.; Brammer, L.; Bruton, E. A.; Orpen, A. G. *Chem Commun* **1998**, 653.

(42) Kumar, D.; Sastry, G. N.; Goldberg, D. P.; de Visser, S. P. *J. Phys. Chem. A* **2012**, *116*, 582.

(43) Kumar, D.; Thiel, W.; de Visser, S. P. *J. Am. Chem. Soc.* **2011**, *133*, 3869.

(44) Park, M. J.; Lee, J.; Suh, Y.; Kim, J.; Nam, W. *J. Am. Chem. Soc.* **2006**, *128*, 2630.

(45) Park, J.; Morimoto, Y.; Lee, Y. M.; Nam, W.; Fukuzumi, S. *J. Am. Chem. Soc.* **2012**, *134*, 3903.

(46) Seo, M. S.; Jang, H. G.; Kim, J.; Nam, W. *Bull. Korean Chem. Soc.* **2005**, *26*, 971.

(47) Sastri, C. V.; Lee, J.; Oh, K.; Lee, Y. J.; Lee, J.; Jackson, T. A.; Ray, K.; Hirao, H.; Shin, W.; Halfen, J. A.; Kim, J.; Que, L., Jr.; Shaik, S.; Nam, W. *Proc. Natl. Acad. Sci. U. S. A.* **2007**, *104*, 19181.

(48) Latifi, R.; Sainna, M. A.; Rybak-Akimova, E. V.; de Visser, S. P. *Chem.-Eur. J.* **2013**, *19*, 4058.

(49) Wilson, S. A.; Chen, J.; Hong, S.; Lee, Y. M.; Clemancey, M.; Garcia-Serres, R.; Nomura, T.; Ogura, T.; Latour, J. M.; Hedman, B.; Hodgson, K. O.; Nam, W.; Solomon, E. I. *J. Am. Chem. Soc.* **2012**, *134*, 11791.

(50) McDonald, A. R.; Guo, Y. S.; Vu, V.; Bominaar, E. L.; Münck, E.; Que, L., Jr. *Chem. Sci.* **2012**, *3*, 1680.

(51) Neese, F. *Coord. Chem. Rev.* **2009**, *253*, 526.

(52) Kaizer, J.; Klinker, E. J.; Oh, N. Y.; Rohde, J. U.; Song, W. J.; Stubna, A.; Kim, J.; Münck, E.; Nam, W.; Que, L., Jr. *J. Am. Chem. Soc.* **2004**, *126*, 472.

(53) Lim, M. H.; Rohde, J. U.; Stubna, A.; Bukowski, M. R.; Costas, M.; Ho, R. Y. N.; Munck, E.; Nam, W.; Que, L. *Proc. Natl. Acad. Sci. U. S. A.* **2003**, *100*, 3665.

(54) Grapperhaus, C. A.; Mienert, B.; Bill, E.; Weyhermuller, T.; Wieghardt, K. *Inorg. Chem.* **2000**, *39*, 5306.

(55) Rohde, J. U.; In, J. H.; Lim, M. H.; Brennessel, W. W.; Bukowski, M. R.; Stubna, A.; Münck, E.; Nam, W.; Que, L., Jr. *Science* **2003**, *299*, 1037.

(56) Company, A.; Prat, I.; Frisch, J. R.; Mas-Balleste, R.; Guell, M.; Juhasz, G.; Ribas, X.; Munck, E.; Luis, J. M.; Que, L.; Costas, M. *Chem.-Eur. J.* **2011**, *17*, 1622.

(57) Bautz, J.; Bukowski, M. R.; Kerscher, M.; Stubna, A.; Comba, P.; Lienke, A.; Münck, E.; Que, L., Jr. *Angew. Chem. Int. Ed.* **2006**, *45*, 5681.

(58) England, J.; Martinho, M.; Farquhar, E. R.; Frisch, J. R.; Bominaar, E. L.; Münck, E.; Que, L., Jr. *Angew. Chem. Int. Ed.* **2009**, *48*, 3622.

(59) Bigi, J. P.; Harman, W. H.; Lassalle-Kaiser, B.; Robles, D. M.; Stich, T. A.; Yano, J.; Britt, R. D.; Chang, C. J. *J. Am. Chem. Soc.* **2012**, *134*, 1536.

(60) Fujimori, D. G.; Barr, E. W.; Matthews, M. L.; Koch, G. M.; Yonce, J. R.; Walsh, C. T.; Bollinger, J. M., Jr.; Krebs, C.; Riggs-Gelasco, P. J. *J. Am. Chem. Soc.* **2007**, *129*, 13408.

(61) Eser, B. E.; Barr, E. W.; Frantorn, P. A.; Saleh, L.; Bollinger, J. M., Jr.; Krebs, C.; Fitzpatrick, P. F. *J. Am. Chem. Soc.* **2007**, *129*, 11334.

(62) Hoffart, L. M.; Barr, E. W.; Guyer, R. B.; Bollinger, J. M., Jr.; Krebs, C. *Proc. Natl. Acad. Sci. U. S. A.* **2006**, *103*, 14738.

(63) Krebs, C.; Price, J. C.; Baldwin, J.; Saleh, L.; Green, M. T.; Bollinger, J. M. *Inorg. Chem.* **2005**, *44*, 742.

(64) Pestovsky, O.; Stoian, S.; Bominaar, E. L.; Shan, X. P.; Münck, E.; Que, L., Jr.; Bakac, A. *Angew. Chem. Int. Ed.* **2005**, *44*, 6871.

4. 6. Appendix A. Supplementary Spectra and DFT coordinates

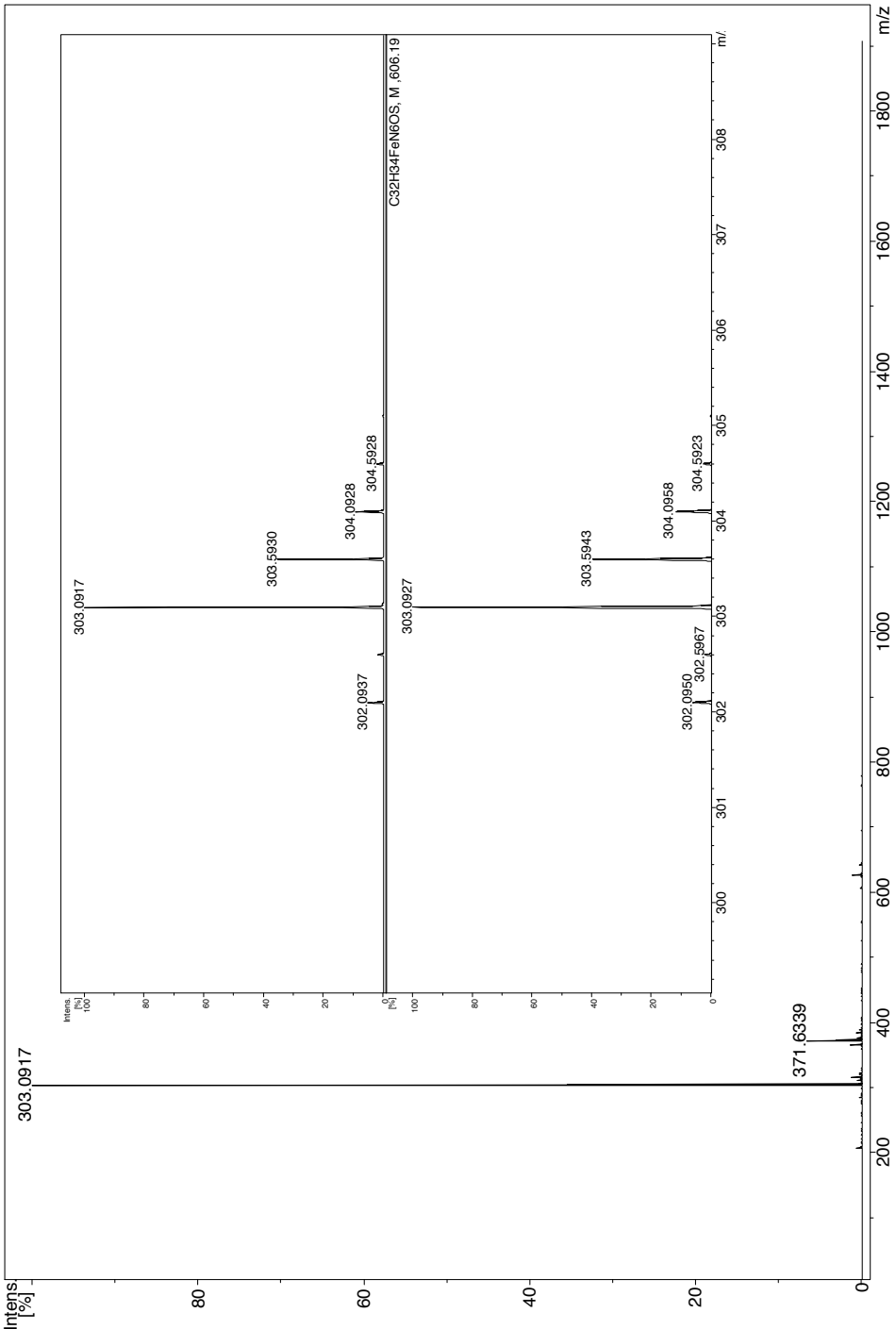

Figure 4. 13. Cryo-UHR ESI-ToF mass spectrum of $[Fe^{II}(N3Py^{amide}SR)]^{2+}$ ($[\mathbf{1} - 2BF_4]^{2+}$) at -40 °C in MeCN/MeOH. Inset: top = experimental, bottom = simulated spectrum for $[C_{32}H_{34}FeN_6OS]^{2+}$.

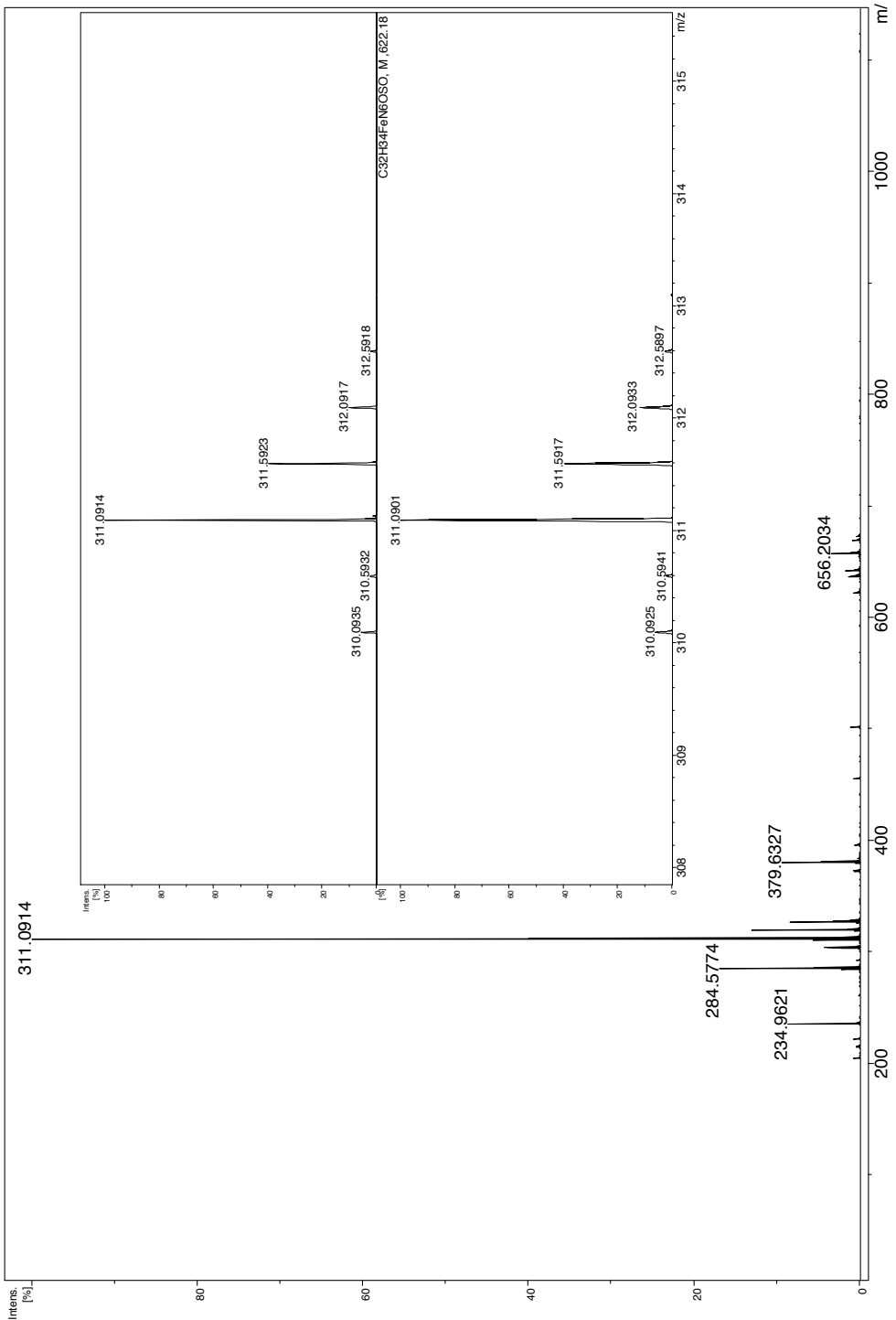

Figure 4. 14. Cryo-UHR ESI-ToF mass spectrum of $[Fe^{IV}(O)(N3Py^{amide}SR)]^{2+}$ ($[\mathbf{2}]^{2+}$) at -40 °C in MeCN/MeOH. Inset: top = experimental, bottom = simulated spectrum for $[C_{32}H_{34}FeN_6O_2S]^{2+}$.

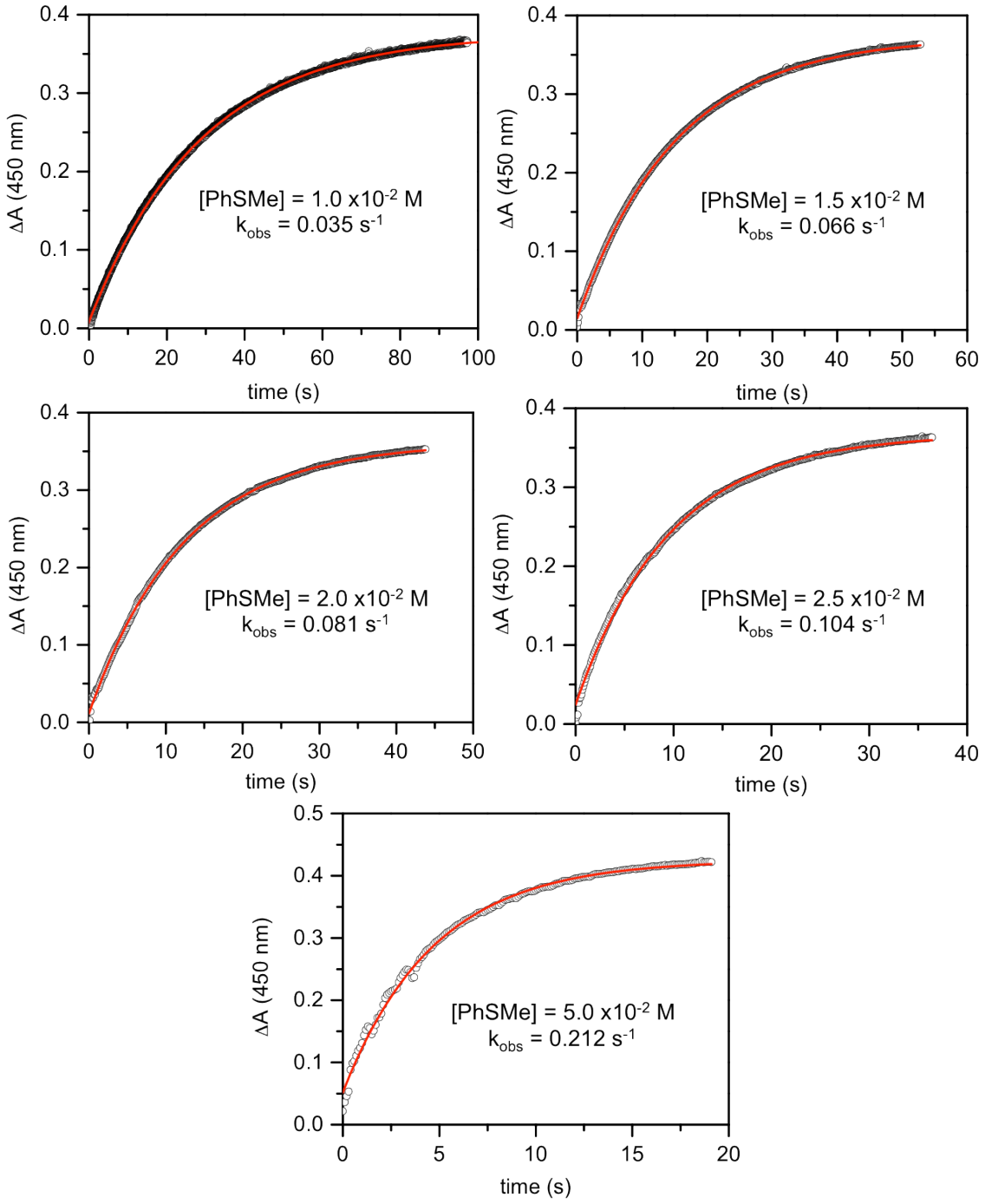

Figure 4. 15. Plots for $\Delta A_{(450nm)}$ versus time for the reaction of $[Fe^{IV}(O)(N3Py^{amide}SR)]^{2+}$ with PhSMe in CH_3CN/CH_3OH ([PhSMe] = 1.0 $x10^{-2}$ – 5.0 $x10^{-2}$ M). Experimental = open circles; best fit = red line.

Cartesian coordinates of DFT calculated structures.

$^{1}[Fe^{II}(N3Py^{amide}SR)]^{2+}$

26	-0.09757	-0.611783	0.371692
8	-1.030409	-1.01577	2.063982
16	-0.597811	1.722522	0.700252
7	0.799787	-0.328836	-1.414015
6	-2.012969	2.387765	-0.292597
1	-2.864199	1.758374	-0.016265
6	-2.356173	3.86748	-0.019712
1	-2.523649	4.031362	1.052636
1	-1.526626	4.519099	-0.319723
6	-3.564418	4.187235	-0.784227
7	-4.526453	4.335739	-1.418168
6	0.82058	2.617649	0.050525
6	1.262357	3.741645	0.756208
6	1.510173	2.177629	-1.098822
6	2.367159	4.470261	0.305282
1	0.73333	4.05074	1.653055
6	2.621055	2.915867	-1.526207
6	3.045962	4.056189	-0.839088
1	2.687772	5.356262	0.845433
1	3.148691	2.615707	-2.429044
1	3.899308	4.619192	-1.205386
6	0.997011	1.063469	-1.982849
1	0.007326	1.340443	-2.362417
6	-1.504166	-1.095353	-1.994576
6	-4.057448	-1.361198	-1.02202
6	-2.547397	-1.265865	-2.89309
1	-5.056991	-1.482614	-0.612632
1	-2.355934	-1.311063	-3.961064
6	-2.954834	-1.170015	-0.174343
6	-3.850598	-1.394688	-2.39432
1	-4.689858	-1.530509	-3.070564
7	-1.706849	-1.017145	-0.650536
7	0.624127	-2.474574	0.133813
6	0.22015	-3.654221	0.637542
6	1.720766	-2.457532	-0.664013
1	-0.647367	-3.621403	1.287423
6	2.429392	-3.606959	-0.994035
6	1.999552	-4.83135	-0.470144
1	3.29897	-3.553723	-1.643213
1	2.531159	-5.748415	-0.70848
7	1.698039	-0.217393	1.140915
6	2.067105	0.186301	2.368983

6	2.656544	-0.406372	0.202335
1	1.260353	0.318781	3.082438
6	4.005364	-0.192821	0.458146
6	4.3849	0.226535	1.737029
1	4.747985	-0.35475	-0.318015
1	5.432303	0.396364	1.970523
6	0.880598	-4.851363	0.362565
6	3.400298	0.411629	2.707842
1	-1.832114	2.234043	-1.360739
6	-0.044545	-1.079885	-2.41359
6	2.092159	-1.036612	-1.067664
7	-3.161595	-1.140667	1.22048
1	0.521078	-5.779747	0.795062
1	3.657828	0.721995	3.715628
1	0.072538	-0.657281	-3.418318
1	0.304417	-2.114488	-2.472722
1	2.816676	-1.019066	-1.893677
1	1.650907	0.974211	-2.861524
6	-2.257066	-1.141432	2.259603
6	-2.805677	-1.336511	3.68251
1	-4.126769	-1.236889	1.512391
6	-2.277757	-0.173885	4.560138
1	-1.18596	-0.133864	4.550048
1	-2.66653	0.796156	4.231766
1	-2.598035	-0.322201	5.595621
6	-2.232658	-2.68531	4.199377
1	-2.553348	-2.846588	5.232999
1	-2.599884	-3.537926	3.614968
1	-1.139563	-2.68599	4.184352
6	-4.348173	-1.376234	3.751128
1	-4.663471	-1.48971	4.792338
1	-4.81833	-0.446655	3.402475
1	-4.782556	-2.237749	3.224349

$^{3}[Fe^{IV}(O)(N3Py^{amide}SR)]^{2+}$

26	0.052835	-0.020757	-0.045694
16	-1.136154	2.089055	0.324624
6	-2.782267	2.239344	-0.658584
6	-3.428848	3.623213	-0.447736
6	-4.704308	3.674496	-1.163590
7	-5.717883	3.679503	-1.750349
1	-3.600468	3.811558	0.619013
1	-2.771958	4.418568	-0.819973
1	-3.399958	1.442557	-0.240233
1	-2.585274	2.036450	-1.712220

6	-0.035580	3.389114	-0.428318
6	0.073874	4.595445	0.271784
6	0.913675	5.608275	-0.213121
6	1.657354	5.394749	-1.376820
6	1.555026	4.176016	-2.057741
6	0.706222	3.151191	-1.602039
6	0.513694	1.936203	-2.479202
7	0.782346	0.542222	-1.920129
6	0.169830	-0.440271	-2.898917
6	-1.216461	-0.838929	-2.462935
7	-1.468593	-0.850782	-1.107396
6	-2.680020	-1.343609	-0.657267
7	-2.897838	-1.388264	0.710557
6	-4.090648	-1.790439	1.369974
8	-5.110199	-2.093246	0.728781
6	-4.073215	-1.871884	2.904080
6	-5.357541	-1.161687	3.410646
1	-5.326140	-0.084075	3.205584
1	-6.243542	-1.577144	2.926229
1	-5.448998	-1.303021	4.492866
6	-4.152057	-3.384559	3.267329
1	-4.204954	-3.494863	4.355892
1	-5.042770	-3.841165	2.828319
1	-3.269212	-3.930463	2.911621
6	-2.824386	-1.247040	3.559219
1	-2.714143	-0.182071	3.315322
1	-2.921705	-1.321312	4.647338
1	-1.898498	-1.767900	3.287317
1	-2.104057	-1.139702	1.297861
6	-3.654495	-1.783620	-1.589903
6	-3.389068	-1.730494	-2.946984
6	-2.149713	-1.251348	-3.399395
1	-1.912745	-1.216185	-4.456688
1	-4.139591	-2.063651	-3.654147
1	-4.595259	-2.145405	-1.204116
1	0.149547	-0.003133	-3.902119
1	0.801245	-1.329187	-2.959094
6	2.250666	0.246070	-1.633339
6	2.295198	-1.224546	-1.230552
7	1.260913	-1.547803	-0.404297
6	1.143987	-2.792012	0.107167
6	2.078488	-3.780497	-0.213832
6	3.143171	-3.465631	-1.065841
6	3.258523	-2.163974	-1.582786
1	4.073065	-1.898342	-2.246482
1	3.875524	-4.220236	-1.329461

1	1.967530	-4.773771	0.203197
1	0.309673	-2.971003	0.771669
6	2.643520	1.016237	-0.383109
7	1.696210	0.914750	0.589422
6	1.935076	1.378337	1.836897
6	3.158975	1.978622	2.148879
6	4.132297	2.108010	1.152362
6	3.873120	1.618284	-0.138057
1	4.616461	1.694953	-0.923476
1	5.084069	2.575848	1.376999
1	3.344343	2.333710	3.155121
1	1.145914	1.238857	2.564773
1	2.895934	0.469174	-2.488838
1	-0.526613	1.895623	-2.818032
1	1.133415	2.044397	-3.377956
1	2.121354	4.028634	-2.972563
1	2.307416	6.173056	-1.760573
1	0.981769	6.550706	0.318236
1	-0.490537	4.748486	1.184931
8	-0.371158	-0.564297	1.456453

$^{5}[Fe^{IV}(O)(N3Py^{amide}SR)]^{2+}$

26	0.004018	-0.200749	-0.007543
16	-1.216514	2.231970	0.389987
6	-2.899526	2.562436	-0.484983
6	-3.401798	3.994737	-0.214001
6	-4.698625	4.192546	-0.865769
7	-5.732052	4.314677	-1.403887
1	-3.501805	4.169222	0.863803
1	-2.688000	4.731848	-0.599899
1	-3.564380	1.815400	-0.046686
1	-2.785315	2.369215	-1.553050
6	-0.034971	3.393472	-0.455685
6	0.239396	4.609059	0.181015
6	1.169337	5.498521	-0.376961
6	1.822624	5.165391	-1.566655
6	1.550042	3.944077	-2.192074
6	0.626056	3.032816	-1.648283
6	0.303856	1.783328	-2.431028
7	0.711341	0.411583	-1.870148
6	0.148104	-0.617077	-2.834765
6	-1.257754	-0.994205	-2.443263
7	-1.544759	-0.996042	-1.088659
6	-2.780027	-1.457243	-0.659949
7	-3.023628	-1.491547	0.698946

6	-4.239214	-1.867675	1.339895
8	-5.243014	-2.175427	0.678155
6	-4.263064	-1.905880	2.875087
6	-5.539471	-1.145524	3.327737
1	-5.474454	-0.076193	3.091202
1	-6.425237	-1.553103	2.836854
1	-5.657839	-1.250600	4.411093
6	-4.397186	-3.404560	3.279941
1	-4.499197	-3.477594	4.367906
1	-5.281055	-3.850742	2.817889
1	-3.515215	-3.983343	2.980114
6	-3.015000	-1.293494	3.543964
1	-2.881993	-0.234940	3.284443
1	-3.135338	-1.345881	4.630749
1	-2.094428	-1.838160	3.301868
1	-2.239734	-1.254047	1.302675
6	-3.744501	-1.872189	-1.614864
6	-3.442535	-1.833270	-2.963928
6	-2.178121	-1.391579	-3.394171
1	-1.920596	-1.372264	-4.446566
1	-4.184437	-2.149827	-3.687411
1	-4.702612	-2.210086	-1.251308
1	0.172183	-0.220384	-3.854826
1	0.781646	-1.504583	-2.819521
6	2.210373	0.259651	-1.631180
6	2.469086	-1.204733	-1.281806
7	1.528191	-1.709672	-0.437217
6	1.655953	-2.958086	0.062588
6	2.750522	-3.758902	-0.283490
6	3.713662	-3.253861	-1.163854
6	3.574595	-1.951538	-1.674902
1	4.313003	-1.540399	-2.353640
1	4.564338	-3.860679	-1.451591
1	2.843004	-4.754014	0.132827
1	0.879528	-3.294954	0.738161
6	2.565546	1.042039	-0.373089
7	1.654528	0.867839	0.625429
6	1.897307	1.335038	1.872956
6	3.084256	2.013828	2.160732
6	4.017280	2.219128	1.137959
6	3.757427	1.724960	-0.150378
1	4.471717	1.865914	-0.953174
1	4.940240	2.750109	1.340598
1	3.273037	2.373266	3.164540
1	1.134905	1.143497	2.617963
1	2.792874	0.583732	-2.499840

1	-0.773238	1.695815	-2.596242
1	0.778053	1.860206	-3.417341
1	2.044636	3.704275	-3.128706
1	2.531403	5.854155	-2.012445
1	1.374277	6.443061	0.114019
1	-0.267586	4.861828	1.105678
8	-0.438717	-0.740200	1.484566

4. 7. Appendix B. X-ray Crystallography.

General

All reflection intensities were measured at 110(2) K using a KM4/Xcalibur (detector: Sapphire3) with enhance graphite-monochromated Mo *K*α radiation (λ = 0.71073 Å) under the program CrysAlisPro (Versions 1.171.35.11 or 1.171.36.24 Agilent Technologies, 2011-2012). The program CrysAlisPro (Versions 1.171.35.11 or 1.171.36.24 Agilent Technologies, 2011-2012) was used to refine the cell dimensions. Data reduction was done using the program CrysAlisPro (Versions 1.171.35.11 or 1.171.36.24 Agilent Technologies, 2011-2012). The structures were solved with the program SHELXS-97 (Sheldrick, 2008), and refined on F^2 with SHELXL-97 (Sheldrick, 2008). Analytical numeric absorption corrections based on a multifaceted crystal model were applied using CrysAlisPro (Versions 1.171.35.11 or 1.171.36.24 Agilent Technologies, 2011-2012). The temperatures of the data collections were controlled using the system Cryojet (manufactured by Oxford Instruments). The H atoms (unless otherwise specified) were placed at calculated positions using the instructions AFIX 13, AFIX 23, AFIX 43 or AFIX 137 with isotropic displacement parameters having values 1.2 or 1.5 times *U*eq of the attached C or N atoms. For the structure of **3**, the H atom attached to N6 was found from Fourier difference maps, and its atomic coordinates were refined freely.

Crystal Structure of $[Fe^{II}(N3Py^{amide}SR)](BF_4)_2 \bullet MeCN$

Data were collected at 110 (2) K after the crystal had been flash-cooled from room temperature. Three crystallographically independent BF_4^- counterions are disordered.

Two of the BF_4^- anions are found to be disordered over two orientations [occupancy factors for major components refine to 0.646(6) and 0.53(3)], while one is more severely disordered over 3 orientations [the three occupancy factors refine to 0.688(3), 0.214(3), and 0.099(2)].

Fw = 821.24, red thick lath, 0.39 × 0.25 × 0.15 mm^3, triclinic, *P*-1 (no. 2), a = 12.7152(3), b = 17.1863(3), c = 17.3225(4) Å, α = 89.9635(17), β = 81.5135(19), γ = 81.8096(18)°, V = 3705.00(14) $Å^3$, Z = 4, D_x = 1.472 g cm^{-3}, μ = 0.543 mm^{-1}, abs. corr. range: 0.851–0.934. 45414 Reflections were measured up to a resolution of $(\sin \theta/\lambda)_{max}$ = 0.62 $Å^{-1}$. 14972 Reflections were unique (R_{int} = 0.0320), of which 11595 were observed [$I > 2\sigma(I)$]. 1129 Parameters were refined using 579 restraints. $R1/wR2$ [$I > 2\sigma(I)$]: 0.0386/0.0995. $R1/wR2$ [all refl.]: 0.0552/0.1072. S = 1.056. Residual electron density found between –0.33 and 0.67 e $Å^{-3}$.

Crystal Structure of $[Fe^{II}(Cl)(N3Py^{amide}SR)](BF_4)$

The structure is ordered. The H atom attached to N6 was found from Fourier difference maps, and its atomic coordinates were refined freely. Fw = 728.82, irregular yellow block, 0.31 × 0.24 × 0.12 mm^3, monoclinic, *C*2/*c* (no. 15), a = 25.4707(3), b = 9.98637(13), c = 25.8674(3) Å, β = 94.8579(12)°, V = 6555.99(14) $Å^3$, Z = 8, D_x = 1.477 g cm^{-3}, μ = 0.665 mm^{-1}, abs. corr. range: 0.870–0.947. 24531 Reflections were measured up to a resolution of $(\sin \theta/\lambda)_{max}$ = 0.62 $Å^{-1}$. 6622 Reflections were unique (R_{int} = 0.0387), of which 5537 were observed [$I > 2\sigma(I)$]. 431 Parameters were refined. $R1/wR2$ [$I > 2\sigma(I)$]: 0.0317/0.0777. $R1/wR2$ [all refl.]: 0.0418/0.0817. S = 1.055. Residual electron density found between -0.39 and 0.47 e $Å^{-3}$.

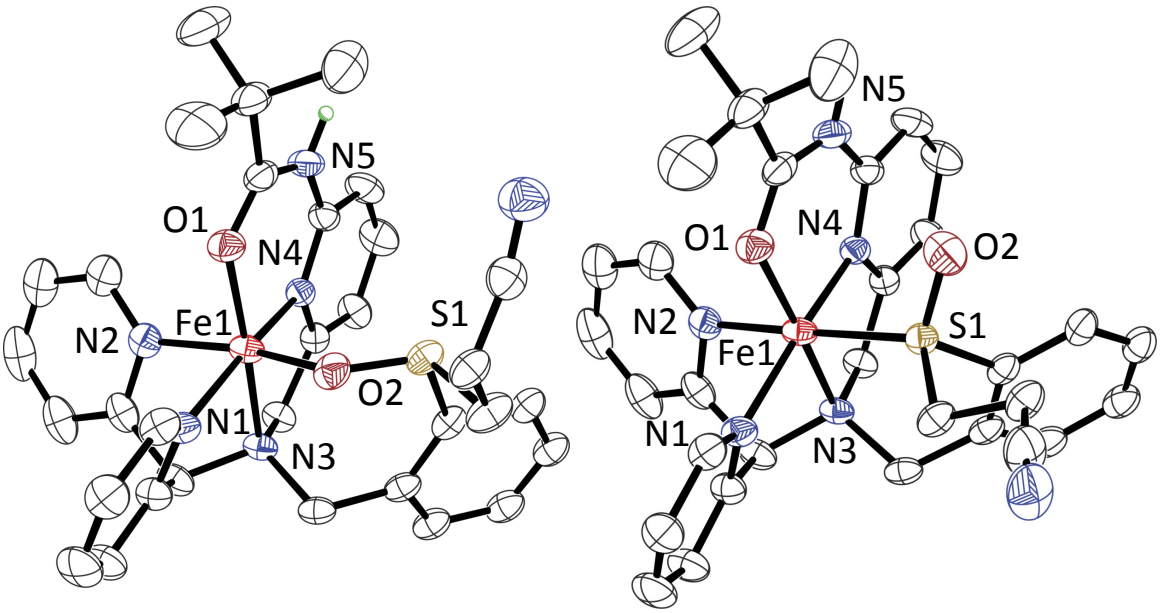

Figure 4. 16. Displacement ellipsoid plots (50% probability level) of the O-bound (left) and S-bound (right) dications of $[Fe^{II}(N3Py^{amide}S(O)R)](BF_4)_2$ •0.5 CH_3CN. H-atoms have been omitted, with the exception of the amide N-H.

Crystal Structure of $[Fe^{II}(N3Py^{amide}S(O)R)](BF_4)_2$ •0.5 CH_3CN

The structure is disordered because there are two possible modes of coordination on the Fe metal center in the crystal lattice. Some parts of the Fe complex are found to be disordered over 3 orientations. In two of the three orientations, the sixth coordination is achieved *via* S1, and occurs about 80% of the time. In the third orientation, the sixth coordination is achieved *via* O2. Both counterions are found to be disordered over two orientations [both occupancy factors for major components refine to 0.550(2)]. The lattice uncoordinated MeCN molecule is found to be disordered as the solvent molecule is found at a site of inversion symmetry. The crystal lattice also contains some CH_2Cl_2 solvent molecules disordered over another inversion center, but with probable occupancies lower than 1; their contributions were then taken out using the program

SQUEEZE for the final refinement. All details of the SQUEEZE refinement are provided in the final CIF file.

Fw = 1633.42,* orange-red lath, 0.48 × 0.31 × 0.12 mm^3, triclinic, *P*-1 (no. 2), a = 10.1678(3), b = 11.9592(3), c = 15.8456(3) Å, α = 92.0341(18), β = 96.166(2), γ = 108.703(2)°, V = 1809.49(8) $Å^3$, Z = 1, D_x = 1.499 g cm^{-3},* μ = 0.557 mm^{-1},* abs. corr. range: 0.804–0.940. 29353 Reflections were measured up to a resolution of $(\sin \theta/\lambda)_{max}$ = 0.62 $Å^{-1}$. 7300 Reflections were unique (R_{int} = 0.0347), of which 6311 were observed [$I > 2\sigma(I)$]. 788 Parameters were refined with 1162 restraints. $R1/wR2$ [$I > 2\sigma(I)$]: 0.0475/0.1232. $R1/wR2$ [all refl.]: 0.0543/0.1271. S = 1.050. Residual electron density found between –0.75 and 0.58 e $Å^{-3}$.

* excluding the contribution of the unresolved residual electron density

4. 8. Appendix C: Magnetization data for $[Fe^{II}(N3Py^{amide}SR)](BF_4)_2$

There is some ambiguity about the spin state of the starting iron(II) complex, $[Fe^{II}(N3Py^{amide}SR)](BF_4)_2$. The Fe-N(py) bond distances are all < 2.0 Å, consistent with a l.s. (S = 0) iron(II) complex, however the ^{1}H-NMR is paramagnetic at room temperature, consistent with a h.s. (S = 2) iron(II) complex. In an effort to determine the spin state of the ion, we attempted Evan's method measurements. An amount of $[Fe^{II}(N3Py^{amide}SR)](BF_4)_2$ (14 mg, 0.018 mmol) was dissolved in 0.4 mL CD_3CN (with TMS) and placed in the NMR sample tube. The Evan's method insert was then filled with 0.2 mL of the CD_3CN/TMS mixture, and was also placed in the NMR sample tube. The ^{1}H NMR spectrum of $[Fe^{II}(N3Py^{amide}SR)](BF_4)_2$, recorded at 25°C, shows two distinct TMS peaks (0.00 and -0.69 ppm, **Figure 4. 17**) due to the effect of a paramagnetic center on the TMS in solution. The difference between these two peaks (in Hz) can be related to the effective magnetic moment, μ_{eff}, of $[Fe^{II}(N3Py^{amide}SR)](BF_4)_2$ using equation 4. 3, where $\Delta\nu$ is the difference between TMS peaks in Hz, T is the temperature in Kelvin, f is the magnetic field in MHz, and M is the concentration of Fe. The effective magnetic moment (μ_{eff}) can then be related to the spin quantum number (S) using equation 4. 4, where g is the gyromagnetic ratio of an electron. Solving these equations with the Evan's method data gives an overall spin for $[Fe^{II}(N3Py^{amide}SR)](BF_4)_2$ of S = 0.95. Of the possible spin states for Fe^{II}, a value of S = 0.95 is closest to an overall S = 1 complex, which would correspond to an extremely rare example of an intermediate-spin (is) iron(II) compound. An overall S = 1 complex is unlikely, so we attempted SQUID measurements in collaboration with the McQueen lab to see if we could observe spin crossover behavior, or assign the spin state more accurately.

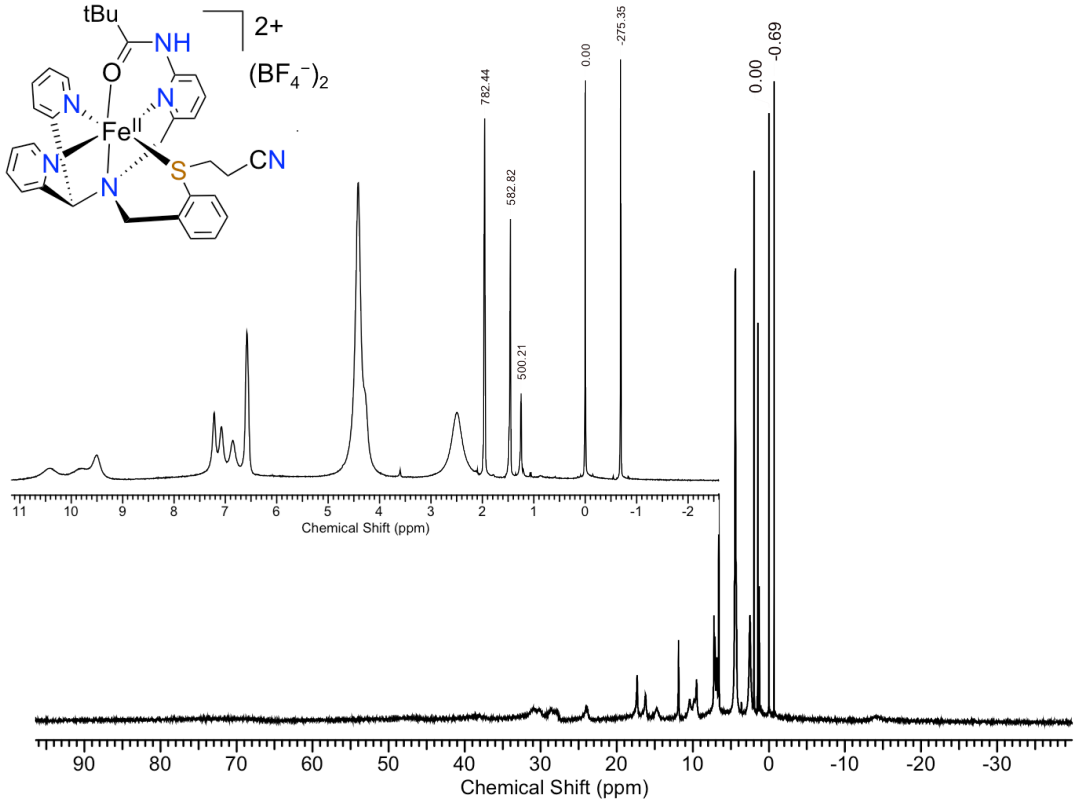

Figure 4. 17. Evan's method ^{1}H-NMR of [Fe^{II}(N3Py^{amide}SR)](BF$_4$)$_2$. [Fe] = 45 mM, volume = 0.4 mL. Chemical shifts are given in ppm (full spectrum) or Hz (inset).

$$\mu_{eff} = 0.0618\sqrt{\frac{d\Delta T}{2fM}}$$

equation 4. 3

$$\mu_{eff} = g\sqrt{S(S+1)}$$

equation 4. 4

A sample of solid [Fe^{II}(N3Py^{amide}SR)](BF$_4$)$_2$ (24.8 mg, 0.032 mmol) was placed in a plastic holder, and measuring the magnetic susceptibility ($\chi - \chi_0$) as a function of temperature gives the Curie-Weiss analysis shown in **Figure 4. 18** (top). The Curie constant, *C*, is then obtained from the slope of this line (slope = 1/*C*). The Curie constant is confirmed by plotting ($\chi - \chi_0$)*T versus temperature (**Figure 4. 18**, bottom), as

evidenced by the plateau at ~0.5 at T > 50K. The experimental value for *C* allows for the calculation of μ_{eff} (equation 4. 3), and ultimately *S* (equation 4. 4). Interestingly, the magnetic susceptibility measurement and Evan's method gives an effective magnetic moment (μ_{eff}) of 1.9, which corresponds to an overall $S = 0.6$ complex. A value of $S = 0.6$ does not match any of the possible Fe^{II} spin states, and with no obvious spin-crossover that might obscure the data, the complex is currently being re-investigated.

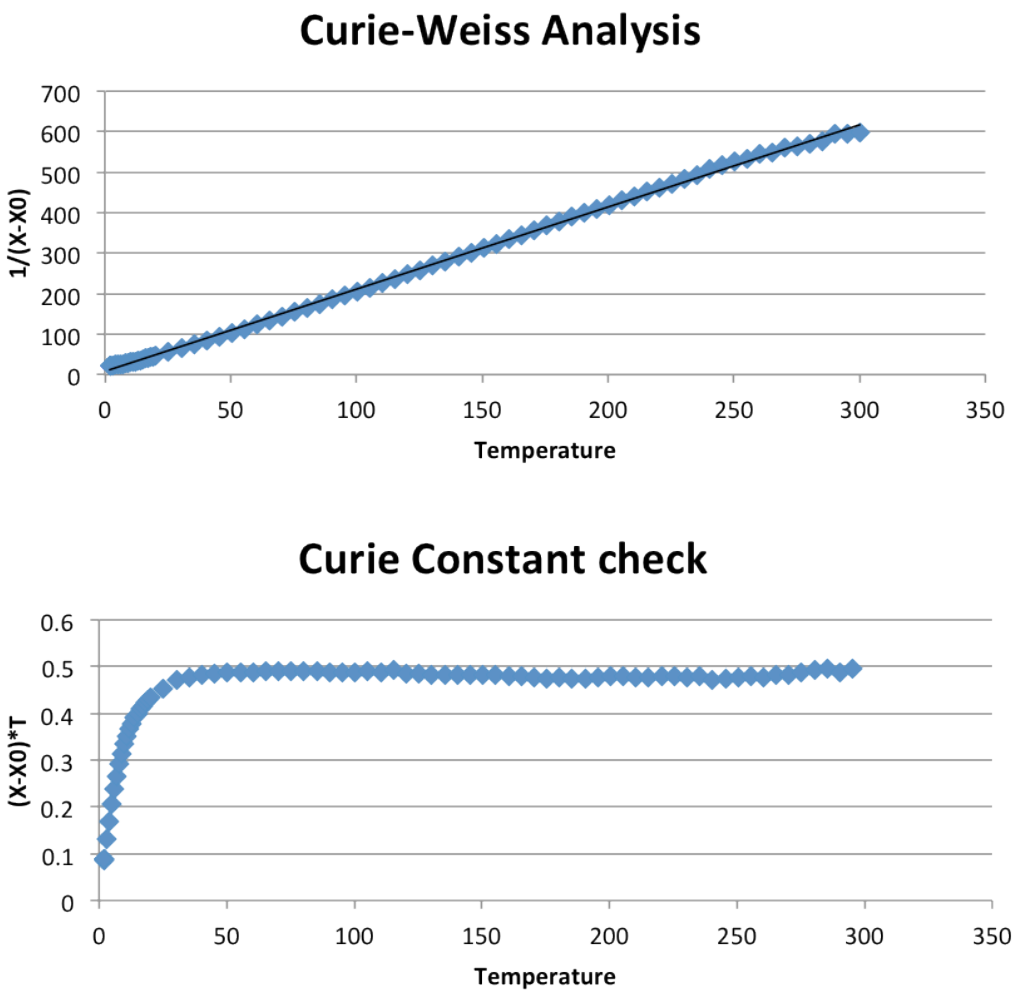

Figure 4. 18. Magnetic susceptibility data for $[Fe^{II}(N3Py^{amide}SR)](BF_4)_2$ from 2 – 300 K.

Chapter 5. Synthesis and Characterization of Sulfide-ligated Hydroperoxo and Alkylperoxo Iron(III) Complexes with a Pendant Amide H-Bond Donor in the Second Coordination Sphere

This work was co-written with the following authors:

Leland R. Widger, Yunbo Jiang, Tzuhsiung Yang, Maxime A. Siegler, Pierre Möenne-Loccoz, Devesh Kumar, Sam P. de Visser and David P. Goldberg

Manuscript in Preparation

5. 1. Introduction

Iron-(hydro)peroxo and (alkyl)peroxo species are postulated to be critical intermediates in a number of biologically relevant processes, from the utilization of dioxygen for substrate oxidation, to the processing and detoxification of reactive oxygen-derived species (ROS).[1-5] Some specific examples of enzymes involved in this chemistry include isopenicillin N-synthase (IPNS),[6] superoxide reductase (SOR),[7] aromatic amino acid hydroxylase (AAH),[8] Bleomycin,[9] and cysteine dioxygenase (CDO) (**Figure 5. 1**).[10] In one case, the alkylperoxo intermediate of an extradiol ring-cleaving dioxygenase, homoprotocatechuate 2,3-dioxygenase (2,3-HPCD), was structurally characterized by X-ray crystallography.[2] The physical and spectroscopic properties of these species have been studied in a number of inorganic model complexes,[11-25] but most of these systems utilize polyamino/polypyridyl ligands, and the incorporation of sulfur or other heteroatoms is rare.[23,25-29] In addition, little work has been done to determine the effect of secondary sphere interactions, such as hydrogen-bonding networks, on the structures and spectroscopic properties of iron-peroxo complexes. Recently our lab has focused on determining the first and second coordination sphere effects on non-heme iron model

complexes, including the incorporation of S-donors in the first coordination sphere, and oxidizable substrates or H-bond donors in the second coordination sphere.[30-33]

The thiolate-ligated complex $[Fe^{II}(N3PyS)(CH_3CN)](BF_4)_2$ was among the first examples of a biomimetic iron(II) complex to undergo S-oxygenation with O_2 to yield a doubly-oxygenated sulfinate product.[30] This complex was also useful for studying the fundamental electronic structure and photolability of complexes while employing NO• as a surrogate for O_2.[31] We have examined secondary coordination sphere effects by utilizing the aryl appended complexes, $[Fe^{II}(N4Py^{2Ph})(NCCH_3)](BF_4)_2$ and $[Fe^{II}(N4Py^{amide,2Ph})(NCCH_3)](BF_4)_2$. Without a stabilizing H-bond donor positioned near the open site on iron, the alkylperoxo complex $[Fe^{III}(N4Py^{2Ph})(OO^tBu)]^{2+}$ undergoes rapid O-O bond cleavage to give an $Fe^{IV}(O)$ intermediate. The $Fe^{IV}(O)$ is then situated for attack of the appended aryl group, giving the arene-hydroxylated product. However, in the presence of an amide H-bond donor, $[Fe^{III}(N4Py^{amide,2Ph})(OO^tBu)]^{2+}$ is stabilized and only the alkylperoxo-iron(III) complex is observed.[32] We also determined the influence of first and second coordination sphere modifications in a system in which an equatorial sulfide donor was included in the 1st-coordination sphere and an amide H-bond donor was included in the 2nd-coordination sphere. The $[Fe^{II}(N3Py^{amide}SR)](BF_4)_2$ starting material was shown to react with O-atom donors to give $[Fe^{IV}(O)(N3Py^{amide}SR)]^{2+}$ in CH_3CN at -40 °C. This complex is a rare example of a metastable $Fe^{IV}(O)$ complex with a pendant sulfide donor, and it does not undergo *intramolecular* oxygen-atom transfer (OAT) to the sulfide group. However, this complex does exhibit rapid *intermolecular* OAT to *exogenous* sulfide substrates (PhSMe), and it was proposed that amide H-bond donation

to the terminal oxo ligand was causing the significant rate accelerations seen for intermolecular OAT.[33]

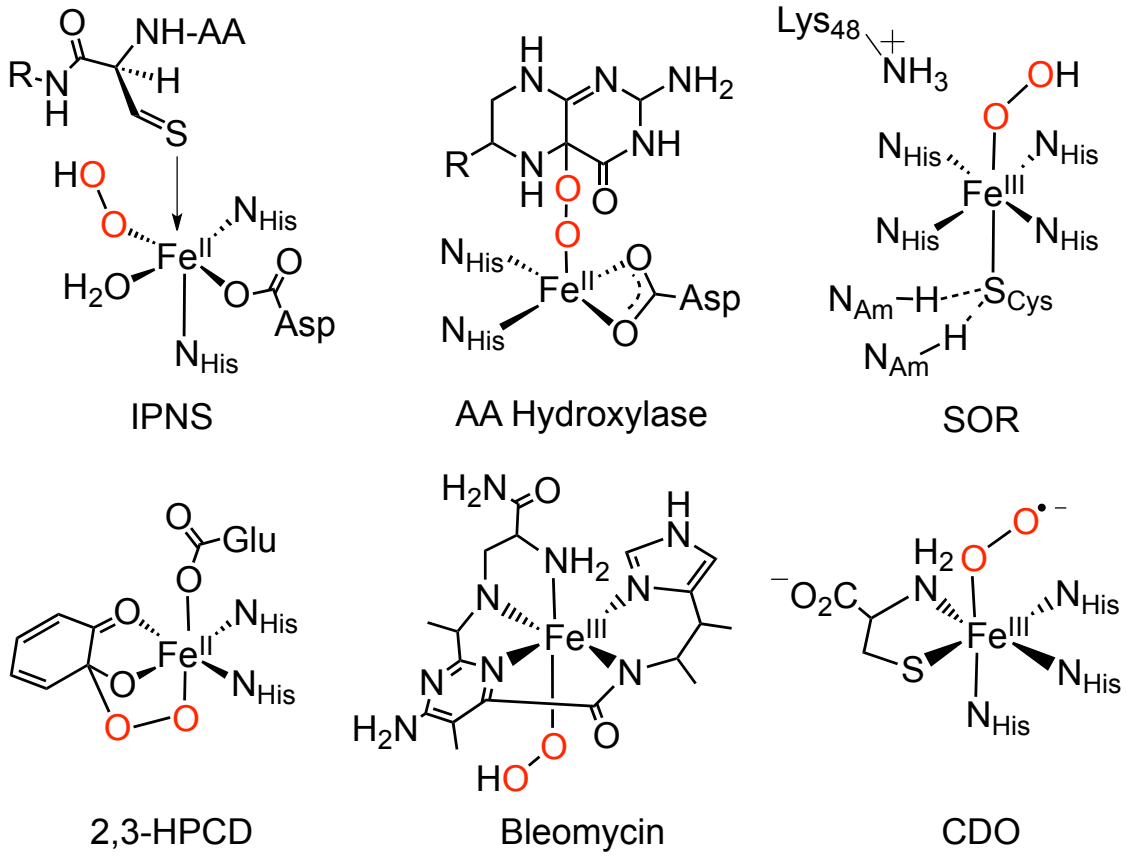

Figure 5. 1. Selected examples of iron-dioxygen complexes in biology.

Herein we report the synthesis and characterization of Fe(III)-OOH and –OO^{t}Bu complexes derived from two biomimetic starting compounds, [Fe^{II}(N3PySR)(MeCN)](BF$_4$)$_2$ and [Fe^{II}(N3Py^{amide}SR)](BF$_4$)$_2$, shown in **Scheme 5. 1**. These complexes were synthesized by metallation with Fe(BF$_4$)$_2$ of their respective purified ligand precursors. Both [Fe^{II}(N3PySR)(MeCN)](BF$_4$)$_2$ and [Fe^{II}(N3Py^{amide}SR)](BF$_4$)$_2$ possess a sulfide ligand in the first coordination sphere, while [Fe^{II}(N3Py^{amide}SR)](BF$_4$)$_2$ incorporates a single amide N-H group within H-bonding distance of the preferred binding site for anionic ligands. We demonstrate the generation

of meta-stable Fe^{III}-OO(H/R) complexes in the presence of the sulfide donor ligands starting from $[Fe^{II}(N3PySR)(MeCN)](BF_4)_2$ and $[Fe^{II}(N3Py^{amide}SR)](BF_4)_2$. The influence of a 1st-coordination sphere sulfide donor and a 2nd-coordination sphere H-bond donor on the stability and spectroscopic properties of the (hydro/alkyl)peroxo complexes is assessed.

5. 2. Experimental Section

General Considerations

All reagents were purchased from commercial vendors and used without further purification unless noted otherwise. The N3PySR ligand[30] and $[Fe^{II}(N3Py^{amide}SR)](BF_4)_2$[33] were synthesized as previously reported. All reactions were carried out under an atmosphere of N_2 inside a glovebox or under Ar by standard Schlenk and vacuum line techniques. UV-visible spectra were recorded on a Varian Cary 50 spectrophotometer. Electron paramagnetic resonance (EPR) spectra were obtained on a Bruker EMX EPR spectrometer controlled with a Bruker ER 041 X G microwave bridge at 15 or 77 K. The EPR spectrometer was equipped with a continuous-flow liquid He cryostat and an ITC503 temperature controller made by Oxford Instruments, Inc. NMR was performed on a Bruker Avance 400 MHz FT-NMR spectrometer at 25 ºC. Elemental analysis was performed by Atlantic Microlab Inc., Norcross, GA. LDI-ToF mass spectra were obtained using a Bruker Autoflex III Maldi ToF/ToF instrument (Billerica, MA). Samples were dissolved in CH_2Cl_2 and deposited on the target plate in the absence of any added matrix. Samples were irradiated with a 355 nm UV laser and mass-analyzed by ToF mass spectrometry in the reflectron mode. Resonance Raman spectra were recorded at 110 K using a backscattering geometry with a McPherson 2061/207 spectrograph and a

liquid-N_2-cooled CCD camera. The 568 and 647 nm excitations were obtained from a Kr and Ar ion laser, respectively (Innova 300, Coherent). Longpass filters (RazorEdge, Semrock) were used to attenuate the Raleigh scattering. The samples were kept at 110 K inside a liquid-N_2 coldfinger and spun continuously to prevent photodamage. Frequencies were calibrated relative to an aspirin standard and are accurate to ± 1 cm^{-1}.

Synthesis of Reported Compounds

$[Fe^{II}(N3PySR)(CH_3CN)](BF_4)_2$

The free ligand N3PySEt (399 mg, 0.89 mmol) was dissolved in CH_3CN (10 mL). A slurry of $Fe(BF_4)_2 \bullet 6H_2O$ (298 mg, 0.88 mmol) in CH_3CN (10 mL) was added dropwise to the ligand, affording a red suspension. The mixture was allowed to stir for 2 h, and filtered through celite. Diffusion of diethyl ether into a CH_3CN solution afforded dark red blocks after two days. Yield: 409 mg (68%). ^1H NMR ($CDCl_3$): δ 9.48 (2H), 9.34 (1H), 8.23 (1H), 8.14 (1H), 7.99 (2H), 7.76 (1H), 7.70 (1H), 7.56 (1H), 7.44 (3H), 7.21 (2H), 6.81 (1H), 6.71 (1H), 4.40 (1H), 4.26 (1H), 3.88 (1H), 3.66 (1H), 3.10 (1H), 2.73 (1H) 2.60 (1H). *Anal Calc*. for $C_{29}H_{28}B_2F_8N_6SFe$: C, 48.24; H, 3.91; N, 11.64. Found: C, 48.22; H, 3.93; N, 11.70.

$[Fe^{II}(N3Py^{amide}SR)(F/N_3)](BF_4) \bullet CH_3CN$ (F = 67%, N_3 = 33%)

A stock solution of NaN_3 (5.8 mg in 0.5 mL MeOH) was prepared, and 50 μL of this solution was added to $[Fe^{II}(N3Py^{amide}SR)](BF_4)_2$ (6.5 mg, 9 μmol) dissolved in 0.5 mL MeCN. Vapor diffusion of Et_2O into the mixture resulted in a small amount of yellow crystals suitable for X-ray structure determination, which were separated manually from the bulk material. UV-vis (CH_3CN): λ_{max} = 355, 430 nm, ε = 1620, 1680 M^{-1} cm^{-1}.

$[Fe^{III}(N3PySR)(OOH)]^{2+}$

A solution of $[Fe^{II}(N3PySR)](BF_4)_2$ (0.8 mM) was prepared in MeCN before H_2O_2 (30%, 5.0 equiv) was added. The yellow solution immediately turned red, then brown. Monitoring by UV-vis (**Figure 5. 5**) showed the peaks corresponding to $[Fe^{II}(N3PySR)](BF_4)_2$ (λ_{max} = 350, 450 nm) decay with isosbestic conversion to a new spectrum (λ_{max} = 550 nm) that corresponds to $[Fe^{II}(N3PySR)(OOH)]^{2+}$. The hydroperoxo complex ($[Fe^{II}(N3PySR)(OOH)]^{2+}$) was formed within 60 s and immediately began to decay to a brown species with no prominent UV-vis features. UV-vis: λ_{max} = 542 nm, ε = 1000 M^{-1} cm^{-1}; EPR: g = [2.17, 2.11, 1.97]; rR: ν(Fe-O) = 615, 629, 647 and 644 cm^{-1}, ν(O-O) = 809 cm^{-1}.

$[Fe^{III}(N3Py^{amide}SR)(OOH)]^{2+}$

An amount of $[Fe^{II}(N3Py^{amide}SR)](BF_4)_2$ (1.25 mg, 1.7 μmol) was dissolved in 4.0 mL of MeCN and cooled to -40 °C. A solution of H_2O_2 (0.88 M, 25 equiv, 0.05 mL) in MeCN was added and the color immediately began to change from orange to purple. Monitoring by UV-vis (Fig. 6) revealed full formation of $[Fe^{II}(N3Py^{amide}SR)(OOH)]^{2+}$ (λ_{max} = 556 nm) within 30 min. UV-vis: λ_{max} = 567 nm, ε = 900 M^{-1} cm^{-1}; EPR: g = [2.17, 2.16, 1.95]; rR: ν(Fe-O) = 612 cm^{-1}, ν(O-O) = 800 cm^{-1}.

$[Fe^{III}(N3PySR)(OO^tBu)]^{2+}$

A solution of $[Fe^{II}(N3PySR)](BF_4)_2$ (0.8 mM) was prepared in MeCN and cooled to -40 °C. A solution of tBuOOH (5.5 M, 10.0 equiv) diluted in MeCN was added, and the yellow solution immediately turned green, then blue. Monitoring by UV-vis (**Figure 5. 8**) showed the peaks corresponding to $[Fe^{II}(N3PySR)](BF_4)_2$ decay with isosbestic conversion to a new spectrum (λ_{max} = 660 nm) that corresponds to

$[Fe^{II}(N3PySR)(OOtBu)]^{2+}$. UV-vis: λ_{max} = 600 nm, ε = 1670 M^{-1} cm^{-1}; EPR: g = [2.14, 2.08, 1.96]; rR: ν(Fe-O) = 700 cm^{-1}, ν(O-O) = 797 cm^{-1}.

$[Fe^{III}(N3Py^{amide}SR)(OO^{t}Bu)]^{2+}$

A solution of $[Fe^{II}(N3Py^{amide}SR)](BF_4)_2$ (1.1 mM) in MeCN was prepared and cooled to -40 °C. A solution of tBuOOH (5.5 M, 10 equiv) in MeCN was then added and allowed to stir for 20 min. The orange solution of $[Fe^{II}(N3Py^{amide}SR)](BF_4)_2$ turns green and finally deep blue, as monitoring by UV-vis (**Figure 5. 9**) shows the decay of the peaks corresponding to $[Fe^{II}(N3Py^{amide}SR)](BF_4)_2$ with the isosbestic growth of a new peak (λ_{max} = 621 nm) corresponding to $[Fe^{II}(N3Py^{amide}SR)(OOtBu)]^{2+}$ UV-vis: λ_{max} = 620 nm, ε = 2000 M^{-1} cm^{-1}; EPR: g = [2.17, 2.11, 1.96]; rR: ν(Fe-O) = 691 cm^{-1}, ν(O-O) = 797 cm^{-1}

Secondary amine (iii)

Primary amine (**i**) (825 mg, 2.5 mmol) and aldehyde (**ii**) (468 mg, 2.5 mmol) were dissolved in a 1:1 mixture of $CHCl_3$/MeOH. Molecular sieves (4 Å) were added and the mixture was stirred under Ar for 48 h. Excess $NaBH_3CN$ (315 mg, 5.0 mmol) was added and allowed to mix for 2h before being quenched with 1M HCl. The crude reaction mixture was concentrated, dissolved in $CHCl_3$, washed with H_2O, dried and re-concentrated, before being purified on neutral alumina (EtOAc/hexanes) to give 680 mg (53%) of secondary amine **iii** as a pale yellow solid. ^{1}H-NMR ($CDCl_3$): δ 8.09–8.07 (m, 4H), 7.72 (t, 2H), 7.63 (d, 2H), 7.54-7.49 (m, 6H), 7.46-7.42 (m, 6H), 5.30 (s, 1H), 4.06 (s, 2H), 3.06 (t, 2H), 2.47 (t, 2H).

N3Py^{amide,2Ph}SR

Secondary amine (**iii**) (200 mg, 0.4 mmol) and Cs_2CO_3 (196 mg, 0.6 mmol) were combined in 100 mL MeCN, followed by bromide (**iv**) (109 mg, 0.4 mmol) and NaI (90 mg, 0.6 mmol). After stirring for 72 h, the crude mixture as filtered through celite and concentrated. The crude solid was dissolved in $CHCl_3$, washed with H_2O, dried, and purified by column chromatography on neutral silica to give 272 mg (97%) of the final ligand as a pale yellow solid. ^{1}H-NMR ($CDCl_3$): δ 8.07–8.03 (m, 5H), 7.92-9.90 (m, 2H), 7.73 (t, J = 8.1 Hz, 2H), 7.67 (dd, J = 8.8, 1.0 Hz, 2H), 7.60 (t, J = 7.8 Hz, 2H), 7.50-7.39 (m, 9H), 7.33 (dd, J = 7.6, 1.5 Hz, 1H), 7.25 (dd, J = 7.6, 1.3 Hz, 1H), 7.19 (td, 7.5, 1.8 Hz, 1H), 5.53 (s, 1H), 4.29 (s, 2H), 4.06 (s, 2H), 2.94 (t, J = 7.1 Hz, 2H), 2.37 (t, J = 7.1 Hz, 2H), 1.31 (s, 9H); ^{13}C NMR ($CDCl_3$): d 177.2, 160.1, 159.1, 156.5, 150.8, 141.8, 139.8, 138.7, 137.1, 133.0, 131.4, 130.4, 129.1, 128.9, 127.9, 127.8, 127.3, 123.0, 119.1, 118.8, 118.3, 111.8, 72.0, 57.5, 54.6, 51.9, 40.0, 30.1, 27.8, 18.2, 8.6. FAB-MS (+): *m/z* = 703.32127 $[M + H]^+$.

[Fe^{II}(N3Py^{amide,2Ph}SR)](BF$_4$)$_2$

The free ligand N3Py^{amide,2Ph}SR (461 mg, 0.66 mmol) was dissolved in 5 mL MeCN before $Fe(BF_4)_2$•$6H_2O$ (221 mg, 0.66 mmol) was added. After stirring for 2 h, the yellow solution was filtered through celite and vapor diffusion of Et_2O gave [Fe^{II}(N3Py^{amide,2Ph}SR)](BF$_4$)$_2$ as yellow crystals suitable for X-ray structure determination (510 mg, 83% yield). ^{1}H-NMR (CD_3CN): δ 80.67, 65.78, 64.29, 63.25, 53.03, 47.52, 32.37, 24.80, 20.33, 19.42, 13.40, 11.65, 9.19, 8.22, 7.38, 6.22, 4.08, 3.50, 2.33, 1. 17, 0.45, -0.45, -2.33, -14.63, -32.73. LDI-MS: *m/z* = 757.6 $[M-H]^+$. UV-vis (CH_3CN):

λ_{max} = 405 nm, e = 2650 M^{-1} cm^{-1}. *Anal Calc*. for ($C_{32}H_{34}B_2F_8FeN_6OS$): Predicted: C, 56.68, H, 4.54; N, 9.01; Found: C, 56.53; H 4.72; N, 9.44

Deprotection of N3Py^{amide}SR and N3Py^{amide2Ph}SR.

Procedure adapted from Ref [41]. The protected ligand (1.1 mmol) was dissolved in THF before tBuOK (5.0 equiv, 5.5 mmol) was added dropwise as a suspension in THF. The solution changed in color from pale orange, to dark red, and finally a very dark brown. The mixture was allowed to stir at r.t. for 2 h before being acidified with 4 M HCl and concentrated. The residue was dissolved in EtOH and placed in the freezer overnight. The solids were filtered off and the filtrate was concentrated before being dissolved in CH_2Cl_2. A solution of $NaHCO_3$ (aq) was added, and the organic layer was separated, dried, and concentrated. The crude product was then purified by column chromatography on neutral alumina (EtOAc/Hexanes) to give the pure product (~15% yield).

[Fe^{II}(N3Py^{amide,2Ph}S)(CH$_3$CN)](BF$_4$)$_2$ and [(Fe(N3Py^{amide2Ph}S)$_2$Fe(CH$_3$CN)$_3$].

The deprotected ligand, N3Py^{amide,2Ph}S(H) (250 mg, 0.38 mmol), was dissolved in 7 mL THF, before $Fe(BF_4)_2$ (130 mg, 0.38 mmol) was added. The mixture was allowed to stir overnight before being concentrated. The residue was dissolved in CH3CN then filtered, and vapor diffusion of Et_2O into this solution gave small amounts of crystalline [Fe^{II}(N3Py^{amide,2Ph}S)(CH$_3$CN)](BF$_4$)$_2$ or [Fe(N3Py^{amide,2Ph}S)$_2$Fe(CH$_3$CN)$_3$]. These structures were not refined, and the compounds were not pursued for further characterization.

5. 3. Results and Discussion

Synthesis and Characterization

Metallation of the ligand N3PySR with $Fe(BF_4)_2$ in MeCN, followed by vapor diffusion of Et_2O into the resulting solution gave dark red blocks of $[Fe^{II}(N3PySR)](BF_4)_2$ in 68% yield (**Scheme 5. 1**). The structure of the cation of $[Fe^{II}(N3PySR)](BF_4)_2$ is shown in **Figure 5. 2**, and structural data are summarized in **Table 5. 1**. The ferrous ion is bound in a pseudo-octahedral geometry by three pyridyl and an aryl sulfide donor in the equatorial plane, with a tertiary nitrogen donor and solvent nitrile molecule occupying the axial positions. The Fe-N bond distances (1.9260(14)-1.9969(13) Å, **Table 5. 2**) are consistent with a low spin (l.s.) iron(II) center. The spin state was also confirmed by observation of a diamagnetic ^{1}H-NMR spectrum in $CDCl_3$.

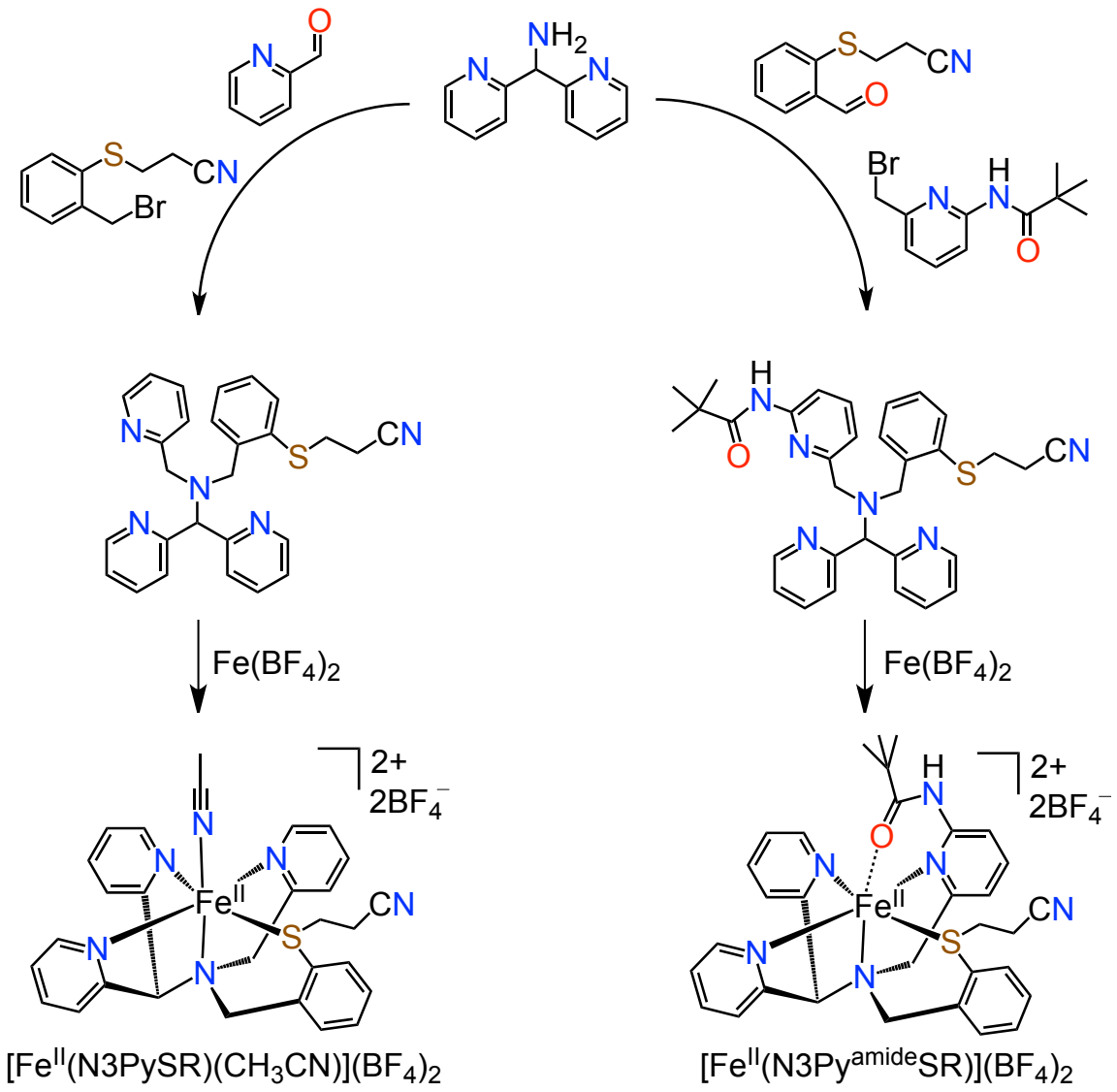

Scheme 5. 1. Convergent syntheses of $[Fe^{II}(N3PySR)(CH_3CN)](BF_4)_2$ and $[Fe^{II}(N3Py^{amide}SR)](BF_4)_2$.

Metallation of the ligand $N3Py^{amide}SR$ with $Fe(BF_4)_2$, followed by vapor diffusion of Et_2O into the resulting dark orange solution yielded dark red crystals of $[Fe^{II}(N3Py^{amide}SR)](BF_4)_2$ in 88% yield. The structure of the cation of $[Fe^{II}(N3Py^{amide}SR)](BF_4)_2$ (**Figure 5. 3**) was reported previously and is repeated here for comparison with the other complexes.[33] As in $[Fe^{II}(N3PySR)](BF_4)_2$, the ferrous ion is bound in a pseudo-octahedral geometry with three pyridyl and one aryl sulfide donor in

the equatorial plane, with the tertiary nitrogen donor occupying the axial position. In $[Fe^{II}(N3Py^{amide}SR)](BF_4)_2$ however, the amide ligand has displaced the bound solvent molecule and is coordinated through the amide oxygen.

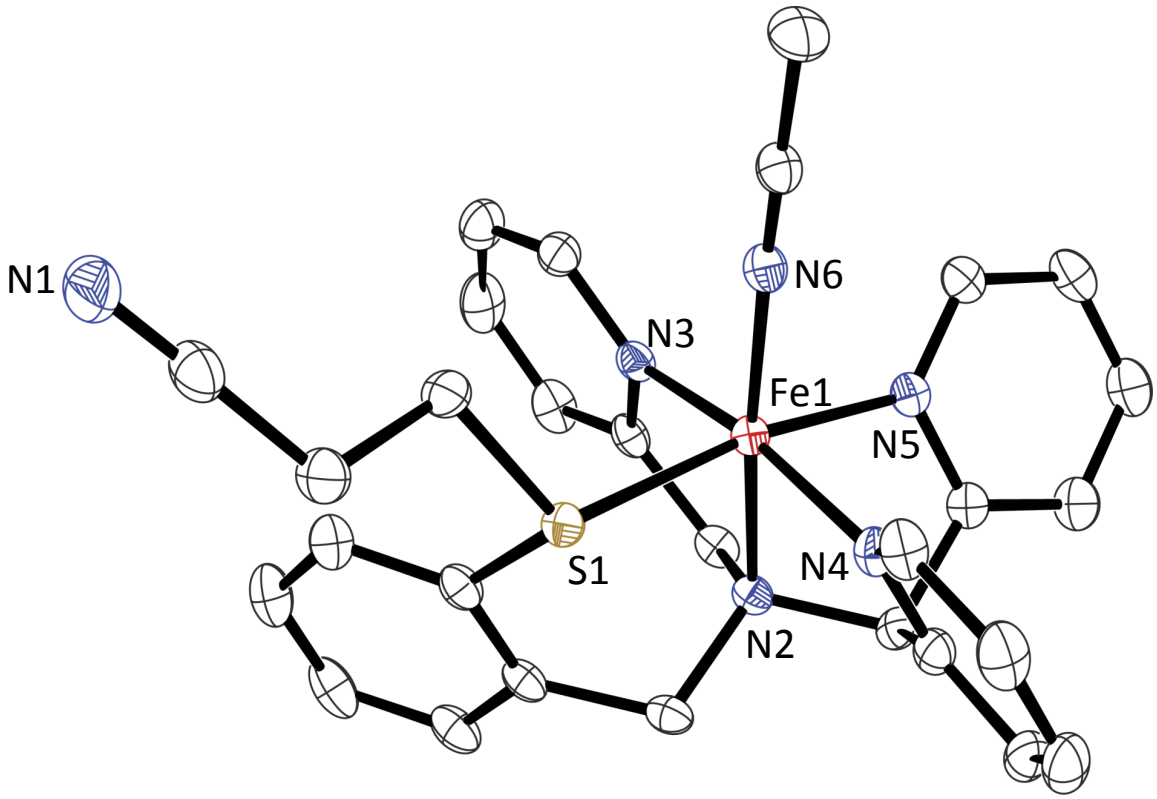

Figure 5. 2. Displacement ellipsoid plot of the cation of $[Fe^{II}(N3PySR)](BF_4)_2$ shown at the 50% probability level. H-atoms are removed for clarity.

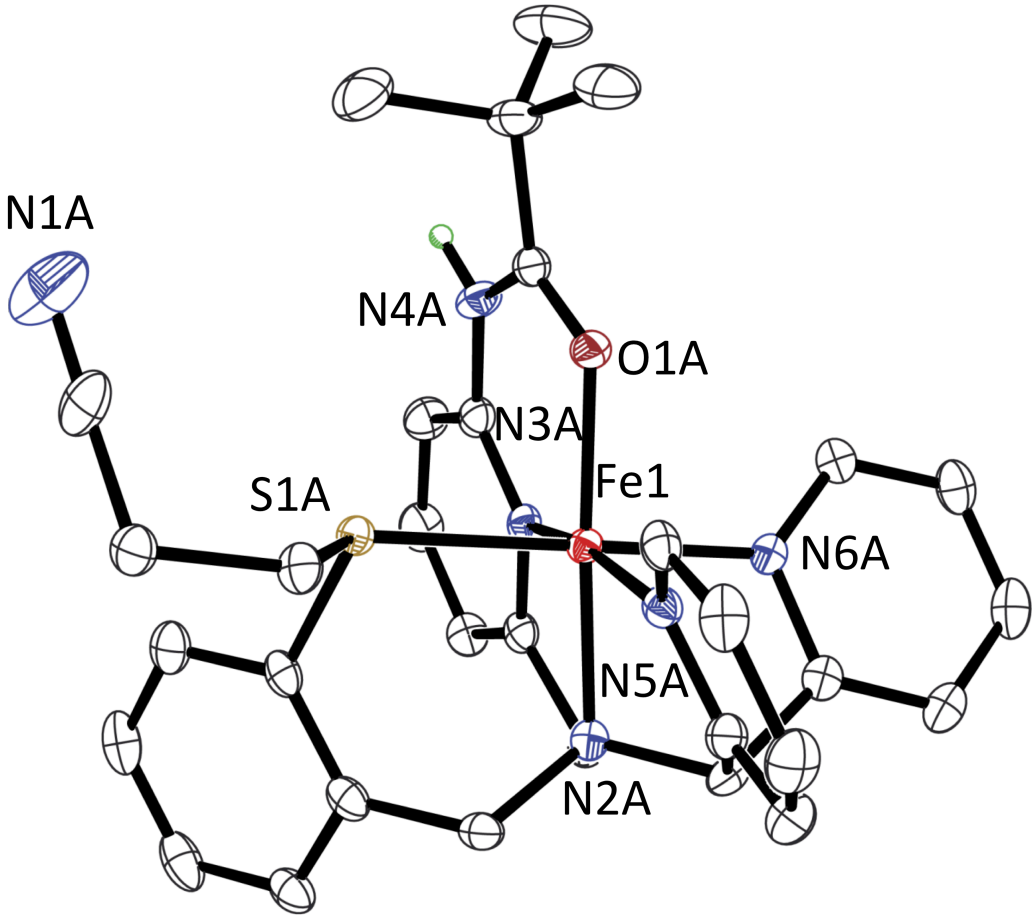

Figure 5. 3. Displacement ellipsoid plot for the cation of $[Fe^{II}(N3Py^{amide}SR)](BF_4)_2$ shown at the 50% probability level. H-atoms, except the amide N-H, are removed for clarity.

When the propionitrile protecting group of the ligand for $[Fe^{II}(N3PySR)](BF_4)_2$ is removed prior to metal binding, the corresponding Fe^{II}-thiolate complex is accessed, which has been shown to undergo sulfur oxidation in the presence of O_2.[30] However, in $[Fe^{II}(N3PySR)](BF_4)_2$ and $[Fe^{II}(N3Py^{amide}SR)](BF_4)_2$, the sulfide donor appears to make these complexes stable toward O_2, with no visible decomposition under aerobic conditions.

Prior to attempting to make iron-peroxo complexes from $[Fe^{II}(N3PySR)](BF_4)_2$ and $[Fe^{II}(N3Py^{amide}SR)](BF_4)_2$, we wanted to test the substitution chemistry of $[Fe^{II}(N3Py^{amide}SR)](BF_4)_2$ toward anionic donors to show that the amide group could be

displaced and reoriented into a favourable hydrogen-bonding position. We also wanted to confirm whether hydrogen bonding would be favored with the anionic ligands found in the axial position. Stirring of $[Fe^{II}(N3Py^{amide}SR)](BF_4)_2$ with 1.0 equiv NaN_3 in MeCN, followed by vapor diffusion of Et_2O into the solution produced a mixture of crystals suitable for X-ray structure determination. A small amount of yellow crystals could be manually separated from the bulk orange material, and X-ray structure determination revealed the new compound, $[Fe^{II}(N3Py^{amide}SR)(F/N_3)](BF_4)_2$. The structure of $[Fe^{II}(N3Py^{amide}SR)(F/N_3)](BF_4)_2$ clearly shows that the amide C=O donor has been displaced, and there is a mixture of F^- (67%) and N_3^- (33%) anions that are occupying the desired axial position. The Fe^{II}-N(py) distances (2.1703(16) – 2.2448(13) Å) for **3** are indicative of a hs ferrous center, and the difference in Fe-F and Fe-N_3 distances allows for reliable determination of the N_3^- ligand despite its low occupancy. The N_3^--containing component of $[Fe^{II}(N3Py^{amide}SR)(F/N_3)](BF_4)_2$ is shown in **Figure 5. 4**, as it more closely resembles the structure of an anionic peroxo ligand. The source of fluoride for the F^--containing component of $[Fe^{II}(N3Py^{amide}SR)(F/N_3)](BF_4)_2$ can be assigned to BF_4^-. This structure shows that the axial amide carbonyl is labile, and can be displaced by anionic donors. The structure of $[Fe^{II}(N3Py^{amide}SR)(F/N_3)](BF_4)_2$ also shows that the pendant amide is positioned such that H-bonding interactions to anionic ligands are favoured (N6---N7 = 2.914(16) Å, N6---F1 = 2.784(5) Å, N6-H-N7 = 174(2)°, N6-H-F1 = 170(2)°). This complex provides good evidence that Fe-OO(H/R) complexes will likely exhibit the same H-bonding interaction.

Table 5. 1. Summary of the Crystallographic data for $[Fe^{II}(N3PySR)](BF_4)_2$, $[Fe^{II}(N3Py^{amide}SR)(F/N_3)](BF_4)_2$ and $[Fe^{II}(N3Py^{amide,2Ph}SR)](BF_4)_2$.

Complex	$[Fe^{II}(N3PySR)](BF_4)_2$	$[Fe^{II}(N3Py^{amide}SR)(F/N_3)](BF_4)_2 \bullet CH_3CN$	$[Fe^{II}(N3Py^{amide,2Ph}SR)](BF_4)_2$
Formula	$C_{29}H_{28}B_2F_8FeN_6S$	$C_{34}H_{37}BF_{4.67}FeN_8OS$	$C_{44}H_{42}B_2F_8FeN_6OS$
Formula weight	722.10	761.13	932.37
T (K)	110	110	110
Color, morphology	dark red, irregular shape	yellow, lath	yellow, block
Class	triclinic	orthorhombic	triclinic
Space group	*P*-1	*Pbcn*	*P-1*
a (Å)	10.6689(2)	35.1087(4)	10.4419(3)
b (Å)	12.0355(2)	10.08753(9)	14.5834(3)
c (Å)	13.0403(3)	19.9277(2)	17.2950(4)
α (°)	80.5885(18)	N/A	90.6304(19)
β (°)	88.0024(18)	N/A	105.768(2)
γ (°)	68.543(2)	N/A	106.791(2)
V (Å^3)	1536.85(5)	7057.59(12)	2415.01(10)
ϱ (g cm^{-3})	1.560	1.433	1.282
μ (mm^{-1})	0.640	4.546	0.425
$(\sin\theta/\lambda)_{max}$ (Å^{-1})	0.65	0.62	0.62
No. reflections collected	35673	44026	29736
No. unique reflections	7051	6942	9709
R_{int}	0.0247	0.0273	0.0305
No. variable parameters	425	511	648
R_1 [$I > 2\sigma(I)$]	0.0325	0.0322	0.0401
wR_2 [$I > 2\sigma(I)$]	0.0877	0.0791	0.1117
R_1 [all data]	0.0373	0.0366	0.0475
R_2 [all data]	0.0905	0.0821	0.1155
Goodness-of-fit (GOF) on F^2	1.061	1.026	1.102
Largest difference in hold and peak (e A^{-3})	-0.50, 0.63	-0.33, 0.63	-0.46, 0.58

Table 5. 2. Selected bond distances (Å) and angles (°) for $[Fe^{II}(N3PySR)](BF_4)_2$.

Bond lengths		Bond angles	
Fe1 N6	1.9260(14)	N6 Fe1 N4	94.41(6)
Fe1 N4	1.9569(13)	N6 Fe1 N3	97.35(6)
Fe1 N3	1.9619(13)	N4 Fe1 N3	168.23(6)
Fe1 N5	1.9790(13)	N6 Fe1 N5	94.24(5)
Fe1 N2	1.9969(13)	N4 Fe1 N5	86.41(5)
Fe1 S1	2.2848(4)	N3 Fe1 N5	92.09(5)
		N6 Fe1 N2	175.10(5)
		N4 Fe1 N2	83.35(5)
		N3 Fe1 N2	84.88(5)
		N5 Fe1 N2	81.29(5)
		N6 Fe1 S1	93.13(4)
		N4 Fe1 S1	87.26(4)
		N3 Fe1 S1	92.70(4)
		N5 Fe1 S1	170.63(4)
		N2 Fe1 S1	91.12(4)

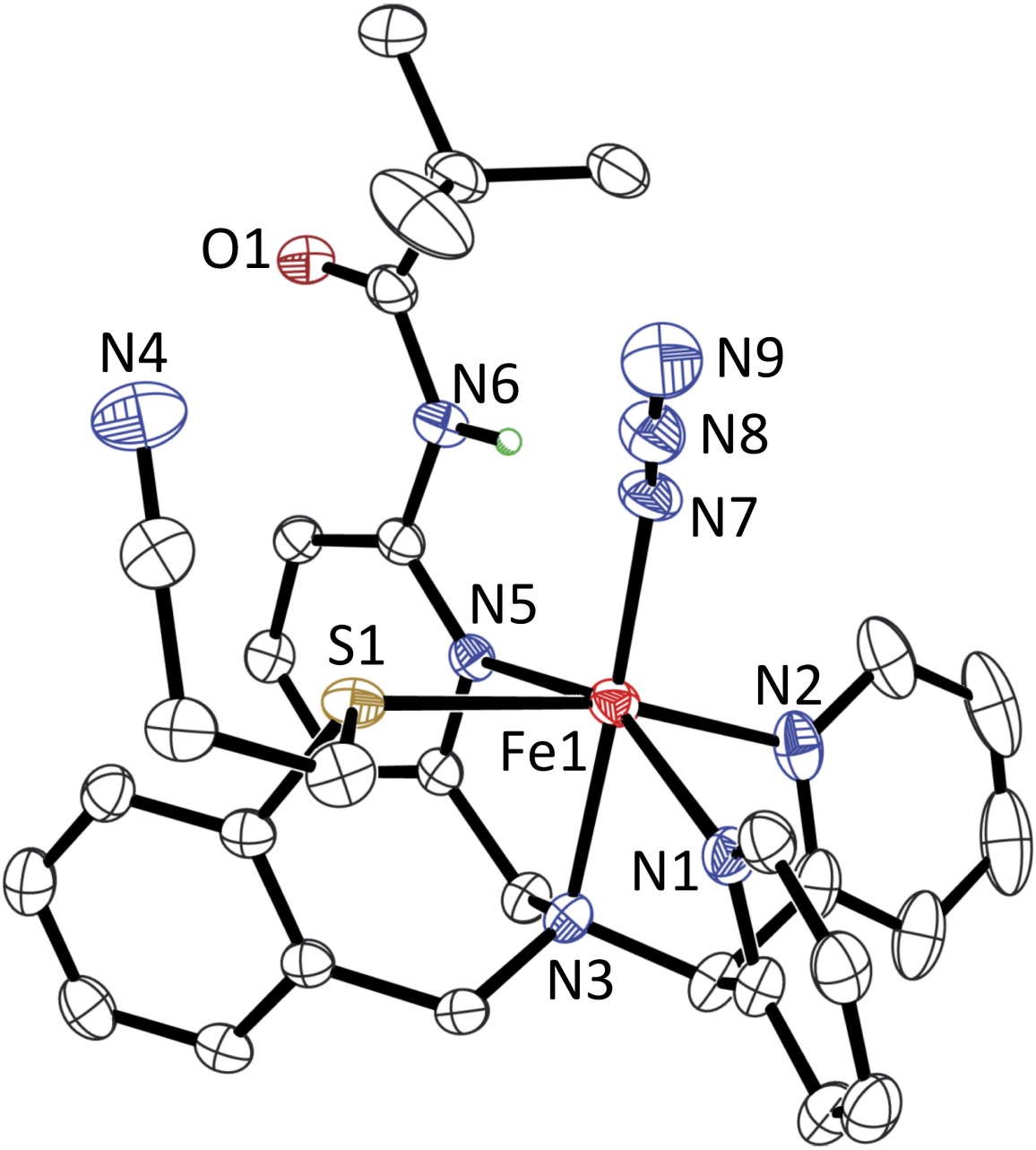

Figure 5. 4. Displacement ellipsoid plot of the N_3^--containing disordered component of the cation of $[Fe^{II}(N3Py^{amide}SR)(F/N_3)](BF_4)_2$ shown at the 50% probablility level. H-atoms, except the amide N-H, are removed for clarity.

Table 5. 3. Selected bond lengths (Å) and angles (°) for $[Fe^{II}(N3Py^{amide}SR)(F/N_3)](BF_4)_2$.

Bond lengths		Bond Angles	
Fe1 F1	1.850(4)	F1 Fe1 N2	98.05(14)
Fe1 N7	2.063(14)	N7 Fe1 N2	105.6(5)
Fe1 N2	2.1703(16)	F1 Fe1 N1	108.09(14)
Fe1 N1	2.1892(14)	N7 Fe1 N1	102.8(4)
Fe1 N3	2.2012(14)	N2 Fe1 N1	82.68(6)
Fe1 N5	2.2448(13)	F1 Fe1 N3	173.68(12)
Fe1 S1	2.6007(5)	N7 Fe1 N3	176.6(4)
		N2 Fe1 N3	77.62(6)
		N1 Fe1 N3	76.14(5)
		F1 Fe1 N5	98.62(14)
		N7 Fe1 N5	103.3(4)
		N2 Fe1 N5	95.76(5)
		N1 Fe1 N5	153.22(5)
		N3 Fe1 N5	77.41(5)
		F1 Fe1 S1	94.88(14)
		N7 Fe1 S1	87.7(5)
		N2 Fe1 S1	166.53(5)
		N1 Fe1 S1	96.89(4)
		N3 Fe1 S1	89.18(4)
		N5 Fe1 S1	78.52(4)

Fe^{III}-OOH Complexes

The ferrous complex $[Fe^{II}(N3PySR)](BF_4)_2$ reacts with excess H_2O_2 at 25 °C (**Figure 5. 5**) to generate a new transient red species ($t_{½}$ = 1 min). Monitoring the reaction by UV-vis shows isosbestic conversion of the peaks corresponding to $[Fe^{II}(N3PySR)](BF_4)_2$ (360, 430 nm), into a new spectrum (λ_{max} = 542 nm, ε = 1000 M^{-1} cm^{-1}). The peak at 542 nm is characteristic of a hydroperoxo-to-iron(III) LMCT band. Attempts to trap this species by generation at -40 °C were unsuccessful, leading only to decomposition, with no observable UV-vis peaks corresponding to the new species. Samples of for analysis by EPR and resonance Raman were therefore prepared at 25 °C and flash-frozen after mixing for 1 min. From EPR and rR (*vide infra*) the new species is assigned as the Fe^{III}-OOH complex $[Fe^{III}(OOH)(N3PySR)]^{2+}$.

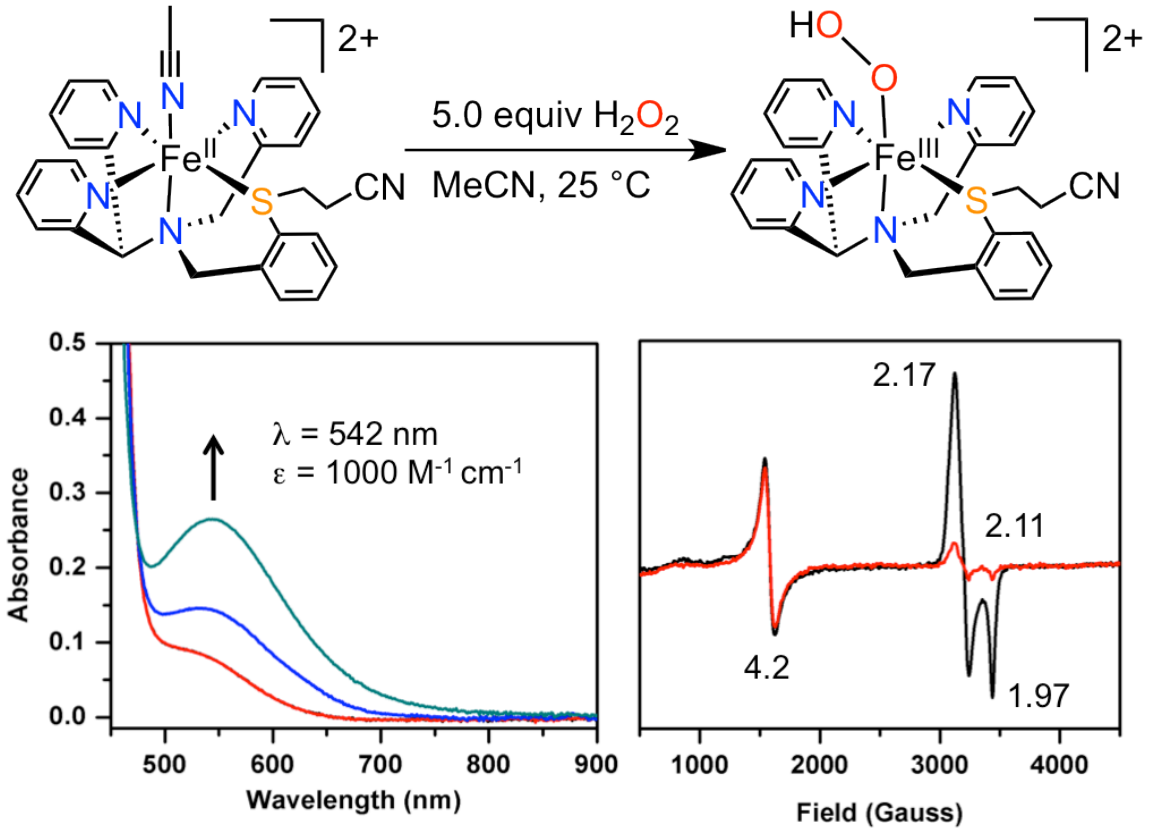

Figure 5. 5. Formation of $[Fe^{III}(N3PySR)(OOH)]^{2+}$ (top). Changes in the electronic absorption spectrum for the reaction of $[Fe^{III}(N3PySR)](BF_4)_2$ + H_2O_2 in CH_3CN, at 25 °C, red = 0 s, blue = 30 s, green = 60 s (bottom left). X-band EPR spectra of the reaction mixture of $[Fe^{III}(N3PySR)](BF_4)_2$ + H_2O_2, flash frozen after mixing at 25 °C for 1 min (black line) and 3 min (red line) (bottom right). EPR parameters: T = 77 K, Frequency = 9.46 GHz, Power = 2.01 mW.

The ferrous complex $[Fe^{II}(N3Py^{amide}SR)](BF_4)_2$ reacts with excess H_2O_2 at -40 °C (**Figure 5. 6**), and changes in color from orange to deep purple over the course of 30 min. The new purple species persists for at least several hours at -40 °C, but immediately decays upon warming to 25 °C. Monitoring by low-temperature UV-vis spectroscopy shows isosbestic conversion from $[Fe^{II}(N3Py^{amide}SR)](BF_4)_2$ (350, 450 nm) to a new peak (λ_{max} = 567 nm, ε = 900 M^{-1} cm^{-1}) that is characteristic of a hydroperoxo-to-iron(III)

LMCT band. The EPR and rR spectra (*vide infra*), confirmed that the new species is the Fe^{III}-OOH complex, $[Fe^{III}(N3Py^{amide}SR)(OOH)]^{2+}$.

The X-band EPR spectra of $[Fe^{III}(N3PySR)(OOH)]^{2+}$ and $[Fe^{III}(N3Py^{amide}SR)(OOH)]^{2+}$ are shown in **Figure 5. 5** and **Figure 5. 6**, respectively. Both complexes show axial spectra corresponding to ls iron(III) centers with signals at g = 2.17, 2.11, 1.97, for $[Fe^{III}(N3PySR)(OOH)]^{2+}$ and g = 2.20, 2.16, 1.95, for $[Fe^{III}(N3Py^{amide}SR)(OOH)]^{2+}$. These values are a good match for Fe^{III}-OOH complexes reported in the literature.[18] The mononuclear complex $[Fe^{III}(N4Py)(OOH)]^{2+}$ in methanol has a signal at g = 2.17, 2.12 and 1.97,[13] while the TPA analogue $[Fe^{III}(TPA)(OOH)]^{2+}$ affords a spectrum with g = 2.17, 2.15 and 1.96 in acetone/acetonitrile.[34] EPR spectra of reaction mixtures of $[Fe^{III}(N3PySR)(OOH)]^{2+}$, taken at different timepoints (1 – 5 min) clearly show the rapid decomposition of the ls-Fe^{III} signal at room temperature. Samples frozen after 1 min show a relatively strong ls-Fe^{III} signal along with an additional signal at g = 4.2. After 3 minutes, the ls-Fe^{III} signal appears to be mostly decayed, and after 5 min no ls-Fe^{III} signal is observed. The peak at g = 4.2 does not increase with the decay of the Fe^{III}-OOH feature, indicating it is not a decomposition product and is likely a byproduct of Fe^{III}-OOH formation. The peak at g = 4.2 is much more prominent in $[Fe^{III}(N3PySR)(OOH)]^{2+}$ relative to that seen in the spectrum of $[Fe^{III}(N3Py^{amide}SR)(OOH)]^{2+}$, which was prepared at -40 °C and frozen after 30 min, allowing for full formation of $[Fe^{III}(N3Py^{amide}SR)(OOH)]^{2+}$ with much less possibility for decay.

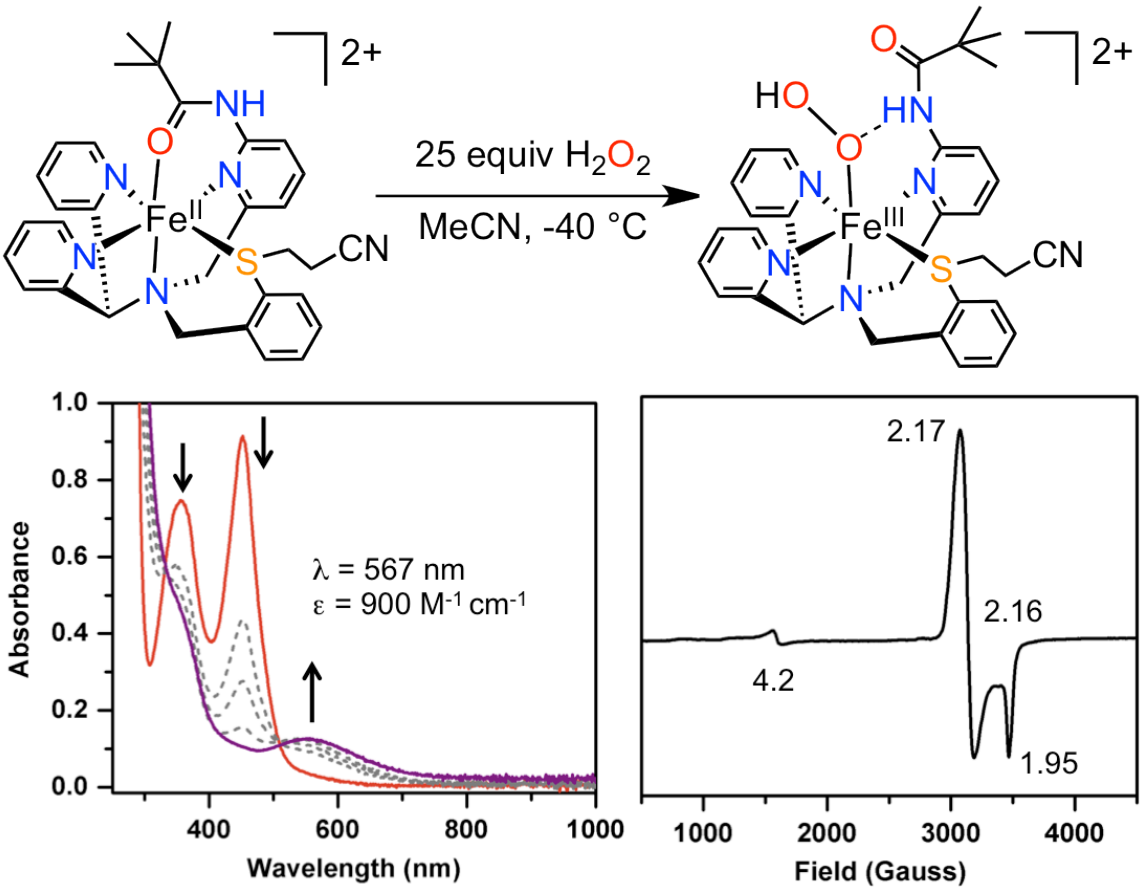

Figure 5. 6. Formation of $[Fe^{III}(OOH)(N3Py^{amide}SR)]^{2+}$ (top). Changes in the electronic absorption spectrum for the reaction of $[Fe^{II}(N3Py^{amide}SR)](BF_4)_2 + H_2O_2$ in CH_3CN, over 30 min at -40 °C (bottom left)**.** X-band EPR spectrum of the reaction mixture of $[Fe^{II}(N3Py^{amide}SR)](BF_4)_2 + H_2O_2$, flash frozen after mixing at -40 °C for 30 min. EPR parameters: T = 77 K, Frequency = 9.46 GHz, Power = 2.01 mW.

The identity of the Fe^{III}-OOH complex $[Fe^{III}(OOH)(N3PySR)]^{2+}$ was confirmed by RR spectroscopy, and the spectra are shown in **Figure 5. 7**. Frozen CD_3CN solutions were analyzed at 110 K with a 568 nm laser excitation to avoid overlap of RR bands with non-resonant vibrations from CH_3CN. The RR spectra of $[Fe^{III}(OOH)(N3PySR)]^{2+}$ show a cluster of bands in the ν(Fe-O) region with prominent bands at 615, 629, 647 and 664 cm^{-1}, and two bands at 787 and 809 cm^{-1} in the ν(O-O) region (**Figure 5. 7a**).

Labeled samples prepared with $H_2{}^{18}O_2$ exhibits greatly simplified spectra with unique ν(Fe-O) and ν(O-O) modes at 590 and 763 cm^{-1}, respectively. RR spectra of samples prepared with D_2O_2 in the presence of excess D_2O also show a single set of ν(Fe-O) and ν(O-O) bands at 607 cm^{-1} and 809 cm^{-1}. These data clearly indicate that the complexity of the RR spectra of unlabeled $[Fe^{III}(OOH)(N3Py^{amide}SR)]^{2+}$ results from vibrational coupling of the Fe-O-O-H unit with internal vibrations of the (N3PyS) ligand. Using Hooke's law to calculate the ν(^{16}O-^{16}O) frequency based on an isolated diatomic oscillator with a ν(^{18}O-^{18}O) at 763 cm^{-1} leads to a 809 cm^{-1} value that matches the ν(O-O) mode seen in D_2O and the sharper component of the doublet observed with unlabeled $[Fe^{III}(OOH)(N3PySR)]^{2+}$. Accordingly, the 809 cm^{-1} band is assigned to the ν(Fe-O) mode of $[Fe^{III}(OOH)(N3PySR)]^{2+}$. Using the same approach to interpret the RR bands observed in the ν(Fe-O) region is less successful,[35] presumably because of admixture between Fe-O stretch and Fe-O-O bend vibrations, as seen previously with other Fe(III)-hydroperoxo complexes.[13,36]

The pendant amide complex $[Fe^{III}(N3Py^{amide}SR)(OOH)]^{2+}$ was also studied by RR spectroscopy under the same conditions (**Figure 5. 7**b). In contrast with $[Fe^{III}(OOH)(N3PySR)]^{2+}$, the RR spectra of $[Fe^{III}(N3Py^{amide}SR)(OOH)]^{2+}$ shows no evidence of vibrational coupling and assigning the ν(Fe-O) and ν(O-O) bands is straightforward. The unlabeled complex shows a single ν(O-O) mode at 800 cm^{-1} that downshifts to 756 cm^{-1} with samples prepared with $H_2{}^{18}O_2$ and that is unchanged in samples prepared with D_2O_2 in the presence of excess D_2O. A single band at 612 cm^{-1} in the ν(Fe-O) region shifts to 593 cm^{-1} with $H_2{}^{18}O_2$ and to 607 cm^{-1} with D_2O_2. Comparing ν(Fe-O) and ν(O-O) frequencies for $[Fe^{III}(OOH)(N3PySR)]^{2+}$ and

$[Fe^{III}(N3Py^{amide}SR)(OOH)]^{2+}$ with previously characterized Fe(III)-OOH complexes (**Table 5. 4**), confirms their identity and suggests that the amide H-bond donor group exerts limited influence on the Fe-O-O unit.

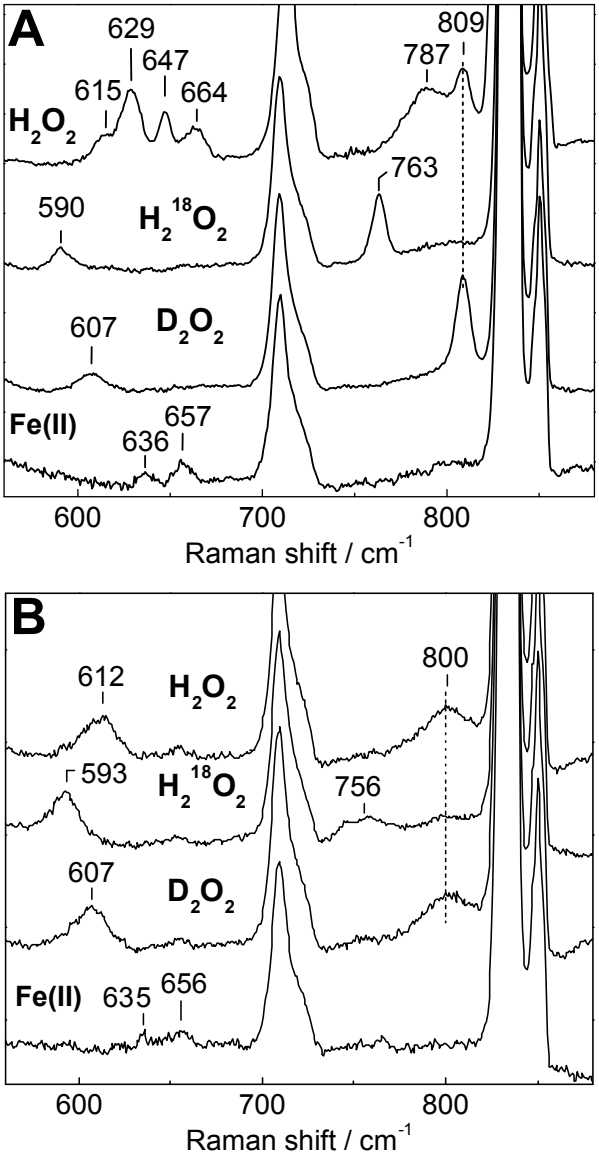

Figure 5. 7. Resonance Raman spectra for $[Fe^{III}(OOH)(N3PySR)]^{2+}$ (a) and $[Fe^{III}(OOH)(N3Py^{amide}SR)]^{2+}$ (b). Black = (hydro)peroxo, Red = Deuterium-incorporated, Blue = ^{18}O labeling, Green = Starting material (a = $[Fe^{II}(N3PySR)](BF_4)_2$, b = $Fe^{II}(N3Py^{amide}SR)](BF_4)_2$.

Table 5. 4. Comparison of RR data for ls non-heme Fe^{III}-OOH complexes

Complex	ν(Fe-O), [ν(O-O)]	$\Delta^{18}O_2$	ΔD_2O
$[Fe^{III}(N3PySR)(OOH]^{2+}$	615, [809]	-25, [-46]	-8, [0]
$[Fe^{III}(N3Py^{amide}SR)(OOH)]^{2+}$	612, [800]	-19, [-44]	-5, [0]
[a]$[Fe^{III}(N4Py)(OOH)]^{2+}$	632, [790]	-16, [-44]	-5, [0]
[b]$[Fe^{III}(TPA)(OOH)]^{2+}$,	624, [803]	-19, [44]	-3, [0]

[a]Ref 13, [b]Ref 37

Comparison of the RR data for complexes $[Fe^{III}(N3PySR)(OOH]^{2+}$ and $[Fe^{III}(N3Py^{amide}SR)(OOH)]^{2+}$ with $[Fe^{III}(N4Py)(OOH)]^{2+}$ reveals a 19 ±2 cm^{-1} downshift in ν(Fe-O), and a 10 to 19 cm^{-1} (for $[Fe^{III}(N3Py^{amide}SR)(OOH)]^{2+}$ and $([Fe^{III}(N3PySR)(OOH]^{2+}$, respectively) upshift of the Δν(O-O) upon incorporation of the thioether donor. This effect of the equatorial sulfide donor on ν(O-O) contrasts a previous study, where the replacement of an axial triflate (OTf^-) ligand with aryl-thiolate donors (ArS^-) in hs $[Fe^{III}(Me_4[15]aneN_4)(SAr)(OOR)]^+$ complexes was shown to have little influence on ν(O-O) (Δν(O-O) = 1 cm^{-1}).[23] In contrast, the effect of the equatorial sulfide donor on ν(Fe-O) in $[Fe^{III}(N3PySR)(OOH]^{2+}$ and $[Fe^{III}(N3Py^{amide}SR)(OOH)]^{2+}$ is similar to the effect previously seen for the aryl-thiolate complexes, in which inclusion of sulfur induced a lowering of this band.

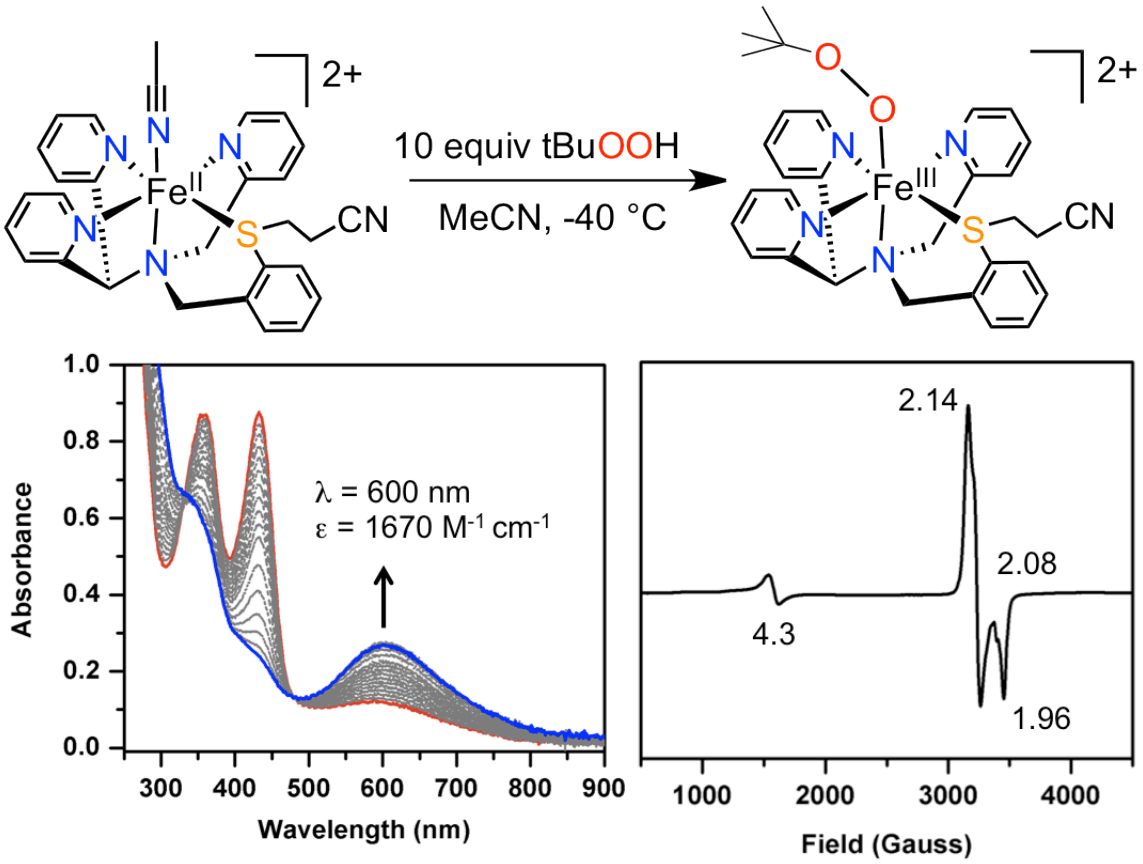

Figure 5. 8. Formation of $[Fe^{III}(OOtBu)(N3PySR)]^{2+}$ (top). Changes in the electronic absorption spectrum for the reaction of $[Fe^{II}(N3PySR)](BF_4)_2$ + tBuOOH in CH_3CN, over 10 min at -40 °C (bottom left)**.** X-band EPR spectrum of the reaction mixture of $[Fe^{II}(N3PySR)](BF_4)_2$ + tBuOOH, flash frozen after mixing at -40 °C for 15 min. EPR parameters: T = 77 K, Frequency = 9.46 GHz, Power = 2.01 mW.

Fe^{III}-OO^{t}Bu Complexes

The ferrous complex $[Fe^{II}(N3PySR)](BF_4)_2$ reacts with 10 equiv of ^{t}BuOOH (**Figure 5. 8**) at -40 °C in MeCN to give a new deep blue species that persists at low temperature for 15 – 20 min before slowly decaying. Monitoring the reaction by UV-vis spectroscopy shows the isosbestic conversion of the peaks corresponding to $[Fe^{II}(N3PySR)](BF_4)_2$, into a new spectrum ($\lambda_{max}$ = 600 nm, ε = 1670 $M^{-1}cm^{-1}$) that is

characteristic of an alkylperoxo-to-iron(III) LMCT band and is in good agreement with similar compounds reported in the literature.[14,29] The UV-vis spectra reveal that $[Fe^{II}(N3PySR)](BF_4)_2$ reacts with tBuOOH to form the new species within 10 min, but is only stable for a short period and begins to decay after 15 min. The new species is assigned as the alkylperoxo complex $[Fe^{III}(OOtBu)(N3PySR)]^{2+}$.

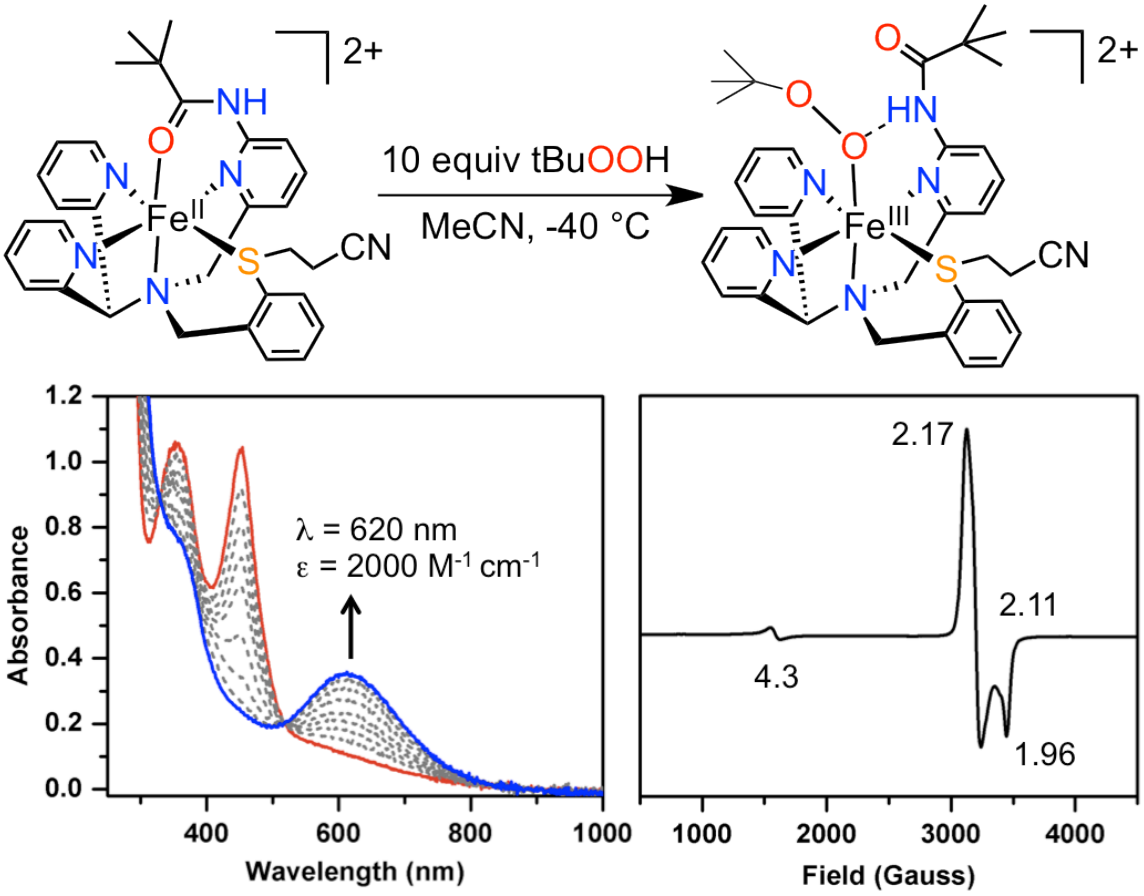

Figure 5. 9. Formation of $[Fe^{III}(OOtBu)(N3Py^{amide}SR)]^{2+}$ (top). Changes in the electronic absorption spectrum for the reaction of $[Fe^{II}(N3Py^{amide}SR)](BF_4)_2$ + tBuOOH in CH_3CN, over 10 min at -40 °C (bottom left)**.** X-band EPR spectrum of the reaction mixture of $[Fe^{II}(N3Py^{amide}SR)](BF_4)_2$ + tBuOOH, flash frozen after mixing at -40 °C for 15 min. EPR parameters: T = 77 K, Frequency = 9.46 GHz, Power = 2.01 mW.

The ferrous complex $[Fe^{II}(N3Py^{amide}SR)](BF_4)_2$ also reacts with tBuOOH at -40 °C to give a deep blue solution, similar to that seen for $[Fe^{II}(N3PySR)](BF_4)_2$. This new complex (**Figure 5. 9**) is formed via isosbestic conversion from $[Fe^{II}(N3Py^{amide}SR)](BF_4)_2$, to a new spectrum characteristic for Fe^{III}-OOR complexes (λ_{max} = 625 nm, ε = 2000 $M^{-1}cm^{-1}$) within 15 min. As seen for $[Fe^{III}(OOtBu)(N3PySR)]^{2+}$, the new complex is not stable at -40 °C, and slowly decays to a broad, featureless spectrum over 1 h. This species is assigned as the ferric-alkylperoxo complex, $[Fe^{III}(OO^tBu)(N3Py^{amide}SR)]^{2+}$.

It has been shown that a lowering in energy of peroxo-to-iron(III) charge transfer bands can be correlated with an increasing number of pyridine ligands bound to the iron center, as the π-accepting ability of py ligands lowers the energy of LMCT bands.[18,38] It is therefore interesting to compare the energy of the LMCT band for $[Fe^{III}(OOtBu)(N3PySR)]^{2+}$ and $[Fe^{III}(OOtBu)(N3Py^{amide}SR)]^{2+}$ to the parent $[Fe^{III}(OOtBu)(N4Py)]^{2+}$ compound (560 nm, 2400 M^{-1} cm^{-1}).[15] Relative to N4Py, the sulfide-ligated complexes exhibit bands that are shifted to lower energy by 40 nm for $[Fe^{III}(OOtBu)(N3PySR)]^{2+}$, and 60 nm for $[Fe^{III}(OO^tBu)(N3Py^{amide}SR)]^{2+}$. These shifts indicate that replacement of a pyridine with a sulfide donor causes a significant lowering of the energy of the LMCT band. This change is consistent with stabilization of the metal acceptor orbital caused by the weaker ligand field presented by the sulfide donor. In addition, the LMCT bands for both the (hydro) and (alkyl)peroxo-iron(III) complexes are further stabilized by the addition of the H-bond donor, as evidenced by the ~20 nm red-shift in the absorption band for both $[Fe^{III}(OOH)(N3Py^{amide}SR)]^{2+}$ and

$[Fe^{III}(OO^tBu)(N3Py^{amide}SR)]^{2+}$, relative to the non H-bonded $[Fe^{III}(OOH)(N3PySR)]^{2+}$ and $[Fe^{III}(OOtBu)(N3PySR)]^{2+}$.

The X-band EPR spectra for $[Fe^{III}(OO^tBu)(N3PySR)]^{2+}$ and $[Fe^{III}(OO^tBu)(N3Py^{amide}SR)]^{2+}$ (**Figure 5. 8** and **Figure 5. 9**) show that the alkylperoxo species are also low-spin iron(III) with g values of 2.14, 2.08, 1.96 ($[Fe^{III}(OO^tBu)(N3PySR)]^{2+}$), and 2.17, 2.11, 1.96 ($[Fe^{III}(OO^tBu)(N3Py^{amide}SR)]^{2+}$), that are in good agreement with similar compounds previously reported in the literature.[14,28,29] As seen with the hydroperoxo complexes, spectra of $[Fe^{III}(OO^tBu)(N3PySR)]^{2+}$ and $[Fe^{III}(OO^tBu)(N3Py^{amide}SR)]^{2+}$ do show a small peak at g = 4.3, consistent with a small amount of high-spin decomposition product.

Resonance Raman spectra of $[Fe^{III}(OO^tBu)(N3PySR)]^{2+}$ and $[Fe^{III}(OO^tBu)(N3Py^{amide}SR)]^{2+}$ were collected on frozen samples in CD_3CN at 110 K with 467 nm laser excitation. Shown in **Figure 5. 10**, the spectrum of $[Fe^{III}(OO^tBu)(N3PySR)]^{2+}$ shows two resonance-enhanced vibrations at 700 and 797 cm^{-1} that are in the expected range for ν(Fe-O) and ν(O-O), respectively. The spectrum of $[Fe^{III}(OO^tBu)(N3Py^{amide}SR)]^{2+}$ shows similar bands at 691 and 797 cm^{-1}. Unfortunately, no rR spectrum is reported for $[Fe^{III}(N4Py)(OOtBu)]^{2+}$, but these data do closely match reported results for $[Fe^{III}(TPA)(OH_n)(OOtBu)]^{n+}$ (**Table 5. 5**) and the ν(O-O) values below 800 cm^{-1} are consistent with the ls configuration of $[Fe^{III}(OO^tBu)(N3PySR)]^{2+}$ and $[Fe^{III}(OO^tBu)(N3Py^{amide}SR)]^{2+}$.[22] While there is no influence exerted by the presence of the H-bond donor on the O-O bond in $[Fe^{III}(OO^tBu)(N3Py^{amide}SR)]^{2+}$, the Fe-O bond is downshifted by 9 cm^{-1} relative to $[Fe^{III}(OO^tBu)(N3PySR)]^{2+}$. We attempted to exchange the amide N-H for N-D in complexes $[Fe^{III}(OOH)(N3Py^{amide}SR)]^{2+}$ and

$[Fe^{III}(OO^tBu)(N3Py^{amide}SR)]^{2+}$, but despite much effort were not able to observe any significant change in the rR spectra. The lack of an observable shift may indicate a relatively weak H-bonding interaction, or the small expected shift (1 – 3 cm^{-1}) may be difficult to observe given the broadness of the peaks for these complexes.

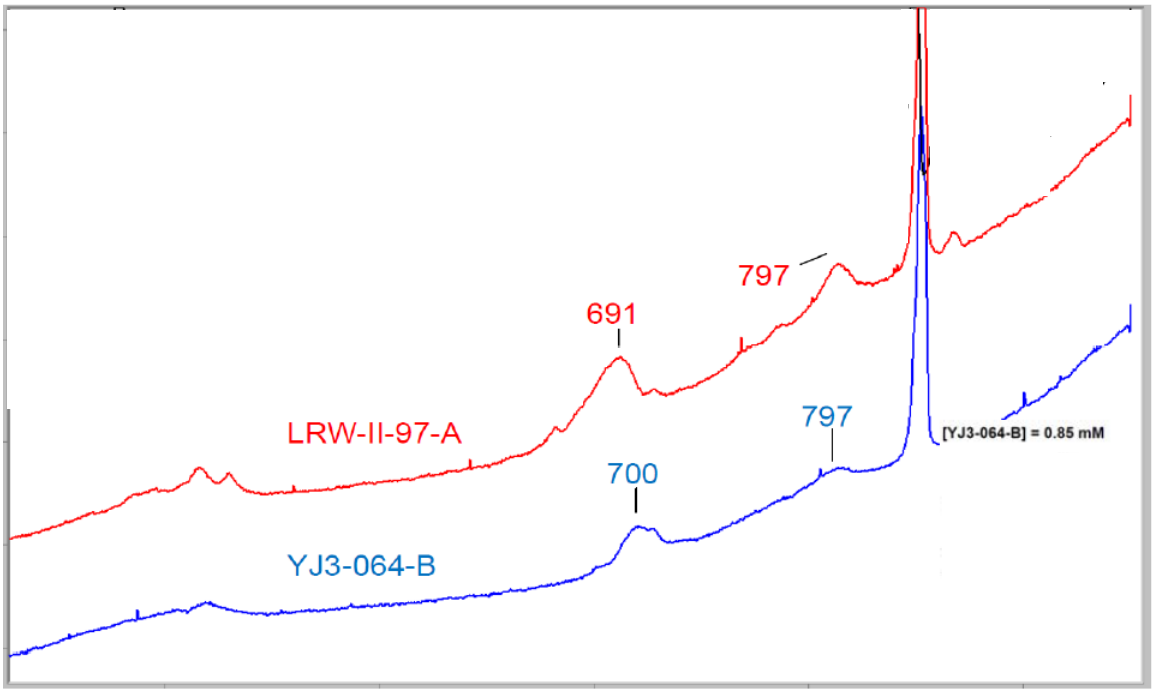

Figure 5. 10. Resonance Raman spectra of $[Fe^{III}(OO^tBu)(N3Py^{amide}SR)]^{2+}$ (red) and $[Fe^{III}(OO^tBu)(N3PySR)]^{2+}$ (blue).

Table 5. 5. Comparison of RR data for ls non-heme Fe^{III}-OOtBu complexes

Complex	ν(Fe-O)	ν(O-O)	Reference
$[Fe^{III}(N3PySR)(OOtBu)]^{2+}$	700	796	This Work
$[Fe^{III}(N3Py^{amide}SR)(OOtBu)]^{2+}$	691	796	This Work
$[Fe^{III}(TPA)(OH_n)(OOtBu)]^{2+}$	696	796	22
$[Fe^{III}([15]aneN_4)(SPh)(OOtBu)]^{+}$	612	803	23

Density Functional Theory

Density functional computations at the UB3LYP-D level of theory were utilized to model the (hydro/alkyl)peroxo complexes (see Appendix B for details). Initial geometry optimizations were performed in *Gaussian*-09 with different basis sets on the lowest lying doublet, quartet, and sextet spin states for $[Fe^{III}(OOH)(N3Py^{amide}SR)]^{2+}$, and the doublet spin state was found to be the ground state by 1.5 and 8.5 kcal mol^{-1} over the sextet and quartet spin states, respectively. This doublet (S = ½) ground state reproduces the experimental ground state determined by EPR for $[Fe^{III}(OOH)(N3Py^{amide}SR)]^{2+}$, as well as for the other peroxo complexes. The geometry for $[Fe^{III}(OOtBu)(N3Py^{amide}SR)]^{2+}$ was optimized by the same density functional theory with equivalent basis sets and approximations in *Orca* to allow for faster convergence. The optimized geometries for $[Fe^{III}(OOH)(N3Py^{amide}SR)]^{2+}$ and $[Fe^{III}(OOtBu)(N3Py^{amide}SR)]^{2+}$ (**Figure 5. 11**) are consistent with the proposed structures for complexes, where the iron(III) center is bound in a pseudo-octahedral geometry by the equatorial pyridine and sulfide donors, with the tertiary amine and (hydro/alkyl)peroxide ligands occupying the axial positions. The structures also show that the pendant amide H-bond donor has reoriented in both cases, and reveals an NH---O hydrogen bond, with calculated N---O distances of 2.774 Å ($[Fe^{III}(OOH)(N3Py^{amide}SR)]^{2+}$) and 2.815 Å ($[Fe^{III}(OOtBu)(N3Py^{amide}SR)]^{2+}$) and angles of 158.1° ($[Fe^{III}(OOH)(N3Py^{amide}SR)]^{2+}$) and 153.3° ($[Fe^{III}(OOtBu)(N3Py^{amide}SR)]^{2+}$).

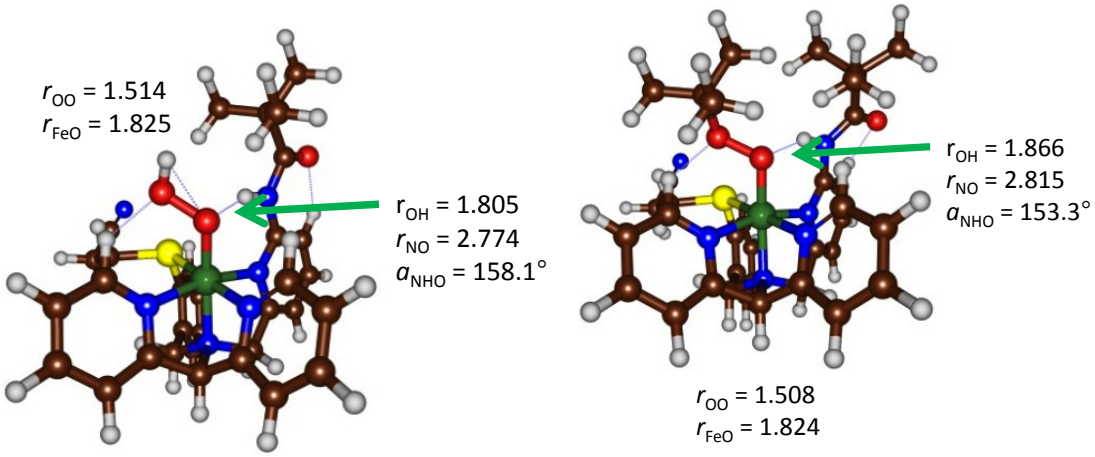

Figure 5. 11. DFT optimized structures of $[Fe^{III}(OOH)(N3Py^{amide}SR)]^{2+}$ (left) and $[Fe^{III}(OOtBu)(N3Py^{amide}SR)]^{2+}$ (right). See Appendix B for computational details.

Steric Influences in the Secondary Coordination Sphere

In further efforts to stabilize the Fe^{III}-OO(H/R) species, we synthesized the new ligand shown in **Scheme 5. 2**. The resulting complex, $[Fe^{II}(N3Py^{amide,2Ph}SR)](BF_4)_2$, incorporates two phenyl substituents in the second coordination sphere, providing additional steric protection around the putative peroxide binding site (**Figure 5. 12**). The synthesis of the $N3Py^{amide,2Ph}SR$ ligand is shown in **Scheme 5. 2**. The key synthetic step, incorporation of the phenyl substituents onto the pyridine rings, was accomplished in high yield using Suzuki-Miyaura cross coupling reaction.[32] Metallation of the free ligand with $Fe(BF_4)_2$ was accomplished by stirring in MeCN, and single crystals of $[Fe^{II}(N3Py^{amide,2Ph}SR)](BF_4)_2$ were grown from vapor diffusion of Et_2O into the solution. The light yellow crystals reveal Fe-N bond distances (2.1842 - 2.2267 Å, **Table 5. 6**) consistent with a high-spin (hs) iron(II) center. As in $[Fe^{II}(N3Py^{amide}SR)](BF_4)_2$, the iron(II) ion is bound in a pseudo-octahedral geometry with the 3 pyridine donors and aryl sulfide occupying the equatorial positions, while the tertiary amine and the amide

carbonyl are bound in the axial positions. The incorporated phenyl substituents are projected orthogonal to the pseudo-equatorial plane, and are oriented to provide significant steric protection around the axial binding site. In contrast to low-spin $[Fe^{II}(N3PySR)](BF_4)_2$ and $[Fe^{II}(N3Py^{amide}SR)](BF_4)_2$, as well as some other hs Fe^{II} complexes,[28,32] $[Fe^{II}(N3Py^{amide,2Ph}SR)](BF_4)_2$ does not react with H_2O_2 or tBuOOH to afford the corresponding ferric-peroxo complexes, and appears to only undergo outer-sphere oxidation upon addition of a large excess of oxidant (150 equiv). The lack of reactivity may be due to significant steric encumbrance around the metal center with incorporation of the new phenyl substituents.

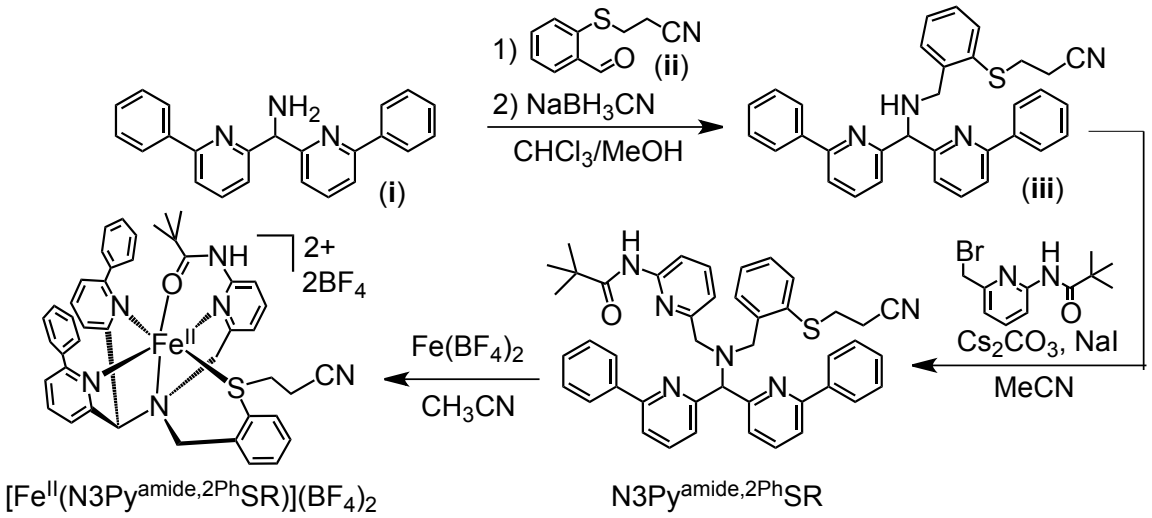

Scheme 5. 2. Synthesis of the ligand precursor ($N3Py^{amide,2Ph}SR$) to $[Fe^{II}(N3Py^{amide,2Ph}SR)](BF_4)_2$.

Table 5. 6. Selected bond distances (Å) and angles (°) for $[Fe^{II}(N3Py^{amide,2Ph}SR)](BF_4)_2$.

Bond lengths		Bond angles	
Fe1 O1	2.0085(13)	O1 Fe1 N4	83.37(6)
Fe1 N4	2.1842(16)	O1 Fe1 N3	159.27(6)
Fe1 N3	2.1954(15)	N4 Fe1 N3	76.66(6)
Fe1 N1	2.1959(15)	O1 Fe1 N1	111.24(6)
Fe1 N2	2.2267(16)	N4 Fe1 N1	98.60(6)
Fe1 S1	2.6097(5)	N3 Fe1 N1	77.62(6)
		O1 Fe1 N2	120.85(6)
		N4 Fe1 N2	154.51(6)
		N3 Fe1 N2	78.35(6)
		N1 Fe1 N2	80.75(6)
		O1 Fe1 S1	83.97(4)
		N4 Fe1 S1	84.45(4)
		N3 Fe1 S1	88.61(4)
		N1 Fe1 S1	164.70(4)
		N2 Fe1 S1	90.05(4)

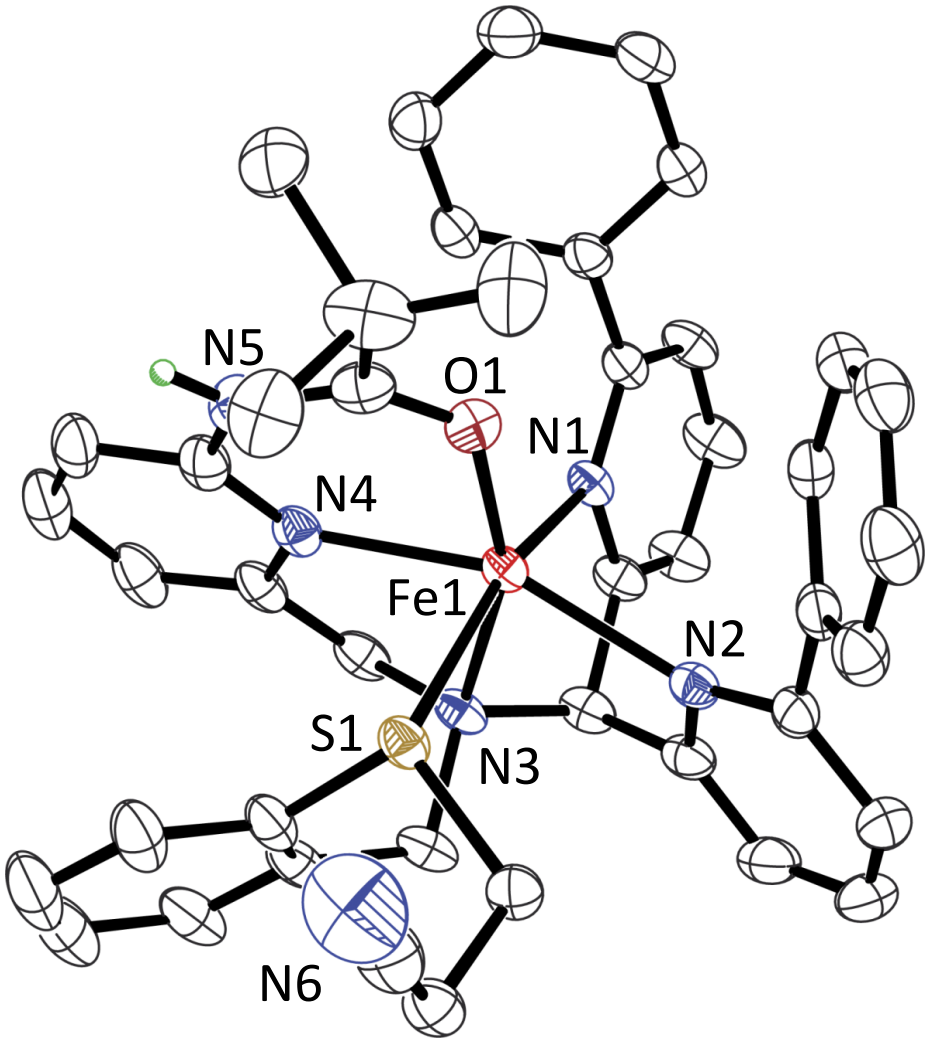

Figure 5. 12. Displacement ellipsoid plot of the cation of $[Fe^{II}(N3Py^{amide,2Ph}SR)](BF_4)_2$ shown at the 50% probability level. H-atoms, except the amide N-H, are removed for clarity.

Synthesis of pendant thiolate ($N3Py^{amide}S$) complex.

Due to our success with the sulfide-ligated complex, $[Fe^{II}(N3Py^{amide}SR)](BF_4)_2$, we wanted to expand on this series and make the corresponding anionic thiolate-ligated derivative, $[Fe^{II}(N3Py^{amide}S)](BF_4)$, which would serve as a comparison to the previously reported $[Fe^{II}(N3PyS)](BF_4)$.[30,31] The key deprotection step (**Scheme 5. 3**) was attempted

under identical conditions as previously reported,[30,41] and allowed for isolation of a clean product that was characterized by ^{1}H-NMR (**Figure 5. 13**). In the ^{1}H-NMR spectrum of the isolated product, the methine C-H and thiolate S-H are both missing, indicating a possible C-S bond formation under the deprotection conditions. This was confirmed when the 2Ph-containing ligand was metallated and yellow crystals were obtained from CH_3CN/Et_2O (**Figure 5. 14**). The Fe-N bond distances are consistent with a hs FeII center, and are listed in **Table 5. 7**. This reaction has been repeated several times, under aerobic and anaerobic conditions, as well as with several different bases (KOtBu, DBU, *n*-BuLi). In almost every case the same C-S coupling product was obtained, except when DBU or *n*-BuLi were used as the base and no reaction was observed by TLC. Additionally, attempts were made to reduce the isolated C-S coupled product with $NaBH_4$, but again no reaction was observed by TLC.

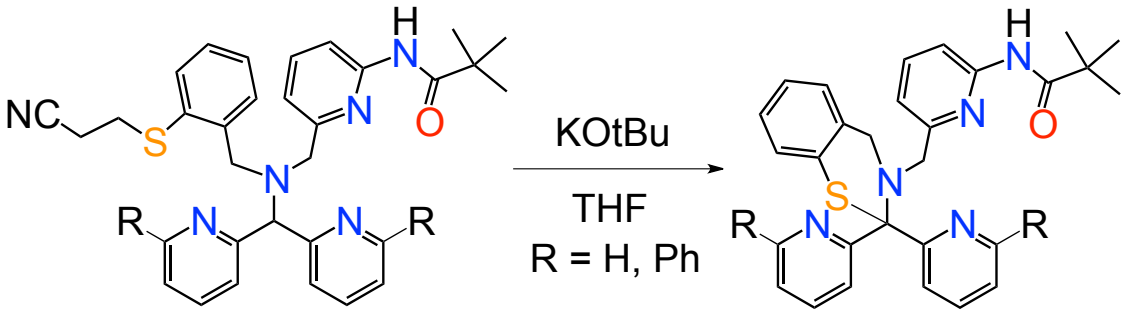

Scheme 5. 3. Attempted deprotection of N3Py^{amide}SR with KOtBu gives C-S coupled product.

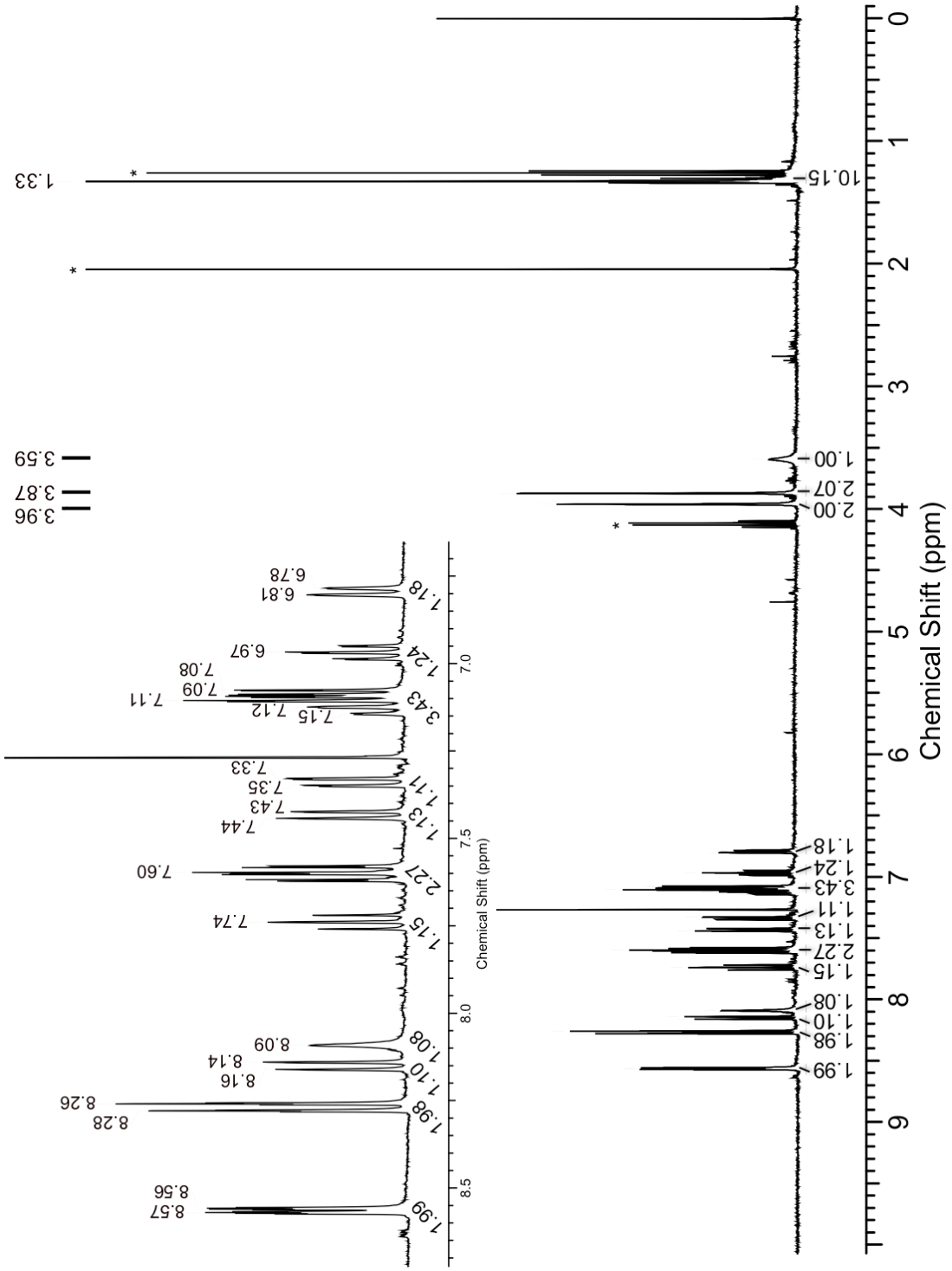

Figure 5. 13. ^{1}H-NMR of the C-S coupled product from the deprotection of N3Py^{amide}SR with KOtBu in $CDCl_3$ at 25 °C.* Indicates EtOAc impurity.

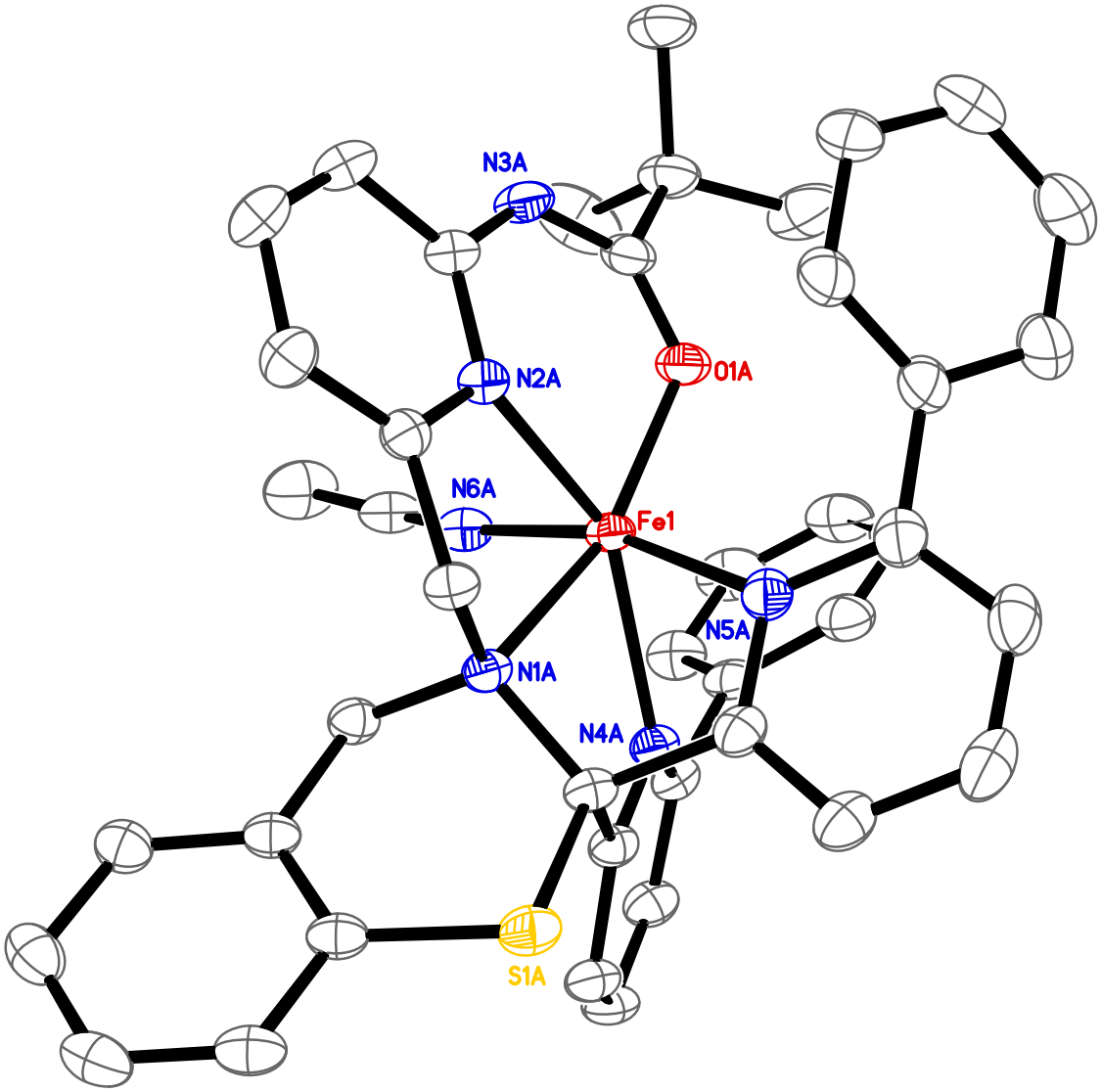

Figure 5. 14. Thermal ellipsoid plot (50% probability level) of the dication of $[Fe^{II}(N3Py^{amide,2Ph}S)(CH_3CN)](BF_4)_2$, resulting from the metallation of the C-S coupled ligand. H-atoms are removed for clarity.

Table 5. 7. Selected bond distances (Å) and angles (°) for $[Fe^{II}(N3Py^{amide,2Ph}S)(CH_3CN)](BF_4)_2$

Bond Distances		Bond Angles	
Fe1-O1A	2.0287(16)	O1A-Fe1-N6A	85.21(7)
Fe1-N6A	2.147(2)	O1A-Fe1-N2A	83.70(7)
Fe1-N2A	2.1728(18)	N6A-Fe1-N2A	89.89(7)
Fe1-N5A	2.2179(19)	O1A-Fe1-N5A	106.88(7)
Fe1-N1A	2.2235(18)	N6A-Fe1-N5A	165.63(7)
Fe1-N4A	2.2573(18)	N2A-Fe1-N5A	98.97(7)
		O1A-Fe1-N1A	160.00(6)
		N6A-Fe1-N1A	96.36(7)
		N2A-Fe1-N1A	76.39(7)
		N5A-Fe1-N1A	74.99(7)
		O1A-Fe1-N4A	124.69(7)
		N6A-Fe1-N4A	85.90(7)
		N2A-Fe1-N4A	150.69(7)
		N5A-Fe1-N4A	80.83(7)
		N1A-Fe1-N4A	75.28(7)

Interestingly, in only one reaction the desired deprotected ligand ($N3Py^{amide,2Ph}SH$) was obtained (**Scheme 5. 3**, R = Ph). The free ligand was characterized by ^{1}H-NMR (**Figure 5. 15**) and was then metallated with $Fe(BF_4)_2$. Single crystals were grown from CH_3CN/Et_2O, although the crystalline material obtained from this reaction was not

sufficient for refinement. However, a partial data set was obtained that showed a trinuclear-iron structure, where two $[Fe^{II}(N3Pyamide,2PhS)]^{+}$ complexes are bridged via the thiolate ligands to a central $Fe(CH_3CN)_x$ (see **Figure 5. 16**).

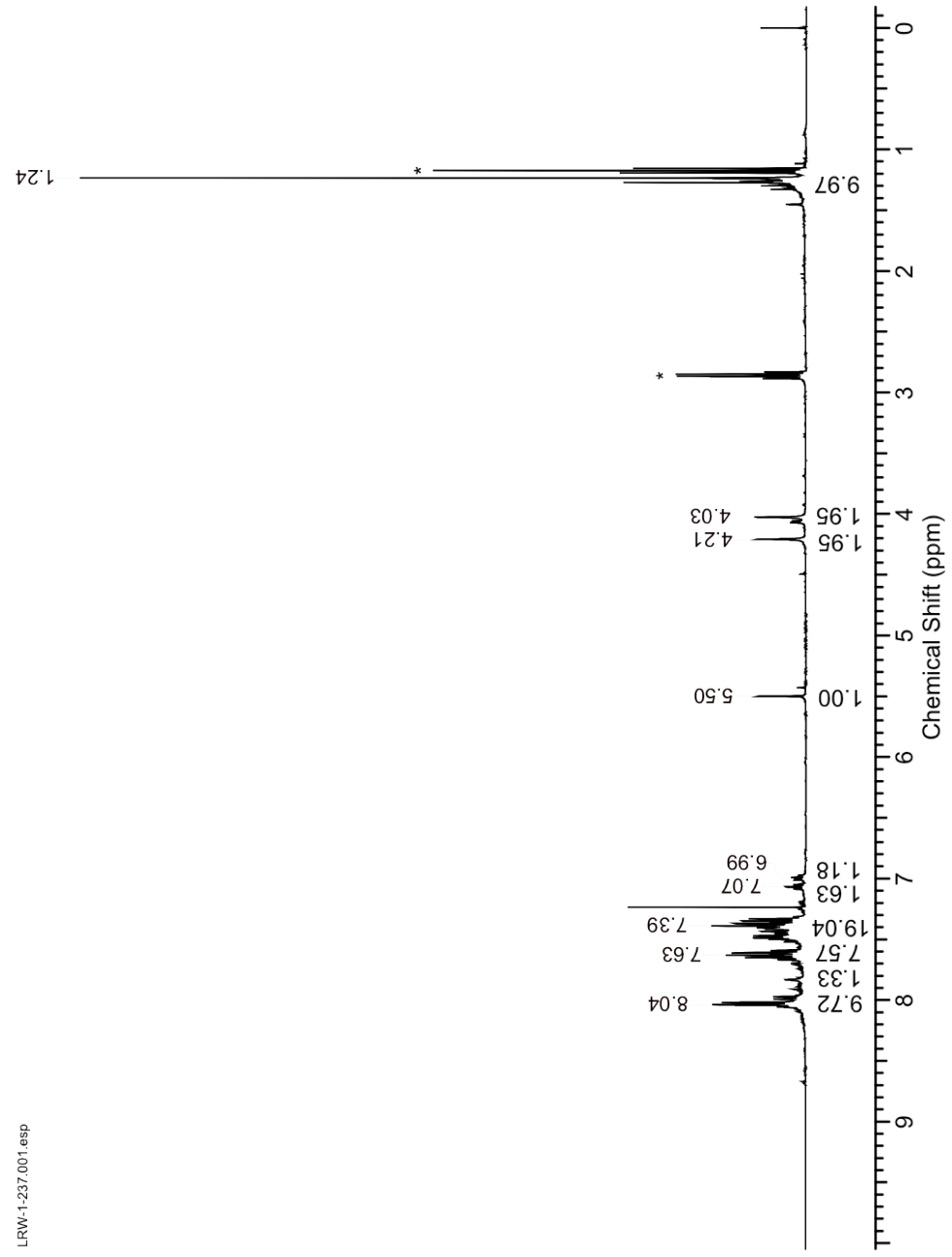

Figure 5. 15. ^{1}H-NMR of the ligand $N3Py^{amide,2Ph}SH$ in $CDCl_3$ at 25 °C.

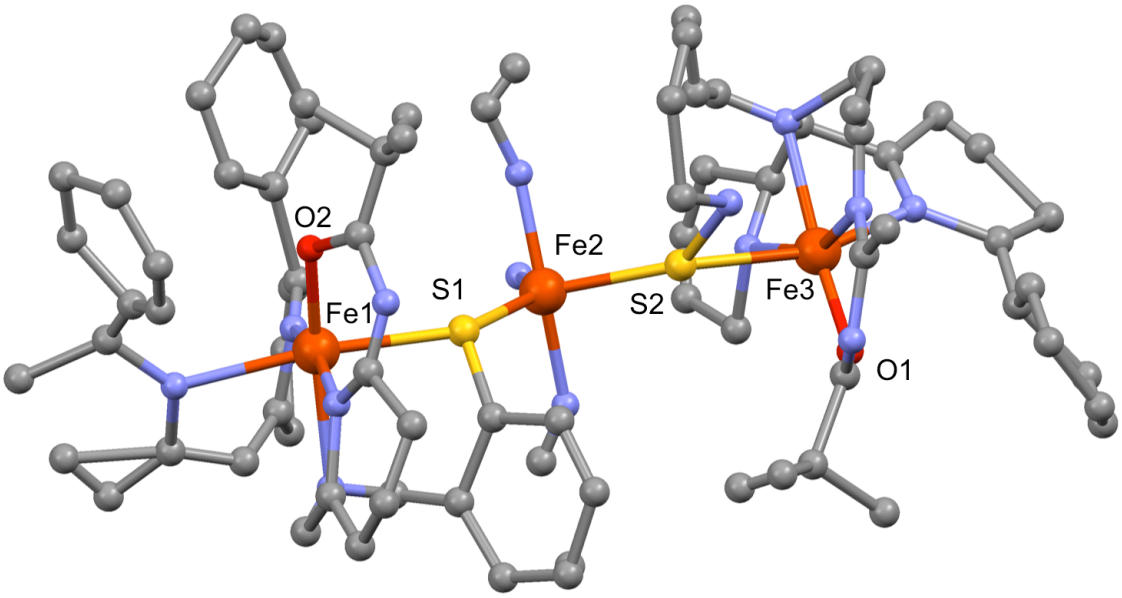

Figure 5. 16. Atomic connectivity plot of [(Fe(N3Py^{amide2Ph}S)$_2$Fe(CH$_3$CN)$_3$] based on initial refinement from metallation of N3Py^{amide,2Ph}SH with Fe(BF$_4$)$_2$ (R_1 [I > 2σ(*I*)] = 17.9%). H-atoms are removed for clarity.

5. 4. Conclusions

We have synthesized a series of new biomimetic iron(II) model complexes that incorporate a pendant sulfide ligand in the equatorial plane. The new iron(II) complexes, [Fe^{II}(N3PySR)](BF$_4$)$_2$ and [Fe^{II}(N3Py^{amide}SR)](BF$_4$)$_2$, react to generate rare examples of Fe^{III}-hydroperoxo and -alkylperoxo complexes with a pendant sulfide donor. These peroxo species were characterized by UV-vis, EPR and resonance Raman spectroscopy. All four peroxo complexes are low-spin species with rhombic EPR resonances centered around g = 2, and ν(O-O) at 800 ± 10 cm^{-1}. The hydroperoxo and alkylperoxo complexes

show ν(Fe-O) at 618 ± 5 cm^{-1} and ν(Fe-O) at 695 ± 5 cm^{-1}, respectively, which are also in the expected range for ls peroxo species. The UV-vis data show a significant decrease in the energy of the alkylperoxo-to-iron(III) charge transfer bands, indicating that incorporation of a sulphide donor in the first coordination sphere likely stabilizes the key metal acceptor orbital for the LMCT bands in $[Fe^{III}(OOtBu)(N3PySR)]^{2+}$ and $[Fe^{III}(OO^{t}Bu)(N3Py^{amide}SR)]^{2+}$. Modification of the second coordination sphere by addition of a single H-bond donor was also shown to affect the properties of these nonheme Fe complexes. Structural characterization of the azide/fluoride-ligated complex $[Fe^{II}(N3Py^{amide}SR)(F/N_3)](BF_4)_2$, showed that the axial amide ligand was indeed labile toward displacement by anionic donors, and that formation of a single hydrogen bond between the amide N-H and anionic ligands in the open site is favoured. The inclusion of an amide H-bond donor in the 2^{nd}-coordination sphere also appears to stabilize the peroxo-to-iron LMCT band by ~20 nm in both the hydro- and alkylperoxo cases. In contrast, the RR spectra of the peroxo complexes are minimally affected by the addition of the amide H-bond donor. The largest change corresponds to a 9 cm^{-1} downshift of the ν(Fe-O) in the Fe^{III}-OOtBu complex $[Fe^{III}(OOtBu)(N3Py^{amide}SR)]^{2+}$. It appears that the addition of the phenyl substituents in $[Fe^{II}(N3Py^{amide,2Ph}SR)](BF_4)_2$ inhibits formation of the Fe^{III}-OO(H/R) complexes, and further work is needed to tease out the factors that contribute to this 2^{nd}-coordination sphere effect. The results presented here suggest that both 1^{st}- and 2^{nd}-coordination sphere effects can be employed by nonheme iron complexes and proteins to subtly tune the Fe-O and O-O interactions in Fe^{III}-OO(H/R) species.

5. 5. References

(1) Kovaleva, E. G.; Neibergall, M. B.; Chakrabarty, S.; Lipscomb, J. D. *Acc. Chem. Res.* **2007**, *40*, 475.

(2) Kovaleva, E. G.; Lipscomb, J. D. *Science* **2007**, *316*, 453.

(3) Solomon, E. I.; Decker, A.; Lehnert, N. *Proc. Natl. Acad. Sci. U. S. A.* **2003**, *100*, 3589.

(4) Costas, M.; Mehn, M. P.; Jensen, M. P.; Que, L., Jr. *Chem. Rev.* **2004**, *104*, 939.

(5) Solomon, E. I.; Wong, S. D.; Liu, L. V.; Decker, A.; Chow, M. S. *Curr. Opin. Chem. Biol.* **2009**, *13*, 99.

(6) Roach, P. L.; Clifton, I. J.; Hensgens, C. M. H.; Shibata, N.; Schofield, C. J.; Hajdu, J.; Baldwin, J. E. *Nature* **1997**, *387*, 827.

(7) Santos-Silva, T.; Trincão, J.; Carvalho, A. L.; Bonifàcio, C.; Auchére, F.; Raleiras, P.; Moura, I.; Moura, J. J. G.; Romão, M. J. *J. Biol. Inorg. Chem.* **2006**, *11*, 548.

(8) Bruijnincx, P. C. A.; van Koten, G.; Klein Gebbink, R. J. M. *Chem. Soc. Rev.* **2008**, *37*, 2716.

(9) Que, L., Jr. *J. Biol. Inorg. Chem.* **2004**, *9*, 684.

(10) Ye, S.; Wu, X.; Wei, L.; Tang, D. M.; Sun, P.; Bartlam, M.; Rao, Z. H. *J. Biol. Chem.* **2007**, *282*, 3391.

(11) Vasbinder, M. J.; Bakac, A. *Inorg. Chem.* **2007**, *46*, 2921.

(12) Roelfes, G.; Lubben, M.; Chen, K.; Ho, R. Y. N.; Meetsma, A.; Genseberger, S.; Hermant, R. M.; Hage, R.; Mandal, S. K.; Young, V. G.; Zang, Y.; Kooijman, H.; Spek, A. L.; Que, L., Jr.; Feringa, B. L. *Inorg. Chem.* **1999**, *38*, 1929.

(13) Roelfes, G.; V, V.; Chen, K.; Ho, R. Y. N.; Rohde, J. U.; Zondervan, C.; la Crois, R. M.; Schudde, E. P.; Lutz, M.; Spek, A. L.; Hage, R.; Feringa, B. L.; Münck, E.; Que, L., Jr. *Inorg. Chem.* **2003**, *42*, 2639.

(14) Kim, J.; Larka, E.; Wilkinson, E. C.; Que, L., Jr. *Angew. Chem. Int. Ed.* **1995**, *34*, 2048.

(15) Rohde, J. U.; Torelli, S.; Shan, X. P.; Lim, M. H.; Klinker, E. J.; Kaizer, J.; Chen, K.; Nam, W. W.; Que, L., Jr. *J. Am. Chem. Soc.* **2004**, *126*, 16750.

(16) Dey, A.; Solomon, E. I. *Inorg. Chim. Acta* **2010**, *363*, 2762.

(17) Simaan, A. J.; Dopner, S.; Banse, F.; Bourcier, S.; Bouchoux, G.; Boussac, A.; Hildebrandt, P.; Girerd, J. J. *Eur. J. Inorg. Chem.* **2000**, 1627.

(18) Martinho, M.; Banse, F.; Sainton, J.; Philouze, C.; Guillot, R.; Blain, G.; Dorlet, P.; Lecomte, S.; Girerd, J. J. *Inorg. Chem.* **2007**, *46*, 1709.

(19) Anastasi, A. E.; Lienke, A.; Comba, P.; Rohwer, H.; McGrady, J. E. *Eur. J. Inorg. Chem.* **2007**, 65.

(20) Bukowski, M. R.; Comba, P.; Limberg, C.; Merz, M.; Que, L., Jr.; Wistuba, T. *Angew. Chem. Int. Ed.* **2004**, *43*, 1283.

(21) Lehnert, N.; Ho, R. Y. N.; Que, L., Jr.; Solomon, E. I. *J. Am. Chem. Soc.* **2001**, *123*, 12802.

(22) Lehnert, N.; Ho, R. Y. N.; Que, L., Jr.; Solomon, E. I. *J. Am. Chem. Soc.* **2001**, *123*, 8271.

(23) Namuswe, F.; Hayashi, T.; Jiang, Y. B.; Kasper, G. D.; Sarjeant, A. A. N.; Moënne-Loccoz, P.; Goldberg, D. P. *J. Am. Chem. Soc.* **2010**, *132*, 157.

(24) Jiang, Y. B.; Telser, J.; Goldberg, D. P. *Chem. Commun.* **2009**, 6828.

(25) Stasser, J.; Namuswe, F.; Kasper, G. D.; Jiang, Y. B.; Krest, C. M.; Green, M. T.; Penner-Hahn, J.; Goldberg, D. P. *Inorg. Chem.* **2010**, *49*, 9178.

(26) Shearer, J.; Scarrow, R. C.; Kovacs, J. A. *J. Am. Chem. Soc.* **2002**, *124*, 11709.

(27) Kitagawa, T.; Dey, A.; Lugo-Mas, P.; Benedict, J. B.; Kaminsky, W.; Solomon, E.; Kovacs, J. A. *J. Am. Chem. Soc.* **2006**, *128*, 14448.

(28) Krishnamurthy, D.; Kasper, G. D.; Namuswe, F.; Kerber, W. D.; Sarjeant, A. A. N.; Moënne-Loccoz, P.; Goldberg, D. P. *J. Am. Chem. Soc.* **2006**, *128*, 14222.

(29) Namuswe, F.; Kasper, G. D.; Sarjeant, A. A. N.; Hayashi, T.; Krest, C. M.; Green, M. T.; Moënne-Loccoz, P.; Goldberg, D. P. *J. Am. Chem. Soc.* **2008**, *130*, 14189.

(30) McQuilken, A. C.; Jiang, Y. B.; Siegler, M. A.; Goldberg, D. P. *J. Am. Chem. Soc.* **2012**, *134*, 8758.

(31) McQuilken, A. C.; Ha, Y.; Sutherlin, K. D.; Siegler, M. A.; Hodgson, K. O.; Hedman, B.; Solomon, E. I.; Jameson, G. N. L.; Goldberg, D. P. *J. Am. Chem. Soc.* **2013**, *135*, 14024.

(32) Sahu, S.; Widger, L. R.; Quesne, M. G.; de Visser, S. P.; Matsumura, H.; Moënne-Loccoz, P.; Siegler, M. A.; Goldberg, D. P. *J. Am. Chem. Soc.* **2013**, *135*, 10590.

(33) Widger, L. R.; Davies, C. G.; Yang, T.; Siegler, M.A.; Troeppner, O.; Jameson, G. N. L.; Ivanović-Burmazović, I.; Goldberg, D. P. *Submitted*.

(34) Kim, C.; Chen, K.; Kim, J. H.; Que, L., Jr. *J. Am. Chem. Soc.* **1997**, *119*, 5964.

(35) Calculations based on an isolated diatomic oscillator with a ν (Fe-^{18}O) at 590 cm^{-1} predict a ν (Fe-^{16}O) at 617 cm^{-1}, which does not match any of the most

prominent bands seen in the ν(Fe-O) region of the RR spectra of unlabeled $[Fe^{II}(N3PySR)(OOH)]^{2+}$, nor the 607 cm^{-1} frequency observed in D_2O.

(36) Lehnert, N.; Neese, F.; Ho, R. Y. N.; Que, L., Jr.; Solomon, E. I. *J. Am. Chem. Soc.* **2002**, *124*, 10810.

(37) Payeras, A. M. I.; Ho, R. Y. N.; Fujita, M.; Que, L., Jr. *Chem.-Eur. J.* **2004**, *10*, 4944.

(38) Girerd, J. J.; Banse, F.; Simaan, A. J. *Struct. Bond.* **2000**, *97*, 145.

(39) Neese, F.; Wennmohs, F.; Hansen, A.; Becker, U. *Chem. Phys.* **2009**, *356*, 98.

(40) Kendall, R. A.; Früchtl, H. A. *Theor. Chem. Acc.* **1997**, *97*, 158.

(41) Belle, C.; Bougault, C.; Averbuch, M. T.; Durif, A.; Pierre, J. L.; Latour, J. M.; Le Pape, L. *J. Am. Chem. Soc.* **2001**, *123*, 8053.

5. 6. Appendix A: Crystallographic Information:

General

All reflection intensities were measured at 100(2) ($[Fe^{II}(N3Py^{amide}SR)(F/N_3)]BF_4$) using a SuperNova diffractometer (equipped with Atlas detector) with Cu *K*α radiation (mirror optics, λ = 1.54178 Å) or at 110(2) K (compounds ($[Fe^{II}(N3Py^{amide}SR)]BF_4$ and ($[Fe^{II}(N3Py^{amide,2Ph}SR)](BF_4)_2$) K using a KM4/Xcalibur (detector: Sapphire3) with enhance graphite-monochromated Mo *K*α radiation (λ = 0.71073 Å) under the program CrysAlisPro (Versions 1.171.35.11 ($[Fe^{II}(N3Py^{amide}SR)]BF_4$ and ($[Fe^{II}(N3Py^{amide,2Ph}SR)](BF_4)_2$) or 1.171.36.24 ($[Fe^{II}(N3Py^{amide}SR)(F/N_3)]BF_4$) Agilent Technologies, 2011-2013). The same program was used to refine the cell dimensions and data reduction. The structure was solved with the program SHELXS-97 or SHELXS-2013 and was refined on F^2 with SHELXL-97 or SHELXL-2013 (Sheldrick, 2008). Analytical numeric absorption corrections based on a multifaceted crystal model were applied using CrysAlisPro. The temperature of the data collection was controlled using the system Cryojet (manufactured by Oxford Instruments). The H atoms were placed at calculated positions using the instructions AFIX 13, AFIX 23, AFIX 43 or AFIX 137 with isotropic displacement parameters having values 1.2 or 1.5 times *U*eq of the attached C atoms. For $(Fe^{II}(N3Py^{amide}SR)(F/N_3)]BF_4$, the H atom of the amide group (*i.e.*, H atom attached to N6) was found from difference Fourier map, and its coordinates and isotropic temperature factor were refined freely.

$[Fe^{II}(N3PySR)(CH_3CN)](BF_4)_2$

The structure is ordered.

Fw = 722.10, dark red irregular shape, 0.47 × 0.39 × 0.14 mm^3, triclinic, *P*-1 (no. 2), a = 10.6689(2), b = 12.0355(2), c = 13.0403(3) Å, α = 80.5885(18), β = 88.0024(18), γ = 68.543(2)°, V = 1536.85(5) $Å^3$, Z = 2, D_x = 1.560 g cm^{-3}, μ = 0.640 mm^{-1}, abs. corr. range: 0.806–0.929. 35673 Reflections were measured up to a resolution of $(\sin \theta/\lambda)_{max}$ = 0.65 $Å^{-1}$. 7051 Reflections were unique (R_{int} = 0.0247), of which 6258 were observed [$I > 2\sigma(I)$]. 425 Parameters were refined. $R1/wR2$ [$I > 2\sigma(I)$]: 0.0325/0.0877. $R1/wR2$ [all refl.]: 0.0373/0.0905. S = 1.061. Residual electron density found between –0.50 and 0.63 e $Å^{-3}$.

$[Fe^{II}(N3Py^{amide}SR)(F/N_3)](BF_4)$

The structure is mostly ordered. At the sixth coordination site (axial position), there is a mixture of F^- / N_3^-. F^- is found to be coordinated to Fe^{II} about 67 % of the time, whereas N_3^- is coordinated to the metal center the rest of the time. All refined occupancy factors are provided in the CIF file. The crystal lattice contains some amount of solvent molecules (MeCN). The two MeCN molecules per asymmetric unit are found to be located at sites of two-fold axial symmetry, and thus their occupancy factors must be 0.5.

Fw = 761.13, yellow lath, 0.30 × 0.18 × 0.04 mm^3, orthorhombic, *Pbcn* (no. 60), a = 35.1087(4), b = 10.08753(9), c = 19.9277(2) Å, V = 7057.59(12) $Å^3$, Z = 8, D_x = 4.546 g cm^{-3}, μ = 1.433 mm^{-1}, abs. corr. range: 0.389–0.808. 44026 Reflections were measured up to a resolution of $(\sin \theta/\lambda)_{max}$ = 0.62 $Å^{-1}$. 6942 Reflections were unique (R_{int} = 0.0273), of which 6307 were observed [$I > 2\sigma(I)$]. 511 Parameters were refined using 56

restraints. $R1/wR2$ [$I > 2\sigma(I)$]: 0.0322/0.0791. $R1/wR2$ [all refl.]: 0.0366/0.0821. S = 1.026. Residual electron density found between –0.33 and 0.63 e Å^{-3}.

[Fe^{II}(N3Py^{amide,2Ph}SR)](BF$_4$)$_2$

The structure is mostly ordered except for one of the two BF_4^- counterions, which is found to be disordered over two orientations (occupancy factors for the major components: 0.574(4)). The structure also contains some very disordered lattice acetonitrile solvents molecules with occupancies likely to be lower than 1; their contributions were then taken out using the program SQUEEZE for the final refinement (all details about the SQUEEZE procedure have been embedded in the cif file).

Fw = 932.37,* yellow block, 0.43 × 0.21 × 0.19 mm^3, triclinic, *P*-1 (no. 2), a = 10.4419(3), b = 14.5834(3), c = 17.2950(4) Å, α = 90.6304(19), β = 105.768(2), γ = 106.791(2)°, V = 2415.01(10) Å^3, Z = 2, D_x = 1.282 g cm^{-3},* μ = 0.425 mm^{-1},* abs. corr. range: 0.876–0.942. 29736 Reflections were measured up to a resolution of $(\sin\theta/\lambda)_{max}$ = 0.62 Å^{-1}. 9709 Reflections were unique (R_{int} = 0.0305), of which 8130 were observed [$I > 2\sigma(I)$]. 648 Parameters were refined with 265 restraints. $R1/wR2$ [$I > 2\sigma(I)$]: 0.0401/0.1117. $R1/wR2$ [all refl.]: 0.0475/0.1155. S = 1.102. Residual electron density found between –0.46 and 0.58 e Å^{-3}. *excluding the contribution of the unresolved residual electron density.

[Fe^{II}(N3Py^{amide,2Ph}S)(CH$_3$CN)](BF$_4$)$_2$

The structure was solved and refined in the centrosymmetric space group $P2_1/n$ with Z' = 2. The asymmetric unit contains two crystallographically independent Fe(II) complex, four BF_4^- counterions, and four uncoordinated acetonitrile molecules. The structure is

mostly ordered; two of the four counterions are found to be disordered over two or three orientations [occupancy factors of the major components: 0.808(3) and 0.609(3)].

The final refinement against F^2 was good. The R factor [$F^2 > 2\sigma(F^2)$] is about 0.044. The final difference Fourier map was flat. The other residual peaks were no larger than 0.66 e Å^{-3}.

$[C_{43}H_{40}FeN_6OS](BF_4)_2 \bullet 2(CH_3CN)$, Fw = 1000.45, irregular yellow-orange block, 0.55 × 0.47 × 0.28 mm^3, monoclinic, $P2_1/n$ (no. 14), a = 19.36862(16), b = 19.32888(17), c = 25.0655(2) Å, β = 92.0667(8)°, V = 9377.76(14) Å^3, Z = 8, D_x = 1.417 g cm^{-3}, μ = 0.444 mm^{-1}, abs. corr. range: 0.831–0.923. 76241 Reflections were measured up to a resolution of (sin $\theta/\lambda)_{max}$ = 0.62 Å^{-1}. 18420 Reflections were unique (R_{int} = 0.0418), of which 14946 were observed [$I > 2\sigma(I)$]. 1346 Parameters were refined with 419 restraints. $R1/wR2$ [$I > 2\sigma(I)$]: 0.0439/0.1083. $R1/wR2$ [all refl.]: 0.0578/0.1159. S = 1.023. Residual electron density found between –0.47 and 0.66 e Å^{-3}.

5. 7. Appendix B: Density Functional Calculations

General Methods

Density functional theory calculations were performed using the *Gaussian*-09 and *Orca* software packages.[1] We used the unrestricted hybrid density functional method UB3LYP-D with dispersion correction due to Grimme.[2–4] Geometries were optimized without constraints using the LACVP basis set on iron and 6-31G on the rest of the atoms in *Gaussian*-09[5] and an equivalent set, LANLDZ basis set on iron and 6-31G on the rest of the atoms in *Orca* including the auxiliary basis sets def2-SVP/J and def2-SVP/K for the RIJCOSX approximation.[39,40] Subsequently, improved energies were obtained at single point level with an LACV3P+ basis set on iron and 6-311+G* on the rest of the atoms in *Gaussian*-09.[5] Geometry optimizations converged to local minima with real frequencies only. Although we calculated $[Fe^{III}OOH(N3PyS)]^{2+}$ in the lowest lying doublet, quartet and sextet spin states, under all conditions the doublet spin state was the ground state which matches the experimental data and provides a good calibration of our method. Subsequent calculations for all other species were preformed on the doublet spin state only. This is in good agreement with DFT calculations of the iron(III)-hydroperoxo species in heme enzymes, such as cytochrome P450, where also a doublet spin ground state was found.[6] By contrast, in nonheme iron(III)-hydroperoxo complexes with trigonal bipyramidal conformation typically a high-spin ground state is found.[7]

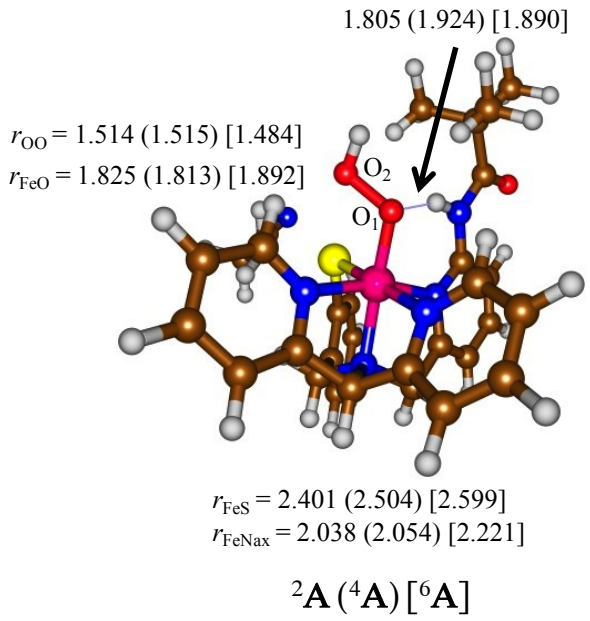

Figure 5. 17. Optimized geometries of ^{2,4,6}[Fe^{III}(OOH)(N3Py^{amide}SR)]$^{2+}$ as calculated with UB3LYP-D in *Gaussian*-09, with bond lengths in angstroms. (**A** = [Fe^{III}(OOH)(N3Py^{amide}SR)]$^{2+}$)

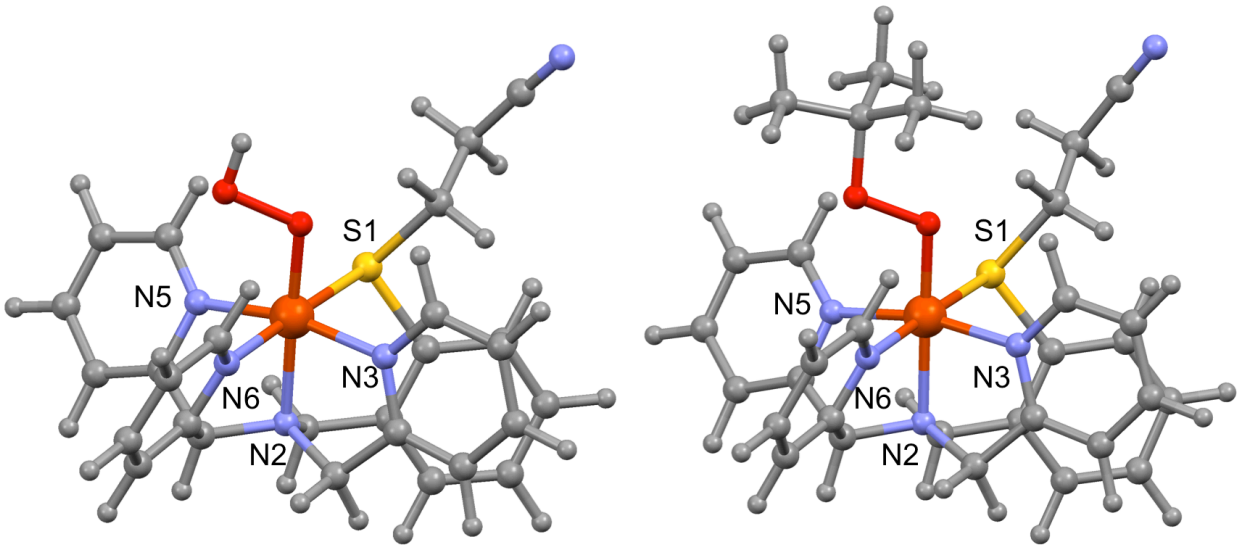

Figure 5. 18. Optimized geometries of ^{2}[Fe^{III}OOH(N3PySR)]$^{2+}$ (left) and ^{2}[Fe^{III}(OOtBu)(N3PySR)]$^{2+}$ (right) as calculated UB3LYP-D in *Orca*. Relevant bond distances are given in Table 5. 8.

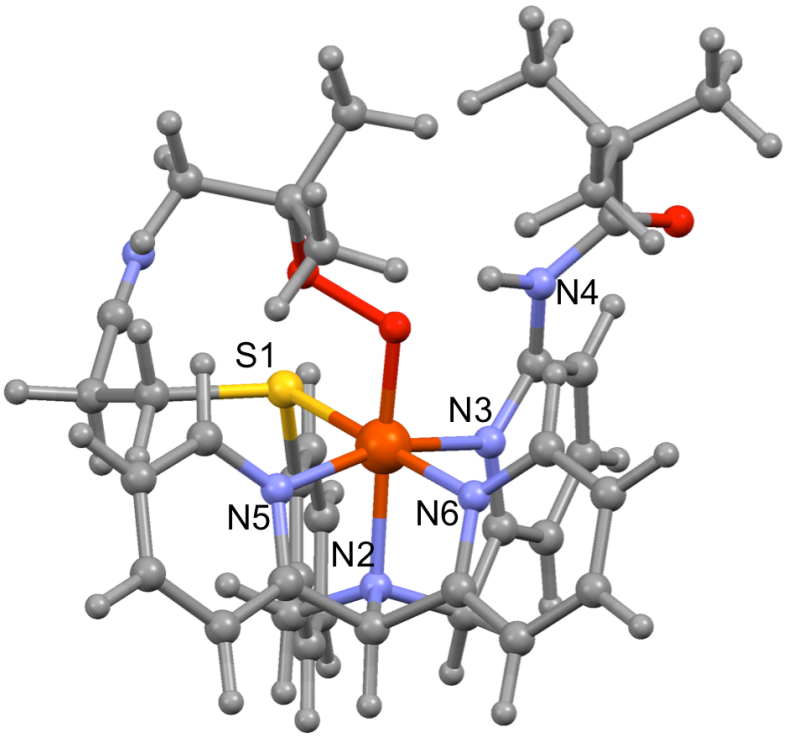

Figure 5. 19. Optimized geometry $^{2}[Fe^{III}(OOtBu)(N3PySR)]^{2+}$, as calculated with UB3LYP-D in *Orca*. Relevant bond distances are given in Table 5. 8.

Table 5. 8. Selected bond distances (Å) and angles (°) for DFT calculated structures[a]

	^{2}[Fe^{III}(OOH)(N3PySR)]$^{2+}$	^{2}[Fe^{III}(OOH)(N3Py^{amide}SR)]$^{2+}$	^{2}[Fe^{III}(OOtBu)(N3PySR)]$^{2+}$	^{2}[Fe^{III}(OOtBu)(N3Py^{amide}SR)]$^{2+}$
Fe-O	1.81	1.83	1.80	1.82
Fe-N2	2.06	2.04	2.06	2.06
Fe-N3	1.98	2.03	1.98	2.04
Fe-N5	1.96	1.98	1.96	1.97
Fe-N6	1.99	2.01	1.98	2.02
Fe-S1	2.43	2.39	2.43	2.39
N4-O	N/A	2.74	N/A	2.82
N4-H--O	N/A	158.4	N/A	153.3

[a] calculated with UB3LYP-D in *Orca*

Table 5. 9. Absolute and relative energies, zero point energies and free energies from optimized geometries of ^{2,4,6}**A**, as calculated at the UB3LYP-D level of theory in *Gaussian*-09. (**A** = $[Fe^{III}(OOH)(N3Py^{amide}SR)]^{2+}$). Absolute energies are in au and relative energies are in kcal mol^{-1}

(a)

B1 -> LACVP						
Multip	E	E+ZPE	G	ΔE^a	$\Delta E+ZPE^a$	ΔG^a
^{2}**A**	-2315.480194	-2314.843475	-2314.914353	0.00	0.00	0.00
^{4}**A**	-2315.459681	-2314.825428	-2314.897378	12.87	11.32	10.65
^{6}**A**	-2315.460588	-2314.827056	-2314.902791	12.30	10.30	7.26

[a] with respect to $^2[Fe^{III}(OOH)(N3Py^{amide}SR)]^{2+}$.

(b)

B2 -> LACV3P+*				
Multip	E	E+ZPE	ΔE^a	$\Delta E+ZPE^a$
^{2}**A**	-2316.379551	-2315.742832	0.00	0.00
^{4}**A**	-2316.363612	-2315.729359	10.00	8.45
^{6}**A**	-2316.374026	-2315.740494	3.47	1.47

[a] with respect to $^2[Fe^{III}(OOH)(N3Py^{amide}SR)]^{2+}$.

Table 5. 10. Group spin densities and group charges from UB3LYP-D optimized geometries of ^{2,4,6}**A**, as calculated in *Gaussian*-09. (**A** = $[Fe^{III}(OOH)(N3Py^{amide}SR)]^{2+}$)

	Spin densities					Charges				
	Fe	O_1	O_2H	S	Rest	Fe	O_1	O_2H	S	Rest
^{2}**A**	0.91	0.16	0.01	-0.03	-0.05	0.50	-0.37	0.04	0.60	1.23
^{4}**A**	2.76	0.09	0.00	-0.01	0.16	0.64	-0.37	0.05	0.54	1.13
^{6}**A**	3.97	0.36	0.07	0.14	0.47	0.79	-0.42	0.09	0.49	1.05

Table 5. 11. Group spin densities and group charges of UB3LYP-D/LACV3P+*// UB3LYP-D/LACVP calculations of ^{2,4,6}**A**, as calculated in *Gaussian*-09. (**A** = $[Fe^{III}(OOH)(N3Py^{amide}SR)]^{2+}$)

	Spin densities					Charges				
	Fe	O_1	O_2H	S	Rest	Fe	O_1	O_2H	S	Rest
^{2}**A**	0.94	0.14	0.01	-0.03	-0.06	0.16	-0.27	-0.01	0.48	1.64
^{4}**A**	2.83	0.06	0.00	-0.01	0.12	0.31	-0.29	0.05	0.39	1.54
^{6}**A**	4.12	0.29	0.06	0.14	0.38	0.31	-0.31	0.09	0.35	1.55

Table 5. 12. Group spin densities and group charges of UB3LYP-D optimized geometries of **^{2}B, ^{2}C, ^{2}D**, as calculated in *Orca*. (**B** = $[Fe^{III}(OOH)(N3PySR)]^{2+}$, **C** = $[Fe^{III}(OOtBu)(N3PySR)]^{2+}$, **D** = $[Fe^{III}(OOtBu)(N3Py^{amide}SR)]^{2+}$)

	Spin densities					Charges				
	Fe	O_1	O_2R^a	S	Rest	Fe	O_1	O_2R^a	S	Rest
^{2}**B**	0.85	0.21	0.02	-0.02	-0.06	0.57	-0.38	0.05	0.57	1.19
^{2}**C**	0.77	0.26	0.04	-0.01	-0.06	0.54	-0.37	0.15	0.56	1.12
^{2}**D**	0.85	0.20	0.02	-0.02	-0.05	0.49	-0.37	0.12	0.61	1.15

[a]R = H for ^{2}**B**, R = tBu for ^{2}**C** and ^{2}**D**

References

1. (a) Frisch, M. J.; Trucks, G. W.; Schlegel, H. B.; Scuseria, G. E.; Robb, M. A.; Cheeseman, J. R.; Scalmani, G.; Barone, V.; Mennucci, B.; Petersson, G. A.; Nakatsuji, H.; Caricato, M.; Li, X.; Hratchian, H. P.; Izmaylov, A. F.; Bloino, J.; Zheng, G.; Sonnenberg, J. L.; Hada, M.; Ehara, M.; Toyota, K.; Fukuda, R.; Hasegawa, J.; Ishida, M.; Nakajima, T.; Honda, Y.; Kitao, O.; Nakai, H.; Vreven, T.; Montgomery, Jr., J. A.; Peralta, J. E.; Ogliaro, F.; Bearpark, M.; Heyd, J. J.; Brothers, E.; Kudin, K. N.; Staroverov, V. N.; Keith, T.; Kobayashi, R.; Normand, J.; Raghavachari, K.; Rendell, A.; Burant, J. C.; Iyengar, S. S.; Tomasi, J.; Cossi, M.; Rega, N.; Millam, J. M.; Klene, M.; Knox, J. E.; Cross, J. B.; Bakken, V.; Adamo, C.; Jaramillo, J.; Gomperts, R.; Stratmann, R. E.; Yazyev, O.; Austin, A. J.; Cammi, R.; Pomelli, C.; Ochterski, J. W.; Martin, R. L.; Morokuma, K.; Zakrzewski, V. G.; Voth, G. A.; Salvador, P.; Dannenberg, J. J.; Dapprich, S.; Daniels, A. D.; Farkas, O.; Foresman, J. B.; Ortiz, J. V.; Cioslowski, J.; Fox, D. J. *Gaussian* 09, Revision C.01,Gaussian, Inc., Wallingford CT, 2010. (b) Neese, F. *Wiley Interdiscip. Rev.: Comput. Mol. Sci.* **2012**, *2*, 73.
2. Becke, A. D. *J. Chem. Phys.* **1993**, *98*, 5648–5652.
3. Lee, C.; Yang, W.; Parr, R. G. *Phys. Rev. B* **1988**, *37*, 785–789.
4. Schwabe, T.; Grimme, S. P*hys. Chem. Chem. Phys.* **2007**, *9*, 3397–3406.
5. Hay, P. J.; Wadt, W. R. *J. Chem. Phys.* **1985**, *82*, 270–283.
6. Porro, C. S.; Sutcliffe, M. J.; de Visser, S. P. *J. Phys. Chem. A* **2009**, *113*, 11635–11642.
7. Vardhaman, A. K.; Sastri, C. V.; Kumar, D.; de Visser, S. P. *Chem. Commun.* **2011**, *47*, 11044–11046.

Cartesian coordinates of calculated structures

Gaussian Optimized Geometries:

^{2}[Fe^{III}(N3PySR)(OOH)]$^{2+}$

26	0.100658000	0.084331000	0.005221000
16	0.115724000	-0.008359000	2.404593000
6	0.535140000	-0.867202000	5.432925000
6	0.439425000	-1.976660000	4.486571000
1	-0.603238000	-2.314313000	4.441466000
1	1.031625000	-2.828760000	4.845922000
6	0.942074000	-1.607163000	3.082075000
1	0.757820000	-2.423601000	2.383941000
1	2.000891000	-1.344722000	3.077314000
6	-1.670144000	-0.237654000	2.858905000
6	-2.138145000	0.503079000	3.948405000
1	-1.459517000	1.133103000	4.511136000
6	-3.486378000	0.404084000	4.321965000
1	-3.848225000	0.970199000	5.172518000
6	-4.351501000	-0.427320000	3.604032000
1	-5.392557000	-0.511807000	3.894233000
6	-3.873379000	-1.154702000	2.506598000
1	-4.550591000	-1.800124000	1.954658000
6	-2.527402000	-1.069899000	2.114121000
6	-2.048581000	-1.841644000	0.910206000
1	-2.844959000	-2.505717000	0.552131000
1	-1.179579000	-2.457690000	1.144370000
6	-2.732735000	0.063497000	-0.553654000
1	-3.699126000	-0.317199000	-0.213227000
1	-2.795272000	0.187090000	-1.638698000
6	-2.429427000	1.392105000	0.080008000
6	-3.452068000	2.273164000	0.380910000
1	-4.484105000	1.980457000	0.231244000
6	-3.119151000	3.543408000	0.877389000
1	-3.897294000	4.255137000	1.127372000
6	-1.790132000	3.895155000	1.039046000
1	-1.494816000	4.868729000	1.398201000
6	-0.770650000	2.962387000	0.726230000
6	1.149483000	4.508749000	1.175370000
6	2.685060000	4.554045000	1.140288000
6	3.221150000	4.056660000	-0.228529000
1	2.988979000	3.003666000	-0.429255000
1	4.310291000	4.167806000	-0.247913000
1	2.812449000	4.658122000	-1.048665000
6	3.133798000	6.014711000	1.355743000

1	4.227129000	6.061633000	1.369442000
1	2.752145000	6.407924000	2.300709000
1	2.765892000	6.662525000	0.554381000
6	3.226932000	3.670500000	2.298045000
1	2.903326000	2.627632000	2.215691000
1	2.886247000	4.052836000	3.265662000
1	4.322107000	3.700329000	2.292591000
6	-1.229287000	-1.740713000	-1.468308000
1	-2.034700000	-2.387473000	-1.827768000
6	0.003758000	-2.514699000	-1.051629000
6	0.323018000	-3.813169000	-1.425513000
1	-0.375830000	-4.406091000	-2.003818000
6	1.571972000	-4.331207000	-1.044760000
1	1.850104000	-5.341507000	-1.322035000
6	2.453785000	-3.526552000	-0.315693000
1	3.430769000	-3.891934000	-0.024481000
6	2.068527000	-2.230224000	0.040445000
1	2.701536000	-1.550892000	0.592542000
6	-0.788089000	-0.723871000	-2.508310000
6	-1.014841000	-0.773307000	-3.877865000
1	-1.596101000	-1.577579000	-4.313337000
6	-0.473075000	0.247275000	-4.678288000
1	-0.632400000	0.237749000	-5.750389000
6	0.270582000	1.273854000	-4.083480000
1	0.698985000	2.069214000	-4.680457000
6	0.460783000	1.266042000	-2.698204000
1	1.030515000	2.023033000	-2.176882000
7	0.579337000	0.072135000	6.129972000
7	-1.647033000	-0.933817000	-0.246465000
7	-1.101953000	1.700172000	0.273361000
7	0.571060000	3.263740000	0.825845000
1	1.203222000	2.508374000	0.572715000
7	0.857509000	-1.744571000	-0.315161000
7	-0.064518000	0.279857000	-1.944194000
8	0.454208000	5.483862000	1.498595000
1	3.481455000	0.991863000	0.775113000
8	1.723298000	0.910450000	-0.085114000
8	2.667993000	0.490828000	1.021413000

^{4}[Fe^{III}(N3Py^{amide}SR)(OOH)]$^{2+}$

26	-0.011786000	0.110853000	-0.000902000
16	-0.010011000	0.079843000	2.503174000
6	1.162466000	-0.321576000	5.496418000
6	1.983617000	-0.829229000	4.402098000
1	1.735744000	-1.882779000	4.224928000

1	3.044216000	-0.797680000	4.689238000
6	1.819026000	-0.017021000	3.112603000
1	2.419557000	-0.448021000	2.316244000
1	2.078742000	1.034068000	3.245040000
6	-0.702931000	-1.590373000	2.908315000
6	-1.613900000	-1.642612000	3.967407000
1	-1.828683000	-0.751053000	4.544532000
6	-2.225402000	-2.861571000	4.293413000
1	-2.926022000	-2.904906000	5.119175000
6	-1.917763000	-4.013813000	3.563781000
1	-2.380404000	-4.960084000	3.819683000
6	-1.005546000	-3.948999000	2.503277000
1	-0.765314000	-4.851077000	1.948262000
6	-0.388315000	-2.736847000	2.152625000
6	0.575099000	-2.697285000	0.992831000
1	0.792451000	-3.719646000	0.659923000
1	1.519860000	-2.227843000	1.267129000
6	-1.340875000	-2.426230000	-0.589956000
1	-1.442260000	-3.478272000	-0.309921000
1	-1.438979000	-2.362397000	-1.677033000
6	-2.417350000	-1.589051000	0.045541000
6	-3.655958000	-2.120414000	0.359669000
1	-3.845336000	-3.180353000	0.244662000
6	-4.657310000	-1.246259000	0.819160000
1	-5.638522000	-1.629220000	1.074323000
6	-4.401721000	0.111962000	0.937394000
1	-5.155621000	0.811991000	1.262167000
6	-3.112939000	0.601652000	0.616298000
6	-3.606067000	3.033841000	0.968336000
6	-2.920493000	4.408063000	0.939044000
6	-2.194540000	4.624028000	-0.416716000
1	-1.362323000	3.925729000	-0.571962000
1	-1.784746000	5.638830000	-0.445560000
1	-2.892370000	4.522206000	-1.254892000
6	-4.000858000	5.494696000	1.117343000
1	-3.529020000	6.482109000	1.125680000
1	-4.546816000	5.356849000	2.053838000
1	-4.729685000	5.461751000	0.302145000
6	-1.907868000	4.480221000	2.115943000
1	-1.124519000	3.717014000	2.041062000
1	-2.415673000	4.346744000	3.076522000
1	-1.432299000	5.466667000	2.122634000
6	1.010236000	-2.020603000	-1.394122000
1	1.148951000	-3.060804000	-1.703540000
6	2.314580000	-1.373582000	-0.957265000
6	3.590513000	-1.824139000	-1.275314000

1	3.732718000	-2.761196000	-1.800920000
6	4.688724000	-1.029570000	-0.902954000
1	5.696613000	-1.355426000	-1.132407000
6	4.471186000	0.187552000	-0.245797000
1	5.300116000	0.826033000	0.033750000
6	3.160823000	0.576277000	0.052121000
1	2.914746000	1.500397000	0.557981000
6	0.428298000	-1.164315000	-2.509270000
6	0.466171000	-1.452182000	-3.868301000
1	0.885793000	-2.385303000	-4.224982000
6	-0.052123000	-0.501304000	-4.764763000
1	-0.038224000	-0.698839000	-5.830383000
6	-0.582632000	0.698837000	-4.275996000
1	-0.982429000	1.446223000	-4.949329000
6	-0.590323000	0.926759000	-2.896267000
1	-0.976969000	1.833446000	-2.449650000
7	0.450296000	0.100197000	6.322665000
7	0.038933000	-1.930772000	-0.215975000
7	-2.128420000	-0.258455000	0.195590000
7	-2.761597000	1.936099000	0.685534000
1	-1.791532000	2.144123000	0.469173000
7	2.112511000	-0.207539000	-0.286619000
7	-0.096476000	0.003156000	-2.048099000
8	-4.808217000	2.877239000	1.229098000
1	0.789479000	3.465339000	0.855917000
8	0.038052000	1.921781000	-0.081920000
8	0.885903000	2.498773000	1.032979000

^{6}[Fe^{III}(N3PySR)(OOtBu)]$^{2+}$

26	-0.055098000	0.222454000	0.021775000
16	0.126410000	-0.005830000	2.604005000
6	1.396058000	-0.795984000	5.508322000
6	2.144223000	-1.201368000	4.323187000
1	1.839638000	-2.216928000	4.034895000
1	3.216252000	-1.248930000	4.562250000
6	1.967621000	-0.231767000	3.148690000
1	2.533273000	-0.574936000	2.284485000
1	2.267787000	0.786412000	3.406707000
6	-0.653964000	-1.652358000	2.952736000
6	-1.558957000	-1.693263000	4.017449000
1	-1.727994000	-0.809904000	4.621536000
6	-2.221420000	-2.892093000	4.316442000
1	-2.916964000	-2.926833000	5.147037000
6	-1.965172000	-4.037701000	3.557480000
1	-2.463102000	-4.971214000	3.794876000

6	-1.055713000	-3.983984000	2.493957000
1	-0.853916000	-4.881453000	1.916483000
6	-0.391151000	-2.790023000	2.165243000
6	0.563227000	-2.766494000	0.995277000
1	0.765272000	-3.794750000	0.666731000
1	1.518213000	-2.313873000	1.268046000
6	-1.359166000	-2.415298000	-0.558408000
1	-1.518951000	-3.463477000	-0.288863000
1	-1.469424000	-2.341042000	-1.644082000
6	-2.411252000	-1.543959000	0.087372000
6	-3.650375000	-2.065718000	0.413177000
1	-3.840896000	-3.126342000	0.305702000
6	-4.650865000	-1.191305000	0.872618000
1	-5.629823000	-1.574254000	1.136856000
6	-4.397054000	0.167033000	0.977877000
1	-5.152365000	0.868353000	1.296729000
6	-3.112591000	0.659347000	0.647143000
6	-3.661468000	3.093157000	0.910385000
6	-2.997151000	4.476967000	0.844763000
6	-2.275868000	4.662876000	-0.518494000
1	-1.434284000	3.972395000	-0.653108000
1	-1.882181000	5.683216000	-0.577977000
1	-2.975723000	4.527608000	-1.350847000
6	-4.094317000	5.551868000	0.991409000
1	-3.637001000	6.546139000	0.969985000
1	-4.638092000	5.434480000	1.932186000
1	-4.822227000	5.483741000	0.177768000
6	-1.985707000	4.603347000	2.016839000
1	-1.192535000	3.846915000	1.973238000
1	-2.492357000	4.498763000	2.982077000
1	-1.522457000	5.595851000	1.987012000
6	1.007070000	-2.024046000	-1.351044000
1	1.211613000	-3.051126000	-1.672786000
6	2.282056000	-1.323628000	-0.899063000
6	3.574890000	-1.753525000	-1.178503000
1	3.743941000	-2.699088000	-1.680392000
6	4.650896000	-0.932779000	-0.801767000
1	5.669022000	-1.244898000	-1.004608000
6	4.397969000	0.292992000	-0.173571000
1	5.208546000	0.952816000	0.110007000
6	3.075780000	0.662768000	0.088567000
1	2.805335000	1.592072000	0.573228000
6	0.423451000	-1.198036000	-2.492062000
6	0.480600000	-1.541064000	-3.838805000
1	0.915109000	-2.484491000	-4.148924000
6	-0.035899000	-0.637476000	-4.783039000

1	-0.003171000	-0.879849000	-5.839223000
6	-0.591146000	0.574560000	-4.352524000
1	-0.991374000	1.288194000	-5.061946000
6	-0.622801000	0.856452000	-2.983706000
1	-1.035908000	1.774706000	-2.585459000
7	0.751857000	-0.445432000	6.419476000
7	0.032184000	-1.985939000	-0.193136000
7	-2.121231000	-0.206705000	0.232190000
7	-2.784697000	1.999931000	0.698097000
1	-1.809464000	2.234699000	0.529853000
7	2.046914000	-0.146369000	-0.258958000
7	-0.122649000	-0.020858000	-2.085457000
8	-4.868984000	2.924876000	1.131880000
1	0.774782000	3.674652000	0.973051000
8	0.027108000	2.110465000	0.100957000
8	0.947612000	2.711383000	1.097328000

Orca Optimized Geometries:

^{2}[Fe^{III}(OOH)(N3PySR)]$^{2+}$

26	0.042620000	0.138099000	-0.062918000
16	1.352259000	0.743369000	-2.021181000
6	2.867158000	-0.403162000	-1.940523000
6	4.083177000	0.189054000	-2.681771000
6	5.200137000	-0.743794000	-2.513282000
7	6.039314000	-1.541642000	-2.336152000
1	3.872489000	0.335960000	-3.748508000
1	4.345864000	1.169202000	-2.265816000
1	3.064233000	-0.497251000	-0.871784000
1	2.563189000	-1.367470000	-2.350921000
6	0.379311000	0.038598000	-3.436179000
6	1.002084000	-0.693317000	-4.449380000
1	2.067592000	-0.887731000	-4.428726000
6	0.241997000	-1.167500000	-5.528846000
1	0.729377000	-1.728745000	-6.318588000
6	-1.130101000	-0.897700000	-5.592847000
1	-1.717033000	-1.247610000	-6.434310000
6	-1.741436000	-0.163479000	-4.569086000
1	-2.802234000	0.067666000	-4.624406000
6	-1.001361000	0.308894000	-3.472253000
6	-1.694641000	1.082510000	-2.378997000
1	-1.192611000	2.030513000	-2.167860000
1	-2.728158000	1.299489000	-2.675279000
7	-1.743663000	0.306094000	-1.064380000

6	-2.300637000	-1.081192000	-1.285692000
1	-2.983572000	-1.320994000	-0.463648000
1	-2.875814000	-1.112822000	-2.215602000
6	-1.185953000	-2.096225000	-1.309192000
6	-1.343343000	-3.365507000	-1.866642000
1	-2.266765000	-3.622472000	-2.372993000
6	-0.302919000	-4.294675000	-1.755867000
1	-0.410782000	-5.285188000	-2.183024000
6	0.871988000	-3.931140000	-1.081750000
1	1.691327000	-4.630165000	-0.964655000
6	0.976146000	-2.646813000	-0.549947000
1	1.847738000	-2.305748000	-0.008569000
7	-0.030268000	-1.743981000	-0.678414000
6	-2.485087000	1.099392000	0.009682000
1	-3.515082000	1.325879000	-0.281315000
6	-1.651485000	2.345695000	0.245913000
6	-2.132826000	3.634456000	0.434224000
1	-3.194724000	3.843100000	0.368065000
6	-1.207970000	4.655880000	0.708327000
1	-1.551700000	5.673647000	0.855636000
6	0.154689000	4.347190000	0.793926000
1	0.886733000	5.114192000	1.013492000
6	0.574523000	3.026638000	0.598787000
1	1.607541000	2.720733000	0.678327000
7	-0.319494000	2.053173000	0.323116000
6	-2.393679000	0.279702000	1.284138000
6	-3.384762000	0.122297000	2.244655000
1	-4.371830000	0.542748000	2.090795000
6	-3.065843000	-0.577001000	3.422080000
1	-3.814616000	-0.710047000	4.195038000
6	-1.775518000	-1.094911000	3.590258000
1	-1.498509000	-1.628175000	4.491282000
6	-0.829111000	-0.918901000	2.576141000
1	0.184813000	-1.282084000	2.650824000
7	-1.148670000	-0.246081000	1.450716000
8	1.610087000	-0.069165000	0.810266000
8	1.661587000	0.665053000	2.123531000
1	2.564043000	0.416802000	2.436505000

^{2}[Fe^{III}(OOH)(N3Py^{amide}SR)]$^{2+}$

26	0.028958850	0.001609873	0.218482875
16	-0.134677441	-0.220229653	2.592128253
6	0.617341470	-1.878948685	3.198341354
6	0.093294494	-2.273631496	4.591160974
6	0.279121530	-1.216650527	5.586291929

7	0.403245402	-0.324322905	6.334582580
1	-0.972000110	-2.532279230	4.539368976
1	0.629054046	-3.180050099	4.905310303
1	0.385681216	-2.656496008	2.468694622
1	1.689273787	-1.673277355	3.205388676
6	-1.932767029	-0.502766761	2.925003074
6	-2.462585157	0.109170552	4.065551612
1	-1.823729295	0.704604938	4.708746895
6	-3.814654897	-0.084558035	4.388554605
1	-4.224881704	0.378056908	5.279079219
6	-4.620520709	-0.884718110	3.570671833
1	-5.659172559	-1.057678095	3.830409210
6	-4.081700901	-1.475479642	2.419395135
1	-4.708296526	-2.097183718	1.785746623
6	-2.731241601	-1.294734906	2.080128634
6	-2.183264447	-1.963703143	0.845766342
1	-2.963817502	-2.585714476	0.388308380
1	-1.330279448	-2.602527928	1.082148721
7	-1.715734409	-0.970685452	-0.208046188
6	-2.789350286	0.051614492	-0.487005491
1	-3.759422154	-0.328040402	-0.155391526
1	-2.847333868	0.213281217	-1.568840373
6	-2.474699664	1.359123556	0.187202467
6	-3.484769260	2.268996517	0.441536691
1	-4.514641200	2.003948561	0.231476291
6	-3.139073288	3.526805250	0.962707943
1	-3.908752047	4.252427657	1.198728707
6	-1.806492742	3.851107691	1.163033685
1	-1.496536996	4.819633228	1.524265779
6	-0.801582320	2.899559560	0.863845321
7	-1.149807039	1.635940108	0.432483520
7	0.545000086	3.197584900	0.917424890
6	1.129471222	4.484762370	0.997421150
6	2.635796794	4.523227764	0.708576509
6	2.947856165	3.810592438	-0.635611128
1	2.811906543	2.723717323	-0.575267490
1	3.993263846	4.004368119	-0.900446836
1	2.318656683	4.211132789	-1.440389602
6	3.085043604	5.994106340	0.604030911
1	4.162404687	6.027680184	0.404433301
1	2.872736528	6.536022817	1.530136651
1	2.560715828	6.503242793	-0.210597872
6	3.383266933	3.825436409	1.874742667
1	3.064427611	2.781646773	1.996844937
1	3.196279901	4.346643569	2.820242523
1	4.461399009	3.849259312	1.675984221

8	0.462173320	5.495893777	1.257754232
1	1.173913959	2.410751431	0.756706743
6	-1.236527831	-1.690821732	-1.467219980
1	-2.028162242	-2.300343915	-1.913311589
6	-0.034949789	-2.508950376	-1.037878458
6	0.310142157	-3.765727945	-1.517139040
1	-0.340960589	-4.285979563	-2.210783205
6	1.518424025	-4.338111961	-1.082944859
1	1.821244804	-5.314196112	-1.444714825
6	2.331393765	-3.629426391	-0.190503721
1	3.270451401	-4.042998179	0.156522478
6	1.925695088	-2.367677069	0.257049158
1	2.515037333	-1.756870642	0.927125260
7	0.757944476	-1.827094131	-0.159085369
6	-0.738198659	-0.600517064	-2.401811828
6	-0.960041012	-0.501169220	-3.770265859
1	-1.551724448	-1.245720315	-4.290502160
6	-0.404034635	0.594799426	-4.454995628
1	-0.571535942	0.710651019	-5.520338554
6	0.357150931	1.538613223	-3.753534954
1	0.798479488	2.387581874	-4.260916349
6	0.538186375	1.381624007	-2.375746395
1	1.104213534	2.079960397	-1.775125851
7	-0.008820884	0.330788957	-1.730109966
8	1.677882417	0.776917670	0.333123080
8	2.485234293	0.301797893	1.523706280
1	3.327615026	0.796148558	1.384457880

^{2}[Fe^{III}(OOtBu)(N3PySR)]$^{2+}$

26	0.043626217	0.067232455	-0.105660890
16	1.335845556	0.680958322	-2.071052183
6	2.837965277	-0.479553504	-1.998630599
6	4.078770958	0.130890278	-2.680872442
6	5.198535037	-0.787349250	-2.460521986
7	6.036361269	-1.574874055	-2.236886420
1	3.915367725	0.278994412	-3.755859520
1	4.309299339	1.112354833	-2.248537142
1	3.002732832	-0.610988140	-0.928247953
1	2.541537972	-1.427471608	-2.450687474
6	0.333546914	-0.000700982	-3.475982866
6	0.928563952	-0.737201002	-4.502399329
1	1.992156064	-0.945011252	-4.500048893
6	0.143256853	-1.198345567	-5.569326723
1	0.608346355	-1.763419608	-6.369800816
6	-1.226318123	-0.910865248	-5.607546501

1	-1.833103335	-1.251544512	-6.438735144
6	-1.809348959	-0.170829345	-4.571588486
1	-2.867900032	0.074036759	-4.607162600
6	-1.044182154	0.289701614	-3.487176500
6	-1.709205666	1.074783492	-2.382679520
1	-1.185397262	2.012474555	-2.177612482
1	-2.741404400	1.313950050	-2.667298931
7	-1.755531599	0.298334438	-1.070810029
6	-2.352400859	-1.072445718	-1.285253059
1	-2.999865942	-1.309378663	-0.434275586
1	-2.971965946	-1.079403486	-2.187234284
6	-1.260035118	-2.108360064	-1.371972386
6	-1.447827797	-3.351137708	-1.977381159
1	-2.384508815	-3.574333186	-2.475219512
6	-0.417221035	-4.296617608	-1.929418612
1	-0.547132895	-5.265851765	-2.397353213
6	0.776023481	-3.978525745	-1.264424181
1	1.587504262	-4.693234518	-1.196540195
6	0.908179991	-2.719632586	-0.679582717
1	1.792832040	-2.410858819	-0.139256517
7	-0.086029257	-1.798497989	-0.752834977
6	-2.447021701	1.107309892	0.025239690
1	-3.474813671	1.371944336	-0.240785831
6	-1.566970521	2.324023628	0.253633370
6	-1.998075717	3.628658753	0.457185030
1	-3.052499457	3.876852604	0.412768506
6	-1.032055040	4.615153140	0.715127675
1	-1.335784278	5.644353454	0.870668523
6	0.320567406	4.257661844	0.771474133
1	1.083789519	4.998722413	0.973674737
6	0.687802310	2.923653882	0.565948716
1	1.710727191	2.578742413	0.617232066
7	-0.246074048	1.985155433	0.305445963
6	-2.354533964	0.275880807	1.293614275
6	-3.320885541	0.160547717	2.285295407
1	-4.291843234	0.626531466	2.165020554
6	-2.997305390	-0.557206667	3.450242967
1	-3.725607873	-0.655206284	4.247605685
6	-1.730155772	-1.140427873	3.573170846
1	-1.450452666	-1.693084876	4.461695649
6	-0.809303468	-1.002819611	2.530367650
1	0.189096656	-1.410865911	2.571242894
7	-1.130505509	-0.305579289	1.420710262
8	1.608725455	-0.180005380	0.748497627
8	1.656053341	0.489743222	2.084265894
6	3.043782264	0.351345410	2.669309470

6	3.383220067	-1.128631970	2.830160607
1	4.339183466	-1.231375619	3.355687364
1	3.473506687	-1.616982374	1.854695958
1	2.614600332	-1.636620055	3.424017441
6	4.035761971	1.080512624	1.766668728
1	5.044059653	1.001208849	2.188695807
1	3.778778531	2.143874551	1.689706322
1	4.048479857	0.632897703	0.767618989
6	2.853097629	1.056426820	4.015877273
1	3.814387504	1.081392657	4.541011730
1	2.131043475	0.518621754	4.637839127
1	2.505939636	2.085656260	3.871554721

^{2}[Fe^{III}(OOtBu)(N3Py^{amide}SR)]$^{2+}$

26	0.083683900	0.122611887	-0.088486276
16	0.233281512	-0.337842956	2.258283561
6	0.855369172	-1.550554785	5.105915248
6	0.524690551	-2.535811995	4.075067166
1	-0.552966436	-2.739758203	4.108308207
1	1.038729113	-3.483547212	4.286434289
6	0.937801159	-2.074980157	2.664312036
1	0.595854507	-2.786676216	1.911885357
1	2.016384033	-1.928864071	2.580804015
6	-1.532810659	-0.525806491	2.778131858
6	-1.908555768	0.109800774	3.964505942
1	-1.167830362	0.634577643	4.557281426
6	-3.245033665	0.046087606	4.388427306
1	-3.541047517	0.537525578	5.308510301
6	-4.183582899	-0.664391215	3.632121007
1	-5.211955006	-0.736093197	3.969393993
6	-3.794851599	-1.289460419	2.440033450
1	-4.525891666	-1.836965386	1.852270028
6	-2.466706008	-1.222228344	1.989728448
6	-2.100717894	-1.838928074	0.662201764
1	-2.952453615	-2.411890882	0.272599011
1	-1.242760429	-2.506912380	0.744127727
6	-2.804869333	0.291646059	-0.398650755
1	-3.768287334	-0.117895378	-0.082779080
1	-2.909504244	0.653841218	-1.426565234
6	-2.387707425	1.433199603	0.481855940
6	-3.316438313	2.184495063	1.178393080
1	-4.360430495	1.896633494	1.169925175
6	-2.867001484	3.302299479	1.899085048
1	-3.558571594	3.887384286	2.493703535
6	-1.533479564	3.676044984	1.826722004

1	-1.167355808	4.566865788	2.310335182
6	-0.629605642	2.901266940	1.062858925
6	1.064809168	4.676901714	0.750744861
6	2.479616467	4.924420034	0.223607867
6	2.753247766	4.099377226	-1.059378089
1	2.687858600	3.017648513	-0.900935435
1	3.764156086	4.322112574	-1.418380268
1	2.045129147	4.386051606	-1.847655739
6	2.642252342	6.419995846	-0.112306632
1	3.667516361	6.599362079	-0.456542140
1	2.444026690	7.038693275	0.766553044
1	1.948344346	6.723532243	-0.903270069
6	3.455080780	4.551801190	1.371369352
1	3.282333759	3.537830512	1.743837722
1	3.328534115	5.252586493	2.203882258
1	4.488146898	4.624025602	1.010505790
6	-1.458042244	-1.386084289	-1.738744129
1	-2.321727681	-1.926253652	-2.138355120
6	-0.252584304	-2.278964663	-1.534567658
6	-0.038371048	-3.516512735	-2.127961570
1	-0.789299019	-3.949282883	-2.779271134
6	1.166795692	-4.189758950	-1.858752398
1	1.367616172	-5.154269547	-2.311224259
6	2.097697809	-3.604324218	-0.993991686
1	3.030188988	-4.101243019	-0.753574792
6	1.816404135	-2.356988190	-0.429116075
1	2.482895639	-1.838058106	0.238808991
6	-1.027670150	-0.231150134	-2.628478263
6	-1.380200426	-0.026512107	-3.957188039
1	-2.044989826	-0.716702122	-4.464259338
6	-0.854804341	1.097759923	-4.618699702
1	-1.120045911	1.294021526	-5.651529854
6	0.003738847	1.966235074	-3.932651470
1	0.424715630	2.836083667	-4.421627999
6	0.317446738	1.702498536	-2.595852876
1	0.969042940	2.334841903	-2.010264303
7	1.103281720	-0.712480914	5.885508412
7	-1.743963153	-0.778998196	-0.370322368
7	-1.043819871	1.729168972	0.476573711
7	0.666494394	3.316332462	0.813459740
1	1.317838737	2.591897421	0.511776518
7	0.667589923	-1.704342315	-0.704963809
7	-0.198869325	0.624062367	-1.971882627
8	0.308437568	5.592152836	1.111019889
8	1.740446046	0.884085547	-0.110919463
8	2.713045889	0.143217218	0.771838904

6	4.151873841	0.227006375	0.260201039
6	4.195575596	0.009902357	-1.248017305
1	5.234041755	0.098077200	-1.586455339
1	3.602028495	0.770967830	-1.760711007
1	3.821722991	-0.980971154	-1.527653616
6	4.805174092	-0.912094830	1.052631987
1	5.886885371	-0.882060170	0.875655299
1	4.444269867	-1.897728322	0.738992430
1	4.634672023	-0.782457407	2.128058314
6	4.753022454	1.567564735	0.654170937
1	5.831826804	1.545580235	0.456094786
1	4.596452261	1.757876862	1.720155067
1	4.322611172	2.380676929	0.074936969

Appendix A. Design and Synthesis of Macrocyclic N4S Ligands with a Pendant Anionic Thiolate Donor

As we are interested in the design and synthesis of novel ligand scaffolds that incorporate mixed nitrogen and sulfur donor sets, one direction of our research has been toward accessing macrocyclic ligands that incorporate four neutral N-donors in a single plane, with an anionic S(thiolate) donor in a pseudo-axial position *trans* to an open binding site. We sought target ligands that would allow future flexibility, where the sterics and/or electronics of the ligand could be altered, so we could explore the effects of these changes on the properties of biologically-relevant FeO_x complexes.

We attempted a synthetic approach where a linear poly(amino/alkyl) fragment would be utilized in a macrocyclization reaction with an electrophile to form 14-membered macrocyclic structures. These macrocycles would then allow for the formation of stable 5 and 6-membered chelate rings with the donor atoms and central Fe ion. Despite significant effort, the key macrocyclization step for these ligands proved unsuccessful and we decide to pursue other projects before I was able to successfully synthesize these target molecules. However, there is literature precedence for similar

cyclization reactions using slightly different reagents. One possible problem could be the stability of the thiol, and it may be advantageous to seek alternate routes for protecting this donor until the macrocycle is fully formed. Another possibility is using a metal ion to pre-organize the poly(amino/alkyl) chain prior to cyclization. There is some preliminary evidence for the formation of dimeric structures that would result from the nucleophile and electrophile not reacting in the proper 1:1 form.

Macrocyclic N4S-[14]-ane with a pendant aryl-thiolate donor

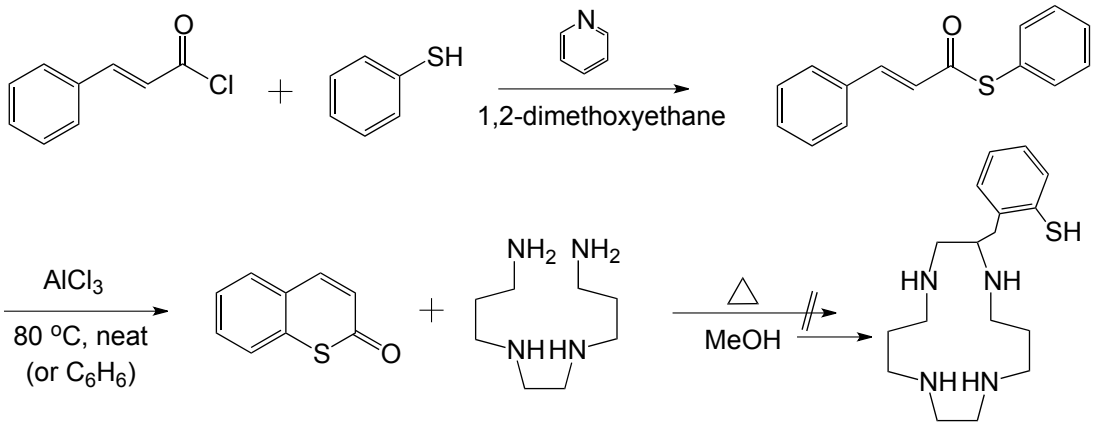

Scheme A. 1. Proposed synthesis of [14]-ane macrocyclic ligand.

The proposed synthesis of the macrocyclic ligand, 2-((1,4,8,11-tetraazacyclotetradecan-1-yl)methyl)benzenethiol, is shown in **Scheme A. 1**. A straightforward acylation of thiophenol with cinnamoyl-chloride affords the thoiester, phenyl thiol(2-ethylcinnamate) in 80% yield. The synthesis of thiocoumarin is then accomplished with $AlCl_3$, either neat or in benzene. The key macrocyclization step with thiocoumarin and *N*,*N*'-(ethane-1,2-diyl)bis(propane-1,3-diamine) was adapted from a literature procedure where the ester-containing coumarin used. According to the

literature, this reaction should be preformed under dilute conditions (MeOH, reflux) to avoid the formation of dimeric products. The reaction was attempted several times, and allowed to reflux for >2 weeks while monitoring by TLC. Little reaction progress was observed, and in only one case evidence of a product spot observed by TLC. Purification of this compound proved difficult, as it co-eluted with unreacted starting material, but crude ^{1}H-NMR suggested that it may be the 2:1 (thiocoumarin : amine) adduct. I then attempted to template the poly(amino/alkyl) donor around a Zn^{2+} ion in order to preorganize the primary amines for attack on the same molecule of thiocoumarin. Unfortunately, it appears that this mitigated the nucleophilicity such that the amines are unable to attack thiocoumarin. One would predict that a thioester is more reactive than an ester, so attack by the amine on thiocoumarin should be more facile than the literature reaction that utilizes an ester.

Experimental

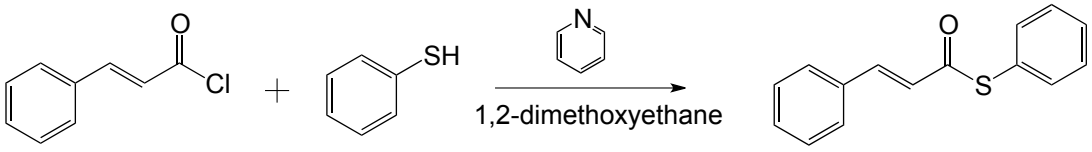

Phenyl thiol-(2-ethylcinnamate). Procedure adapted from Ref 1. Thiophenol (2.24 g, 20.3 mmol) was added to a solution of cinnamoyl chloride (20.3 mmol, 3.5 M) in 1,2-dimethoxyethane. The solution was cooled to 0 °C while pyridine (21.3 mmol, 1.7 mL) was added slowly, causing the reaction mixture to turn yellow. The reaction mixture eventually formed a white precipitate as the solution lost the yellow color. The mixture was allowed to warm to rt overnight before being diluted with H_2O and extracted with $CHCl_3$. The organic layer was then washed with 5% NaOH, H_2O and brine before being dried and concentrated. The crude product was recrystallized from MeOH and EtOH to give the desired product as white crystals.

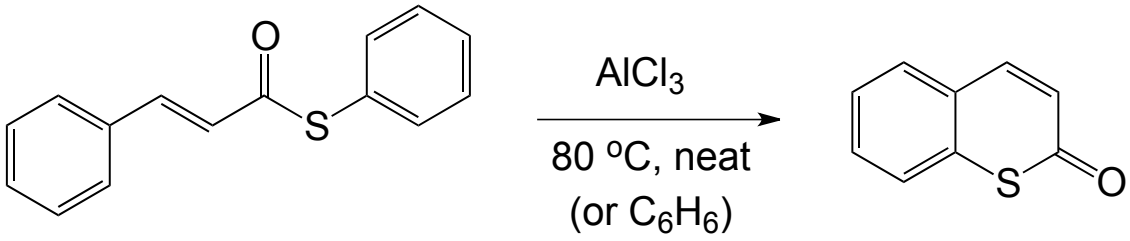

Thiocoumarin. Procedure adapted from Ref 2. Phenyl Thiol-(2-ethylcinnamate) (3.5 g, 15 mmol) and $AlCl_3$ (6 g, 45 mmol) were heated to 80 °C under a drying tube for 4 h. Note: This reaction can be done neat or in solution with C_6H_6 (150 mL), which makes little difference. Upon completion, the reaction mixture was quenched and purified by column chromatography on silica with EtOAc/Hexanes. ^1H NMR ($CDCl_3$, 25 °C): δ 7.73 (d, 1H), 7.61 (d, 1H), 7.52 – 7.45 (m, 2H), 7.39 (t, 1H), 6.55 (d, 1H).

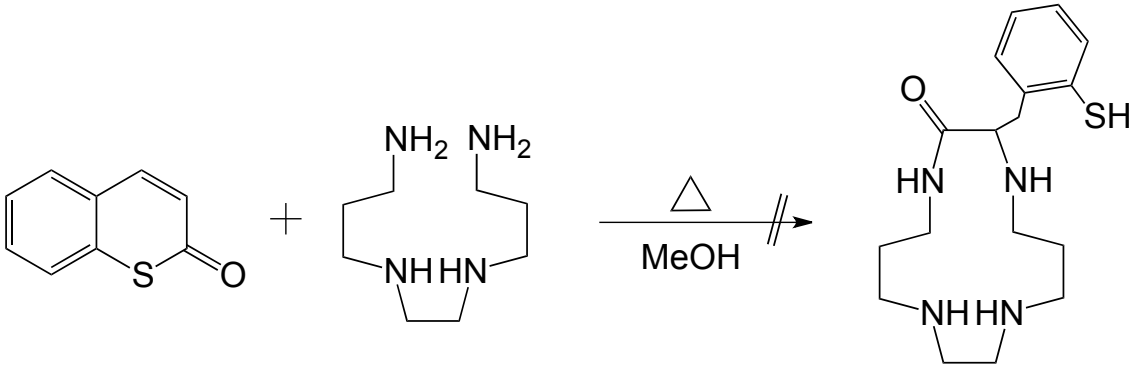

4-(2-mercaptobenzyl)-1,4,8,11-tetraazacyclotetradecan-2-one. Procedure adapted from Ref 3. A 0.05 M solution of Thiocoumarin (3.1 g, 19 mmol) and tetramine (3.5 mL, 19 mmol) was refluxed in dry MeOH for 14 d. One product, identified by TLC was purified by chromatography on silica ($MeOH/CH_2Cl_2/NH_3(aq)$). NMR was inconclusive, product could possibly be the 2:1 adduct (m/z = 499).

*Note: This reaction was also attempted by pre-mixing 1.0 equiv $ZnCl_2$ with the tetramine in order to template the geometry of the amine. No reaction was observed.

N4S macrocyclic bis(imino)pyridine with pendant alkyl-thiolate

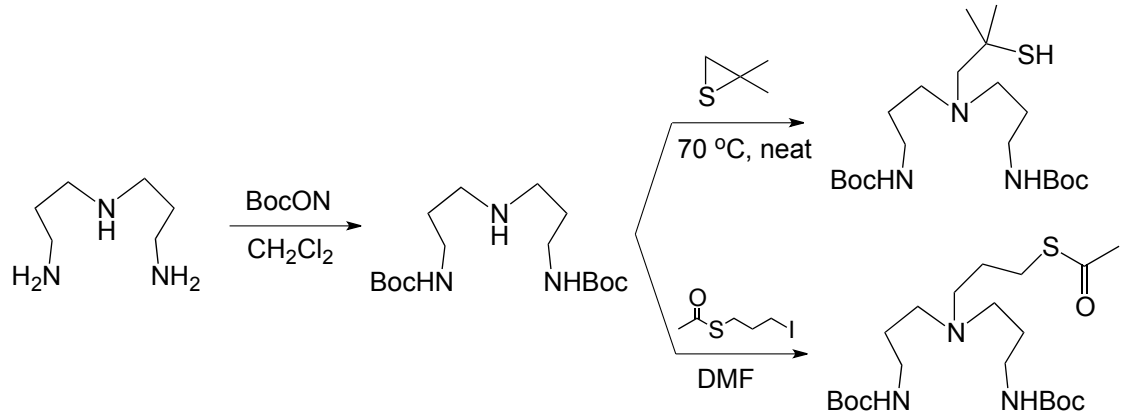

Scheme A. 2. Proposed synthesis of amine.

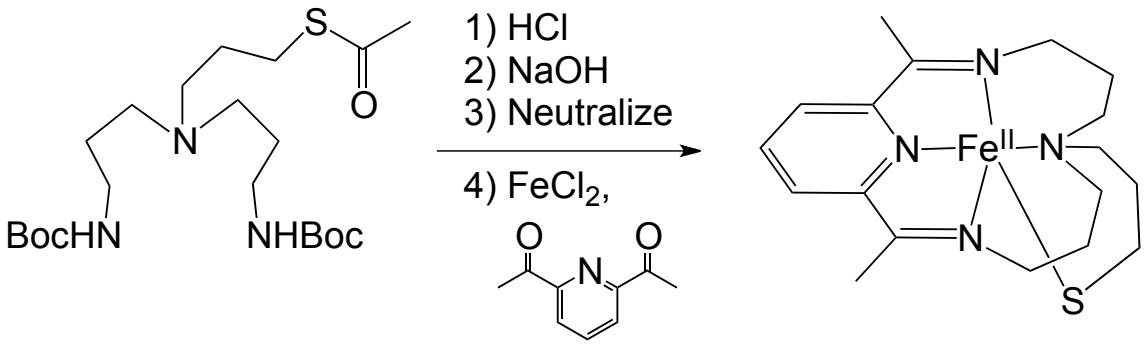

Scheme A. 3. Deprotection and template synthesis of bis(imino)pyridine macrocycle with pendant thiolate.

Another synthetic strategy involved alkylation of a secondary amine with an alkyl-thiolate arm (**Scheme A. 2**) and then preforming a Schiff-base condensation onto diacyl pyridine to give a desired N4S 14-membered macrocyclic ligand (**Scheme A. 3**). This strategy has a number of steps that are reported in the literature, and were previously preformed in our lab by Dr. Gary Kasper. The key cyclization step (**Scheme A. 3**) is reported for the un-substituted linear triamine (N-(3-aminopropyl)propane-1,3-diamine) and diacylpyridine in the presence of Ni(II). This literature reaction was repeated

successfully prior to undertaking the synthesis described herein. Again, the key cyclization step was not successful in my hands and it is unclear whether this was due to the instability of the alkyl-thiolate donor giving mixtures of products that inhibited crystallization, or if the condensation reaction failed to proceed altogether.

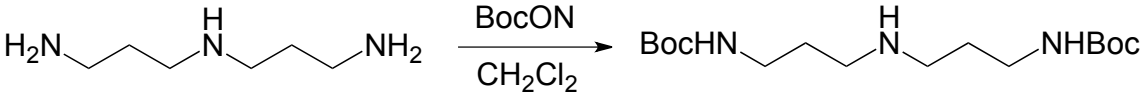

***N*,*N*'-(azanediylbis(propane-3,1-diyl))bis(2,2-dimethylpropanamide).** *N*-(3-aminopropyl)propane-1,3-diamine (533 mg, 4.1 mmol) and BocON (2 g, 8.1 mmol) were stirred in CH_2Cl_2 for 16 h. The crude reaction mixture was concentrated, dissolved in EtOAc, then washed with 5% NaOH and H_2O before being dried and concentrated. ^{1}H NMR ($CDCl_3$, 25 °C): δ 5.20 (br, 1.5 H), 3.30 – 3.10 (br, 4H), 2.65 (t, 4H), 1.75 – 1.55 (br, 5 H), 1.45 (s, 18H).

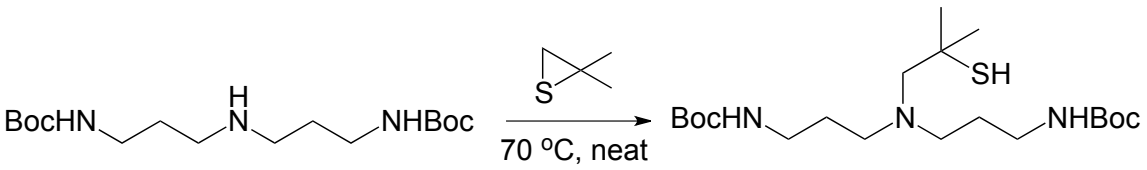

***N*,*N*'-(((2-mercapto-2-methylpropyl)azanediyl)bis(propane-3,1-diyl))bis(2,2-dimethyl propanamide).** Procedure adapted from Ref 4. Assuming quantative yield from Boc protection step, the thiirane (0.42 mL, 4.1 mmol) was added to the secondary amine (932 mg, 4.1 mmol) neat and allowed to stir under Ar for 24 h. This product was not purified due to concerns about stability of the alkyl-thiol, and used crude in subsequent steps.

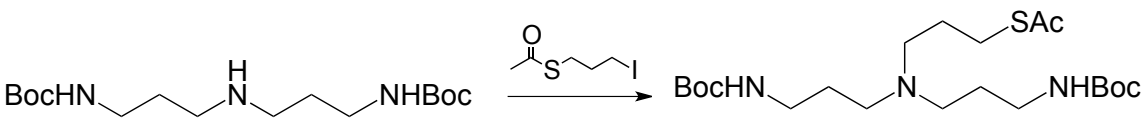

(3-(bis(3-pivalamidopropyl)amino)propyl) ethanethioate. Procedure adapted from Ref 5. An amount of 3-iodioproponyl thioacetate (976 mg, 4.0 mmol) was slowly added to a stirring solution of the amine (938 mg, 4.1 mmol) and Cs_2CO_3 (717 mg, 2.2 mmol) in DMF. Upon completion (by TLC) water was added and the mixture was extracted with EtOAc. The organic layer was dried with brine and MgSO4 and concentrated. The crude yellow oil was purified by column chromatography on silica with CH_2Cl_2/MeOH to give 670 mg (32%) of purified product. ^{1}H NMR ($CDCl_3$, 25 °C): δ (5.25 (br, 2H), 3.17 (br, 4H), 2.86 (t, 2H), 2.41 (t, 6H), 2.32 (s, 3H), 1.75 – 1.60 (m, 6H), 1.42 (s, 18H).

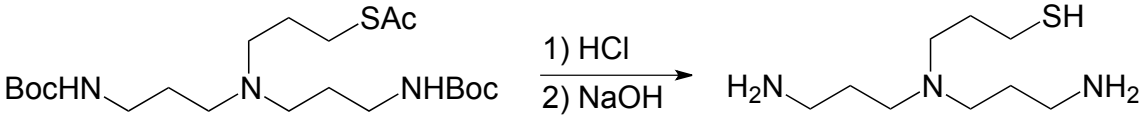

Deprotection. Procedure partially adapted from Ref 5. An amount of the protected starting material (100 mg, 0.22 mmol) was mixed with 0.2 mL of 4 M HCl in dioxane for 24 h. Excess NaOH, as a solution in MeOH) was then added and allowed to stir for an additional 12 h. The reaction mixture was neutralized with HCl in dioxane and concentrated. This compound was not isolated and characterized for purity due to concerns over stability. The crude product was used in the template reaction as a crude product.

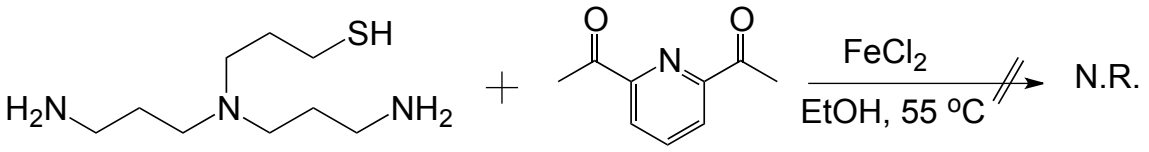

Template reaction. Procedure partially adapted from Ref 5. An amount of $FeCl_2$ (28 mg, 0.22 mmol) and diacylpyridine (36 mg, 0.22 mg) were dissolved in 2 mL of EtOH and heated to 55 °C for 4 h. The reaction mixture was concentrated and dissolved in CH_2Cl_2 before being filtered through celite. The filtrate was pale blue and leaving a large amount of purple precipitate that was dissolved in MeOH. Multiple attempts at crystallization gave only fine powders. Many variations of this template reaction were attempted, all failed to give crystalline product or a promising ion peak in the ESI-MS.

Appendix B. Reaction of N4S Fe^{II}-bis(imino)pyridine complexes with superoxide.

Reactions of [Fe^{II}(LN3S)(py)](OTf) and [Fe^{II}(LN3S)(DMAP)](OTf) were examined with potassium superoxide (KO_2), solubilized by 18-crown-6. The reactions with [Fe^{II}(LN3S)(py)](OTf) and [Fe^{II}(LN3S)(DMAP)](OTf) are identical, therefore preliminary studies were preformed on [Fe^{II}(LN3S)(py)](OTf) only. Upon addition of KO_2/18-C-6 to solutions of [Fe^{II}(LN3S)(py)](OTf), the reaction mixture exhibits an immediate color change from dark brown to deep purple, which could possibly be an Fe^{III}-OO intermediate (**Scheme B. 1**).

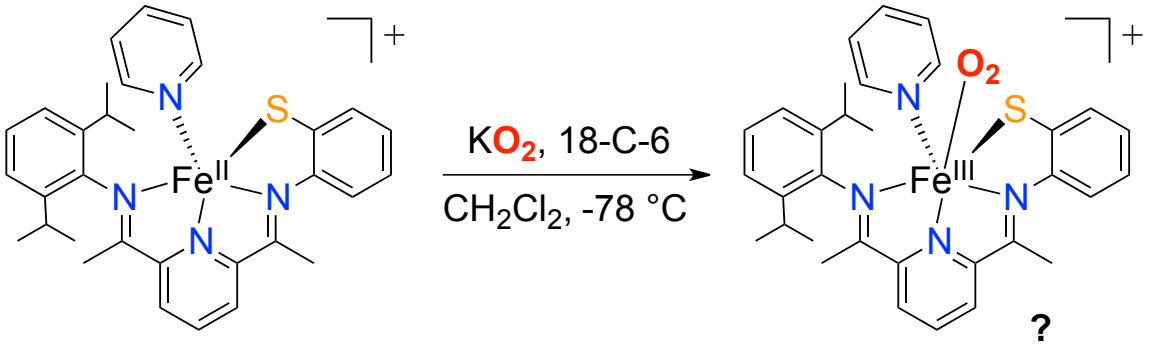

Scheme B. 1. Proposed intermediate formed from reaction of [Fe^{II}(LN3S)(py)](OTf) with KO_2/18-C-6.

The superoxide solution used for these reactions is prepared by vigorously stirring potassium superoxide (100 mg, 1.4 mmol) and 18-crown-6 (380 mg, 1.4 mmol) in approximately 10 mL of Acetonitrile inside the glovebox overnight before filtering through a pad of celite and determining the concentration by UV-Vis in DMSO. Typical concentrations are between 10 and 20 mM.

In a typical reaction, [Fe^{II}(LN3S)(py)](OTf) (7.0 mg, 0.01 mmol) is dissolved in 5.0 mL of methylenechloride inside the glovebox and placed in a dip probe flask equipped with a small stir bar. A separate vial, capped with a septum, containing the

superoxide solution is also prepared inside the glovebox before both are brought out and placed under an argon atmosphere. The dip probe optics are placed into the flask with positive argon flow and the reaction flask is brought to the desired temperature. After an initial scan of the starting material, the 1.0 equivalent of superoxide solution (1.0 mL, 10mM) is added in one portion. The scan rate is typically set for every 0.2 sec for the first minute, every 30 seconds until the 5 minute mark and 1 minute for the remainder of the experiment (usually 90 minutes).

These reactions are reproducible and have been done >10 times, in varying solvents and at different temperatures. In every case, three peaks with similar λ_{max} and relative intensities are observed although the molar absorptivity of the peaks varies greatly with temperature and solvent changes. The starting complex is a very dark red-brown color that turns to a purple intermediate upon addition of superoxide. If left at room temperature for several days, the purple color is completely gone and the solution is a rusty-red color. However at low temperature (-80ºC) the solution was observed to remain purple for at least 3 weeks.

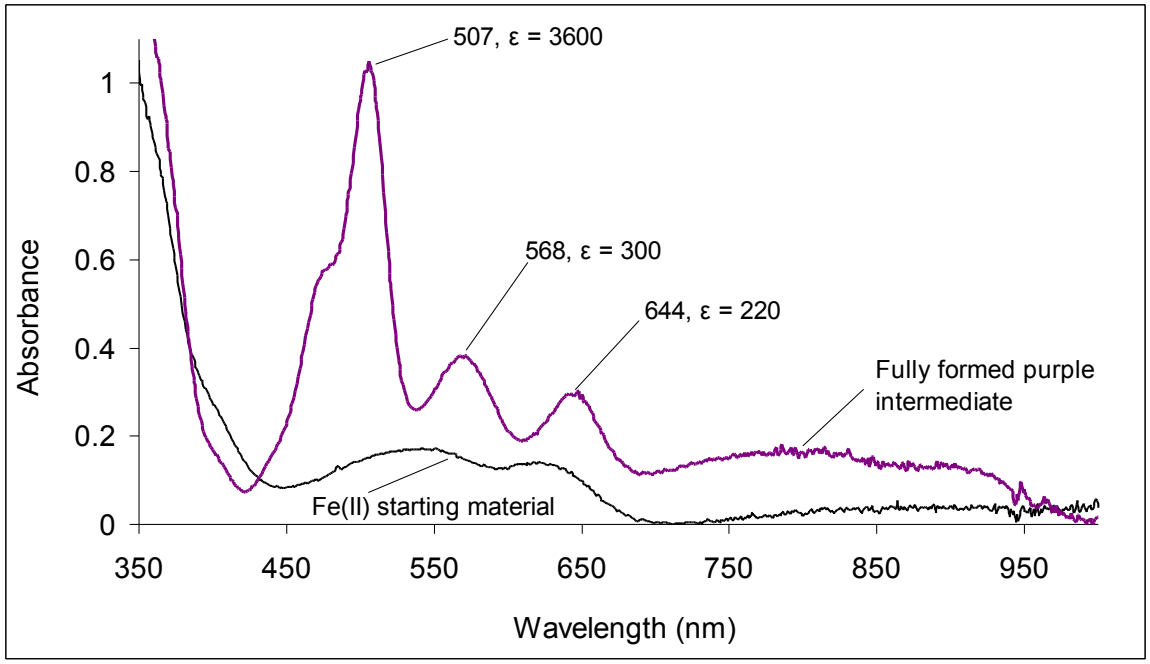

Figure B. 1. Changes in the electronic absorption spectrum upon addition of 1.0 equiv KO_2/18-C-6 to $[Fe^{II}(LN_3S)(py)](OTf)$.

When monitoring the reaction of $[Fe^{II}(LN_3S)(py)](OTf)$ + KO_2/18-C-6 by UV-vis, the absorption spectrum changes, from a broad featureless spectrum characteristic of $[Fe^{II}(LN_3S)(py)](OTf)$, to a spectrum with three distinct peaks at 510, 560 and 640 nm (**Figure B. 1**). This reaction gives similar results in CH_2Cl_2/MeCN and THF/MeCN mixtures at -78 °C. In every case, three peaks with similar λ_{max} and relative molar absorptivities are observed, although the molar absorptivities vary with solvent and temperature. If the purple species is warmed to room temperature, the UV-vis spectrum exhibits significant changes within the time of warming. Over a longer period, decomposition is observed as the purple color is converted to a rusty-red color. If the purple species is stored at low temperature (-80 ºC), the solution remains purple for at least three weeks. The decomposition spectrum (**Figure B. 2**) is characterized by a

decrease in the absorbance around 510 nm while the λ_{max} shifts slightly higher to about 515 or 520 nm. At the same time, the absorbance at 560 nm decreases initially but then increases in intensity and shifts to a slightly lower λ_{max} and the absorbance at 654 nm disappears. Decomposition is begins after about 30 minutes at room temperature and is not observed at -78ºC, however when a low temperature reaction is warmed to room temperature decomposition begins.

Attempts to characterize this species by X-ray crystallography have so far been unsuccessful, most likely due to the presence of K^+/18-C-6 salts that crystallize preferentially. In lieu of structural characterization, preliminary efforts have been made to further characterize this intermediate by EPR and resonance-Raman spectroscopy, although thus far it has been difficult to get consistent results due to the instability of the complex during sample preparation.

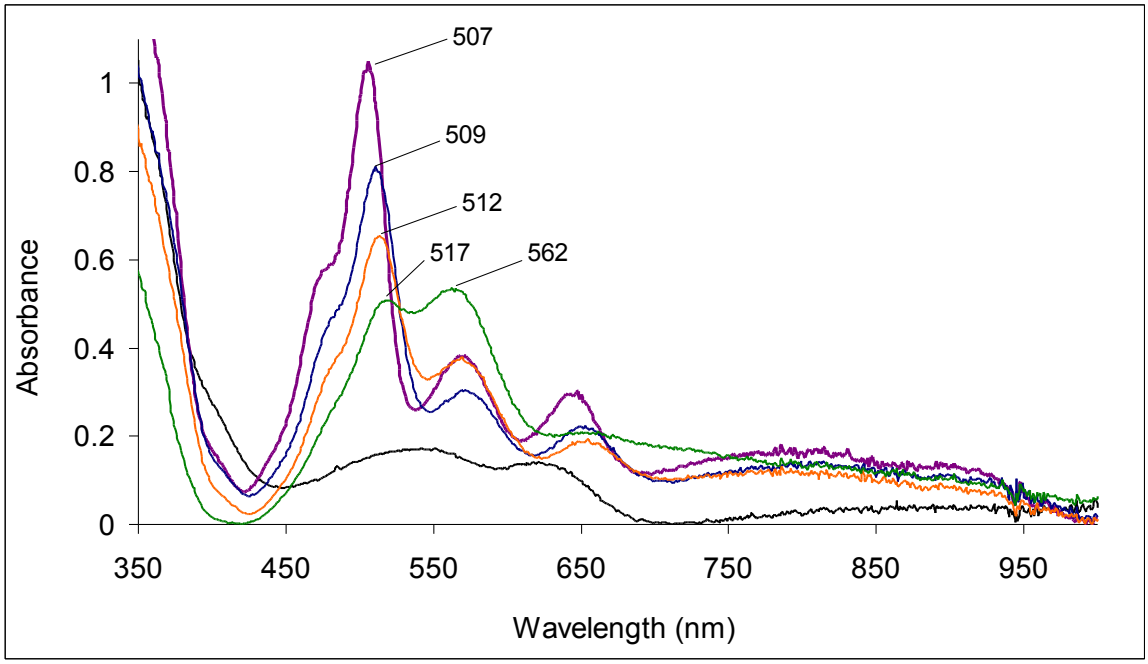

Figure B. 2. Changes in the electronic absorption spectrum upon warming the reaction mixture of $Fe^{II}(LN_3S)(py)](OTf)$ + KO_2/18-C-6 to room temperature. Black =

$Fe^{II}(LN_3S)(py)](OTf)$, Purple = fully formed intermediate, green = final spectrum at room temperature after 2 h.

X-band EPR measuerments were preformed on frozen solutions of the crude reaction mixture of $Fe^{II}(LN_3S)(py)](OTf)$ + 1.0 equiv KO_2/18-C-6. The spectrum in **Figure B. 3** shows a sharp axial signal centered at g = 2.02 consistent with a ls Fe^{III} ion. When the reaction is preformed in the presence of MeOH (100 equiv), the observed signal is centered at g = 2.03 and is rhombic (**Figure B. 4**).

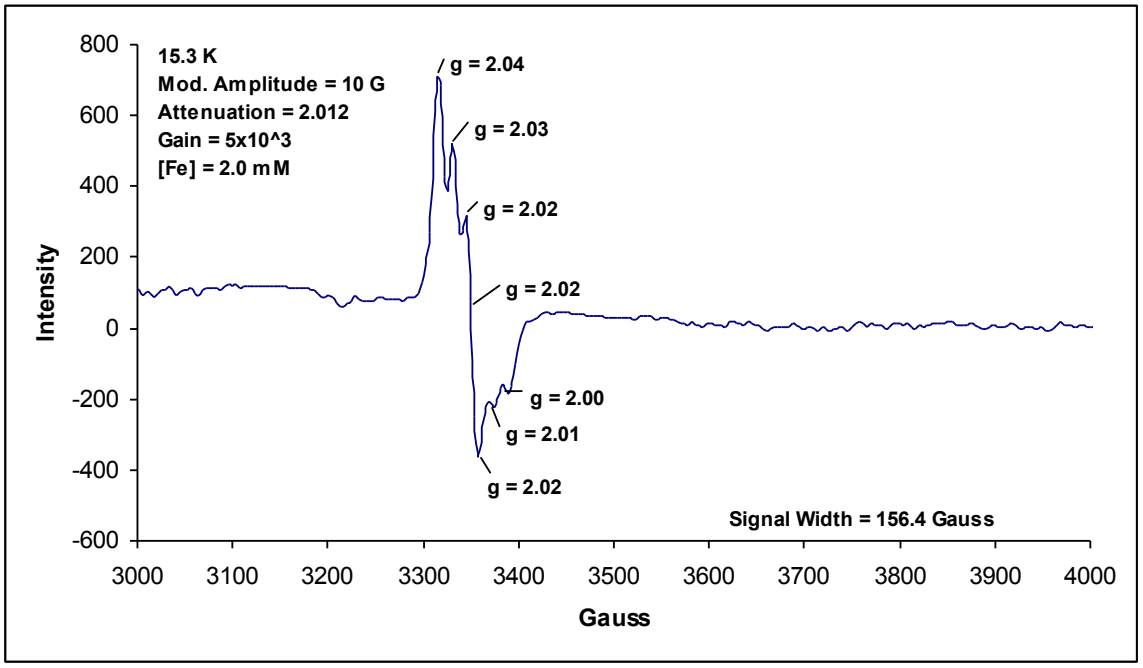

Figure B. 3. X-band EPR spectrum of the crude reaction mixture of $Fe^{II}(LN_3S)(py)](OTf)$ + 1.0 equiv KO_2/18-C-6 at 15 K.

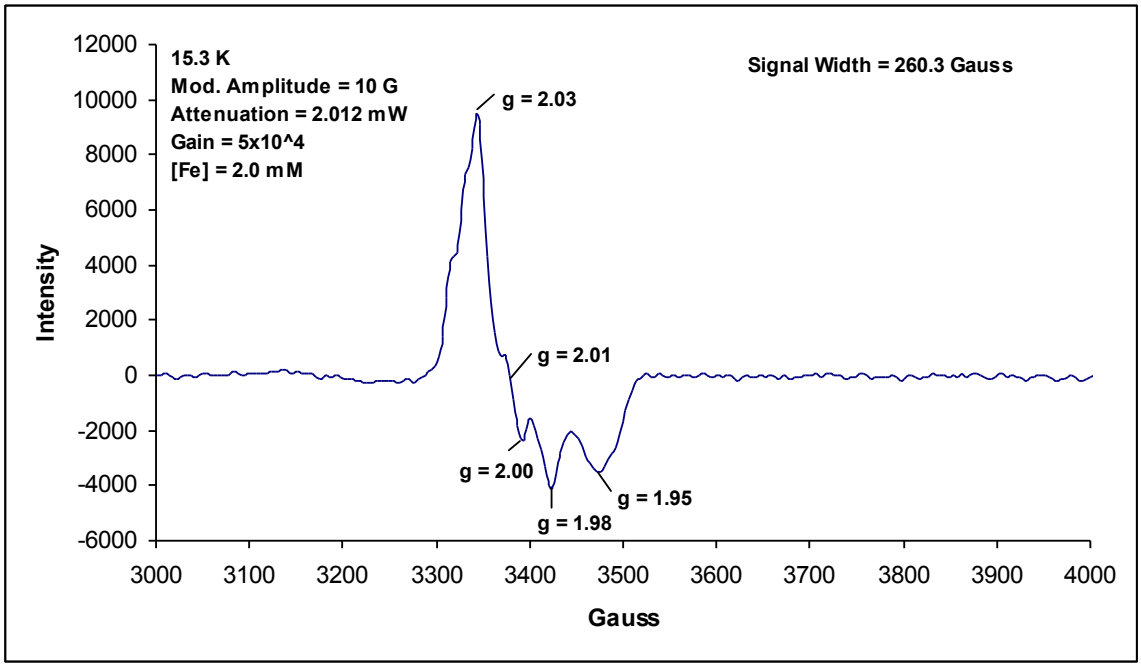

Figure B. 4. X-band EPR spectrum of the crude reaction mixture of $Fe^{II}(LN_3S)(py)](OTf)$ + 1.0 equiv KO_2/18-C-6 in the presence of 100 equiv MeOH at 15 K.

Preliminary resonance Raman was preformed on the crude reaction mixture of $Fe^{II}(LN_3S)(py)](OTf)$ + 1.0 equiv KO_2/18-C-6 by T. Hayashi & P. Moënne-Loccoz at Oregon Health and Science University. The ^{16}O and ^{18}O-samples showed poor match in terms of the sample color (^{18}O-samples looked brownish, as opposed to purple) and rR spectra. Nevertheless, each set of samples were consistent from sample to sample. The rR spectra of ^{16}O-samples taken with 514, 568 and 647 nm excitation (**Figure B. 5**, **Figure B. 6** and **Figure B. 7**, respectively and are compared in **Figure B. 8**) showed numerous bands in the mid-frequency region, most of which originating from benzene and pyridine ring out-of-plane vibrations. Despite the poor match between the ^{16}O and ^{18}O-samples, the spectra taken with 568-nm excitation show relatively good match between the ^{16}O and ^{18}O-samples. However, no candidate for ν(Fe-O) or ν(O-O) modes was observed.

Furthermore, All the spectra were taken on both static and spinning samples and visual inspection confirmed that no photodamage occurred during data acquisition. Each spectrum was normalized based on the solvent band at 390 or 921 cm^{-1}. It should be noted that ^{18}O-labeled potassium superoxide had been purchased from Icon Isotopes and stored for several years prior to use. Attempts to synthesize fresh $K^{18}O_2$ did not produce better samples.

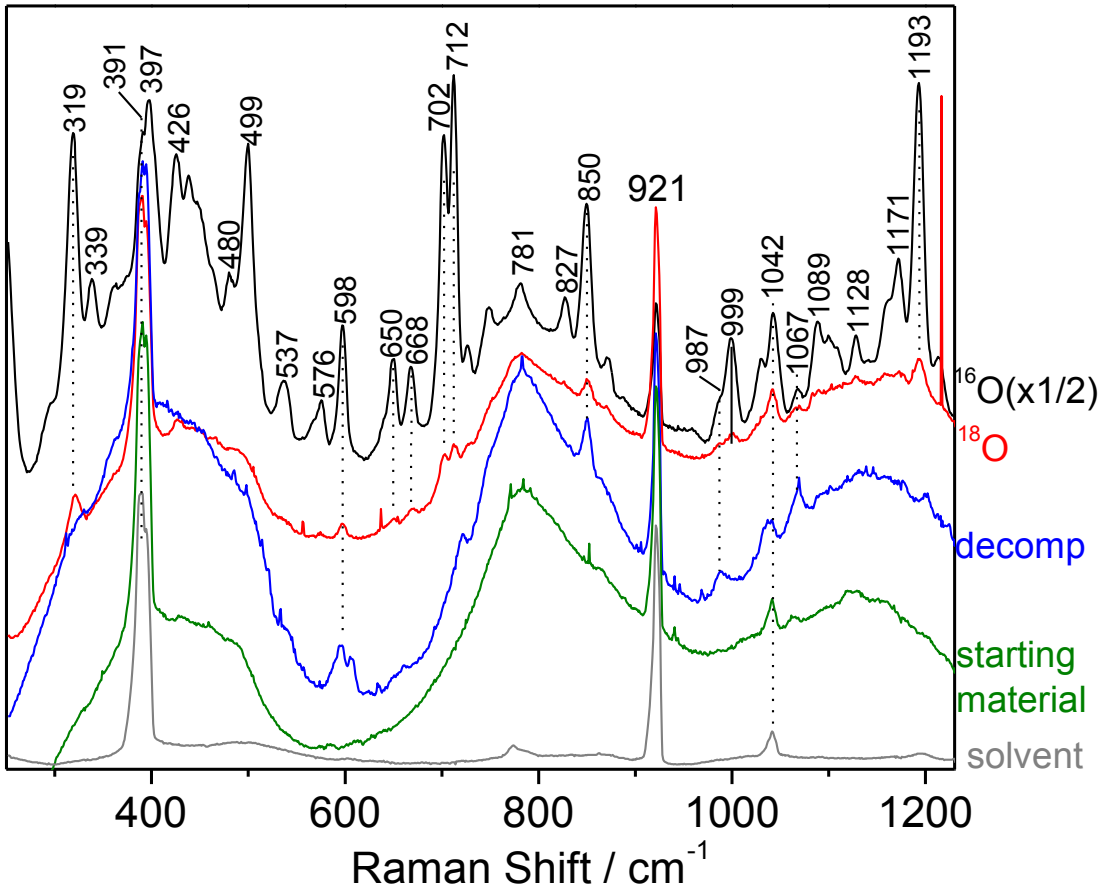

Figure B. 5. Resonance Raman spectra of $Fe^{II}(LN_3S)(py)](OTf)$ + 1.0 equiv KO_2/18-C-6 with 514 nm excitation. Conditions: 19 mW laser power at sample, 150 μm Slit, and 1200 g/mm grating.

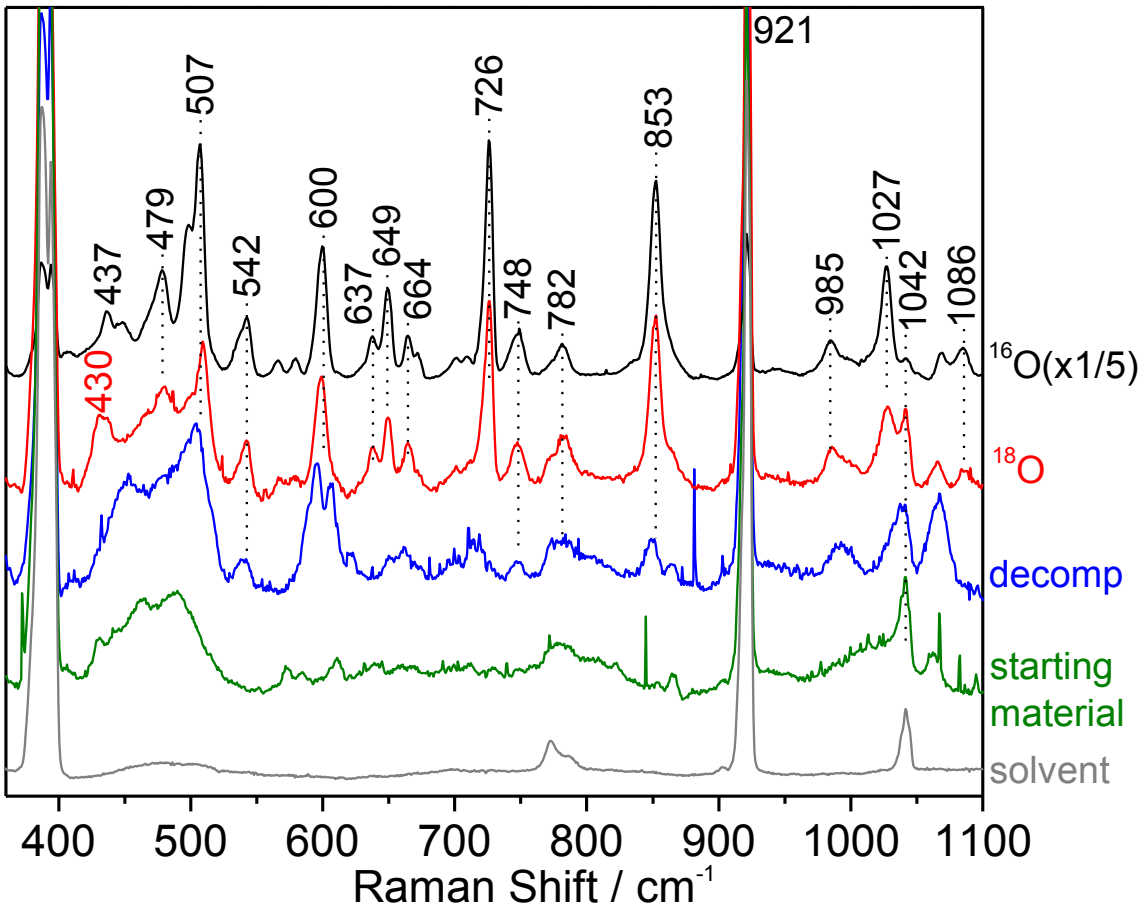

Figure B. 6. Resonance Raman spectra of $Fe^{II}(LN_3S)(py)](OTf)$ + 1.0 equiv KO_2/18-C-6 with 647 nm excitation. Conditions: 35 mW laser power at sample, 150 μm Slit, and 1200 g/mm grating.

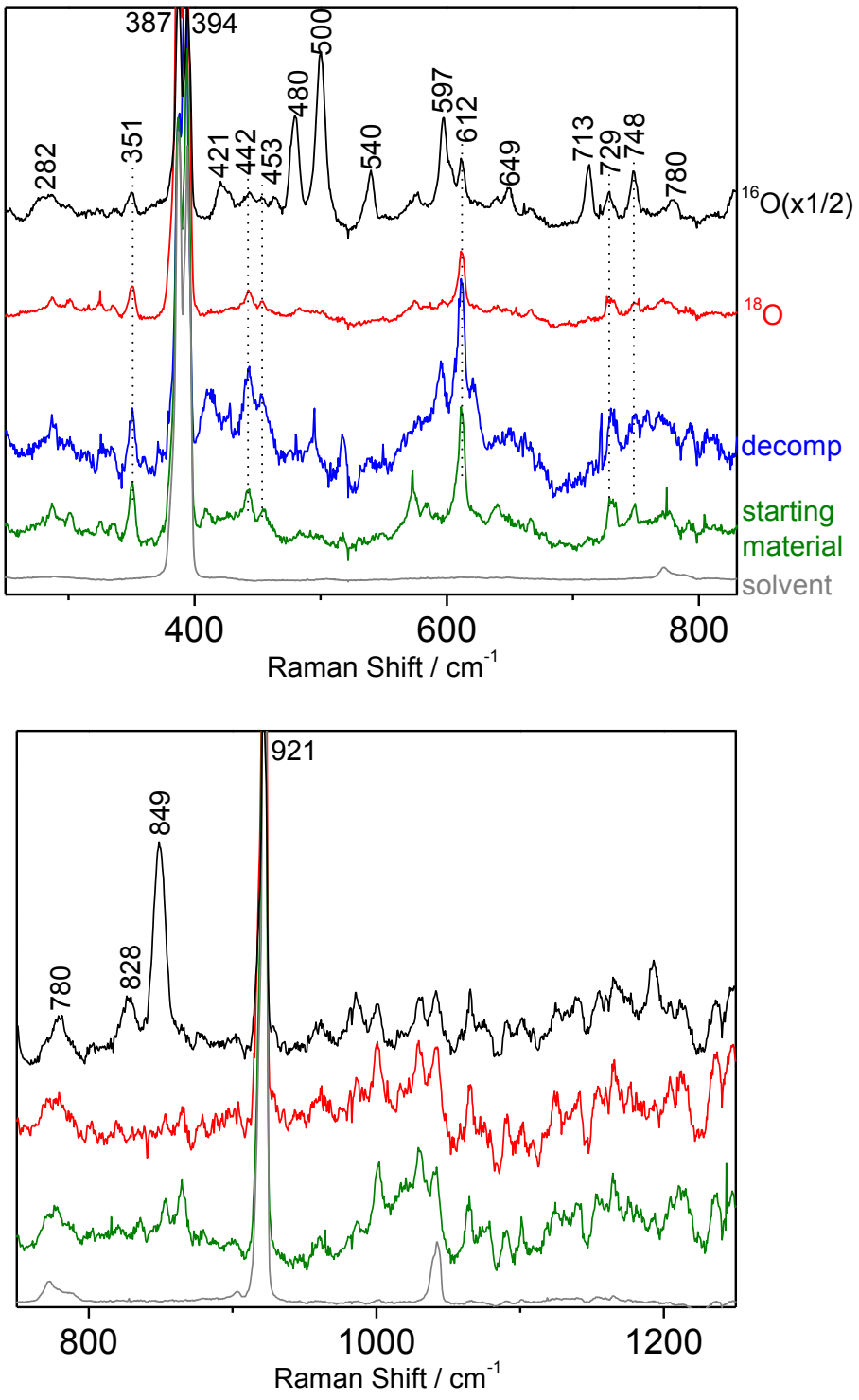

Figure B. 7. Resonance Raman spectra of $Fe^{II}(LN_3S)(py)](OTf)$ + 1.0 equiv KO_2/18-C-6 with 568 nm excitation. 86 mW laser power at sample, 150 μ m Slit, and 1200 g/mm grating.

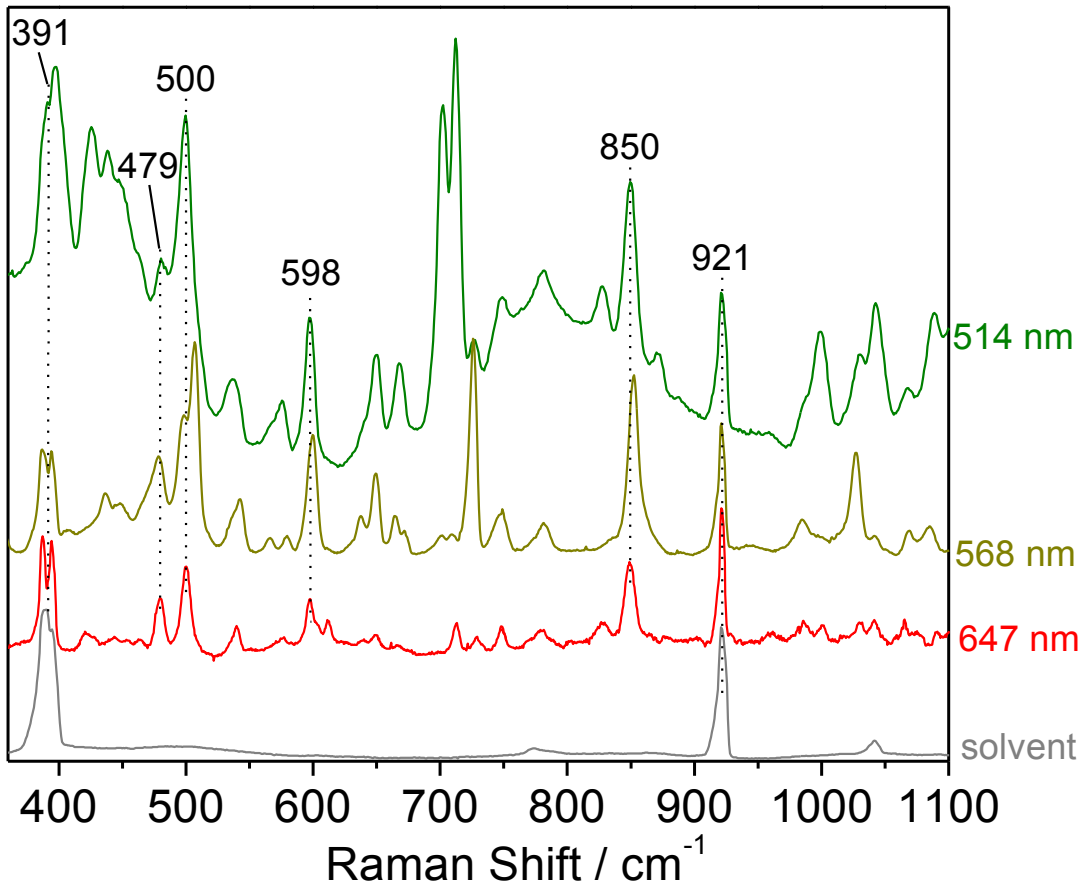

Figure B. 8. Comparison of the RR spectra of the ^{16}O-sample taken with 514, 568, and 647-nm excitation.

References

(1) Manimaran, T.; Thiruvengadam, T. K.; Ramakrishnan, V. T. *Synthesis-Stuttgart* **1975**, 739.

(2) Zhong, P.; Xiong, Z. X.; Huang, X. *Synth. Commun.* **2000**, *30*, 2793.

(3) Kimura, E.; Koike, T.; Uenishi, K.; Hediger, M.; Kuramoto, M.; Joko, S.; Arai, Y.; Kodama, M.; Iitaka, Y. *Inorg. Chem.* **1987**, *26*, 2975.

(4) Ohta, T.; Tachiyama, T.; Yoshizawa, K.; Yamabe, T.; Uchida, T.; Kitagawa, T. *Inorg. Chem.* **2000**, *39*, 4358.

(5) Kitagawa, T.; Dey, A.; Lugo-Mas, P.; Benedict, J. B.; Kaminsky, W.; Solomon, E.; Kovacs, J. A. *J. Am. Chem. Soc.* **2006**, *128*, 14448.

(6) McQuilken, A. C.; Jiang, Y. B.; Siegler, M. A.; Goldberg, D. P. *J. Am. Chem. Soc.* **2012**, *134*, 8758.

(7) McQuilken, A. C.; Ha, Y.; Sutherlin, K. D.; Siegler, M. A.; Hodgson, K. O.; Hedman, B.; Solomon, E. I.; Jameson, G. N. L.; Goldberg, D. P. *J. Am. Chem. Soc.* **2013**, *135*, 14024.

(8) Belle, C.; Bougault, C.; Averbuch, M. T.; Durif, A.; Pierre, J. L.; Latour, J. M.; Le Pape, L. *J. Am. Chem. Soc.* **2001**, *123*, 8053.

(9) Jiang, Y. B.; Widger, L. R.; Kasper, G. D.; Siegler, M. A.; Goldberg, D. P. *J. Am. Chem. Soc.* **2010**, *132*, 12214.

Curriculum Vita

Leland Robert Widger was born in Syracuse, NY to Gary and Sandra Widger on October 23, 1984. He received a New York State Regents diploma from Liverpool High School in 2002. From there, Leland attended Eckerd College in St. Petersburg, FL where he received a B. S. in Biology in 2006. While at Eckerd, Leland conducted research with Dr. Catherine Dayton and Prof. David Grove. He then moved to Cortland, NY where he conducted research with Prof. Francis Rossi at SUNY Cortland. In 2007, Leland relocated to Baltimore where he worked under Prof. Joe Kao at the University of Maryland Biotechnology Institute before beginning his graduate studies at The Johns Hopkins University. Leland joined the research group of Prof. David Goldberg in 2009, where his dissertation research has focused on the synthesis and characterization of inorganic model complexes with mixed N/S donor sets, inspired by the nonheme iron centers in Cysteine Dioxygenase and Superoxide Reductase. Leland received his M.A. in 2010, and completed his Ph.D. in 2014.